

**ANALYZING FALLING WEIGHT DEFLECTOMETER DATA ON CURLED AND
WARPED CONCRETE SLABS**

by

Kevin D. Alland

B.S. Case Western Reserve University, 2010

Submitted to the Graduate Faculty of
Swanson School of Engineering in partial fulfillment
of the requirements for the degree of
Doctor of Philosophy

University of Pittsburgh

2018

UNIVERSITY OF PITTSBURGH
SWANSON SCHOOL OF ENGINEERING

This dissertation was presented

by

Kevin Alland

It was defended on

March 20, 2018

and approved by

John Brigham, Ph.D., Assistant Professor
Department of Engineering, Durham University

Andrew Bunger, Ph.D., Associate Professor
Department of Civil and Environmental Engineering, University of Pittsburgh

Donald Janssen, Ph.D., Associate Professor Emeritus
Department of Civil and Environmental Engineering, University of Washington

Lev Khazanovich, Ph.D., Professor
Department of Civil and Environmental Engineering, University of Pittsburgh

Dissertation Director: Julie Vandebossche, Ph. D., Associate Professor
Department of Civil and Environmental Engineering, University of Pittsburgh

Copyright © by Kevin Alland

2018

ANALYZING FALLING WEIGHT DEFLECTOMETER DATA ON CURLED AND WARPED CONCRETE SLABS

Kevin Alland, PhD

University of Pittsburgh, 2018

Falling weight deflectometer testing (FWD) is a non-destructive testing method for pavements, which involves measuring the response of a pavement to a falling weight. For jointed plain concrete pavements (JPCP), the response of the pavement to the FWD load can be used to backcalculate the pavement layer properties, estimate the performance of the joints, and detect voids. Temperature and moisture gradients in the concrete layer of JPCPs induce curvature in the slab, altering the support conditions of the slab throughout the day. This change in support condition can have a significant effect on FWD testing results.

A combination of computational analyses, interpretation of field trials, and statistical analysis was used to evaluate the effect of slab curvature when interpreting FWD data. It was determined that backcalculation of the modulus of subgrade reaction (k-value), is sensitive to slab curvature, if the equivalent linear temperature gradient (ELTG) in the slab is less than 0.5 °F/in especially for pavements with stiff supporting layers. A backcalculation procedure was developed to backcalculate the modulus of subgrade reaction using FWD testing when positive temperature gradients are present. The measured load transfer efficiency (LTE) for doweled JPCP slabs was

found to be at a minimum when the slab is approximately flat and increase as a positive or negative temperature gradient develops. The measured differential deflection for doweled slabs was found to be at a maximum when the slab is approximately flat or with a negative temperature gradient, depending on the condition of the dowels. A void detection model for doweled JPCP pavements was developed using LASSO logistic regression, which outperforms currently available void detection techniques. Finally, a temperature prediction model was developed, which predicts the pavement temperature profile as a function of the weather conditions. The developed models are all packaged in the University of Pittsburgh FWD Analysis of Concrete Slabs (PITT-FACS) web tool, so that they can easily be used by practitioners.

TABLE OF CONTENTS

NOMENCLATURE.....	XXVII
1.0 INTRODUCTION.....	1
1.1 BACKGROUND AND PROBLEM STATEMENT	3
1.2 RESEARCH OBJECTIVE AND OUTLINE	6
2.0 FIELD DATA COLLECTION FOR JPCP PAVEMENTS	9
2.1 TESTING PROCEDURES.....	11
2.1.1 Test Plan A	11
2.1.2 Test Plan B.....	14
2.2 TESTING INFORMATION.....	15
2.2.1 I-79 Test Plan A (5/8/2017).....	15
2.2.2 SR-22 Doweled Test Plan A (4/25/2017)	18
2.2.3 SR-22 Undoweled Test Plan A (4/27/2017)	21
2.2.4 I-79 Test Plan B (10/1/2017).....	25
2.2.5 SR-22 Doweled/Undoweled Test Plan B (10/1/2017)	29
2.3 LABORATORY TESTING RESULTS.....	32
2.3.1 Specimen Information	32
2.3.2 Test Results.....	34
3.0 BACKCALCULATION	36
3.1 INTRODUCTION	36

3.2	EFFECT OF SLAB CURVATURE ON THE BACKCALCULATED K-VALUE.....	39
3.2.1	FIELD TRIALS	39
3.2.2	Analysis of LTPP SMP Sections and MnROAD Cells	46
3.3	COMPUTATIONAL ANALYSIS.....	59
3.4	PAVEMENT ME SENSITIVITY ANALYSIS.....	66
3.5	BACKCALCULATION FOR CURLED AND WARPED SLABS	72
3.5.1	Forward Calculation.....	73
3.5.2	ANN Backcalculation of k-value Using Midslab Testing.....	75
3.5.3	ANN Backcalculation of k-value Using Midslab and Transverse Joint Testing	79
3.5.4	Optimization method.....	89
3.6	CONCLUSIONS	99
4.0	JOINT PERFORMANCE.....	101
4.1	INTRODUCTION	101
4.1.1	Joint Performance Testing.....	101
4.1.2	Slab Curvature Effects on Estimated Joint Performance.....	103
4.2	FIELD TRIALS	105
4.3	COMPUTATIONAL ANALYSIS.....	122
4.3.1	Model Description.....	122
4.3.2	Results of Analysis	128
4.3.3	Evaluation of the Mechanics Contributing to the Observed Behavior	139
4.4	ANALYSIS OF LTPP AND MNROAD DATA	144
4.4.1	Distribution Analysis.....	144
4.4.2	ANOVA of SMP and MnROAD Sections.....	157

4.5	EVALUATION OF THE PREVALENCE OF FAULTING	163
4.5.1	Pennsylvania Pavement Management System	163
4.5.2	Analysis of Faulting in the LTPP Database.....	166
4.6	SENSITIVITY OF THE PAVEMENT ME REFLECTIVE CRACKING MODEL TO MEASURED LTE.....	179
4.7	CONCLUSIONS AND RECOMMENDATIONS	184
5.0	VOID DETECTION	185
5.1	INTRODUCTION	185
5.1.1	Background	185
5.1.2	Research Database Development	188
5.1.3	Performance of Existing Void Detection Methods	192
5.1.4	LASSO Logistic Regression Classifier.....	202
5.2	RESULTS	206
5.2.1	Performance of Developed Classifier	206
5.2.2	Validation	210
5.2.3	Sensitivity analysis	224
5.3	CONCLUSION	227
6.0	TEMPERATURE PROFILE PREDICTION	228
6.1	INTRODUCTION	228
6.2	LITERATURE REVIEW	231
6.2.1	Existing Heat Transfer Models.....	231
6.2.2	Research Utilizing Heat Transfer Models	241
6.3	DEVELOPMENT OF A TEMPERATURE PROFILE PREDICTION MODEL FOR FWD TESTING	243
6.3.1	Data Sources.....	244
6.3.2	Processing Weather Datasets.....	249

6.3.3	Finite Difference Method	255
6.3.4	Sensitivity Analysis	263
6.3.5	Comparison Between Data Sources	275
6.3.6	Validation and Tuning	279
6.4	ALLOWABLE TESTING TIMES	295
6.5	CONCLUSION	309
7.0	CONCLUDING REMARKS AND FUTURE WORK	310
APPENDIX A DAILY PLOTS OF TEMPERATURE PREDICTIONS AT		
	VALIDATION SECTIONS	313
	MNROAD CELL 52.....	313
	MNROAD CELL 53.....	327
	ATLANTA HARTSFIELD-JACKSON INTERNATIONAL AIRPORT	342
	SR-22 SMART PAVEMENT	357
	LTPP SECTION 37-0201.....	371
APPENDIX B PITT-FACS WEB TOOL USER’S GUIDE.....		
	FIELD DATA COLLECTION NOTES.....	383
	STEP 1: ACCESS THE WEBSITE	383
	STEP 2: ENTER THE REQUIRED INFORMATION ABOUT THE PAVEMENT TESTED.....	383
	STEP 3: SELECT WHETHER TEMPERATURE HOLES WERE USED TO MEASURE THE PAVEMENT TEMPERATURE PROFILE.	384
	STEP 4: IF THE PAVEMENT TEMPERATURE PROFILE WAS NOT MEASURED, ENTER GEOGRAPHICAL INFORMATION FOR THE PAVEMENT, SO THAT THE PAVEMENT TEMPERATURE PROFILE CAN BE MEASURED.....	384
	STEP 5: FORMAT THE INPUT DATA FILES.	388
	STEP 6: UPLOAD THE FWD DATA FILE, AND SUPPLEMENTAL DATA FILE	397

STEP 7: ENTER THE USER'S EMAIL ADDRESS	397
ABBREVIATIONS.....	408
BIBLIOGRAPHY	409

LIST OF TABLES

Table 1.1. Evaluation parameters determined from each FWD test location on JPCP	2
Table 1.2. FWD Derived Evaluation Parameters Required for Each Rehabilitation Strategy	3
Table 2.1. Structural properties of field trial sections	10
Table 2.2. Thermocouple depths at SR-22 field trial sections.....	14
Table 2.3. Sensor offsets (I-79 Test Plan A).....	16
Table 2.4. FWD testing pass information (I-79, Test Plan A)	17
Table 2.5. Sensor offsets (I-79 Test Plan A).....	19
Table 2.6. FWD testing pass information (SR-22 Doweled, Test Plan A).....	20
Table 2.7. Sensor offsets (I-79 Test Plan A).....	22
Table 2.8. FWD testing pass information (SR-22 Undoweled, Test Plan A)	24
Table 2.9. Sensor offsets (I-79 Test Plan B).....	27
Table 2.10. FWD testing pass information (I-79, Test Plan B)	28
Table 2.11. Sensor offsets (SR-22 Doweled/Undoweled, Test Plan B).....	30
Table 2.12. FWD testing pass information (I-79, Test Plan B)	31
Table 2.13. Thickness of concrete cores by location (I-79).....	34
Table 2.14. Final dimensions of concrete cores by location (I-79)	35
Table 2.15. Laboratory testing results (I-79).....	35
Table 3.1. Sensitivity analysis inputs.....	67
Table 3.2. Forward calculation parameter ranges.....	74
Table 3.3. Marginal R ² values showing the importance of k-value to forward calculation.....	78
Table 4.1. Field test section properties.....	105
Table 4.2. ELTG ranges for distribution analysis groups.....	145

Table 4.3. Statistics describing distributions of transformed joint efficiency parameters in LTPP database.	152
Table 4.4. ANOVA for LTE at LTPP and MnROAD sections	159
Table 4.5. ANOVA for DD at LTPP and MnROAD sections	161
Table 4.6. Faulting prediction logistic regression model.....	170
Table 4.7. Logistic regression model to predict faulting with raw FWD data.....	173
Table 4.8. Logistic regression model to predict faulting with z-scores for DD and LTE	174
Table 4.9. GEE logistic regression model to predict faulting with raw DD and LTE	176
Table 4.10. GEE logistic regression model to predict faulting with z-scores for DD and LTE.....	178
Table 4.11. AC overlay of JPCP sensitivity analysis.....	180
Table 5.1. Plots evaluated to estimate “true” void detection model	190
Table 5.2. Z-score of difference in means between classes for predictors.....	195
Table 6.1. CMS/EICM model material properties.....	234
Table 6.2. HIPERPAV I model solar radiation.....	236
Table 6.3. HIPERPAV I model material properties	237
Table 6.4. HIPERPAV II model material properties	239
Table 6.5. NIST model material properties	241
Table 6.6. ASOS sky condition estimates.....	245
Table 6.7. MERRA2 variables used in temperature profile prediction tool.....	248
Table 6.8. Estimate of cloud fractions for ASOS sky conditions	251
Table 6.9. Baseline values for the sensitivity analysis	264
Table 6.10. Evaluation of the agreement between the MERRA2 and ASOS datasets	277
Table 6.11. Tuning section pavement information	280
Table 6.12. Tuned thermal material properties for each dataset	282
Table 6.13. Comparison between measured and predicted ELTG for the tuning sections	284
Table 6.14. Comparison between measured and predicted WAT for the tuning sections	284
Table 6.15. Hypothesis testing results comparing the variability of temperature prediction model residuals using the MERRA2 dataset and ASOS dataset	284
Table 6.16. Validation section information.....	287

LIST OF FIGURES

Figure 1.1 Typical FWD testing locations	2
Figure 1.2. Influence of temperature and moisture gradients on FWD testing.....	5
Figure 2.1. Location of field trials on I-79 near Bridgeville, PA (base map is from PennDOT PMS website, originally derived from Google Maps)	9
Figure 2.2. Location of field trials on SR-22 near Murrysville, PA (base map is from PennDOT PMS website, originally derived from Google Maps)	10
Figure 2.3. Field trials testing locations (Test Plan A).....	12
Figure 2.4. Depth of temperature holes used at I-79 test section	13
Figure 2.5. Field trial testing locations (Test Plan B)	15
Figure 2.6. Test section layout (I-79, Test Plan A)	16
Figure 2.7. ELTG and WAT during testing period (I-79 Test Plan A).....	18
Figure 2.8. Test section layout (SR-22 doweled, Test Plan A).....	19
Figure 2.9. ELTG and WAT during testing period (SR-22 Doweled, Test Plan A).....	21
Figure 2.10. Test section layout (SR-22 undoweled, Test Plan A)	22
Figure 2.11. ELTG and WAT during testing period (SR-22 Undoweled, Test Plan A)	25
Figure 2.12. Test section layout (I-79, Test Plan B)	26
Figure 2.13. ELTG and WAT during testing period (I-79, Test Plan B)	29
Figure 2.14. Test section layout (SR-22 Doweled/Undoweled, Test Plan B)	30
Figure 2.15. ELTG and WAT during testing period (SR-22 Doweled/Undoweled, Test Plan B)	32
Figure 2.16. Concrete cores (I-79)	33
Figure 2.17. Bottom surface of the PCC slab (I-79).....	34
Figure 3.1. Backcalculated k-value (I-79, 5/8/2016)	40
Figure 3.2. Backcalculated k-value (I-79, 10/1/2017).....	40

Figure 3.3. Backcalculated k-value (SR-22 doweled, 4/25/2016)	41
Figure 3.4. Backcalculated k-value (SR-22 doweled, 10/1/2017).	41
Figure 3.5. Backcalculated k-value (SR-22 undoweled, 4/26/2017)	42
Figure 3.6. Backcalculated k-values (SR22 undoweled, 10/2/2017).....	42
Figure 3.7. Comparison of midslab deflection basins between doweled and undoweled sections with an ELTG of -1.0 °F/in (SR-22, Fall 2017)	44
Figure 3.8. Backcalculated k-value (LTPP Section 04-0215, Arizona)	47
Figure 3.9. Backcalculated k-value (LTPP Section 06-3042, California).....	48
Figure 3.10. Backcalculated k-value (LTPP Section 18-3002, Indiana)	48
Figure 3.11. Backcalculated k-value (LTPP Section 31-3018, Nebraska).....	49
Figure 3.12. Backcalculated k-value (LTPP Section 37-0201, North Carolina)	49
Figure 3.13. Backcalculated k-value (LTPP Section 49-3011, Utah).....	50
Figure 3.14. Backcalculated k-value (LTPP Section 53-3813, Washington).....	50
Figure 3.15. Backcalculated k-value (LTPP Section 83-3802, Manitoba).....	51
Figure 3.16. Backcalculated k-value (LTPP Section 89-3015, Quebec)	51
Figure 3.17. Backcalculated k-value (MnROAD Cell 5)	52
Figure 3.18. Backcalculated k-value (MnROAD Cell 6)	52
Figure 3.19. Backcalculated k-value (MnROAD Cell 7)	53
Figure 3.20. Backcalculated k-value (MnROAD Cell 8)	53
Figure 3.21. Backcalculated k-value (MnROAD Cell 9)	54
Figure 3.22. Backcalculated k-value (MnROAD Cell 10)	54
Figure 3.23. Backcalculated k-value (MnROAD Cell 11)	55
Figure 3.24. Backcalculated k-value (MnROAD Cell 13)	55
Figure 3.25. Backcalculated k-value (MnROAD Cell 52)	56
Figure 3.26. Backcalculated k-value (MnROAD Cell 53)	56
Figure 3.27. Example of daily linear regression (LTPP Section 04-0215, 7/22/1996)	58
Figure 3.28. Comparison of regression slope to k-value intercept for FWD tests at LTPP SMP sections.....	58
Figure 3.29. Computational analysis on the effect of true subgrade stiffness on the relationship between slab curvature and backcalculated k-value.....	61
Figure 3.30. Computational analysis of the effect of joint spacing on the relationship between CLTG and backcalculated k-value.....	64

Figure 3.31. Computational analysis of the effect of stabilized base stiffness on the relationship between CLTG and backcalculated k-value	65
Figure 3.32. Sensitivity of Pavement ME distress predictions to k-value (8 in thick slab, 15-ft joint spacing) .	68
Figure 3.33. Sensitivity of Pavement ME distress predictions to k-value (8 in thick slab, 20-ft joint spacing) .	69
Figure 3.34. Sensitivity of Pavement ME distress predictions to k-value (12 in thick slab, 15-ft joint spacing)	69
Figure 3.35. Sensitivity of Pavement ME distress predictions to k-value (12 in thick slab, 20-ft joint spacing)	70
Figure 3.36. Performance of ANN trained using midslab data on test set	76
Figure 3.37. Proposed test plan	79
Figure 3.38. Performance of proposed backcalculation method on test set (CLTG is an input)	80
Figure 3.39. Performance of proposed backcalculation method on test set (CLTG is not an input)	82
Figure 3.40. Performance of proposed backcalculation method on test set (CLTG is an input, with simulated noise in the test set).....	83
Figure 3.41. Performance of proposed backcalculation technique on factorial of CLTG and k-values	84
Figure 3.42. Validation of two test location ANN backcalculation model (I-79, 10/1/2017)	85
Figure 3.43. Validation of two test location ANN backcalculation model (SR-22 Doweled, 10/2/2017)	86
Figure 3.44. Validation of two test location ANN backcalculation model (SR-22 Undoweled, 10/2/2017)	86
Figure 3.45. Validation of adjusted two test location ANN backcalculation model (I-79, 10/1/2017)	88
Figure 3.46. Validation of adjusted two test location ANN backcalculation model (SR-22 Doweled, 10/2/2017)	88
Figure 3.47. Validation of adjusted two test location ANN backcalculation model (SR-22 Undoweled, 10/2/2017)	89
Figure 3.48. Validation of optimization framework based backcalculation (I-79, 5/8/2016)	91
Figure 3.49. Validation of optimization framework based backcalculation (I-79, 10/1/2017)	92
Figure 3.50. Validation of optimization framework based backcalculation (SR-22 Doweled, 4/25/2016)	92
Figure 3.51. Validation of optimization framework based backcalculation (SR-22 Doweled, 10/2/2017)	93
Figure 3.52. Validation of optimization framework based backcalculation (SR-22 Undoweled, 4/26/2016).....	93
Figure 3.53. Validation of optimization framework based backcalculation (SR-22 Undoweled, 10/2/2017).....	94
Figure 3.54. Validation of optimization framework based backcalculation with constant slab stiffness (I-79, 5/8/2016)	96
Figure 3.55. Validation of optimization framework based backcalculation with constant slab stiffness (I-79, 10/1/2017)	96

Figure 3.56. Validation of optimization framework based backcalculation with constant slab stiffness (SR-22 Doweled, 4/25/2016).....	97
Figure 3.57. Validation of optimization framework based backcalculation with constant slab stiffness (SR-22 Doweled, 10/2/2017).....	97
Figure 3.58. Validation of optimization framework based backcalculation with constant slab stiffness (SR-22 Undoweled, 4/26/2016)	98
Figure 3.59. Validation of optimization framework based backcalculation with constant slab stiffness (SR-22 Undoweled, 10/2/2017)	98
Figure 4.1. Example of strain gages indicating joint lock-up (SR-22 8/11/2017).....	107
Figure 4.2. Evaluation of SR-22 joint “lock-up” (4/25/2016)	108
Figure 4.3. Evaluation of SR-22 joint “lock-up” (5/8/2016)	109
Figure 4.4. Evaluation of SR-22 joint “lock-up” (10/1/2017)	109
Figure 4.5. Evaluation of SR-22 joint “lock-up” (10/2/2017)	110
Figure 4.6. Measured LTE at I-79 (5/8/2016, 9,000 lb nominal load level)	111
Figure 4.7. Measured LTE at I-79 (5/8/2016, 16,000 lb nominal load level)	111
Figure 4.8. Measured LTE at I-79 (10/1/2017, 9,000 lb nominal load level)	112
Figure 4.9. Measured LTE at I-79 (10/1/2017, 16,000 lb nominal load level)	112
Figure 4.10. Measured LTE at SR-22 doweled section (4/25/2016, 9,000 lb nominal load level)	113
Figure 4.11. Measured LTE at SR-22 doweled section (4/25/2016, 16,000 lb nominal load level)	113
Figure 4.12. Measured LTE at SR-22 doweled section (10/2/2017, 9,000 lb nominal load level)	114
Figure 4.13. Measured LTE at SR-22 doweled section (10/2/2017, 16,000 lb nominal load level)	114
Figure 4.14. Measured normalized DD at I-79 (5/8/2016, 9,000 lb nominal load level)	117
Figure 4.15. Measured normalized DD at I-79 (5/8/2016, 16,000 lb nominal load level)	117
Figure 4.16. Measured normalized DD at I-79 (10/1/2017, 9,000 lb nominal load level)	118
Figure 4.17. Measured normalized DD at I-79 (10/1/2017, 16,000 lb nominal load level)	118
Figure 4.18. Measured normalized DD at SR-22 (4/25/2016, 9,000 lb nominal load level)	119
Figure 4.19. Measured normalized DD at SR-22 (4/25/2016, 16,000 lb nominal load level)	119
Figure 4.20. Measured normalized DD at SR-22 (10/2/2017, 9,000 lb nominal load level)	120
Figure 4.21. Measured normalized DD at SR-22 (10/2/2017, 16,000 lb nominal load level)	120
Figure 4.22. Geometry of EverFE dowel looseness implementation	124
Figure 4.23. Estimated dowel looseness from ALF testing after 25,000 load cycles (Vandenbossche 2017)....	126

Figure 4.24. Estimated dowel looseness from ALF testing after 5,000,000 load cycles (Vandenbossche 2017)	126
Figure 4.25. LTE predicted by the computational analysis with discretely modeled dowel looseness	129
Figure 4.26. DD predicted by the computational analysis with discretely modeled dowel looseness	129
Figure 4.27. LTE predicted by the computational analysis utilizing a dense liquid interaction between the dowel and slab	133
Figure 4.28. DD predicted by the computational analysis utilizing a dense liquid interaction between the dowel and slab	134
Figure 4.29. Comparison between LTE predicted by the computational analysis with a 9,000 and 16,000 lb load (2 mils dowel looseness)	135
Figure 4.30. Comparison between DD predicted by the computational analysis with a 9,000 and 16,000 lb load (2 mils dowel looseness)	136
Figure 4.31. Comparison between DD predicted by the computational analysis with a 9,000 and 16,000 lb load (4 mils dowel looseness)	138
Figure 4.32. Position of dowel bar in socket before and after loading (1 mil of dowel looseness)	140
Figure 4.33. Position of dowel bar in socket before and after loading (1.25 °F/in CLTG)	142
Figure 4.34. Estimated kernel density PDF of LTE in the LTPP database (9,000 lb nominal load level)	146
Figure 4.35. Estimated kernel density PDF of LTE in the LTPP database (16,000 lb nominal load level)	146
Figure 4.36. Estimated kernel density PDF of DD in the LTPP database (9,000 lb nominal load level)	147
Figure 4.37. Estimated kernel density PDF of DD in the LTPP database (16,000 lb nominal load level)	147
Figure 4.38. Estimated kernel density PDF of transformed LTE in the LTPP database (9,000 lb nominal load level)	148
Figure 4.39. Estimated kernel density PDF of transformed LTE in the LTPP database (16,000 lb nominal load level)	149
Figure 4.40. Estimated kernel density PDF of transformed DD in the LTPP database (9,000 lb nominal load level)	149
Figure 4.41. Estimated kernel density PDF of transformed DD in the LTPP database (16,000 lb nominal load level)	150
Figure 4.42. Bonferroni confidence intervals for transformed LTE in the LTPP database (9,000 lb nominal load level)	153
Figure 4.43. Bonferroni confidence intervals for transformed LTE in the LTPP database (16,000 lb nominal load level)	153
Figure 4.44. Bonferroni confidence intervals for transformed DD in the LTPP database (16,000 lb nominal load level)	154
Figure 4.45. Bonferroni confidence intervals for transformed DD in the LTPP database (16,000 lb nominal load level)	155
Figure 4.46. Measured LTE at I-79 field trials adjusted based on distributions in LTPP database	156

Figure 4.47. Measured DD at I-79 field trials adjusted based on distributions in LTPP database	157
Figure 4.48. Measured LTE and DD from ALF testing with 1.5-in dia epoxy coated steel dowel bars.....	162
Figure 4.49. Sensitivity analysis of Pavement ME AC over JPCP reflective cracking model (k=150 psi/in) ..	181
Figure 4.50. Sensitivity analysis of Pavement ME AC over JPCP reflective cracking model (slab thickness = 8 in)	183
Figure 5.1: Example of scatterplots used to identify the time of void development.....	190
Figure 5.2. CDF plot of normalized deflection for void and no void classes.....	193
Figure 5.3. CDF plot of deflection ratio for void and no void classes.....	193
Figure 5.4. CDF plot of void parameter for void and no void classes	194
Figure 5.5. Accuracy of normalized deflection stump classifier	196
Figure 5.6. Accuracy of deflection ratio stump classifier	196
Figure 5.7. Accuracy of void parameter stump classifier	197
Figure 5.8. ROC curves of stump classifiers.....	197
Figure 5.9. Accuracy of normalized deflection stump classifier by ELTG group	199
Figure 5.10. Accuracy of deflection ratio stump classifier by ELTG group	199
Figure 5.11. Accuracy of void parameter stump classifier by ELTG group	200
Figure 5.12. ROC curve for normalized deflection classifier by ELTG group	200
Figure 5.13. ROC curve for deflection ratio classifier by ELTG group	201
Figure 5.14. ROC curve for void parameter classifier by ELTG group	201
Figure 5.15: Work flow diagram used to select and train LASSO logistic regression classifier	204
Figure 5.16. Cross validated accuracy of LASSO classifier and normalized deflection classifier	207
Figure 5.17. ROC curves of LASSO classifier and normalized deflection classifier	208
Figure 5.18. Accuracy of LASSO Classifier by ELTG group	209
Figure 5.19: ROC curve for LASSO classifier by ELTG group	209
Figure 5.20. LASSO classifier validation (SR-22, Joint 1)	211
Figure 5.21. LASSO classifier validation (SR-22, Joint 2)	212
Figure 5.22. LASSO classifier validation (SR-22, Joint 3)	212
Figure 5.23. LASSO classifier validation (SR-22, Joint 4)	213
Figure 5.24. LASSO classifier validation (SR-22, Joint 5)	213
Figure 5.25. LASSO classifier validation (SR-22, Joint 6)	214
Figure 5.26. LASSO classifier validation (SR-22, Joint 7)	214

Figure 5.27. LASSO classifier validation (SR-22, Joint 8)	215
Figure 5.28. LASSO classifier validation (I-79, Joint 1).....	215
Figure 5.29. LASSO classifier validation (I-79, Joint 2).....	216
Figure 5.30. LASSO classifier validation (I-79, Joint 3).....	216
Figure 5.31. LASSO classifier validation (I-79, Joint 4).....	217
Figure 5.32. LASSO classifier validation (I-79, Joint 5).....	217
Figure 5.33. LASSO classifier validation (I-79, Joint 6).....	218
Figure 5.34. LASSO classifier validation (I-79, Joint 7).....	218
Figure 5.35. LASSO classifier validation (MnROAD Cell 8, Joint 4)	220
Figure 5.36. LASSO classifier validation (MnRoad Cell 8, Joint 3).....	221
Figure 5.37. LASSO classifier validation (MnROAD Cell 8, Joint 10)	221
Figure 5.38. LASSO classifier validation (MnROAD Cell 8, Joint 9)	222
Figure 5.39. Lasso classifier performance (LTPP Section 05-0215, all joints)	223
Figure 5.40. Sensitivity of classifier to k-value	224
Figure 5.41. Sensitivity of classifier to elastic modulus of the PCC layer	225
Figure 5.42. Sensitivity of classifier to LTE.....	225
Figure 5.43. Sensitivity of classifier to void parameter	226
Figure 6.1. Heat transfer in concrete pavements	230
Figure 6.2. ASOS stations in and near Pennsylvania.....	247
Figure 6.3. MERRA2 grid points in and near Pennsylvania.....	249
Figure 6.4. ASOS stations used for barycentric interpolation (I-79).....	250
Figure 6.5. MERRA2 grid points used for bilinear interpolation (I-79).....	254
Figure 6.6. Analysis length required for convergence (4/6/2014, 7-in slab).....	258
Figure 6.7. Analysis length required for convergence (4/8/2014, 7-in slab).....	259
Figure 6.8. Analysis length required for convergence (4/18/2014, 7-in slab).....	259
Figure 6.9. Analysis length required for convergence (4/6/2014, 12-in slab).....	260
Figure 6.10. Analysis length required for convergence (4/14/2014, 12-in slab)	260
Figure 6.11. Analysis length required for convergence (4/18/2014, 12-in slab)	261
Figure 6.12. Analysis length required for convergence (4/6/2014, 20-in slab)	261
Figure 6.13. Analysis length required for convergence (4/14/2014, 20-in slab)	262

Figure 6.14. Analysis length required for convergence (4/24/2014, 20-in slab)	262
Figure 6.15a. Sensitivity of ELTG to concrete thermal conductivity (4/10/2014)	265
Figure 6.15b. Sensitivity of WAT prediction to concrete thermal conductivity (4/10/2014)	265
Figure 6.16a. Sensitivity of ELTG prediction to base conductivity (4/10/2014)	267
Figure 6.16b. Sensitivity of WAT prediction to base conductivity (4/10/2014)	267
Figure 6.17a. Sensitivity of ELTG prediction to emissivity (4/10/2014)	269
Figure 6.17b. Sensitivity of WAT prediction to emissivity (4/10/2014)	269
Figure 6.18a. Sensitivity of ELTG prediction to albedo (4/10/2014)	270
Figure 6.18b. Sensitivity of WAT prediction to albedo (4/10/2014)	270
Figure 6.19a. Sensitivity of ELTG prediction to specific heat capacity (4/10/2014)	272
Figure 6.19b. Sensitivity of WAT prediction to specific heat capacity (4/10/2014)	272
Figure 6.20a. Sensitivity of ELTG prediction to net longwave irradiation model (4/10/2014)	274
Figure 6.20b. Sensitivity of WAT prediction to net longwave irradiation model (4/10/2014)	274
Figure 6.21. Randomly selected locations for comparing MERRA2 and ASOS datasets	276
Figure 6.28. Location of ASOS station and MERRA2 grid points used for interpolation (Ohio SPS sections)	287
Figure 6.23. Comparison between measured and predicted temperature profile (I-79, 5/8/2016)	288
Figure 6.24. Comparison between measured and predicted temperature profile (I-79, 10/1/2017)	288
Figure 6.25. Comparison between measured and predicted temperature profile (39-0203, 9/22/2004)	289
Figure 6.26. Comparison between measured and predicted temperature profile (39-0203, 6/17/2014)	289
Figure 6.27. Comparison between measured and predicted temperature profile (39-0205, 9/9/2004)	290
Figure 6.28. Comparison between measured and predicted temperature profile (39-0207, 9/21/2004)	290
Figure 6.29. Comparison between measured and predicted temperature profile (39-0207, 6/5/2014)	291
Figure 6.30. Comparison between measured and predicted temperature profile (39-0260, 6/3/2014)	291
Figure 6.31. Comparison between measured and predicted temperature profile (39-0262, 9/21/2004)	292
Figure 6.32. Comparison between measured and predicted temperature profile (39-0262, 6/6/2014)	292
Figure 6.33. Cloud packing effect (Mannarano 1998)	294
Figure 6.34. Example of improved performance of temperature prediction using estimated sky condition (LTPP Section 39-0205, 9/9/2004)	295
Figure 6.35. Allowable testing times for PennDOT Engineering District 1 (sunny days)	298
Figure 6.36. Allowable testing times for PennDOT Engineering District 2 (sunny days)	298

Figure 6.37. Allowable testing times for PennDOT Engineering District 3 (sunny days)	299
Figure 6.38. Allowable testing times for PennDOT Engineering District 4 (sunny days)	299
Figure 6.39. Allowable testing times for PennDOT Engineering District 5 (sunny days)	300
Figure 6.40. Allowable testing times for PennDOT Engineering District 6 (sunny days)	300
Figure 6.41. Allowable testing times for PennDOT Engineering District 8 (sunny days)	301
Figure 6.42. Allowable testing times for PennDOT Engineering District 9 (sunny days)	301
Figure 6.43. Allowable testing times for PennDOT Engineering District 10 (sunny days)	302
Figure 6.44. Allowable testing times for PennDOT Engineering District 11 (sunny days)	302
Figure 6.45. Allowable testing times for PennDOT Engineering District 12 (sunny days)	303
Figure 6.46. Allowable testing times for PennDOT Engineering District 1 (cloudy days)	303
Figure 6.47. Allowable testing times for PennDOT Engineering District 2 (cloudy days)	304
Figure 6.48. Allowable testing times for PennDOT Engineering District 3 (cloudy days)	304
Figure 6.49. Allowable testing times for PennDOT Engineering District 4 (cloudy days)	305
Figure 6.50. Allowable testing times for PennDOT Engineering District 5 (cloudy days)	305
Figure 6.51. Allowable testing times for PennDOT Engineering District 6 (cloudy days)	306
Figure 6.52. Allowable testing times for PennDOT Engineering District 8 (cloudy days)	306
Figure 6.53. Allowable testing times for PennDOT Engineering District 9 (cloudy days)	307
Figure 6.54. Allowable testing times for PennDOT Engineering District 10 (cloudy days)	307
Figure 6.55. Allowable testing times for PennDOT Engineering District 11 (cloudy days)	308
Figure 6.56. Allowable testing times for PennDOT Engineering District 12 (cloudy days)	308
Figure A.1. MnROAD Cell 52 (4/1/2011).....	313
Figure A.2. MnROAD Cell 52 (4/1/2011).....	314
Figure A.3. MnROAD Cell 52 (4/3/2011).....	314
Figure A.4. MnROAD Cell 52 (4/4/2011).....	315
Figure-A.5. MnROAD Cell 52 (4/5/2011)	315
Figure A.6. MnROAD Cell 52 (4/6/2011).....	316
Figure A.7. MnROAD Cell 52 (4/8/2011).....	316
Figure A.8. MnROAD Cell 52 (4/9/2011).....	317
Figure A.9. MnROAD Cell 52 (4/10/2011).....	317
Figure A.10. MnROAD Cell 52 (4/11/2011).....	318

Figure A.11. MnROAD Cell 52 (4/12/2011).....	318
Figure A.12. MnROAD Cell 52 (4/13/2011).....	319
Figure A.13. MnROAD Cell 52 (4/15/2011).....	319
Figure A.14. MnROAD Cell 52 (4/16/2011).....	320
Figure A.15. MnROAD Cell 52 (4/17/2011).....	320
Figure A.16. MnROAD Cell 52 (4/18/2011).....	321
Figure A.17. MnROAD Cell 52 (4/19/2011).....	321
Figure A.18. MnROAD Cell 52 (4/20/2011).....	322
Figure A.19. MnROAD Cell 52 (4/21/2011).....	322
Figure A.20. MnROAD Cell 52 (4/22/2011).....	323
Figure A.21. MnROAD Cell 52 (4/23/2011).....	323
Figure A.22. MnROAD Cell 52 (4/24/2011).....	324
Figure A.23. MnROAD Cell 52 (4/25/2011).....	324
Figure A.24. MnROAD Cell 52 (4/26/2011).....	325
Figure A.25. MnROAD Cell 52 (4/27/2011).....	325
Figure A.26. MnROAD Cell 52 (4/28/2011).....	326
Figure A.27. MnROAD Cell 52 (4/29/2011).....	326
Figure A.28. MnROAD Cell 52 (4/30/2011).....	327
Figure A.29. MnROAD Cell 53 (4/1/2011).....	327
Figure A.30. MnROAD Cell 53 (4/2/2011).....	328
Figure A.31. MnROAD Cell 53 (4/3/2011).....	328
Figure A.32. MnROAD Cell 53 (4/4/2011).....	329
Figure A.33. MnROAD Cell 53 (4/5/2011).....	329
Figure A.34. MnROAD Cell 53 (4/6/2011).....	330
Figure A.35. MnROAD Cell 53 (4/7/2011).....	330
Figure A.36. MnROAD Cell 53 (4/8/2011).....	331
Figure A.37. MnROAD Cell 53 (4/9/2011).....	331
Figure A.38. MnROAD Cell 53 (4/10/2011).....	332
Figure A.39. MnROAD Cell 53 (4/11/2011).....	332
Figure A.40. MnROAD Cell 53 (4/12/2011).....	333

Figure A.41. MnROAD Cell 53 (4/13/2011).....	333
Figure A.42. MnROAD Cell 53 (4/14/2011).....	334
Figure-A.43. MnROAD Cell 53 (4/15/2011)	334
Figure A.44. MnROAD Cell 53 (4/16/2011).....	335
Figure A.45. MnROAD Cell 53 (4/17/2011).....	335
Figure A.46. MnROAD Cell 53 (4/18/2011).....	336
Figure A.47. MnROAD Cell 53 (4/19/2011).....	336
Figure A.48. MnROAD Cell 53 (4/20/2011).....	337
Figure A.49. MnROAD Cell 53 (4/21/2011).....	337
Figure A.50. MnROAD Cell 53 (4/22/2011).....	338
Figure A.51. MnROAD Cell 53 (4/23/2011).....	338
Figure A.52. MnROAD Cell 53 (4/24/2011).....	339
Figure A.53. MnROAD Cell 53 (4/25/2011).....	339
Figure A.54. MnROAD Cell 53 (4/26/2011).....	340
Figure A.55. MnROAD Cell 53 (4/27/2011).....	340
Figure A.56. MnROAD Cell 53 (4/28/2011).....	341
Figure A.57. MnROAD Cell 53 (4/29/2011).....	341
Figure A.58. MnROAD Cell 53 (4/30/2011).....	342
Figure A.59. Atlanta Hartsfield-Jackson Airport (4/1/2010)	342
Figure A.60. Atlanta Hartsfield-Jackson Airport (4/2/2010)	343
Figure A.61. Atlanta Hartsfield-Jackson Airport (4/3/2010)	343
Figure A.62. Atlanta Hartsfield-Jackson Airport (4/4/2010)	344
Figure A.63. Atlanta Hartsfield-Jackson Airport (4/5/2010)	344
Figure A.64. Atlanta Hartsfield-Jackson Airport (4/6/2010)	345
Figure A.65. Atlanta Hartsfield-Jackson Airport (4/7/2010)	345
Figure A.66. Atlanta Hartsfield-Jackson Airport (4/8/2010)	346
Figure A.67. Atlanta Hartsfield-Jackson Airport (4/9/2010)	346
Figure A.68. Atlanta Hartsfield-Jackson Airport (4/10/2010)	347
Figure A.69. Atlanta Hartsfield-Jackson-Airport (4/11/2010).....	347
Figure A.70. Atlanta Hartsfield-Jackson Airport (4/12/2010)	348

Figure A.71. Atlanta Hartsfield-Jackson Airport (4/13/2010)	348
Figure A.72. Atlanta Hartsfield-Jackson Airport (4/14/2010)	349
Figure A.73. Atlanta Hartsfield-Jackson Airport (4/15/2010)	349
Figure A.74. Atlanta Hartsfield-Jackson Airport (4/16/2010)	350
Figure A.75. Atlanta Hartsfield-Jackson Airport (4/17/2010)	350
Figure A.76. Atlanta Hartsfield-Jackson Airport (4/18/2010)	351
Figure A.77. Atlanta Hartsfield-Jackson Airport (4/19/2010)	351
Figure A.78. Atlanta Hartsfield-Jackson Airport (4/20/2010)	352
Figure-A.79. Atlanta Hartsfield-Jackson Airport (4/21/2010)	352
Figure A.80. Atlanta Hartsfield-Jackson Airport (4/22/2010)	353
Figure A.81. Atlanta Hartsfield-Jackson Airport (4/23/2010)	353
Figure A.82. Atlanta Hartsfield-Jackson Airport (4/24/2010)	354
Figure A.83. Atlanta Hartsfield-Jackson Airport (4/25/2010)	354
Figure A.84. Atlanta Hartsfield-Jackson Airport (4/26/2010)	355
Figure A.85. Atlanta Hartsfield-Jackson Airport (4/27/2010)	355
Figure A.86. Atlanta Hartsfield-Jackson Airport (4/28/2010)	356
Figure A.87. Atlanta Hartsfield-Jackson Airport (4/29/2010)	356
Figure A.88. Atlanta Hartsfield-Jackson Airport (4/30/2010)	357
Figure A.89. SR-22 Smart Pavement (4/1/2014)	357
Figure A.90. SR-22 Smart Pavement (4/2/2014)	358
Figure A.91. SR-22 Smart Pavement (4/3/2014)	358
Figure A.92. SR-22 Smart Pavement (4/4/2014)	359
Figure A.93. SR-22 Smart Pavement (4/5/2014)	359
Figure A.94. SR-22 Smart Pavement (4/6/2014)	360
Figure A.95. SR-22 Smart Pavement (4/7/2014)	360
Figure A.96. SR-22 Smart Pavement (4/8/2014)	361
Figure A.97. SR-22 Smart Pavement (4/9/2014)	361
Figure A.98. SR-22 Smart Pavement (4/10/2014).....	362
Figure A.99. SR-22 Smart Pavement (4/11/2014).....	362
Figure A.100. SR-22 Smart Pavement (4/12/2014).....	363

Figure A.101. SR-22 Smart Pavement (4/13/2014).....	363
Figure A.102. SR-22 Smart Pavement (4/14/2014).....	364
Figure A.103. SR-22 Smart Pavement (4/15/2014).....	364
Figure A.104. SR-22 Smart Pavement (4/17/2014).....	365
Figure A.105. SR-22 Smart Pavement (4/18/2014).....	365
Figure A.106. SR-22 Smart Pavement (4/19/2014).....	366
Figure A.107. SR-22 Smart Pavement (4/21/2014).....	366
Figure A.108. SR-22 Smart Pavement (4/22/2014).....	367
Figure A.109. SR-22 Smart Pavement (4/23/2014).....	367
Figure A.110. SR-22 Smart Pavement (4/24/2014).....	368
Figure A.111. SR-22 Smart Pavement (4/25/2014).....	368
Figure A.112. SR-22 Smart Pavement (4/26/2014)	369
Figure A.113. SR-22 Smart Pavement (4/27/2014).....	369
Figure A.114. SR-22 Smart Pavement (4/28/2014).....	370
Figure A.115. SR-22 Smart Pavement (4/29/2014).....	370
Figure A.116. SR-22 Smart Pavement (4/30/2014).....	371
Figure-A.117. LTPP Section 37-0201 (4/1/2003)	371
Figure A.118. LTPP Section 37-0201 (4/2/2003)	372
Figure A.119. LTPP Section 37-0201 (4/3/2003)	372
Figure A.120. LTPP Section 37-0201 (4/4/2003)	373
Figure A.121. LTPP Section 37-0201 (4/5/2003)	373
Figure A.122. LTPP Section 37-0201 (4/6/2003)	374
Figure A.123. LTPP Section 37-0201 (4/8/2003)	374
Figure A.124. LTPP Section 37-0201 (4/9/2003)	375
Figure A.125. LTPP Section 37-0201 (4/10/2003)	375
Figure A.126. LTPP Section 37-0201 (4/11/2003)	376
Figure A.127. LTPP Section 37-0201 (4/12/2003)	376
Figure A.128. LTPP Section 37-0201 (4/13/2003)	377
Figure A.129. LTPP Section 37-0201 (4/15/2003)	377
Figure A.130. LTPP Section 37-0201 (4/16/2003)	378

Figure A.131. LTPP Section 37-0201 (4/17/2003)	378
Figure A.132. LTPP Section 37-0201 (4/18/2003)	379
Figure A.133. LTPP Section 37-0201 (4/19/2003)	379
Figure A.134. LTPP Section 37-0201 (4/20/2003)	380
Figure A.135. LTPP Section 37-0201 (4/21/2003)	380
Figure A.136. LTPP Section 37-0201 (4/22/2003)	381
Figure A.137. LTPP Section 37-0201 (4/23/2003)	381
Figure A.138. LTPP Section 37-0201 (4/24/2003)	382
Figure B.1 . Geographical information tool	385
Figure B.2. NOAA climatic normals tool	387
Figure B.3. Climatic normals output file	388
Figure B.4. File formatting tool interface	389
Figure B.5. Fields for temperature hole information	390
Figure B.6. Fields for pyranometer reading information	391
Figure B.7 . Field for sky condition estimate information	392
Figure B.8. Selection of FWD file location	393
Figure B.9. Form for temperature hole measurements	394
Figure B.10. Form to record pyranometer measurements	395
Figure B.11. Form to record sky conditions	396
Figure B.12. Screenshot of Pitt-FACS interface	398
Figure B.13. Screenshot of Pitt-FACS interface (continued)	399

NOMENCLATURE

Abbreviation	Meaning
AASHTO	Association of State Highway and Transportation Officials
ACPA	American Concrete Pavement Association
ALF	Accelerated Loading Frame
ANN	Artificial Neural Network
ANOVA	Analysis of Variance
API	Application Program Interface
AREA	Normalized Area Parameter
ASCE	American Society of Civil Engineers
ASOS	Automated Surface Observation System
ATB	Asphalt Treated Base
ATL	Atlanta Hartsfield-Jackson International Airport
AWOS	Automated Weather Observation System
BTU	British Thermal Unit
CDF	Cumulative Distribution Function
CF	Cloud Factor
CLTG	Cumulative Linear Temperature Gradient
CMS	Climatic-Materials-Structural Analysis Program
COV	Coefficient of Variation
CPR	Concrete Pavement Restoration
CTB	Cement Treated Base
CTE	Coefficient of Thermal Expansion
DBR	Dowel Bar Retrofit
DD	Differential Deflection
DISC	Data Information Services Center
DMI	Distance Measuring Instrument
DR	Deflection Ratio
EICM	Enhanced Integrated Climatic Model
ELTG	Equivalent Linear Temperature Gradient
EWRI	Environmental and Water Resources Institute

FAA	Federal Aviation Administration
FDM	Finite Difference Method
FDR	Full Depth Repair
FEM	Finite Element Method
FHWA	Federal Highway Administration
FWD	Falling Weight Deflectometer
GAMO	Global Assimilation and Modeling Observations
GEE	General Error Estimation
GEOS	Goddard Earth Observation System Model
GPS	General Pavement Sections
HIPERPAV	High Performance Concrete Paving Software
IAU	Incremental Analysis Units
JCP	Jointed Concrete Pavement
JPCP	Jointed Plain Concrete Pavement
JRCP	Jointed Reinforced Concrete Pavement
KHC	Korean Highway Corporation
LASSO	Least Absolute Shrinkage and Selection Operator
LCB	Lean Concrete Base
LOWESS	Locally Weighted Estimates Using Sum of the Squares
LTE	Load Transfer Efficiency
LTPP	Long Term Pavement Performance Program
MAT	Mean Annual Temperature
MERRA2	Modern Era Reanalysis for Research and Applications
MLE	maximum likelihood estimates
MMT	Mean Monthly Temperature
MNR52	Minnesota Road Research Facility Cell 52
MNR52	Minnesota Road Research Facility Cell 53+B103
MnROAD	Minnesota Road Research Facility
MOR	Modulus of Rupture
MSE	Mean Squared Error
NARR	North American Regional Reanalysis
NASA	National Aeronautics and Space Administration
NIST	National Institute of Standards and Technology
NOAA	National Oceanic and Atmospheric Administration
NSRDB	National Solar Radiation Database
NWS	National Weather Service
PDF	Probability Distribution Function
PDR	Partial Depth Repair
PennDOT	Pennsylvania Department of Transportation

PITT-FACS	University of Pittsburgh Falling Weight Deflectometer Analysis for Concrete Slabs
PMS	Pavement Management System
QCLCD	Quality Controlled Local Climatic Database
RH	Relative Humidity
ROC	Receiver Operator Characteristic Curve
RPPR	Rigid Pavement Performance and Rehabilitation
SHRP	Strategic Highway Research Program
SMP	Seasonal Monitoring Program
SPS	Specific Pavement Sections
UBOL	Unbonded Overlay
ULCD	Unedited Local Climatic Database
UTC	Universal Time Coordinated
VP	Void Parameter
WAT	Weighted Average Temperature

1.0 INTRODUCTION

Falling Weight Deflectometer (FWD) Testing is a pavement evaluation strategy, which measures pavement deformation under a dynamic load. A FWD consists of a package of weights that are dropped onto a buffer, which rests on a load plate. This mechanism applies an impulse load ranging from 25-80 ms in duration. A set number of accelerometers are seated onto the pavement at varying distances from the load plate and measure the acceleration, which occurs due to the dynamic loading. The acceleration measurements are integrated twice to calculate displacement. A plot of the maximum displacement calculated for each sensor against the locations of the sensors is called the deflection basin. A FWD can be used for pavement evaluation at the network level, and for selecting and designing rehabilitation alternatives at the project level.

At the project level, FWD testing is a valuable tool for obtaining the necessary inputs required to select and design rehabilitation strategies. FWD testing of Jointed Plain Concrete Pavements (JPCP) is performed at several different locations on the slab. A map of typical FWD testing locations for a project level analysis can be seen in Figure 1.1.

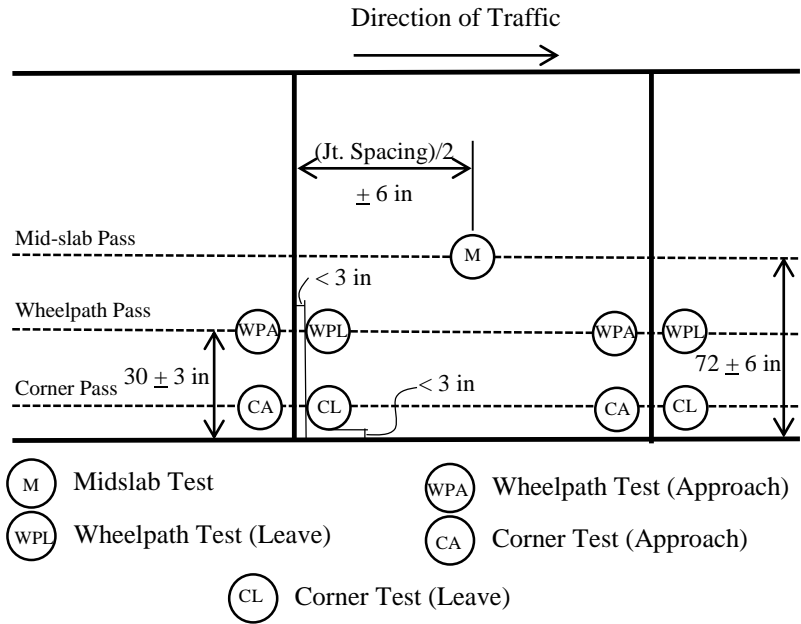


Figure 1.1 Typical FWD testing locations

The FWD test results are used to calculate evaluation parameters. The evaluation parameters typically calculated using FWD test results at each of the typical test locations can be seen in Table 1.1. Evaluation parameters determined from each FWD test location on JPCP.

Table 1.1. Evaluation parameters determined from each FWD test location on JPCP

Test location	Evaluation Parameters
Midslab	Elastic modulus of the concrete layer (E_{pcc}) Elastic modulus of the stabilized base layer (E_{base}) Modulus of subgrade reaction (k-value)
Wheelpath	Load transfer efficiency (LTE)* Differential deflection (DD)*
Corner	Location of voids beneath the slab (Void Detection)

**These parameters are sometimes calculated in the corner of the slab*

These evaluation parameters can be used as indicators for concrete pavement restoration activities, and inputs into pavement design procedures, such as the Pavement ME Design Guide (ARA Inc. 2004). The FWD derived evaluation parameters, which can be used as inputs into the rehabilitation modules in the Pavement ME Design Guide, can be seen in Table 1.2. FWD Derived Evaluation Parameters Required for Each Rehabilitation Strategy.

Table 1.2. FWD Derived Evaluation Parameters Required for Each Rehabilitation Strategy

Rehab Strategy	Parameters
Pavement ME Design Guide Inputs	
Concrete Pavement Restoration (CPR)	E_{pcc} , E_{base} , k-value
Bonded Concrete Overlay	E_{pcc} , E_{base} , k-value
Unbonded Concrete Overlay	E_{pcc} , E_{base} , k-value
HMA Overlay	E_{pcc} , E_{base} , k-value, LTE
CPR Activity Selection	
Subsealing	void locations
Load transfer restoration	DD, LTE

The Pavement ME Design Guide assumes that the pavement is uniformly supported. Therefore, to accurately utilize the analysis modules in the design guide, all voids should be located and repaired using subsealing.

1.1 BACKGROUND AND PROBLEM STATEMENT

FWD testing results can be influenced by several environmental factors. The volume of the concrete slab is affected by the mean temperature and moisture levels of the concrete slab. As the temperature of the slab increases, the coefficient of thermal expansion (CTE) of the concrete, will

cause the slab to expand. In addition, as concrete dries the volume of the slab will decrease due to drying shrinkage. The volume of the slab will have an effect on the width of the pavement joints. A decrease in joint width can affect the effective load transfer through aggregate interlock and dowels. The volume of the slab can increase to a point where the joints are completely closed (joint lock-up) this leads to very effective load transfer between slabs and can cause restraint to slab curvature.

Temperature and moisture gradients through the depth of the slab induce curvature in the slab due to temperature curling and moisture warping, respectively. A positive temperature gradient, the top of the slab is warmer than the bottom of the slab, will lead to negative curvature, as the top of the slab expands more than the bottom of the slab. The opposite is true for a negative temperature gradient.

Moisture changes in concrete pavement often lead to positive curvature. Monitoring of moisture sensors in Illinois and Pennsylvania has shown that most of the drying occurs in the top few inches of the pavement (Janssen 1987, Nassiri 2011). In unique situations, such as an arid environments or concrete experience autogenous shrinkage, some drying may occur in the lower layers of the pavement. However, additional drying will occur at the surface due to convection and evaporation. This results in a moisture gradient, with the top of the slab being dryer than the bottom of the slab, causing the top of the slab to shrink more than the bottom of the slab. This leads to positive curvature. The total curvature of the slab is a superposition of the curvature caused by the temperature gradient, and curvature caused by the moisture gradient.

The curvature of the slab can lead to changes in the support conditions at the edges of the slab for positive curvature, and in the middle of the slab for negative curvature. This change in

support conditions can have a large effect on FWD testing results. The effect of temperature and moisture gradients on the pavement shape and FWD testing is illustrated in Figure 1.2.

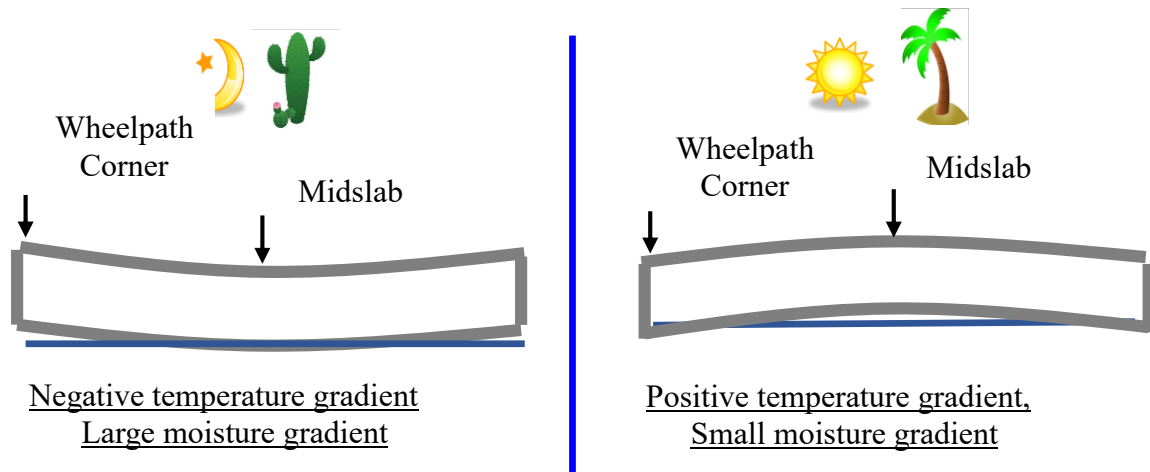


Figure 1.2. Influence of temperature and moisture gradients on FWD testing

Previous research at the Minnesota Road Research Facility (MnROAD), and analysis of the Federal Highway Administration (FHWA) Long-term Pavement Performance (LTPP) Database, have indicated that the slab curvature does affect at least some of the pavement evaluation parameters calculated from FWD test data (Khazanovich et al. 2003; Khazanovich et al. 2001; Vandebossche 2003; Vandebossche and Snyder 2004). More details on previous research into the effect of slab curvature on FWD testing is provided in Chapters 3-5 . However, no tools have been developed to affectively account of this effect. FHWA provides guidance that FWD testing should be performed when the slab is approximately flat. However, no tools are available to predict when a pavement will be approximately flat. In addition, limiting testing to times when the slab is approximately flat can be impractical. It is possible for a slab to transition from a negative temperature gradient to a positive temperature gradient in less than one hour.

Therefore, a toolset, which can be used to reduce the sensitivity of the pavement evaluation parameters to the slab curvature during FWD testing, will allow engineers to make more informed pavement rehabilitation decisions, and more accurately design overlays.

1.2 RESEARCH OBJECTIVE AND OUTLINE

The primary objective of this study is to develop a toolset, which reduces the effect of slab curvature during FWD testing on the backcalculated k-value, joint performance parameters (LTE and DD), and the detection of voids. For each of these parameters, the influence of slab curvature using currently available methods is evaluated, and techniques are developed to decrease this influence. This research is conducted through a combination of computational analysis, statistical analysis of the LTPP and MnROAD datasets, and field trials conducted in Western Pennsylvania. The field trials are described in Chapter 2 .

Chapter 3 describes the research effort used to evaluate the effect of slab curvature on the backcalculated k-value. The effect of slab curvature on this parameter is evaluated using the field trials and the LTPP and MnROAD datasets. A computational model based on the finite element method (FEM) is used to validate the trends observed in the field data. The potential effect of the bias caused by these trends is evaluated using a sensitivity analysis of the Pavement ME design procedure. The computational model is also used to develop and evaluate several methods of reducing the effect of slab curvature on the backcalculated k-value. The field trials are used to validate these methods.

Chapter 4 describes the research effort used to evaluate and account for the effect of slab curvature on the LTE and DD calculated using FWD testing for doweled JPCPs. Data from the

field trials and LTPP dataset are used to evaluate the influence of slab curvature on these parameters. A FEM based computational model is then used to validate the observations from the field data and explore the mechanism driving these trends. Historical test data from the LTPP database is used to adjust these parameters for the slab curvature during FWD testing.

There are currently no evidence-based criterion for evaluating what values of LTE and DD necessitate pavement rehabilitation, such as a dowel bar retrofit (DBR) or full depth repair (FDR). FHWA currently provides guidance on cutoff values for these parameters, but this guidance is based on “rule of thumb,” not direct evaluation of the relationship between these parameters and faulting. Therefore, a statistical analysis is performed evaluating the correlation of these parameters and future pavement distress. A sensitivity analysis of the effect of LTE on the predicted distress in the HMA overlay of JPCP in the Pavement ME Design Guide is also conducted.

Chapter 5 describes the research involved in developing a statistical model to detect voids beneath the slab, while accounting for slab curvature during FWD testing. This chapter also describes the procedure used to develop and evaluate the performance of the statistical model. The performance of the model is also compared to the performance of existing tools. In addition, the sensitivity of the model to each of the predictors is evaluated.

The toolset developed in Chapters 3, 4, 5 required the temperature gradient in the slab to be known at the time of testing. The temperature profile during the field trials and during FWD testing at LTPP sections and MnROAD is directly measured, either using temperature holes or embedded thermocouples. However, these measurements may not be practical for routine FWD testing. Therefore, a temperature prediction model, based on 1-D heat transfer, was developed using the finite difference method. Chapter 6 describes the research involved in developing and

evaluating this tool. The sensitivity of the model to thermal material properties was evaluated using a sensitivity analysis. Two data sources were considered to be included in the temperature prediction model, the Automated Surface Observation System (ASOS) dataset, and the Modern Era Retrospective analysis for Research and Applications version 2 (MERRA2) dataset. The ASOS dataset is a cooperative effort between the National Oceanic and Atmospheric Administration (NOAA), the Federal Aviation Administration (FAA) and the Department of Defense (DoD). The MERRA2 dataset is developed by the National Aeronautics and Space Administration (NASA). The weather data from the two datasets were compared. Five instrumented pavement sections were used to tune the thermal material properties in the model for each dataset. The tuning sections were also used to compare the variance of the residuals for each data source. The performance of the tuned model was also evaluated using test sections, which were not used to tune the model.

The final chapter, Chapter 7 includes conclusions and recommendations for future work. The user's guide for the University of Pittsburgh FWD Analysis of Concrete Slabs (Pitt-FACS), a web tool developed based on the results of this research, is included in Appendix B at the end of this dissertation.

2.0 FIELD DATA COLLECTION FOR JPCP PAVEMENTS

To directly evaluate the effect of slab curvature on FWD testing results, field trials were conducted on five test dates at three test sections in Western Pennsylvania. The tested sections were PennDOT control section 0525 on southbound I-79, near Bridgeville, PA, and a portion of PennDOT control section B01, on westbound SR-22 near Murrysville, PA. The tested portion of PennDOT control section B01 consisted of the doweled and undoweled cells of the PennDOT Smart Pavement. The specific locations of the test sections within the control sections can be seen in Figure 2.1 and Figure 2.2.

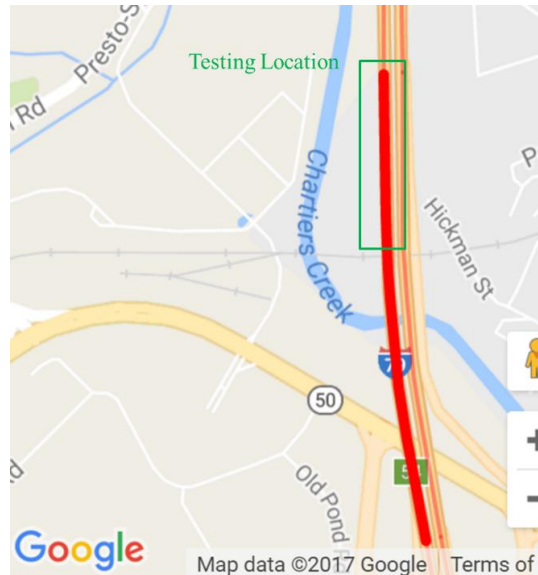


Figure 2.1. Location of field trials on I-79 near Bridgeville, PA (base map is from PennDOT PMS website, originally derived from Google Maps)



Figure 2.2. Location of field trials on SR-22 near Murrysville, PA (base map is from PennDOT PMS website, originally derived from Google Maps)

The structural properties of each of the test sections can be seen in Table 2.1. Structural properties of field trial sections.

Table 2.1. Structural properties of field trial sections

Section	Test Dates	Thickness (in)	Jt. Spacing (ft)	Base/Subbase	Dowels/ Tie Bars
I-79	5/8/2016, 10/1/2017	12	20	Open graded subbase (4 in) PennDOT 2A* (5 in)	Yes
SR-22 Doweled	4/25/2016, 10/2/2017	12-14	15	Asphalt Stabilized base (4 in) PennDOT 2A* (8 in)	Yes
SR-22 Undoweled	4/27/2016 10/2/2017	13	15	Asphalt Stabilized base (4 in) PennDOT 2A* (8 in)	No
*PennDOT 2A is a subbase material defined in (PennDOT 2011)					

The I-79 section has a tied concrete shoulder. The SR-22 sections have a concrete curb and gutter, which is tied for the doweled section, and untied for the undoweled section.

2.1 TESTING PROCEDURES

During these trials, FWD testing and traffic control was provided by PennDOT. The University of Pittsburgh verified proper alignment of the test locations and measured and recorded the pavement temperatures. Testing during the field trials utilized two separate test plans. The first three test dates, in the Spring of 2016, utilized Test Plan A, whereas the final two test dates, in the Fall of 2017, utilized Test Plan B. Following testing in the Spring of 2017, three cores were pulled from the I-79 section to validate the slab thickness, and measure the coefficient of thermal expansion, static elastic modulus, and compressive strength of the concrete. Cores were not taken from the SR-22 section as these tests were performed on cores from the SR-22 section soon after construction and are available in the final construction report (Wells et al. 2005).

2.1.1 Test Plan A

Test Plan A was developed to produce FWD testing results at the corner of the slab, in the wheelpath and at midslab over the full range of ELTGs experienced by the test section in a day. To ensure testing occurred over the full range of the gradients, FWD testing occurred from approximately 5:30 am to 5:00 pm. The testing locations utilized in test plan A can be seen in Figure 2.3. At each location, three seating drops (no data recorded) were performed at the 12,000 lb nominal load level, followed by four testing drops each, at the 9,000 lb, 12,000 lb and 16,000 lb nominal load levels in that order.

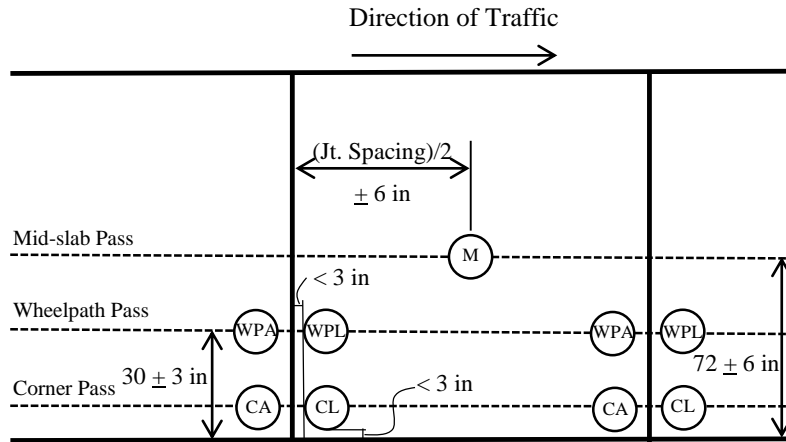


Figure 2.3. Field trials testing locations (Test Plan A)

To ensure that at least one testing pass of each type was performed before the temperature gradient began increasing after sunrise, the first three passes occurred in the order: *corner, wheelpath, midslab*. Previous research indicated that void detection is the FWD testing parameter most influenced by slab curvature. Therefore, after the first three passes, the passes were conducted in the following order: *corner, midslab, corner, wheelpath*. This pass order was repeated throughout the testing period.

At the I-79 section, temperature holes were used to measure the pavement temperature profile according to the LTPP test protocol (Schmalzer 2011). The depths of the holes used can be seen in Figure 2.4. Due to buildup of drilling fines in the bottom of the hole it was difficult to drill the deepest hole within the specifications in the LTPP test procedure without drilling into the base layer. The first attempt to drill the hole resulted in the drill bit reaching the base layer before the top of the compacted drilling fines at the bottom of the hole reached the specified depths in the LTPP test procedure. This hole was abandoned and a second hole was drilled to a depth slightly less than the depth specified in the LTPP test procedure. The localized temperature gradients at

the bottom of the slab are very small. Therefore, it is unlikely that this deviation has a large impact on the measured pavement temperature profile.

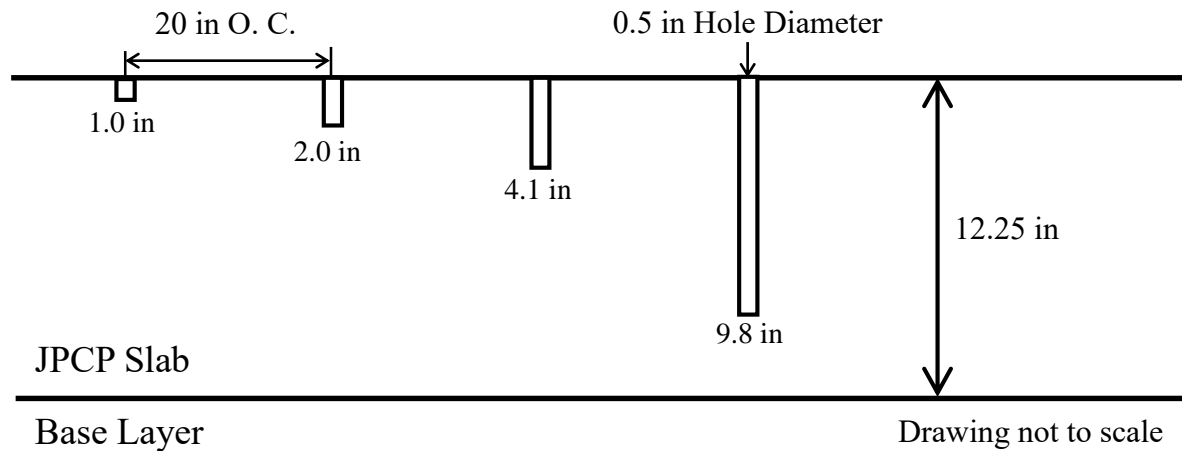


Figure 2.4. Depth of temperature holes used at I-79 test section

The temperature in each hole was measured at five-minute intervals using a thermocouple wire read by a datalogger. The bottom 0.5 in of each hole was filled with mineral oil to provide thermal conductivity between the concrete and the thermocouple. The tops of the holes were sealed using duct tape to prevent convective heat transfer between the hole and the air.

The SR-22 Smart Pavement contains embedded thermocouples, which were used to measure the temperature profile of the slab throughout the testing periods (Wells et al. 2005). Therefore, no temperature holes were required at SR-22. Thermocouples 16-22, which are located at midslab in the doweled section, were used to calculate the temperature gradient. The depths of these thermocouples can be seen in Table 2.2. Thermocouple depths at SR-22 field trial sections.

Table 2.2. Thermocouple depths at SR-22 field trial sections

Sensor	Depth (in)
TC16	0.5
TC17	1.6
TC18	2.9
TC19	5.9
TC20	10.1
TC21	12.0
TC22	12.5

2.1.2 Test Plan B

Test plan B was developed to validate a backcalculation procedure, which was developed using computational data. Details of this procedure can be seen in Chapter 3. A secondary goal of Test Plan B is to provide additional test points at intermediate temperature gradients for passes at midslab and in the wheelpath. The testing occurred from approximately 6:30 am to 4:30 pm. Testing utilizing Test Plan B occurred in the fall, during which days are shorter than the late spring when Test Plan A was utilized. This allowed the peak gradients to be captured during a shorter testing period. The testing locations utilized in Test Plan A can be seen in Figure 2.5. The drop sequence used in Test Plan A was also used in Test Plan B.

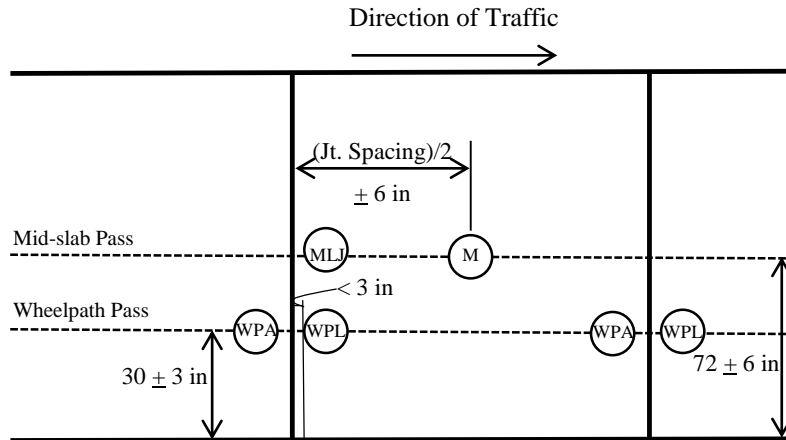


Figure 2.5. Field trial testing locations (Test Plan B)

The FWD testing passes were conducted in the following order: *midslab, midslab, wheelpath*. The temperature holes and thermocouples utilized for Test Plan A were also utilized for Test Plan B. The ELTG was calculated using the method of equivalent strains (Janssen and Snyder 2000). The results and analysis of the FWD field trials can be seen in Chapters 3, 4, and 5.

2.2 TESTING INFORMATION

2.2.1 I-79 Test Plan A (5/8/2017)

Testing utilizing Test Plan A at I-79 was performed over a 380-foot long section. To increase testing efficiency, every three slabs were tested. The layout of the test section can be seen in Figure 2.6.

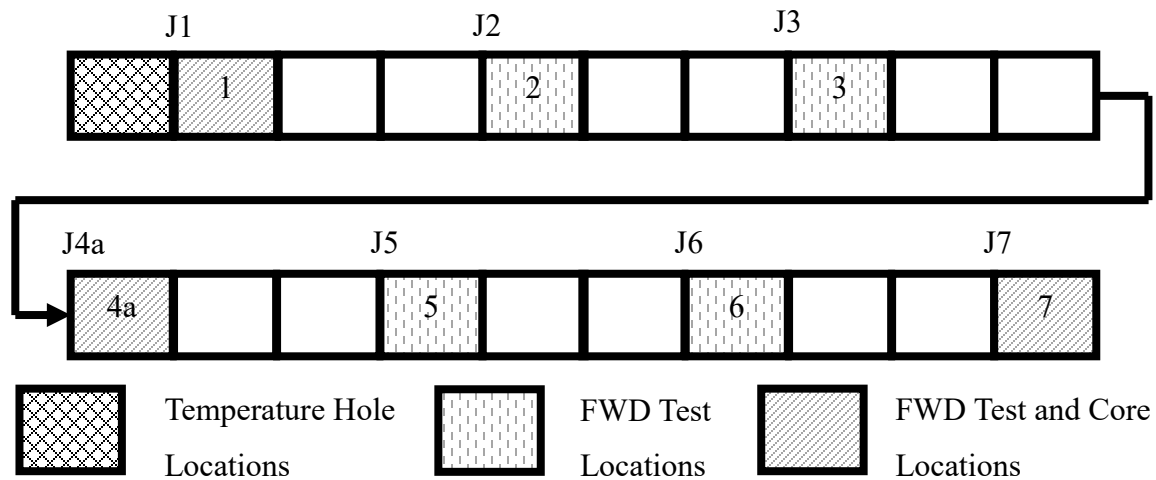


Figure 2.6. Test section layout (I-79, Test Plan A)

The sensor offset used for this test date can be seen in Table 2.3.

Table 2.3. Sensor offsets (I-79 Test Plan A)

Sensor	Offset (in)
1	0
2	-12
3	8
4	12
5	18
6	24
7	36
8	60

The weather during FWD testing of I-79 on 5/8/2017 consisted of sunny conditions with an ambient temperature ranging from 47 °F at 6:12 am to 64 °F at 4:59 pm. Approximately 0.2 in of

precipitation occurred the night prior to testing, ending at approximately 2:00 am. The average time, ELTG, and WAT at each of the FWD testing passes can be seen in Table 2.4.

Table 2.4. FWD testing pass information (I-79, Test Plan A)

Pass	Time	ELTG (°F/in)	WAT (°F)
Corner			
C1	6:30	-0.8	63
C2	7:45	-0.9	62
C3	9:00	-0.6	61
C4	9:45	0.2	65
C5	10:45	1.0	65
C6	12:15	1.7	71
C7	13:15	2.2	77
C8	15:15	2.5	84
C9	16:15	2.6	82
Wheelpath			
WP1	7:05	-0.9	63
WP2	10:15	0.5	66
WP3	12:50	2.0	73
WP4	14:45	2.4	83
WP5	16:50	2.5	83
Midslab			
MS1	7:25	-0.9	62
MS2	9:20	-0.2	62
MS3	11:10	1.2	68
MS4	13:45	2.3	80
MS5	15:45	2.8	82

The ELTG and WAT throughout the testing period can be seen in Figure 2.7.

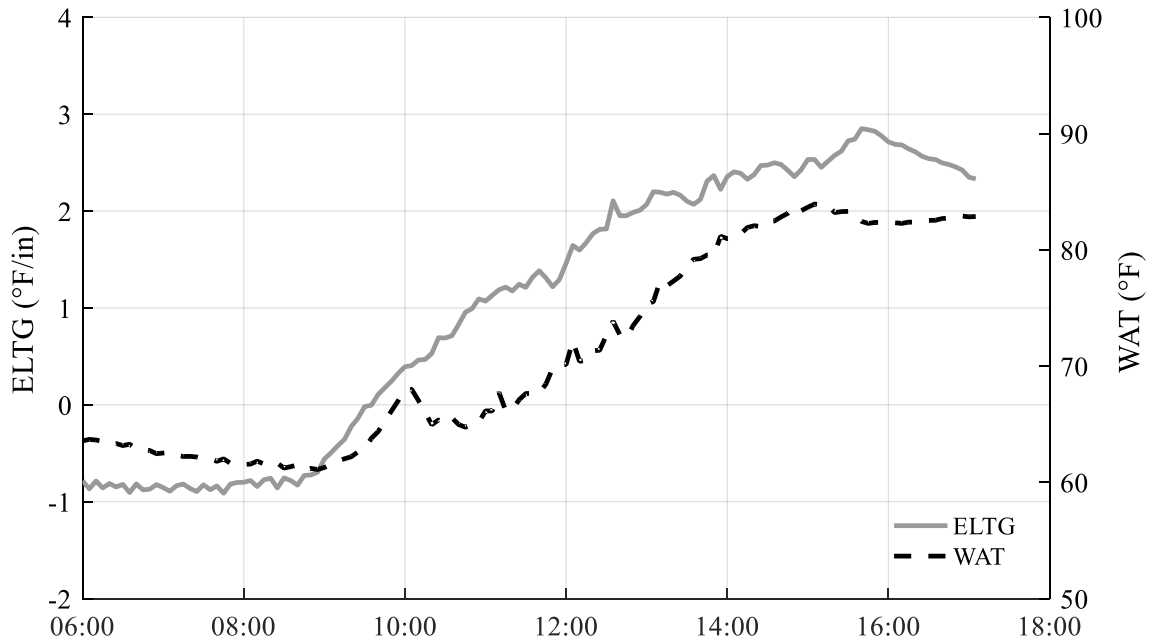


Figure 2.7. ELTG and WAT during testing period (I-79 Test Plan A)

2.2.2 SR-22 Doweled Test Plan A (4/25/2017)

The doweled test section at SR-22 consists of two cells, each consisting of three slabs. These cells are separated by 8 slabs (approximately 120 ft). The layout of the test section can be seen in Figure 2.8.

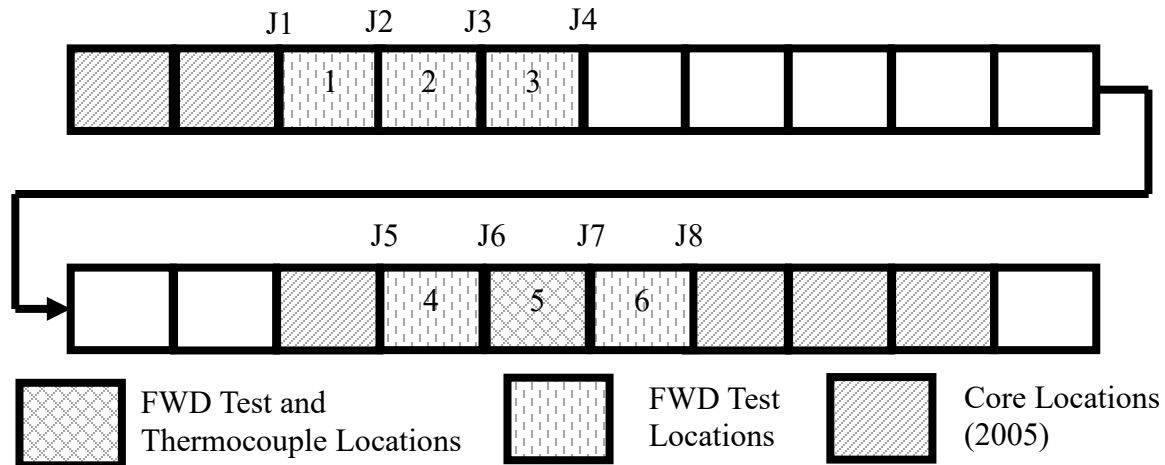


Figure 2.8. Test section layout (SR-22 doweled, Test Plan A)

The sensor offset utilized for the doweled section at SR-22, for Test Plan A, can be seen in Table 2.5.

Table 2.5. Sensor offsets (I-79 Test Plan A)

Sensor	Offset (in)
1	0
2	-12
3	8
4	12
5	18
6	24
7	36
8	60

The weather during testing consisted of sunny conditions with an ambient temperature ranging from 42 °F at 5:36 am to 89 °F at 4:28 pm. The average time, ELTG, and WAT at each of the FWD testing passes can be seen in Table 2.6.

Table 2.6. FWD testing pass information (SR-22 Doweled, Test Plan A)

Pass	Times	ELTG (°F/in)	WAT (°F)
Corner			
C1	5:45	-1.2	60
C2	7:15	-1.1	59
C3	8:30	-0.6	59
C4	9:45	0.4	62
C5	11:00	1.4	65
C6	12:45	2.3	71
C7	13:45	2.7	75
C8	14:45	2.9	77
C9	16:00	2.7	80
C10	16:30	2.4	80
Wheelpath			
WP1	6:30	-1.2	59
WP2	8:00	-0.9	59
WP3	10:30	1.0	64
WP4	13:15	2.5	73
WP5	15:30	2.8	79
Midslab			
MS1	6:45	-1.1	59
MS2	9:15	0.0	61
MS3	14:15	2.9	76
MS4	16:15	2.6	80

The ELTG and WAT throughout the testing period can be seen in Figure 2.9.

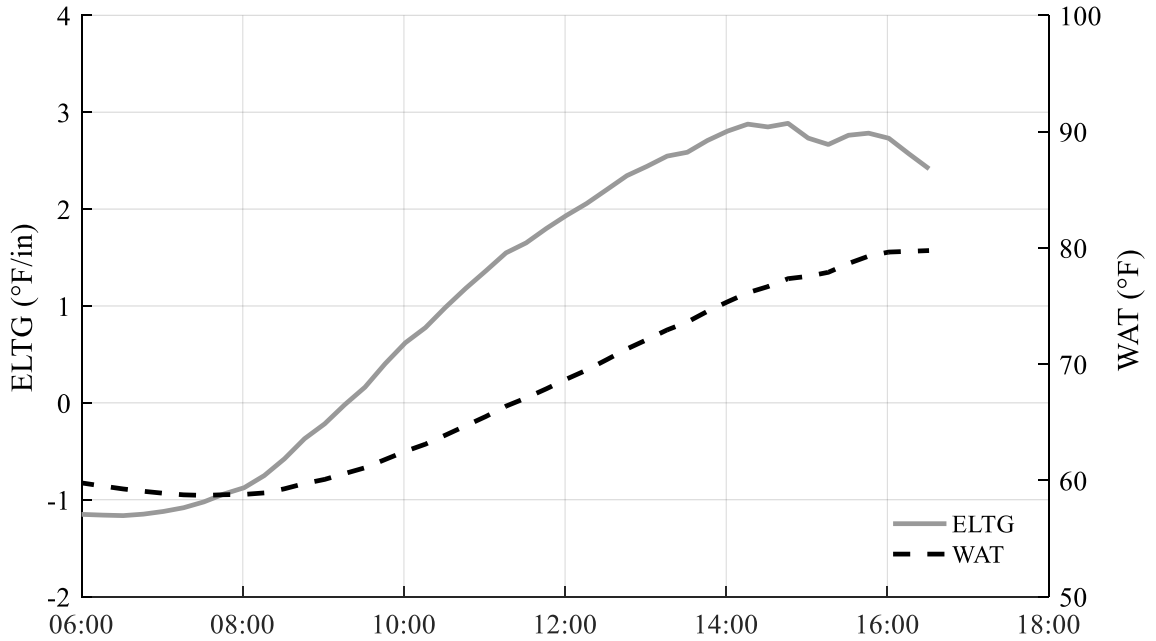


Figure 2.9. ELTG and WAT during testing period (SR-22 Doweled, Test Plan A)

2.2.3 SR-22 Undoweled Test Plan A (4/27/2017)

The undoweled section at SR-22 consists of 6 continuous slabs. The transition slabs at each end of the undoweled section are doweled on the joint adjacent to the doweled cells, and undoweled on the joint adjacent to the undoweled section. The layout of the undoweled section can be seen in Figure 2.10.

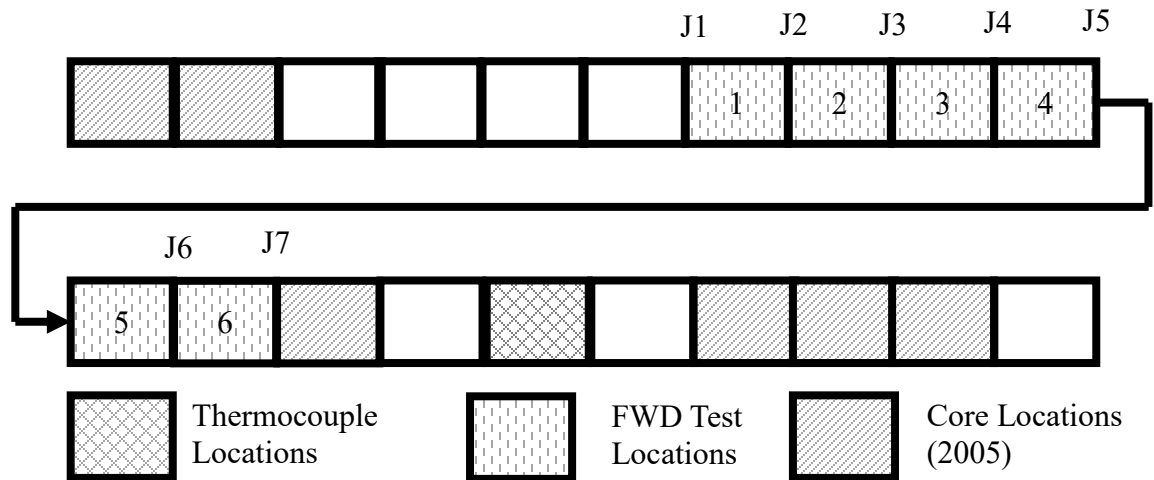


Figure 2.10. Test section layout (SR-22 undoweled, Test Plan A)

The sensor offset used on the test date for the doweled section at SR-22, for Test Plan A, can be seen in Table 2.7.

Table 2.7. Sensor offsets (I-79 Test Plan A)

Sensor	Offset (in)
1	0
2	-12
3	8
4	12
5	18
6	24
7	36
8	60

The weather during testing consisted of mostly cloudy conditions with an ambient temperature ranging from 53 °F at 5:30 am to 65°F at 4:13 pm. Approximately 0.2 in of precipitation occurred the day before testing, ending at approximately 8:00 am. The average time, ELTG, and WAT at each of the FWD testing passes can be seen in Table 2.8.

Table 2.8. FWD testing pass information (SR-22 Undoweled, Test Plan A)

Pass	Times	ELTG (°F/in)	WAT (°F)
Corner			
C1	6:45	-0.7	66
C2	7:45	-0.4	66
C3	8:30	0.0	67
C4	9:45	0.4	68
C5	10:30	0.9	70
C6	11:30	0.9	71
C7	12:45	0.9	72
C8	13:45	1.1	73
C9	14:30	1.2	74
C10	15:30	1.3	75
Wheelpath			
WP1	6:15	-0.7	66
WP2	7:15	-0.6	66
WP3	9:30	0.4	68
WP4	11:00	0.9	71
WP5	13:15	0.9	72
WP6	15:00	1.3	75
Midslab			
MS1	6:30	-0.7	66
MS2	8:15	-0.1	67
MS3	10:15	0.7	69
MS4	12:30	0.9	72
MS5	14:15	1.2	74

The ELTG and WAT throughout the testing period can be seen in Figure 2.11.

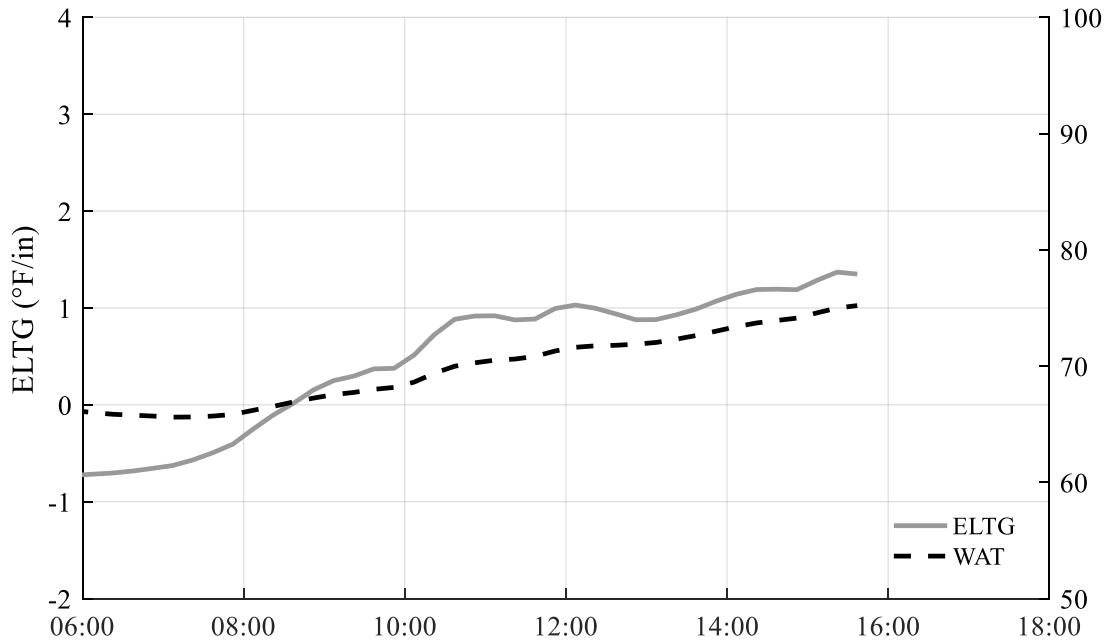


Figure 2.11. ELTG and WAT during testing period (SR-22 Undoweled, Test Plan A)

2.2.4 I-79 Test Plan B (10/1/2017)

The testing layout for Test Plan B at I-79 was slightly modified from the test layout from Test Plan A. To avoid testing on a core location, Slab and Joint 4 were each moved to the next slab downstream. Slab 1 could not be moved because the joint sealant had melted into the pavement texture 1 slab downstream. This prevented the load from being properly seated at the MLJ test location. To increase testing efficiency, every three slabs were tested. Similarly, Slab 7 was not tested due to a core hole. This location was not replaced, resulting in only six joints and slabs being tested. This decreased the total time required for each test pass, and therefore increased the number of passes performed. The layout of the test section can be seen in Figure 2.12.

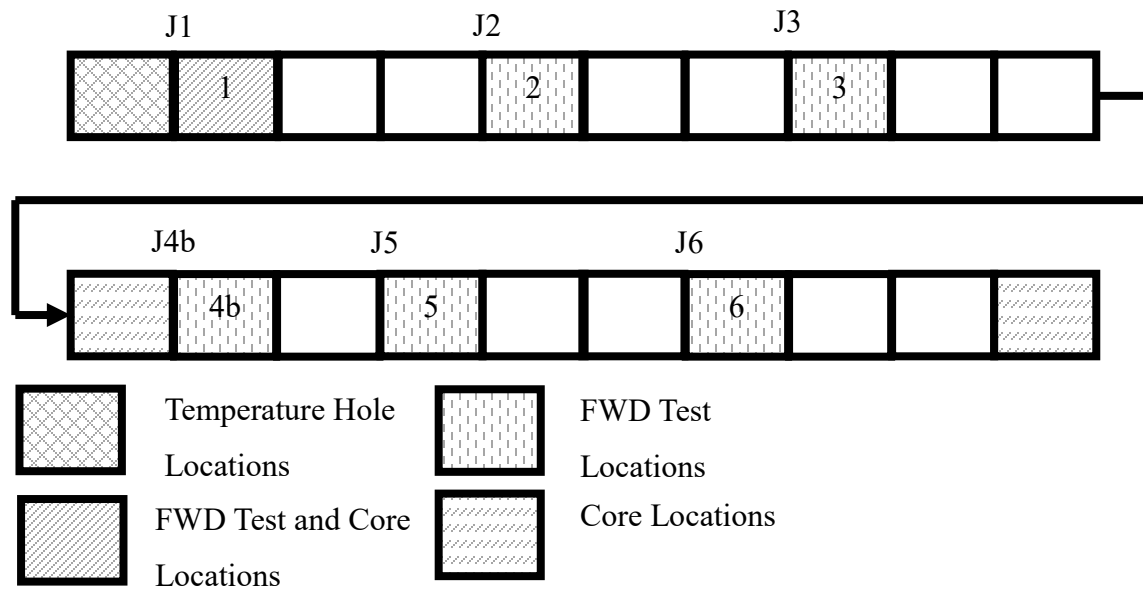


Figure 2.12. Test section layout (I-79, Test Plan B)

PennDOT provided an FWD with PennDOT’s standard sensor layout, rather than the previously used layout. It was determined that the time required to change the sensor spacing would delay the start of testing long enough to miss the time-period when negative ELTGs were present in the pavement. Therefore, the PennDOT standard layout was used. The computational analysis dataset described in Chapter 3 showed strong agreement between the backcalculated k-value using the two sensor arrangements with an R^2 of 1.00 and a slope of 1.01. The PennDOT standard sensor offset used for this test date can be seen in Table 2.9.

Table 2.9. Sensor offsets (I-79 Test Plan B)

Sensor	Offset (in)
1	0
2	-12
3	12
4	24
5	36
6	48
7	60

The weather during FWD testing of I-79 on 5/8/2017 consisted of clear conditions until 1:00 pm, then partly cloudy conditions. The ambient temperature ranged from 41 °F at 7:00 am to 66 °F at 3:31 pm. The average time, ELTG, and WAT at each of the FWD testing passes can be seen in Table 2.10.

Table 2.10. FWD testing pass information (I-79, Test Plan B)

Pass	Times	ELTG (°F/in)	WAT (°F)
Wheelpath			
WP1	8:00	-0.9	54
WP2	9:30	-1.1	55
WP3	10:50	0.1	58
WP4	12:10	1.0	65
WP5	13:30	1.7	71
WP6	14:55	1.8	76
Midslab			
MS1	8:30	-1.2	55
MS2	9:00	-1.2	55
MS3	9:55	-0.8	55
MS4	10:20	-0.4	56
MS5	11:15	0.5	60
MS6	11:40	0.7	62
MS7	12:35	1.3	67
MS8	13:05	1.5	69
MS9	13:55	1.8	72
MS10	14:25	1.9	74

The ELTG and WAT throughout the testing period can be seen in **Figure 2.13**.

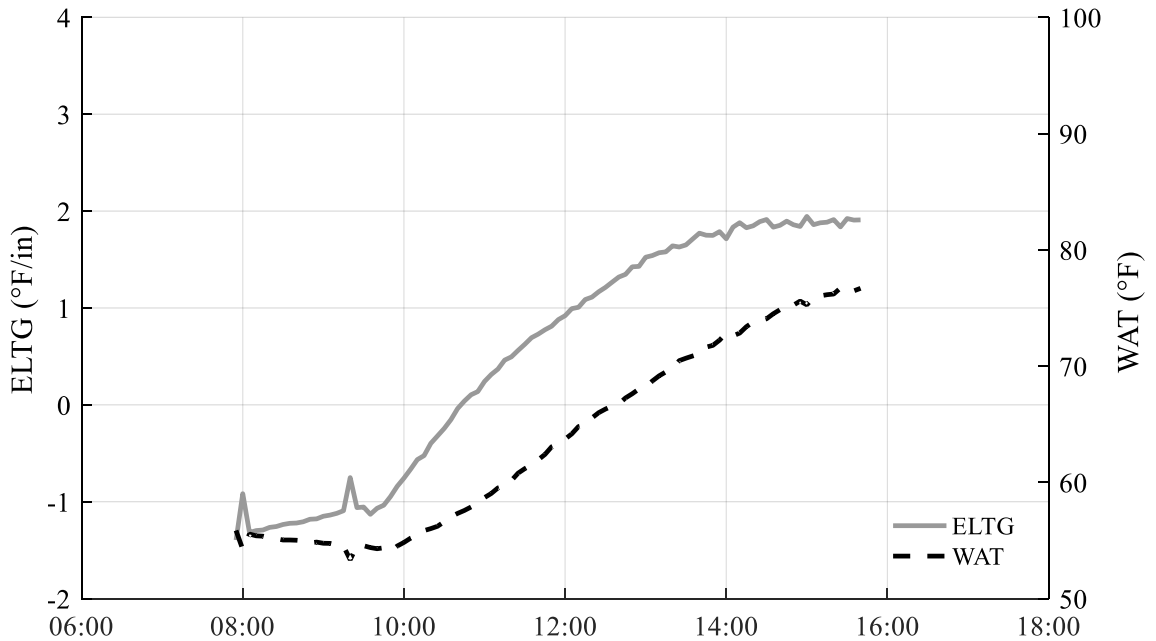


Figure 2.13. ELTG and WAT during testing period (I-79, Test Plan B)

2.2.5 SR-22 Doweled/Undoweled Test Plan B (10/1/2017)

Only one test date was available to implement Test Plan B at SR-22. Therefore, testing was performed on the same day on Slabs 4, 5, and 6 of both the doweled and undoweled sections. The layout of the test section can be seen in Figure 2.14.

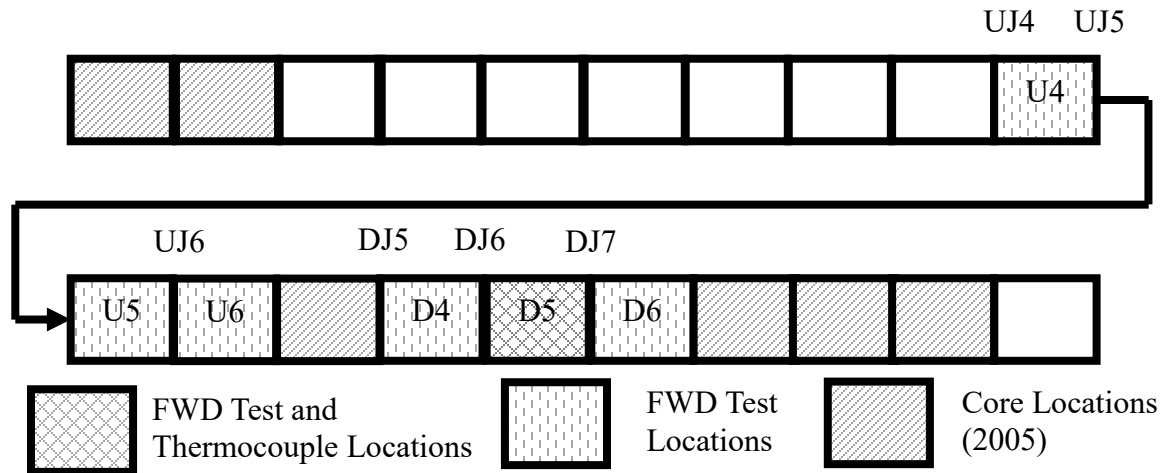


Figure 2.14. Test section layout (SR-22 Doweled/Undoweled, Test Plan B)

An attempt was made to modify the sensors to match the sensors used for Test Plan A. However, a different FWD was used for testing in the Fall of 2017 (Test Plan B) than was used in the Spring of 2016 (Test Plan A). The FWD used for Test Plan B has a bar that could not be removed in the field, which prevented the installation of a sensor at an 8-inch offset. Therefore, the sensor offsets shown in Table 2.11, were used for this test data.

Table 2.11. Sensor offsets (SR-22 Doweled/Undoweled, Test Plan B)

Sensor	Offset (in)
1	0
2	-12
3	12
4	18
5	24
6	36
7	60

The weather during FWD testing of SR-22 on 10/2/2017 consisted of scattered clouds. The ambient temperature ranged from 41 °F at 7:00 am to 73 °F at 3:01 pm. The average time, ELTG, and WAT at each of the FWD testing passes can be seen in Table 2.12.

Table 2.12. FWD testing pass information (I-79, Test Plan B)

Pass	Times	ELTG (°F/in)	WAT (°F)
Wheelpath			
WP1	8:00	-1.2	58
WP2	9:15	-0.5	59
WP3	10:30	0.4	62
WP4	11:45	1.2	66
WP5	13:00	1.8	69
WP6	14:15	2.0	73
Midslab			
MS1	7:30	-1.3	58
MS2	8:15	-1.1	58
MS3	8:45	-0.8	59
MS4	9:30	-0.3	60
MS5	10:00	0.0	61
MS6	10:45	0.6	63
MS7	11:15	0.9	64
MS8	12:00	1.3	67
MS9	12:30	1.5	68
MS10	13:30	1.9	71
MS11	13:45	1.8	71
MS12	15:00	1.9	74
MS9	13:55	1.8	72
MS10	14:25	1.9	74

The ELTG and WAT throughout the testing period can be seen in Figure 2.15.

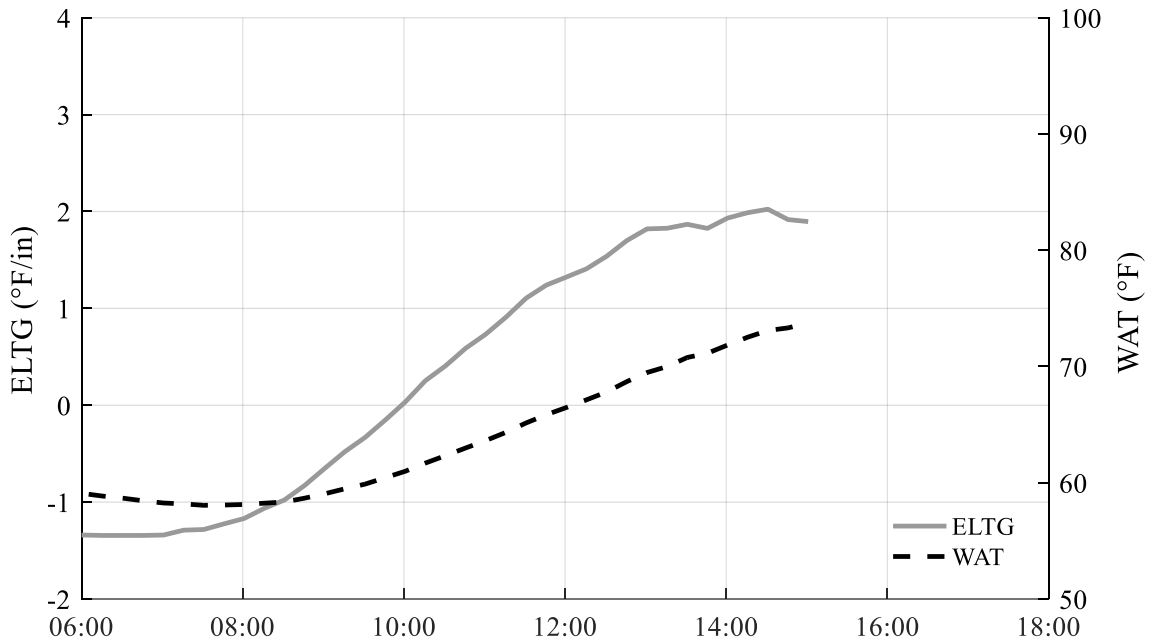


Figure 2.15. ELTG and WAT during testing period (SR-22 Doweled/Undoweled, Test Plan B)

2.3 LABORATORY TESTING RESULTS

2.3.1 Specimen Information

Three cores were taken from PennDOT control section 0525 of southbound I-79 near Bridgeville, PA on August 2nd, 2016. The first core was taken from Slab 1, approximately 10 ft from the start of the test section. The second core was taken from Slab 4, approximately 190 ft from the start of the test section. The third core was taken from Slab 6, approximately 310 ft from the start of the test section. All cores were taken at the midslab testing location. Images of the three cores can be seen in Figure 2.16.



Figure 2.16. Concrete cores (I-79)

The thickness of the cores ranged from 11.5 in to 12.2 in. The bottom surface of the concrete slab is very rough because it is directly on top of the open graded subbase, as can be seen in Figure 2.17. This leads to variability in the pavement thickness even within the same core. An average slab thickness was estimated for each core. The thicknesses of the cores are summarized in Table 2.13.



Figure 2.17. Bottom surface of the PCC slab (I-79)

Table 2.13. Thickness of concrete cores by location (I-79)

	Core Location		
	Slab 1	Slab 4	Slab 7
Concrete Thickness (in)	12	12.2	11.5

2.3.2 Test Results

The compressive strength, modulus of elasticity, Poisson's ratio, and coefficient of thermal expansion of the concrete cores were determined by the University of Pittsburgh. The concrete cores were cut with a diamond-bladed saw prior to testing to ensure the ends of the specimens were flat and perpendicular to the longitudinal axis. The final dimensions of the cores are summarized in Table 2.14.

Table 2.14. Final dimensions of concrete cores by location (I-79)

	Core Location		
	Slab 1	Slab 4	Slab 7
Average Length (in)	11.76	11.39	11.47
Average Diameter (in)	5.79	5.79	5.81

A summary of the test results is included in Table 2.15.

Table 2.15. Laboratory testing results (I-79)

Core	Compressive Strength, σ (psi)	Modulus of Elasticity, E (psi)	Poisson's Ratio, μ	Coefficient of Thermal Expansion, α ($\mu\epsilon/^\circ\text{F}$)
1	7710	4.48×10^6	0.17	5.64
2	8270	4.38×10^6	0.22	6.01
3	7830	4.35×10^6	0.18	5.67

3.0 BACKCALCULATION

3.1 INTRODUCTION

The deflection basin measured by FWD testing can be used to backcalculate the structural layer properties of a JPCP. Backcalculation is usually performed using FWD testing at midslab to minimize the influence of boundary conditions, such as joints or the pavement edge. Most backcalculation techniques for JPCP assume that the pavement acts as a flexural plate on a dense liquid foundation. The behavior of the pavement structure in response to an applied load is defined by the flexural stiffness of the flexural plate, and the modulus of subgrade reaction (k-value). The stiffness of stabilized base layers is considered in the stiffness of the flexural plate. The stiffness of an unstabilized base layer is considered in the k-value. The plate stiffness and k-value have traditionally been estimated using:

- A closed form solution based on the unique relationship between the normalized area parameter (AREA) and the radius of relative stiffness (ℓ) (Ioannides et al. 1989)
- An iterative solution based on minimizing the mean squared error (MSE) between the measured deflection basin and the theoretical deflection basin described by Kelvin-Bessel functions (Korenev 1954)

Backcalculation has also been performed using artificial neural networks (ANN) (Bayrak and Ceylan 2009); Khazanovich and Roesler 1997).

Estimating the structural properties of an in situ rigid pavement is important for:

- Evaluating the uniformity of conditions along a project. Large changes in backcalculated structural properties along a project, especially the k-value, can indicate non-uniformity along a project. These changes are possibly due to distinct geological features, such as a large cut or fill region. Variations in support conditions along a project may necessitate dividing a rehabilitation into subprojects and applying different treatments to the subprojects.
- Developing inputs for designing overlays, and predicting the future life of a pavement following a restoration (ARA Inc. 2004). The concrete pavement rehabilitation module within the AASHTO Pavement ME design procedure can be used to predict future distress in a pavement following a CPR project, and can help an engineer decide between using a CPR or other rehabilitation alternatives, such as an overlay. The backcalculated k-value and modulus of elasticity of the slab are included as Level 1 inputs into the following modules in the Pavement ME Design Guide (ARA Inc. 2004) :
 - CPR
 - Bonded concrete overlays of concrete
 - Unbonded concrete overlays
- Evaluating whether regions of loss of support occur beneath the slab. Detecting areas of loss of support often involves comparing deflections measured using the FWD in the corner of the slab to the expected deflections from a computational model. Backcalculated structural parameters are necessary for developing an accurate computational model. The ratio between the measured deflection and the theoretical deflection is an important predictor for detecting voids, which is described in Chapter 5 .

Slab curvature due to temperature and moisture gradients affects the response of a pavement to applied loads, and therefore affects the results of FWD testing. When a pavement is curled upwards due to negative temperature and/or moisture gradients, the edges of the slab can have greatly reduced support, increasing the deflection when a load is applied near the slab edge. When a pavement is curled downward due to a positive temperature gradient, the interior of the slab can have greatly reduced support, increasing the deflection when a load is applied at midslab. The changes in the deflection basin due to slab curvature can lead to inaccuracy in the backcalculation process.

A study at the Minnesota Road Research Facility (MnROAD) found that the ELTG, an indicator of slab curvature, influenced the backcalculated k-value for thinner slabs (7.5 in), but not for thicker slabs (10 in) (Vandenbossche and Snyder 2004). An analysis of the LTPP SMP projects compared backcalculated k-values from FWD tests at the same location on the same day. Half of the sections evaluated, 8 of 16, have a mean coefficient of variation (COV) for any one day greater than 10%. All 16 sections have at least one test date where the within day coefficient of variation is greater than 10% (Khazanovich et al. 2001). The prior analysis did not tie this variation directly to slab curvature or a temperature gradient. However, physically, slab curvature is likely the major contributor to variation in the backcalculated k-value within a one day period. The within day variance in the backcalculated elastic modulus of the concrete layer was also evaluated. The daily variance in the backcalculated elastic modulus was less than the within day variance in the backcalculated k-value (Khazanovich and Roesler 1997). This indicates slab curvature is more influential on the backcalculated k-value than the backcalculated E_{pcc} .

A better understanding of the effect of slab curvature on the backcalculated k-value, including the factors which determine the magnitude of the effect, is important for establishing

design inputs and predicting future distresses. The effect of slab curvature on k-value was evaluated using data from field trials in Pennsylvania, the LTPP SMP sections, and a computational analysis. It is also important to understand if errors in backcalculating the k-value significantly affect pavement management decision making. Therefore, a sensitivity analysis was conducted to determine the effect of variation in k-value on future pavement life predictions using the AASHTO Pavement ME design procedure. Finally, strategies for minimizing the errors in backcalculated k-values caused by curling and warping were developed and evaluated.

3.2 EFFECT OF SLAB CURVATURE ON THE BACKCALCULATED K-VALUE

3.2.1 FIELD TRIALS

The five field trials in Western Pennsylvania, which are described in Chapter 2 were used to observe the influence of slab curvature on the k-value backcalculated from FWD deflection measurements. The k-value was backcalculated for each test at the 16,000 lb nominal load level, at each sensor, using the closed form solution (Hall 1992; Ioannides et al. 1989). The k-values backcalculated from each sensor were then averaged to calculate a single estimate of k-value for each section. The observed relationship between backcalculated k-value and ELTG for each field trial can be seen in Figure 3.1 to Figure 3.6. The k-value input in the Pavement ME rehabilitation modules requires a dynamic k-value. Therefore, all k-values reported in this report are dynamic k-values, and have not been adjusted for consistency with values measured using the plate load test.

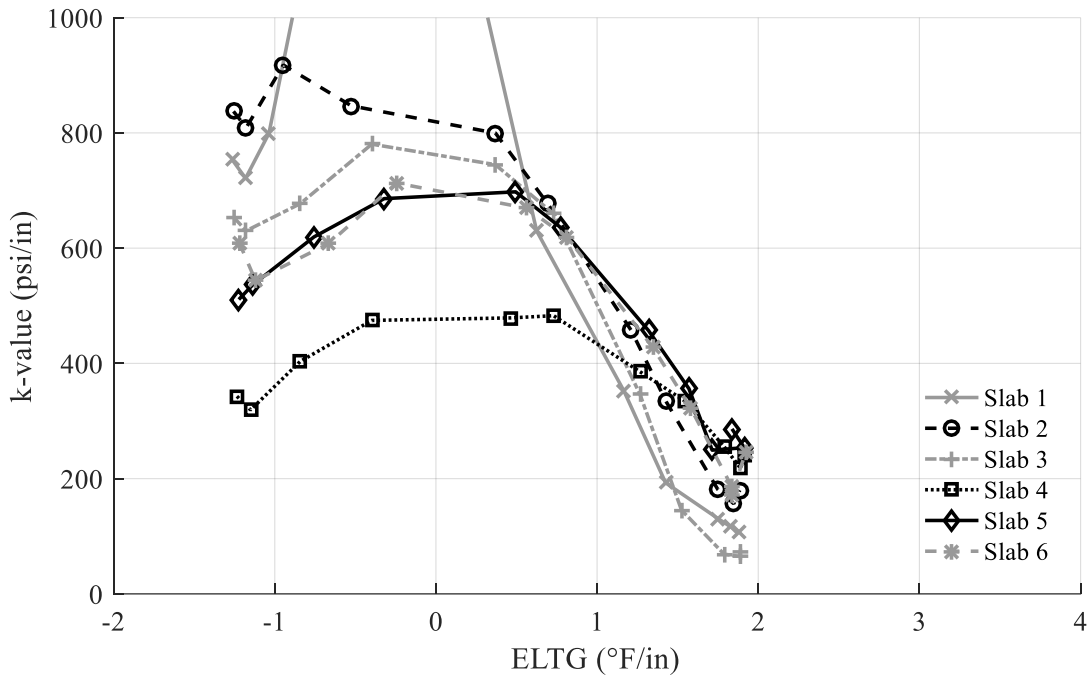


Figure 3.1. Backcalculated k-value (I-79, 5/8/2016)

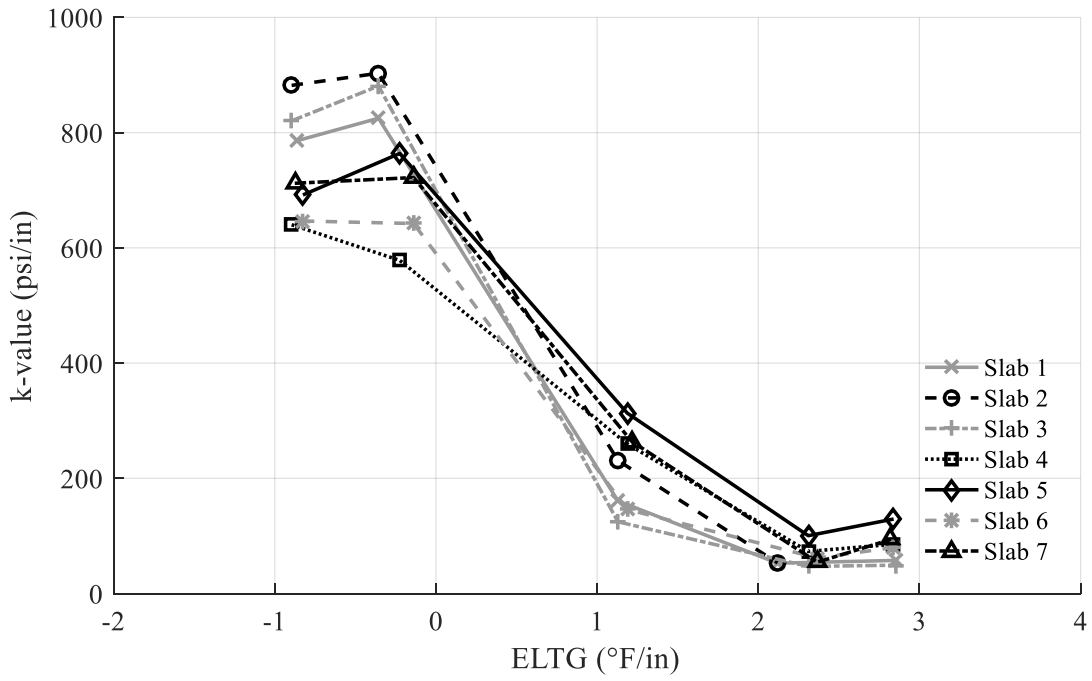


Figure 3.2. Backcalculated k-value (I-79, 10/1/2017)

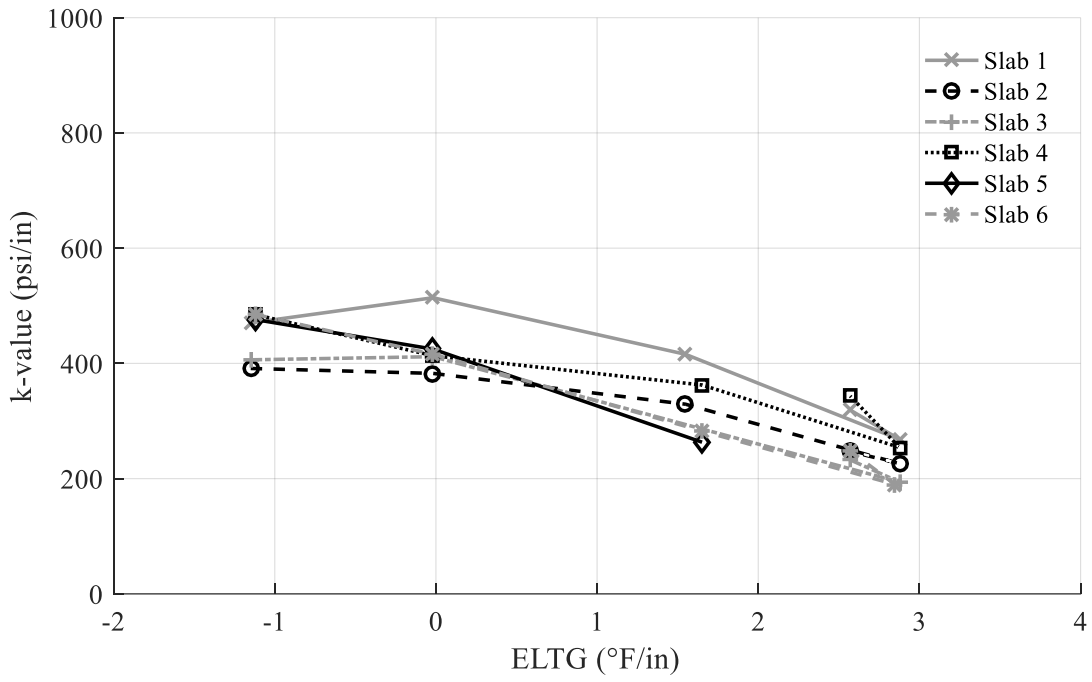


Figure 3.3. Backcalculated k-value (SR-22 doweled, 4/25/2016)

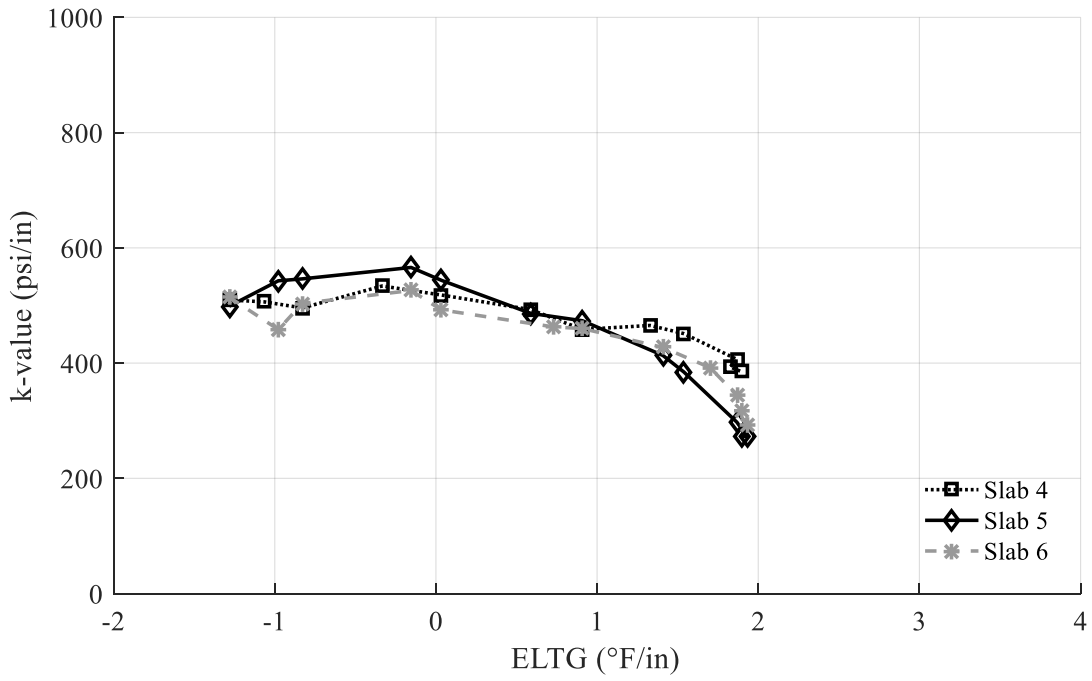


Figure 3.4. Backcalculated k-value (SR-22 doweled, 10/1/2017).

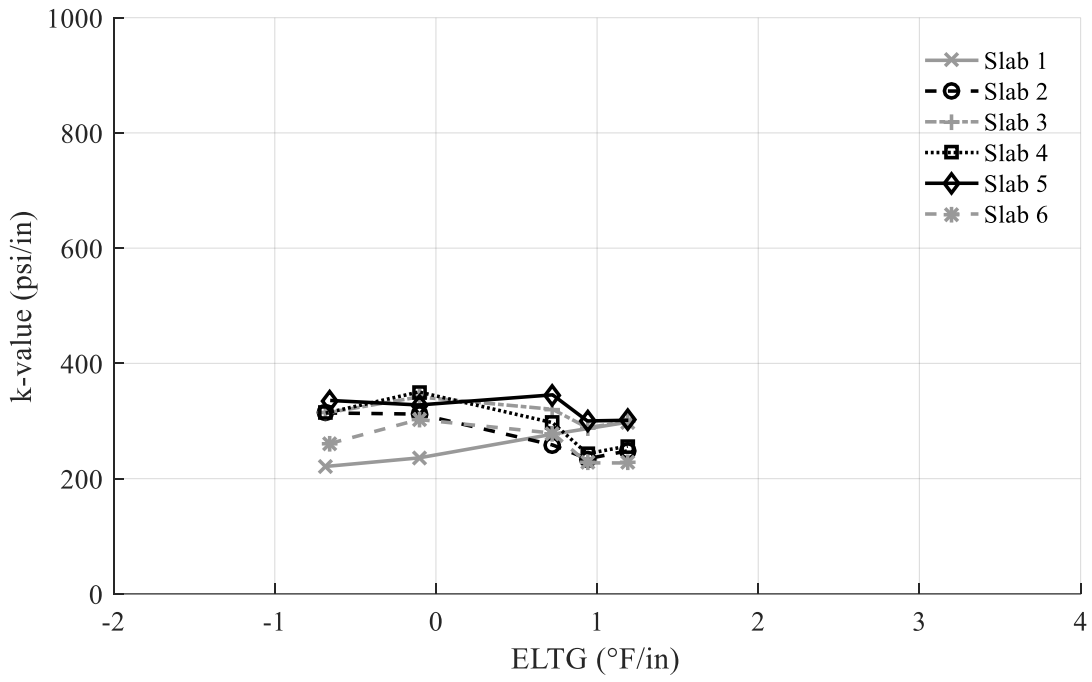


Figure 3.5. Backcalculated k-value (SR-22 undoweled, 4/26/2017)

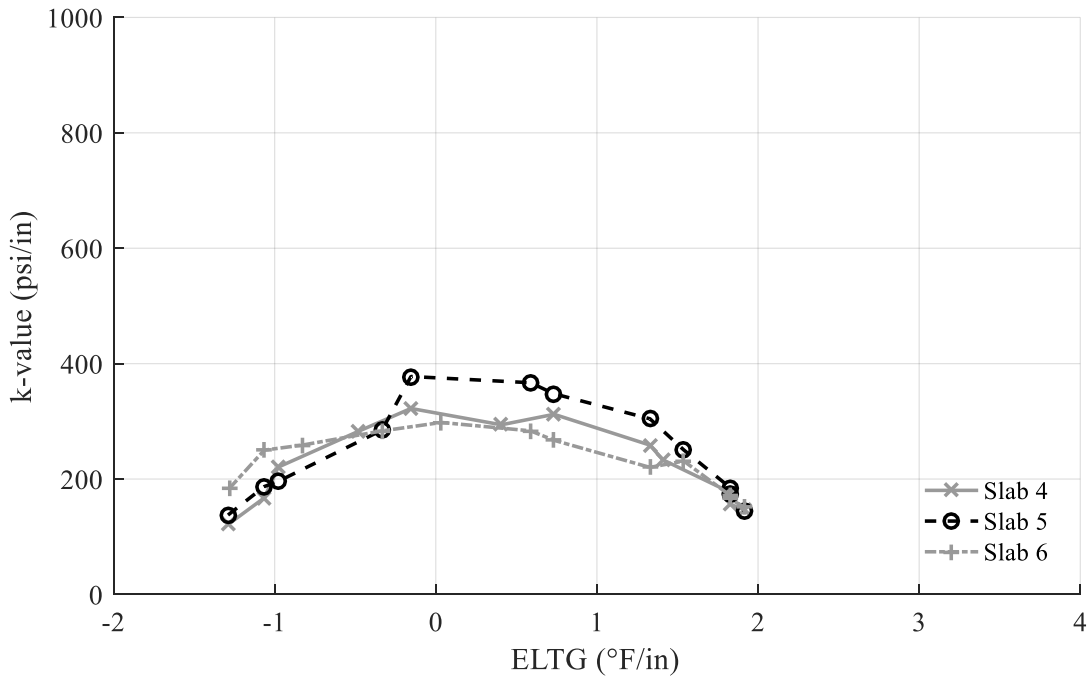


Figure 3.6. Backcalculated k-values (SR22 undoweled, 10/2/2017)

For all three sections, the backcalculated k-value is affected by slab curvature when a positive ELTG is present. For the I-79 section, the backcalculated k-value decreases rapidly as the ELTG increases. The backcalculated k-values in 2016 reach a minimum value, around 50 psi/in, at an ELTG of around 2 °F/in. During the 2017 test date, the ELTG also decreases rapidly. However, the maximum ELTG is less than 2 °F/in, and the k-value does not level off at a minimum value. It is likely that the backcalculated k-value would reach a minimum value and level off, if larger gradients were present on this test date. The doweled section at SR-22 also exhibits a decrease in backcalculated k-value as the ELTG increases, on both test dates. However, this rate of decrease is much lower than the rate of decrease at I-79.

The undoweled section at SR-22 does not show a significant relationship between ELTG and k-value during the Spring 2016 test date. However, cloudy conditions limited the range of ELTG experienced on this date. The testing on this section in 2016 showed a maximum k-value when the slab is approximately flat, and a lower k-value with a positive or negative ELTG. The maximum k-value for the undoweled section is lower than the maximum k-value for the doweled section on both test dates.

This is unexpected as the two cells of the doweled section are on opposing sides of the undoweled section. To investigate this difference, the deflection basins for the doweled and undoweled sections were compared. An example of this comparison, with an ELTG of -1.0 °F/in can be seen in Figure 3.7.

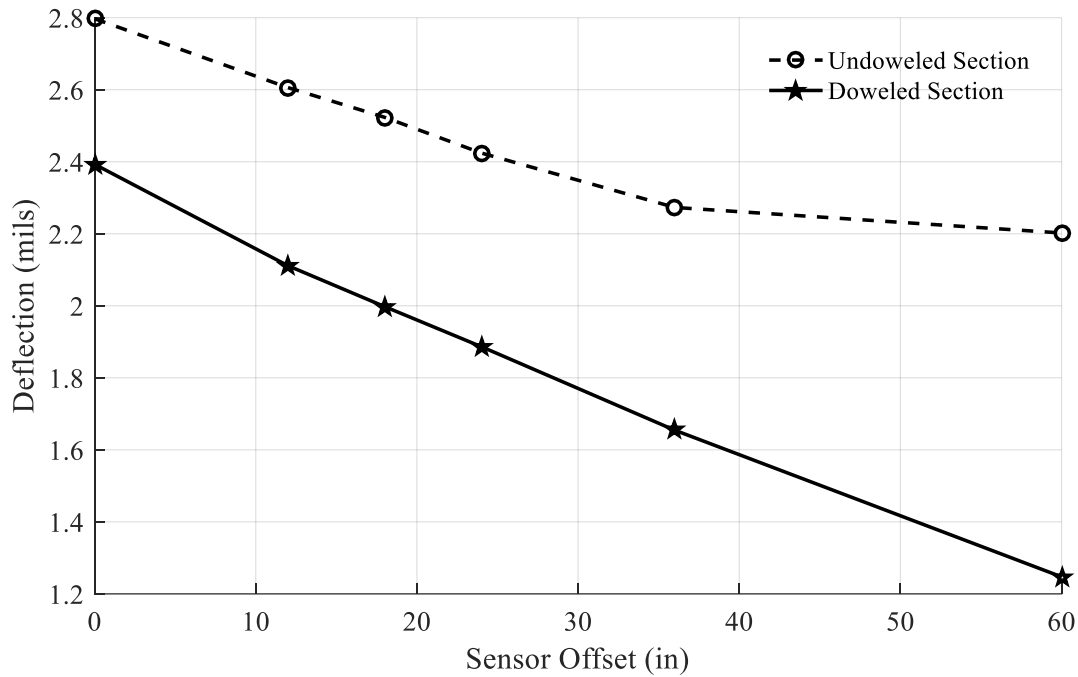


Figure 3.7. Comparison of midslab deflection basins between doweled and undoweled sections with an ELTG of -1.0 °F/in (SR-22, Fall 2017)

The undoweled section experiences a sharp inflection point after an offset of 36 inches. In contrast, the deflection basin for the doweled section is nearly linear. This likely indicates that the additional curvature in the undoweled section, due to the lack of restraint, causes the slab to have reduced support 60 inches from the center of the slab, 18 inches from the joint. This results in the additional deflection in the areas which have reduced support, and results in a lower backcalculated k-value.

The difference in the rate at which the backcalculated k-value decreases with increased ELTG between the I-79 test section and the doweled section at SR-22 is likely due to the variation in the amount of upward deflection at midslab due to positive ELTGs. The joint spacing at I-79 is 20 ft, whereas the joint spacing at SR-22 is 15 ft. An FEM analysis has shown that for a 12 in slab and a k-value of 500 psi/in, more upward deflection will occur midslab with a 20-ft joint spacing

than for a 15-ft joint spacing. Also, the asphalt stabilized base at SR-22 will restrain curvature, due to the additional weight bonded to the bottom of the slab, while the granular base at I-79 will not. FWD testing at midslab can be used to estimate if a slab is bonded to the base by evaluating whether the backcalculated elastic modulus of the slab is closer to expected values assuming a parallel plate model (assuming no bond between the slab and the base) and a composite plate model, assuming full bond between the slab and the base. A vast majority of FWD testing of concrete pavements on stabilized bases in the LTPP database indicates that the slabs are bonded to the base (Khazanovich and Roesler 1997). It should be noted that a study of airfield pavements has found that composite action occurs between the slab and the base, even when a gap occurs at the corner of the slab. This could be due to friction between the slab and the base, or the possibility of a partial bond, where the slab is bonded to the base at the interior of the slab, and debonded near the edges. A push-off test at the SR-22 Smart pavement shortly after paving resulted in rupture of the base layer prior to debonding between the base and the slab (Wells et al. 2005).

These factors likely lead to the middle of the slab having greatly reduced support at I-79 under smaller positive ELTGs than at SR-22. This may explain the rapid decrease in backcalculated k-value with increasing ELTG at I-79, and the more gradual decrease at SR-22. If very large positive gradients were observed at SR-22 during the field tests, it is possible that the backcalculated k-value would have reached a minimum value and stabilized.

The maximum k-value backcalculated from testing at negative ELTGs is also higher at I-79 than it is for either section at SR-22. The maximum k-value is a good estimate of the “true k-value” subgrade stiffness, the k-value that corresponds to the physical stiffness of the supporting layers, when the slab is fully supported. The estimate of the “true” k-value at I-79 is higher than

the estimate of the “true” k-value at SR-22, indicating that the supporting layers are likely stiffer at I-79 than at SR-22.

When positive ELTGs occur, stiff supporting layers will reduce the amount of curvature that is absorbed by the elasticity of the foundation, which increases upward deflection at the center of the slab. This will increase the impact of positive ELTGs on backcalculated k-values. It is not possible to determine the relative impact of joint spacing, base type, and the true stiffness of the supporting layers on the relationship between ELTG and backcalculated k-value solely from the field trials in Pennsylvania.

3.2.2 Analysis of LTPP SMP Sections and MnROAD Cells

The effect of the true stiffness of the supporting layers on the relationship between slab curvature and backcalculated k-value was evaluated using the LTPP SMP sections, and sections from MnROAD. The SMP sections are tested more frequently than other LTPP sections, sometimes with multiple test passes at midslab occurring within a single day. Previous analysis of these sections has revealed significant variation in backcalculated k-values between FWD tests performed at the same location on the same day (Khazanovich et al. 2001). However, some sections showed significantly more within day variation than others, possibly indicating that slab curvature has a larger effect on the backcalculated k-value for these particular sections.

Testing at MnROAD sections is performed often. However, with the exception of testing performed for previous research relating to the effect of slab curvature on FWD testing results, multiple passes are not performed on the same day. Previous research at MnROAD found that ELTG had a significant impact on slab curvature for the thin sections (7.5 in), but not for the thick sections (10 in) (Vandenbossche and Snyder 2004).

The relationship between ELTG and k-value for each of the SMP sections and MnROAD sections can be seen in Figure 3.8 to Figure 3.25. To limit the effect of a frozen subgrade on the results, only tests where the WAT is greater than 40 °F were considered in the analysis to minimize the potential that the subgrade is frozen. However, in locations where there has been a deep freeze, such as at MnROAD, LTPP Section 83-3802 (Manitoba), and LTPP Section 89-3015 (Quebec), the subgrade can still be frozen when the WAT of the slab is greater than 40 °F.

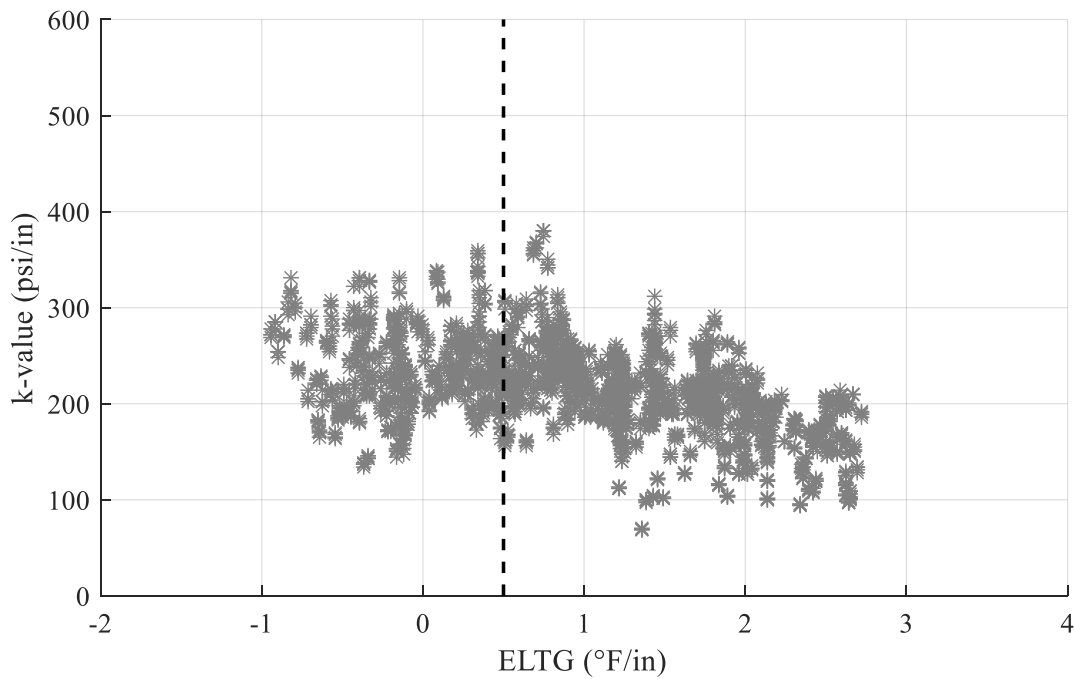


Figure 3.8. Backcalculated k-value (LTPP Section 04-0215, Arizona)

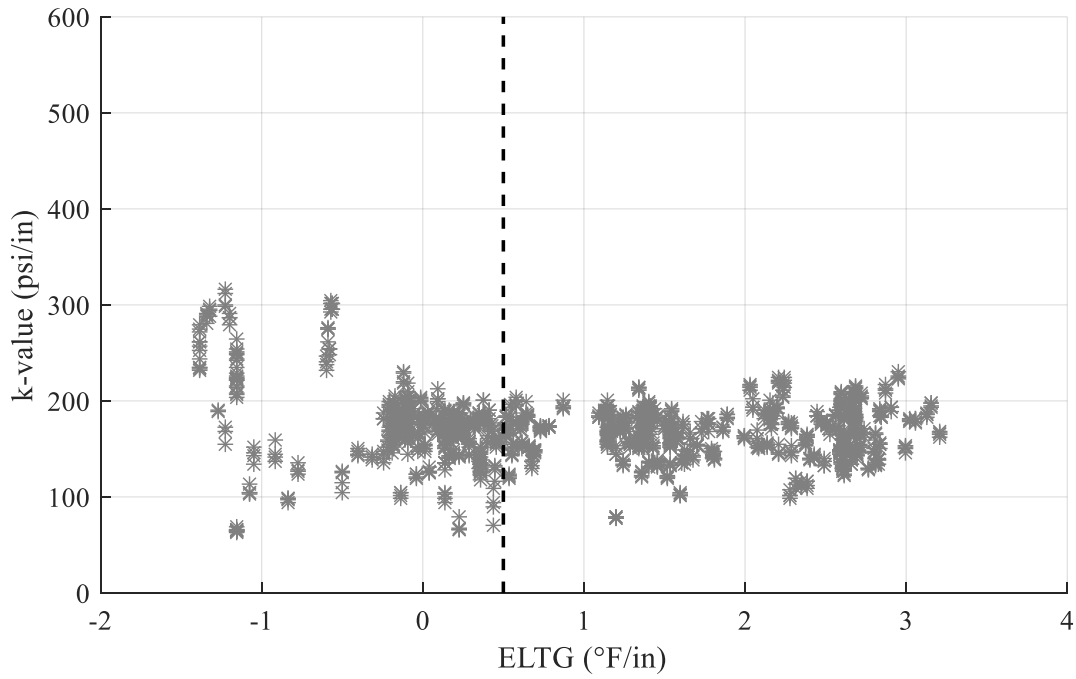


Figure 3.9. Backcalculated k-value (LTPP Section 06-3042, California)

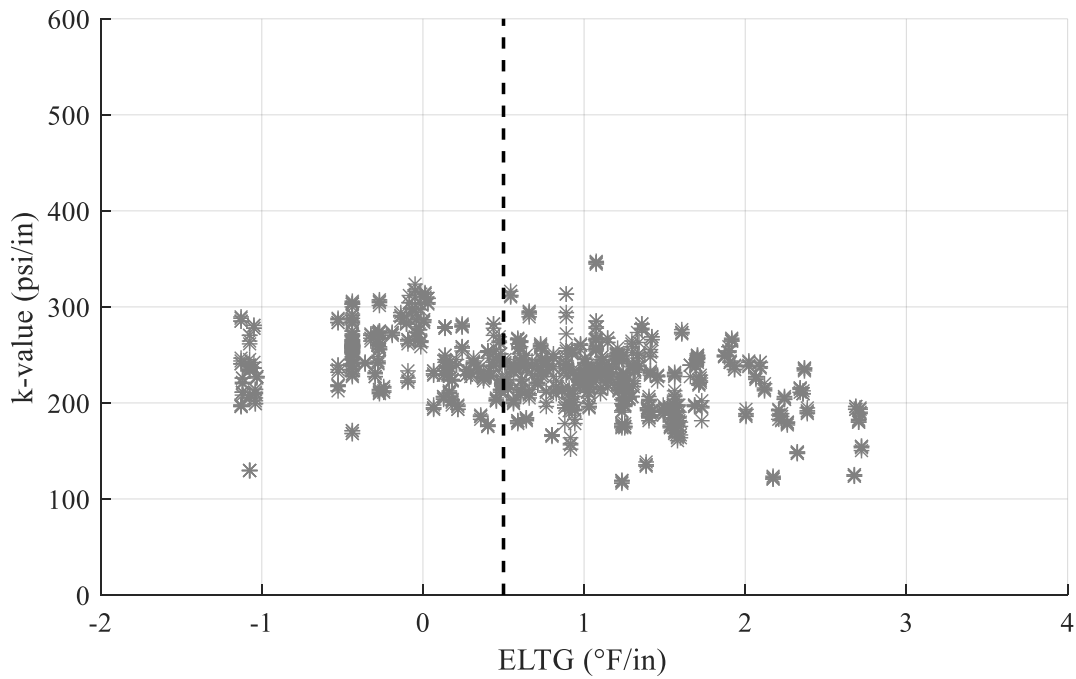


Figure 3.10. Backcalculated k-value (LTPP Section 18-3002, Indiana)

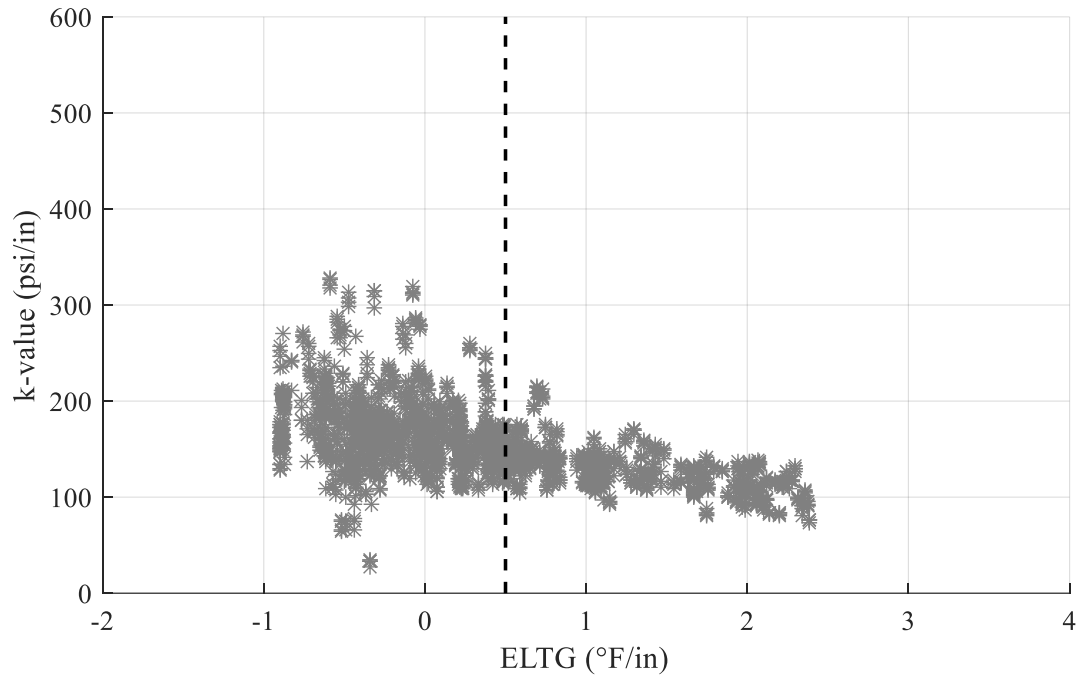


Figure 3.11. Backcalculated k-value (LTPP Section 31-3018, Nebraska)

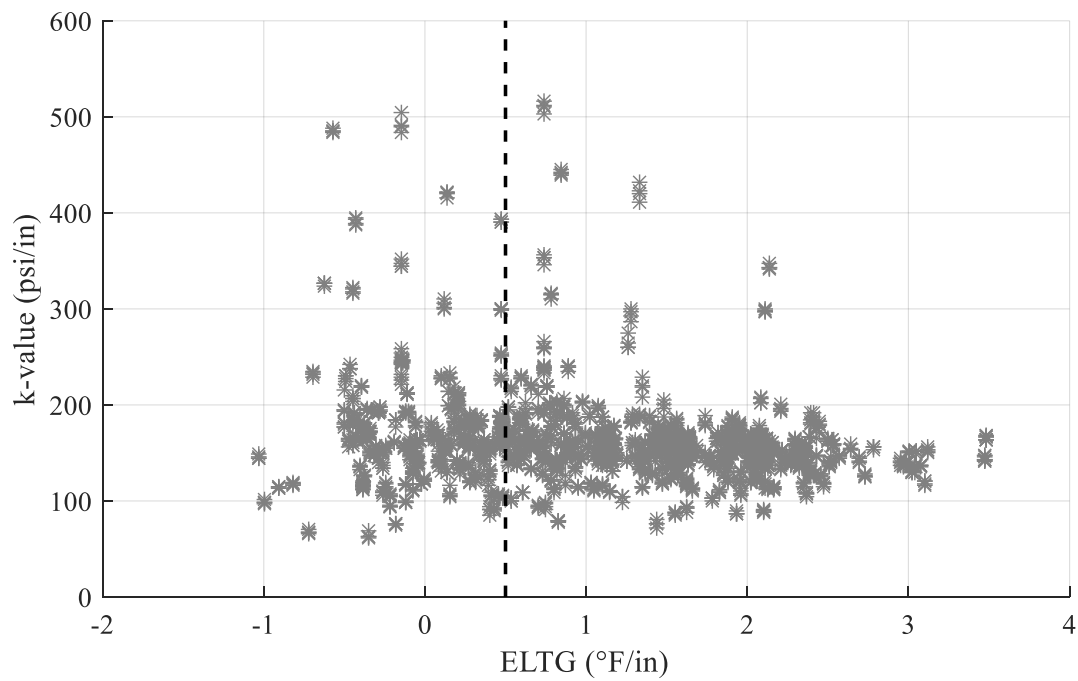


Figure 3.12. Backcalculated k-value (LTPP Section 37-0201, North Carolina)

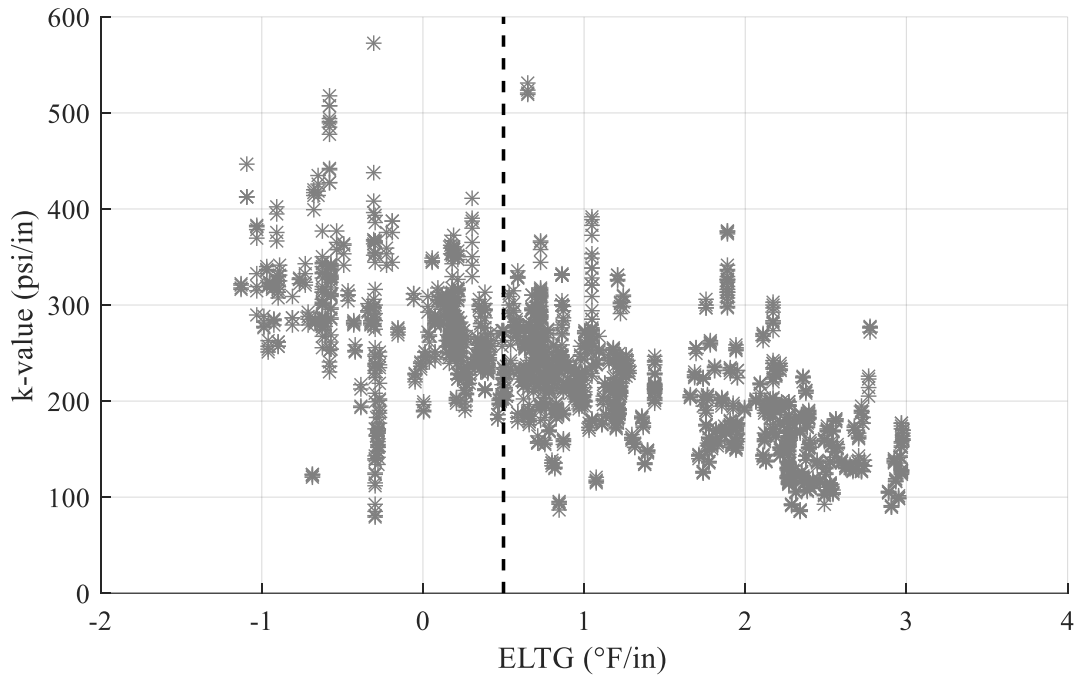


Figure 3.13. Backcalculated k-value (LTPP Section 49-3011, Utah)

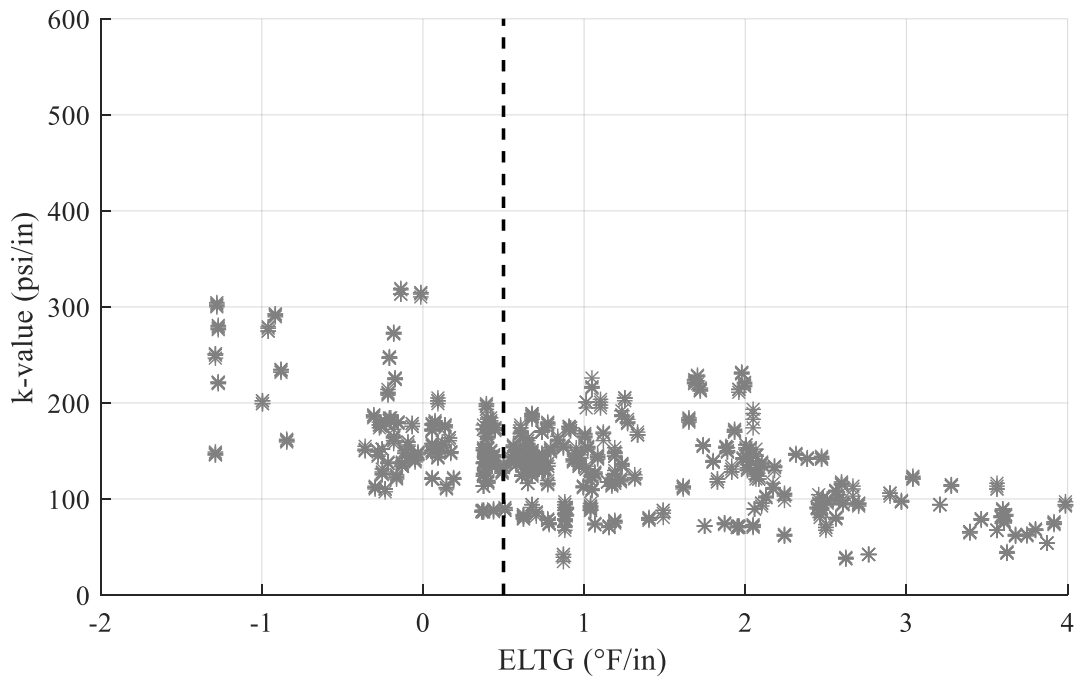


Figure 3.14. Backcalculated k-value (LTPP Section 53-3813, Washington)

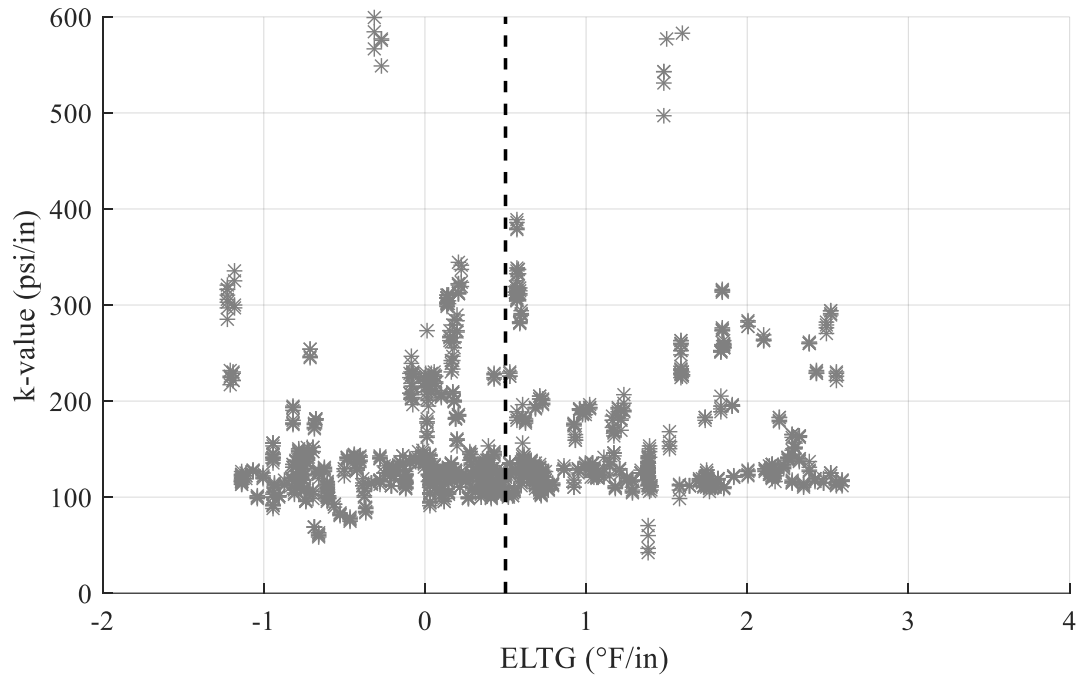


Figure 3.15. Backcalculated k-value (LTPP Section 83-3802, Manitoba)

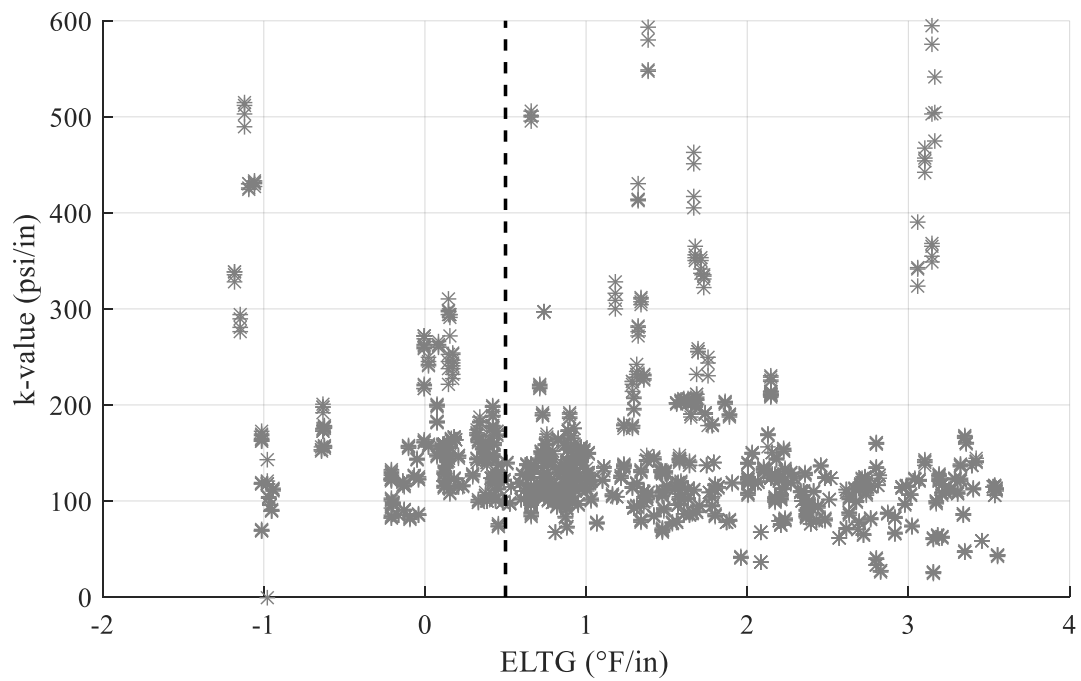


Figure 3.16. Backcalculated k-value (LTPP Section 89-3015, Quebec)

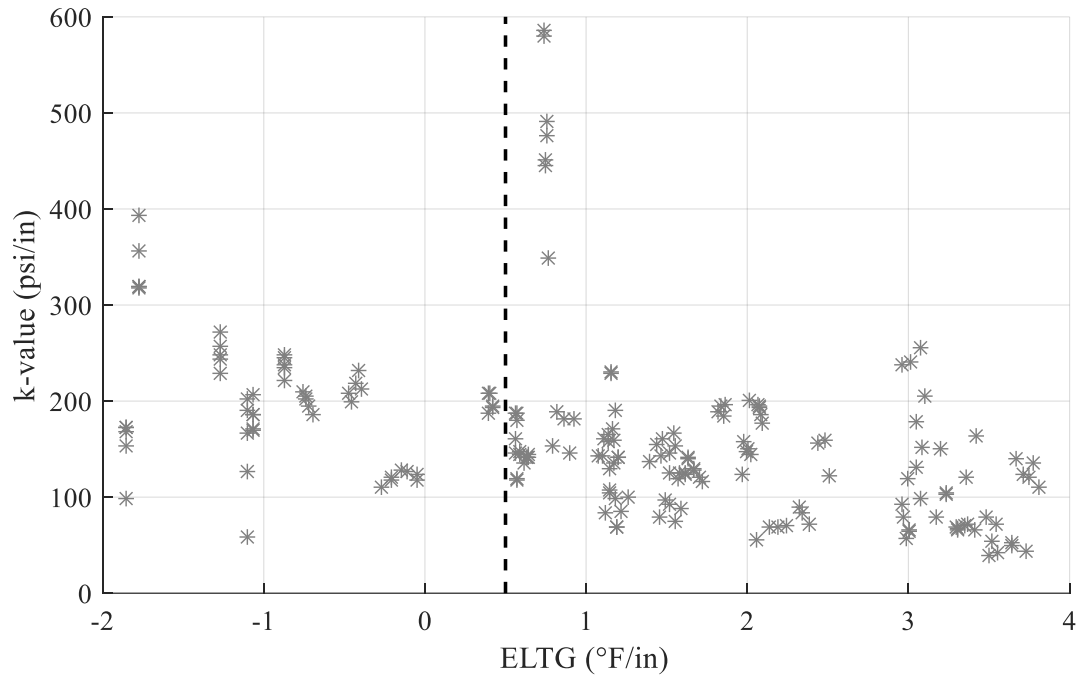


Figure 3.17. Backcalculated k-value (MnROAD Cell 5)

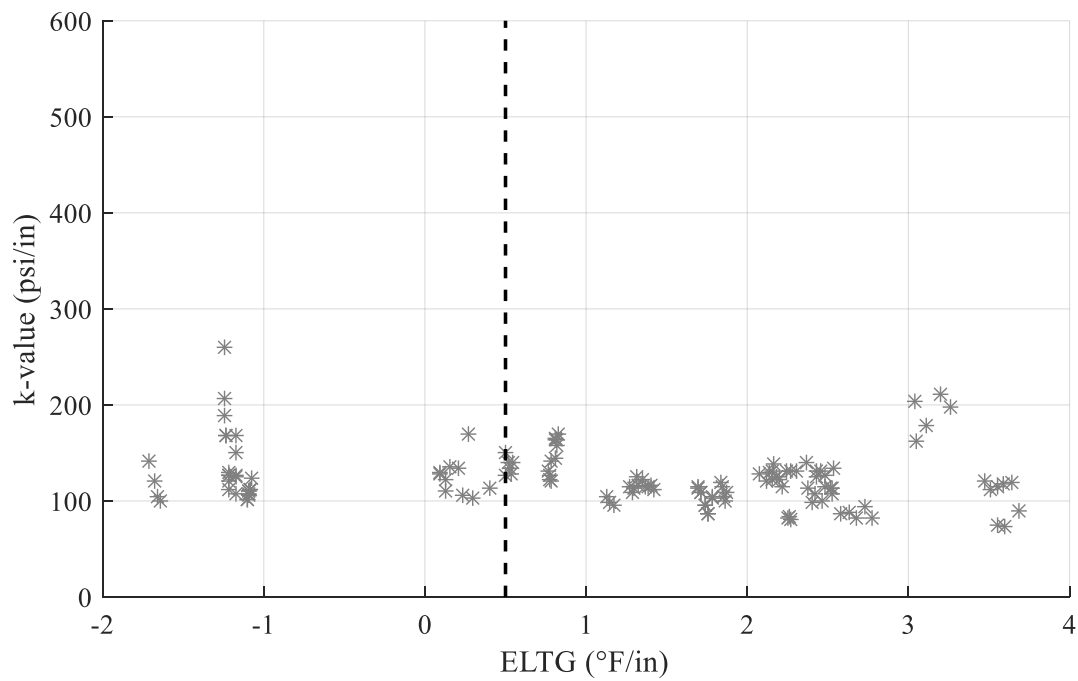


Figure 3.18. Backcalculated k-value (MnROAD Cell 6)

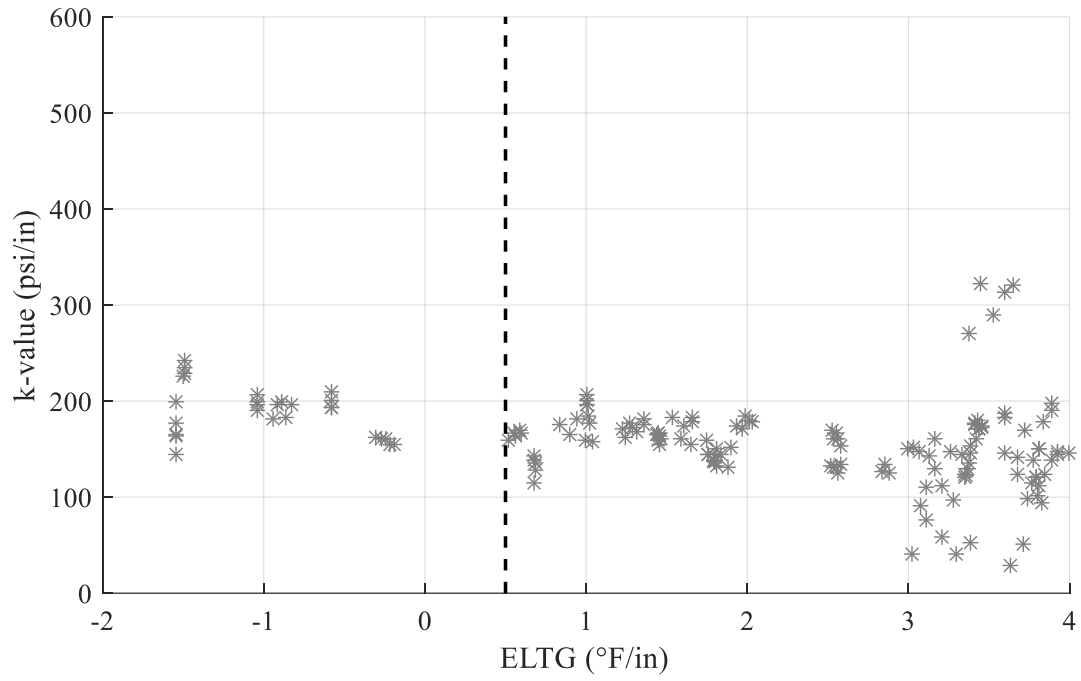


Figure 3.19. Backcalculated k-value (MnROAD Cell 7)

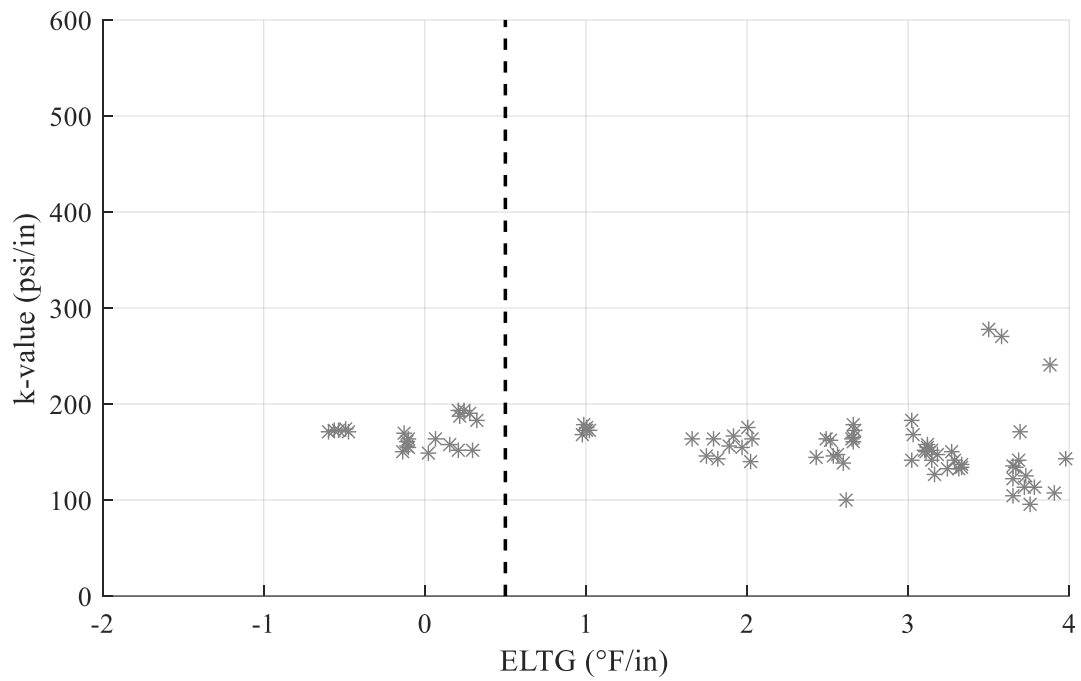


Figure 3.20. Backcalculated k-value (MnROAD Cell 8)

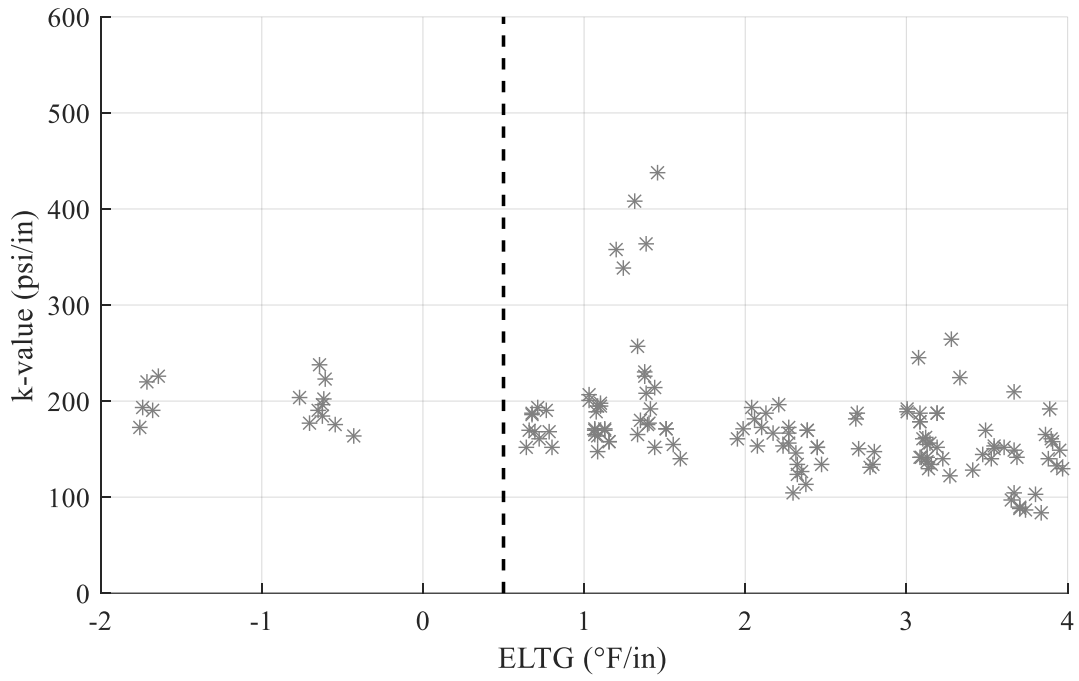


Figure 3.21. Backcalculated k-value (MnROAD Cell 9)

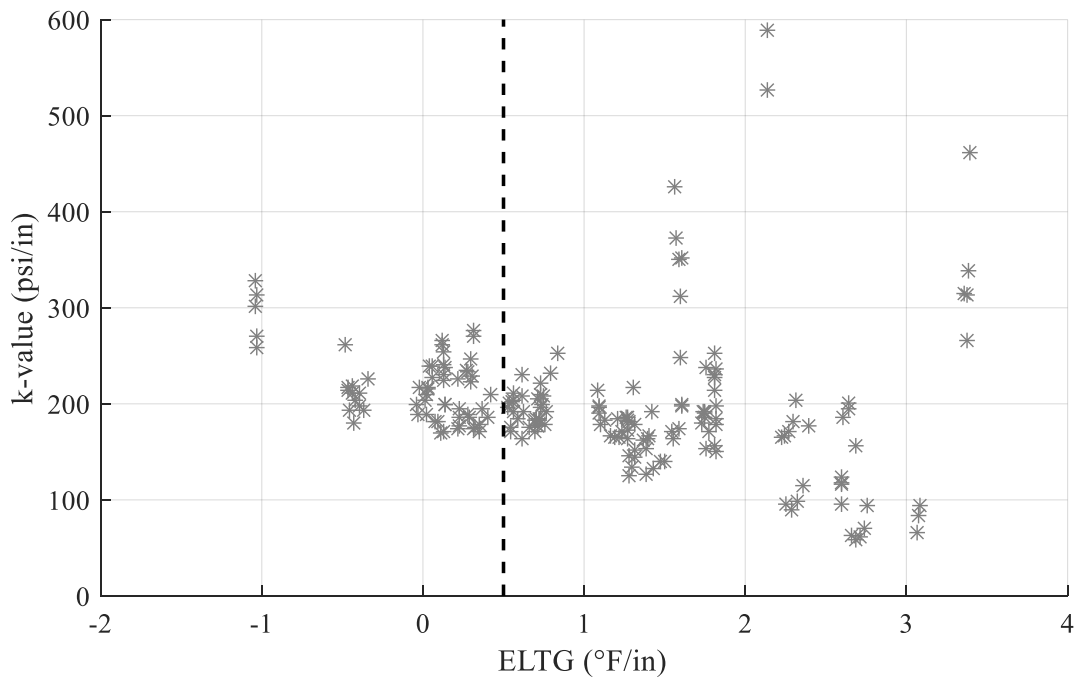


Figure 3.22. Backcalculated k-value (MnROAD Cell 10)

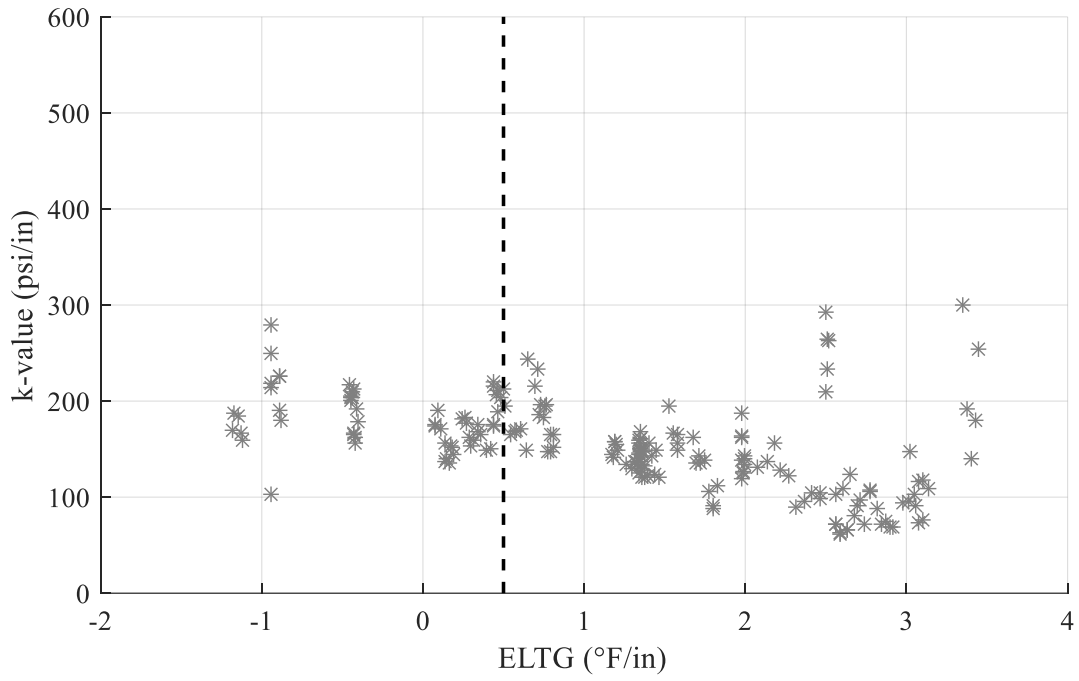


Figure 3.23. Backcalculated k-value (MnROAD Cell 11)

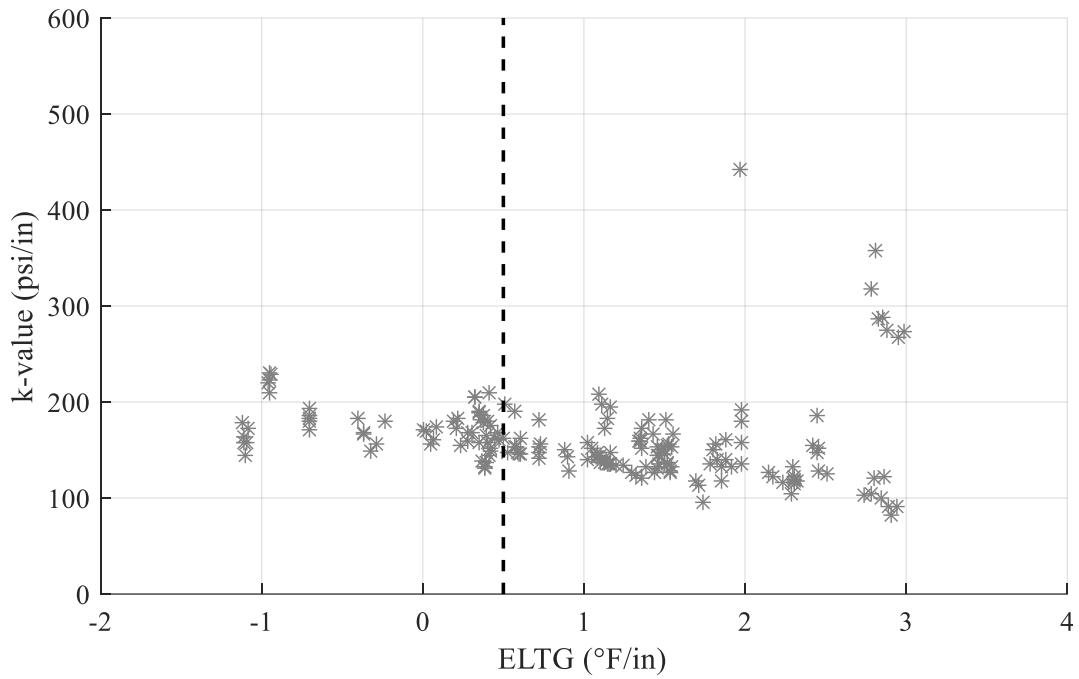


Figure 3.24. Backcalculated k-value (MnROAD Cell 13)

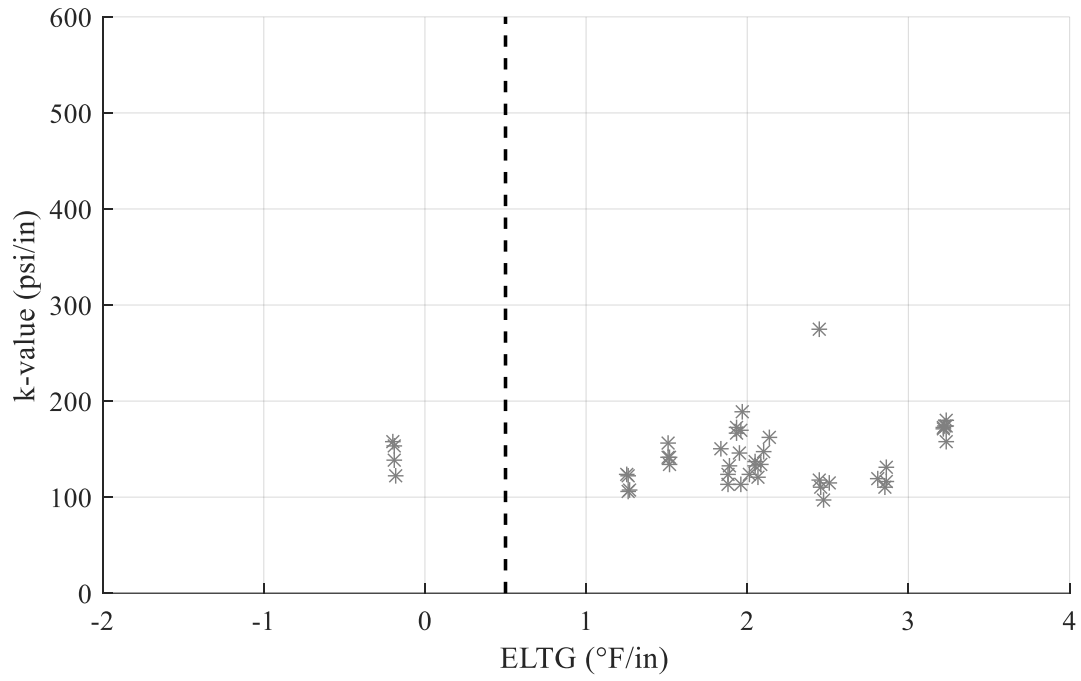


Figure 3.25. Backcalculated k-value (MnROAD Cell 52)

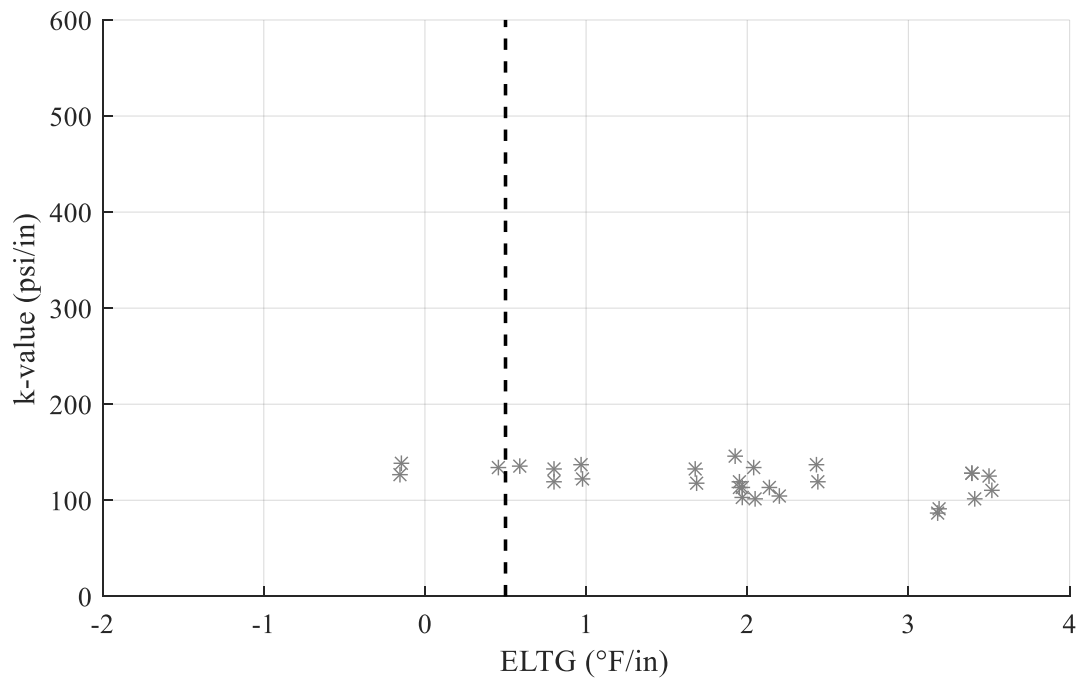


Figure 3.26. Backcalculated k-value (MnROAD Cell 53)

As observed in the field trials in Pennsylvania, the backcalculated k-value is affected less by negative ELTGs than by positive ELTGs. The measured ELTG is fairly consistent for most sections with an ELTG less than 0.5 °F/in, which is shown with a dashed line. Some sections show a significant decrease in ELTG with an increasing temperature gradient, while other sections do not. This is consistent with the previous research, which showed significant within day variation for some sections, but not for others.

To evaluate the effect of the true stiffness of the supporting layers on the relationship between ELTG and k, individual test dates, where more than one midslab pass was performed, were evaluated. For each test date at LTPP SMP sections where multiple test passes are conducted with a positive ELTG, a linear regression was fit between ELTG and backcalculated k-value from tests with a positive ELTG. The k-value intercept of this regression is an estimate of the k-value which would be backcalculated if the test were performed on an approximately flat slab, and therefore, indicative of the true stiffness of the subgrade. The slope of the regression is indicative of the magnitude of the effect slab curvature has on the backcalculated k-value. An example of one of these regressions can be seen in Figure 3.27. The individual regression lines are summarized in Figure 3.28, in order to show the relationship between the slope and intercept of the individual regressions.

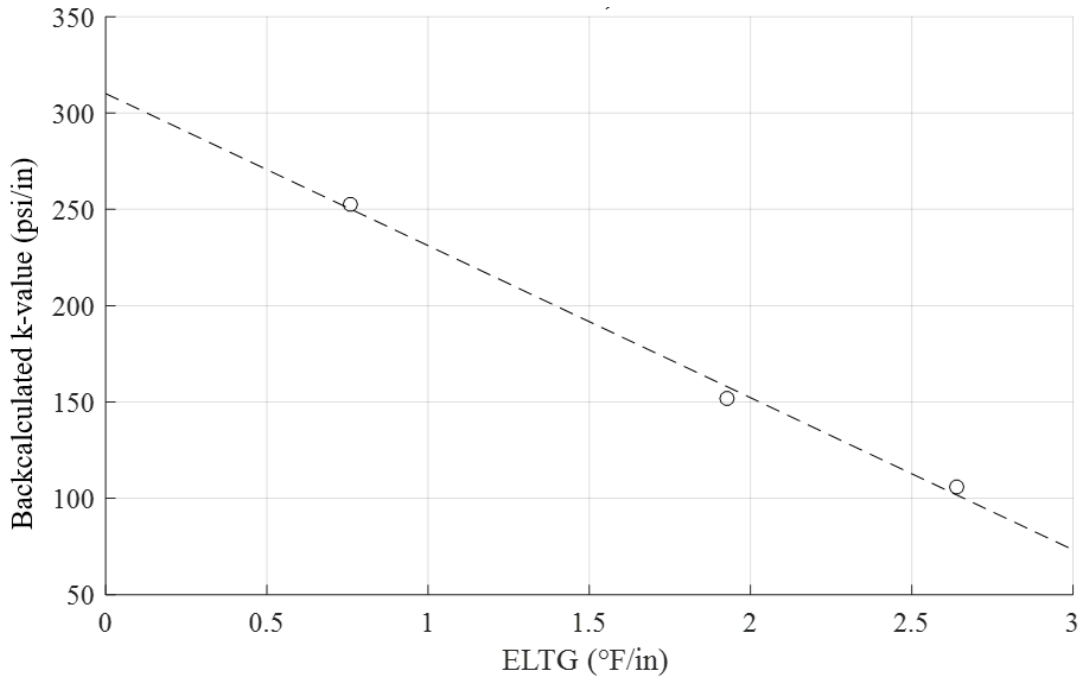


Figure 3.27. Example of daily linear regression (LTPP Section 04-0215, 7/22/1996)

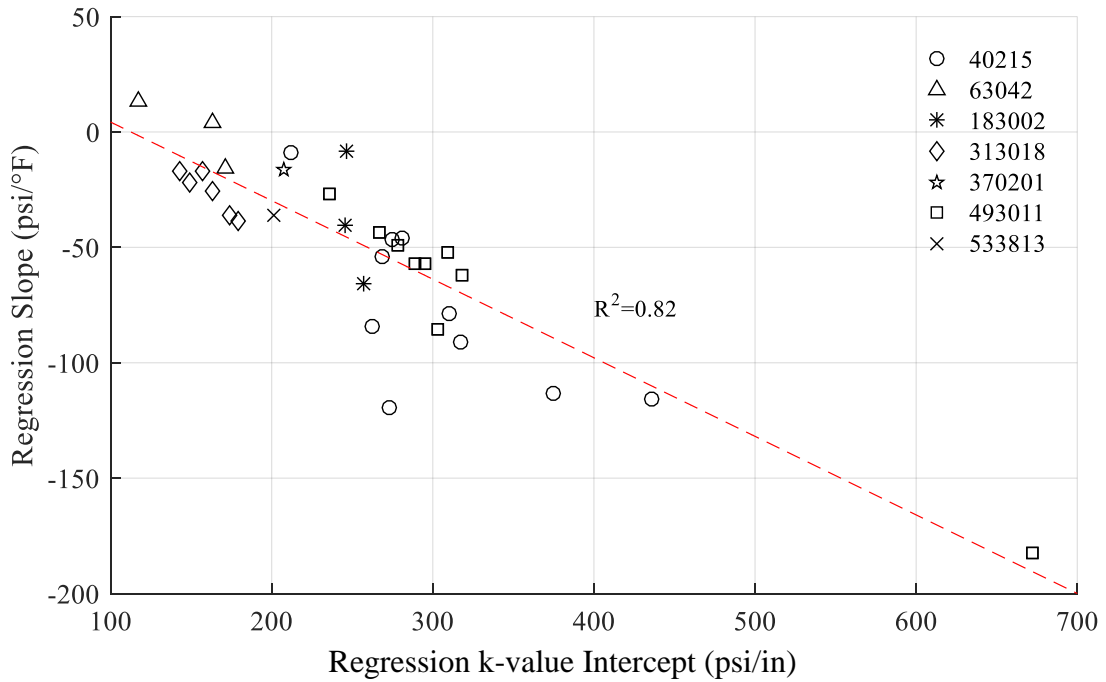


Figure 3.28. Comparison of regression slope to k-value intercept for FWD tests at LTPP SMP sections

There is a strong negative correlation between the slope of the daily regression model and the backcalculated k-value intercept of the regression model (y intercept in Figure 3.27). This supports the hypothesis that slab curvature has a larger effect on the backcalculated k-value when the “true” k-value is higher.

3.3 COMPUTATIONAL ANALYSIS

The effect of the “true” k-value and slab length on the relationship between the slab curvature and backcalculated k-value was further explored using a computational analysis. A 9-slab pavement system was modeled in the finite element method (FEM) program ABAQUS. The system consisted of two 12-ft wide driving lanes, and a 6-ft wide tied concrete shoulder. Three 15-ft long slabs were modeled for each lane and the shoulder. The pavement structure consists of:

- 10 in concrete slab, with a modulus of elasticity of 4 million psi
- 4-in thick asphalt stabilized base (bonded to the slab), with a modulus of elasticity of 300,000 psi
- A dense liquid foundation with a stiffness that varies between 150 and 750 psi/in.

Shear springs provide load transfer at the transverse and longitudinal joints. The stiffness of the shear springs was set so that the deflection load transfer efficiency (LTE) was 85% at the transverse joints, and 50% at the longitudinal joints, using the equations developed by Croveti (1994). Rotational springs are provided at transverse joints to simulate the rotational restraint provided by steel dowel bars. The stiffness of the rotational springs was determined using the classical solution proposed by Friberg (1940). Assuming infinitely stiff concrete, the rotational stiffness of a dowel bar should be equal to the flexural stiffness of the steel bar. However, due to a combination of

elastic behavior and damage of the concrete surrounding the dowel, the slope of the dowel at the joint will not be parallel to the centerline of the concrete at the face of the joint. This angle can be estimated using the Friberg solution. The stiffness of the springs was then solved so that combined rotation due to elastic bending of the bar and the slope of the bar at the face of the joint was equal to the rotation. For 1.5-in diameter steel dowel bars, in concrete with a dense liquid interaction between the bar and the concrete with a stiffness of 1.5 million psi/in, and a joint width of 0.25 in, the flexural stiffness of the springs is 385 kip-in/radian.

An FWD load is simulated as a static load applied to the middle of the center slab on an 11.8-in square loading area. A static load with a dynamic layer stiffness was used to match the pavement response models in the Pavement ME Design Guide (ARA Inc. 2004). The 16,000 lb load level, the highest nominal load level typically used on highway pavements, was used in this analysis to maximize the possibility that the load will force the stabilized base into contact with the dense liquid foundation. Deflections were recorded 0 in, 8 in, 12 in, 18 in, 24 in, 36 in, and 60 in from the middle of the load plate to simulate FWD sensors. A mesh convergence study was conducted, and convergence was achieved with 6 in x 6 in x 5 in 20 node quadratic brick elements with reduced integration on the loaded slab, and 12 in x 12 in x 10 in 20 node quadratic brick elements with reduced integration on the other slabs. The mesh was adjusted slightly to allow the boundaries of the load plate to correspond with element boundaries. The k-value of the dense liquid foundation was varied between 150 psi/in and 750 psi/in in 100 psi/in increments. For each k-value, the composite linear temperature gradient (CLTG) was varied between -2.5 °F/in and 5 °F/in in increments of 0.25 °F/in. The CLTG accounts for slab curvature due to transient temperature gradients (ELTG), built in curvature, and transient moisture gradients. The CLTG is typically considered to be approximately 1 °F/in less than the ELTG, but this can vary with the climate and

the mixture design. An analysis during the development of the Pavement ME indicated that the best fit between the measured and predicted distress occurs if a built in temperature difference of $-10\text{ }^{\circ}\text{F}$, equivalent to a gradient of $-0.8\text{ }^{\circ}\text{F}/\text{in}$ for a 10 in slab, or $-1\text{ }^{\circ}\text{F}/\text{in}$ for a 12 in slab. A previous analysis of the strain gauges at the SR-22 Smart found a built in temperature gradient of $-1.0\text{ }^{\circ}\text{F}/\text{in}$ for the restrained section, and $-1.58\text{ }^{\circ}\text{F}/\text{in}$ for the unrestrained section (Asbahan and Vandebossche 2011). An analysis at the Minnesota road research facility and SR-22 smart pavement found similar values for the built in temperature gradient (Alland and Vandebossche 2017). The concrete layer is assumed to have a unit weight of $145\text{ pounds}/\text{ft}^3$. Base layers were assumed to have a unit weight of $120\text{ pounds}/\text{ft}^3$. For each analysis, the k-value was backcalculated from the virtual FWD measurements using the closed form solution. The backcalculated k-value as a function of the CLTG and the “true” k-value can be seen in Figure 3.29.

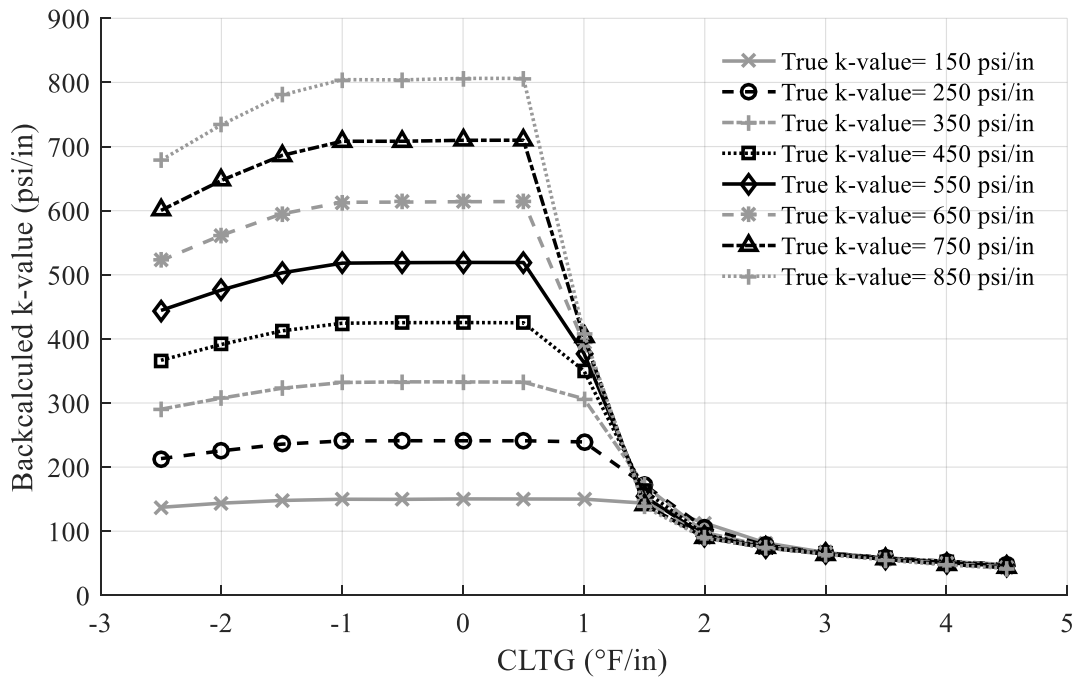


Figure 3.29. Computational analysis on the effect of true subgrade stiffness on the relationship between slab curvature and backcalculated k-value

When a negative CLTG is present, the closed form solution estimates k-values that are relatively close to the “true” k-value. This supports the assumption that k-values backcalculated from FWD tests with a negative ELTG, which is typically greater than the CLTG, provide a good estimate of the “true” k-value. The backcalculated k-value does appear to be affected by large negative CLTGs when the “true” k-value is high, but the effect is much less than for positive CLTGs. At large positive temperature gradients, CLTGs greater than 2 °F/in, the closed form solution estimates approximately the same k-value, regardless of the “true” k-value. If the “true” k-value is small, the backcalculated k-value is similar whether there is a positive or negative CLTG. Whereas, if the “true” k-value is large, there is a substantial difference between the backcalculated k-value at positive and negative CLTGs. This agrees with field data from the LTPP SMP sections, which showed that the relationship between slab curvature and backcalculated k-value depends on the “true” k-value.

In addition to the difference between the maximum and minimum backcalculated k-value, the value of CLTG at which slab curvature first begins to affect the backcalculated k-value is also a function of the “true” k-value. For soft foundations (“true” k-value=150 psi/in), the backcalculated k-value is not greatly affected by slab curvature until CLTG is greater than 1.5 °F/in. For a moderate foundation stiffness (“true” k-value=250-350 psi/in), the backcalculated k-value is significantly affected by slab curvature at a CLTG of 1 °F/in. For stiff foundations, (“true” k-value>450 psi/in), the backcalculated k-value is significantly affected by slab curvature at a CLTG of 0.5 °F/in. The CLTG at which the backcalculated k-value begins to be affected by slab curvature likely corresponds with the middle of the slab having greatly reduced support.

The rate at which the backcalculated k-value decreases with increasing CLTG depends on the “true” k-value. For stiff dense liquid foundations, the backcalculated k-value decreases rapidly

once a gap occurs between the middle of the slab and the supporting layers. For softer dense liquid foundations, the decrease in backcalculated k-value with increasing CLTG is much more gradual. As an illustrative example, the backcalculated k-value with a CLTG of 1.5 °F/in, is slightly greater for a virtual structure with a “true” k-value of 250 psi/in, than for a virtual structure with a “true” k-value of 750 psi/in, indicating the rapid decrease in backcalculated k-value for higher values of the “true” k-value. This behavior is consistent with the field trials in Pennsylvania. In these trials, the backcalculated k-value decreased rapidly with increasing ELTG at the I-79 test section, which has a very high “true” k-value, and decreased more gradually with increasing positive ELTG at the SR-22 sections which have a lower “true” k-value.

The effect of slab length on the relationship between CLTG and backcalculated k-value was also explored using a computational analysis. This analysis is similar to the computational analysis on the “true” stiffness of the k-value, except the “true” k-value is held constant at 450 psi/in, and three different slab lengths are considered, 15 ft and 20 ft. The results of this analysis can be seen in Figure 3.30.

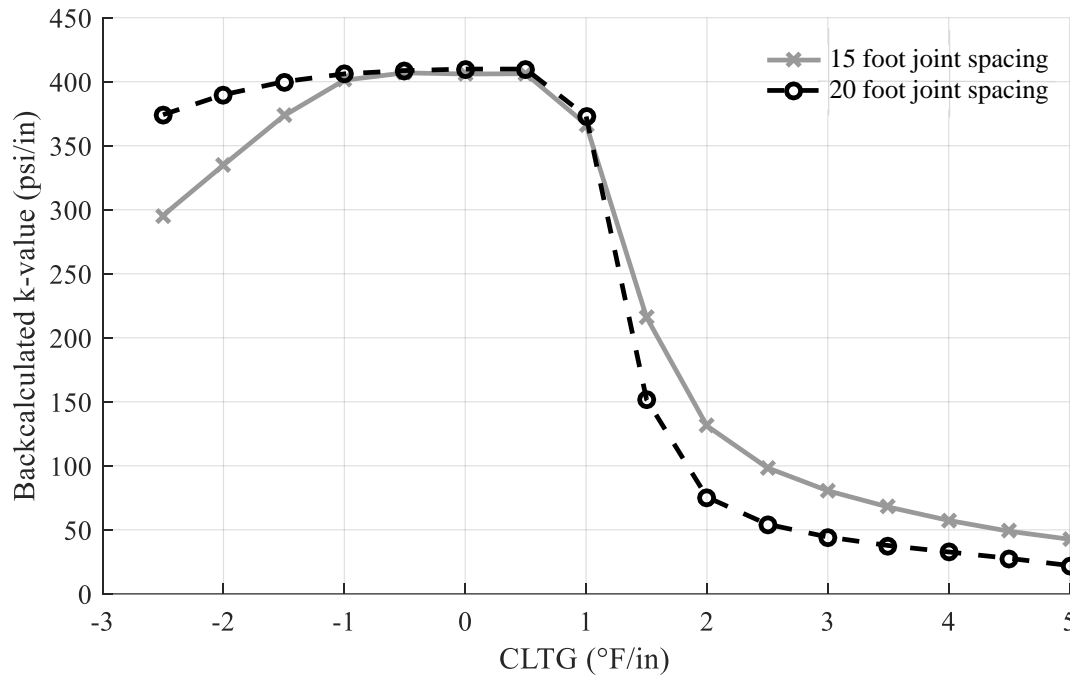


Figure 3.30. Computational analysis of the effect of joint spacing on the relationship between CLTG and backcalculated k-value

This analysis shows that slab length does not have a large effect on the backcalculated k-value of curled and warped slabs. However, the backcalculated k-value decreases more rapidly with increasing CLTG with a slab length of 20-ft, than with a 15-ft slab length.

The effect of restraint due to the base on the relationship between CLTG and the backcalculated k-value was also explored using a computational analysis. Three different structures were analyzed. Like the other computational analyses, each structure consists of a 10 in thick concrete slab on a 4-in asphalt stabilized base, with a k-value of 450 psi/in. The elastic modulus of the layers varies between the structures. The first structure has a modulus of elasticity of the concrete (E_{conc}) of 4.5 million psi, and a modulus of elasticity of the asphalt base E_{base} of 100,000 psi. The second structure has an E_{conc} of 4 million psi, and an E_{base} 300,000 psi. The third

structure has an E_{conc} of 3 million psi and an E_{base} of 780,000 psi. These values were chosen such that the three structures have equivalent composite plate stiffnesses. The backcalculated k-value for these structures can be seen in Figure 3.31.

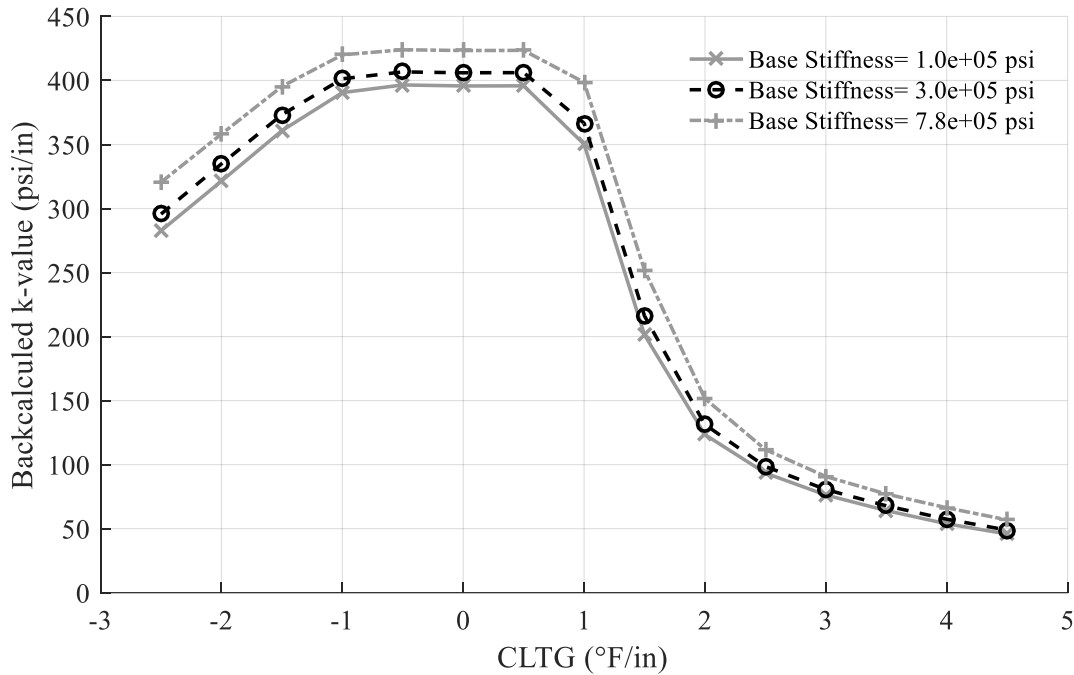


Figure 3.31. Computational analysis of the effect of stabilized base stiffness on the relationship between CLTG and backcalculated k-value

Altering the makeup of the structure, with the same plate stiffness, has only a minor effect on the backcalculated k-value. These differences are likely due to differences in compression of the base layer, a deviation from the assumption that the pavement behavior can be described by plate theory. The structure with the stiffest base has the highest backcalculated k-value. The stiffness of the base does not appear to affect the relationship between CLTG and backcalculated k-value. It should be noted that all joints were assumed to propagate through the base layer. If the joint does not

propagate through the base layer, the stiffness of the base may affect the relationship between CLTG and backcalculated k-value.

This indicates that the differences between the rate at which the backcalculated stiffness decreases with increasing ELTG, between I-79 and SR-22, is likely primarily due to the differences in “true” k-value, and not the variation in slab length or restraint differences from the base.

3.4 PAVEMENT ME SENSITIVITY ANALYSIS

From the analysis of field data and the computational analysis, it is clear that slab curvature has a large effect on the backcalculated k-value estimated from FWD testing, especially with a high “true” k-value. However, it is important to consider whether the inaccuracy in backcalculating the k-value due to slab curvature influences pavement design and maintenance decisions. Therefore, a sensitivity analysis was developed that explored the effect of backcalculated k-value on the predicted life a concrete pavement following a CPR, using the CPR module in Pavement ME. The analysis results are also applicable to the design of a bonded concrete overlay of concrete. The new unbonded overlay (UBOL) design procedure, developed for Pooled Fund Study TPF 5-269 is not sensitive to k-value (Sachs 2016).

The sensitivity analysis was conducted using Pavement ME Version 2.3.1, with national default calibration coefficients (Sachs et. al. 2015). The program defaults were used for the traffic distribution, gradation of the subgrade and subbase, and PCC mixture properties. The design properties considered in the sensitivity analysis can be seen in Table 3.1.

Table 3.1. Sensitivity analysis inputs

General	
Design Type	CPR
Pavement Type	JPCP
Reliability (%)	90
Dowel Diameter (in)	1.5
Climate	
Climate Station	Allegheny County Airport, West Mifflin, PA
Traffic	
ADTT	10,000
Lane Distribution (%)	90
Directional Distribution (%)	50
Base/Subgrade Material Properties	
Base Type	Granular (Crushed Stone)
Base Thickness (in)	4
Base Resilient Modulus (psi)	30,000*
Subgrade Soil Type	A-2-4
Subgrade Resilient Modulus (psi)	16,500*
Concrete Properties	
28-Day Modulus of Rupture (MOR)(psi)	690
28-Day Elastic Modulus (psi)	4.2 million
PCC CTE ($\mu\epsilon/^\circ\text{F}$)	5.5
Sensitivity Parameters	
PCC Thickness (in)	8, 12
Joint Spacing (ft)	15, 20
k-value (psi/in)	100-500 (50 psi/in increments)
<i>*The Pavement ME software scales these values to achieve a backcalculated k-value</i>	

The pavement age at which the pavement reaches the prescribed failure criterion (0.12 in faulting, 10% slabs cracked) was calculated for each pavement structure. The results of the sensitivity analysis can be seen in Figures 3.32 to 3.35. It should be noted that, with the given conditions, the lowest curve on the plot would govern design life. Additional curves are provided to indicate how the design procedure would behave, if that particular mechanism was controlling. Pavement ME only provides the failure criteria for the critical cracking mechanism. Therefore, only the critical cracking mechanism is shown for each test case.

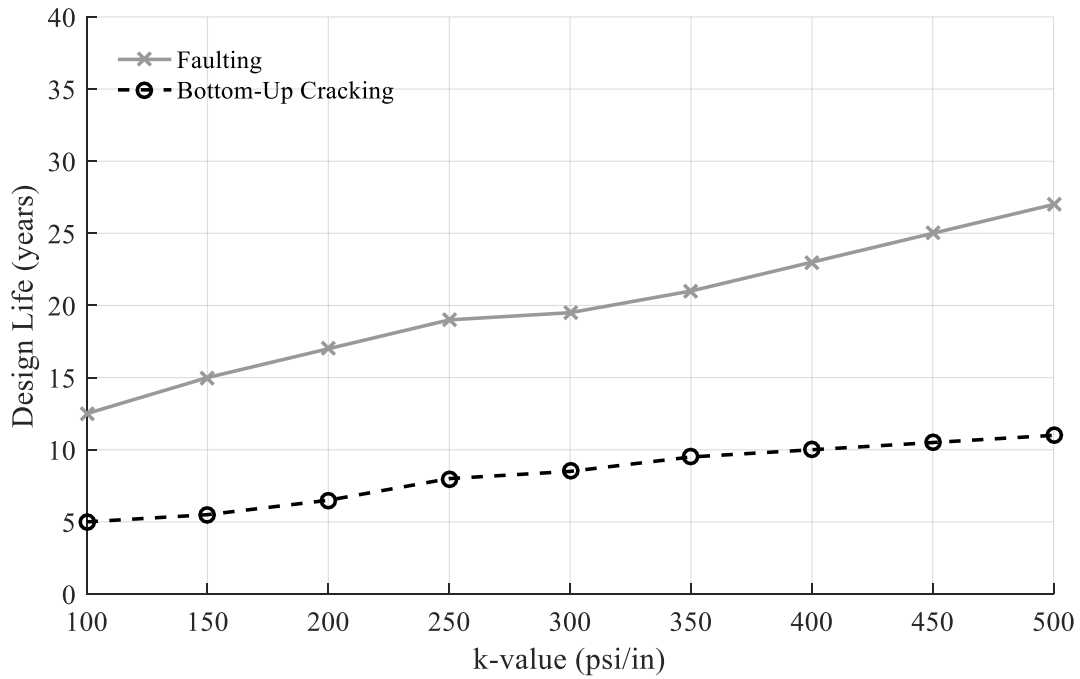


Figure 3.32. Sensitivity of Pavement ME distress predictions to k-value (8 in thick slab, 15-ft joint spacing)

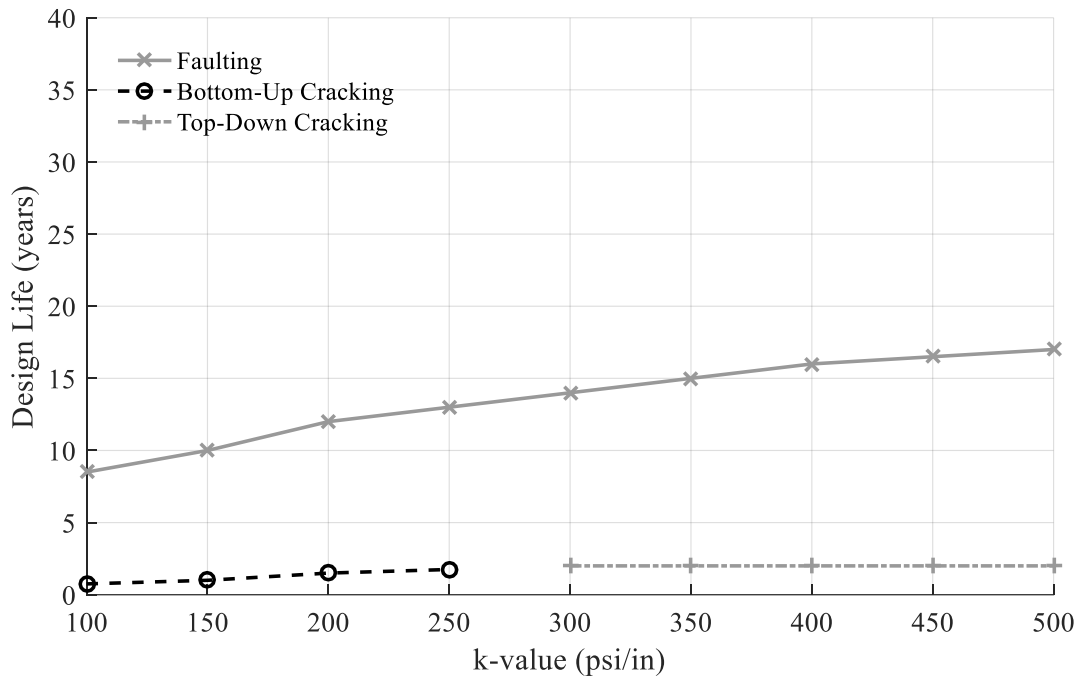


Figure 3.33. Sensitivity of Pavement ME distress predictions to k-value (8 in thick slab, 20-ft joint spacing)

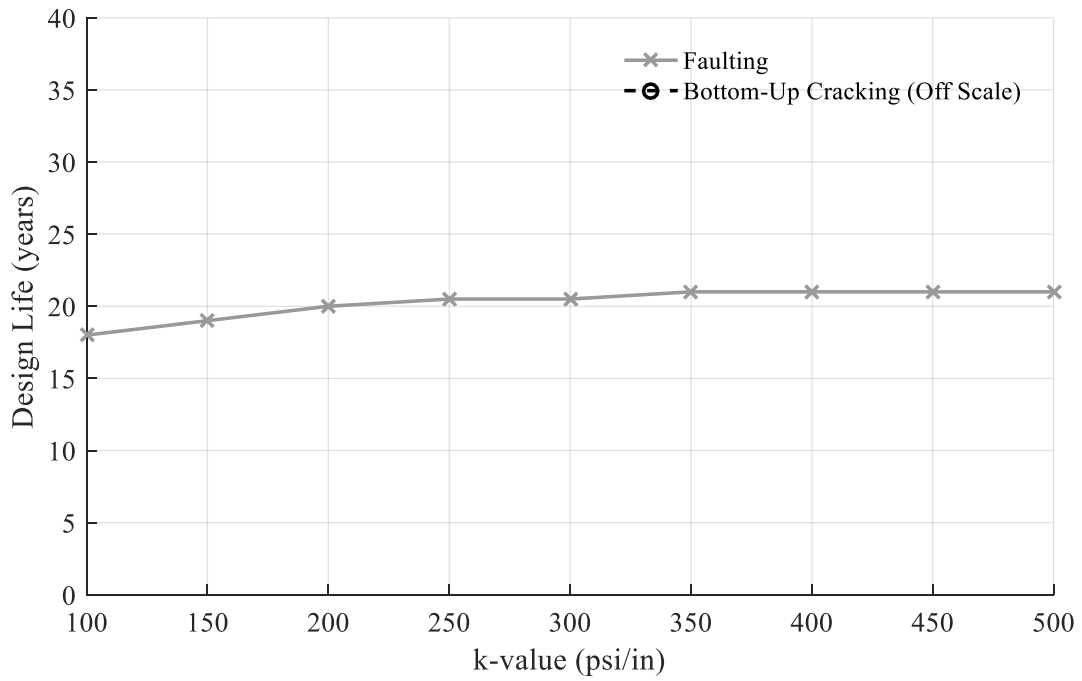


Figure 3.34. Sensitivity of Pavement ME distress predictions to k-value (12 in thick slab, 15-ft joint spacing)

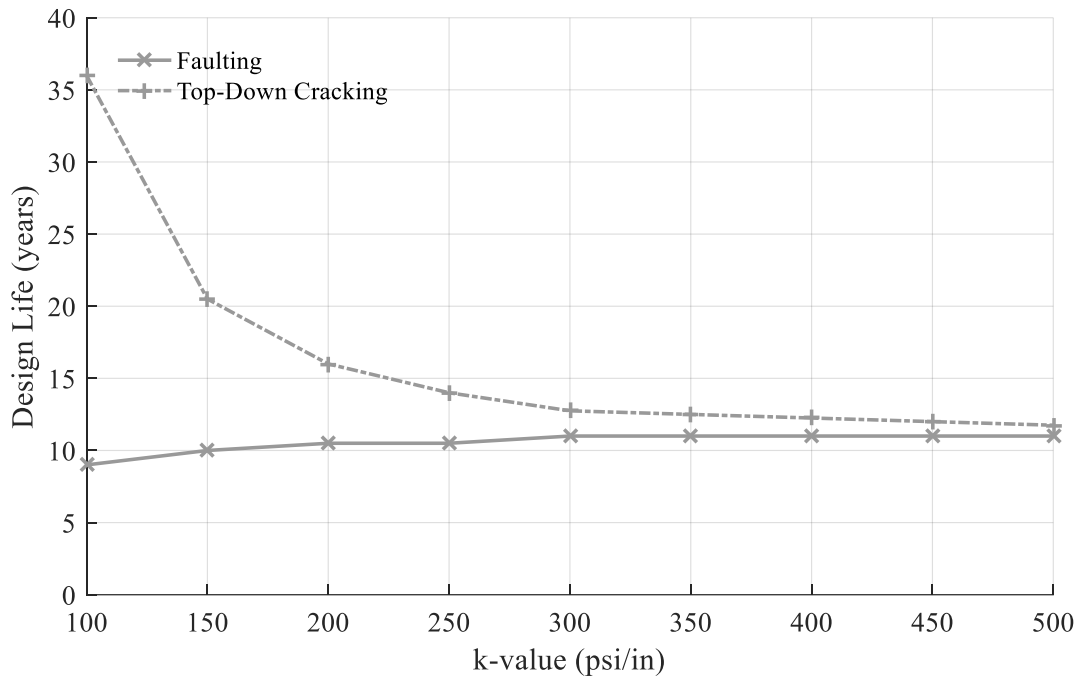


Figure 3.35. Sensitivity of Pavement ME distress predictions to k-value (12 in thick slab, 20-ft joint spacing)

For the pavements with a typical joint spacing, 15 ft, and a thin slab, 8 in (Figure 3.32), Pavement ME predicts that the design life will be controlled by bottom-up cracking, regardless of the k-value. The predicted performance life due to bottom-up cracking is sensitive to k-value. The software predicted design life for a pavement with a k-value of 500 psi/in (12 years) is three times as long as the predicted design life with a k-value of 100 psi/in (4 years). This is due to increased stress under the wheel load with a decreased k-value. The faulting prediction for this structure is also sensitive to k-value. This failure mode does not control the design life, but might if higher performance concrete is used. The software-predicted faulting design life for a pavement with a k-value of 500 psi/in (27 years) is over twice as long as the software-predicted faulting life for a pavement with a k-value of 100 psi/in (13 years). A lower k-value will lead to increased deflection

in the corner of the slab due to vehicle loading. This results in higher differential energy at the transverse joint, and consequently higher faulting predictions.

For a pavement with a typical joint spacing, 15 ft, and thicker slab, 12 in (Figure 3.34), faulting controls the design. The software predicts nearly infinite fatigue life for all k-values in this scenario for both top down and bottom up cracking. The predicted faulting design life for this structure is not very sensitive to k-value. The predicted faulting design life for a pavement with a k-value of 150 psi/in (21 years) is only 14% longer than for a pavement with a k-value of 100 psi/in (18 years). The deflection of the 12-in slab is less dependent on the k-value than the deflection of the 8-in slab, as the thicker slab is able to spread the load out over a larger tributary area of subgrade.

For pavements with a long joint spacing, 20 ft, the controlling failure mode depends on the k-value. For a pavement with a 20-ft joint spacing, and a thin slab, 8 in thick (Figure 3.33), the critical failure mode is bottom up cracking, if the k-value is less than 300 psi/in, and top down cracking, if k-value is greater than 300 psi/in. The service life is significantly shorter for the 8-in slab with a 20-ft joint spacing, than the 8-in slab with a 15-ft joint spacing, due to the additional curling stresses. With large k-values, the stiff foundation prevents the slab from sinking into the foundation, leading to higher tensile stresses at the top of the slab, when negative CLTGs are present.

For pavements with a long joint spacing, 20 ft, and a thick slab, 12 in, (Figure 3.35) the design is controlled by faulting. Like the 12-in slab with a 15-ft joint spacing, the predicted faulting service life is not very sensitive to k-value. At high k-values, greater than 300 psi/in, the predicted service lives due to faulting and top-down cracking are similar. Top-down cracking is not sensitive to k-value, if the k-value is greater than 300 psi/in. If the k-value is less than 300 psi/in, top-down

cracking is very sensitive to the k-value, with a smaller k-value resulting in less cracking. This is due to a smaller k-value allowing the slab to “sink-in” to the foundation, reducing the portion of the slab with reduced support under a negative temperature gradient.

The sensitivity analysis indicates that the variation in backcalculated k-value can have a significant effect on pavement rehabilitation decisions, especially with a thin pavement or longer joint spacing. Field data and a computational analysis has shown that, using current backcalculation techniques, slab curvature can have a large effect on the backcalculated k-value. Therefore, a backcalculation technique that can account for curling and warping of the slab can provide valuable information to pavement engineers.

3.5 BACKCALCULATION FOR CURLED AND WARPED SLABS

Some previous research has been performed on developing a backcalculation procedure for curled and warped concrete slabs. A spreadsheet based procedure has been developed to backcalculate the concrete elastic modulus of curled and warped slabs, but it did not consider the k-value (Ye 2017). However, validation of the procedure revealed that, while the bias in backcalculated k-value due to slab curvature was decreased by using the procedure instead of traditional backcalculation methods, the random variability increased. Another procedure has been proposed, which uses the results of FWD testing at two test locations, midslab and the corner of the slab, as inputs into an ANN that can backcalculate the CLTG. The measured ELTG can then be subtracted from the CLTG to estimate the long-term portion of the CLTG. The CLTG may also be used in the future to backcalculate the k-value and elastic modulus of the slab, while accounting for slab curvature (Bayrak and Ceylan 2009). This procedure is promising, as testing at these two locations at similar

ELTG conditions will ensure the slab is in contact with the foundation for at least one of the test locations. However, there are a few drawbacks to this solution:

- The solution requires testing to be performed at midslab and in the corner of the slab at similar values of ELTG. These tests cannot be performed on the same “pass.” Therefore, this can be difficult to accomplish without greatly limiting the number of slabs that can be tested in a day.
- The solution can be heavily influenced by erosion in the corner of the slab.
- The solution can be influenced by interaction between the slab and shoulder. The interaction between the slab and shoulder is not typically measured during FWD testing.
- The accuracy of the solution can be decreased by the assumption that the subgrade layer acts as a dense liquid. If two computational pavement models, one with a dense liquid foundation and one with an elastic solid foundation, calculate equivalent deflections when loaded at midslab, the elastic solid foundation will calculate less deflection in the corner of the slab. In reality, most base and subgrade materials fall somewhere between a dense liquid and an elastic solid.

While some research has been performed on backcalculation of layer properties for rigid pavements with curled and warped slabs, no method is currently available that backcalculates the k-value with adequate accuracy. This research attempts to develop such a method, as described below.

3.5.1 Forward Calculation

First, a large database of “forward calculation” analyses is required. These forward calculation analyses calculate the deflection at the FWD sensor locations given the structural properties of the

pavement, environmental conditions, and the applied load. A computational FEM model, developed in ABAQUS, was used for forward calculation. This computational model is similar to the computational model used in the sensitivity analysis shown in Figures 3.32 to 3.35. The design features of the computational model were selected using a Monte-Carlo simulation, randomly sampling from uniform distributions spanning the ranges shown in Table 3.2.

Table 3.2. Forward calculation parameter ranges

Design Parameter	Range
Slab Thickness (in)	6 to 16
Base Thickness (in)	3 to 8
Base Elastic Modulus (psi)	50,000 to 500,000
Dowels (indicator variable)	True or False
Shoulder (indicator variable)	True or False
CLTG (°F/in)	-2.5 to 4
LTE (%)	Doweled: 70 to 90, Undoweled: 30 to 99
Joint Spacing (ft)	12 to 20
Lane Width (ft)	12 to 15
k-value (psi/in)	100-850

The base is modeled as a stabilized base, fully bonded to the slab for all analyses. However, the base and slab layer act as a composite layer. Therefore, the analysis can be used for pavements with granular bases, with the slab and base layer in the computational model representing the stiffness of the slab, and the k-value including the granular layer. The test location is located at the center of the travel lane, located 6 ft from the centerline longitudinal joint, even if a widened lane was present in the analysis. A total of 14,143 analyses were conducted sampling from the Monte-Carlo simulation. These analyses can then be used to train a backcalculation procedure.

3.5.2 ANN Backcalculation of k-value Using Midslab Testing

A possible solution for accounting for slab curvature during backcalculation is to utilize an ANN. ANNs have previously been used to perform backcalculation without considering the temperature gradient (Bayrak and Ceylan 2009; Khazanovich and Roesler 1997).

The inputs for the ANN are as follows:

- Normalized 16000 lb deflection beneath the load plate (δ_0)
- Normalized 16000 lb deflection 3 ft. from the load plate (δ_{36}). This deflection sensor was chosen because the mean radius of relative stiffness in the training dataset is 36 in, with a standard deviation of 9 in.
- The normalized area parameter (AREA). The area of the deflection basin, divided by the deflection under the load plate. This parameter is closely related to the radius of relative stiffness (Ioannides et al. 1989).
- CLTG
- Joint spacing
- Slab width
- Presence of dowels (indicator variable)
- Presence of a tied shoulder (indicator variable)

The ANN architecture considers two hidden layers, each with 10 nodes, for a total of 211 degrees of freedom. The data was divided into a training set, and a test set, with 80% of the data in the training set and 20% of the data in the test set. A total of five ANNs were trained on the training set, using the Bayesian regularization training algorithm. This algorithm uses likelihood methods to estimate values of weight decay parameters to improve generalization of the model (MacKay 1992). The Bayesian regularization training algorithm does not require a validation set. Averaging multiple ANNs reduces the variance in ANN training caused by local minima (Hastie et al. 2009). For the remaining 20% of the data, the test set, the backcalculated k-value was estimated using all

five ANNs and was averaged to achieve a single estimate of the k-value, which was then compared to the “true” k-value. The resulting estimates can be seen in Figure 3.36.

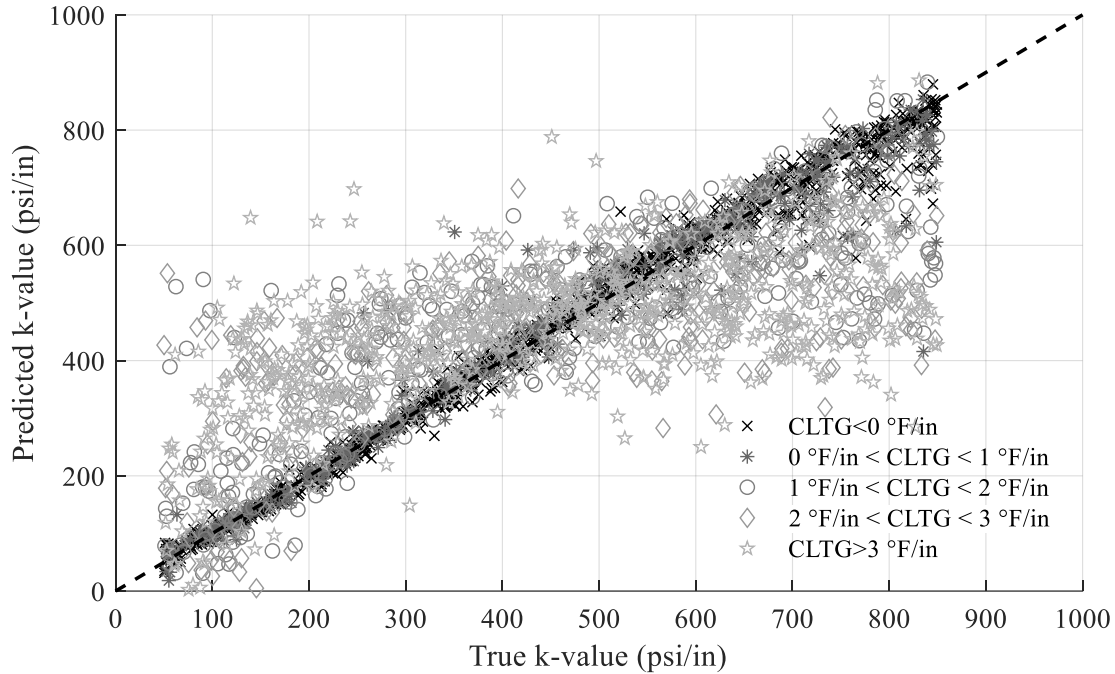


Figure 3.36. Performance of ANN trained using midslab data on test set

The performance of the ANNs appears to be poor, with an overall R^2 of 0.67. A closer investigation of Figure 3.36 indicates that with a CLTG less than 1 °F/in, the ANN performs very well. However, the ANN has very poor performance on tests with large positive CLTGs. With these large values of CLTG, the ANN attempts to minimize MSE by estimating values near the mean value in the database, 450 psi/in. This indicates that testing at midslab with a CLTG greater than 1 °F/in may not provide sufficient information to backcalculate the k-value, even if the CLTG is accounted for in the backcalculation process. This is consistent with Figure 3.29, which shows that the “true” k-value has very little effect on the backcalculated k-value, using traditional backcalculation methods, when the CLTG is greater than 1 °F/in.

This is likely due to the minimal influence that the k-value has on the deflection basin, when CLTG is greater than 1 °F/in. The influence of the “true” k-value on the deflection basin can be accomplished using the concept of marginal R^2 in ANNs (Giam and Olden 2015). In this procedure, two versions of ANNs are trained to predict the parameters describing the deflection basin, δ_0 , δ_{36} , and AREA. The predictors used for these ANNs are as follows:

- Composite plate stiffness of the slab and base layer
- Joint spacing
- Slab width
- Presence of dowels (indicator variable)
- Presence of a tied shoulder (indicator variable)
- k-value

In the first set of ANNs, the correct values are used for all of the inputs. In the second set of ANNs, the k-values are randomly permuted, breaking any association between k-value and the deflection basin, therefore reducing the R^2 value in the test set. The difference in the test set R^2 values between the first and the second set of ANNs, is referred to as the marginal R^2 , and is an indicator of the importance of k-value in forward calculating the parameters that describe the deflection basin.

The marginal R^2 was calculated for each of the three parameters describing the deflection base, δ_0 , δ_{36} , and AREA, for three different ranges of CLTG:

- $CLTG < 1$ °F/in
- 1 °F/in $< CLTG < 3$ °F/in
- $CLTG > 3$ °F/in

Similar to the backcalculation procedure shown in Figure 3.36, for each of the nine analyses, five ANNs were trained and averaged. Test set R^2 values for the ANNs, including the correct k-value,

are all greater than 0.95, indicating that if the k-value is included in the analysis, the ANNs can accurately predict the parameters describing the deflection basin for all CLTG ranges. The resulting marginal R^2 values can be seen in Table 3.3.

Table 3.3. Marginal R^2 values showing the importance of k-value to forward calculation

	CLTG<1 °F/in	1 °F/in<CLTG<3 °F/in	CLTG>3 °F/in
δ_0	0.33	0.28	0.05
δ_{36}	0.52	0.39	0.03
AREA	0.25	0.07	0.02

The marginal R^2 values confirm that with large CLTG values, greater than 3 °F/in, the k-value has minimal effect on the deflection basin. Therefore, it is not possible to backcalculate the k-value solely from midslab testing with large positive values of CLTG. With smaller positive CLTG values, between 1 °F/in and 3 °F/in, the k-value does appear to have some influence on calculating the deflection basin parameters, but much less influence than when CLTG is less than 1 °F/in. This may indicate that the k-value does affect the deflection basin of some structures, but not for others. For example, Figure 3.29 shows that with an ELTG of 1.25 °F/in, a change in “true” k-value from 150 psi/in to 350 psi/in likely affects the deflection basin, but a change in “true” k-value from 550 psi/in to 750 psi/in likely does not.

As a result, it is not possible to accurately backcalculate the k-value solely from testing at midslab when a CLTG greater than 1 °F/in is present. As previously stated, Bayrak et al. (2007) proposed backcalculating the CLTG using FWD testing at midslab and the corner of the slab at similar ELTGs. A similar procedure could be used to backcalculate the k-value. However, as

previously stated, there are several issues with using FWD testing at the corner of the slab for backcalculation of the k-value.

3.5.3 ANN Backcalculation of k-value Using Midslab and Transverse Joint Testing

A possible improved solution is to utilize testing at midslab and testing at mid-lane on the leave side of the transverse joint for backcalculation. This configuration allows the two tests on each slab to be performed in sequence (on the same “pass”) and at nominally the same temperature gradient. In addition, the effect of shear transfer through the subgrade and a tied shoulder are less important for testing at mid-lane adjacent to the transverse joint than they are for testing in the corner of the slab. Finally, erosion in the corner of the slab is unlikely to reach the middle of the lane at the transverse joint. The proposed test plan can be seen in Figure 3.37.

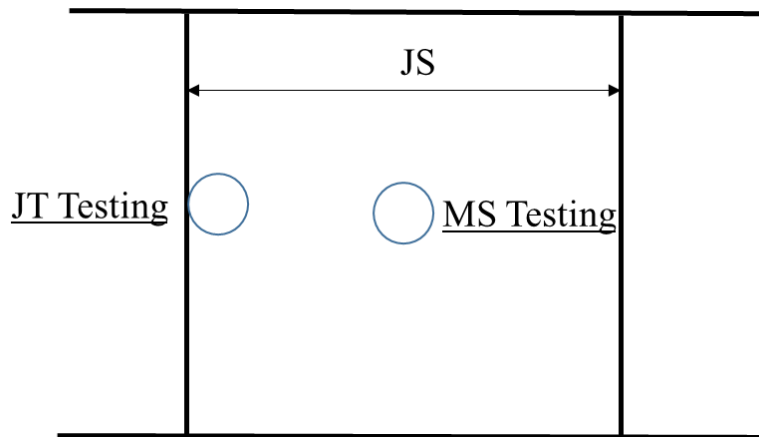


Figure 3.37. Proposed test plan

The forward calculation database was expanded to include testing at mid-lane on the leave side of the transverse joint. A set of five ANNs were trained with the same inputs as the previously described backcalculation database, but with the additional inputs measured from testing adjacent to the joint:

- Measured LTE
- Deflection at the center of the load plate ($\delta_{0,JT}$)
- Deflection 36 in from the load plate ($\delta_{36,JT}$)
- Normalized area parameter ($AREA_{JT}$)

The “true” k-value versus the backcalculated k-value can be seen in Figure 3.38.

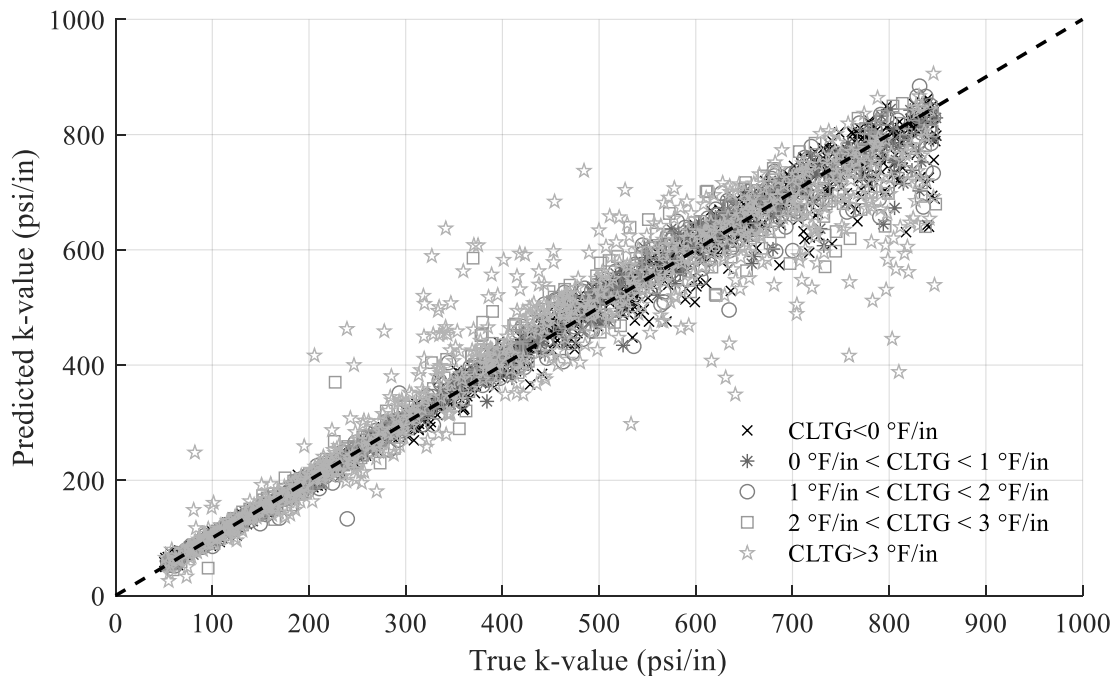


Figure 3.38. Performance of proposed backcalculation method on test set (CLTG is an input)

The prediction is much improved over the prediction using only mid slab testing, with an R^2 of 0.96. A large proportion of the error occurs for sections with a CLTG greater than 3 °F/in. This

loss of accuracy in predicting computational data is likely due to the reduced slab support at mid-lane adjacent to the transverse joints. Analysis of the tests in the LTPP database found that 97.5% of testing occurred with an ELTG < 3 °F/in. The “long-term” portion of the CLTG is nearly always negative due to drying shrinkage. Therefore, it is likely that even a larger portion of tests occur with a CLTG < 3 °F/in. If tests with a CLTG greater than 3 °F/in are not considered, the R² of the model improves to 0.98.

One difficulty in utilizing this model is that it requires the CLTG as an input. While the ELTG can be calculated from a measured or estimated temperature profile, the “long-term” portion of the CLTG is very difficult to estimate. The AASHTO Pavement ME Design Guide uses a “long-term” temperature difference of 10 °F. This corresponds to a long-term portion of the CLTG equal to 1 °F/in for a 10 in slab, or 0.9 °F/in for a 12 in slab. However, this value was selected to provide the best fit between the measured and predicted distress, and is not based on a physical estimate of long-term curvature (ARA 2004). A model was developed to estimate the built-in curl in Pennsylvania (Nassiri and Vandebossche 2012). However, this does not include the effect of short and long-term drying shrinkage, and the effect of built-in curl is likely reduced due to early age creep. Predicting moisture movement, and therefore curvature due to drying shrinkage, is very difficult, and a generalized solution is not available.

To minimize this potential source of error, a set of ANNs, based on the proposed test strategy, was trained such that it “learns” to account for the CLTG without it being explicitly defined. The ANN can recognize that if the midslab deflection is greater than the deflection at the joint, a positive CLTG is likely present. If the midslab deflection is much lower than the deflection at the joint, then a negative CLTG is likely present. A set of five ANNs were trained using similar

inputs to the model shown in Figure 3.38, but without using CLTG as an input. The “true” k-value versus the backcalculated k-value can be seen in Figure 3.39.

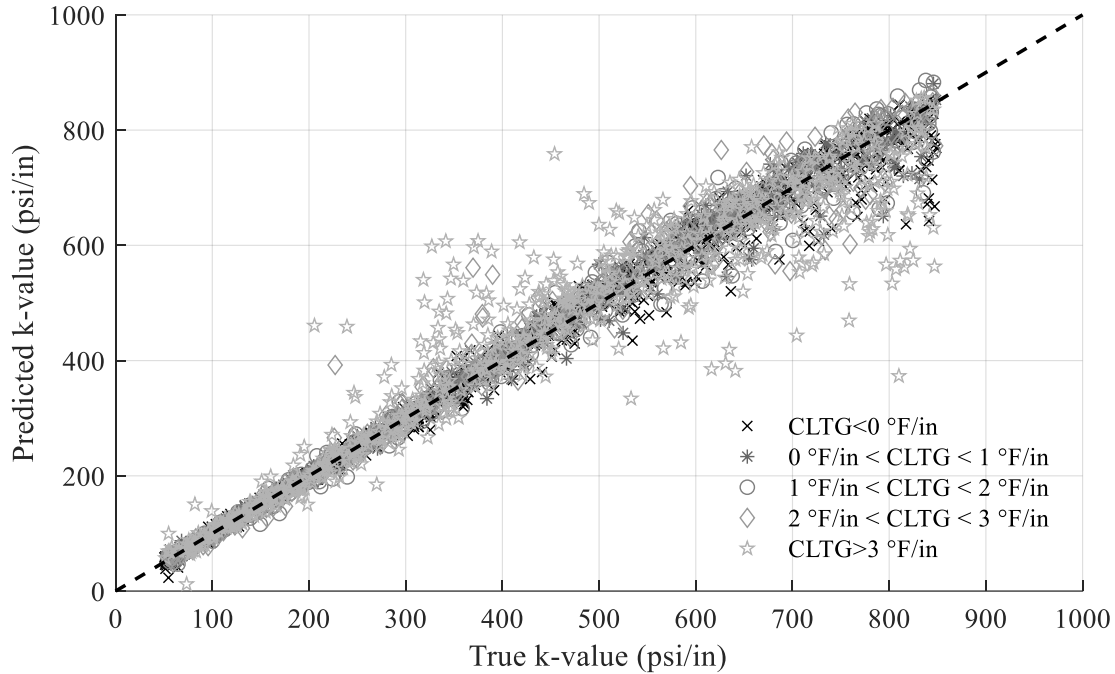


Figure 3.39. Performance of proposed backcalculation method on test set (CLTG is not an input)

Without inputting the CLTG, the R^2 is 0.96, matching the R^2 when the CLTG is defined. If only tests with $CLTG < 3$ °F/in are considered, the R^2 of the model increases to 0.98, again matching the performance where CLTG is an input. This shows that allowing the ANN to account for the CLTG without explicitly entering it can eliminate the errors in estimating CLTG without decreasing prediction accuracy.

An analysis of four instrumented test projects in Pennsylvania demonstrated a standard deviation in built in curl of 0.6 °F/in (Nassiri and Vandebossche 2012). To simulate error in estimating the CLTG, gaussian white noise, with a standard deviation of 0.6 °F/in, and a mean of zero, was added to the CLTG in the test set. In reality, the error in estimating the CLTG is likely

significantly greater than 0.6 °F/in, as there is also error in calculating the ELTG, and in predicting the seasonal and long-term drying shrinkage. The test set was then evaluated using the model trained utilizing CLTG as an input parameter. The “true” k-value versus the measured k-value can be seen in Figure 3.40.

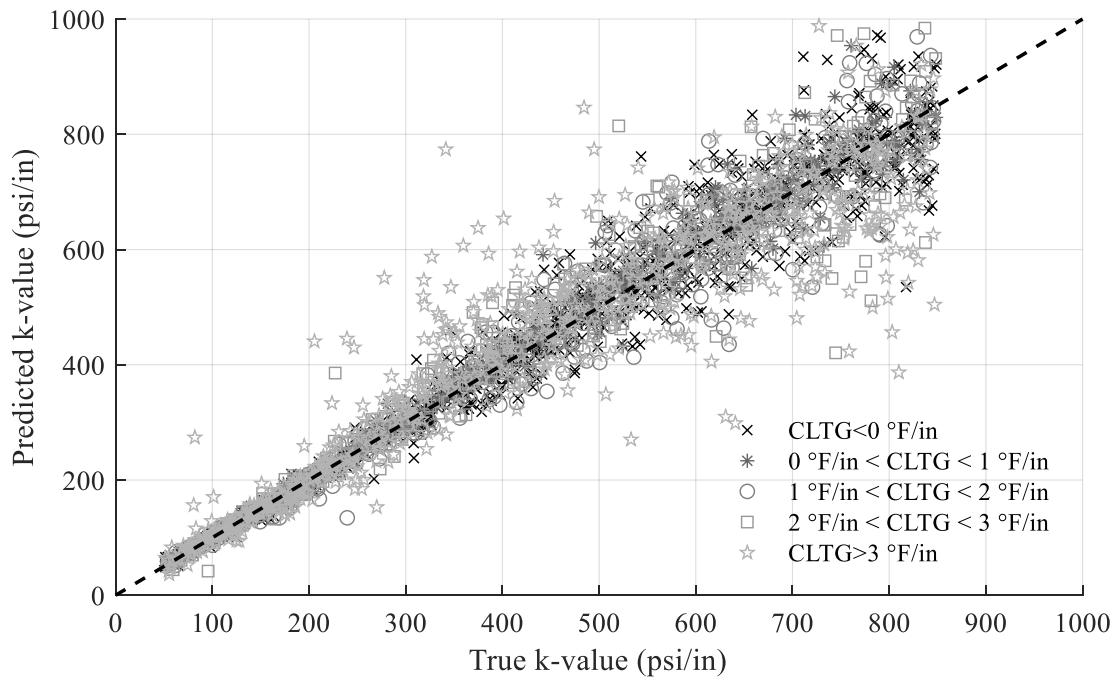


Figure 3.40. Performance of proposed backcalculation method on test set (CLTG is an input, with simulated noise in the test set)

This decreases the R^2 value to 0.92 with all of the data included, and 0.95 when only tests with CLTG less than 3 °F/in were considered. This demonstrates how accuracy of the backcalculation procedure can be improved without explicitly requiring the CLTG as an input.

The model developed without CLTG as an input was used to backcalculate the k-value from the computational analysis shown in Figure 3.29. The backcalculated k-values using the proposed method can be seen in Figure 3.41.

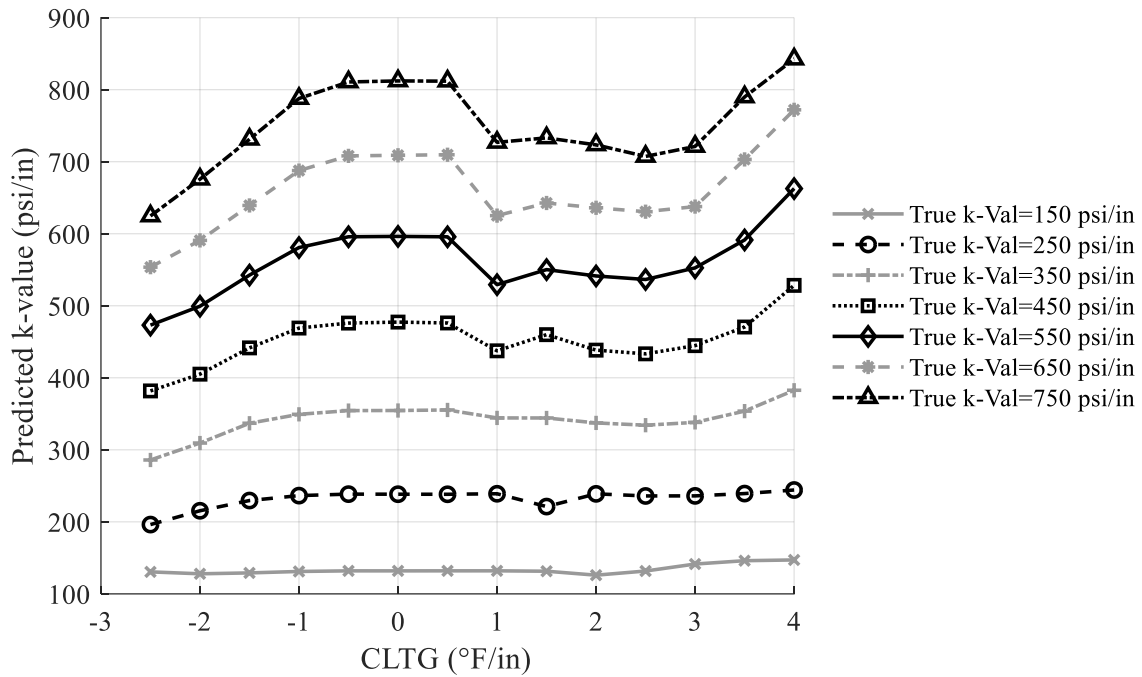


Figure 3.41. Performance of proposed backcalculation technique on factorial of CLTG and k-values

Using the proposed method rather than the traditional method leads to a large improvement in the accuracy of the backcalculated k-values. The model does seem to be over predicting the k-value for stiff k-values, when CLTG is greater than 3 °F/in. As previously mentioned, nearly all the tests in the LTPP database occur with an ELTG less than 3 °F/in, and therefore likely have a CLTG less than 2.5 °F/in.

3.5.3.1 Validation The field trials for the test dates in 2017 were used to validate the developed ANN set shown in Figure 3.38. The field trial test dates in 2016 did not include tests at mid-lane

adjacent to the transverse joint, and therefore could not be used. The backcalculated k-value as a function of ELTG is shown in Figures 3.42 to 3.44.

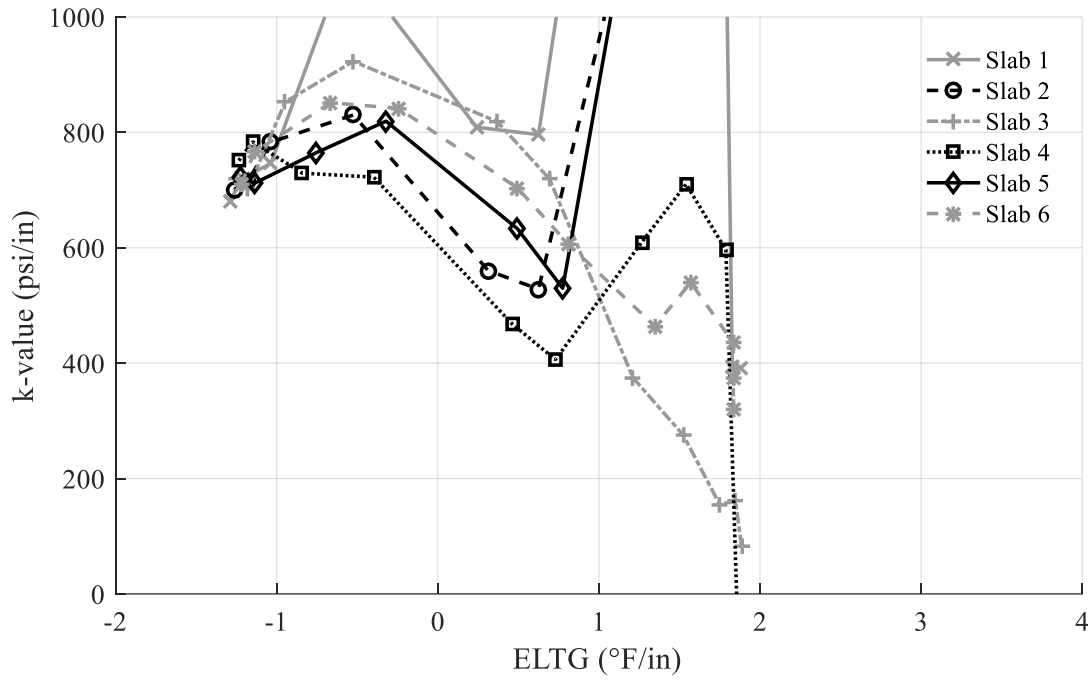


Figure 3.42. Validation of two test location ANN backcalculation model (I-79, 10/1/2017)

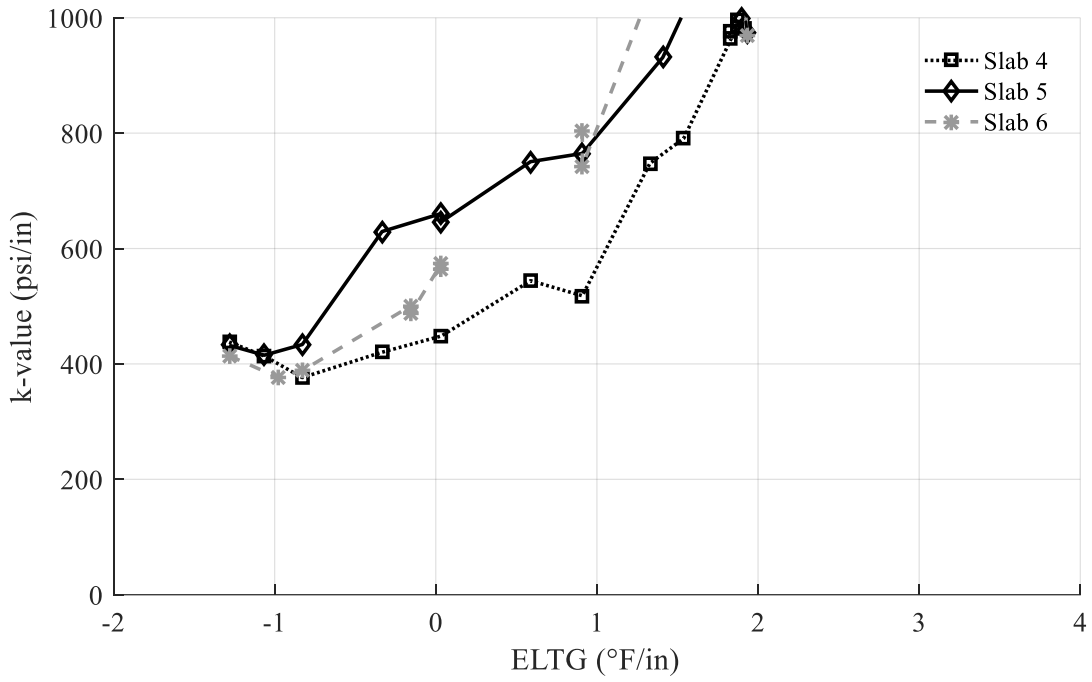


Figure 3.43. Validation of two test location ANN backcalculation model (SR-22 Doweled, 10/2/2017)

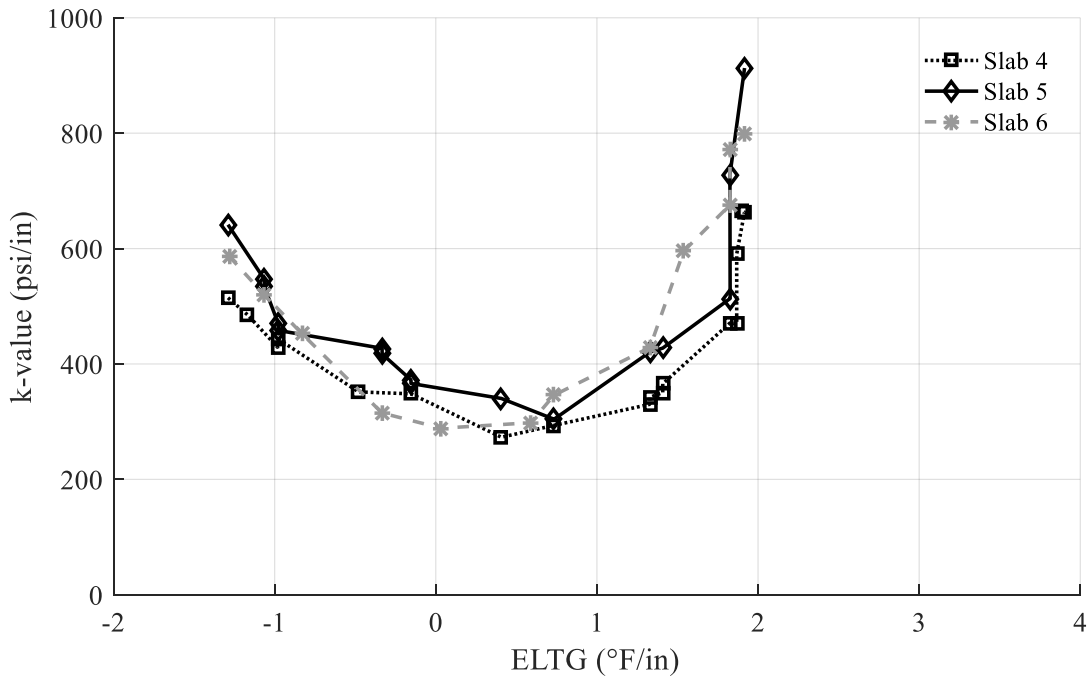


Figure 3.44. Validation of two test location ANN backcalculation model (SR-22 Undoweled, 10/2/2017)

The validation results are generally not optimistic. The backcalculated k-value for the undoweled section at SR-22 does not decrease from the maximum backcalculated k-value as it did when using the AREA method. However, at the I-79 section, the validation indicates that the solution can become unstable with a positive ELTG. This is likely because accurate predictions in the ANN are made possible by evaluating the many non-linear interactions between the input variables. Interactions which may be significant in the training set based on computational analysis, where there is no noise, may not be significant when noise is present. This can lead to significant error when exposed to field measurements, which contain inherent noise. In addition, the computational database used to train the ANNs assumes that all pavement layers are linear elastic materials. The presence of stress softening or stress stiffening layers can lead to bias in these interaction, and consequently unstable results.

A possible improvement may be to introduce noise into the training set. This may allow the Bayesian regularization algorithm to concentrate weight onto interactions that are less sensitive to noise. The ANNs were retrained with random gaussian noise with a signal to noise ratio of 0.1 added to each of the FWD related inputs. This reduces the R^2 of the ANN on computational data to 0.93. The backcalculated k-values from the 2017 field trails, estimated with the adjusted ANNs can be seen in Figures 3.45 to 3.47.

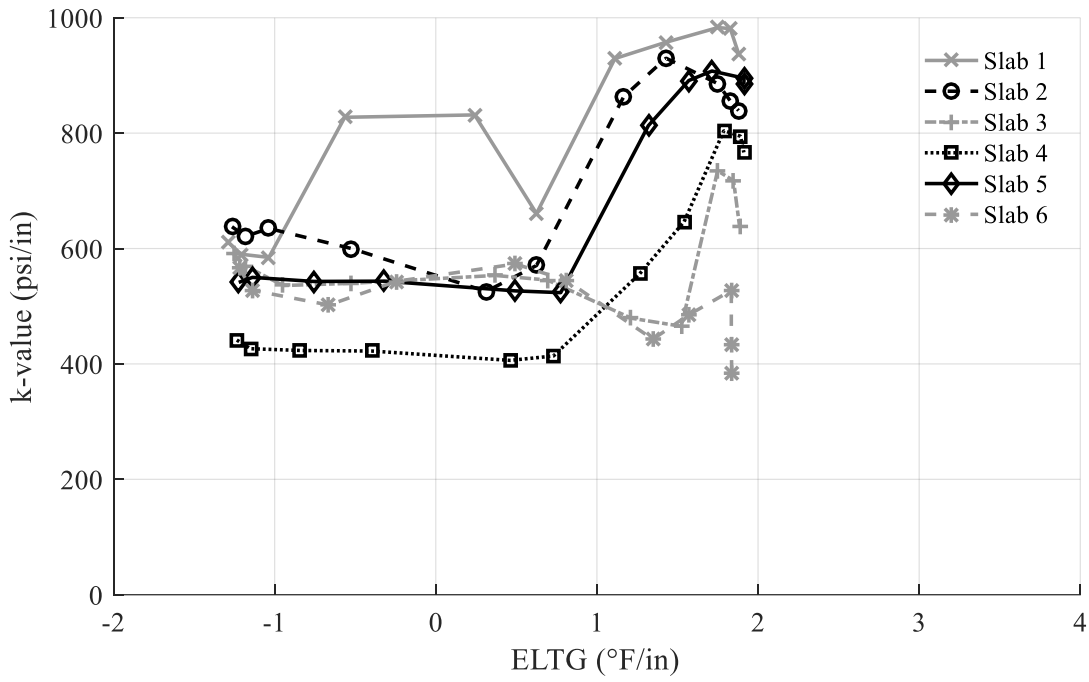


Figure 3.45. Validation of adjusted two test location ANN backcalculation model (I-79, 10/1/2017)

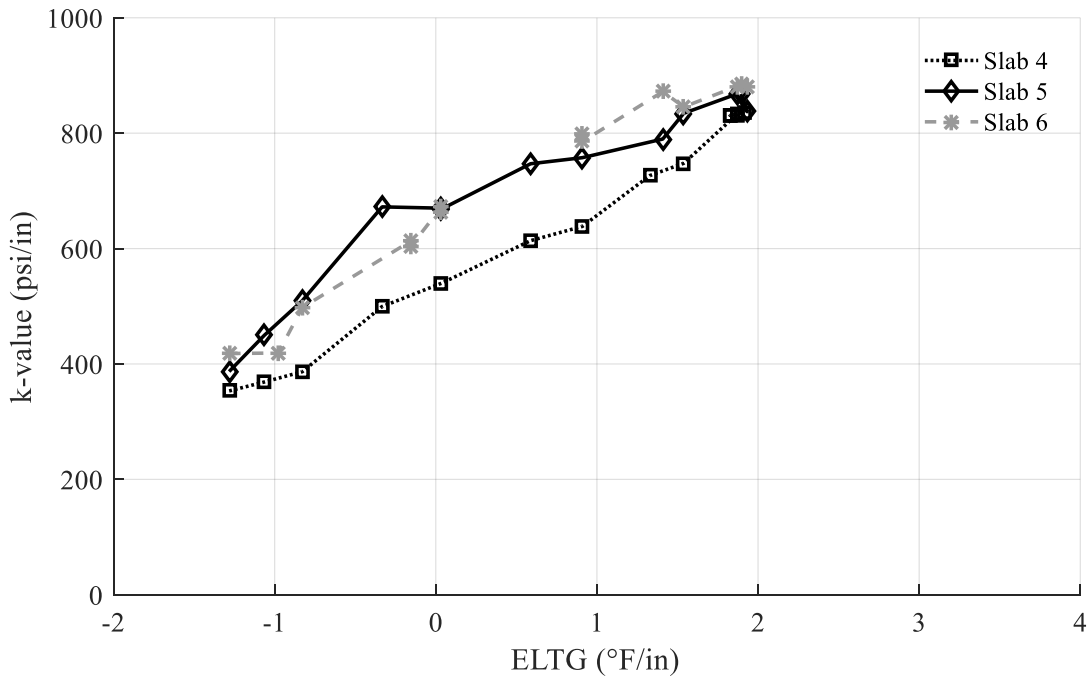


Figure 3.46. Validation of adjusted two test location ANN backcalculation model (SR-22 Doweled, 10/2/2017)

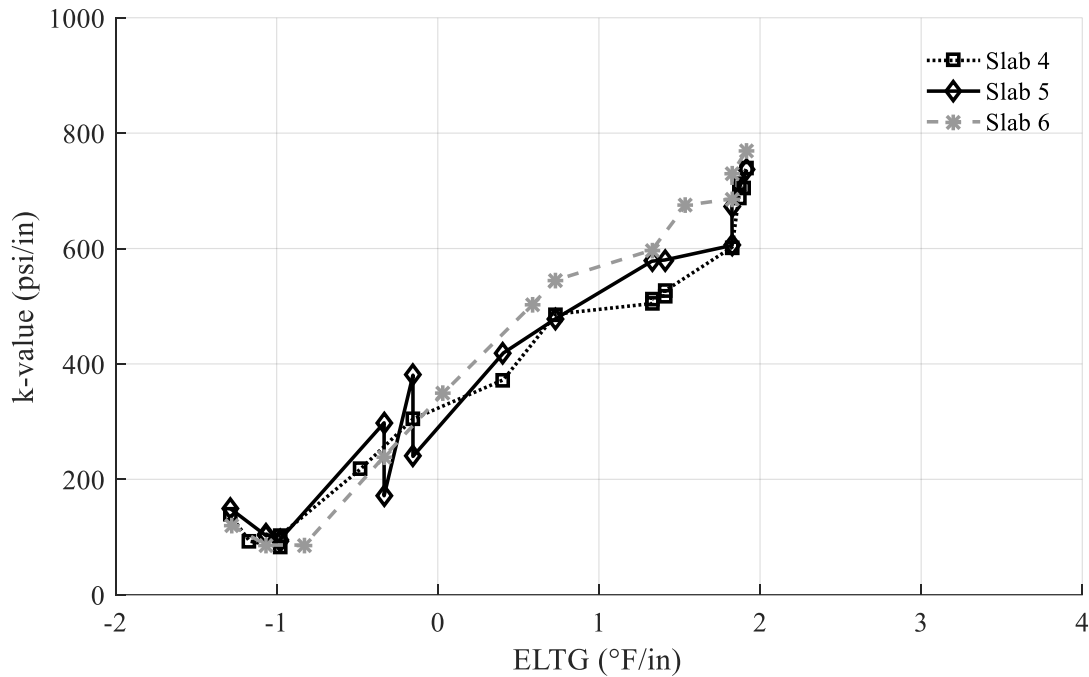


Figure 3.47. Validation of adjusted two test location ANN backcalculation model (SR-22 Undoweled, 10/2/2017)

Introducing noise into training set improves the stability backcalculation predictions at I-79, as can be seen in Figure 3.45. However, the backcalculated k-value at SR-22 appears to increase with temperature gradient, which is undesirable as the stiffness of the supporting layers is not likely changing throughout the day.

3.5.4 Optimization method

Additional stability can be introduced to the backcalculation model by using an optimization framework rather than direct backcalculation using an artificial neural network. Backcalculation of layer properties in asphalt pavements is typically performed by minimizing an objective function, usually mean squared error, between theoretical deflection basins and FWD measured

deflection basins. The measured theoretical deflection basin for asphalt pavements is typically calculated using layered elastic analysis. The forward calculation model used to train the ANN-based backcalculation method can also be used as a forward calculation model for an optimization method.

Based on the analysis shown in Table 3.3, it is unlikely that an optimization-based backcalculation strategy would be effective for testing at midslab when a positive CLTG is present. Therefore, the optimization procedure for backcalculation with positive temperature gradients will need to occur at mid-lane adjacent to the transverse joint or in the wheelpath. The uniformity of the slab support is likely to be better in the wheelpath than at mid-lane under large positive temperature gradients. Therefore, the optimization framework was developed using testing in the wheelpath. An added advantage to utilizing FWD tests in the wheelpath is that it does not require additional FWD drops. Testing is usually performed in the wheelpath for evaluating joints. An optimization method was not developed for tests with an ELTG less than 0.5 °F/in. The AREA method can be used for backcalculation at these locations.

To allow for reasonable computation times for the optimization, an ANN was trained for forward calculation. This ANN estimates the deflection 0 in, 8 in, 12 in, 18 in, 24 in, 36 in, and 60 in from the center of the load as a function of the following inputs:

- k-value
- Radius of relative stiffness
- Joint spacing
- Korenov's non-dimensional curling parameter
- LTE
- Presence of a tied PCC shoulder (indicator variable)
- Presence of dowels (indicator variable)

The k-value and elastic modulus of the slab, which minimize the objective function, was determined using the Nelder-Mead simplex algorithm, also known as the amoeba method. The iterative method is performed until all inputs and the objective function have converged to within a tolerance of 1×10^{-4} . The backcalculated k-value using the AREA method for ELTG values less than $0.5 \text{ }^\circ\text{F/in}$, and the optimization can be seen in Figures 3.48 to 3.53. The most consistent results for the field trials in Pennsylvania was found when the long-term component of the CLTG was $0.75 \text{ }^\circ\text{F/in}$.

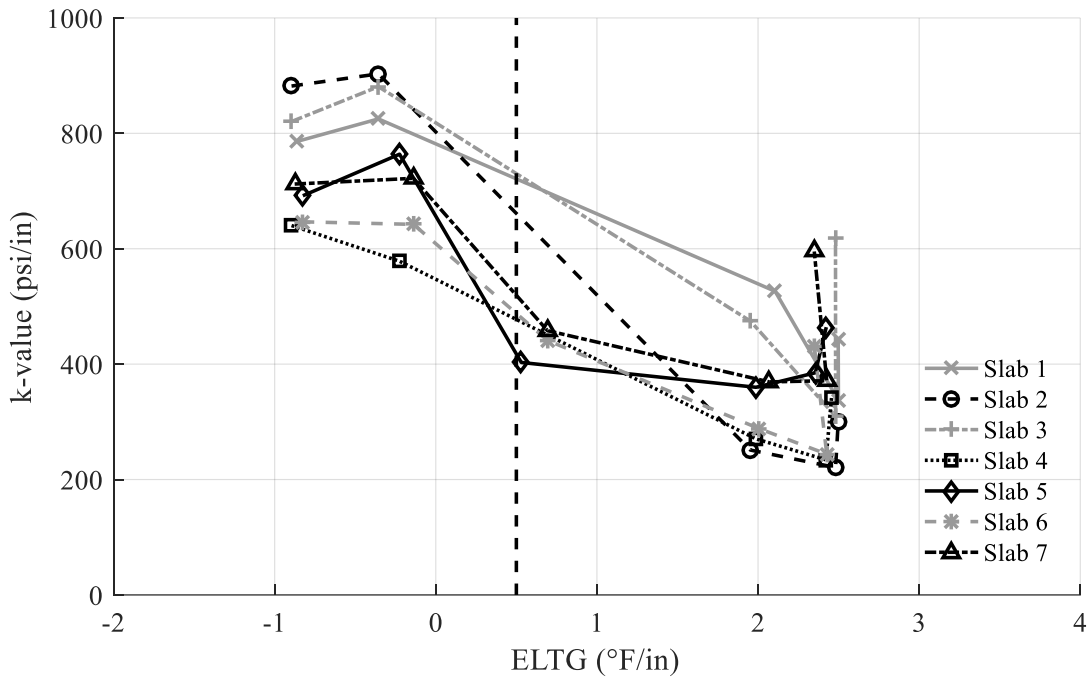


Figure 3.48. Validation of optimization framework based backcalculation (I-79, 5/8/2016)

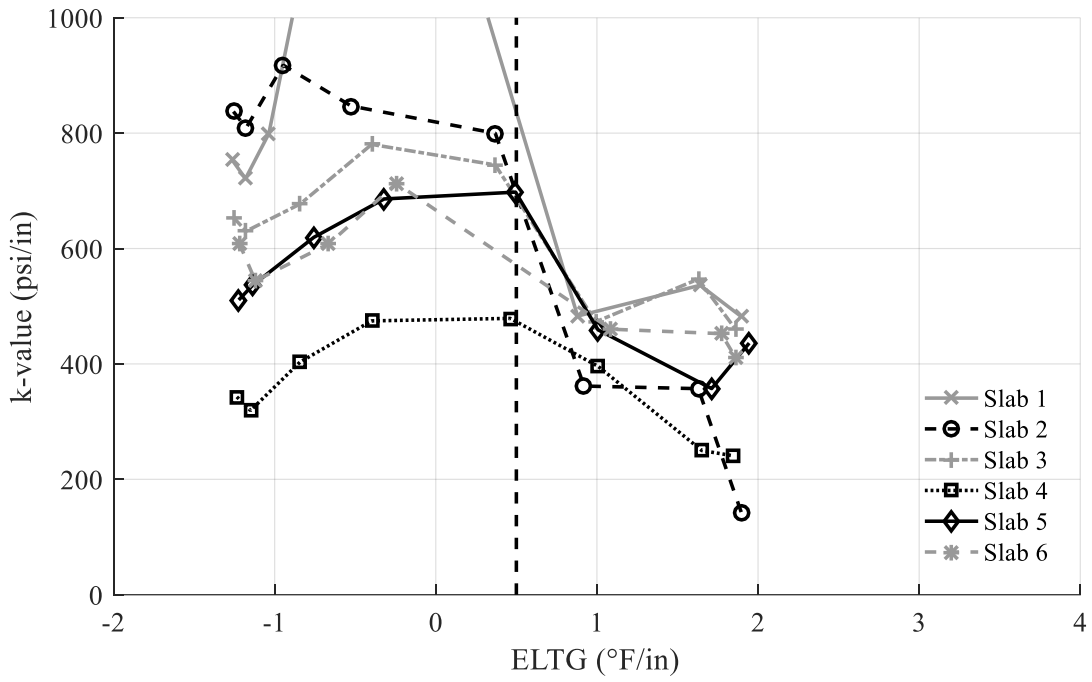


Figure 3.49. Validation of optimization framework based backcalculation (I-79, 10/1/2017)

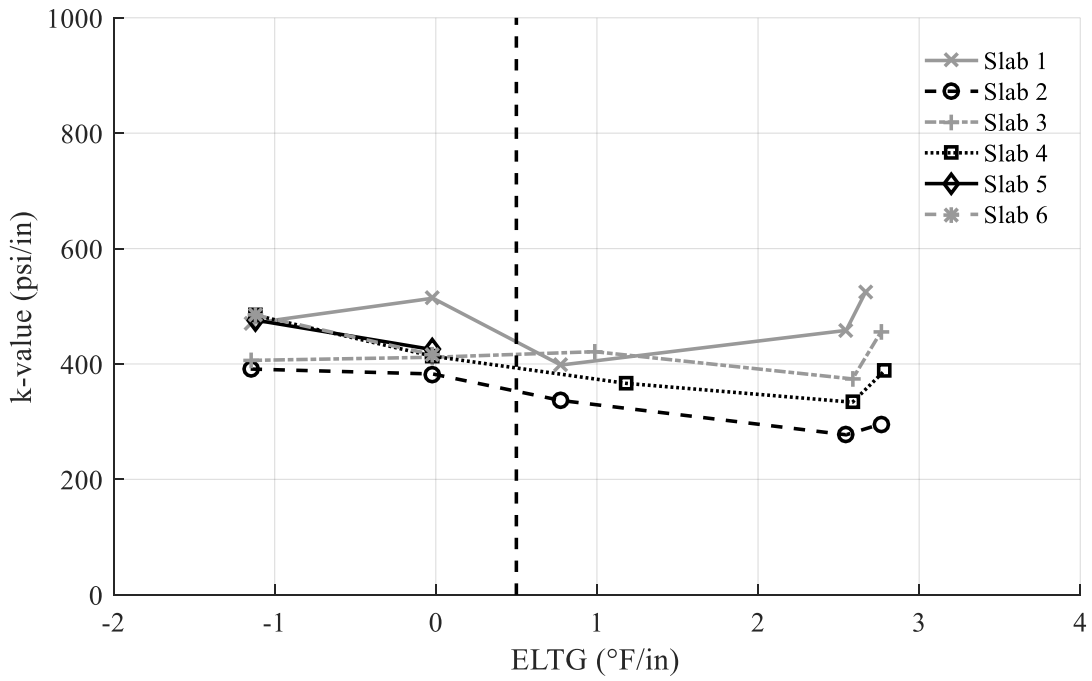


Figure 3.50. Validation of optimization framework based backcalculation (SR-22 Doweled, 4/25/2016)

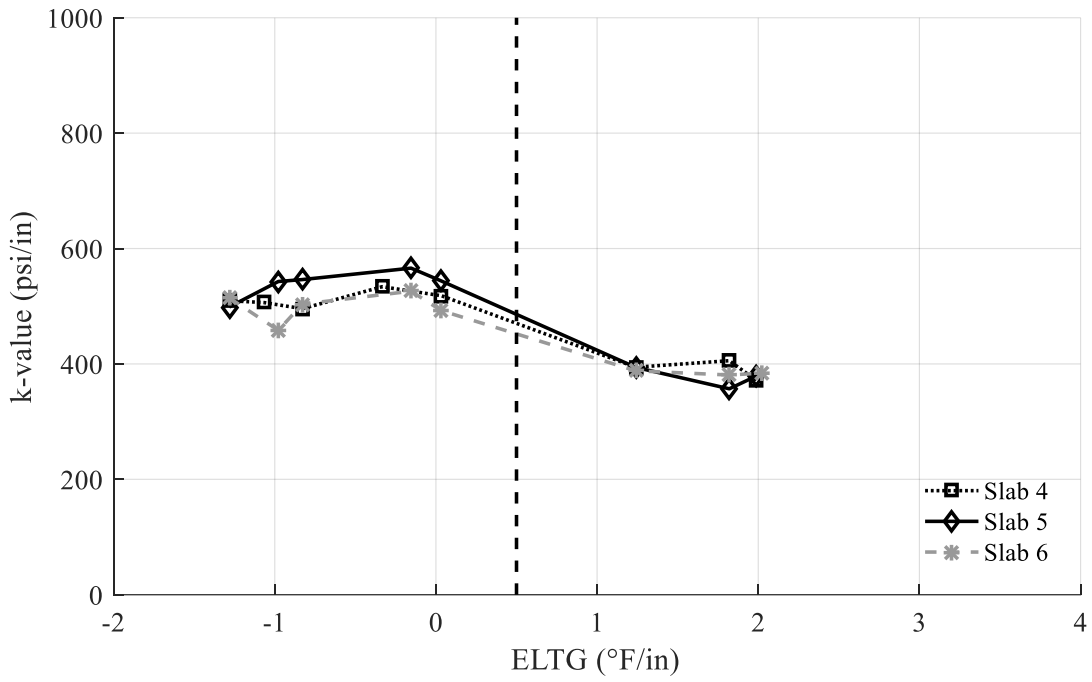


Figure 3.51. Validation of optimization framework based backcalculation (SR-22 Doweled, 10/2/2017)

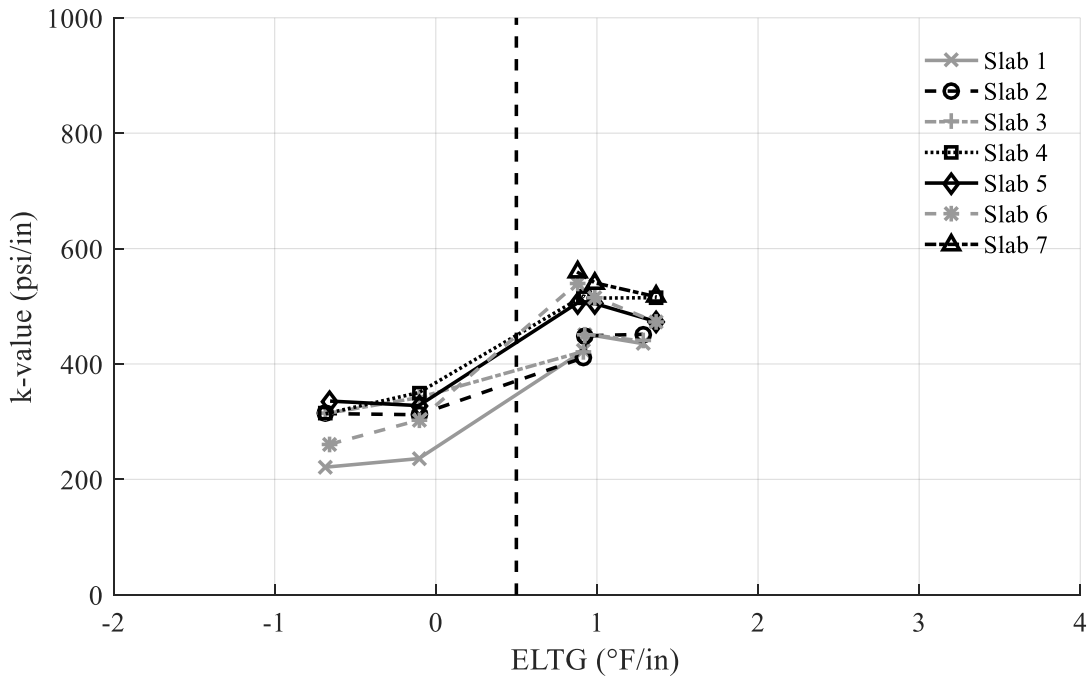


Figure 3.52. Validation of optimization framework based backcalculation (SR-22 Undoweled, 4/26/2016)

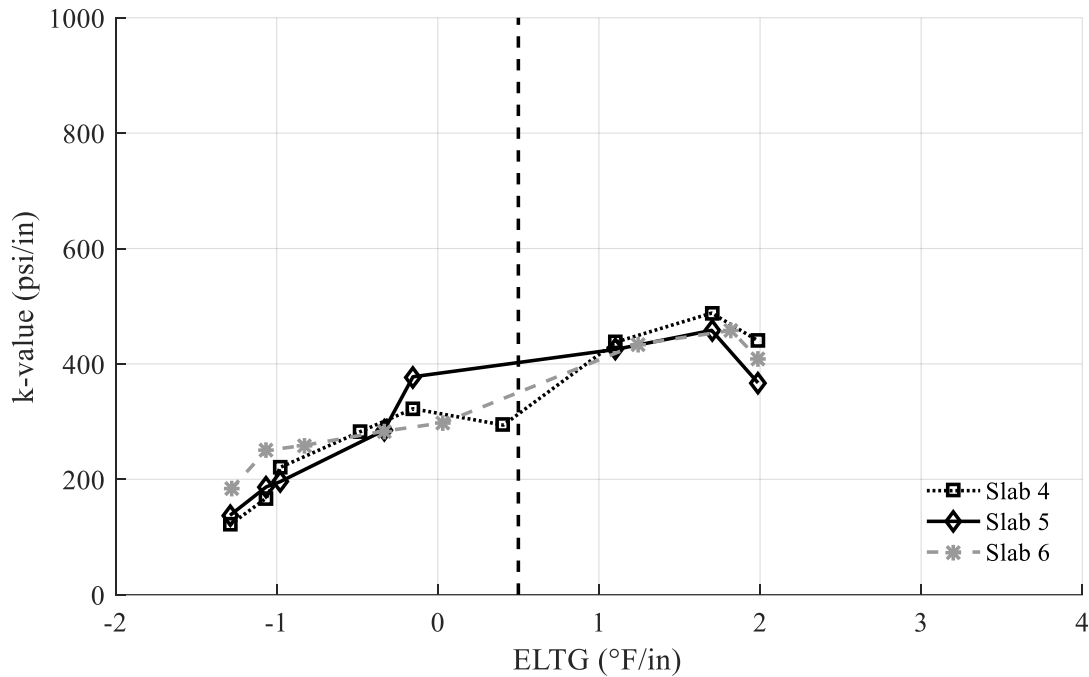


Figure 3.53. Validation of optimization framework based backcalculation (SR-22 Undoweled, 10/2/2017)

The optimization framework appears to be more stable in some cases than the ANN-based backcalculation. Also, the backcalculated k-value at the doweled SR-22 section is not increasing with ELTG using the optimization framework like it is for the ANN backcalculation. The k-value mostly decreases with ELTG for both test dates at the I-79 section, but to a much smaller degree than with the AREA method. The backcalculated k-value for the undoweled section at SR-22 is higher using the optimization framework in the wheelpath than it is using the AREA method. However, the backcalculated k-value using the optimization framework is consistent with the doweled section, whereas the maximum backcalculated k-value using the area method is lower than the doweled section. As previously mentioned, there is no physical reason that these sections should have a different k-value. Therefore, it is possible that the k-value backcalculated using the optimization method is more reasonable than the value estimated using the AREA method.

One concern with this method is that the predicted elastic modulus using this method can occasionally be outside of the expected range for the elastic modulus of concrete. For example, for the SR-22 testing in 2017, the elastic modulus estimated using the optimization method was predicted as high as 15 million psi. This may be due to the rotational restraint at the joint, which is hard to quantify, affecting the deflection basin. Therefore, it is not recommended that the optimization method be used to backcalculate the elastic modulus of the slab.

One way of reducing the bias seen at the I-79 section, and avoid unreasonable values for the slab stiffness would be to backcalculate only the k-value while holding the stiffness of the slab constant. If backcalculation testing on a test date is performed with an ELTG less than 0.5 °F/in, the slab stiffness can be estimated for these sections using the AREA method. The average of these slab stiffness estimates can then be used in the optimization framework to backcalculate the k-value. This method was also evaluated for each of the field trials. The backcalculated k-values can be seen in Figures 3.54 to 3.59.

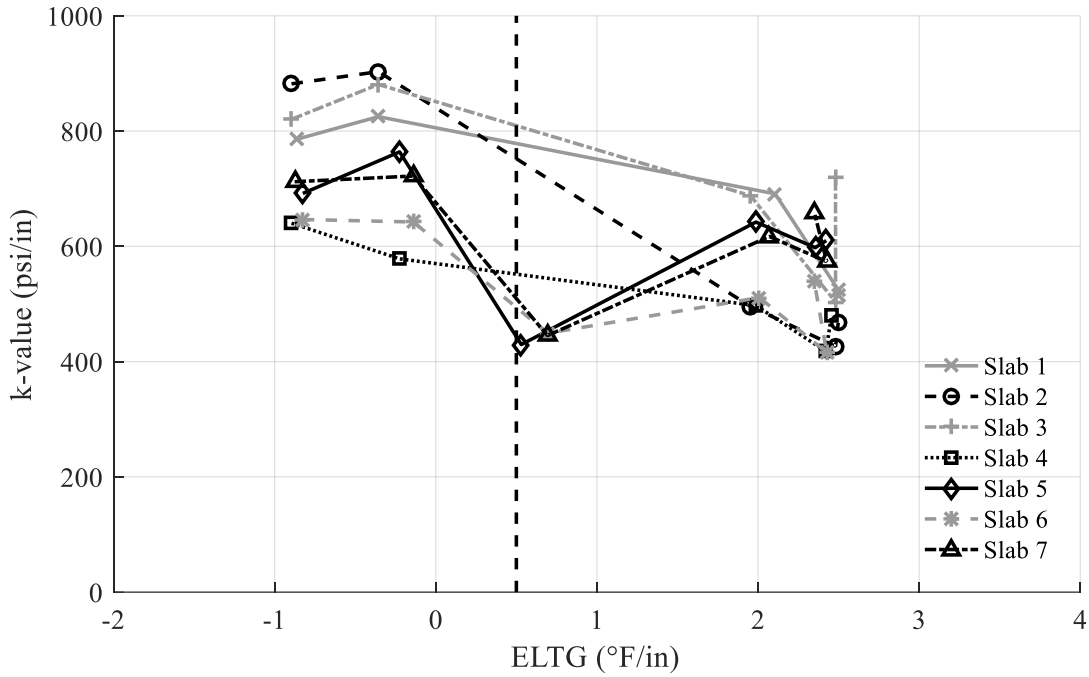


Figure 3.54. Validation of optimization framework based backcalculation with constant slab stiffness (I-79, 5/8/2016)

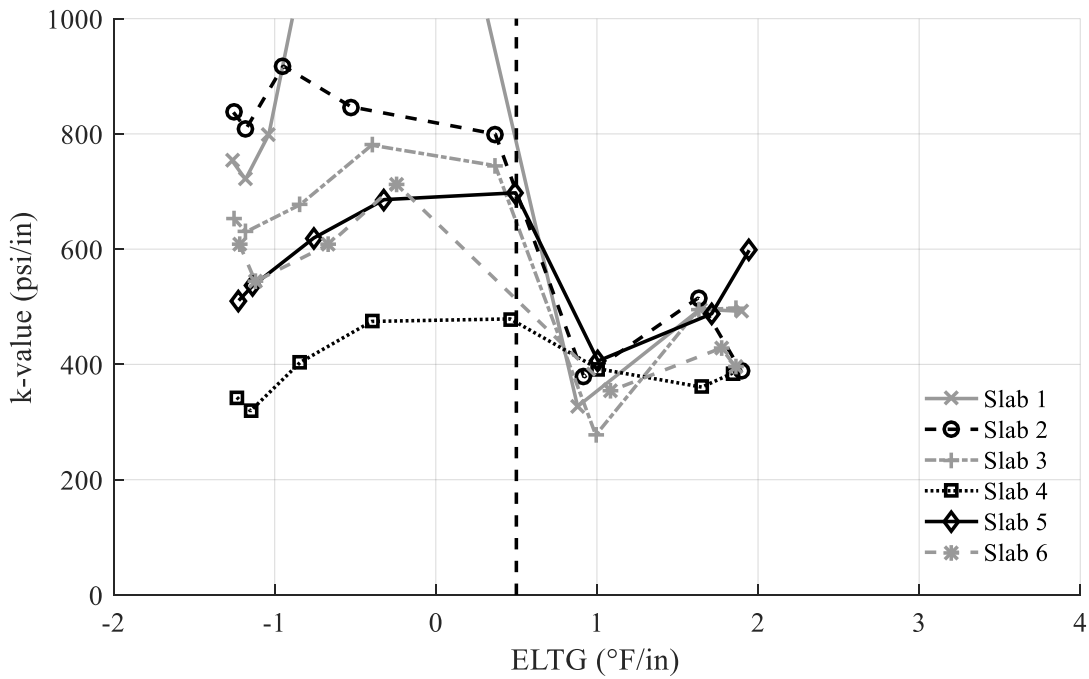


Figure 3.55. Validation of optimization framework based backcalculation with constant slab stiffness (I-79, 10/1/2017)

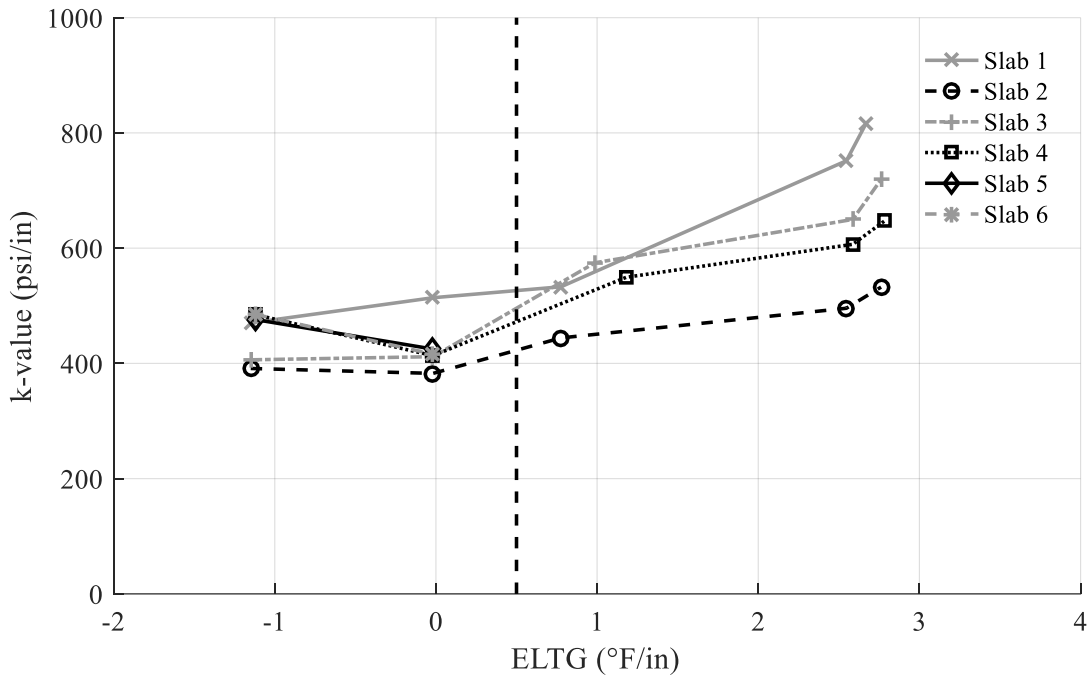


Figure 3.56. Validation of optimization framework based backcalculation with constant slab stiffness (SR-22 Doweled, 4/25/2016)

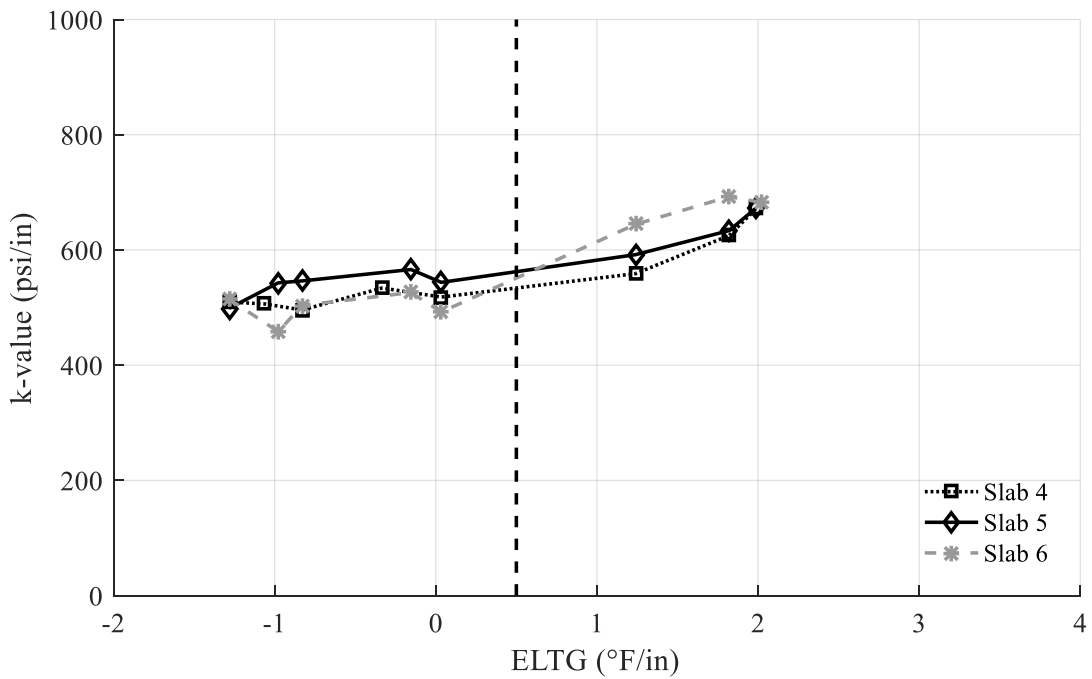


Figure 3.57. Validation of optimization framework based backcalculation with constant slab stiffness (SR-22 Doweled, 10/2/2017)

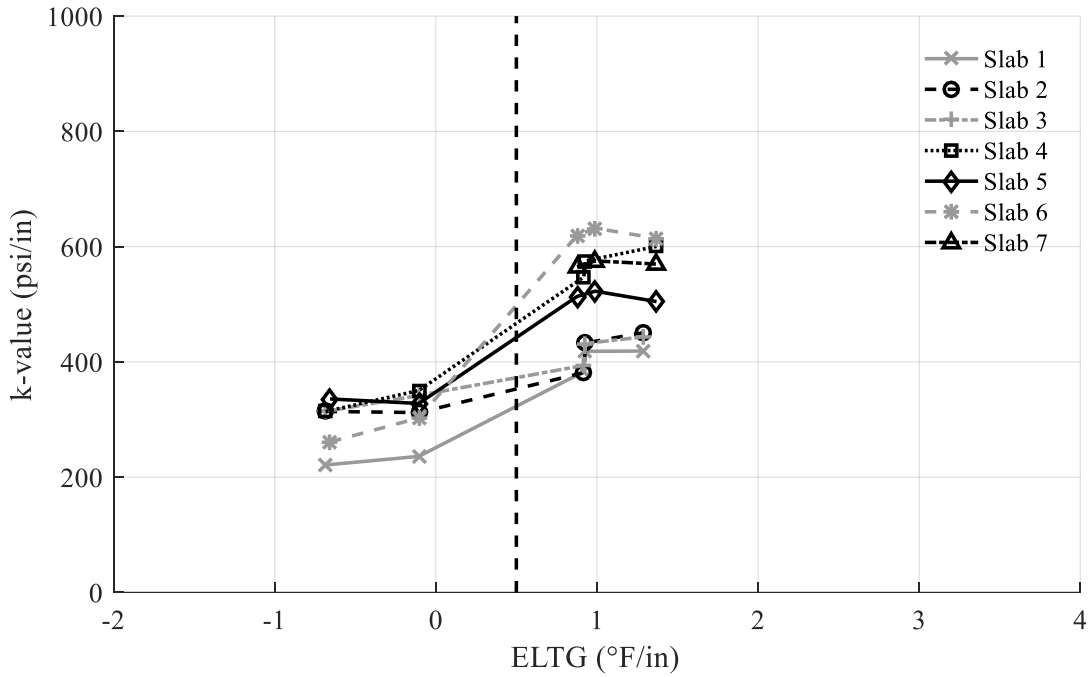


Figure 3.58. Validation of optimization framework based backcalculation with constant slab stiffness (SR-22 Undoweled, 4/26/2016)

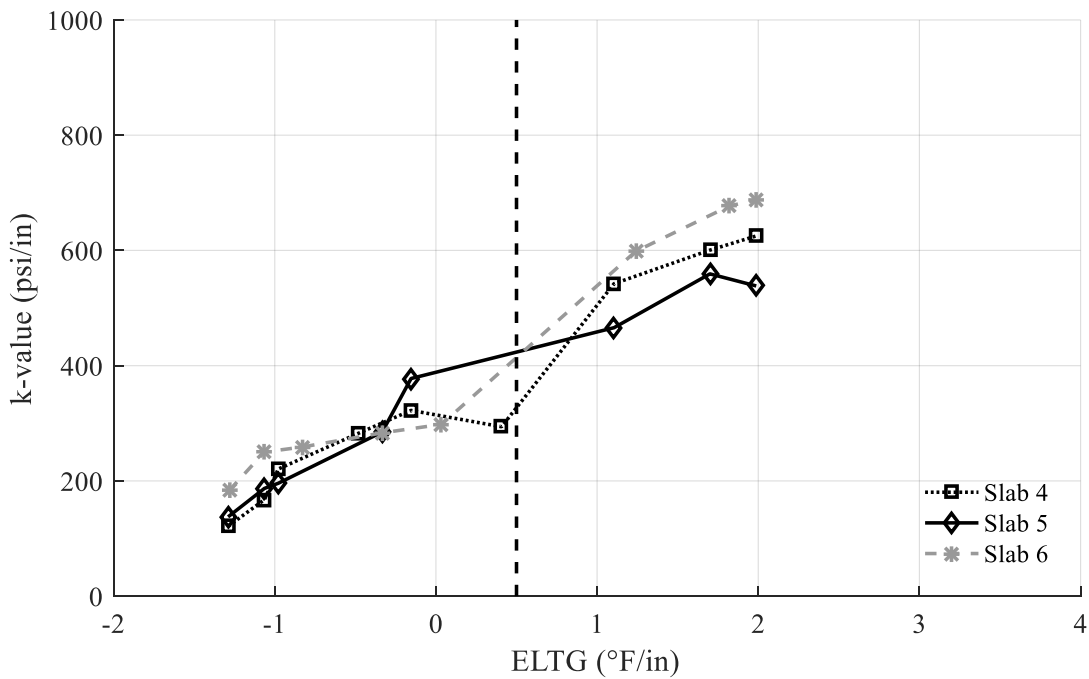


Figure 3.59. Validation of optimization framework based backcalculation with constant slab stiffness (SR-22 Undoweled, 10/2/2017)

Holding the stiffness of the slab constant does not appear to have a major impact on the predicted k-values. This strategy causes the backcalculated k-values found with the optimization framework to be closer to the values calculated with the AREA method at I-79. Therefore, if some midslab tests are available with an ELTG less than 0.5 °F/in on a test date, accuracy may be improved by holding the slab stiffness constant during the optimization framework. As an added benefit, single variable optimization is much more computationally efficient than multi-variable optimization.

3.6 CONCLUSIONS

Slab curvature can have a large influence on the k-value backcalculated from FWD testing. This is especially true when the “true” k-value is high. Errors in estimating the k-value caused by slab curvature can have a significant effect on the predicted distress development using the Pavement ME design procedure. When a large positive ELTG is present, greater than 0.5 °F/in, the k-value has minimal effect on the deflection basin. Therefore, it is not possible to backcalculate the k-value solely from testing at midslab when a positive ELTG is present. Several strategies were evaluated to perform backcalculation when a positive ELTG is present. The procedure with the best performance involved utilizing an optimization framework to minimize the error between measured and predicted deflections. The forward calculation in this framework is performed using an ANN trained with FEM runs that consider slab curvature. Overall, there are issues with all of the methods developed for backcalculating the layer stiffnesses of the concrete layer when a positive temperature gradient is present, if the layer properties are desired for design. Therefore, it

is recommended that testing be performed with an ELTG less than 0.5 °F/in. The optimization method is sufficient for developing a structural model for use in the void detection model, which will be discussed in Chapter 5.

4.0 JOINT PERFORMANCE

4.1 INTRODUCTION

4.1.1 Joint Performance Testing

The overall performance of a jointed concrete pavement (JCP) joint depends on the ability of the joint to prevent the pumping mechanism. Pumping will only occur if four conditions are met:

- Repeated, heavy wheel loads
- Large differential deflections
- Moisture in the base and/or subgrade
- Erodible fines in the base and/or subgrade

Effective joint performance refers to the ability to transfer load across the joint between the slabs, thereby reducing the difference between the deflections in the adjacent slabs and consequently pumping.

Accurate estimates of the joint performance are important for determining whether remedial action, such as a DBR, should be performed at a joint. Joint efficiency is commonly estimated using two parameters, load transfer efficiency (LTE) and differential deflection (DD). These parameters are commonly calculated from falling weight deflectometer (FWD) testing with the load plate in the wheelpath, adjacent to the transverse joint. However, these parameters are

occasionally calculated with the load plate in the corner of the slab. The load transfer efficiency is calculated using Equation 4.1.

$$LTE = \left[\frac{\delta_{UL}}{\delta_L} \right] * 100\% \quad (4.1)$$

where

δ_L = the measured deflection in the center of the load plate (6 in from the center of the joint)

δ_{UL} = the deflection measured 12 in from the center of the load plate, across the joint (6 in from the center of the joint).

There are multiple methods available to correct LTE for bending in the slab. Corrections can be made using deflections from midslab testing, a correlation based on the radius of relative stiffness of the slab, or the normalized area of the deflection basin at the joint. (AASHTO 1993; Khazanovich and Gotlif 2003).

The development of pumping depends on both the portion of deflection that is transferred across the joint and the magnitude of the deflections. Therefore, DD is a useful parameter that considers both the stiffness of the pavement system and the ability of the joint to transfer load. This parameter is calculated using Equation 4.2.

$$DD = \delta_L - \delta_{UL} \quad (4.2)$$

Current guidance by the Federal Highway Administration (FHWA) suggests remedial action should be applied at a joint when LTE is less than 60% or a DD greater than 0.01 in (Applied Pavement Technology 2001).

4.1.2 Slab Curvature Effects on Estimated Joint Performance

The effect of slab curvature on the measured LTE for doweled joints has not been clearly defined in previous research. A study at the Minnesota Road Research Facility (MnROAD), conducted over several test dates in various seasons, did not find a trend relating the measured LTE at doweled joints to the temperature gradient (Vandenbossche 2007). Analysis of the LTPP SMP project found that the LTE at a given joint varied throughout a single day of testing. Five of the 12 doweled SMP sections evaluated had at least one test date with a coefficient of variation (COV) of the mean LTE of at least 10% (Khazanovich and Gotlif 2003). Although this previous research did not perform any analysis to directly tie the observed variation in to temperature gradients or slab curvature, it is likely that this variation is the result of changes in slab curvature.. For most of the sections, the measured LTE was lowest when the first pass of testing was performed (around 10:00 AM), which likely corresponds to the slab being approximately flat, and increased throughout the day as temperature gradients increased (Khazanovich and Gotlif 2003). A study at the Korean Highway Corporation (KHC) Test Road also observed that the measured LTE varied throughout the day. However, unlike the testing from the LTPP test sections, the measured LTE in this study was found to decrease as the temperature gradient increased from a negative temperature gradient in the morning, to a positive temperature gradient in the afternoon, reaching a minimum around 1:00 pm. This behavior was attributed to slab curvature due to negative temperature gradients causing the dowels to “lock-up,” as the dowel comes into contact with the edge of the socket. In this study, the observed relationship between the measured linear temperature gradient and LTE in the two-day test period is much more prevalent than the observed relationship between measured joint width and LTE (Jeong et al 2006). The conflicting results of previous research studies cited above indicate that further study is needed on the behavior of dowels in curled and warped concrete slabs.

Slab curvature can affect the LTE without dowel “lock-up” occurring and affecting the stiffness of the dowel system. A computational analysis of airfield pavements, which models load transfer across the joint using a shear spring, indicates that for a given joint stiffness the estimated LTE from simulated FWD deflections is at a minimum when the slab is flat (Byrum et al. 2011). This is because LTE is estimated from deflection measurements 6 in from the joint. Changes in slab support conditions affect the shape of the deflection basin and, ultimately, the estimated LTE.

Understanding how slab curvature affects the estimated joint efficiency parameters is critical for effectively evaluating JCP joints. In addition, evaluating the mechanics behind this phenomenon is useful for developing computational models of JCP. The effect of slab curvature on LTE and DD of doweled joints was evaluated using three data sources: field trials in Pennsylvania, the LTPP database, and a computational analysis using EverFE v2.24 (Davids 2003).

In addition to evaluating the effect of slab curvature on measured joint efficiency parameters, it is important to evaluate the relationship between these parameters and the development of future distresses. Poor joint efficiency is primarily linked to the development of faulting in JPCP, and the development of reflective cracking in HMA overlays of JPCP. The FHWA recommends thresholds of 60% LTE, or 10 mils DD for defining when load transfer restoration should be performed. However, these recommendations are not based field observations of doweled slabs. Therefore, the relationship between measured joint efficiency and faulting was investigated. This includes an analysis of the prevalence of faulting on JCPs in Pennsylvania, and a statistical analysis between several predictors, including measured joint efficiency, and the development of faulting using the LTPP database. The importance of measured

LTE on the predicted reflective cracking using the Pavement ME design module for HMA overlays of JPCP slabs was evaluated using a sensitivity analysis.

4.2 FIELD TRIALS

To evaluate the effect of slab curvature on LTE, while minimizing the variation in other factors which might influence slab curvature, two doweled concrete pavement sections in Western Pennsylvania were selected for field trials with FWD testing performed on the same joints on the same day. These field trials were described in Chapter 2. The undoweled section of SR-22 was not considered in this analysis. The details of the two pavements can be seen in Table 4.1.

Table 4.1. Field test section properties

Section	I-79	SR-22
Location	Bridgeville, PA	Murrysville, PA
Test Date	5/8/2016	4/25/2016
Slab Thickness	12 in	12-14 in
Base Type	Granular	Asphalt Treated
Joint Spacing	20 ft (skewed)	15 ft

Testing at each section occurred on two test dates, one in the Spring of 2016, and again in the Fall of 2017. In the Spring of 2016, FWD testing was performed from approximately 5:30 am to 5:00 pm. In the Fall of 2017, FWD was performed from approximately 6:30 am to 4:00 pm. These testing windows allowed testing to occur over the full range of temperature gradients. At I-79, the temperature profile was measured using four temperature holes, as described in the LTPP testing protocol (Schmalzer 2011). The section of SR-22 tested, which is part of the PennDOT Smart

Pavement, is heavily instrumented (Wells et al. 2005). Therefore, embedded thermocouples were used to measure the temperature profile in the slab throughout the day. A total of seven joints, testing every third joint, were tested at I-79. The doweled section of SR-22 is comprised of two cells, each consisting of three slabs, with 120 ft between the cells. All four joints were tested at each cell, resulting in a total of eight joints tested. A portion of these joints were tested in the 2017 test dates. Additional information about the field tests is provided in Chapter 2.

Joint “lock-up,” which is a different phenomenon than dowel “lock-up,” may lead to artificially high LTE measurements and low DD measurements. Measurements from vibrating wire strain gages located near the joint of interest can be used to evaluate when joint lock-up occurs by plotting strain against temperature for a 24-hour period. When the joint is not locked up, the strain and temperature will follow an approximately linear pattern. However, if the joint is locked up, this linear relationship will cease and the strain will stop increasing with increasing temperature (Vandenbossche 2001). An example of joint “lock-up” using two strain gages embedded in the SR-22 test section, approximately 1 in from the pavement surface can be seen in Figure 4.1. The strain gauge near the top of the pavement was used to indicate joint lock up as lock-up occurs more often at the top of the slab than the bottom due to the larger diurnal temperature change.

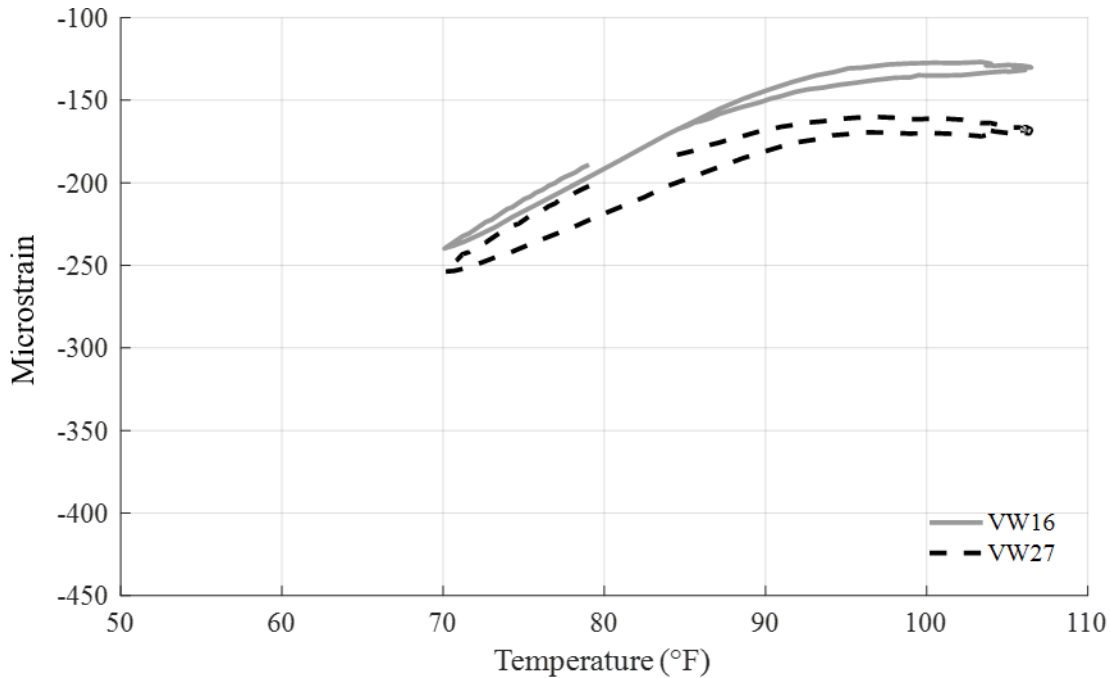


Figure 4.1. Example of strain gages indicating joint lock-up (SR-22 8/11/2017)

The strains shown are corrected for the coefficient of thermal expansion (CTE) of the steel strain gage, but not for the CTE of the concrete. The distinctive ‘kink’ in the plot of strain versus temperature at approximately 92°F indicates that the slab is unable to continue to expand with increasing temperature, resulting in joint ‘lock-up.’ The fact that joint “lock-up” occurs when the strain gages indicate the length of the slab is lower than the length of the slab at set may be due to incompressible materials entering the joint.

The strain versus temperature for each test date at SR-22 was plotted to determine if joint “lock-up” likely occurred. There are no strain gages in the I-79 test section. However, the two test sections are approximately the same thickness and relatively close geographically (30 miles). In addition, the paving mixes used to construct both sections have measured CTEs that are similar, approximately $5.8 \mu\epsilon/^\circ\text{F}$ at I-79, and $5.9 \mu\epsilon/^\circ\text{F}$ at SR-22 (Wells et al. 2005). Assuming that the intrusion of incompressible fines into the joints is also similar, the SR-22 strain gages were used

as a best estimate of joint “lock-up” at the I-79 section. Measurements from two longitudinal strain gages located in the corner of the slab (approximately 1 in below the top of the slab) near the lane-shoulder joint were plotted for each test date and are presented in Figures 4.2 through 4.5.

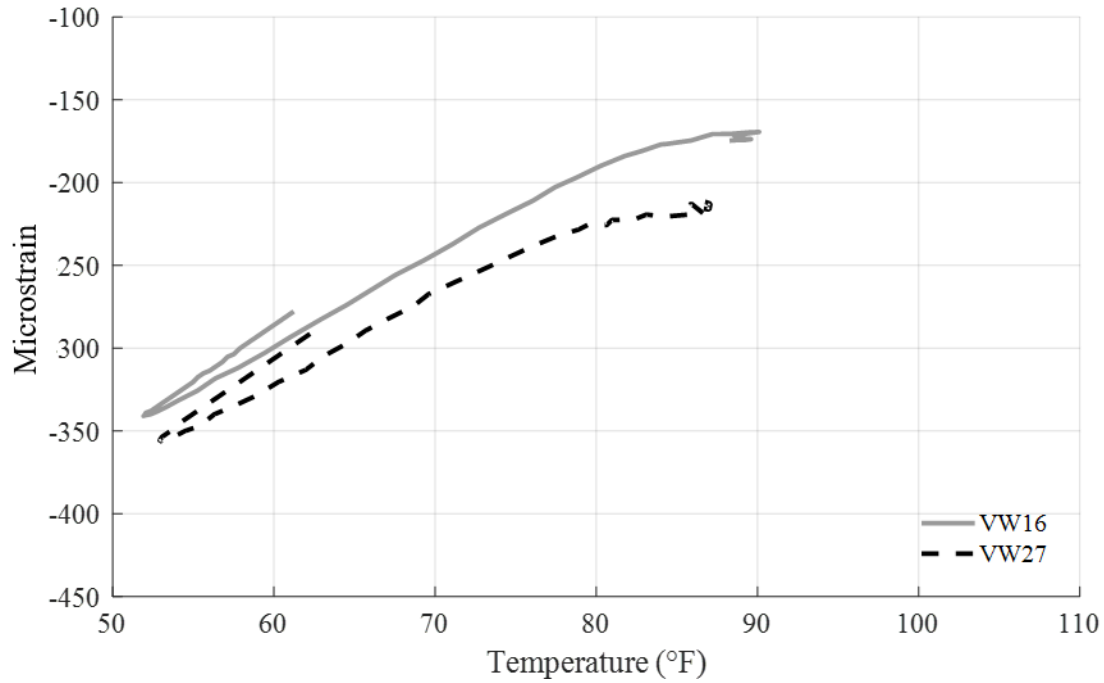


Figure 4.2. Evaluation of SR-22 joint “lock-up” (4/25/2016)

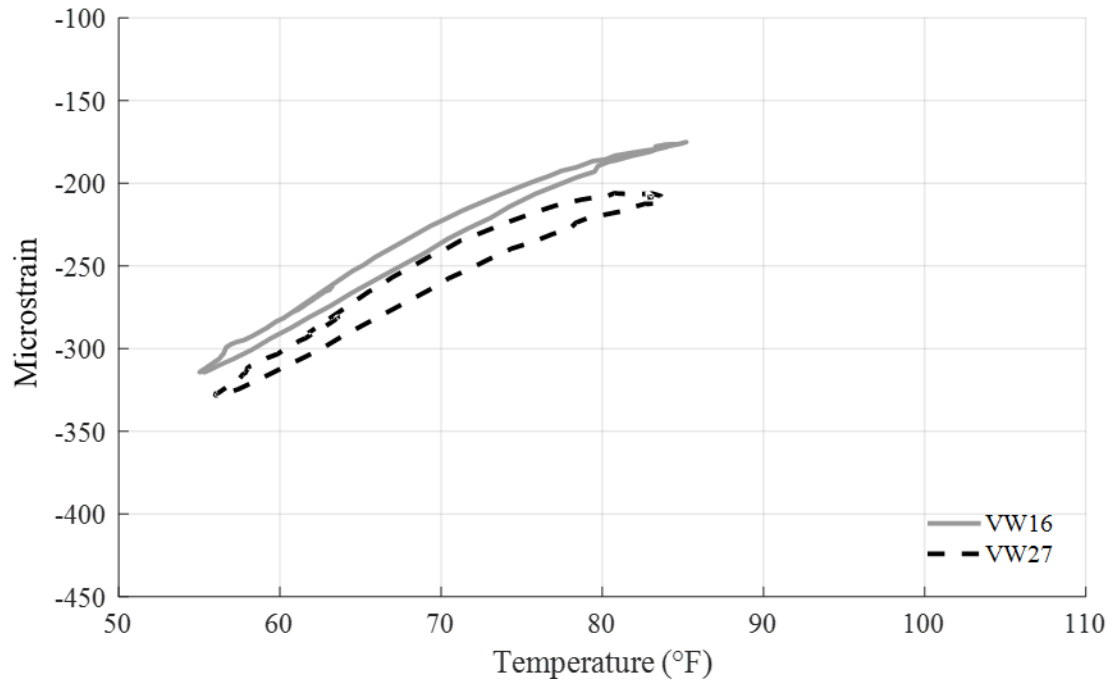


Figure 4.3. Evaluation of SR-22 joint “lock-up” (5/8/2016)

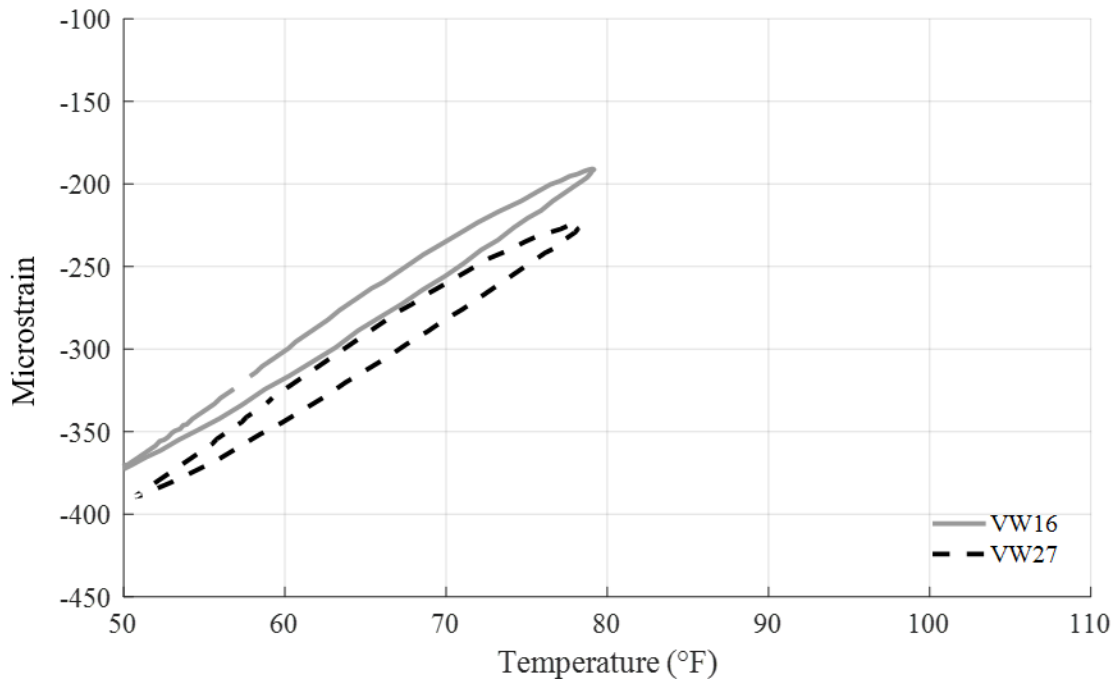


Figure 4.4. Evaluation of SR-22 joint “lock-up” (10/1/2017)

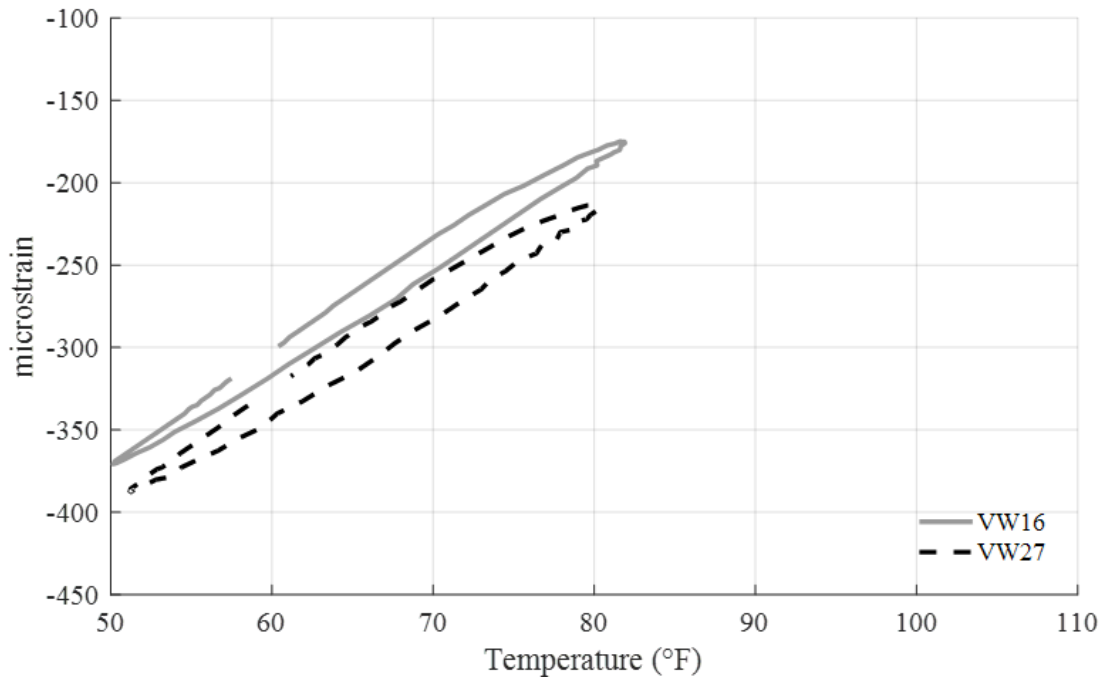


Figure 4.5. Evaluation of SR-22 joint “lock-up” (10/2/2017)

From the graphs, it is clear that joint “lock-up” does not occur on either of the test dates in 2017. However, there does appear to be some joint “lock-up” on April 25, 2016. This lock-up begins at approximately 1:45 pm, just as the ELTG is reaching the daily maximum. In addition, it is also possible that some joint “lock-up” may occur at the very end of testing on 5/8/2016. This should be considered when evaluating the results. The measured LTEs for each of the test dates at the 9,000 and 16,000 lb nominal load levels can be seen in Figures 4.6 through 4.13.

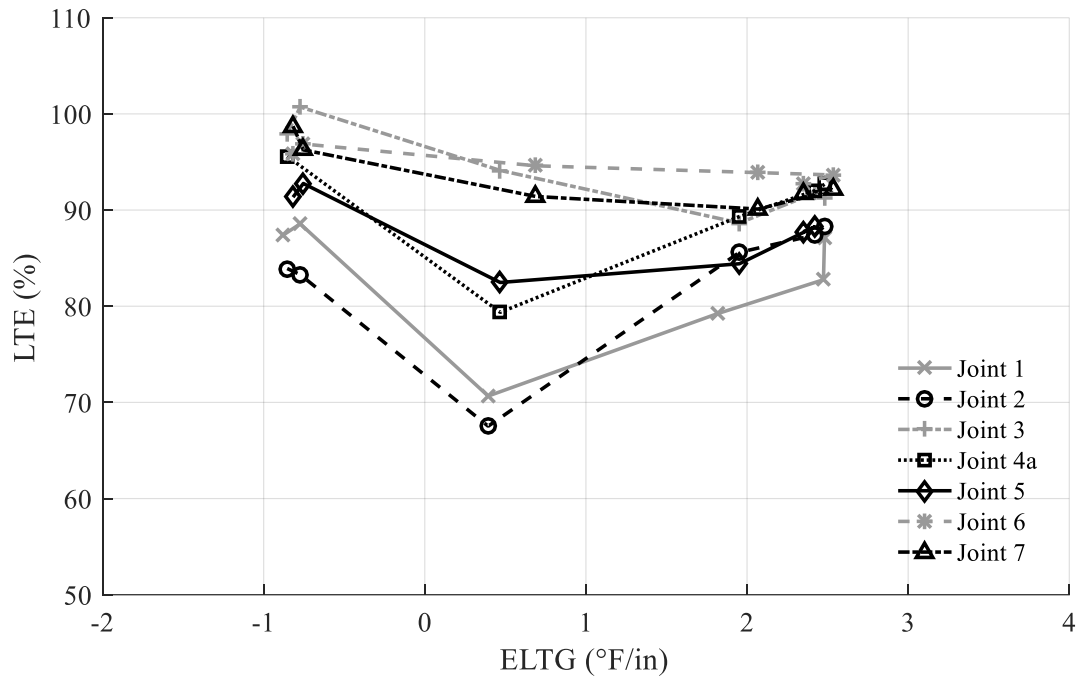


Figure 4.6. Measured LTE at I-79 (5/8/2016, 9,000 lb nominal load level)

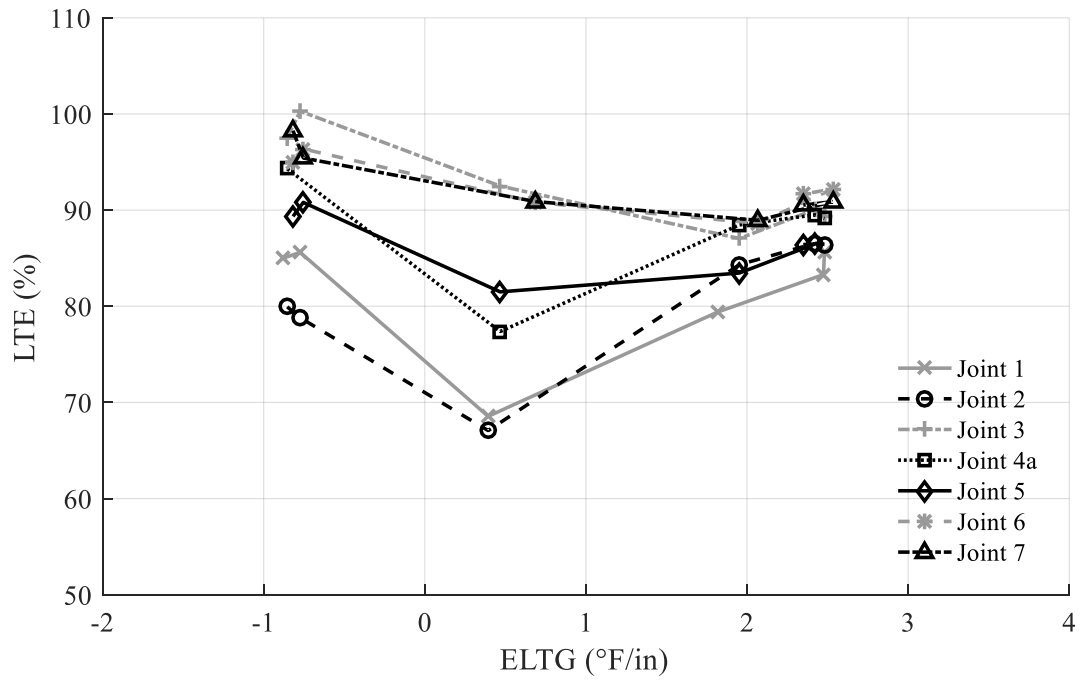


Figure 4.7. Measured LTE at I-79 (5/8/2016, 16,000 lb nominal load level)

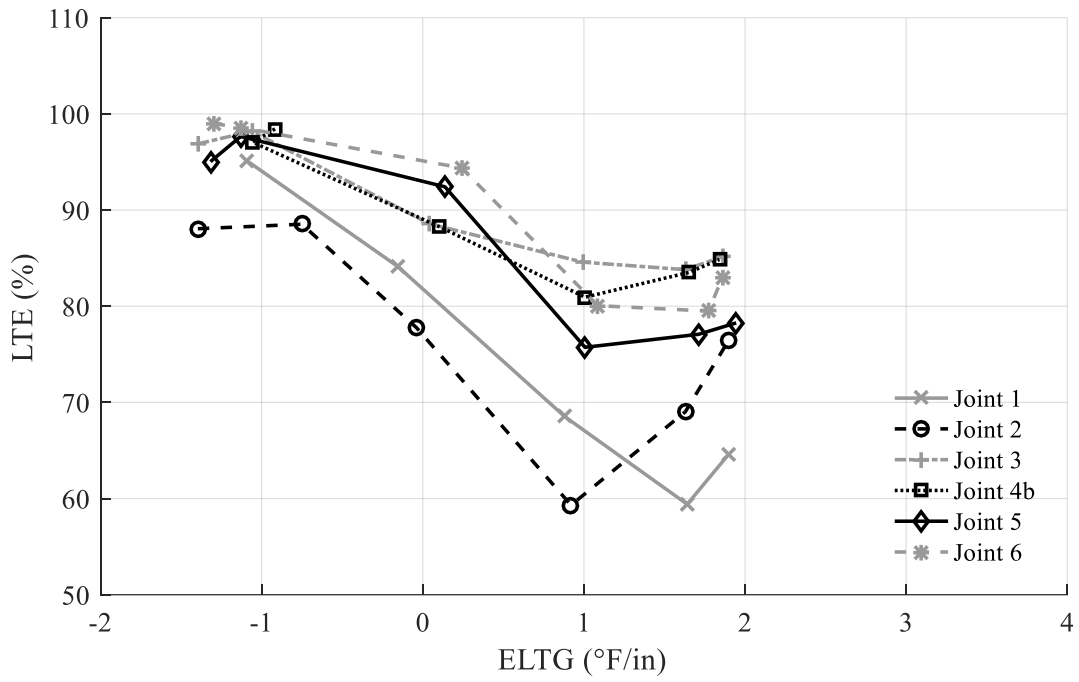


Figure 4.8. Measured LTE at I-79 (10/1/2017, 9,000 lb nominal load level)

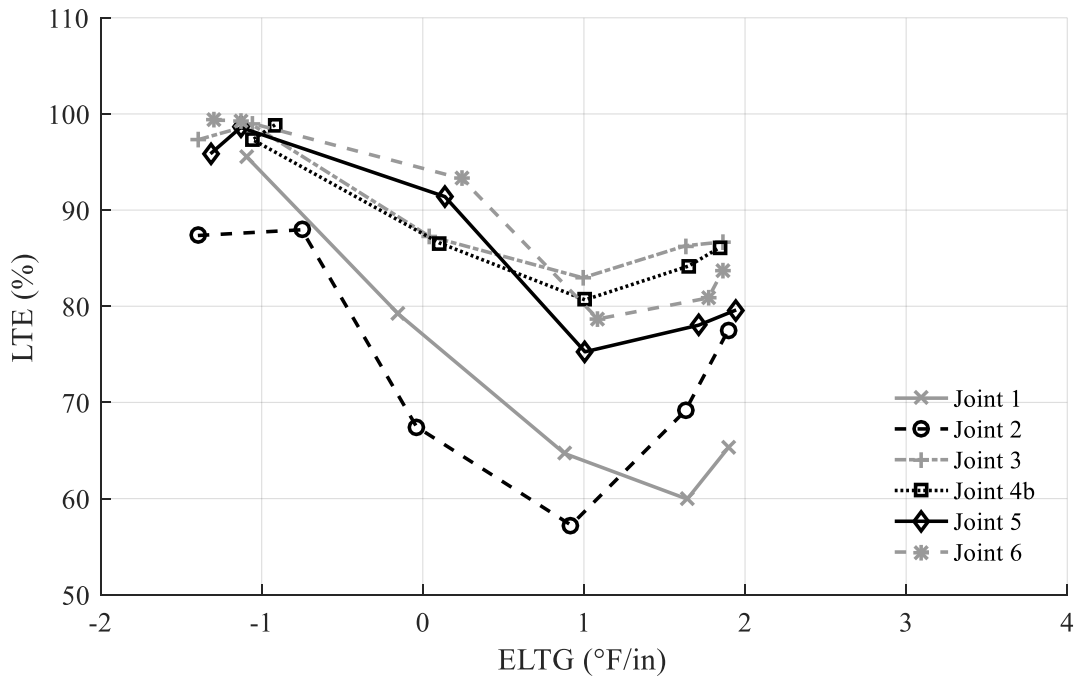


Figure 4.9. Measured LTE at I-79 (10/1/2017, 16,000 lb nominal load level)

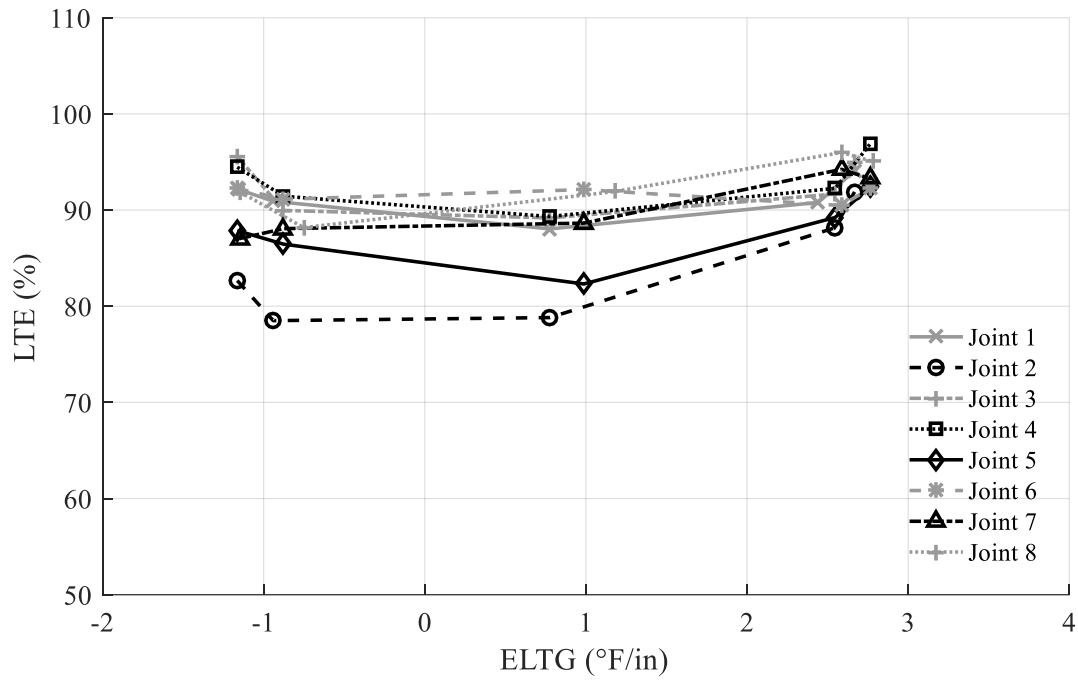


Figure 4.10. Measured LTE at SR-22 doweled section (4/25/2016, 9,000 lb nominal load level)

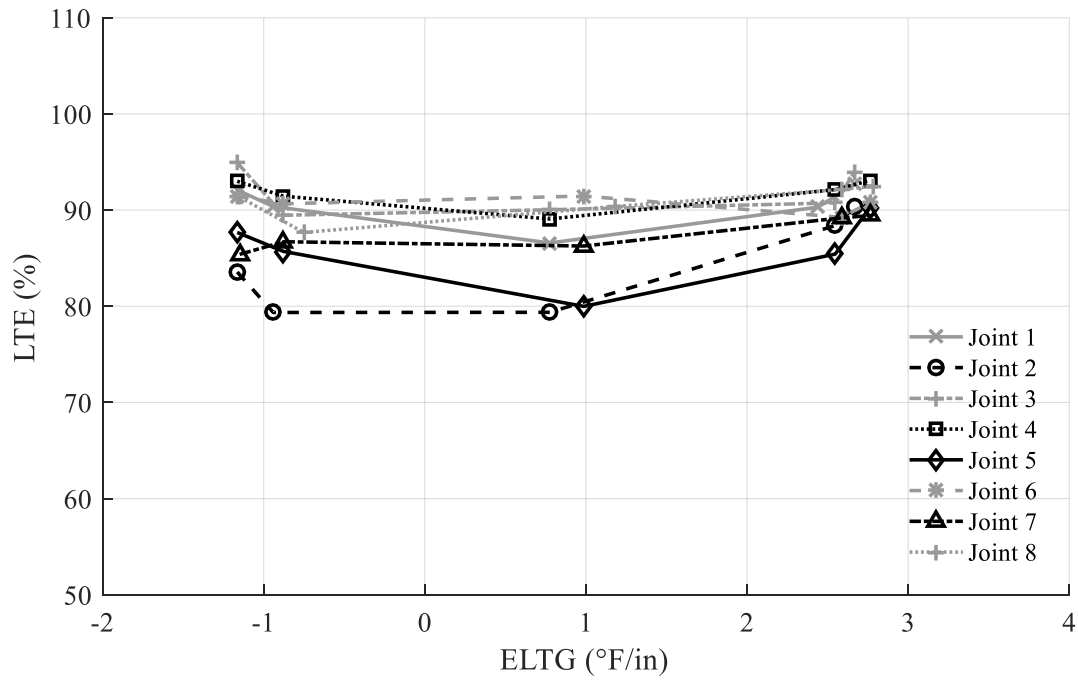


Figure 4.11. Measured LTE at SR-22 doweled section (4/25/2016, 16,000 lb nominal load level)

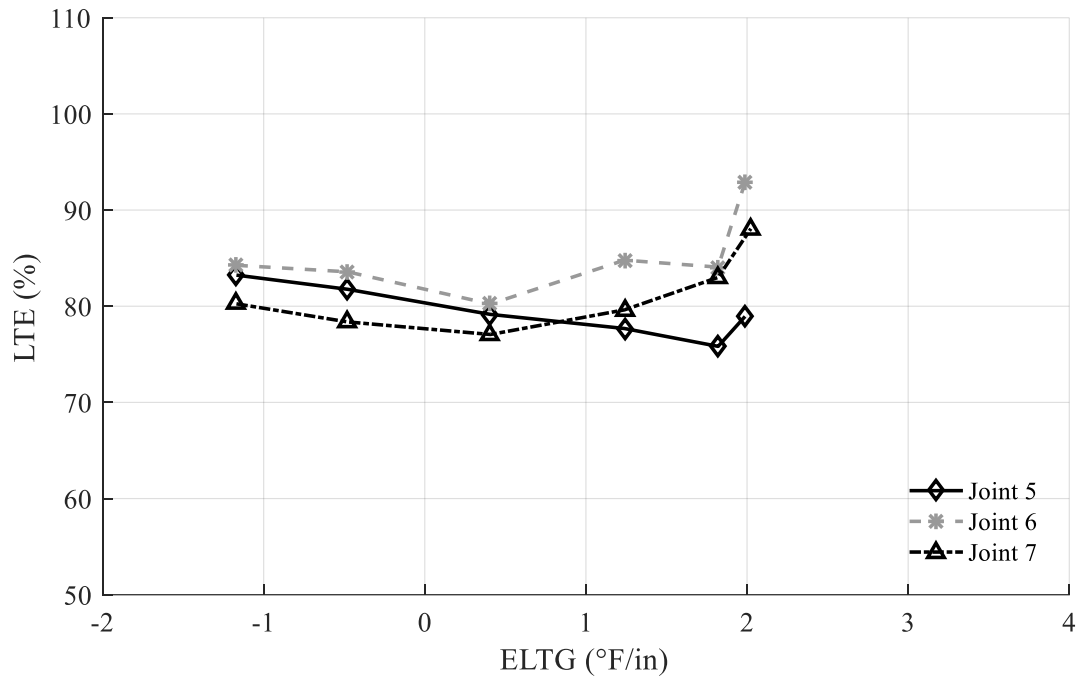


Figure 4.12. Measured LTE at SR-22 doweled section (10/2/2017, 9,000 lb nominal load level)

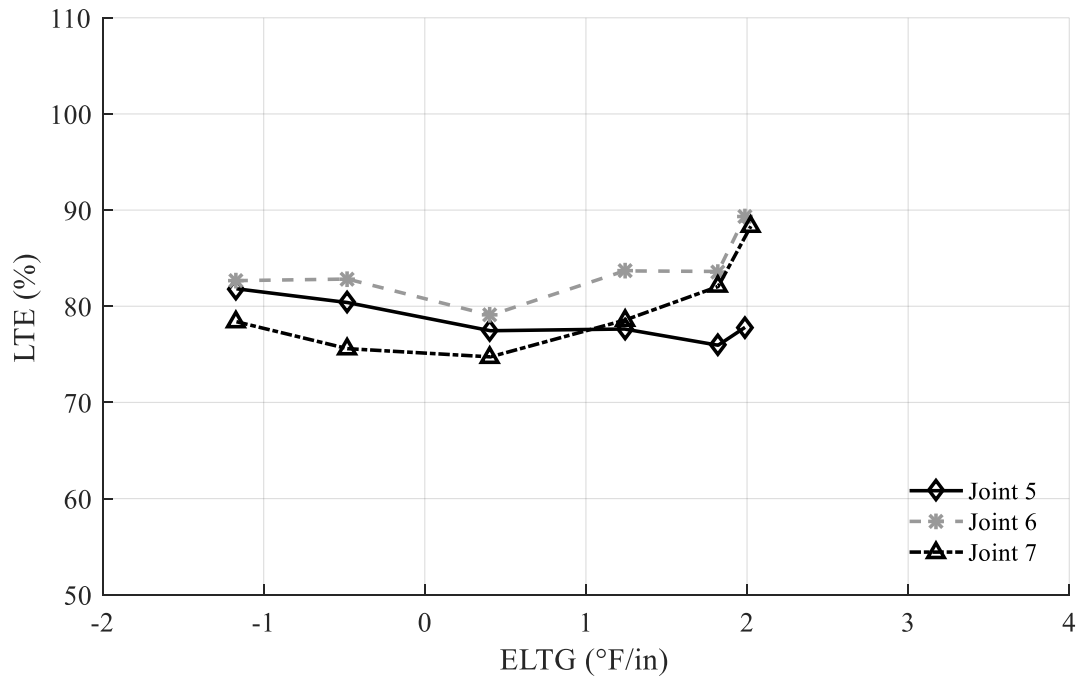


Figure 4.13. Measured LTE at SR-22 doweled section (10/2/2017, 16,000 lb nominal load level)

The primary purpose of the analysis is to evaluate the effect of slab curvature on the measured LTE at each joint. Therefore, the measured LTE is not corrected for slab bending. The measured LTE at each test location of SR-22 is greater than 75% at all test times. When these measurements are corrected for bending, the LTE is greater than 88%, indicating very little dowel looseness. Based on the results of the analysis, testing at SR-22 does not show a large effect of slab curvature on LTE.

However, the joints at I-79 appear to be experiencing more dowel looseness, especially Joints 1 and 2. The section of I-79 is a travel lane upstream of the test section, but transitions into an exit lane near the end of the test section. The joints tested in this section are approximately 60 feet apart. Therefore, the first two joints may experience additional truck loads than the joints further down-stream. Joints 4a and 5 also appear to be experiencing some dowel looseness. It should be noted that a core was taken on the leave slab of joint 4a after the 2016 test date. Therefore, Joint 4b of the 2017 test date is one slab downstream of Joint 4a of the 2016 test date.

On both test dates, the minimum LTE at the joints that exhibit dowel looseness occurs when the ELTG is slightly positive. The LTE increases as positive or negative gradients increase in magnitude. This occurs in both 2016, when joint lockup is possible, and 2017, when joint lockup is unlikely. Long term curvature, which is primarily due to moisture differentials, causes the slab to experience negative curvature when no temperature gradient is present. Therefore, these slightly positive ELTGs likely correspond to approximately flat slabs. The analysis at the KHC test road showed that LTE decreased as the temperature gradient increased similar to the tests at I-79 with a negative or small positive ELTG. However, unlike the tests for Joints 1, 2, 4a, 5 at I-79, the testing at the KHC test road did not show the increase in LTE in the presence of larger positive

temperature gradients (Jeong et al 2006). Joints 3, 6, and 7 at I-79, which appear to be experiencing less dowel looseness, also exhibit this trend. Since the measured LTE at the KHC test road is high (above 85%), it is likely that with more dowel looseness present, the LTE would begin to increase at larger positive temperature gradients (Jeong et al 2006).

It is interesting to note that the minimum LTE of Joint 2 at I-79, which has the lowest LTE at most temperature gradients, occurs at a lower ELTG than the other sections. In addition, it appears from Figure 4.9 that using a 16,000 lb load level results in the LTE increasing less quickly as larger positive or negative gradients develop. There are not enough test points available for the 2016 test date to determine if a similar trend occurred in 2016.

There has not been a lot of previous research on the effect of slab curvature on measured DD. Traditional analysis of concrete pavements, where load transfer at the joint is modeled using shear springs or beam element dowels with dense liquid interactions with the concrete, results in the DD being a maximum when a negative ELTG is present. However, this has not been evaluated with field data. The measured DD normalized to a 9,000 lb load is presented in Figures 4.14 to 4.21 for the test sections.

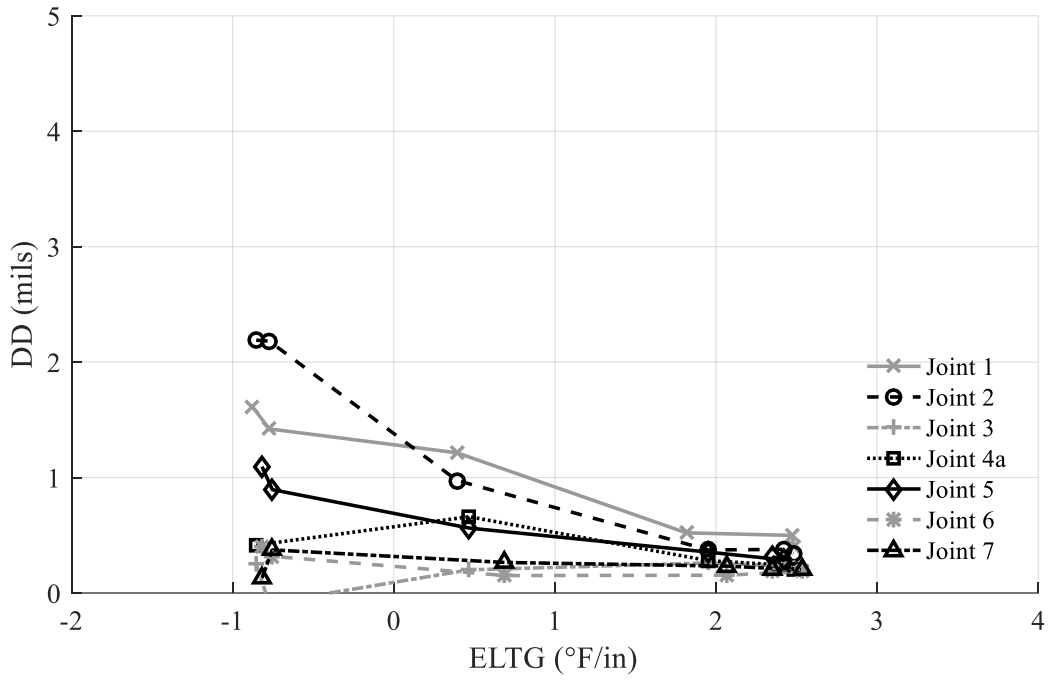


Figure 4.14. Measured normalized DD at I-79 (5/8/2016, 9,000 lb nominal load level)

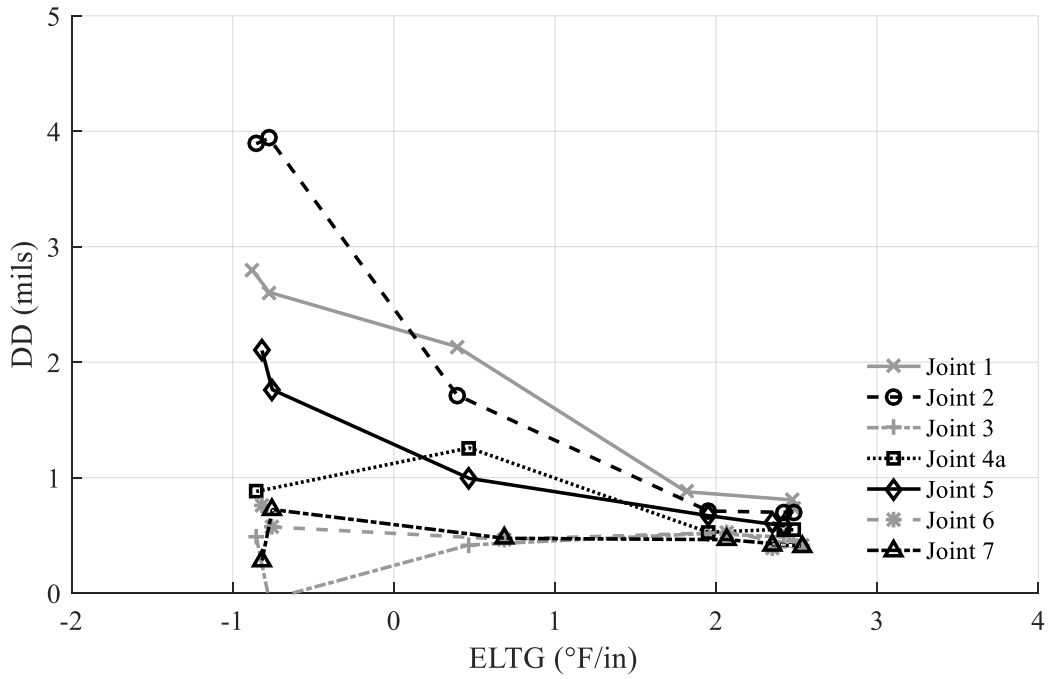


Figure 4.15. Measured normalized DD at I-79 (5/8/2016, 16,000 lb nominal load level)

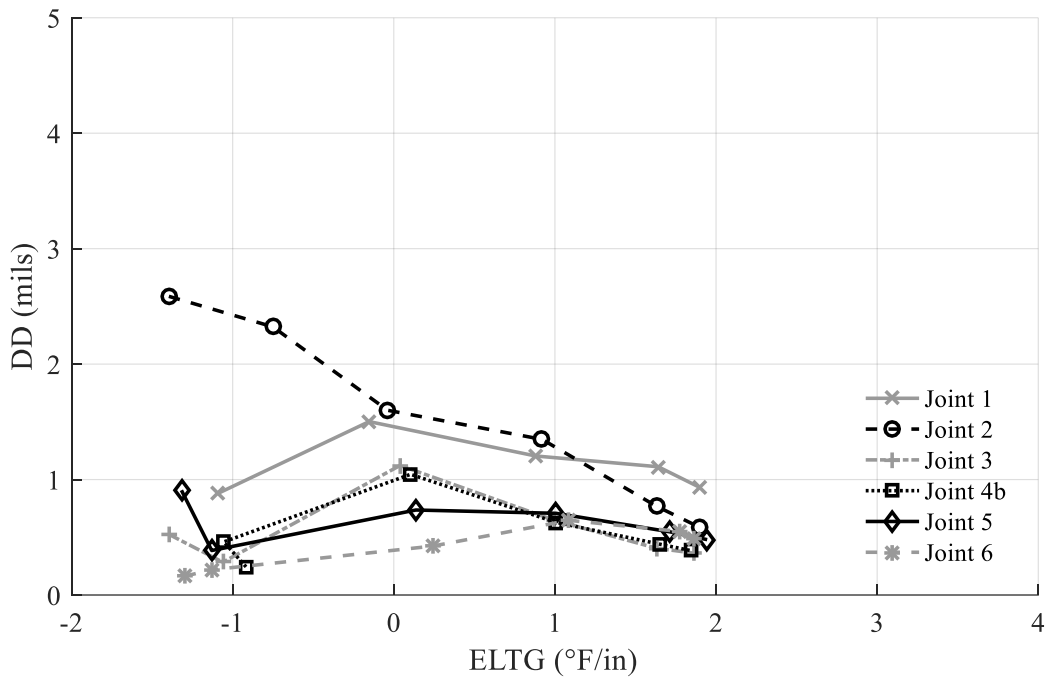


Figure 4.16. Measured normalized DD at I-79 (10/1/2017, 9,000 lb nominal load level)

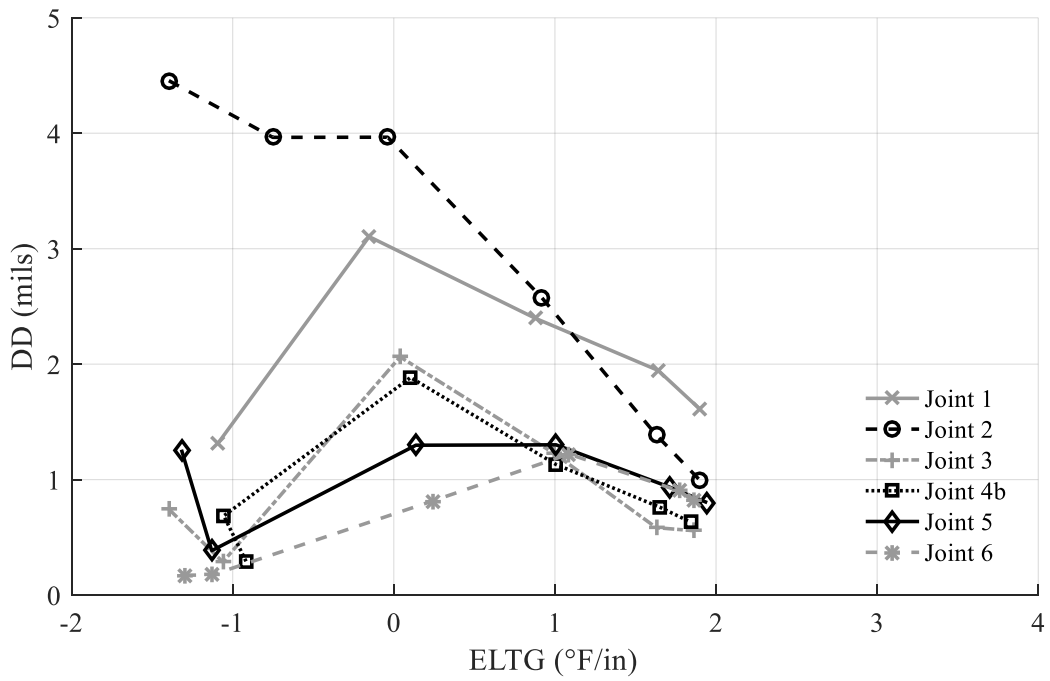


Figure 4.17. Measured normalized DD at I-79 (10/1/2017, 16,000 lb nominal load level)

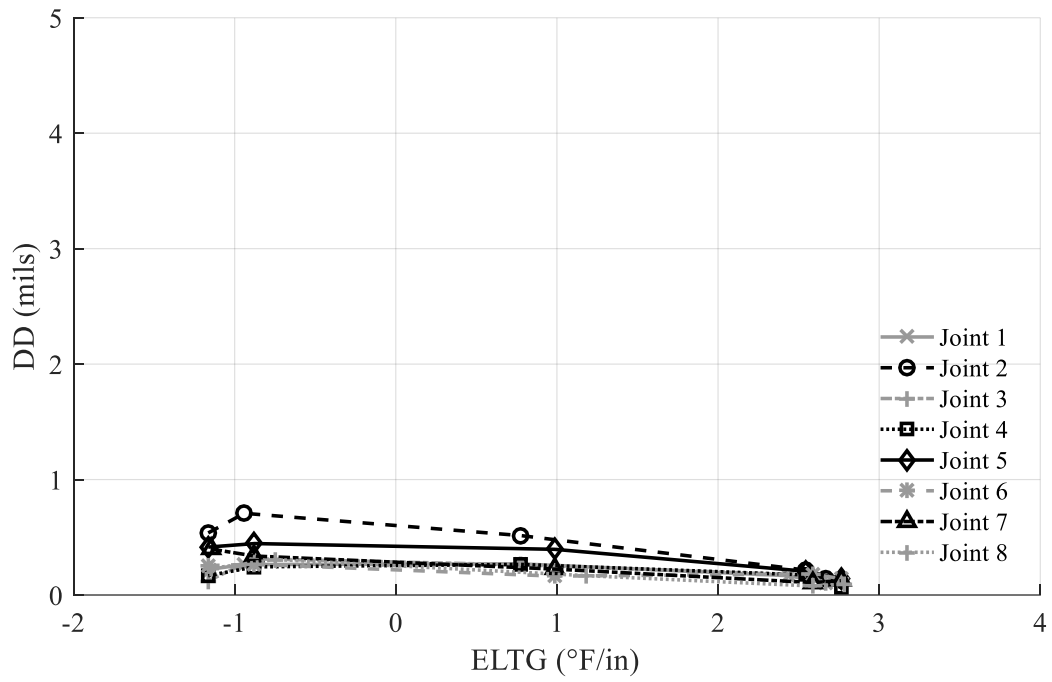


Figure 4.18. Measured normalized DD at SR-22 (4/25/2016, 9,000 lb nominal load level)

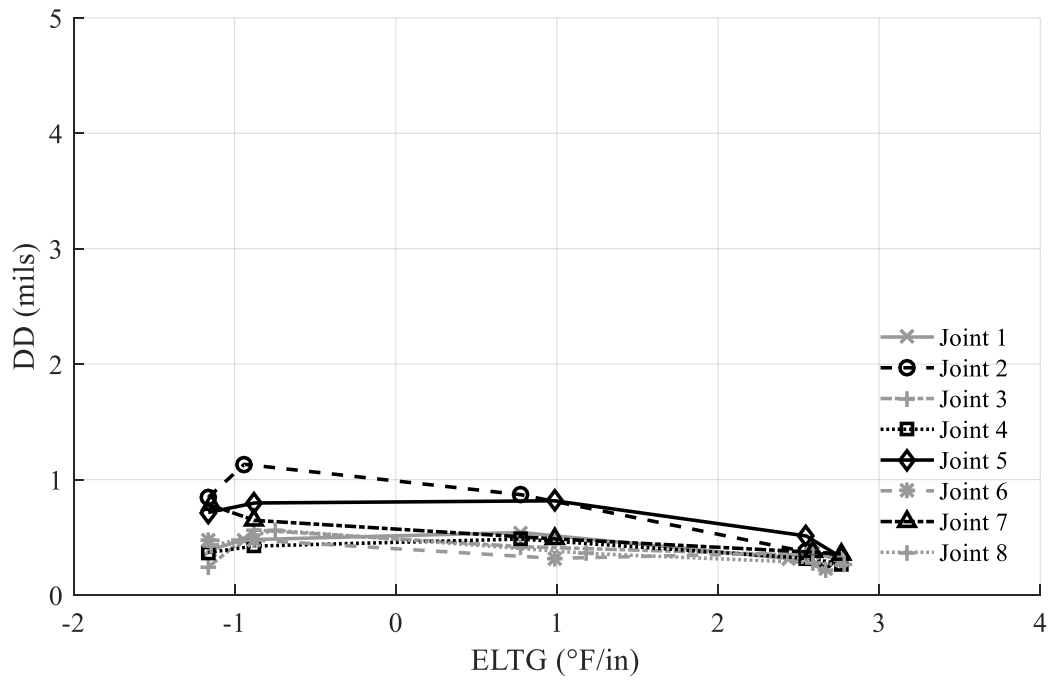


Figure 4.19. Measured normalized DD at SR-22 (4/25/2016, 16,000 lb nominal load level)

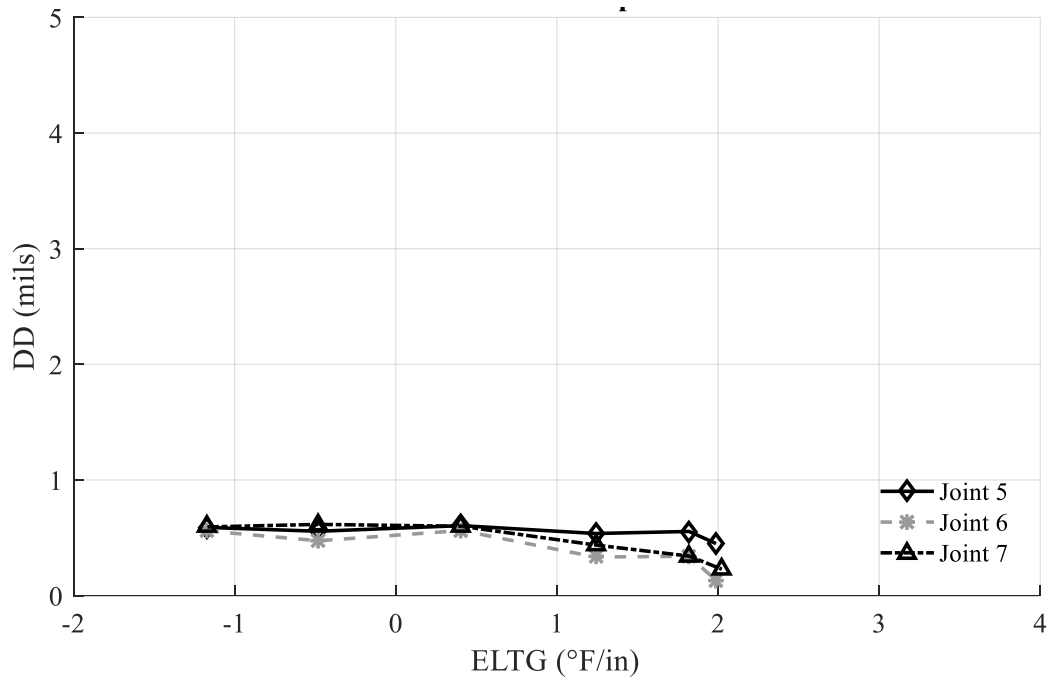


Figure 4.20. Measured normalized DD at SR-22 (10/2/2017, 9,000 lb nominal load level)

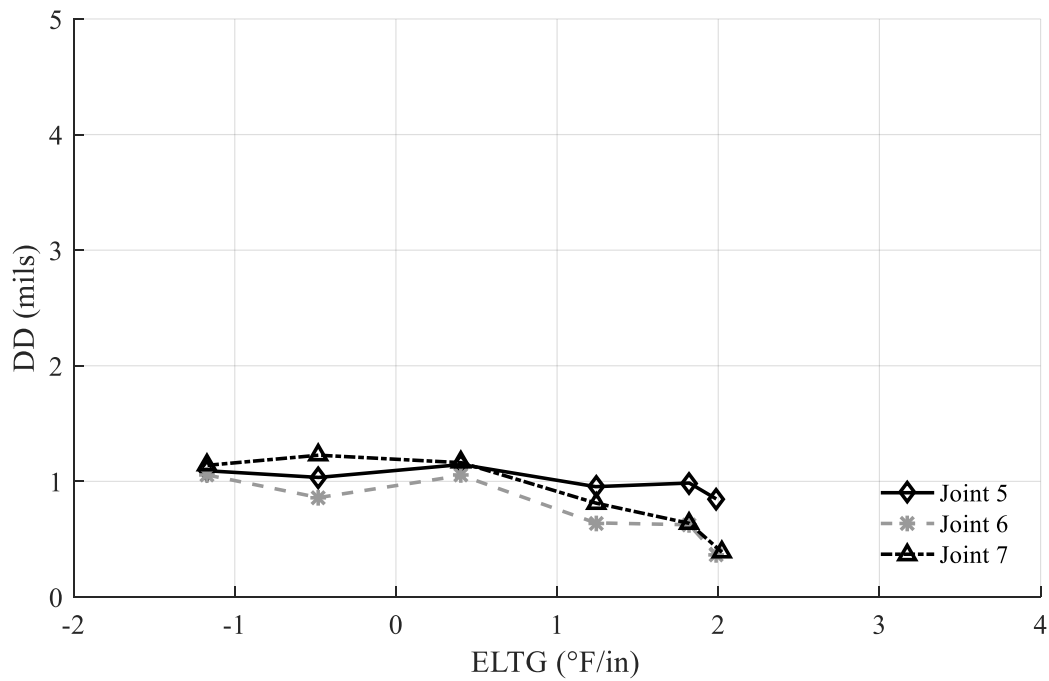


Figure 4.21. Measured normalized DD at SR-22 (10/2/2017, 16,000 lb nominal load level)

Similar to LTE, the DD measurements of the test sections at SR-22 are indicative of minimal dowel looseness. The DD at this test section does not appear to be largely affected by ELTG, except that the DD slightly decreases at larger positive ELTGs. This occurs for both 2016 and 2017 and therefore is not likely due to joint “lock-up.” During testing at the I-79 test section in 2016, the joints that appear to have the most dowel looseness (Joints 1, 2, and 5) have a maximum DD when the peak negative ELTG occurs. Joint 4a has some dowel looseness, but to a lesser degree. The peak DD for this joint occurs when the slab is approximately flat. The peak negative temperature gradient in 2017 was greater than the peak negative temperature gradient in 2016. In 2017, the maximum DD at all joints, except Joint 2, occurs when the slab is approximately flat. At Joint 2, which likely has the most dowel looseness, the maximum DD occurs when the peak negative ELTG is present. It is interesting to note that in 2016 the maximum DD at I-79 Joints 1 and 5 occurred at the peak negative ELTG, approximately -0.9 °F/in. However, in 2017 the DD at these joints is well below the daily maximum when the peak negative ELTG, approximately -1.1 °F/in, is present. This likely indicates that the measured DD decreases rapidly as the negative ELTG approaches a level that will cause the dowel to become “locked-up” against the edge of the socket.

Using the 16,000 lb nominal load level instead of the 9,000 lb nominal load level may provide additional information about the condition of the joint when using DD as the joint efficiency parameter. For example, At I-79, Joint 2, the measured DD with an ELTG around 0 °F/in at the 9,000 lb load level is well below the maximum differential deflection. However, the measured DD with an ELTG around 0 °F/in at the 16,000 lb load level is near the maximum differential deflection.

4.3 COMPUTATIONAL ANALYSIS

4.3.1 Model Description

A computational analysis was performed to validate the trends observed in the field data and explore the mechanisms behind the observations. This study was conducted using the pavement specific finite element model software EverFE v2.24 (Davids 2003). A single structure with varying levels of slab curvature and dowel looseness was analyzed. The pavement of interest consists of a three-slab, single-lane system with no edge support. The modeled structure has a 12-ft lane width with a 15-ft joint spacing. The pavement structure consists of a 10-in thick concrete slab with an elastic modulus of 5 million psi, a 10-in thick granular base with an elastic modulus of 20,000 psi, and a dense liquid foundation with a k-value of 200 psi/in. Load transfer at the transverse joint is provided by 1.25-in diameter dowels spaced at 12-in on center. The slab was modeled using 7-in x 6-in x 5-in 20-node quadratic elements; this element size was shown to produce mesh convergence in previous studies (Davids 1998) and was validated for the present study.

The interaction between the dowel and the joint can be modeled using a dense liquid interaction (Guo et al. 1995; Nishizawa et al. 1989), discretely applying dowel looseness due to socketing (Davids 2000; Guo 1992; Mackiewicz 2015; Maitra et al. 2009), or modeling the concrete using a non-linear damage model (Khazanovich et al. 2008; Prabhu et al. 2009). For this study, the analysis was performed with dowel looseness discretely applied and with a dense liquid interaction between the dowel and the concrete. A comparison between these models can be used to determine whether non-linear behavior due to dowel looseness contributes to the phenomena observed in the field data.

An assumed dense liquid interaction between the concrete and the dowel matches the assumptions used in traditional dowel structural analysis Friberg (1940). This can be accomplished computationally by using embedded dowel elements where the stiffness matrix of the dowel is altered to include the stiffness of the concrete in which the dowel is embedded (Davids 2003, Guo 1992).

EverFE contains a module to model discrete dowel looseness. In this module, each dowel is modeled using 24 three-node, 18 degrees of freedom, quadratic beam elements with 12 elements on each side of the joint and one shear beam element spanning the joint (Davids 2003). Of the 12 elements on each side of the joint, 10 are placed within the area of socketing creating 20 possible locations for contact between the dowel and the concrete. Gap elements are placed between the dowel and the concrete at each location. The number of elements used in this analysis was found to achieve mesh convergence in previous studies and is not adjustable within the EverFE program (Davids 1998). Socketing around the dowel is defined by two parameters, the maximum gap width at the joint, a , and the maximum extent of socketing along the dowel, b . The thickness of the gap element representing the socket is null at a distance b from the joint and increases quadratically to a depth of a at the joint (Davids 2003). The geometry of the EverFE dowel looseness implementation can be seen in Figure 4.22.

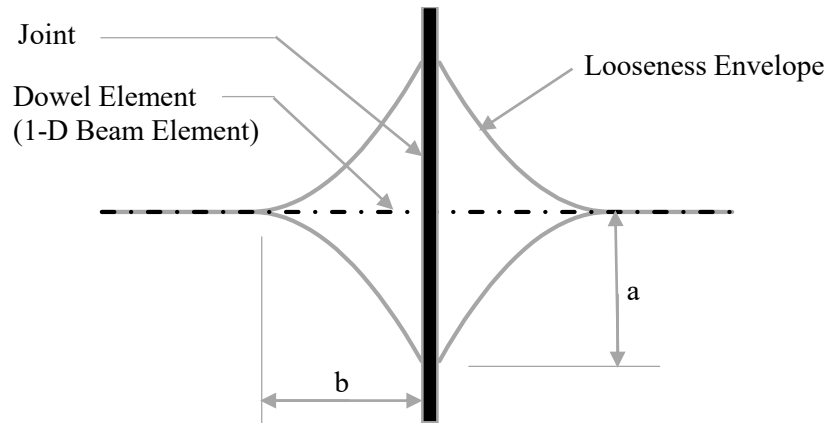


Figure 4.22. Geometry of EverFE dowel looseness implementation

Other analyses considering dowel bar socketing have assumed a constant gap width the full length of the bar (Guo 1992; Maitra et al. 2009) or a gap linearly increasing from null at the embedded end of the dowel to the prescribed dowel looseness at the joint (Mackiewicz 2015). The expected shape of the socket should match the deformed shape of a dowel in an elastic medium, which can be described by a decaying sine wave. A quadratic function can approximate a decaying sine wave well up to the first inflection point. Therefore, the quadratic socket shape used in EverFE is acceptable for this analysis.

In addition to selecting the shape of the dowel socket, it is also necessary to estimate the size of the socket using parameters a and b . The maximum gap width, parameter a , has been estimated as half of the deflection intercept of a plot of DD versus load as a static load is applied (Teller and Cashell 1959). This gap width has also been estimated during dynamic cycling as part of several research projects. Teller and Cashell observed a maximum gap width of up to 3 mils in in-service pavements. A laboratory study, intended to evaluate the performance of dowel bars epoxied in the edge of full-depth repairs, subjected dowel bars anchored into an 18-in x 12-in x

10-in block to 600,000 bidirectional shear loads simulating 9,000-lb single axle loads. The control specimens, consisting of 1-in diameter steel dowel bars cast in the concrete, experienced a maximum gap width of approximately 2 mils after 600,000 load cycles (Synder 1989). Another laboratory study was conducted to estimate dowel looseness as a function of applied loads and concrete material properties. In this study, two 37.5-in x 24-in x 10-in slabs on a neoprene foundation were connected by a dowel. The system was then subjected to loading from two actuators simulating a moving wheel load. The maximum gap width was found to vary between 6 mils and 8 mils after 100,000 load cycles depending on the type of aggregate used in the concrete (Buch and Zollinger 1996). In addition, a dowel bar system, consisting of three 1.5-in diameter epoxy coated steel dowel bars between two 72-in x 60-in x 6-in slabs, was tested in the accelerated loading frame (ALF) at the University of Pittsburgh. The average compressive strength of the concrete was 5,100 psi. The bars were subject to 10 million load cycles. In each cycle, a 9000-lb, 25-Hz half sinusoidal load was applied by actuators on each side of the joint, with a 90-degree phase lag, to simulate a moving wheel load. This loading was followed by a 0.16-sec rest period between each load cycle. At specified intervals during the dynamic testing, a quasi-static load was applied over 5 seconds (Vandenbossche 2017). This static load was used to estimate the dowel looseness. As can be seen in Figures 4.23 and 4.24, the estimated gap width was 1.0 mil after 25,000 load applications (LTE=85%, DD= 6 mils) and 1.8 mils after 5,000,000 load applications (LTE=81%, DD=8 mils). It should be noted that LTE and DD are measured with linear variable displacement transducers (LVDTs) approximately 1 in from the joint and 1 in from the edge of the slab. Therefore, these values cannot be directly compared to LTE and DD measured 6 in from the joint in the wheelpath during FWD testing.

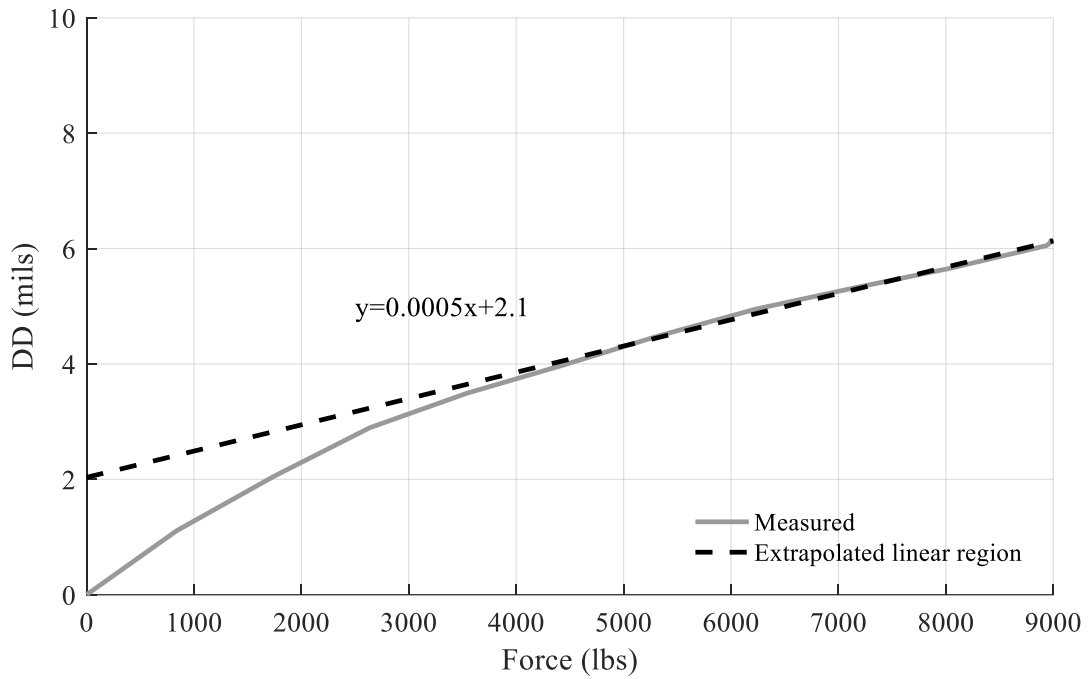


Figure 4.23. Estimated dowel looseness from ALF testing after 25,000 load cycles (Vandenbossche 2017)

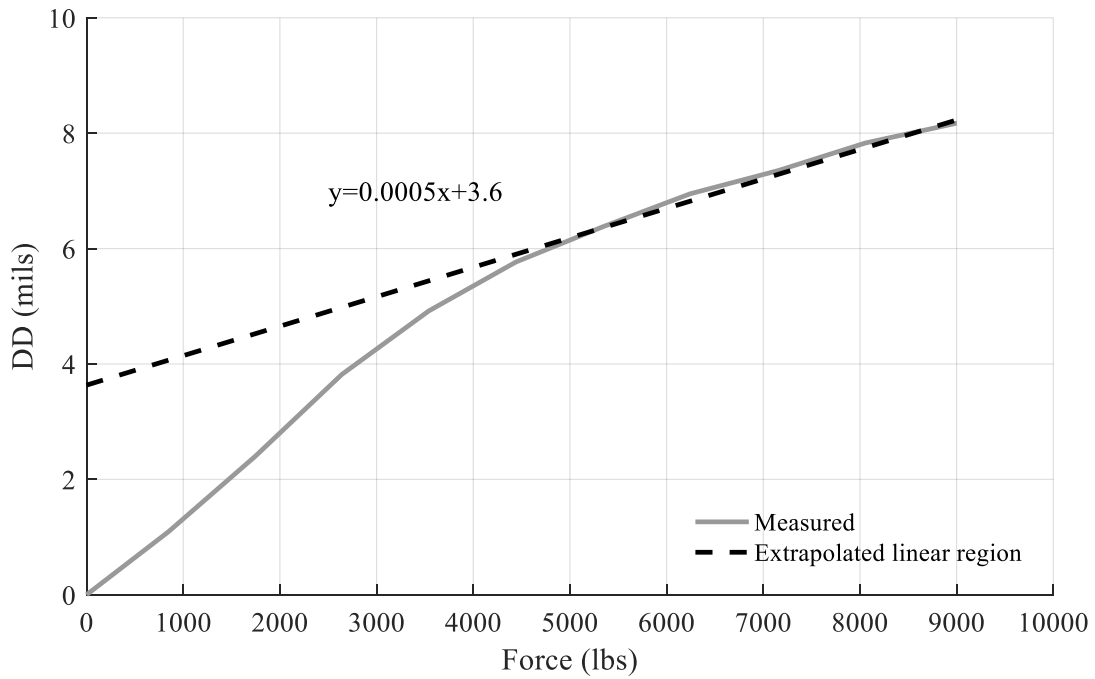


Figure 4.24. Estimated dowel looseness from ALF testing after 5,000,000 load cycles (Vandenbossche 2017)

There is no experimental data available for defining the length of dowel looseness, parameter b . In the development of EverFE, a length of dowel looseness equal to half the embedded dowel length (4.5 in) was used (Davids 1998). However, this value is not based on a computational or experimental analysis of the gap length. A logical approximation of the length of dowel looseness is the location of the first inflection point of the dowel bar deflection within the joint assuming the dowel acts as a beam on an dense liquid foundation (Friberg 1940). The derivative of the deflection within the joint is presented in Equation 4.3.

$$\frac{dy}{dx} = \frac{e^{-\beta x}}{2\beta^2 EI} [(2\beta M_0 - P) * \cos(\beta x) - P \sin(\beta x)] \quad (4.3)$$

Where:

E= the modulus of elasticity of steel (29 million psi)

I= the moment of inertia of the dowel bar ($\pi d^4/64$),

x= the distance along the dowel

P= the applied shear force at the face of the joint

M_0 = the applied moment at the face of the joint.

The moment, M_0 due to an applied wheel load is estimated as $zP/2$, where z is the joint width. The radius of relative stiffness of the bar, β , can be calculated using Equation 4.4.

$$\beta = \sqrt[4]{\frac{Kd}{4EI}} \quad (4.4)$$

Where:

K= the modulus of dowel bar interaction

d= the bar diameter

The location of the first inflection point can be found by setting Equation 4.3 to 0. For a load transferred by a 1.5-in diameter steel dowel across a 0.25-in wide joint with a modulus of dowel bar interaction of 1.5 million psi/in, the first inflection point occurs 4.8 in from the joint. This value agrees well with the value of 4.5 in used in the development and validation of EverFE. Therefore, a value of 4.8 in is used as the length of dowel looseness, b , in this computational analysis. No friction or bond was considered between the dowel and the surrounding concrete.

Based on previous experimental data, three levels of dowel looseness, 1 mil, 2 mils, and 4 mils, were used in the computational analysis with discretely modeled dowel looseness. In addition, three levels of modulus of dowel bar interaction, 1.5 million psi/in, 0.75 million psi/in, and 0.3 million psi/in, were used in the computational analysis with a dense liquid interaction. For each of the six combinations of parameter interaction and model type, analyses were performed with effective composite linear temperature gradients (CLTG) ranging from -3 °F/in to 3°F/in in 0.25 °F/in increments. The composite linear temperature gradient accounts for slab curvature due to the temperature gradient, moisture gradient, and built-in curling. The long-term portion of the CLTG, which is primarily due to the moisture gradient has been found to be around - 1°F/in, as described in Section 3.3. Therefore, the CLTG values used in the computational analysis likely correspond to higher field measured ELTG values.

4.3.2 Results of Analysis

The LTE and DD predicted by the computational analysis with discretely modeled dowel looseness are shown in Figures 4.25 and 4.26, respectively.

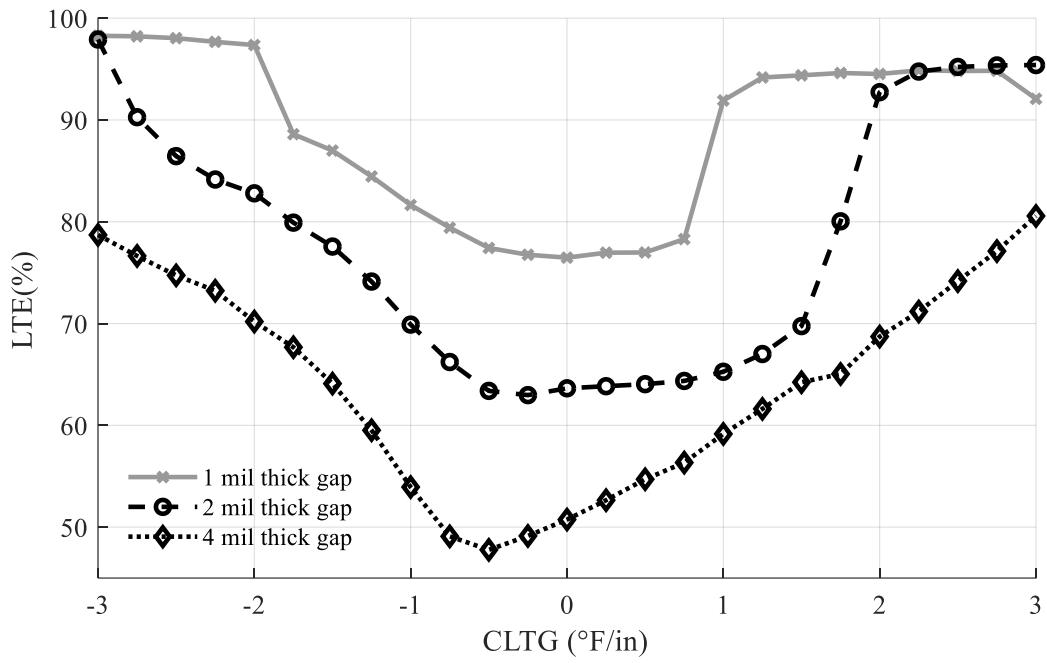


Figure 4.25. LTE predicted by the computational analysis with discretely modeled dowel looseness

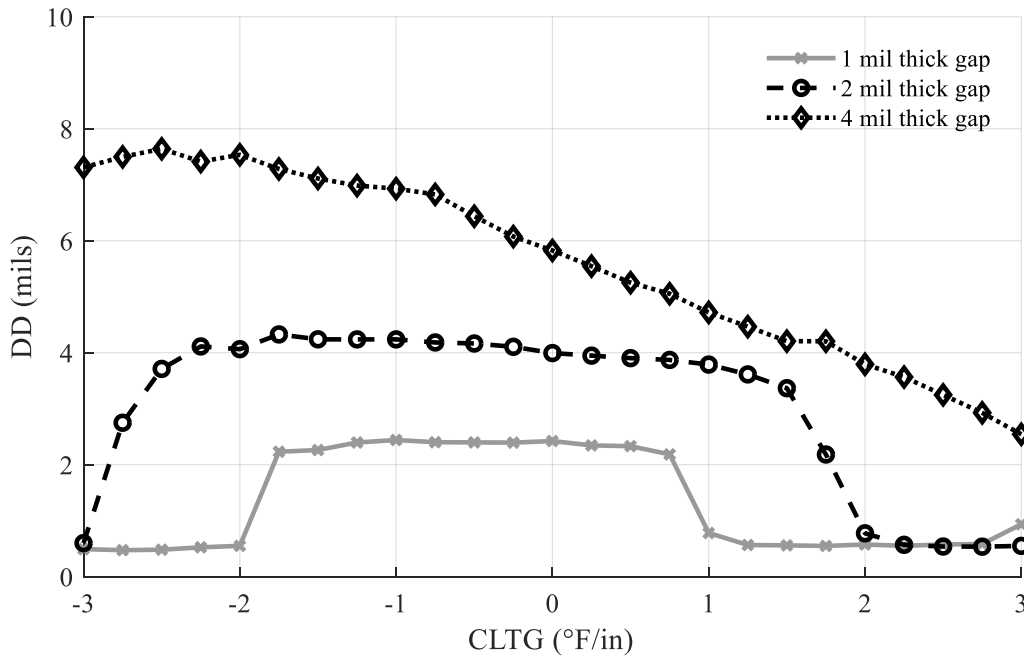


Figure 4.26. DD predicted by the computational analysis with discretely modeled dowel looseness

Several of the phenomenon observed in the field data are also observed in the computational analysis. Like the field data, the minimum LTE from the computational analysis occurs when the slab is approximately flat. For pavements with a gap width of 1 or 2 mils, the maximum DD in the computational analysis also occurs when the slab is approximately flat. For these sections, the DD decreases rapidly once a certain positive or negative ELTG is reached. This is similar to what occurs for Joints 1, 4a, and 5 at I-79 in the field trials. In addition, the computational analysis predicts that for pavements with a gap width of 4 mils the maximum DD occurs at the peak negative temperature gradient, which is similar to what was observed at Joint 2 at I-79.

The minimum LTE from the computational analysis with a gap width of 4 mils occurs at a slightly lower CLTG than the minimum LTE for the lower levels of dowel looseness. This is very much like the observations from the field data at I-79, where the minimum LTE at Joint 2 occurred at a lower ELTG than the other joints. In addition, the computational analysis predicts that for pavements with a gap width of 4 mils, the LTE increases rapidly as the CLTG increases or decreases from CLTG with the minimum LTE. In contrast, for pavements with less dowel looseness, the computational analysis predicts that a range of CLTGs will produce similar LTE measurements. The predicted LTE increases slowly as ELTG decreases at ELTGs lower than the range of ELTGs which produce the minimum predicted LTE. In contrast, the predicted LTE increases rapidly with increasing ELTG at ELTGs higher than the range which produces the minimum LTE. This again is similar to the field data from I-79 in 2017, shown in Figure 4.16 and 4.17. In this data, the LTE increases rapidly as the ELTG increases or decreases from the ELTG at the minimum LTE for Joints 1 and 2, which appear to exhibit the most dowel looseness. For the other joints, a range of ELTGs exist when the LTE is near the minimum.

The computational analysis also shows that the measured DD decreases rapidly as the CLTG reaches critical values of positive and negative CLTG. The rapid decrease in DD at these critical values of CLTG may explain why the DD did not decrease for I-79 Joints 1 and 5 on the 2016 test date but did on the 2017 test date. The critical value of CLTG associated with this rapid decrease in DD for these joints is likely associated with an ELTG between the minimum ELTG on the 2016 test date and the minimum ELTG on the 2017 test date. The range of CLTGs which produce larger DDs increases as the gap width increases. This could explain why the measured DD decreased at negative temperature gradients for Joint 4a at I-79 on the 2016 test date but did not decrease for Joints 1 and 5.

There are some differences between the trends observed in the computational analysis and field data. For example, the computational analysis shows that with a gap width of 1 or 2 mils, the measured differential deflection is nearly constant within the range where significant DD are measured. It is not possible to see the true shape of the relationship between slab curvature and DD for the field trials, as the number of test points is limited by the testing productivity rate. However, it does not appear that the DD measurements reach this constant value.

This difference could be due to several causes. First, the quadratic shape of the dowel socket is an assumption, which may not match reality. Due to the extremely small size of the socket, it is not feasible to verify this shape with destructive testing. In addition, the computational analysis assumes that dowel looseness is uniform for all dowels. In reality, it is expected that dowels near the edge of the pavement, which are loaded more heavily, will develop more looseness. Finally, discretely modeling the dowel looseness with gap elements assumes a binary stiffness of the concrete surrounding the dowel. The concrete is either assumed to have zero stiffness within the gap or full stiffness outside of the gap. In reality, there is likely some damaged

concrete surrounding the dowel, which has a reduced stiffness between zero and the undamaged stiffness of the concrete. Some researchers have used the concrete damage plasticity module in the general-purpose FEM program Abaqus to model the damaged concrete. This research has primarily focused on the behavior of properly installed and misaligned dowels as joints open and close (Khazanovich et al. 2008; Prabhu et al. 2009). This model requires several parameters that are difficult to obtain, such as the confined stress-strain curve, and plastic flow rate of the concrete. In addition, stress softening models, such as the concrete damage plasticity model, are extremely mesh sensitive. Therefore, accurate analysis with this model requires a very computationally expensive fine mesh. An FEM model consisting of a proposed dowel bar test, consisting of eight 1.5-in diameter dowel bars, required 11 GB of memory and 12 hours to run with eight processors running in parallel for a single load cycle. This makes using this model to predict the size and shape of the damaged concrete around the dowel after several million load cycles unfeasible. Some of the discrepancy may also be due to dynamic effects, which are not captured by the static computational analysis. Despite these discrepancies, the EverFE module for modeling dowel looseness allows the computational model to capture the relationship between slab curvature and measured joint efficiency observed in the field trials much better than other available models, such as a dense liquid interaction between the slab and the dowel or modeling load transfer using shear springs.

The LTE predicted by the computational analysis utilizing a dense liquid interaction between the dowel and slab can be seen in Figure 4.27.

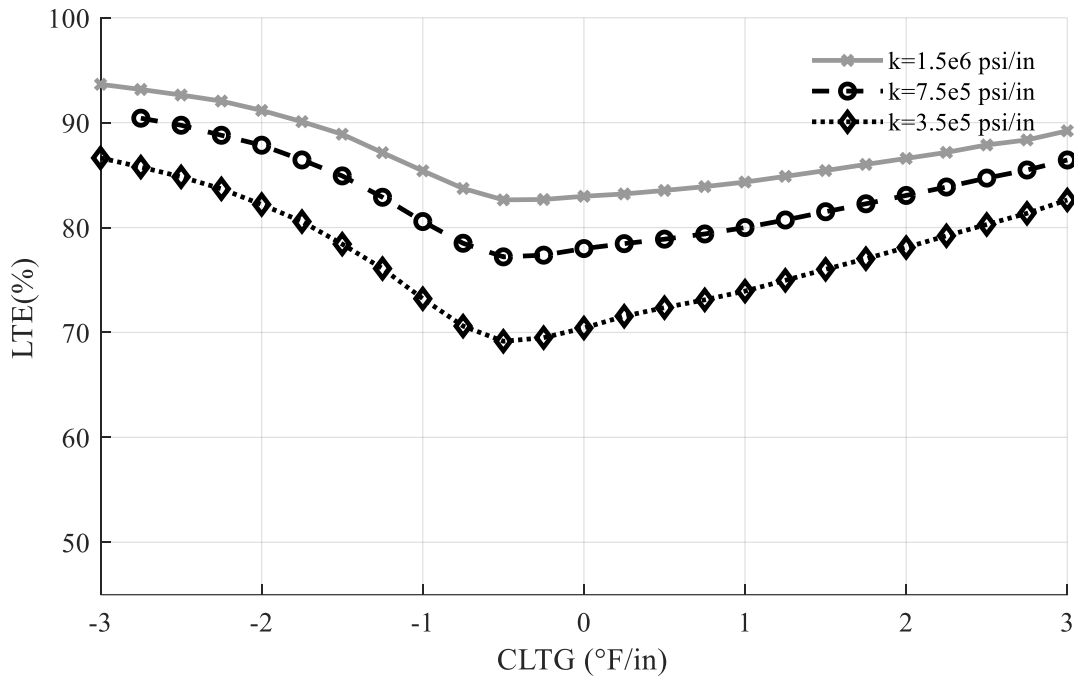


Figure 4.27. LTE predicted by the computational analysis utilizing a dense liquid interaction between the dowel and slab

When the interaction between the slab and dowel is modeled as a dense liquid interaction, the computational analysis still predicts a relationship between slab curvature and measured LTE. The minimum LTE occurs at a slightly negative CLTG, indicating the slab is somewhat curled upwards. However, this effect is smaller than what was observed in the field data and the computational analysis with discretely modeled dowel looseness. In addition, the minimum LTE occurs at approximately the same CLTG and the shape of the curve is similar regardless of the value of the modulus of dowel bar interaction. This also does not match what was observed in the field data and computational analysis. The DD predicted by the computational analysis utilizing a dense liquid interaction between the dowel and the slab is presented in Figure 4.28.

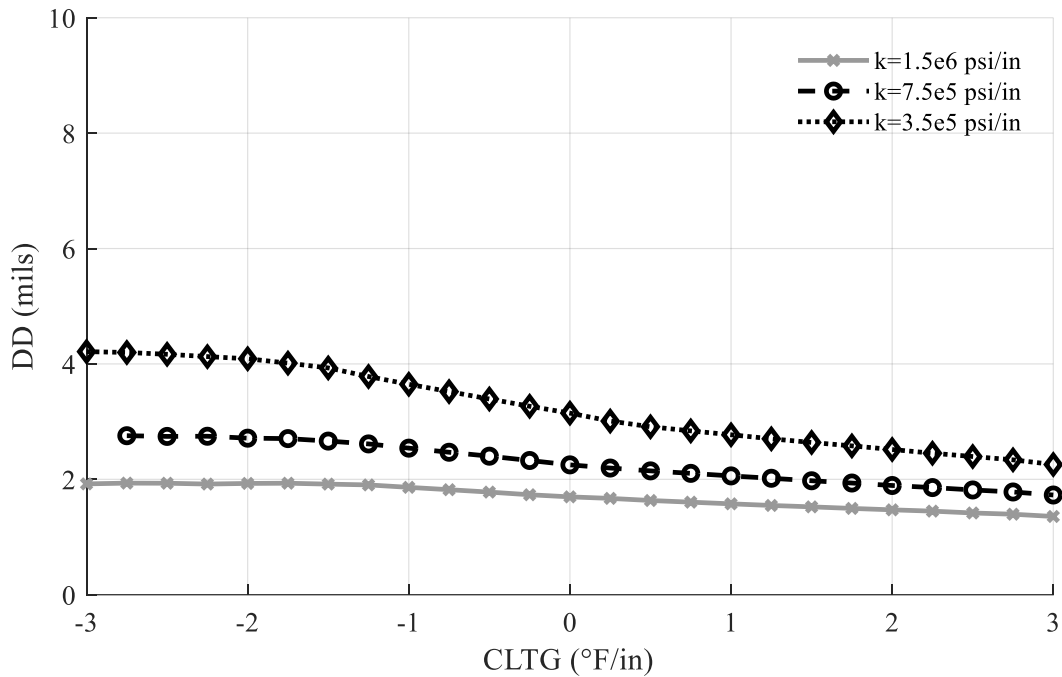


Figure 4.28. DD predicted by the computational analysis utilizing a dense liquid interaction between the dowel and slab

When the interaction between the slab and dowel is modeled as a dense liquid interaction, the computational analysis predicts the DD will increase as the CLTG decreases. This decrease is gradual throughout the typical range of CLTG values that would be observed during the field testing. This does not match the behavior observed in the field trials.

Overall, discretely modeling dowel looseness captures the relationship between slab curvature and joint performance more accurately than using a dense liquid interaction between the dowel and the slab. This indicates that dowel looseness is likely involved in the mechanism behind these trends.

The computational analysis with discretely modeled dowel looseness was also performed with a 16,000 lb load and a gap width of 2 mils. A comparison between the predicted LTE with a 9,000 and 16,000 lb load can be seen in Figure 4.29.

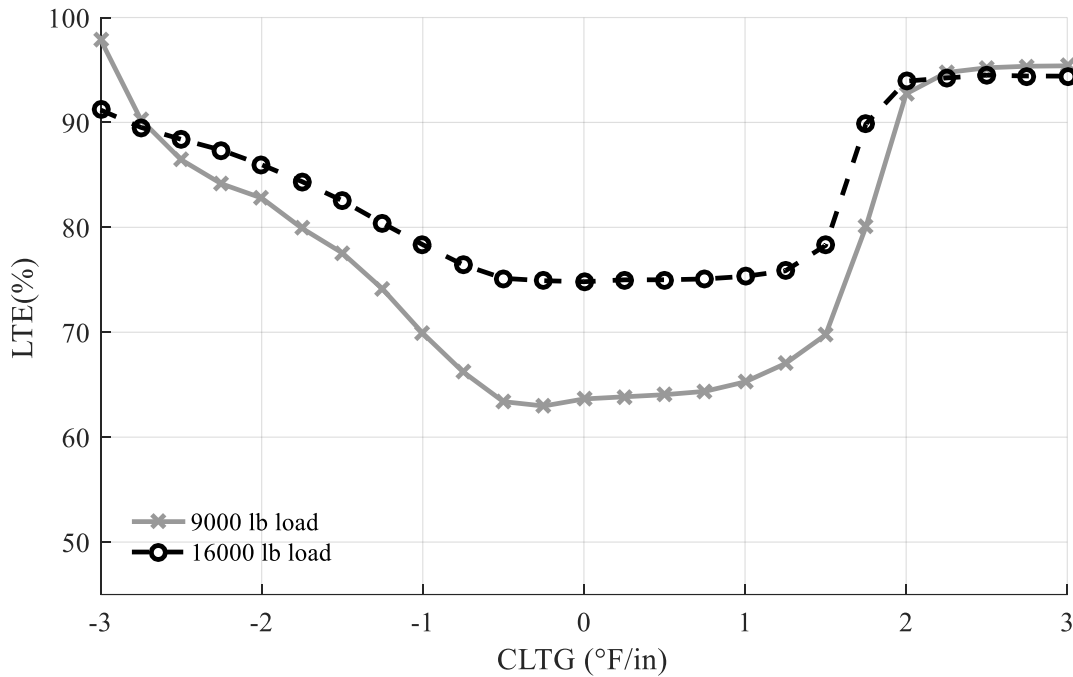


Figure 4.29. Comparison between LTE predicted by the computational analysis with a 9,000 and 16,000 lb load (2 mils dowel looseness)

The minimum LTE predicted by the computational analysis is lower for the 16,000 lb load than it is for the 9,000 lb load. This does not match what was observed in the field data. In the field data, the minimum LTE at each joint was similar for each load level. This discrepancy is likely due to the assumption that the stiffness of concrete is binary, resulting in a reduced stiffness between zero and the undamaged stiffness of the concrete. Therefore, the maximum DD is approximately the same (twice the gap width) for both load levels. However, the maximum deflection is higher for

the 16,000 lb load level, resulting in a lower LTE. If a portion of the concrete surrounding the dowel has a reduced but non-zero stiffness, the 16,000 lb load level would produce larger DD.

The positive CLTG where the LTE begins increasing, $1.75^{\circ}\text{F}/\text{in}$, is the same for both load levels. However, the LTE increases more rapidly in this transition region for the 16,000 lb load level than the 9,000 lb load level. It is impossible to determine if this is the case for the field data due to the small number of test points. In addition, the negative CLTG where the LTE begins increasing is the same for both load levels, but the increase in LTE at negative temperature gradients is more gradual for the 16,000 lb load level than for the 9,000 lb load level. This matches what was observed in the field data.

A comparison between the DD predicted by the computational analysis with a 9,000 and a 16,000 lb load and a gap width of 2 mils is presented in Figure 4.30.

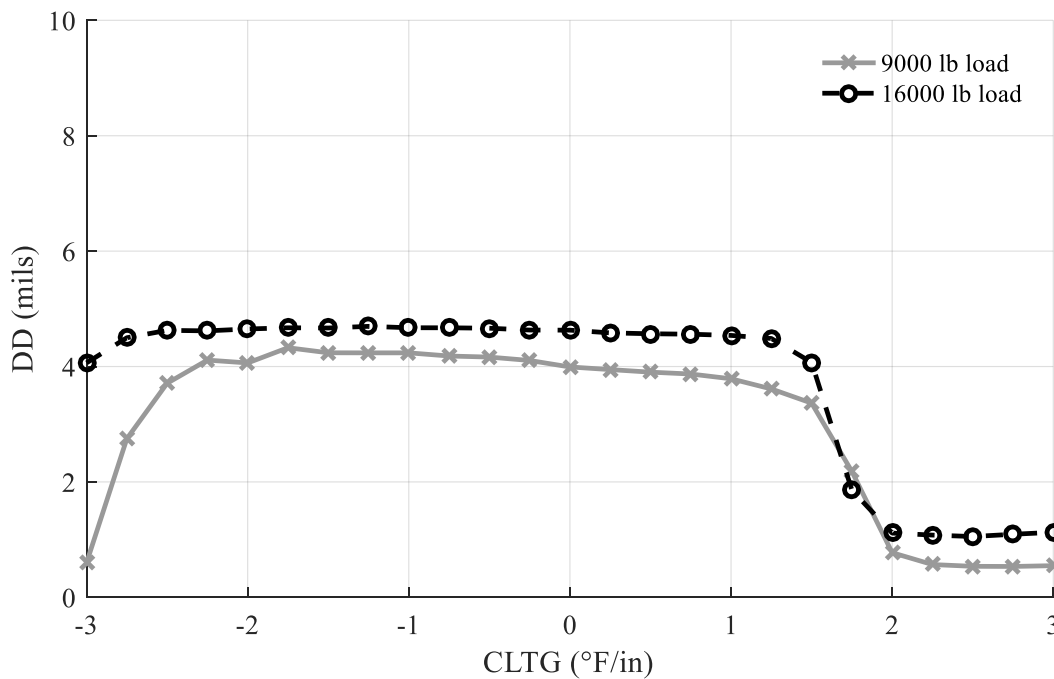


Figure 4.30. Comparison between DD predicted by the computational analysis with a 9,000 and 16,000 lb load (2 mils dowel looseness)

The computational analysis predicts a slightly larger maximum DD for the 16,000 lb load level than the 9,000 lb load level. As previously described, this does not match what was observed in the field data and is likely due to the binary stiffness of the dowel socket. With a 9,000 lb load level, the maximum DD occurs at a CLTG of -1.75 °F/in and decreases slightly until it rapidly decreases at a CLTG of approximately 1.75 °F/in. However, with a 16,000 lb load level, the predicted DD is constant for all DD values greater than this transition zone. In addition, the negative transition occurs at a lower CLTG and DD decreases more rapidly at a CLTG of 1.75 °F/in for the 16,000 lb load level than for the 9,000 lb load level. It is impossible to determine if this phenomenon also occurred in the field due to the small number of test points.

In the I-79 field trials in 2017, the measured DD at Joint 2, which appears to have the most dowel looseness, was closer to the maximum DD for a wider range of ELTGs when a 16,000 lb load was used, than when a 9,000 lb load was used. This can be seen in Figures 4.15 and 4.16. To validate this observation, the computational analysis was also conducted with a 16,000 lb load level and a gap width of 4 mils. A comparison between the predicted DD with a 9,000 and 16,000 lb load can be seen in Figure 4.31.

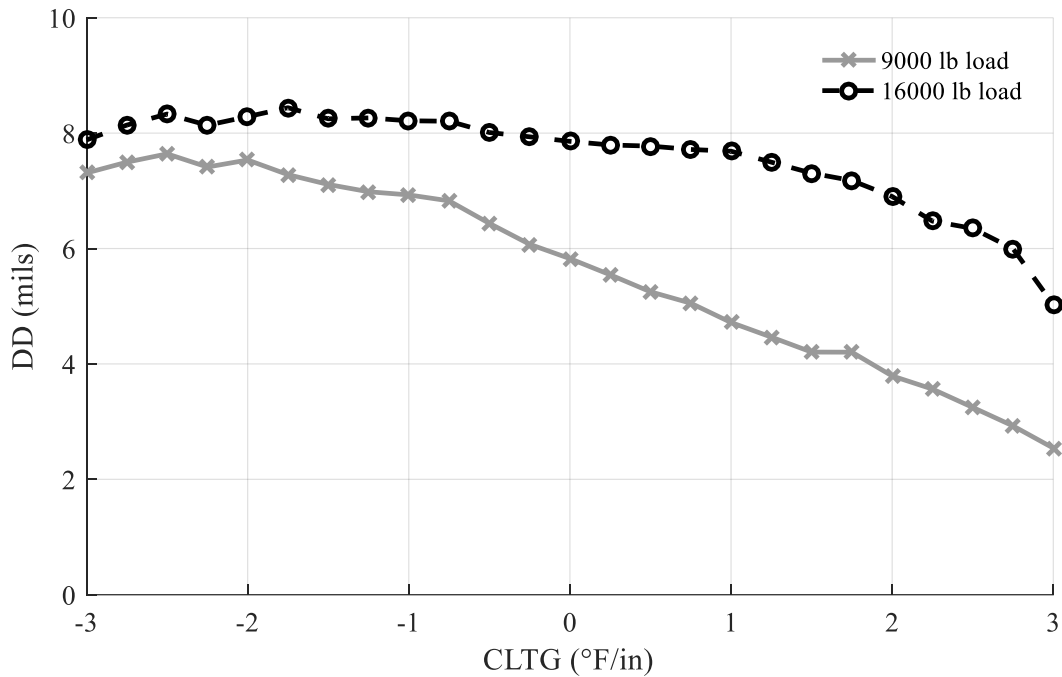


Figure 4.31. Comparison between DD predicted by the computational analysis with a 9,000 and 16,000 lb load (4 mils dowel looseness)

With a 4-mil gap width, the computational analysis predicts the measured DD to be near the maximum DD for a wider range of CLTG values when a 16,000 lb load is used, than when a 9,000 lb load is used. This agrees with the field data, which showed the measured DD near the maximum DD for a wide range of ELTG at Joint 2 of I-79. Overall, the 16,000 lb load level appears to increase the range of ELTG values where dowel looseness can be detected. For example, the computational analysis shows that on a 9,000 lb load would result in a DD of 3.9 mils on a pavement with a gap width of 2 mils around the dowel, and a DD of 4.5 mils for a pavement with a gap width of 4 mils around the dowel. In contrast, a 16,000 lb load would cause 4.5 mils of deflection on a pavement with a gap width of 2 mils around the dowel, and 7.8 mils, on a pavement with a gap width of 4 mils around the dowel. This shows that using a larger load can help differentiate between different levels of dowel looseness, especially at large temperature gradients.

One drawback to using the 16,000 lb load level is that the traditional performance criterion, 60% LTE and/or 10 mils of differential deflection, are based on a 9,000 lb load level and need to be adjusted to account for the use of the 16,000 lb load level.

4.3.3 Evaluation of the Mechanics Contributing to the Observed Behavior

The mechanism driving the relationship between slab curvature and measured joint performance is further investigated by evaluating the interaction between the dowel and the socket before and after loading. Figure 4.32 shows the relationship between the critical dowel (directly below the load plate) and the socket with 1 mil of dowel looseness and a CLTG of 0.75 °F/in, 1.0 °F/in, and 1.25 °F/in. This captures the transition between low DD measurements at high values of CLTG and high DD measurements when the slab is approximately flat.

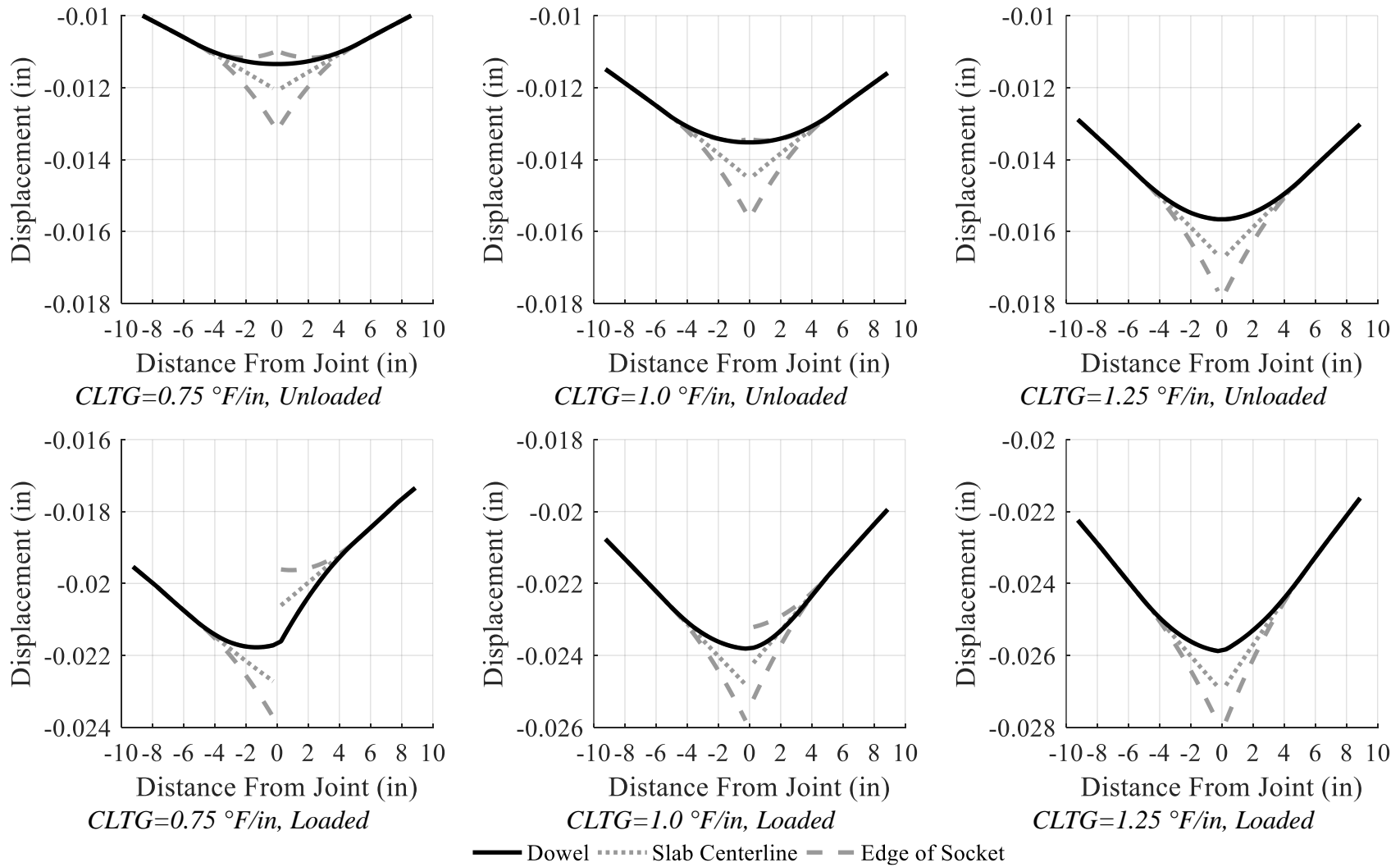


Figure 4.32. Position of dowel bar in socket before and after loading (1 mil of dowel looseness)

At a CLTG of 0.75 °F/in, the predicted DD is near the maximum deflection. At this temperature gradient, the dowel is not in contact with the top of the gap before the load is applied. The load then causes the loaded slab to deflect until the dowel is in contact with the top of the socket on the loaded slab and the bottom of the socket on the unloaded slab. This explains why the peak predicted DD is approximately 2 mils, which is double the size of the socket. At a CLTG of 1.0 °F/in, the dowel is in contact with the top of the gap on both sides of the slab before load is applied. Some preload is likely present in the dowel due to the slab curvature. When load is applied, the dowel is fully effective until the preload in the dowel is reduced. This increases the stiffness of the joint resulting in the dowel not being driven all the way through the gap. It is unclear why using a larger load would create smaller DD in this transition zone, as shown in Figure 4.30. It is possible that more of the load is transferred through bending of the dowel with a larger load, causing less differential deflections. At a CLTG of 1.25 °F/in, the dowel is in contact with the top of the gap before load is applied and a large preload is present in the dowel. The applied load does not cause enough deflection in the loaded slab to completely remove the preload and the dowel remains in contact with the top of the gap on both sides of the joint after loading. This explains the small DDs when load is applied at large positive or negative effective temperature gradients. Figure 4.35 shows the interaction between the critical dowel and the socket with a CLTG of 1.25 °F/in and gap widths of 1, 2, and 4 mils.

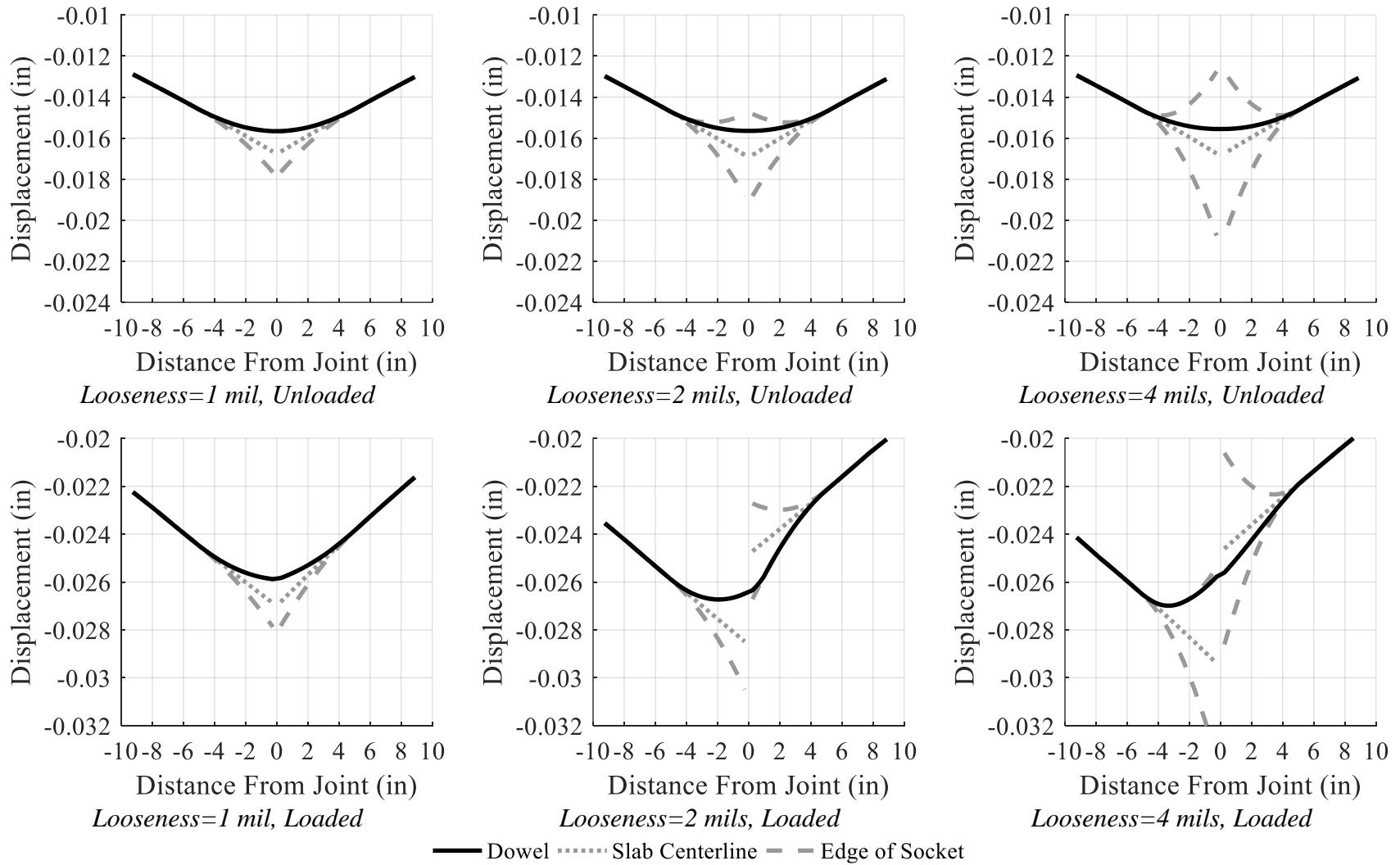


Figure 4.33. Position of dowel bar in socket before and after loading (1.25 °F/in CLTG)

As previously described, with 1 mil of dowel looseness, the load does not cause enough deflection to release the preload between the dowel and the edge of the socket on the unloaded side of the joint. With a gap width of 2 mils, a temperature gradient of 1.25 °F/in is not sufficient to cause the dowel to come in contact with the top of the socket before the load is applied. When the load is applied, the dowel is driven completely through the socket, producing large DD measurements. This explains why a wider range of temperature gradients leads to greater DDs when more dowel looseness is present. A dowel with a gap width of 4 mils is also not in contact with the top of the gap before the load is applied. However, the applied load does not cause enough deflection to drive the dowel completely through the socket. Greater total deflection, which can be caused by a negative CLTG value, or a higher load is required to drive the dowel completely through the socket. This explains why maximum values of DD, which are approximately double the dowel looseness, only occur when there is a negative CLTG with a 9,000 lb load but occur over a much larger range of temperature gradients with a 16,000 lb load.

The computational analysis has shown that dowel looseness is likely a driving factor behind the relationship between slab curvature and measured LTE and DD. The behavior predicted by the computational analysis with discretely modeled dowel looseness matches the behavior observed in the field trials much better than the computational analysis utilizing a dense liquid interaction between the dowel and the slab. However, there are some discrepancies between the behavior observed in the field trials and the behavior predicted by the computational analysis. Future research may be able to more accurately predict field data by using a different gap thickness at each dowel along the joint. In addition, it may be necessary to account for damaged concrete with a reduced stiffness surrounding the gap. This may be possible by using non-linear or piecewise linear spring elements rather than gap elements. Differences between the estimated

stiffness of aggregate interlock and the actual contribution of aggregate interlock in the field may also contribute to the discrepancies between the computational results and trends observed in the field.

4.4 ANALYSIS OF LTPP AND MNROAD DATA

The field trials and computational analysis reveal that slab curvature has an effect on the measured joint performance of doweled pavements. This is especially true when looseness has developed around the dowel. However, these analyses have focused on a limited number of structures. To evaluate the effect of slab curvature on measured joint performance for many structures, a statistical analysis of the LTPP database was conducted. This analysis evaluated the distribution of testing results across all structures in the database to confirm this effect. In addition, an analysis of variance (ANOVA) was conducted on a few of the SMP sections to determine how the effect of slab curvature compares to the effect of other factors, such as fatigue and random error.

4.4.1 Distribution Analysis

The effect of slab curvature on joint performance in the LTPP database was evaluated by dividing the tests into groups based on the measured ELTG during testing. To avoid the effects of joint lock-up and frozen subgrades, only tests with a WAT between 40 °F and 75 °F were considered in the analysis. Duplicate drops within the same FWD seating were averaged and treated as a single test. Treating the duplicate drops independently leads to overly optimistic error measurements because: 1) the duplicate drops are required to be within 1% based on LTPP QA/QC procedures

(and were typically much closer), and 2) they are likely to have correlated error components. The analysis consists of 7,786 tests from 155 test sections. The range of ELTGs for each group and the number of tests in each group are summarized in Table 4.2.

Table 4.2. ELTG ranges for distribution analysis groups

ELTG Range	Number of Tests
-1.5 °F/in < ELTG < -0.5 °F/in	312
-0.5 °F/in < ELTG < 0.5 °F/in	2,252
0.5 °F/in < ELTG < 1.5 °F/in	2,601
1.5 °F/in < ELTG < 2.5 °F/in	1,981
2.5 °F/in < ELTG < 3.5 °F/in	640

Most of the FWD testing occurs during daylight hours, resulting in few tests with an ELTG less than -0.5 °F/in. The tests are well distributed between three groups with -0.5 °F/in < ELTG < 2.5 °F/in. To determine the nature of the distribution of joint efficiency parameters measured within each of these groups, the probability distribution functions (PDF) of the measured parameters were estimated using the non-parametric kernel density smoothing function for the 9,000 and 16,000 lb load levels. These distributions can be seen in Figure 4.34 to 4.37.

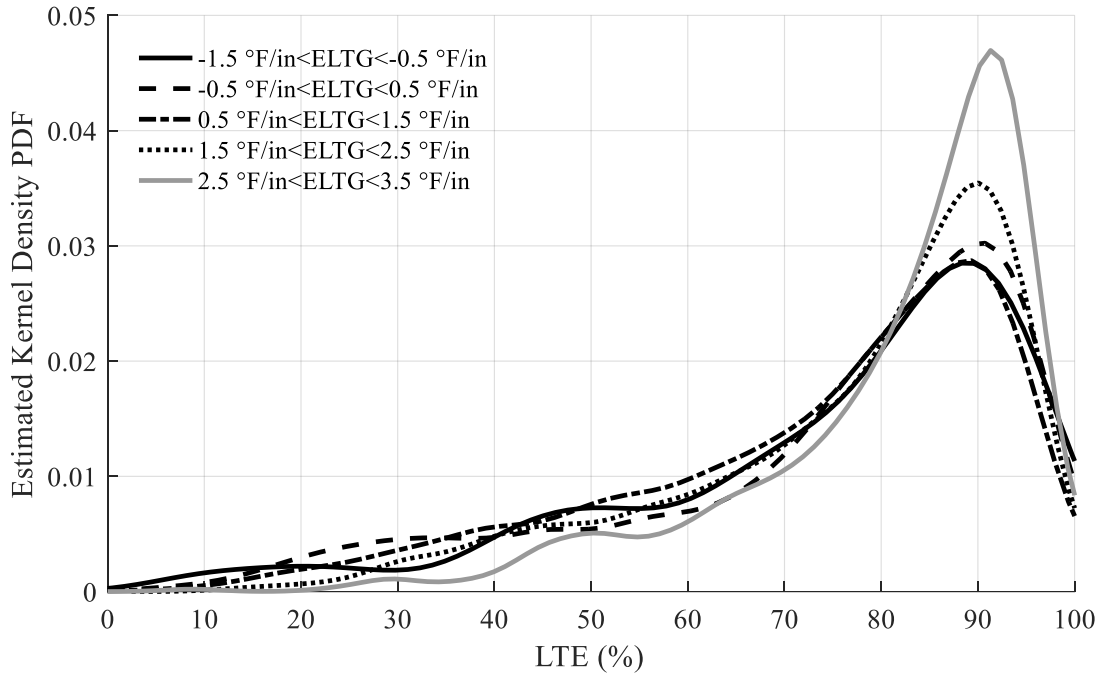


Figure 4.34. Estimated kernel density PDF of LTE in the LTPP database (9,000 lb nominal load level)

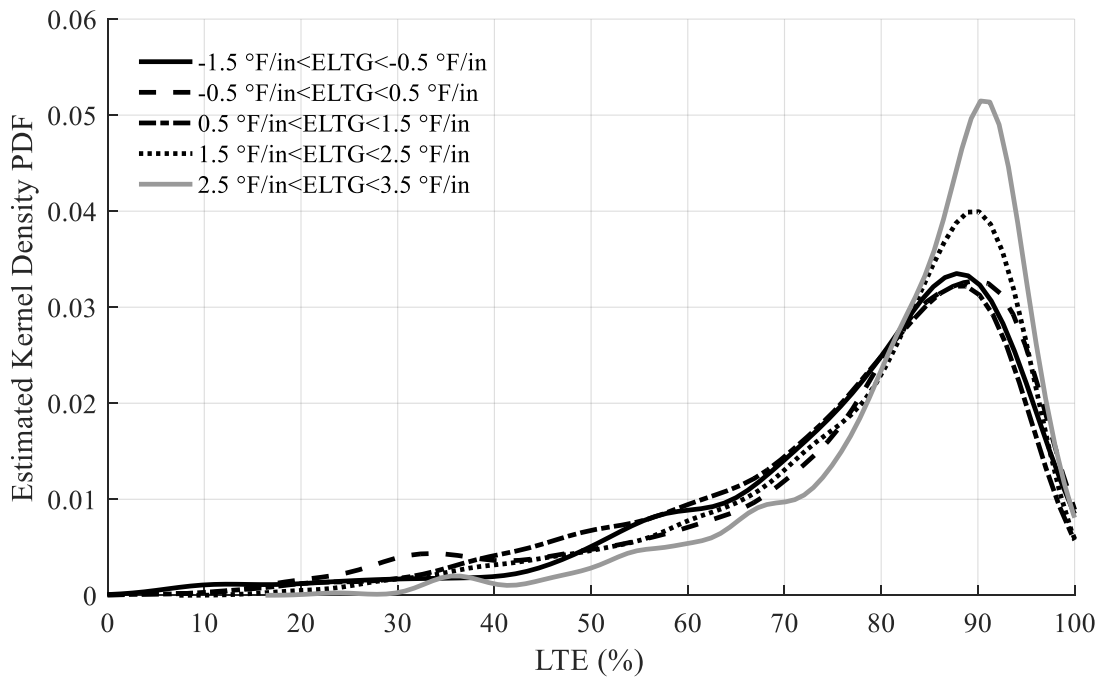


Figure 4.35. Estimated kernel density PDF of LTE in the LTPP database (16,000 lb nominal load level)

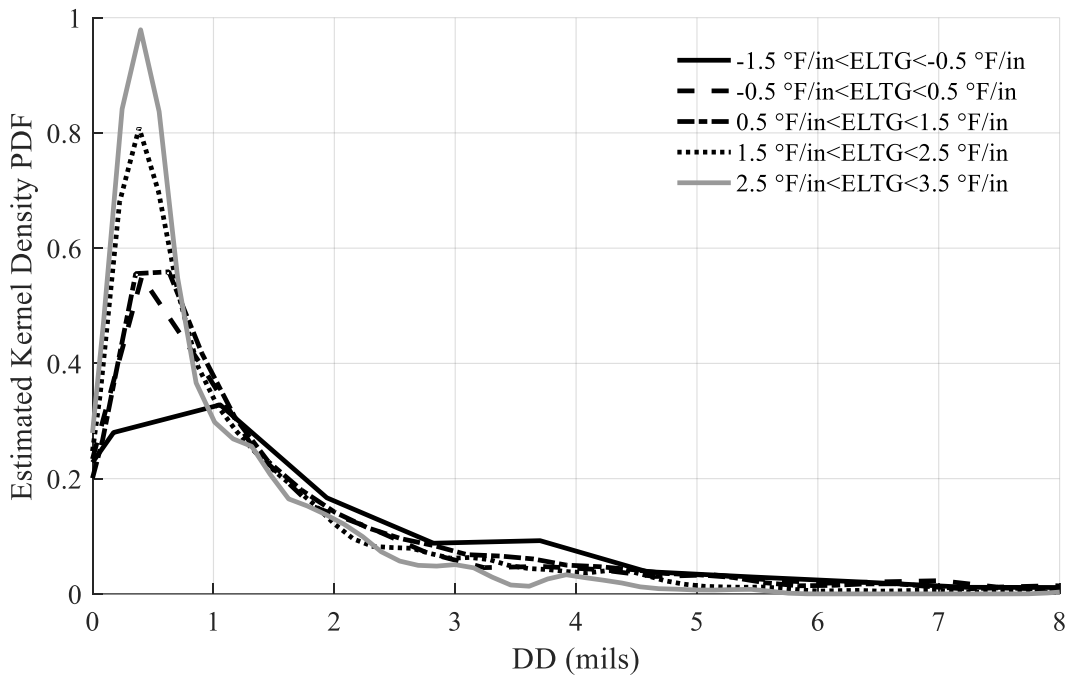


Figure 4.36. Estimated kernel density PDF of DD in the LTPP database (9,000 lb nominal load level)

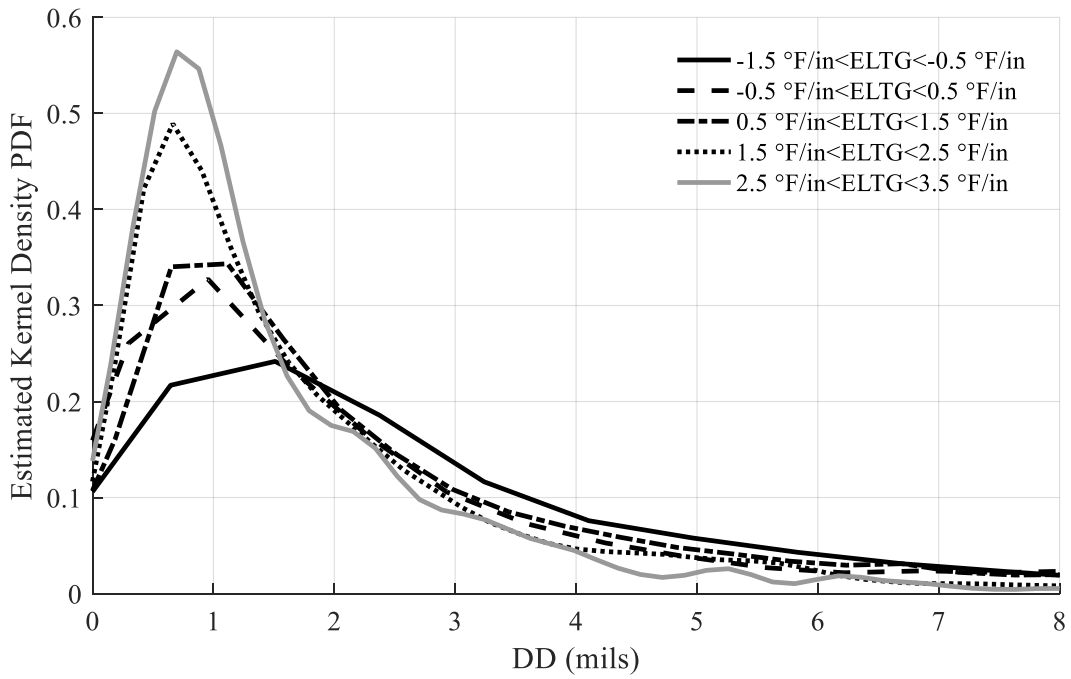


Figure 4.37. Estimated kernel density PDF of DD in the LTPP database (16,000 lb nominal load level)

From these distributions it is clear that pavements with a large positive ELTG tend to have a lower measured DD and higher measured LTE than the other groups. In addition, neither parameter appears to be normally distributed. The DD and compliment of LTE ($1-LTE/100$) for each group appears to be log-normally distributed. Therefore, the LTE was transformed by taking the natural log of $(1-LTE/100)$ and DD was transformed by taking the natural log. The resulting estimated distributions are shown in Figure 4.38 to 4.41.

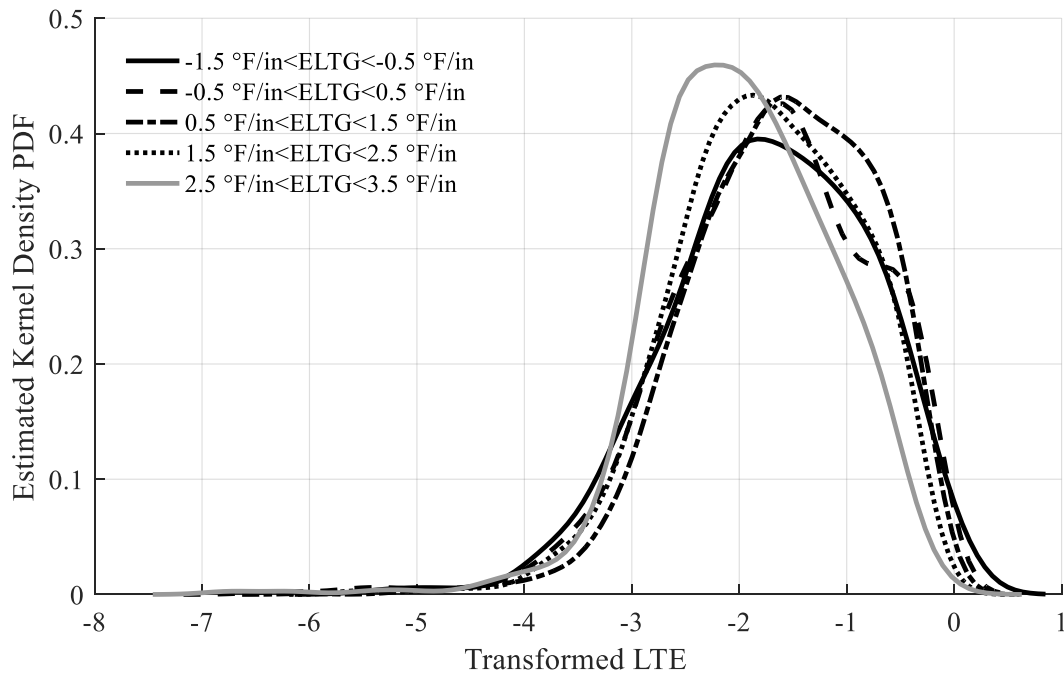


Figure 4.38. Estimated kernel density PDF of transformed LTE in the LTPP database (9,000 lb nominal load level)

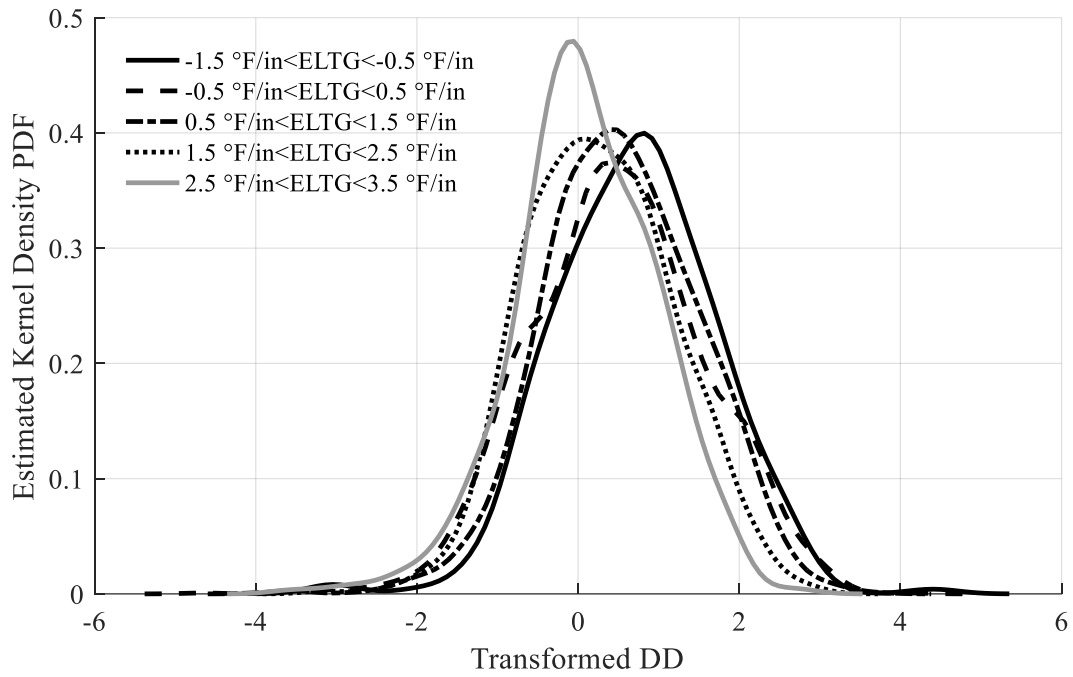


Figure 4.39. Estimated kernel density PDF of transformed LTE in the LTPP database (16,000 lb nominal load level)

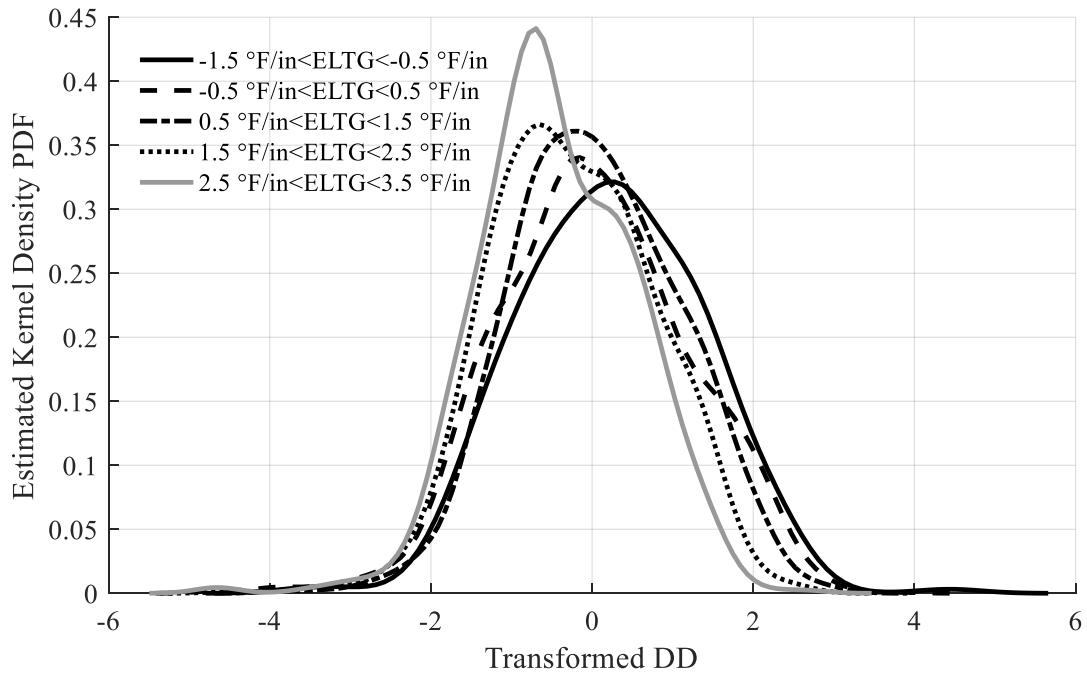


Figure 4.40. Estimated kernel density PDF of transformed DD in the LTPP database (9,000 lb nominal load level)

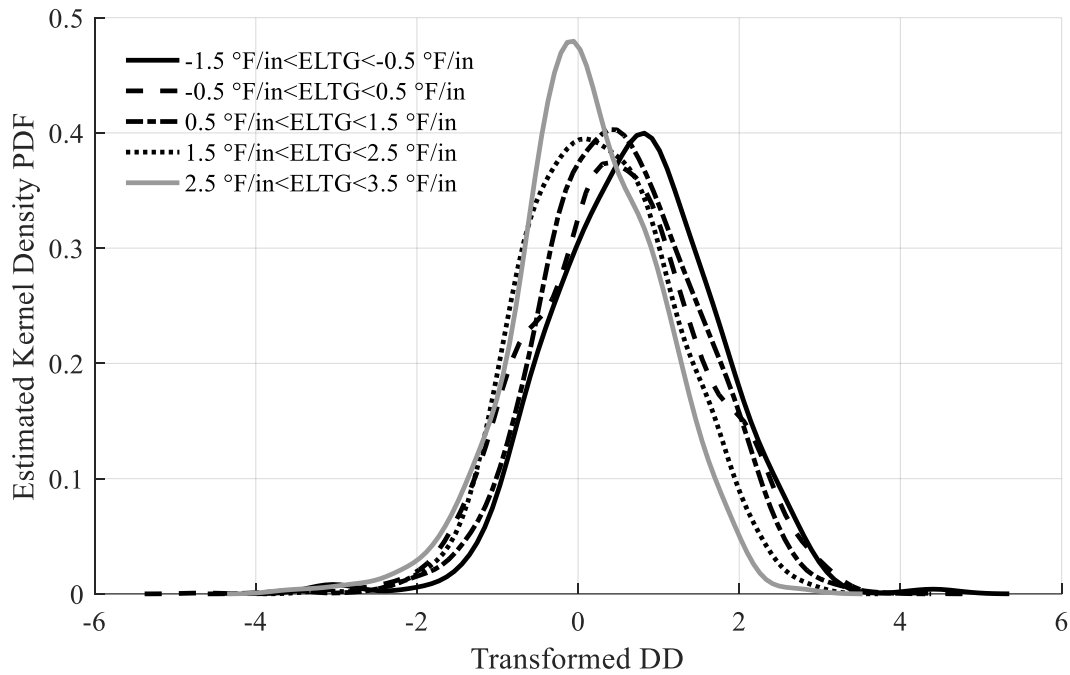


Figure 4.41. Estimated kernel density PDF of transformed DD in the LTPP database (16,000 lb nominal load level)

These distributions are approximately normal, which allows the use of hypothesis testing on the transformed joint efficiency parameters assuming a normal distribution. The mean and standard deviation for each of these ranges can be seen in Table 4.3.

For the transformed LTE and DD at both load levels, Bonferroni confidence intervals with partitioned error were determined for each ELTG group using Equation 4.5.

$$\bar{Y} - t_{\frac{\alpha}{2 * \binom{5}{2}}, N-5} \sqrt{\frac{MSE}{\binom{1}{n_i}}} < Y < \bar{Y} + t_{\frac{\alpha}{2 * 5 * 2}, N-5} \sqrt{\frac{MSE}{\binom{1}{n_i}}} \quad (4.5)$$

where \bar{Y} is the mean value of the group, t is the studentized t-distribution, α is the desired significance level (5%), $\binom{5}{2}$ is the total number of contrasts (10), MSE is the mean squared error of the group, n_i is the number of tests in the group, and N is the total number of tests in all groups.

The effective confidence level for each interval is $\alpha / \binom{5}{2}$ or 0.5%. The confidence intervals of the transformed LTE for both load levels can be seen in Figure 4.42 and 4.43. Confidence intervals that do not overlap indicate a statistically significant contrast.

Table 4.3. Statistics describing distributions of transformed joint efficiency parameters in LTPP database

Group	9,000 lb load nominal load level				16,000 lb load nominal load level			
	Trans. LTE mean	Trans. LTE std. dev.	Trans. DD mean	Trans. DD std. dev.	Trans. LTE mean	Trans. LTE std. dev.	Trans. DD mean	Trans. DD std. dev.
-1.5 °F/in<ELTG<-0.5 °F/in	-1.72	0.90	0.24	1.11	-1.76	0.82	0.72	0.98
-0.5 °F/in<ELTG<0.5 °F/in	-1.71	0.94	0.02	1.17	-1.77	0.87	0.49	1.08
0.5 °F/in<ELTG<1.5 °F/in	-1.60	0.83	0.05	1.03	-1.67	0.79	0.54	0.96
1.5 °F/in<ELTG<2.5 °F/in	-1.76	0.83	-0.24	1.00	-1.82	0.77	0.27	0.92
2.5 °F/in<ELTG<3.5 °F/in	-1.97	0.83	-0.44	0.95	-2.02	0.78	0.10	0.89

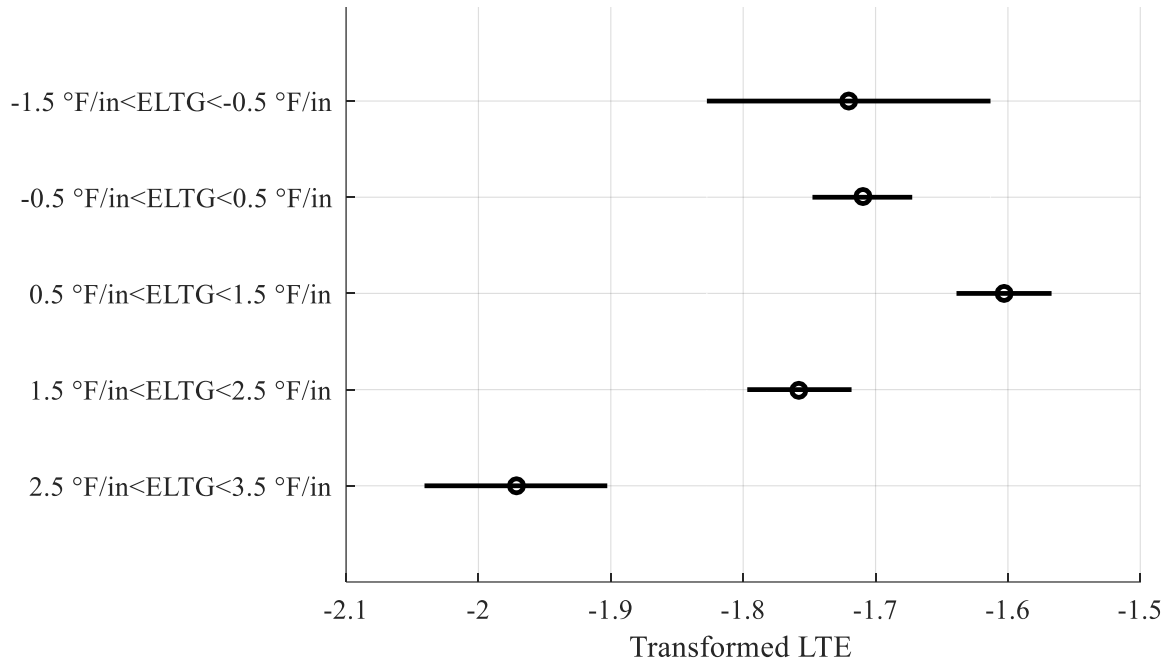


Figure 4.42. Bonferroni confidence intervals for transformed LTE in the LTPP database (9,000 lb nominal load level)

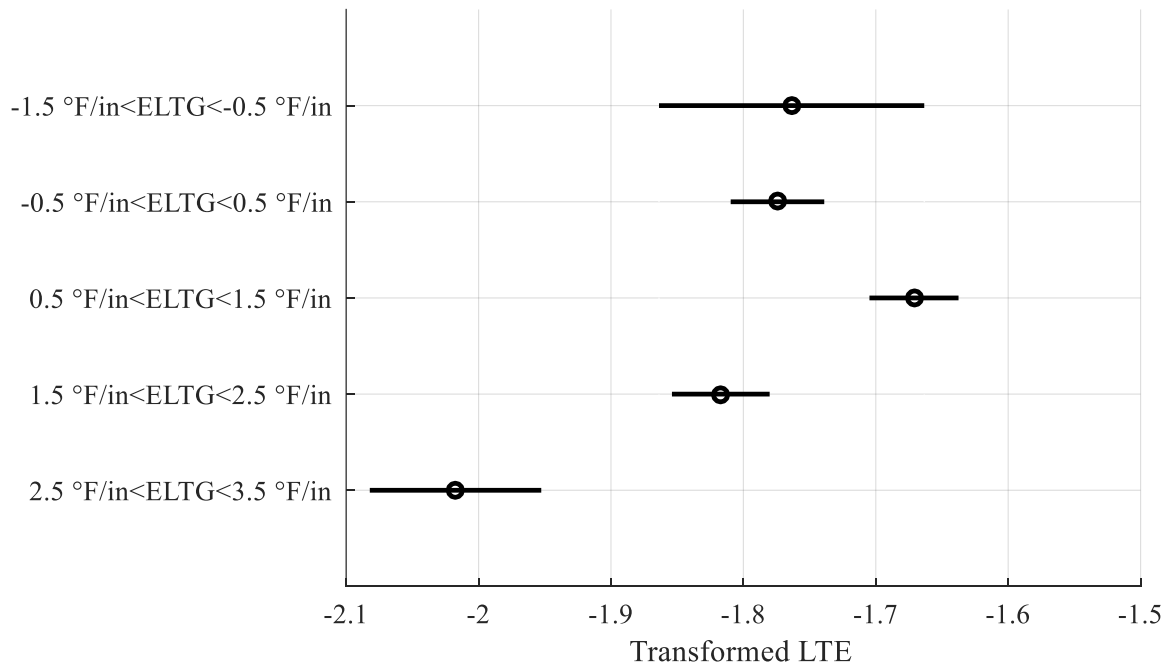


Figure 4.43. Bonferroni confidence intervals for transformed LTE in the LTPP database (16,000 lb nominal load level)

For both load levels, the transformed LTE is lower, which corresponds to a higher LTE, for an ELTG range of 2.5 °F/in to 3.5 °F/in than all other ranges at a statistically significant level. In addition, the group with an ELTG range of 0.5°F/in to 1.5 °F/in has a transformed LTE that is higher, which corresponds to a lower LTE, than all other ranges excluding a range of -1.5 °F/in to -0.5 °F/in at a statistically significant level. This agrees with the field trials and computational analysis, which showed the minimum LTE for most joints occurs at a slightly positive ELTG. The group with an ELTG range of -1.5 °F/in to -0.5 °F/in has significantly fewer tests than the other ranges, resulting in a wide confidence interval.

The confidence intervals of the transformed DD for both load levels can be seen in Figure 4.44 and 4.45.

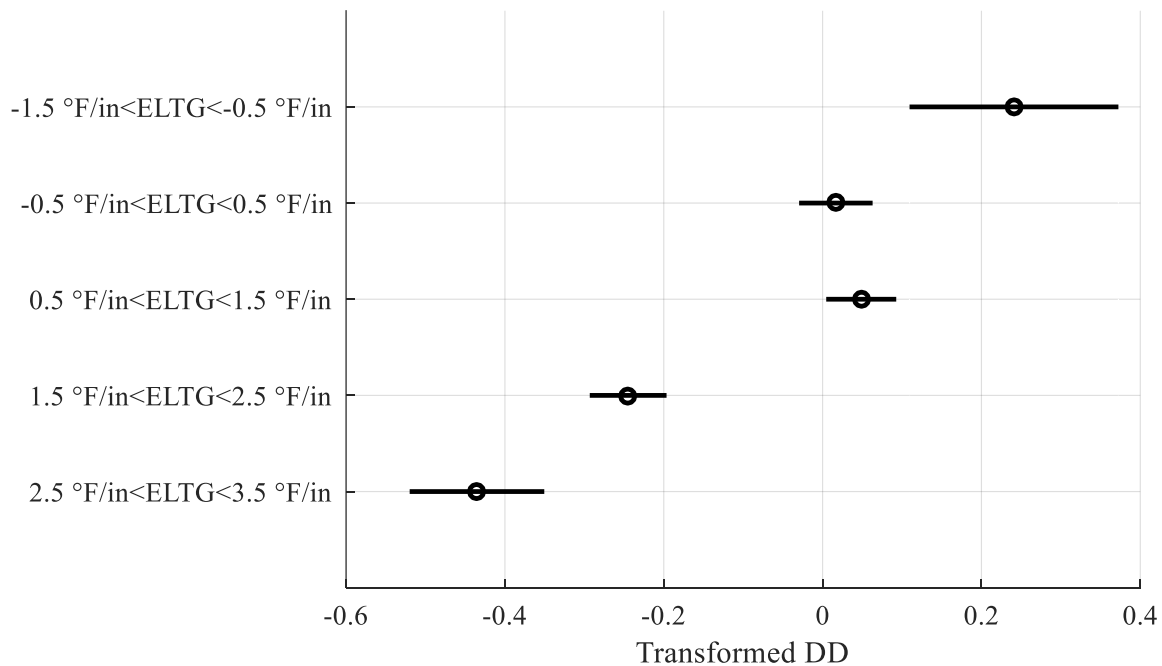


Figure 4.44. Bonferroni confidence intervals for transformed DD in the LTPP database (16,000 lb nominal load level)

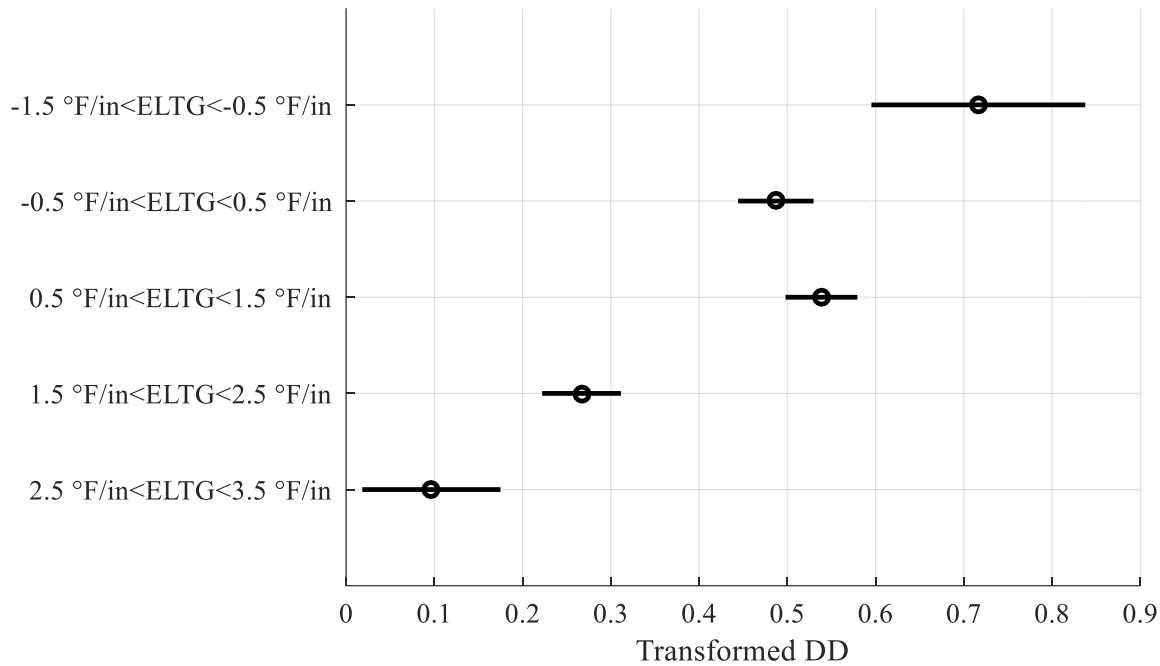


Figure 4.45. Bonferroni confidence intervals for transformed DD in the LTPP database (16,000 lb nominal load level)

Except for the groups with an ELTG range of -0.5 °F/in to 0.5 °F/in and 0.5 °F/in to 1.5 °F/in, all the contrasts are significantly different for both load levels. In addition, the DD decreases as the ELTG increases regardless of the ELTG range or load level. This indicates that a large portion of the joints may be acting like Joint 2 at I-79 and the computational analysis with a gap width of 4 mils.

These distributions can be used to correct the measured joint efficiency parameters for slab curvature. A transformed measured joint efficiency parameter can be converted to a z-variate based on the ELTG group. The statistics for the group with an ELTG range of 0.5 °F/in to 1.5 °F/in, which best corresponds to a flat slab due to the built-in gradient, can then be used to adjust the parameter. The value of the transformed parameter in this range, which has the same z-variate as the measured transformed joint efficiency parameter in the original group, is an estimate of the

adjusted value of the transformed parameter. The inverse transformation can then be performed to determine the value of the adjusted parameter in non-transformed units. The transformed LTE and DD for the field trial at I-79 in October 2017 are shown in Figures 4.46 and 4.47.

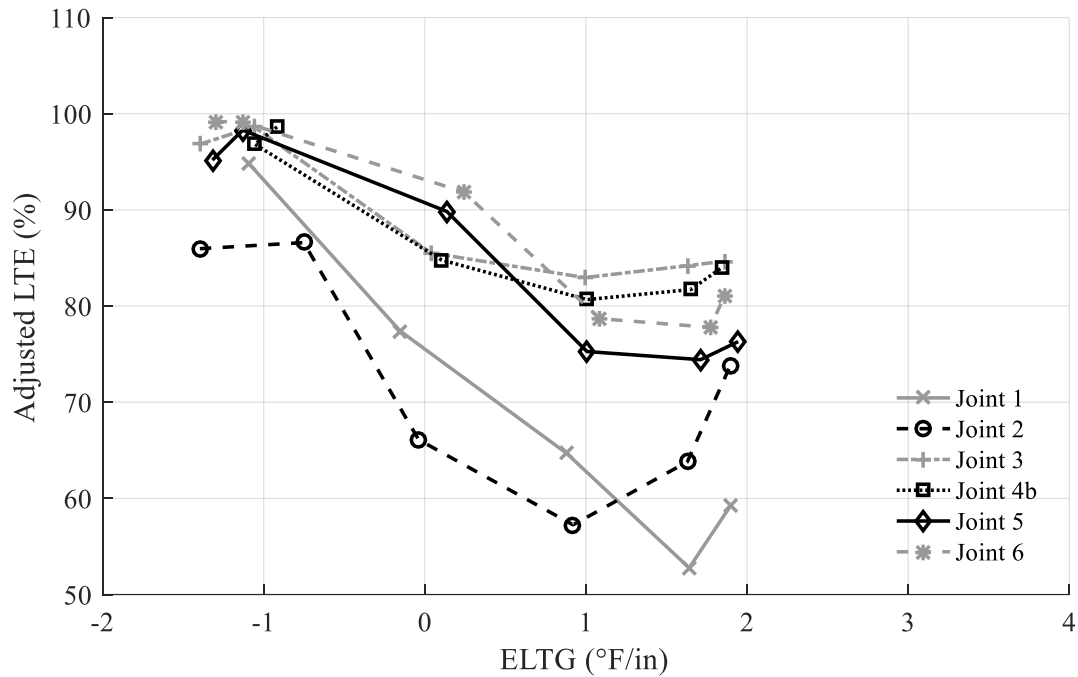


Figure 4.46. Measured LTE at I-79 field trials adjusted based on distributions in LTPP database

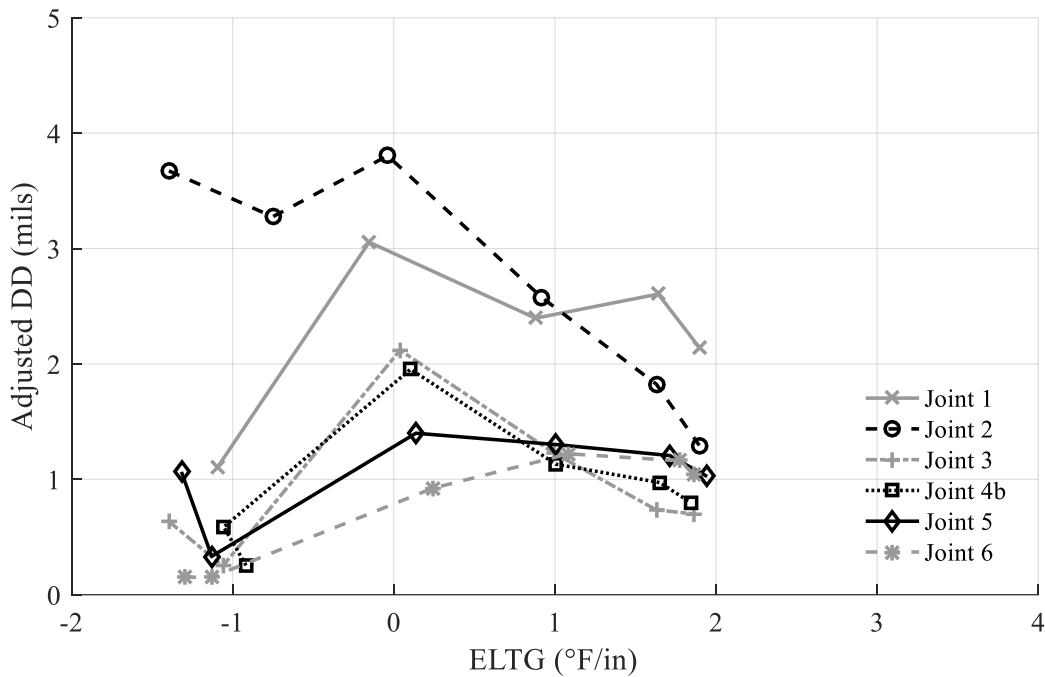


Figure 4.47. Measured DD at I-79 field trials adjusted based on distributions in LTPP database

The effect of slab curvature on both joint efficiency parameters is slightly reduced by utilizing these corrections. However, a significant effect is still present.

4.4.2 ANOVA of SMP and MnROAD Sections

It is evident from the field trials, computational analysis, and statistical analysis of the LTPP database that slab curvature affects the measured LTE and DD. It is important to determine how the magnitude of this effect compares to the magnitude of other factors during testing. Factors that may affect testing results, which include differences between joints and the effect of fatigue loading on dowels, are of interest during FWD testing. The comparison is accomplished by performing an ANOVA on tests at several LTPP SMP and MnROAD sections. The ANOVA was

performed by incrementally fitting linear regression models and calculating the marginal R^2 for each of the following variables:

- Joint number
- WAT
- ELTG
- Pavement age

The joint number is analyzed as a categorical variable and coded as an indicator variable. To approximate the behavior observed in the field trials and computational analysis, a second order relationship between the ELTG and joint efficiency parameters is utilized. It should be noted that the relationship between the predictors and joint efficiency parameters is approximated to be first or second order linear. In reality, these relationships are more complicated. For example, the relationship between ELTG and LTE in the computational analysis and field trials is not truly parabolic. Therefore, it is likely that some variance, which is attributed to random error, may actually be due to one of the predictors. The ANOVA for LTE at four LTPP and five MnROAD sections can be seen in Table 4.4.

Table 4.4. ANOVA for LTE at LTPP and MnROAD sections

Section	Tests	Mean LTE (%)	RMSE (intercept only)	Marginal R-Squared				
				Joints	WAT	ELTG ²	Age	Error
04-0215	398	72	11.8	0.36	0.02	0.04	0.02*	0.57
18-3002	127	80	10.9	0.10	0.09	0.05	0.05*	0.72
37-0201	267	76	14.4	0.29	0.32	0.05	0.01	0.34
89-3015	220	91	5.3	0.10	0.06	0.04	0.00	0.80
MNR 5	269	77	10.3	0.02	0.09	0.05	0.02	0.82
MNR 6	218	81	8.8	0.05	0.17	0.11	0.06	0.61
MNR 7	266	77	7.5	0.16	0.11	0.00	0.02*	0.71
MNR11	240	86	7.2	0.09	0.07	0.01	0.02	0.82
MNR52	67	84	10	0.17	0.55	0.00	0.03*	0.26

Bold indicates predictor is statistically significant at the 95% confidence level

**LTE increases with age*

There is significant variation in the LTE measurements. The variation in LTE measurements is expected to increase as LTE decreases. Therefore, the coefficient of variation for LTE should be defined using Equation 4.6.

$$COV = \frac{MSE}{100 - LTE} \quad (4.6)$$

The average variation within each section is 0.5, indicating significant variation in the measurements. A total of five of the nine sections evaluated have a statistically significant relationship between ELTG and measured LTE at the 95% confidence level. In addition, all sections have a statistically significant relationship between WAT and mean LTE. It should be noted that only tests with a WAT between 40 °F/in and 70 °F/in were evaluated to limit the effect

of frozen subgrades and “locked-up” joints on the results. All nine sections show a larger portion of the variance in LTE is due to WAT than ELTG. This observation holds even if the order of the variables is altered such that ELTG is added into the model before WAT. Eight sections showed a statistically significant trend between pavement age and LTE. However, half of these sections indicate that LTE increases with age, which is the opposite of what is expected. There is no apparent physical reason which would cause LTE to increase as traffic loads are applied. Dowel bar corrosion may cause the gap around the dowel to be filled with iron-oxide, however, this is unlikely as all of the dowel bars are MnROAD are epoxy coated. It is unknown whether the dowels at the LTPP sections were epoxy coated, but based on construction dates in the early 1990s it is likely. Therefore, these relationships are likely spurious, and indicate that there is not a strong relationship between the age of the pavement and LTE for these sections. Overall, while differences in the condition of joints, WAT, ELTG, and age contribute to the large coefficient of variation (COV) within each section, they account for a relatively small amount of the error. Furthermore, even though clear trends between ELTG and LTE are seen during a single day of testing and in the computational analysis, they are less distinct when considering testing throughout the life of a pavement.

The ANOVA for DD at four LTPP and five MnROAD sections can be seen in Table 4.5.

Table 4.5. ANOVA for DD at LTPP and MnROAD sections

Section	Tests	Mean DD (mils)	RMSE (intercept only)	Marginal R-Squared				
				Joints	WAT	ELTG ²	Age	Error
04-0215	398	2.81	1.98	0.25	0.03	0.15	0.03	0.54
18-3002	127	2.17	1.4	0.16	0.04	0.01	0.05	0.74
37-0201	267	3.31	2.81	0.48	0.16	0.05	0.01*	0.30
89-3015	220	0.96	0.86	0.07	0.06	0.07	0.00	0.80
MNR 5	269	3.16	2.2	0.02	0.00	0.12	0.02	0.84
MNR 6	218	2.74	1.58	0.06	0.01	0.27	0.14	0.52
MNR 7	266	2.67	1.01	0.18	0.00	0.05	0.01	0.76
MNR11	240	1.83	1.7	0.09	0.03	0.08	0.02*	0.79
MNR52	67	2.23	1.27	0.21	0.41	0.05	0.06	0.26

Bold indicates predictor is statistically significant at the 95% confidence level

**DD increases with age*

There is also significant within section variance in DD, with a COV of 0.70. Overall, similar to LTE, the explanatory factors only account for a small portion of the variance in DD. Seven of the nine sections showed a statistically significant relationship between DD and both WAT and ELTG. Unlike the ANOVA for LTE, the variance caused by ELTG within each section is greater than the variance caused by WAT at six of the nine sections. The relationship between the age of the pavements and DD is statistically significant for eight of the nine pavements, with DD increasing with age for six of these eight sections. Therefore, two of the pavements that show LTE increasing with age at a statistically significant level (LTPP 04-0215, LTPP 18-3002) also show DD increasing with age. This seems to indicate that total deflection is increasing for these sections and that repeated wheel loading has a larger effect on DD than LTE. . This agrees with observations from the ALF testing performed on doweled slabs at the University of Pittsburgh. Figure 4.48 shows the measured LTE and DD as a function of load applications for the ALF test with 1.5-in diameter epoxy coated steel dowels, described in the computational analysis portion of this report.

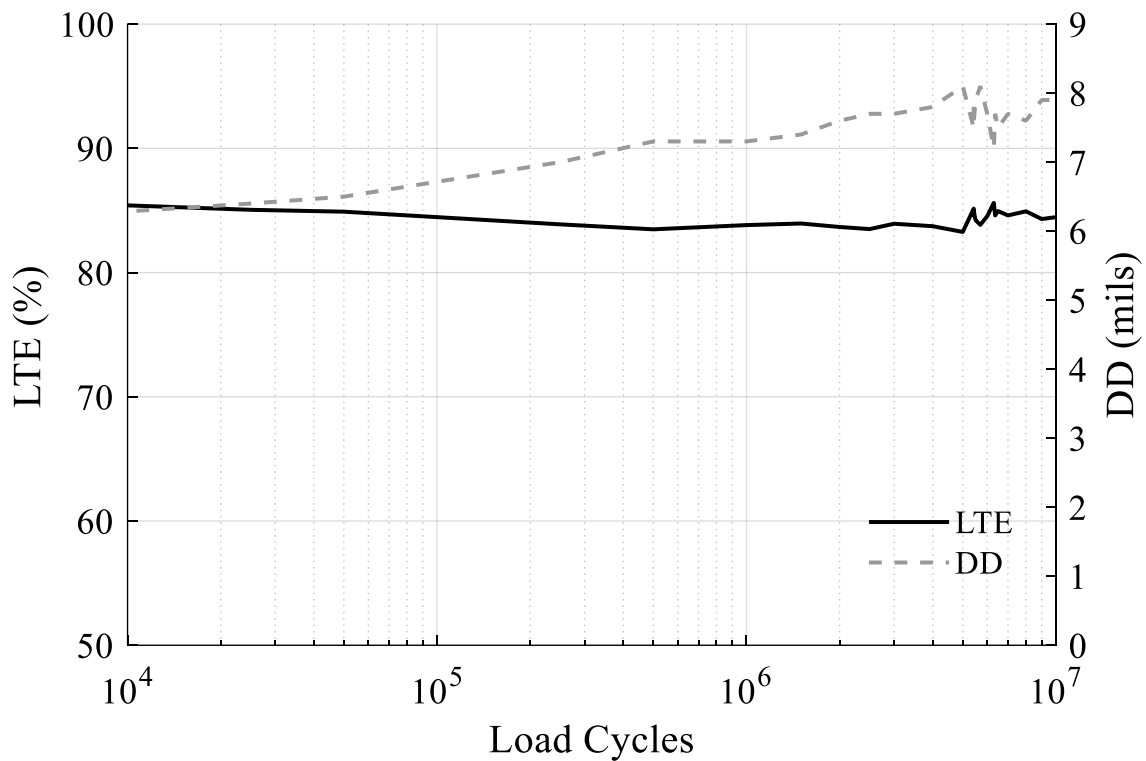


Figure 4.48. Measured LTE and DD from ALF testing with 1.5-in dia epoxy coated steel dowel bars.

In this ALF test, the LTE is relatively constant throughout the test. However, DD increases as additional load cycles are applied. This indicates that the total deflection is increasing as the concrete around the dowel bar degrades, but the LTE is not largely affected by traffic loads after the initial loads are applied.

While it has been shown that slab curvature can have a significant effect on the measured LTE and DD at a joint, random error and undescribed variables account for a much larger portion of the variation in these parameters for tests within the same pavement section. This decreases the utility of FWD measurements to assess the condition of joints. The primary motivation behind measuring joint performance is determining whether future faulting is likely to occur at a joint. Therefore, it is useful to explore the prevalence of faulting in Pennsylvania, and nationally in the

LTPP database, to determine if a link can be drawn between faulting and joint efficiency parameters.

4.5 EVALUATION OF THE PREVALENCE OF FAULTING

4.5.1 Pennsylvania Pavement Management System

The prevalence of faulting in Pennsylvania was evaluated using the PennDOT Pavement Management System (PMS). Only faulting that is defined as moderate (0.25 in < faulting < 0.5 in) and severe (faulting > 0.5 in) is available in the PennDOT PMS. Low severity faulting (0.125 in < faulting < 0.25 in) was not recorded. Therefore, all analysis assumes faulting greater than 0.25 in is of concern. The Pavement ME Design procedure considers an average fault depth of 0.12 in to be failure on interstate pavements and 0.15 in of faulting to be failure on non-interstate pavements. Therefore, it is possible that there is a significant reduction in serviceability due to faulting, without the fault depth reaching the level where it is recorded in the PMS database.

Overall, faulting of 0.25 in or higher does not appear to be a significant factor affecting pavements in the PennDOT network. Looking at the network as a whole, the following observations can be observed:

- Approximately 0.3% of joints surveyed have moderate or severe faulting
- Less than 3% of concrete pavement lane miles are in control sections, the basic unit of roadway in the PMS database, where more than 3% of the joints are experiencing moderate to severe faulting

- Less than 0.6% of concrete pavement lane miles are in a control section where more than 10% of the joints are experiencing moderate to severe faulting
- Lower volume “four-digit” state highways account for 35% of the lane miles with more than 3% of joints faulting and 60% of the lane miles with more than 10% of joints faulting. This is despite “four-digit” state highways accounting for only 9% of concrete pavement lane miles. This may be due to repairs, such as diamond grinding, being performed on higher volume roads, which are experiencing faulting.

It is also important to determine the characteristics of the pavements that are exhibiting faulting. The PennDOT network consists of both jointed reinforced concrete pavement (JRCP) and jointed plain concrete pavement (JPCP). Generally, the JRCP sections tend to be older, with 95% of the JRCP lane miles being built before 1990 and 94% of the JPCP lane miles being built after 1990. Currently, JRCPs accounts for approximately 18% of the total network lane miles, whereas JPCP pavement accounts for 82%. The following observations can be made about the performance of JRCP and JPCP pavements:

- 12% of JRCP lane miles are in a control section with greater than 3% of the joints experiencing faulting
- 63% of lane miles in control sections exhibiting faulting are JRCP
- The average age of JRCP sections with faulting is 48 years and the average age of all JRCP sections is 45 years
- Approximately 1% of JRCP joints have moderate to severe faulting
- 1.2% of JPCP lane miles are in a control section experiencing faulting, accounting for 37% of lane miles in control sections with faulting
- Approximately 0.2% of JPCP joints have moderate or severe faulting
- The average age of JPCP pavements with faulting and the overall age of JPCP sections are both 17 years

The increased faulting exhibited in the JRCP sections may be due to several factors. It is possible that faulting of midslab transverse cracks integral to JRCP design are being recorded as joint faulting, however the provided information from the PennDOT PMS system does not contain any information regarding transverse crack faulting. In addition, the sections are quite old and may have been designed with undersized or uncoated dowels, which have since failed due to corrosion of the bar or crushing of the concrete. Also, the slab length of JRCP pavements is longer than that of JPCP pavements, resulting in longer joints that can increase the stress in the pavement and widen joints, leading to reduced aggregate interlock. Finally, faulting could have occurred at these older sections due to gradual fatigue of the dowel socket and pumping of fine material.

It is also important to note that although faulting is recorded by control section, the design of control sections is not constant. Some control sections contain both JRCP and JPCP. Over 11% of the JPCP pavements with at least 3% faulting are in a control section that also includes JRCP pavement. Based on the faulting rates, it is likely that most of this faulting is in the JRCP sections and the amount of JPCP sections experiencing more than 3% faulting is even lower than previously reported.

Another interesting observation is that JPCP pavements on lower volume “four-digit” state routes experience more faulting than JPCP pavements on larger, higher traffic highways. A total of 9% of JPCP lane miles on “four-digit” state routes experience at least 3% of joints faulting compared to 1.2% for all JPCP pavements. There is not a significant difference between the ages of these groups. PennDOT traditionally uses 1.5 in diameter dowels in JPCP pavements on interstates and primary state highways. It is possible that the lower volume “four-digit” state highways are undoweled or have much smaller dowels, leading to additional faulting. It is also possible that on primary state routes and interstate highways, faulting of less than 0.25 in increases

the roughness of the pavement to a point that corrective action, such as diamond grinding, is taken. Therefore, the faulting is corrected before it reaches the 0.25 in threshold required to be recorded in the PMS database. This highlights the drawbacks to analyzing faulting data with a threshold for recording of 0.25 in. To perform a more meaningful evaluation of faulting in Pennsylvania, it would be necessary for PennDOT to begin recording all faults greater than 0.12 in.

4.5.2 Analysis of Faulting in the LTPP Database

It is apparent that very few JPCP joints on interstates and primary state highways in Pennsylvania experience faulting greater than 0.25 in. However, it is possible that fault depths less than this value are decreasing the serviceability of JPCPs. According to the PennDOT Pavement ME Design User Input Guide, the design mean faulting at failure is 0.15 in for non-interstate highways and 0.12 in for interstate highways (Bhattacharya et al. 2017). Faulting measurements are available at a precision of 0.04 in in the LTPP database. Therefore, this dataset was used to evaluate the prevalence of faulting.

Several previous models have been developed using the LTPP and other datasets to predict the magnitude of faulting at a given time for the design of new JPCP pavements. First, an empirical relationship was developed based on faulting data from six states (Darter et al. 1984). In addition, the principal of differential energy was introduced in the development of the Purdue PUMPS erosion model (Larralde 1984; Vanwijk et al. 1989), where average faulting was related to the difference in subgrade deformation energy between the approach and leave side of the joint. Another model was developed by the American Concrete Pavement Association (ACPA) to predict mean faulting as a function of the cumulative power generated in the subgrade, mean

annual precipitation, and joint spacing for doweled pavements. The presence of drains was also considered for undoweled pavements (Wu et al. 1993) . Additionally, a model was developed based on the initial LTPP general pavement study (GPS) sections as part of the Strategic Highway Research Program (SHRP). This research developed two separate models relating faulting to the cumulative number of ESALs, joint spacing, modulus of subgrade reaction, edge support and dowel diameter for doweled and undoweled pavements. The freezing index and presence of drains were also considered for undoweled pavements (Yu et al. 1998). As part of the FHWA Rigid Pavement Performance and Rehabilitation (RPPR) study, a model that considered the drainage coefficient, base stress, joint spacing, base, freezing index, and precipitation was developed for doweled sections. Also, a model was developed as part of the Nationwide Pavement Cost Model, which utilizes differential energy, annual number of wet days, dowel diameter, AASHTO drainage coefficient, and base type (Titus-Glover et al. 1999). The model used in Pavement ME utilizes an incremental analysis, which considers the differential energy generated, erodibility of the base layer, percentage of the subgrade passing the #200 sieve, annual number of days with greater than 0.1 in of rainfall, and base freezing index (ARA Inc. 2004).

All of these models focus on the prediction of faulting and are not intended to interpret the factors that influence the development of faulting. In addition, it is difficult to predict faulting as a continuous variable for doweled pavements since the precision of the measurement, 0.04 in, is relatively small in relation to the threshold values. Therefore, a model was developed to predict the probability that a fault develops as a binary variable. A positive value represents faults greater than or equal to 0.12 in and a negative value represents faults less than 0.12 in. Since there is inherent scatter in faulting measurements, with faulting values often decreasing by 0.04 in between measurements despite no rehabilitation occurring, a positive measurement is likely an errant

measurement if multiple negative faulting measurements occur after a positive measurement on a single joint. Similarly, if a single negative fault measurement occurs at a time point between positive fault measurements, the negative value is likely an errant measurement. This variation in faulting measurements may be due to variability in the test itself, or the possibility that pavement conditions, such as curling and warping may mask faulting. It is not possible to test if environmental effects significantly affect faulting measurements with the currently available data, as the faulting measurements are not timestamped. In this manner, all joints where some faulting occurs were assigned a time where faulting greater than 0.12 in developed. All measurements before this time are considered negative measurements and all measurements after this point are considered positive measurements. The manual distress surveys in the LTPP database were evaluated to determine the location of partial depth repairs (PDRs), FDRs, and the extent of grinding, which may affect fault measurements. Fault measurements after one of these rehabilitation activities were not considered in the analysis. The dataset used for this analysis consists of 14,531 fault measurements at 2,002 joints and 158 pavement sections.

The probability of a fault in doweled sections was evaluated using a logistic regression model, looking at the probability of faulting as a function of the following variables. The inference space of each of the variables is also shown.

- Base Type (indicator coded categorical variable)
 - ATB: Any asphalt treated base course (3,989 measurements)
 - Granular: Granular, engineered base course (4,483 measurements)
 - CTB: Mixture of soil and cement or aggregate and cement, not performed in a mixing plant (865 measurements)
 - LCB: Lean concrete base mixed at a central plant (3,642 measurements)
 - None: Slab is placed directly on the prepared subgrade (1,558 measurements)
- Freezing Index (°F-days): The average annual number of degree-days below freezing

- 0 to 2,052
- Average Annual Precipitation (in)
 - 8 to 59
- Mean Slab Thickness (in)
 - 7.2 to 13
- Joint Spacing (ft)
 - 13 to 20
- Dowel Diameter (indicator variable)
 - 1.5 in (6,989 measurements)
 - Less than 1.5 in (7,452 measurements)
- Shoulder (indicator variable)
 - Shoulder or widened lane (5,997 measurements)
 - No edge support (8,534 measurements)
- P200 (%): In the base for a granular base, otherwise in the subgrade
 - 1.35 to 97.1
- ESALs: Calculated from LTPP estimates using the trapezoidal rule, better prediction is achieved if ESALs is transformed using \log_{10}
 - 320,000 to 97 million

The results of the fit logistic regression model can be seen in Table 4.6. The granular base course is coded as the default value and is therefore not shown as a predictor. Each of the continuous predictors is centered by the mean and scaled by the standard deviation so that the magnitude of each of the effects can be compared. The weight of each faulting measurement is inversely proportional to the number of faulting measurements at each joint, such that the total weight of each joint is consistent in the analysis. This results in the p-values being based on a t-distribution with the total number of observations equal to the total number of joints, 2,002, not the total number of faulting measurements, 14,531. This accounts for the correlation of faulting measurements at each joint. However, this is conservative since additional information is being

provided and the predictors are changing for each measurement. Therefore, a second p-value, assuming a t-distribution with 14,531 samples, is reported. This p-value is likely unconservative. The calculated p-values form a bracket and the true p-value for each sample is between these values.

Table 4.6. Faulting prediction logistic regression model

	Estimate	P-value	
		n=2,002	n=14,531
Intercept	-3.90	3.20×10^{-7}	4.28×10^{-43}
Base (LCB)	-2.28	2.52×10^{-2}	1.67×10^{-9}
Base (ATB)	1.10	2.88×10^{-1}	4.26×10^{-3}
Base (CTB)	2.95	2.20×10^{-3}	1.67×10^{-16}
Base (none)	2.53	4.70×10^{-5}	6.02×10^{-28}
Freezing Index*	1.42×10^{-1}	4.20×10^{-1}	2.98×10^{-2}
Avg. Annual Precip.*	5.28×10^{-1}	1.38×10^{-1}	6.51×10^{-5}
Mean Thickness*	-2.63×10^{-1}	2.15×10^{-1}	8.41×10^{-4}
Joint Spacing	8.66×10^{-1}	1.24×10^{-4}	4.81×10^{-25}
Dowel Dia.>1.5 in	-1.98	1.74×10^{-2}	1.51×10^{-10}
Drainage	-1.21	3.16×10^{-2}	7.11×10^{-9}
Shoulder/Widened	-8.54×10^{-1}	5.82×10^{-2}	3.39×10^{-7}
P200*	-2.52×10^{-1}	4.67×10^{-1}	5.00×10^{-2}
Log₁₀(Traffic)*	1.48×10^{-1}	9.69×10^{-2}	7.85×10^{-6}

**Predictor is not statistically significant at 95% confidence level assuming n=2,002*
***Predictor is not statistically significant at 95% confidence level assuming n=14,531*

The model has a deviance psuedo-R² of 0.34, which indicates a significant, but not a strong fit. The relationship between predictors and faulting follows the expected relationship. The susceptibility of the base course to faulting in the developed model, from most susceptible to least susceptible, is as follows:

- None
- Cement treated
- Asphalt treated
- Granular
- Lean concrete

This order is logical and illuminates the difference between cemented treated bases and lean concrete bases. The cement treated bases typically contain very little stabilizing agent, tend to have finer gradations than granular bases, and are prone to faulting. In contrast, very little faulting occurs on pavements with plant mixed lean concrete bases. However, these base types are considered to have the same erodibility factor in the Pavement ME Design Guide (ARA Inc. 2004). This analysis indicates that they should be treated separately.

It is not expected that asphalt treated bases are more susceptible to faulting than granular bases. It should be noted that an asphalt treated base is not significantly different from a granular base at a 95% confidence level. In addition, most of the sections with an asphalt treated base were built with subsurface drainage, whereas many of the sections with a granular base were built without drainage. Therefore, it is difficult to differentiate the effect of drainage from the effect of using an asphalt stabilized base. A possible solution may be to perform the analysis on a designed statistical factorial to reduce the effect of this multi-collinearity. However, there is a relatively small number of joints with positive faulting values. Reducing the number of sections considered to the amount required for a balanced factorial would reduce the number of positive measurements to a level where a statistical analysis is not feasible. The freezing index, average annual precipitation, mean concrete thickness, and traffic are not significant at a 95% confidence level assuming $n=2,002$, but are statistically significant assuming $n=14,531$.

The P_{200} value is not statistically significant assuming $n=2,002$, and is on the edge of being statistically significant assuming $n=14,531$. A previous analysis of faulting has shown that CTB are more prone to faulting with a high P_{200} in the base (DeSantis et. al *in print*). This may indicate that if the CTB were treated as an unbound layer, and the P_{200} in the base was considered rather than the P_{200} below the base, this predictor may have been more important.

To evaluate the feasibility of using FWD testing data to provide additional information on the probability of faulting, an expanded data set was developed. Each data point in the combined analysis represents a combination of an FWD test and a faulting measurement. Each faulting measurement is linearly combined with all FWD tests conducted before the faulting measurement, resulting in a large expansion of the database. Each data point is weighted inversely proportional to the total number of FWD tests associated with each faulting measurement multiplied by the number of faulting measurements at each joint. This prevents the later faulting measurements, which are associated with additional previous FWD tests, from dominating the dataset. As a result, each faulting measurement has a weight equal to all other measurements at the same joint. Additionally, the total weight of all joints is consistent across the analysis. This dataset consists of 57,633 combinations. However, each observation is related to multiple sets of predictors and the total number of faulting measurements, is 14,531, as was the case with the previous analysis. Therefore, the p-value is calculated assuming both 2,002 and 14,531 observations. To minimize the effect of slab curvature on the test results, the 16,000 lb nominal load level is used for all FWD testing.

Two new logistic regression models were trained. The first model was performed using FWD measurements scaled and centered across the entire dataset. The resulting model is shown in Table 4.7.

Table 4.7. Logistic regression model to predict faulting with raw FWD data

	Estimate	P-value	
		n=2,002	n=14,531
Intercept	-3.03x10 ⁰	2.79x10 ⁻⁵	1.62x10 ⁻²⁹
LTE**	-7.22x10 ⁻²	7.49x10 ⁻¹	3.90x10 ⁻¹
DD	3.68x10 ⁻¹	1.34x10 ⁻²	2.79x10 ⁻¹¹
Base (LCB)	-3.04x10 ⁰	4.82x10 ⁻³	3.21x10 ⁻¹⁴
Base (ATB)*	-9.61x10 ⁻¹	3.97x10 ⁻¹	2.25x10 ⁻²
Base (CTB)*	1.30x10 ⁰	1.88x10 ⁻¹	3.95x10 ⁻⁴
Base (none)	1.85x10 ⁰	5.50x10 ⁻³	7.72x10 ⁻¹⁴
Freezing Index**	7.88x10 ⁻²	6.67x10 ⁻¹	2.47x10 ⁻¹
Avg. Annual Precip.**	1.82x10 ⁻¹	5.85x10 ⁻¹	1.41x10 ⁻¹
Mean Thickness**	-1.28x10 ⁻²	9.55x10 ⁻¹	8.78x10 ⁻¹
Joint Spacing	8.08x10 ⁻¹	1.12x10 ⁻³	1.70x10 ⁻¹⁸
Dowel Dia.>1.5 in*	-1.58x10 ⁰	5.69x10 ⁻²	2.94x10 ⁻⁷
Drainage**	-2.67*10 ⁻¹	6.53*10 ⁻¹	2.25x10 ⁻¹
Shoulder/Widened	-1.20*10 ⁰	1.02*10 ⁻²	4.47x10 ⁻¹²
P200**	7.48*10 ⁻²	8.33*10 ⁻¹	5.69x10 ⁻¹
Log₁₀ (Traffic)	2.04*10 ⁻¹	3.61*10 ⁻²	1.68x10 ⁻⁸

**Predictor is not statistically significant at the 95% confidence level assuming n=2,002*

***Predictor is not statistically significant at the 95% confidence level assuming n=14,531*

In this model, DD is a statistically significant predictor, but LTE is not. Traffic, which was not significant in the initial prediction model, is a significant predictor with LTE and DD in the model. The dowel diameter, which is a statistically significant predictor in the model without LTE and DD, is not statistically significant if n=2,002 is assumed. This is likely because dowel diameter and FWD joint efficiency measurements are correlated. The effect of having a larger dowel bar is captured in the LTE and DD measurements. Drainage, which was statistically significant assuming n=2,002, is no longer statistically significant if n=14,531 is assumed. Also, the model predicts more faulting for sections with an ATB than with a granular base. This change is likely the result of the model assigning more weight to one of the correlated inputs than the other, rather than a physical difference in the model. The freezing index, average annual precipitation, and mean

thickness are no longer statistically significant if n is assumed to be 14,531. With LTE and DD in the model, the deviance based pseudo-R² increases to 0.37.

The distributions within ELTG groups, described in Table 4.3, were used to calculate z-scores for each of the ELTG tests. The z-scores represent the number of standard deviations each measured joint efficiency parameter is above or below the mean. A logistic regression model was developed using these z-scores instead of the raw LTE and DD. The resulting model can be seen in Table 4.8.

Table 4.8. Logistic regression model to predict faulting with z-scores for DD and LTE

	Estimate	P-value	
		N=2,002	N=14,531
Intercept	-3.31x10 ⁰	3.20x10 ⁻⁶	4.37x10 ⁻³⁶
z-score (LTE)	-1.14x10 ⁰	4.65x10 ⁻²	8.34x10 ⁻⁸
z-score (DD)	1.88x10 ⁰	1.86x10 ⁻⁴	8.16x10 ⁻²⁴
Base (LCB)	-2.75x10 ⁰	7.87x10 ⁻³	8.30x10 ⁻¹³
Base (ATB)*	-1.11x10 ⁰	2.92x10 ⁻¹	4.55x10 ⁻³
Base (CTB)*	1.01x10 ⁰	3.26x10 ⁻¹	8.23x10 ⁻³
Base (none)	1.75x10 ⁰	1.06x10 ⁻²	5.96x10 ⁻¹²
Freezing Index**	6.21x10 ⁻²	7.61x10 ⁻¹	4.12x10 ⁻¹
Avg. Annual Precip.*	2.90x10 ⁻¹	3.73x10 ⁻¹	1.64x10 ⁻²
Mean Thickness*	2.12x10 ⁻¹	3.52x10 ⁻¹	1.23x10 ⁻²
Joint Spacing	7.67x10 ⁻¹	2.46x10 ⁻³	3.52x10 ⁻¹⁶
Dowel Dia.>1.5 in*	-1.44x10 ⁰	7.86x10 ⁻²	2.18x10 ⁻⁶
Drainage**	-2.67x10 ⁻¹	9.39x10 ⁻¹	8.37x10 ⁻¹
Shoulder/Widened	-1.05x10 ⁰	1.98x10 ⁻²	3.48x10 ⁻¹⁰
P200**	1.82x10 ⁻¹	5.98x10 ⁻¹	1.55x10 ⁻¹
Log₁₀(Traffic)	2.23*10 ⁻¹	3.03*10 ⁻²	5.48*10 ⁻⁹

**Predictor is not statistically significant at the 95% confidence level assuming n=2,002*

***Predictor is not statistically significant at the 95% confidence level assuming n=14,531*

The z-score for both LTE and DD are statistically significant predictors in this model. In addition, the magnitude of the coefficients for the z-scores are much larger than the coefficients

for LTE and DD in the model shown in Table 4.8 despite both sets of predictors being scaled and centered. The average annual precipitation and mean thickness are statistically significant predictors if $n=14,531$ is assumed. The deviance based psuedo- R^2 increases to 0.39 when the z-score is used instead of raw DD measurements. This is an indication that modifying the measured joint efficiency parameters based on the distributions in the LTPP database improves the power of FWD measurements to predict faulting.

A better estimate of the statistical significance of each of the predictors can be calculated using the general error estimation method (GEE) (Zeger et al. 1988). This method accounts for the correlation between grouped inputs with a specified variance-covariance matrix. The algorithm accounting for generalized error estimates consists of:

- Prescribing a correlation structure of the data.
 - GEE requires a correlation matrix between each of the measures within a group. Common correlation structures include unstructured (no pattern is assumed in the correlation matrix), exchange (all measures within a group are assumed to have the same correlation), and autocorrelation (measures closer together in time are more correlated than measures further away in time). The exchange correlation structure, which is the simplest correlation structure, is adequate for most applications (Dupont 2009).
- Estimating the parameters using quasi-likelihood
 - This is like the maximum likelihood method but does not require the likelihood function to be defined.
- Estimating the variance-covariance matrix using the Huber-White Sandwich Estimator

- Using the parameter estimates and the variance-covariance matrix to perform hypothesis testing

Two logistic regression models, one using the raw DD and LTE and the other using the z-scores for DD and LTE, were fit using the GEE method. The GEE method is intended for evaluating the importance of predictors, not developing predictive models. Therefore, these models are presented to provide insight into the significance of the predictors. Typical statistics for evaluating the fit of a logistic regression model, such as the deviance based pseudo-R², are not applicable to the GEE method. Therefore, the fit of these models trained with the GEE method are not reported. The model trained with raw DD and LTE measurements can be seen in Table 4.9.

Table 4.9. GEE logistic regression model to predict faulting with raw DD and LTE

	Estimate	P-Value
Intercept		
DD	2.27*10 ⁻¹	1.52*10 ⁻³
LTE*	4.00*10 ⁻⁴	9.96*10 ⁻¹
Base (LCB)	-2.85*10 ⁰	5.04*10 ⁻⁴
Base (ATB)	-1.64*10 ⁰	4.14*10 ⁻²
Base (CTB)*	4.06*10 ⁻¹	5.88*10 ⁻¹
Base (none)	1.52*10 ⁰	1.04*10 ⁻⁴
Freezing Index*	1.80*10 ⁻¹	2.45*10 ⁻¹
Avg. Annual Precip.	8.05*10 ⁻¹	8.08*10 ⁻³
Mean Thickness*	2.93*10 ⁻²	8.42*10 ⁻¹
Joint Spacing	1.08*10 ⁰	1.56*10 ⁻¹⁸
Dowel Dia.>1.5 in	-3.06*10 ⁰	1.22*10 ⁻¹⁶
Drainage*	3.23*10 ⁻¹	4.45*10 ⁻¹
Shoulder/Widened	-7.83*10 ⁻¹	1.46*10 ⁻²
P200*	2.03*10 ⁻¹	5.56*10 ⁻¹
Log₁₀(Traffic)	2.68*10 ⁻¹	3.07*10 ⁻⁵

**Predictor is not statistically significant at the 95% confidence level utilizing the GEE method*

When the GEE method is used to evaluate the importance of predictors, pavements with an asphalt treated base are significantly less susceptible to faulting than pavements with a granular base. This was not the case when using traditional maximum likelihood estimates (MLE) and assuming $n=2,002$ in the hypothesis testing. In addition, the GEE analysis shows the average annual precipitation and dowel diameter are statistically significant predictors, which was also not the case when using MLE and assuming $n=2,002$ in the hypothesis testing. The average annual precipitation was not found to be statistically significant at a 95% confidence level using traditional MLE and assuming $n=14,531$. It is expected that the p-value calculated using GEE would be bound by the two p-values calculated using MLE. However, for this predictor, the p-value was lower than the expected lower bound of the p-value using MLE. This may partially be due to the analysis consisting of 57,633 linear combinations of FWD and faulting measurements. The lower bound of the p-value was estimated using $n=14,531$ since the data points relating to different FWD measurements, but the same faulting measurement, are thought to be highly correlated. However, the results of the GEE analysis show that using MLE with $n=57,633$ may be a better estimator of the lower bound of the p-value. This discrepancy may also be due to the covariance structure of the data affecting the predictors. For example, if fault measurements at a single joint with significant faulting may act as “influence” points for a traditional MLE analysis. However, GEE analysis is more robust to one joint affecting the parameter estimates, due to the correlation terms in the covariance matrix.

The model fit using the GEE method and utilizing the z-score for DD and LTE can be seen in Table 4.10.

Table 4.10. GEE logistic regression model to predict faulting with z-scores for DD and LTE

	Estimate	P-Value
Intercept		
z-score (DD)	$1.23*10^0$	$2.06*10^{-5}$
z-score (LTE)	$9.81*10^{-1}$	$1.09*10^{-3}$
Base (LCB)	$-2.54*10^0$	$8.54*10^{-4}$
Base (ATB)*	$-1.37*10^0$	$8.06*10^{-2}$
Base (CTB)*	$7.41*10^{-1}$	$3.23*10^{-1}$
Base (none)	$1.71*10^0$	$4.00*10^{-5}$
Freezing Index*	$1.72*10^{-1}$	$2.28*10^{-1}$
Avg. Annual Precip.	$1.03*10^0$	$2.27*10^{-3}$
Mean Thickness*	$-4.05*10^0$	$2.05*10^{-1}$
Joint Spacing	$1.05*10^0$	$1.46*10^{-17}$
Dowel Dia.>1.5 in	$-3.37*10^0$	$5.34*10^{-19}$
Drainage*	$4.19*10^{-1}$	$3.40*10^{-1}$
Shoulder/Widened	$-7.14*10^{-1}$	$2.78*10^{-2}$
P200*	$1.41*10^{-1}$	$4.67*10^{-1}$
Log₁₀(Traffic)	$2.69*10^{-1}$	$5.49*10^{-5}$

**Predictor is not statistically significant at the 95% confidence level utilizing the GEE method*

Similar to the model trained using raw DD and LTE, the average annual precipitation and dowel diameter are statistically significant at a 95% confidence level using the GEE model but are not using MLE with n=2,002.

The models utilizing both the MLE and GEE methods were trained using FWD tests over the full range of ELTGs. The z-score was used to adjust the FWD results based on the ELTG at the time of testing. However, the computational analysis using EverFE has shown that it can become difficult to detect dowel looseness at large positive and negative ELTG values. Therefore, tests at these ELTGs likely have limited predictive power, even when utilizing the z-scores for LTE and DD. To evaluate whether an improved model could be developed without these tests, an

additional logistic regression model was fit only using tests with an ELTG between -0.5 °F/in and 2.5 °F/in. The pseudo- R^2 for this model increased to 0.44, which indicates the predictive power of joint efficiency parameters can be increased by avoiding peak positive and negative temperature gradients.

This fit, which includes corrections for slab curvature and limits on the allowable testing range, is still not strong. This is likely due to the large variation in LTE and DD measurements, which makes it difficult to predict future faulting. This weak fit, along with the scarcity of faulting in doweled pavements, may indicate that FWD testing is not the best solution for identifying joints where future faulting is likely to occur. Another possibility would be to perform load transfer restoration, along with diamond grinding, at locations where faulting has already occurred. If a fault is removed with diamond grinding, the underlying factors that led to the development of the fault likely still exist in the pavement. The fault will redevelop if an intervention, such as a DBR, is not applied.

4.6 SENSITIVITY OF THE PAVEMENT ME REFLECTIVE CRACKING MODEL TO MEASURED LTE

In addition to indicating whether future faulting will occur at a joint, the measured LTE can be used as an input into the Pavement ME AC overlay over JPCP module. This module uses a fracture mechanics model to predict the development of reflective cracking in the HMA overlay. The Level 1 inputs for LTE are FWD measured LTE. The Level 3 inputs for LTE are as follows (Titus Glover et al. 2017):

- Doweled joint: 70 percent
- Non-doweled joint with stabilized base course: 50 percent
- Non-doweled joint with granular base course: 30 percent

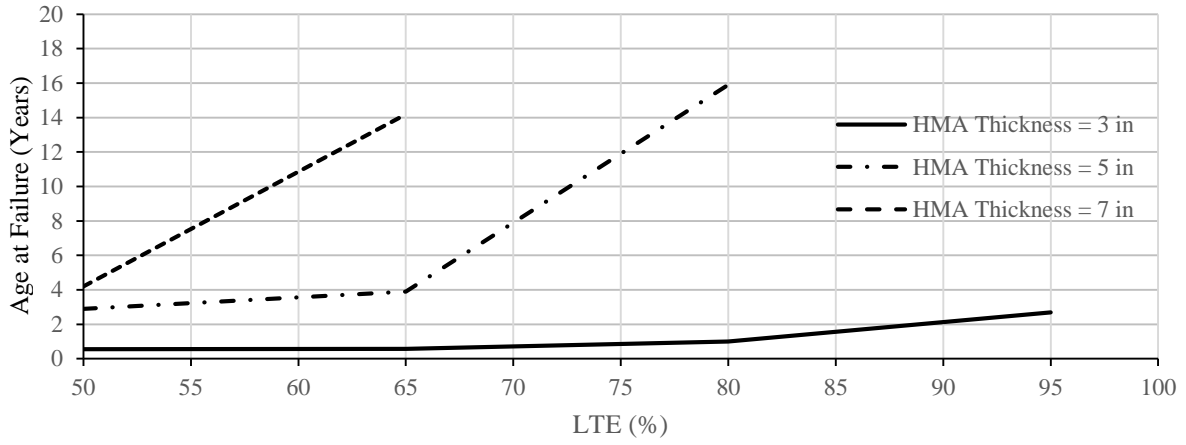
The sensitivity of this module to the LTE input was evaluated. The age at failure, 1500 ft of total transverse cracking per mile at the 50% reliability level, was predicted for a range of LTE, k-value, HMA thickness, and PCC thickness values. The values considered are shown in Table 4.11.

Table 4.11. AC overlay of JPCP sensitivity analysis

LTE	50%	65%	70%	95%
k-value	75 psi/in	150 psi/in	300 psi/in	
HMA Thickness	3 in	5 in		
Slab Thickness	8 in	12 in		

An average one-way ADTT of 5,000 was used in this analysis with a 0% growth rate. This results in an estimated 1 million ESALS/year. A PG 64-22 asphalt binder grade with a default aggregate gradation was used in the analysis. The concrete was assumed to have a static elastic modulus of 4 million psi for this sensitivity analysis as this value corresponds with the assumed concrete strength of 5000 psi in the PennDOT Publication 242 pavement design guide. The Allegheny County Airport weather station was used for the climatic data. The effect of the sensitivity analysis with a constant k-value of 150 psi/in can be seen in Figure 4.49.

Slab Thickness = 8 in



Slab Thickness = 12 in

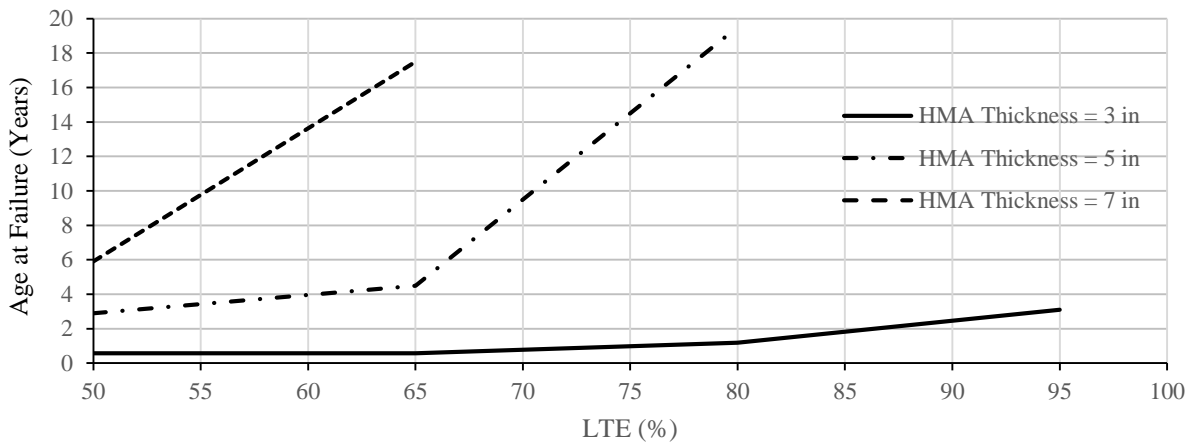
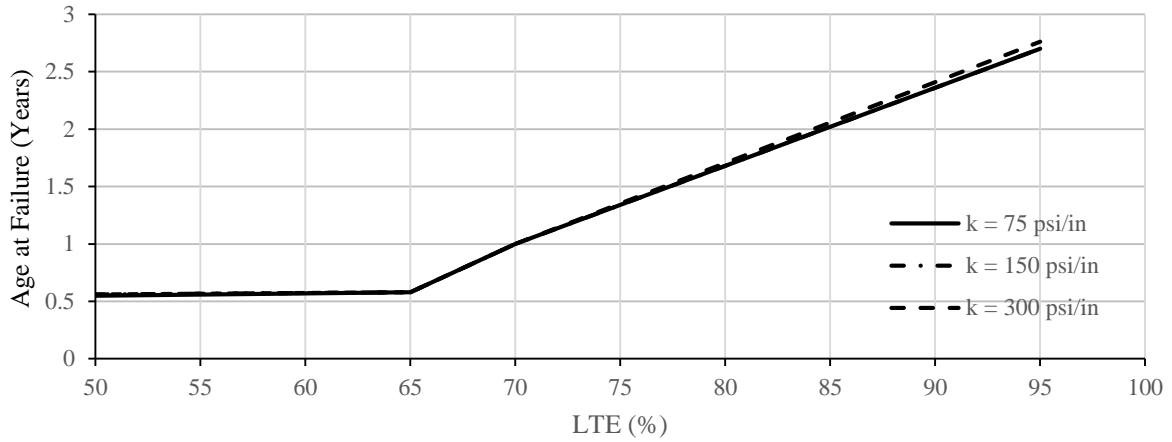


Figure 4.49. Sensitivity analysis of Pavement ME AC over JPCP reflective cracking model (k=150 psi/in)

The analysis shows that the reflective cracking model is very sensitive to LTE and overlay thickness. However, the model does not appear to be sensitive to the thickness of the concrete pavement. The possibility of the LTE and k-value having an interaction was explored by analyzing a structure with an 8-in thick JPCP and a 3 and 5-in thick overlay. The results of the analysis can be seen in Figure 4.50.

HMA Thickness = 3 in



**Note: The y-axis scale on this plot above varies from the plot below for clarity.*

HMA Thickness = 5 in

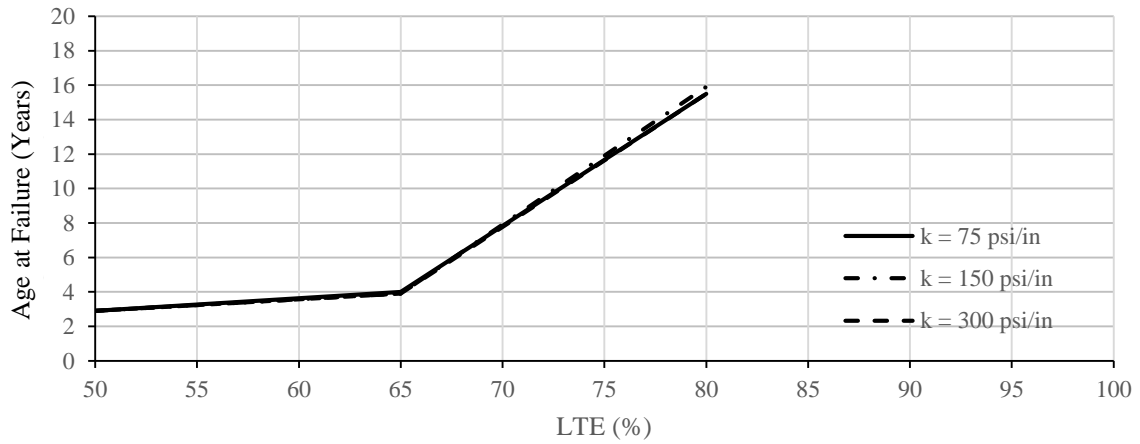


Figure 4.50. Sensitivity analysis of Pavement ME AC over JPCP reflective cracking model (slab thickness = 8 in)

The analysis shows that the reflective cracking model does not appear to be sensitive to k-value. Neither the report detailing the development or the implementation of the model into Pavement ME mention using FWD measured LTE data (Lytton et al. 2010; Titus-Glover et al. 2016). Therefore, it is likely that the Level 3 inputs for LTE were used for calibration. Figure 4.49 and Figure 4.50 indicate that the reflective cracking model is very sensitive to this input. Therefore, using the measured LTE rather than the level three inputs may not be properly represented in the calibration database. In addition, the overall variance in LTE within a section, shown in Table 4.5, can result in a large variance in reflective cracking predictions. Therefore, using Level 3 inputs may result in more reliable reflective cracking predictions. If the measured LTE at a joint is significantly lower than 70%, the pavement life can likely be extended by restoring the LTE with a DBR or FDR prior to placing the overlay.

4.7 CONCLUSIONS AND RECOMMENDATIONS

It is evident from field trials, computational analysis, and statistical analysis that slab curvature can have a significant effect on the measured LTE and DD at a joint. Computational analyses are better able to capture this effect if dowel looseness is discretely modeled, rather than using a dense liquid interaction between the slab and dowel. The variation that can be attributed to slab curvature is only a small portion of total variation observed in repeated measurements within a section. Despite this significant within section variation, measured joint efficiency parameters improve the prediction of future faulting. The prediction is further improved if the measurements are corrected for the ELTG at the time of testing, and/or testing occurs with an ELTG between 0.5 °F/in and 2.5 °F/in.

5.0 VOID DETECTION

5.1 INTRODUCTION

5.1.1 Background

The identification of voids beneath the corner of the slab is important for the successful maintenance and rehabilitation of JPCPs. An untreated void will lead to high tensile stresses at the top of the concrete slab and can eventually cause a corner break. In addition, the overlay design modules in the AASHTO Pavement ME Design Guide assume that the existing pavement is uniformly supported (ARA Inc. 2004). Detection of voids using a FWD consists of performing testing in the corner of the slab, with the load plate tangent to both the transverse joint and the longitudinal lane-shoulder joint. There are several methods for using FWD deflection data to detect if voids are present but they each have limitations. The methods currently available are discussed in this section along with the limitations associated with each of these methods.

Several states have set a threshold for identifying voids based on the standardized deflection under a 9,000 lb load measured in the corner of the slab on the leave side of the joint. For example, PennDOT and the Missouri Department of Transportation assume a void is likely present if the leave corner deflection is greater than 20 mils (MoDOT 2013). This method ignores differences in pavement structures and subgrade support conditions. Alternatively, the normalized

deflection in the leave corner of the slab can be compared to the normalized deflection at similar locations where a void is less likely to occur. These locations include the corner of the slab on the approach side of the same joint, or the leave corner of other joints along the project (AASHTO 1993). These comparisons are limited by the possibility of a large void spanning both sides of the joint, or frequent voids occurring along a project. It is also common to develop a pavement model using the finite element method (FEM), and compare the measured corner deflection to the predicted deflection. The advantage of this method is that the temperature gradient present at the time the FWD testing is performed can be accounted for in the FEM model. This is the only method currently available to account for environmental conditions such as the temperature gradient. However, a FEM model must be developed for each pavement evaluated. To generate this model, assumptions must be made regarding the pavement structure, including the long-term curvature, interface bond conditions and base model. Previous researchers have used multiple passes of FWD testing to estimate the long-term curvature in the slab (Rao and Roesler 2005). However, this is an inverse analysis which assumes that no void is present. Any of these assumptions can influence the accuracy of the prediction. In addition, a threshold level for the ratio between the measured and predicted deflections has not been established.

Another method of void detection is variable load corner deflection analysis. Testing at the leave corner is performed at three different load levels, and a regression line is fit to the load versus deflection data. The deflection intercept of the regression line is considered the void parameter (VP), and is an indication of a non-linear relationship between load and deflection when a void is present (Crovetti 1994). Traditionally, a VP greater than 2 mils is indicative that a void may be present (AASHTO 1993). The void parameter is an indication of whether a void exists, but does not define the size of the void.

Estimating the size of the void can be accomplished using a graphical void size estimator, which takes into account the normalized corner deflection and the bending corrected LTE to predict whether a void exists, and the size of a void (Darter et al. 1985). The estimator is trained using analytical results from a simple FEM model, and does not consider differences between pavement structures, with the exception of LTE. The detection of voids with current methods is often considered more of an art form than a science. Often multiple methods of void detection are performed, and the results are interpreted using “engineering judgement.”

One particular challenge for void detection is accounting for the effect of temperature curling and moisture warping. While performing the FWD testing when a negative temperature gradient is present in the slab, a false positive can result. A false negative can occur when a positive gradient is present at the time of testing. The current void detection techniques cannot distinguish separation between the slab and supporting layers due to slab curvature from a void created by erosion. FEM analysis has shown that the corner deflections are influenced by a negative temperature gradient (Croveti 1994). Analysis of the LTPP database and MnROAD data confirmed that environmental impacts can greatly influence the ability to detect a void (Khazanovich and Gotlif 2003; Vandebossche 2007). While it is accepted that void detection using FWD data is affected by slab curling and warping, there is not a rigorously validated method of accounting for this curvature.

Current guidance from FHWA recommends that FWD testing be performed early in the morning when the slab is flat (AASHTO 1993) . However, in the morning, the temperature gradient in concrete pavements changes rapidly from negative to positive, severely limiting the amount of time testing can be performed on a flat slab (Wells et al. 2006). As part of the present work, the LTPP and MnROAD databases are used to evaluate existing void detection methods at varying

temperature gradients. These databases are then used to train and evaluate a statistical classifier that predicts whether a void exists as a function of FWD testing results and environmental conditions.

5.1.2 Research Database Development

Data available to train and evaluate void detection methods consists of FWD testing from the two previously mentioned long-term research efforts, LTPP and MnROAD. There are three categories of test sections within the LTPP database; General Pavement Sections (GPS), Specific Pavement Sections (SPS), and the Seasonal Monitoring Program (SMP). FWD testing is performed, on average, once every few years on the GPS and SPS sections. Testing is performed as often as once a month on the SMP sections. In addition, some test dates on the SMP sections consist of replicate passes. This allows testing to occur on the same day with varying temperature gradients. Therefore, the SMP sections are used in this analysis. FWD testing at MnROAD is performed four times a year. During a previous study, testing was performed repeatedly over 24 hour periods to capture the full range of temperature gradients (Vandenbossche 2003). Only pavements with doweled joints are being considered in this analysis due to the significant variation between the behavior of doweled and undoweled pavements. Nearly all JPCP pavements in Pennsylvania on primary and interstate routes, where FWD testing is usually performed, are doweled.

An additional challenge for developing and evaluating FWD-based pavement void detection methods is defining the target “true” support conditions for each test. There is currently no practical method to determine whether a void has developed independent of FWD testing. A study has been performed where epoxy is poured into an access hole and allowed to pool in a void (Chapin and White 1993). However, this epoxy test has only been performed on a very limited

basis, and has not been used to determine if voids are present for the pavement sections included in the LTPP or MnROAD databases. Furthermore, only a limited amount of FWD data and no information regarding the environmental conditions was available for the study that utilized epoxy validation. An alternate method of defining when voids are present was used for this study. The history of testing at a single test location is used to identify if and when the development of a void causes a change in the pavement response to FWD loading. This validation technique can only be used at joints where testing is performed often. This method was applied to the LTPP SMP sections and MnROAD sections, in which FWD testing results are available from a minimum of 15 different test dates.

The testing history was evaluated by analyzing scatterplots showing the relationship between FWD testing results and environmental conditions at each test location. The following variables are included on these plots: the equivalent linear temperature gradient calculated using the equivalent strain method (ELTG) (Janssen and Snyder 2000), the VP, ratio of measured deflection to theoretical deflection calculated using a finite element model (DR), and the bending corrected deflection load transfer efficiency in the wheelpath (LTE). The calculation of the theoretical deflection was automated using an artificial neural network. A more detailed description of the model will be presented below. The plots made for each test location, can be seen in Table 5.1. An example of these plots can be seen in Figure 5.1. Within each test location, the time the testing was performed is differentiated with each marker representing all tests within a single year.

Table 5.1. Plots evaluated to estimate “true” void detection model

x-axis	y-axis
ELTG	VP
ELTG	DR
LTE	VP
LTE	DR

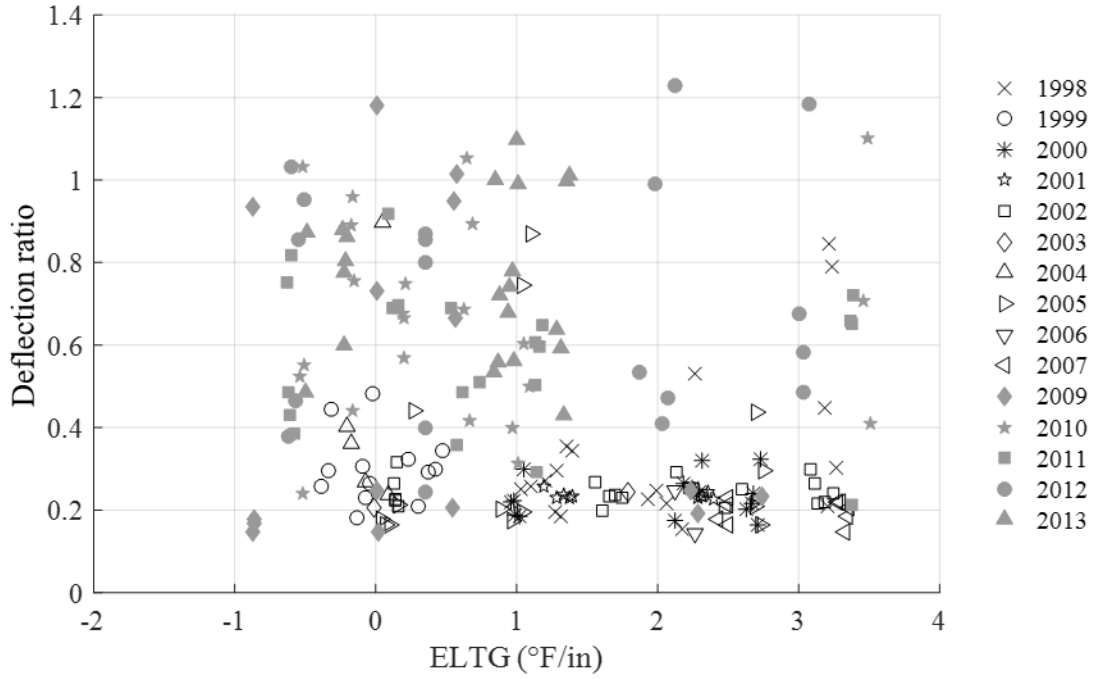


Figure 5.1: Example of scatterplots used to identify the time of void development

A distinct, permanent increase in deflection and/or void parameter that cannot be explained by changes in ELTG or LTE is likely indicative of a void developing beneath the pavement. In this manner, the time at which a void developed was estimated for each test location. For the example plot, there is a distinct difference in the test results shown with open markers (prior to 12/31/2007) and the test results shown with grey filled markers (after 1/1/2009). This indicates a void likely develops between 2007 and 2009. All tests performed prior to this time were classified as “no void” and all tests performed after this time were classified as a “void.” The tests classified as a “void” are shown in grey on the example plot. This procedure was performed at each joint for LTPP Sections 04-0215, 18-3002, 37-0201, 53-3801, and 89-3011, which are all SMP sections, and MnROAD Cells 5, 6, 7, 8, 9, 10, 11, 13, and 52.

The database developed from these sections with the “classified” joint condition contains approximately 4,750 tests, from 121 joints and 14 different pavement structures. Of the 14 sections, 12 are in a wet, freeze climate, one is in a wet, no-freeze climate, and one is in a dry, no-freeze climate. Seven of the sections have a granular base, five have an asphalt stabilized base, and two have a cement stabilized base. The pavement thickness ranges from 7 in to 12 in. The ELTG at the time of testing, calculated using equivalent strain, ranges from -1.5 °F/in to 4 °F/in. The joint spacing ranges from 13 to 20 ft. However, most of the testing where a void occurred was on sections with a joint spacing of 15 ft. Therefore, joint spacing was not used as a predictor. To prevent the behavior of “locked up” joints from influencing the behavior of the classifier, any tests with a slab weighted average temperature (WAT) greater than 75 °F and with a LTE greater than 90% are not included in the dataset.

5.1.3 Performance of Existing Void Detection Methods

This classified database was used to evaluate the performance of existing void detection methods. These techniques are represented by “stump classifiers,” where a void is predicted if a single predictor is greater than or equal to a threshold. Stump classifiers using the VP, normalized 9,000 lb deflection (NormDefl), and DR predictors were developed. Stump classifiers on VP and NormDefl are commonly used in practice. For the LTPP SMP sections and at MnROAD, testing is not performed on the approach corner of the slab. This prevents comparing the deflections on the leave and approach side of the slab to detect voids. In addition, only a select number of joints are tested regularly. Therefore, it is not possible to detect voids by comparing the normalized deflection on the approach side of the joint, in the corner of the slab, to the normalized deflection at adjacent joints. Therefore, the DR parameter was used to classify each joint as having either a “void” or a “no void” condition. This approach is similar to the other two methods in that it compares the measured normalized deflection to a standard deflection, which takes into account characteristics of the pavement structure.

One method of comparing the relative predictive power of these parameters for detecting voids is to compare the distribution of the parameter for two groups. The first group is FWD tests where no void exists. The second group is FWD tests when a void does exist. . This analysis may be slightly biased, as the deflection ratio and void parameter were used to identify the time point which separates the void classes for each joint. However, the development of a void is considered permanent in the analysis. Therefore, comparisons between the classes are meaningful. A larger difference in these distributions is indicative of the parameter having more predictive power. The cumulative distribution plot for these parameters can be seen in Figure 5.2 to 5.4.

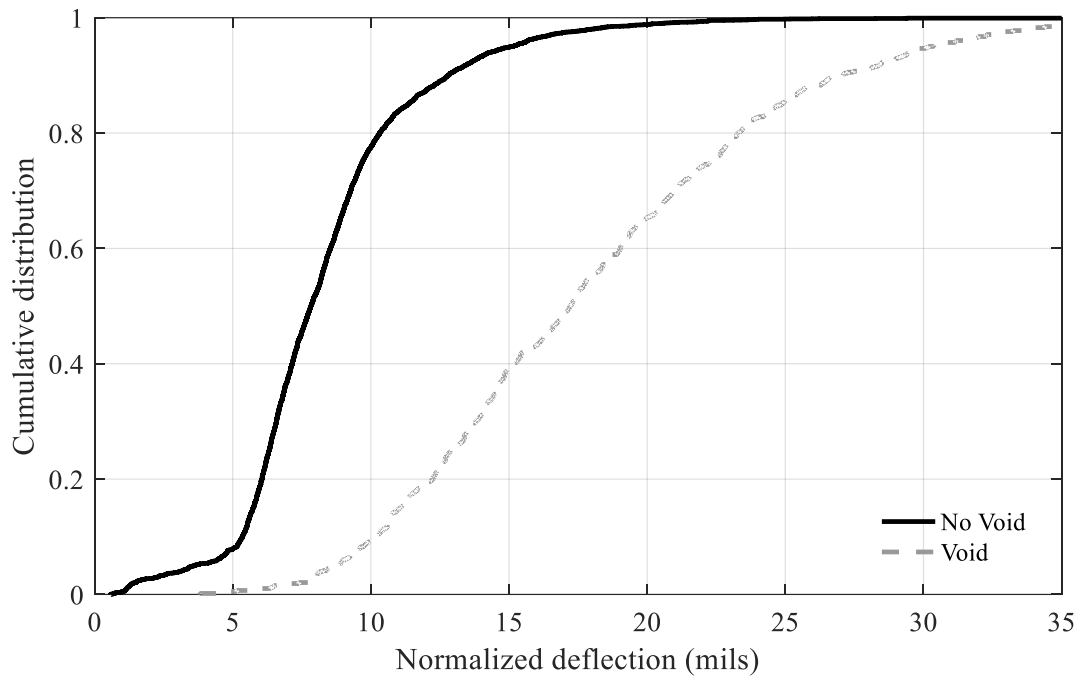


Figure 5.2. CDF plot of normalized deflection for void and no void classes

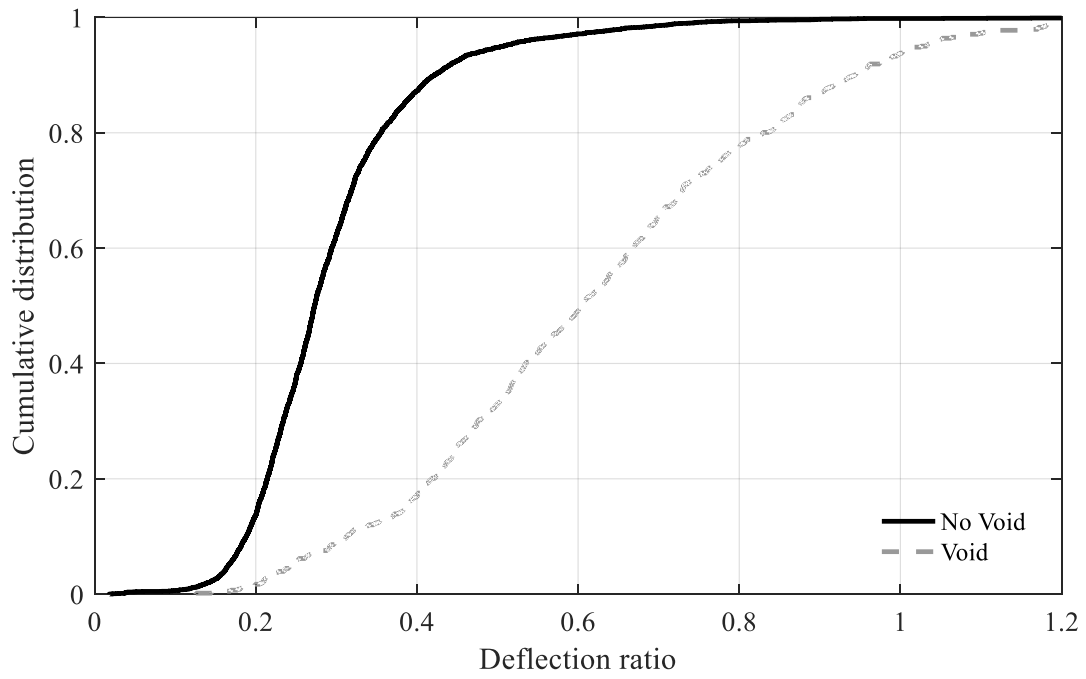


Figure 5.3. CDF plot of deflection ratio for void and no void classes

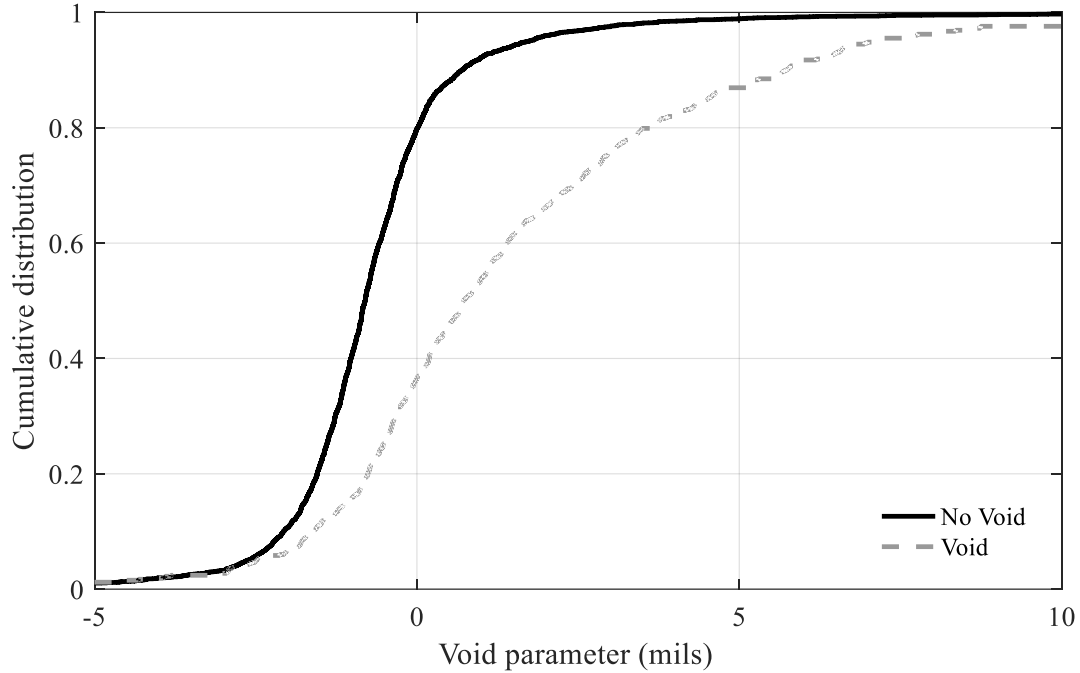


Figure 5.4. CDF plot of void parameter for void and no void classes

The separation between the classes is greater for the normalized deflection and deflection ratio parameters than it is for the void detection parameter. This indicates that the normalized deflection and deflection ratio parameters are better indicators of void development than the void parameter. A paired t-test was performed comparing the classes of each parameter. The classes were different at a statistically significant level for all parameters, with p-values less than 1×10^{-64} for each of the parameters. To compare the separation between the two classes, a z-score was calculated for each of the parameters, using Equation 5.1. The z-scores for each of the parameters can be seen in Table 5.2. The z-scores agree with the cumulative distribution plots, and show that there is more separation between the void classes for the normalized deflection and deflection ratio than there is for the void parameter.

$$Z = \frac{|\bar{X}_1 - \bar{X}_2|}{\sigma_{pooled}} \quad (5.1)$$

Where:

\bar{X}_1 and \bar{X}_2 = the mean parameter value for each of the classes

σ_{pooled} = the pooled standard deviation of the classes

Table 5.2. Z-score of difference in means between classes for predictors

Parameter	z-Score
Normalized Deflection	1.82
Deflection Ratio	1.81
Void Parameter	0.91

The performance of stump classifiers, dividing the classes at a single threshold value, for each of these parameters is evaluated using two curves. The accuracy curve shows the relationship between the accuracy of the classifier and the threshold. The receiver operator characteristic (ROC) curve shows the discriminating power of the classifier by plotting the true positive rate against the false positive rate at varying threshold levels. The closer the ROC curve is to the upper left-hand corner of the plot, the greater the capability of the classifier to discriminate between a void and a no void condition. To allow the accuracy curve to be evaluated in native units, cross validation was not performed on these classifiers. The accuracy and ROC curves for each of the classifiers can be seen in Figure 5.5 to Figure 5.8.

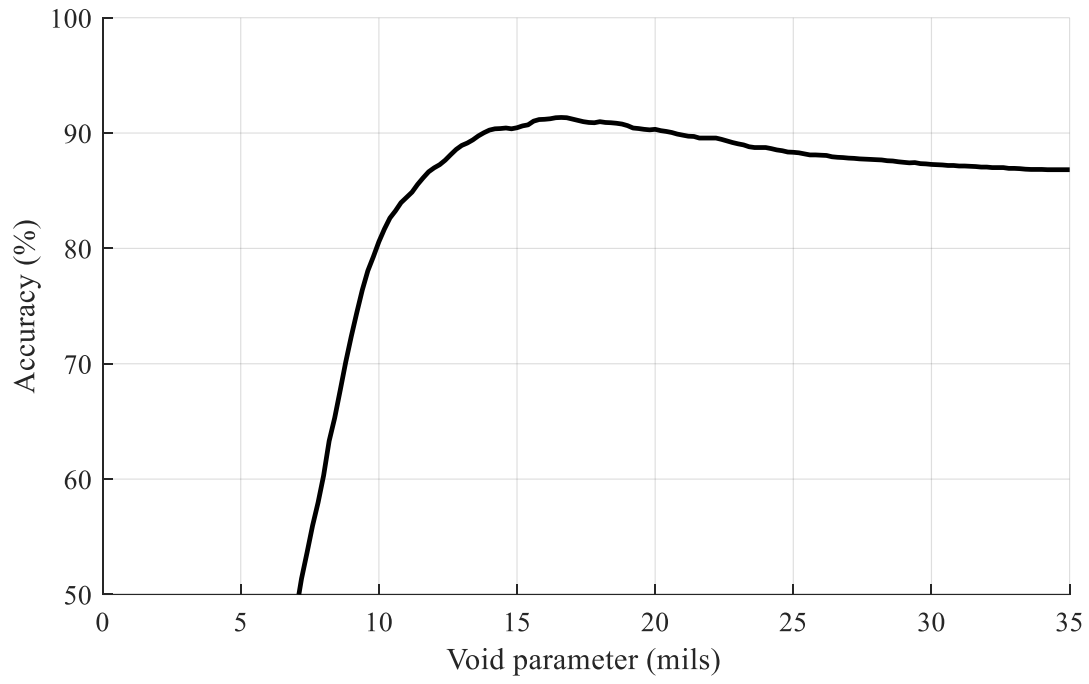


Figure 5.5. Accuracy of normalized deflection stump classifier

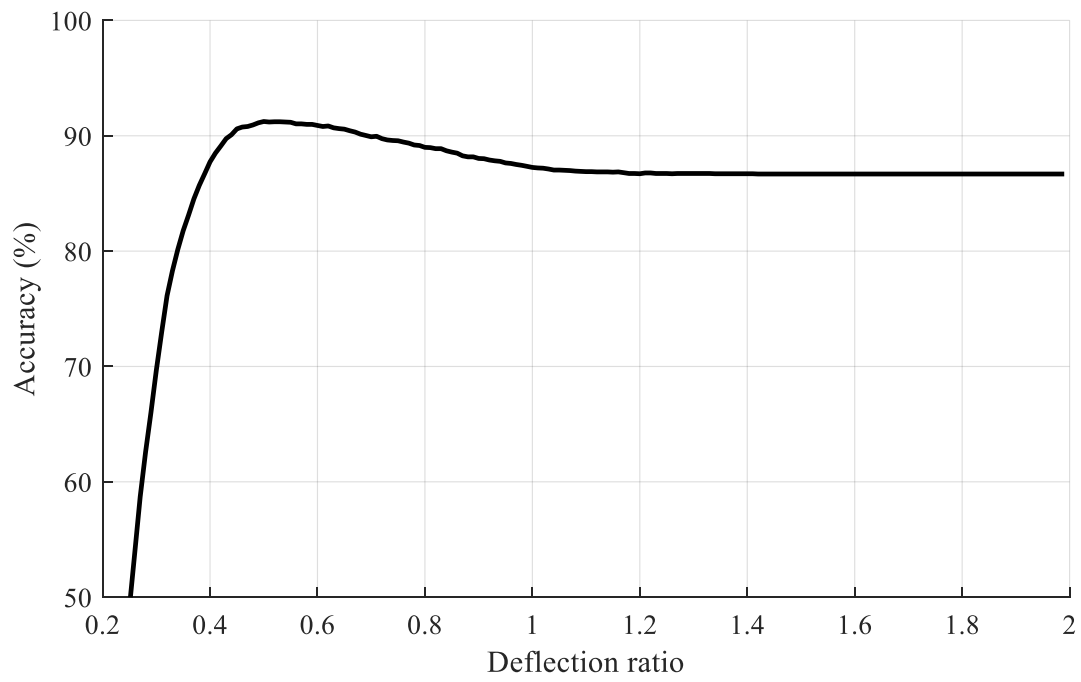


Figure 5.6. Accuracy of deflection ratio stump classifier

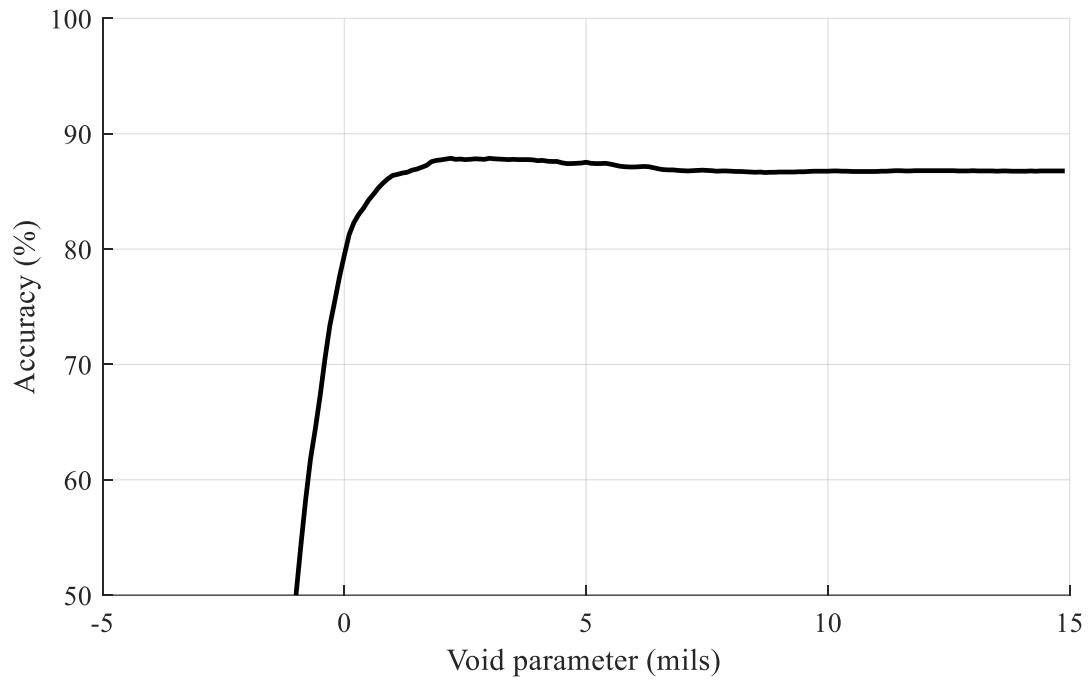


Figure 5.7. Accuracy of void parameter stump classifier

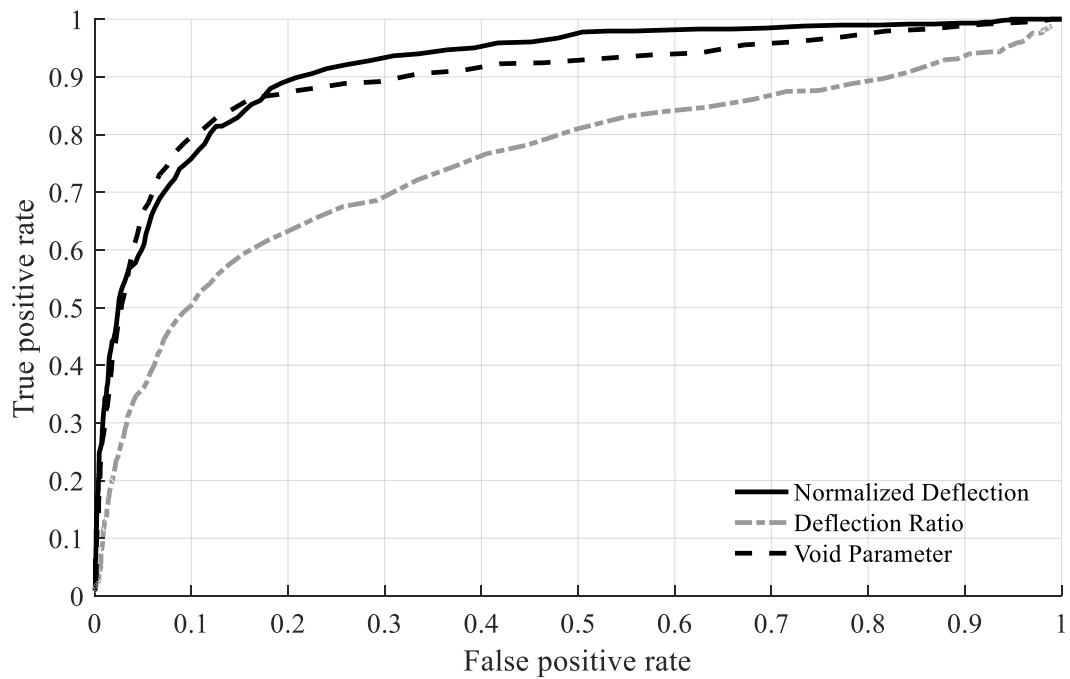


Figure 5.8. ROC curves of stump classifiers

The maximum accuracy for the normalized deflection stump classifier, 0.914, occurs with a threshold of 17 mils deflection. This is similar to the threshold of 20 mils currently used in Pennsylvania. The maximum accuracy for the DR stump classifier, 0.912, occurs with a deflection ratio of approximately 0.56. The ROC curves for these classifiers are similar. It is expected that the deflection ratio classifier would perform better than the normalized deflection classifier as it considers the effect of the pavement structure on deflection. However, large deflections contribute to the pumping mechanism, which causes voids. Therefore, the normalized deflection parameter likely provides additional information on whether a void is likely to develop, along with whether a void currently exists.

Both classifiers perform better than the VP classifier. This agrees with the distribution analysis and the previously mentioned research, which evaluated non-destructive void detection methods using an epoxy injection technique to define the “true” location of voids. This research found that the variable load corner deflection analysis of FWD data did not perform as well as other evaluation tools (Chapin and White 1993). The prior research did not consider deflection based void detection criteria using FWD testing results.

All of the stump classifiers evaluated in the present study are affected by slab curvature. Therefore, the performance of these classifiers was evaluated at different environmental conditions. The range of ELTG values in the dataset was divided into 4 “bins”: negative temperature gradients ($ELTG < -0.5$ °F/in), flat temperature gradients (-0.5 °F/in $< ELTG < 0.5$ °F/in), small positive temperature gradients (0.5 °F/in $< ELTG < 1.5$ °F/in) and large positive temperature gradients ($ELTG > 1.5$ °F/in). The accuracy and ROC curves were then plotted for each ELTG bin and can be seen in Figure 5.9 to 5.14.

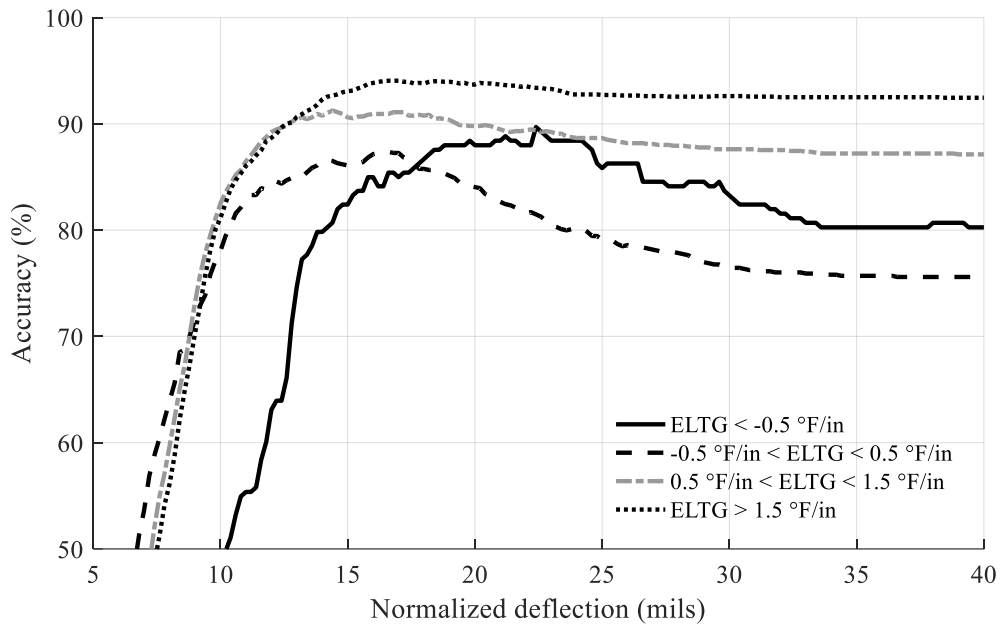


Figure 5.9. Accuracy of normalized deflection stump classifier by ELTG group

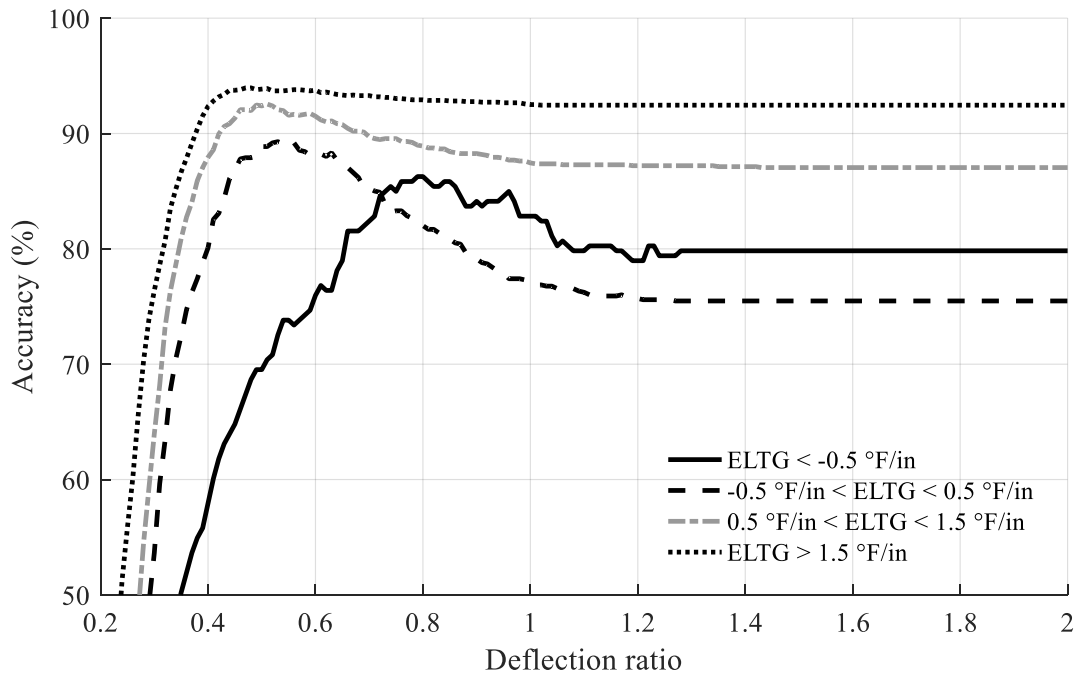


Figure 5.10. Accuracy of deflection ratio stump classifier by ELTG group

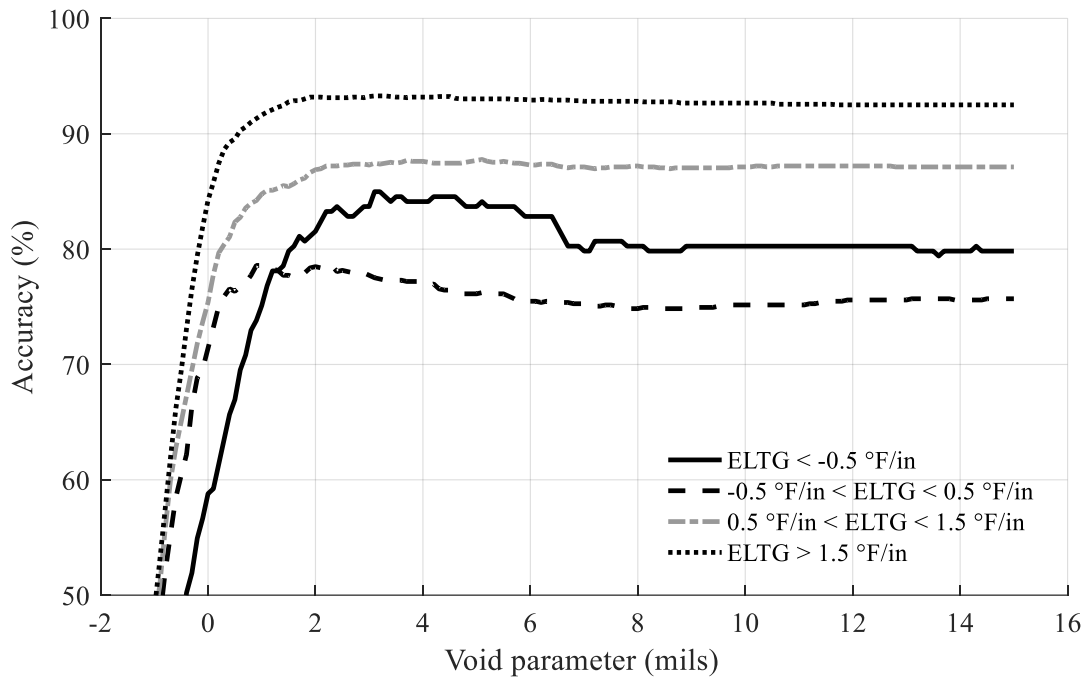


Figure 5.11. Accuracy of void parameter stump classifier by ELTG group

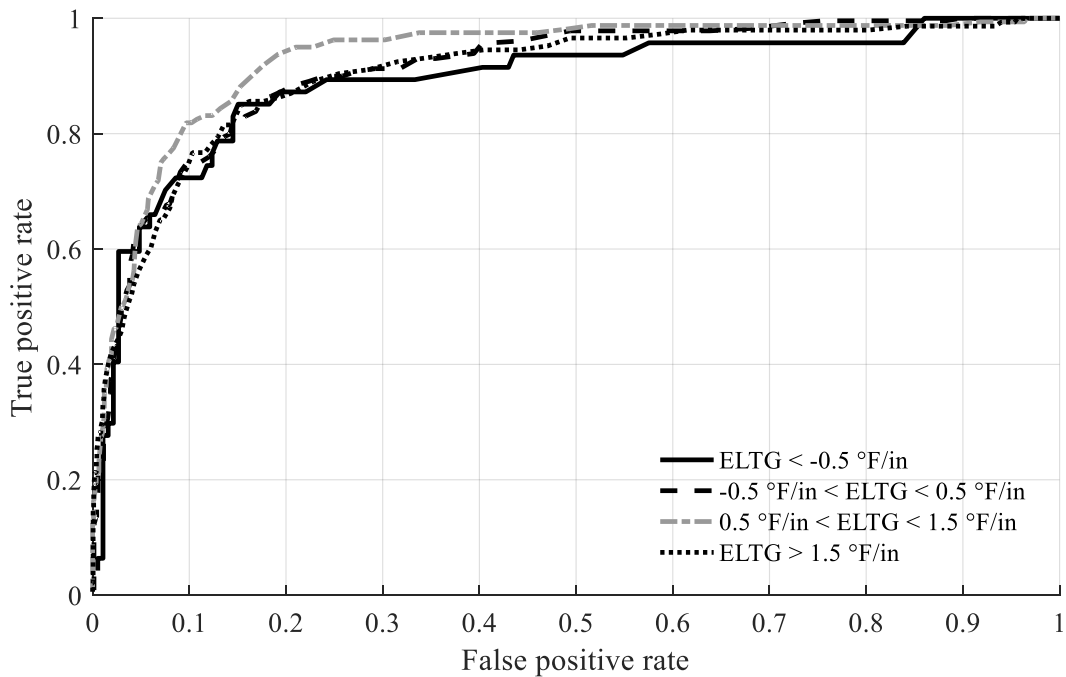


Figure 5.12. ROC curve for normalized deflection classifier by ELTG group

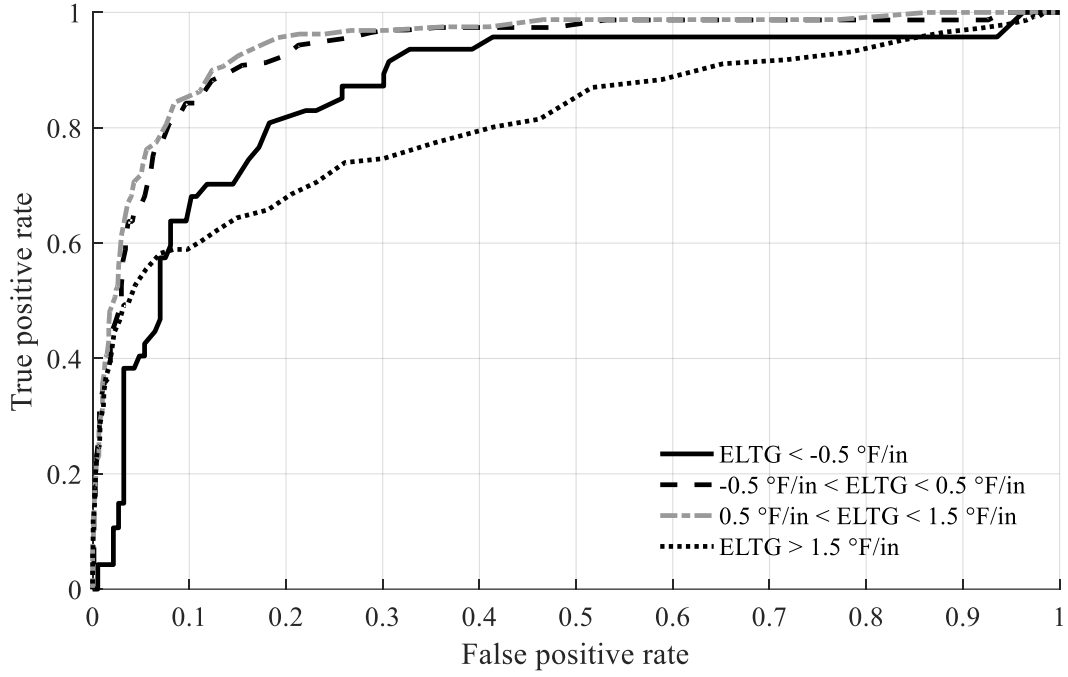


Figure 5.13. ROC curve for deflection ratio classifier by ELTG group

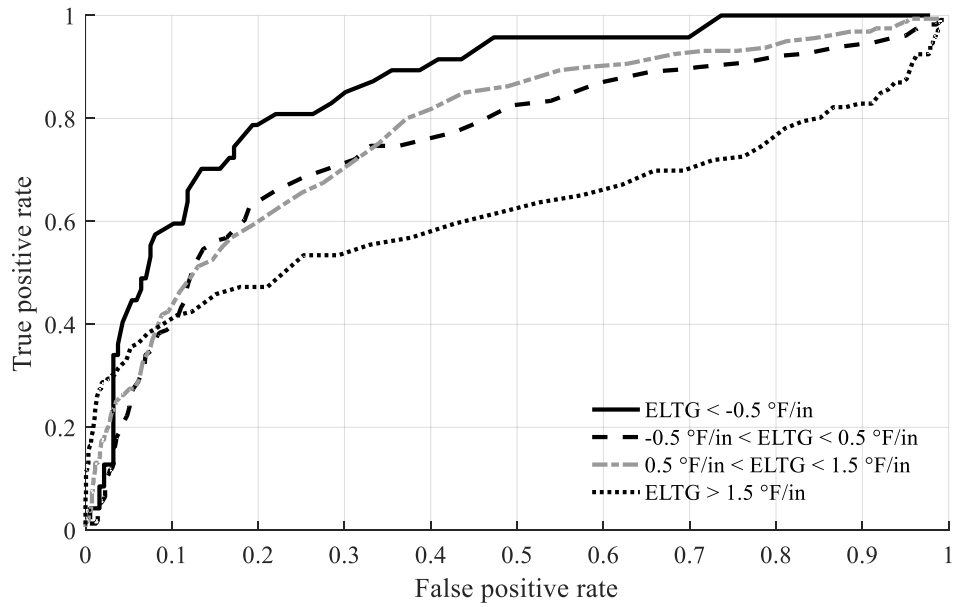


Figure 5.14. ROC curve for void parameter classifier by ELTG group

The ROC curves show that the DR classifier has the most discrimination (curves closest to the upper left-hand corner of the plot) when the ELTG is between -0.5 and 1.5 °F/in. Taking into account the long-term curvature due to drying shrinkage, these bins are likely closest to the flat slab condition assumed when developing the DR parameter. The NormDefl classifier does not discriminate as much as the DR when the ELTG is between -0.5 and 1.5 °F/in, but has better discrimination when there is a negative or a large positive temperature gradient. The VP classifier is only able to exceed the accuracy of a zero sensitivity classifier, a classifier which always predicts no void, when there is a negative temperature gradient. It is possible that this could be attributed to the fact that with a zero or positive temperature gradient condition, the non-linearity of the subgrade behavior may corrupt the signal, masking the presence of a void.

All of the classifiers have somewhat limited performance. The performance of the models can be improved by using a more complex classifier, which takes into account multiple predictors.

5.1.4 LASSO Logistic Regression Classifier

To improve upon the void detection methods currently available, a new classifier was developed using L1 regularized (LASSO) logistic regression. In this method, the logarithm of the odds is modeled as a linear regression model, as can be seen in Equation 5.2.

$$\ln\left(\frac{\text{pr(Void}|X)}{\text{pr(No Void}|X)}\right) = \beta_0 + \beta^T X \quad (5.2)$$

The regression coefficients are chosen by maximizing a penalized maximum likelihood, where a penalty term is applied to the size of the coefficients. The penalized likelihood expression can be seen in Equation 5.3.

$$\sum_{i=1}^n [y_i(\beta_0 + \beta^T x_i) - \ln(1 + \exp(\beta_0 + \beta^T x_i))] - \lambda \sum_{j=1}^p |\beta_j| \quad (5.3)$$

Where n is the total number of tests in the training set, and p is the number of predictors.

The complexity of the model is controlled by the tuning parameter, λ , which is selected using cross-validation. To make the penalty term meaningful, all predictors are scaled by its standard deviation and centered by its mean. A two-level cross validation error estimation process was used to estimate classifier performance, select the tuning parameter, and estimate regression coefficients. To account for correlation between tests from the same test section, cross validation is performed with respect to test section and not with respect to individual tests. A schematic of this process can be seen in Figure 5.15.

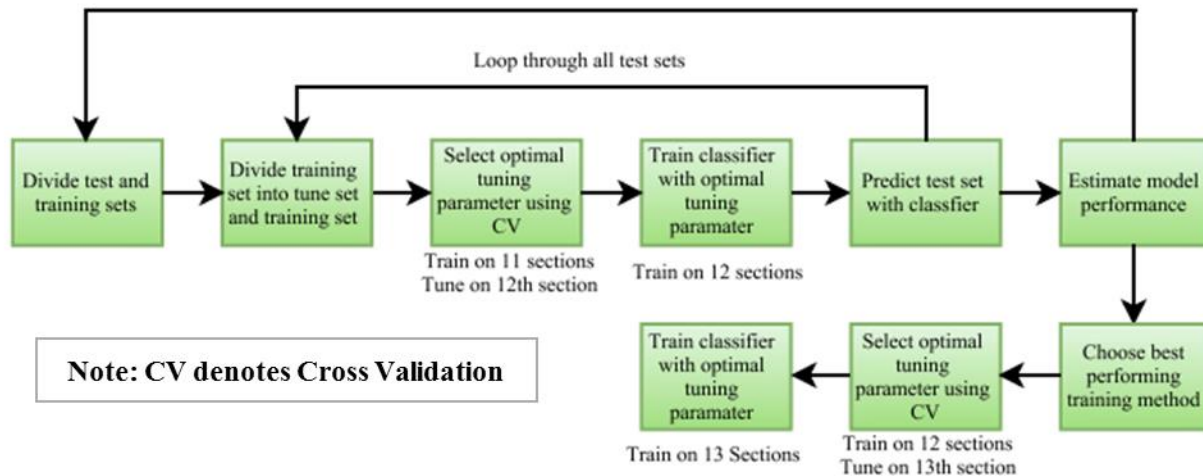


Figure 5.15: Work flow diagram used to select and train LASSO logistic regression classifier

The LASSO logistic regression model consists of eight predictors and first order interactions. The eight predictors are:

- k : The dynamic modulus of subgrade reaction, backcalculated from FWD testing at the center of the slab using the AREA method (Ioannides et al. 1989). For each test date, an average value is used for the entire test section. To minimize the effect of ELTG on the backcalculated k -value, only midslab tests performed when the ELTG was less than 0.5 °F/in were used in the analysis (See Chapter 3 for more information). If no tests were available when the ELTG was less than 0.5 °F/in on a test date, the section average backcalculated k -value for all test dates with an ELTG less than 0.5 °F/in was used.
- ℓ : The dynamic radius of relative stiffness between the slab and subgrade, backcalculated from FWD testing performed at the center of the slab using the AREA method (Ioannides et al. 1989). For each test date, an average value for the entire test section was used. To minimize the effect of ELTG on the backcalculated ℓ , only midslab tests performed when the ELTG less than 0.5 °F/in were used in the analysis (See Chapter 3 for more information). If no tests were available when the ELTG was less than 0.5 °F/in on a test date, the section average backcalculated ℓ for all test dates with an ELTG less than 0.5 °F/in was used.

- **Tcurv**: The slab curvature load that would be induced by a temperature gradient with no restraint. This is calculated by multiplying the ELTG by the coefficient of thermal expansion. The curvature itself, and not the resulting stress, affects the FWD deflections in the corner of the slab. Therefore, the ELTG is calculated based on equivalent strain (Janssen and Snyder 2000). Tcurv is highly related to the non-dimensional temperature curling parameter (ϕ) used in the neural networks incorporated into the American Association of State Highway Transportation Officials (AASHTO) Pavement ME design procedure (ARA Inc. 2004). A preliminary analysis showed models using Tcurv as a predictor performed slightly better than models using ϕ . Using Tcurv instead of ϕ also allows the temperature curvature parameter to be disassociated from k and ℓ .
- **LTE**: The deflection load transfer efficiency. This is calculated as the ratio of the deflection on the unloaded side of the joint to the deflection on the loaded side of the joint in the wheelpath, when testing is performed on the leave side of the joint. A bending correlation factor β , the ratio between the deflection 12 in from the load plate and the deflection directly under the load plate when testing is performed at midslab, was applied to account for bending of the slab (Darter et al. 1985).
- **VP**: The void parameter, as previously described.
- **DR**: The ratio of NormDefl to the deflection predicted by a FEM analysis, assuming flat slab conditions. This calculation was expedited by developing an artificial neural network (ANN) to predict the FEM calculated corner deflection using four variables, (k , ℓ , LTE, and shoulder type). The data set for this ANN consisted of a Monte Carlo simulation of 1008 FEM analyses, varying k (50-800 psi/in), pavement thickness (6-16 in), LTE (30-99%) and the presence of a shoulder (an indicator variable, all tied shoulders were assumed to have a 40% LTE which is the LTE used in the Pavement ME Design Guide). A preliminary analysis showed that when flat slab conditions are assumed, joint spacing was not influential on the corner deflection, and therefore not varied. These runs were divided such that 70% of the data was in the training set, 15% in the validation set, and 15% in the test set. The ANN had two 20 unit, hidden layers and was trained using the MATLAB neural network toolbox, with the Levenberg-Marquadt training algorithm. The ANN was very accurate, with a test set R^2 of 1.00. The ANN is predicting computational data, with no noise, in order to aid in computational efficiency. Therefore, the extremely close fit is

not unexpected. This model assumed a dense liquid foundation, with no shear transfer in the base. In reality the subgrade does have some shear resistance. This difference is more influential in the corner of the slab, than at midslab where layer properties are backcalculated. Therefore, the model over predicts the deflection in the corner of the slab, and values of DR greater than 1.0 are rare. This bias is acceptable, as the FEM model is being used as a variable transformation, and all predictors are scaled and centered before training the logistic regression model.

The normalized deflection parameter is not used, as it is highly correlated with the deflection ratio parameter. Including these two correlated parameters in the model can decrease the generalization of the model. A parameter to account for the potential of drying shrinkage was not included, as only one of the sections in the dataset, LTPP Section 04-0215, is in an arid climate. This does not allow the model to separate the effect of drying shrinkage from the prevalence of voids at this section.

5.2 RESULTS

5.2.1 Performance of Developed Classifier

The LASSO logistic regression classifier can increase the void detection accuracy over the stump classifiers previously presented. The LASSO classifier includes main effects of the 6 predictors and some first order interactions, for a total of 15 degrees of freedom. A model with all main effects and all first order interactions would have 21 degrees of freedom, however 6 of the terms were removed due to the variable selection ability of LASSO logistic regression. The performance of this classifier was evaluated using two-level cross validation, as shown in Figure 5.15. For

comparison, a single predictor logistic regression model is used to estimate the cross validated accuracy and ROC curve of the normalized deflection stump classifier. Stump classifiers predict binary responses, not probabilities, and therefore are not appropriate for developing cross validated accuracy curves. A comparison of the accuracy and ROC curves of the LASSO classifier to the normalized deflection classifier can be seen in Figure 5.16 and 5.17.

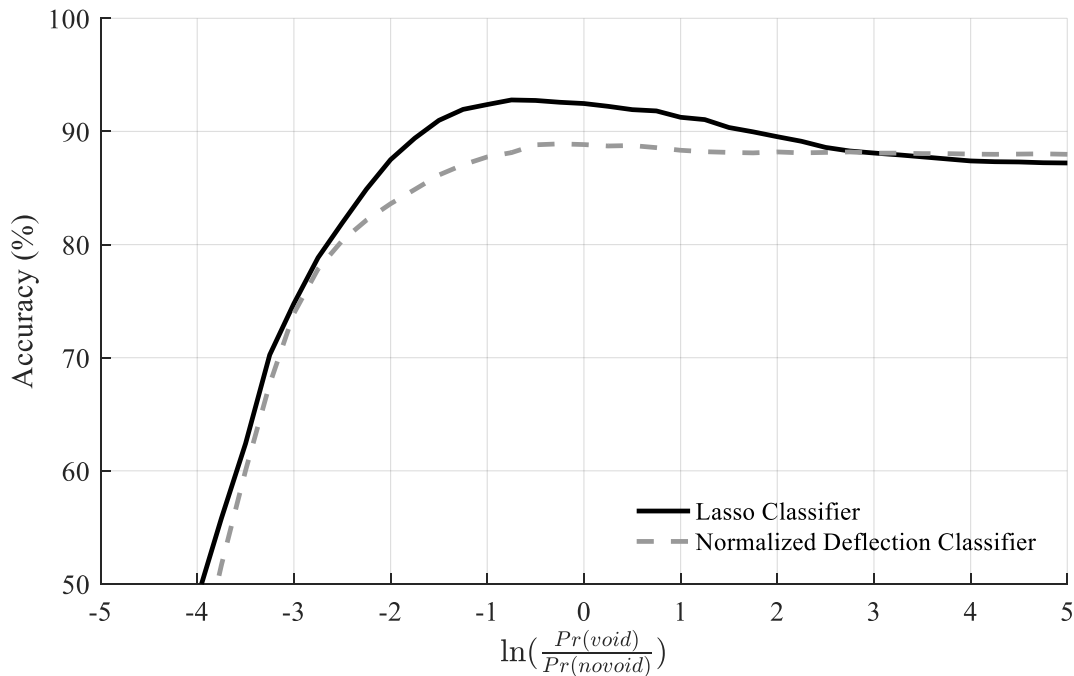


Figure 5.16. Cross validated accuracy of LASSO classifier and normalized deflection classifier

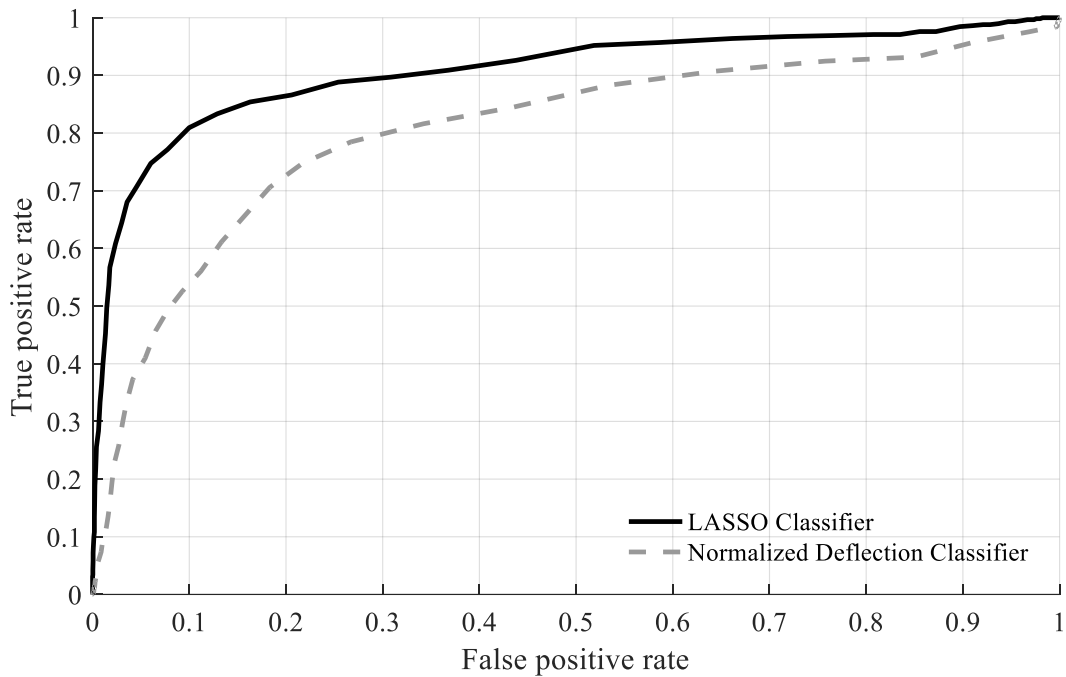


Figure 5.17. ROC curves of LASSO classifier and normalized deflection classifier

Not surprisingly, the LASSO classifier, which considers six inputs, has more discriminating power than the stump classifiers. The LASSO classifier has a cross validated sensitivity, the true positive rate, of 57% and a specificity, the true negative rate, of 98%. The normalized deflection classifier has a cross validated sensitivity of 30% and specificity of 97%. Using the LASSO classifier almost doubles the sensitivity, while increasing the specificity of the model.

A primary goal of the LASSO classifier is to allow testing at any time of the day. Therefore, the performance of the LASSO classifier was evaluated using the same ELTG groups used to evaluate the stump classifiers. The accuracy and ROC curves for each ELTG group can be seen in Figure 5.18 and 5.19.

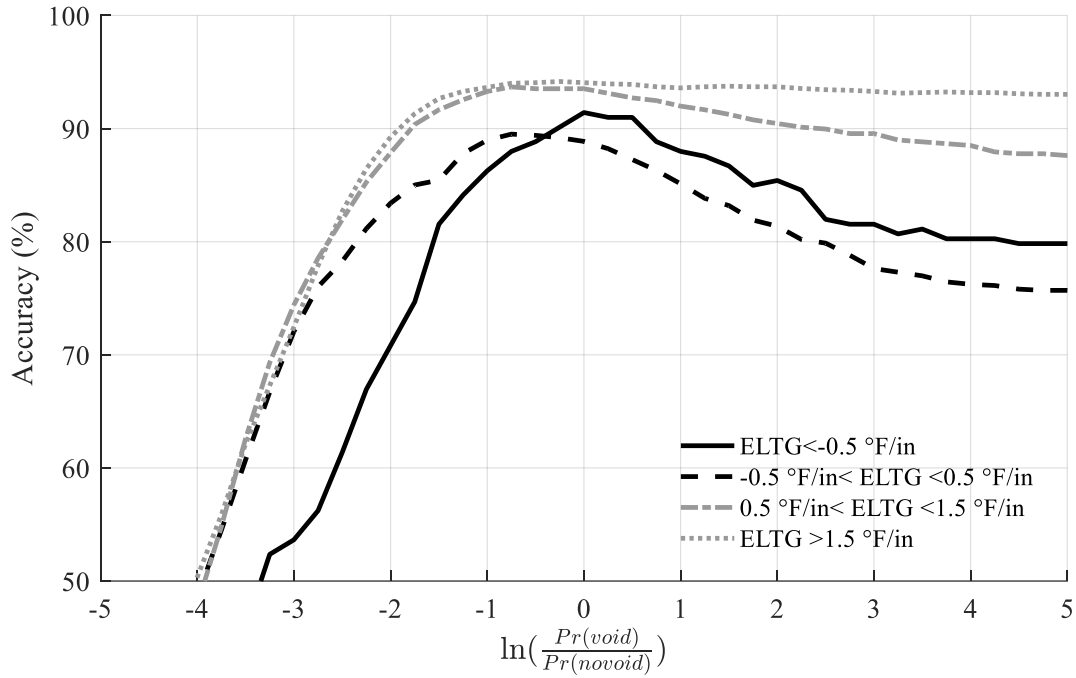


Figure 5.18. Accuracy of LASSO Classifier by ELTG group

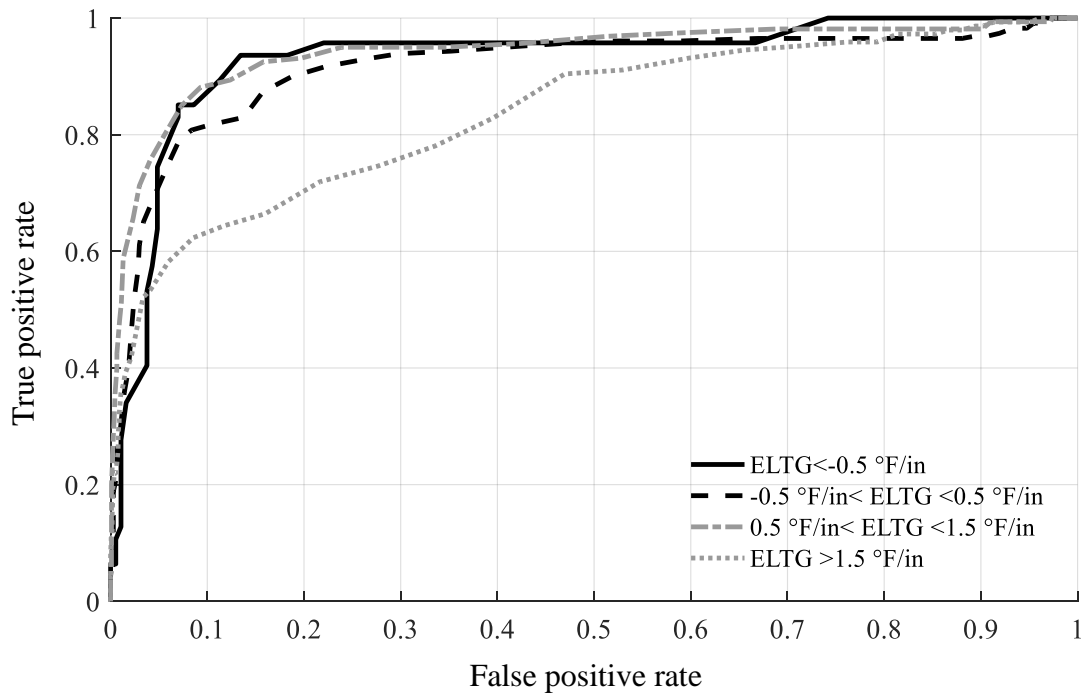


Figure 5.19: ROC curve for LASSO classifier by ELTG group

The maximum accuracy of the LASSO classifier, shown in Figure 5.18, exceeds the maximum accuracy of any of the stump classifiers in each ELTG group. This indicates that using the LASSO classifier performs better than the normalized deflection classifier regardless of the ELTG at the time of testing. The largest increase in performance occurs in the group with an $ELTG < -0.5$ °F/in.

5.2.2 Validation

The two field data collection efforts performed on doweled JPCP pavements in the Spring of 2016, and described in Chapter 2, were used to validate the LASSO classifier. The first data collection site was the doweled section of the PennDOT SMART pavement on US-22 in Murrysville, PA. This section consists of a 12-in instrumented JPCP on an asphalt stabilized base, with 15-foot joint spacing (Wells et al. 2005). A total of 8 joints were tested. The embedded thermocouples in the SMART pavement are used to measure the pavement WAT and ELTG. The second test site was a section of I-79 near Bridgeville, PA. A total of seven joints were tested on I-79. The test joints were spaced 60 feet apart. This section consists of a 12-in JPCP pavement on an open graded granular base, with skewed joints spaced at 20 ft. Temperature holes were drilled in the pavement in accordance with the LTPP testing protocol to measure the pavement WAT and ELTG (Schmalzer 2011).

Testing was performed by PennDOT using a Dynatest FWD in the corner of the slab on the approach and leave side of the joint, in the wheelpath on the approach and leave side of the joint, and at midslab. Testing was performed continuously on the test sections from 5:30 am to 5:00 pm, using the following order: *corner, wheelpath, corner, midslab*. This allowed testing to be performed over a wide range of temperature gradients.

For each test, the LASSO classifier, “cutoff deflection,” was calculated. For a given set of predictors, a measured deflection larger than the cutoff deflection indicates a void is present. The backcalculated k-value and ℓ input parameters were backcalculated from midslab FWD tests performed when an $ELTG < 0.5$ °F/in was present. The average measured LTE at each joint for the entire test day was used as the LTE input parameter in this validation. Testing in the wheelpath is unlikely to occur at the same ELTG as testing in the corner of the slab, making the average LTE at each joint more appropriate as an input than the LTE at a similar ELTG. For each test, a “cutoff value,” the lowest normalized deflection, which would result in the LASSO classifier predicting a void with all the other inputs as measured, is calculated. Figure 5.20 to 5.34 shows the measured normalized deflection, and the “cutoff value” as a function ELTG for each joint at both field trial sections.

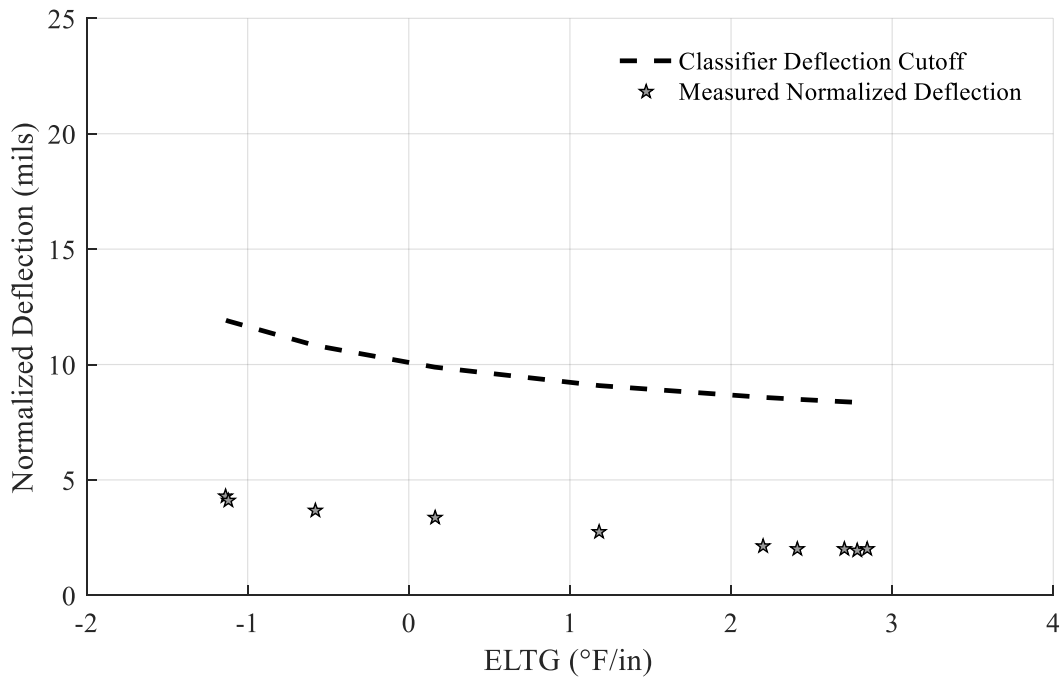


Figure 5.20. LASSO classifier validation (SR-22, Joint 1)

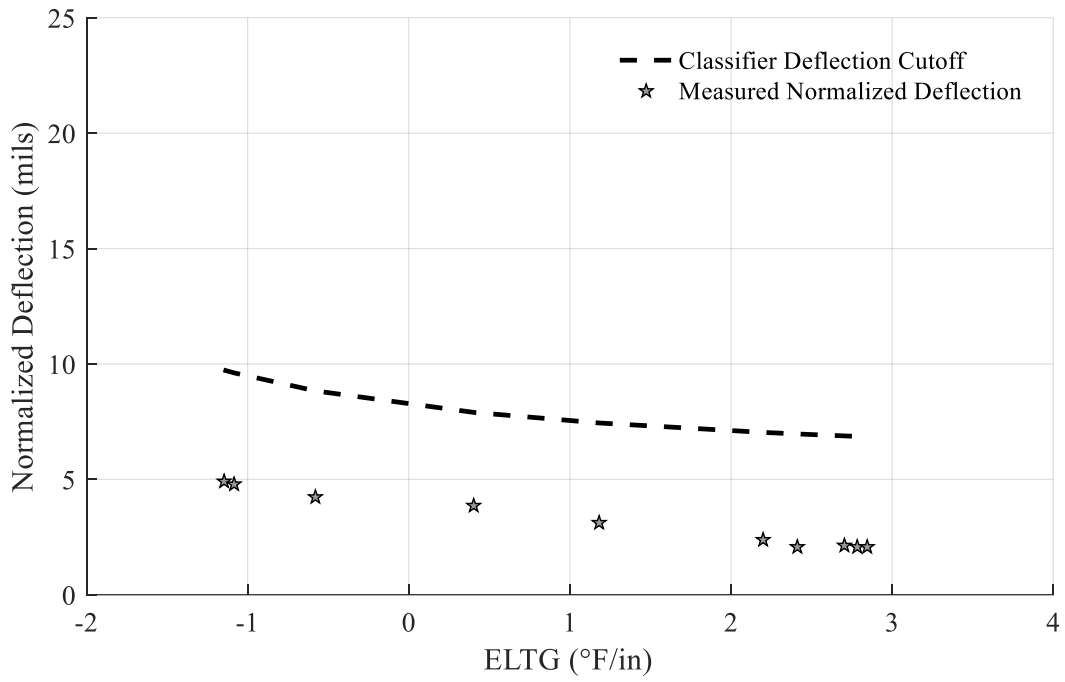


Figure 5.21. LASSO classifier validation (SR-22, Joint 2)

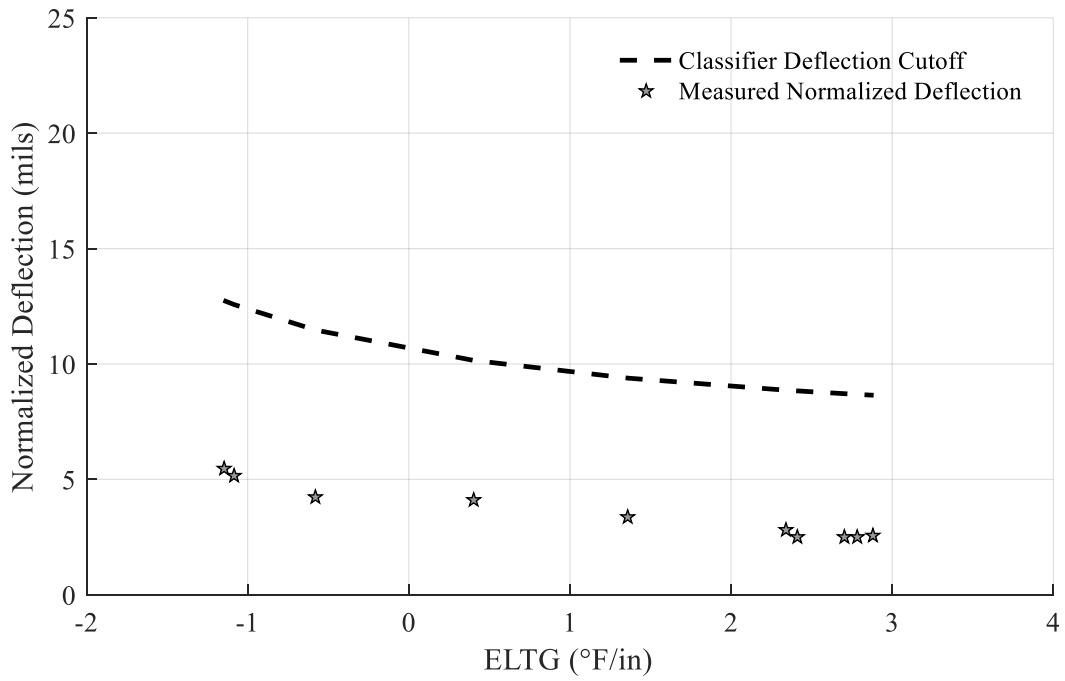


Figure 5.22. LASSO classifier validation (SR-22, Joint 3)

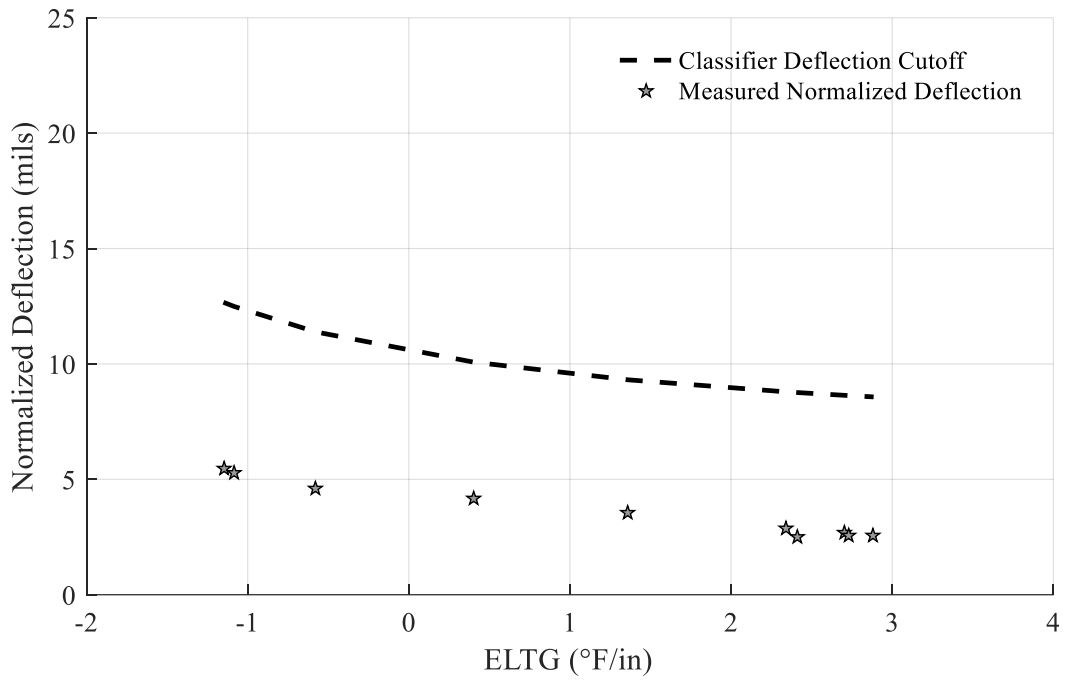


Figure 5.23. LASSO classifier validation (SR-22, Joint 4)

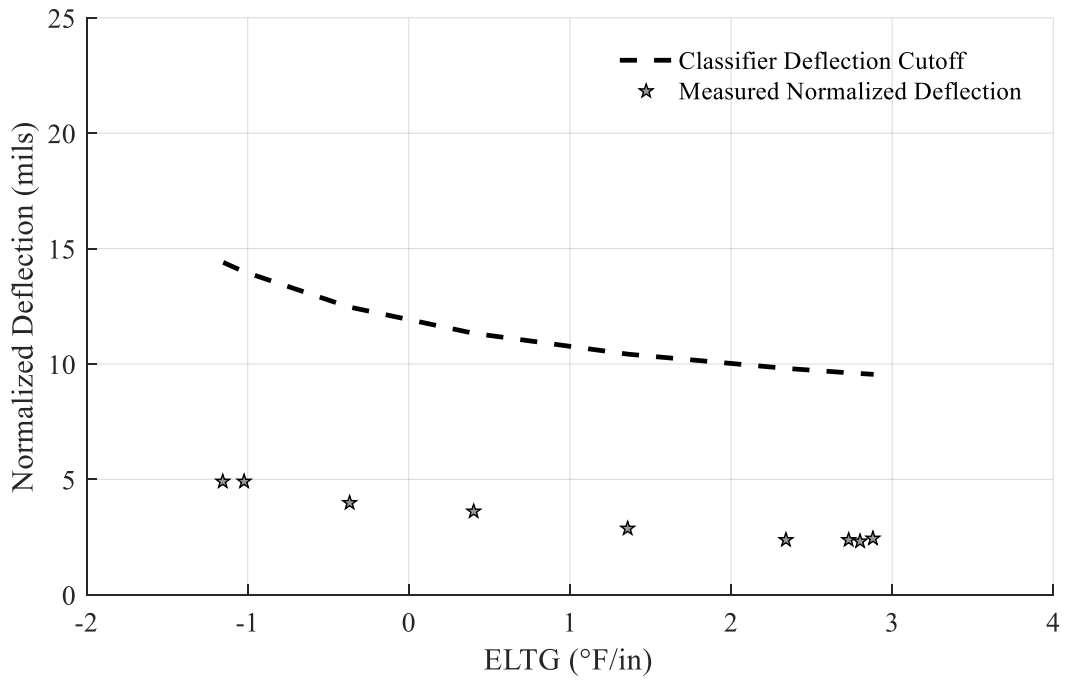


Figure 5.24. LASSO classifier validation (SR-22, Joint 5)

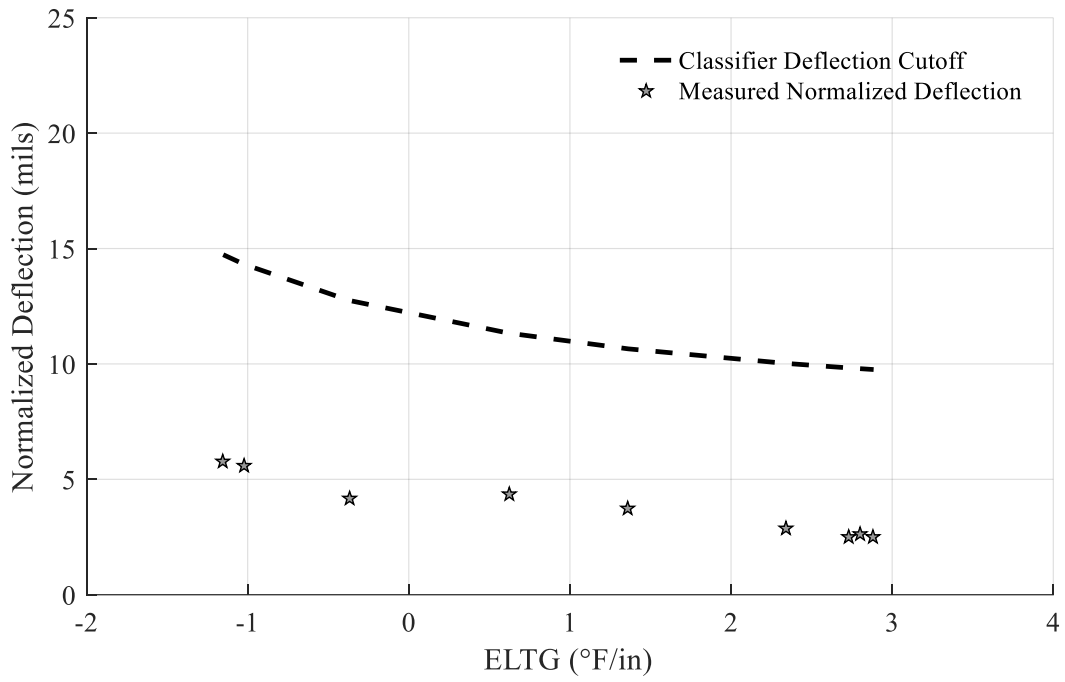


Figure 5.25. LASSO classifier validation (SR-22, Joint 6)

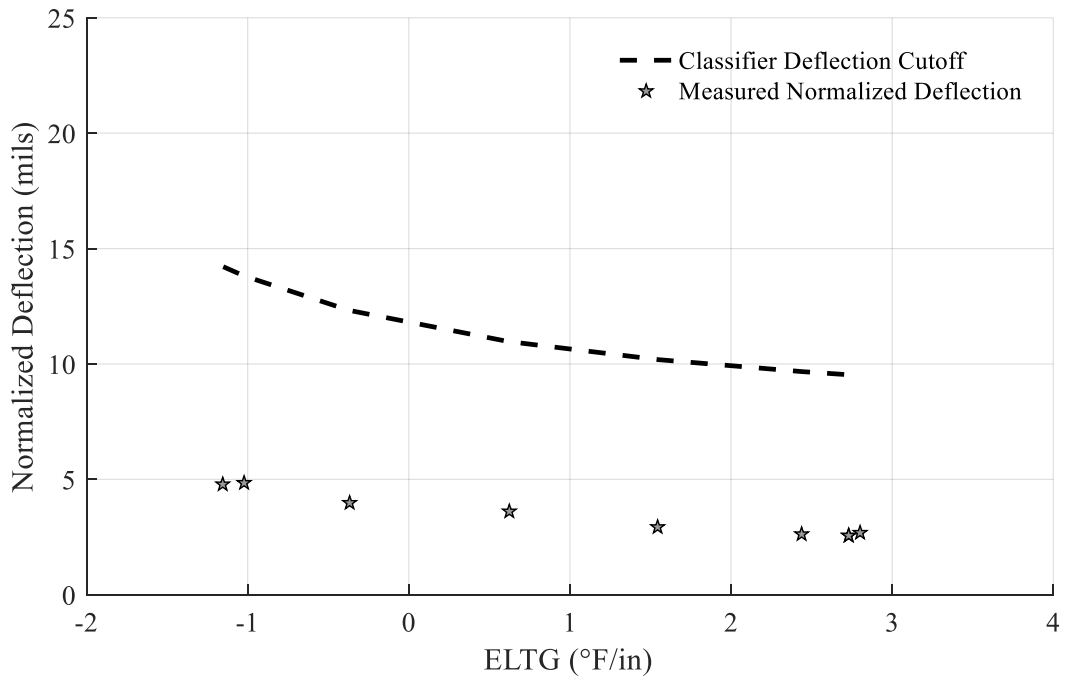


Figure 5.26. LASSO classifier validation (SR-22, Joint 7)

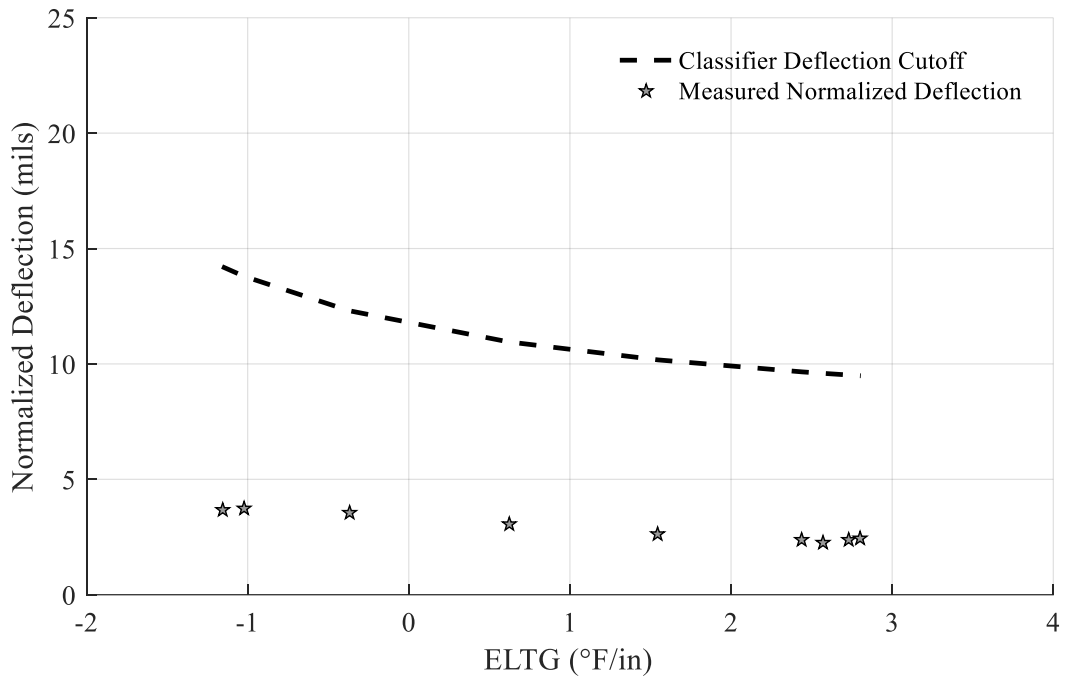


Figure 5.27. LASSO classifier validation (SR-22, Joint 8)

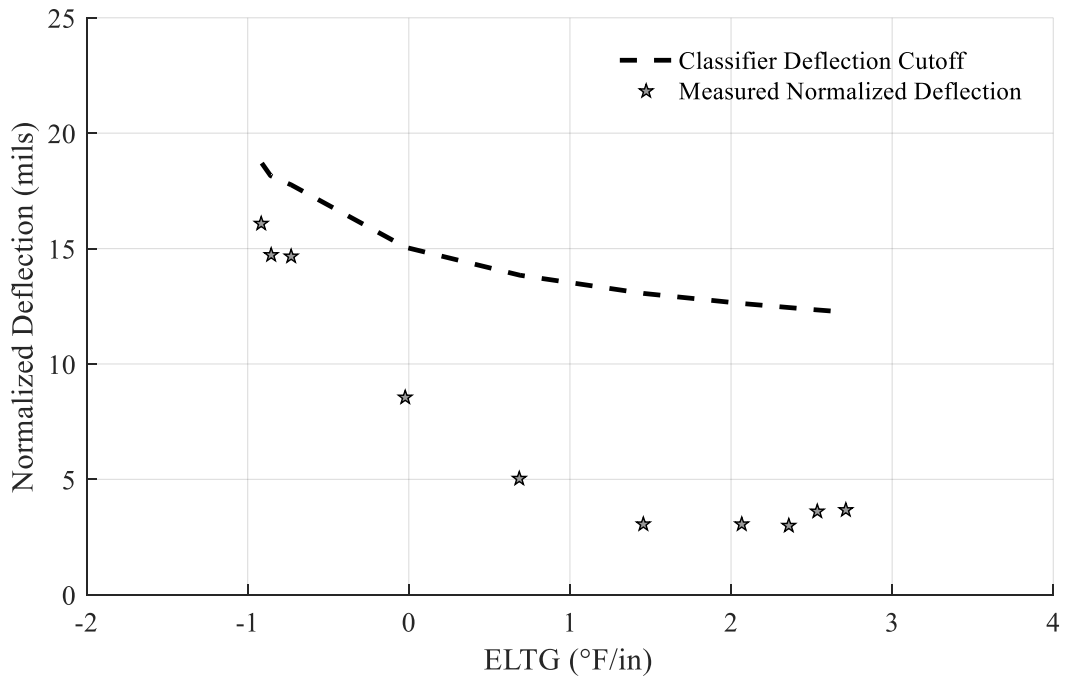


Figure 5.28. LASSO classifier validation (I-79, Joint 1)

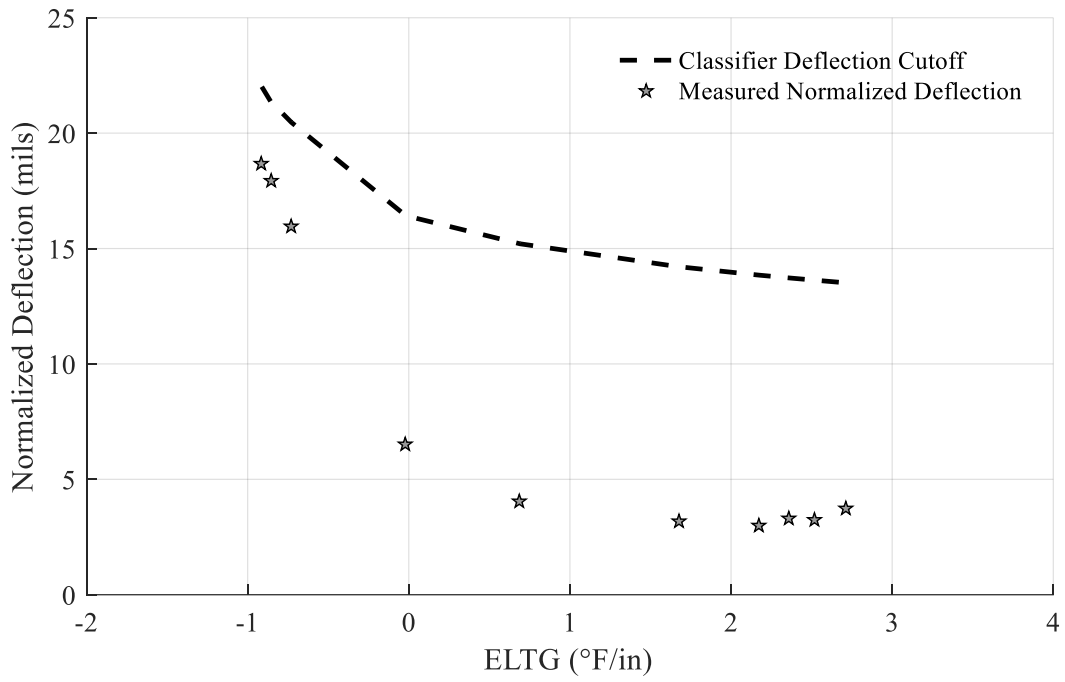


Figure 5.29. LASSO classifier validation (I-79, Joint 2)

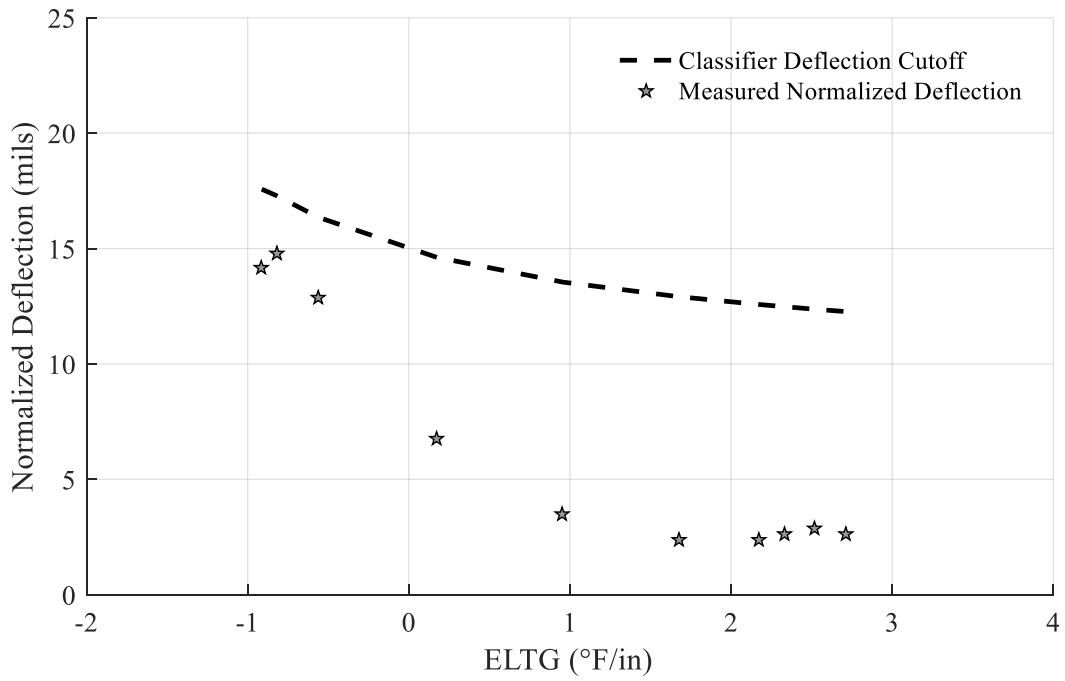


Figure 5.30. LASSO classifier validation (I-79, Joint 3)

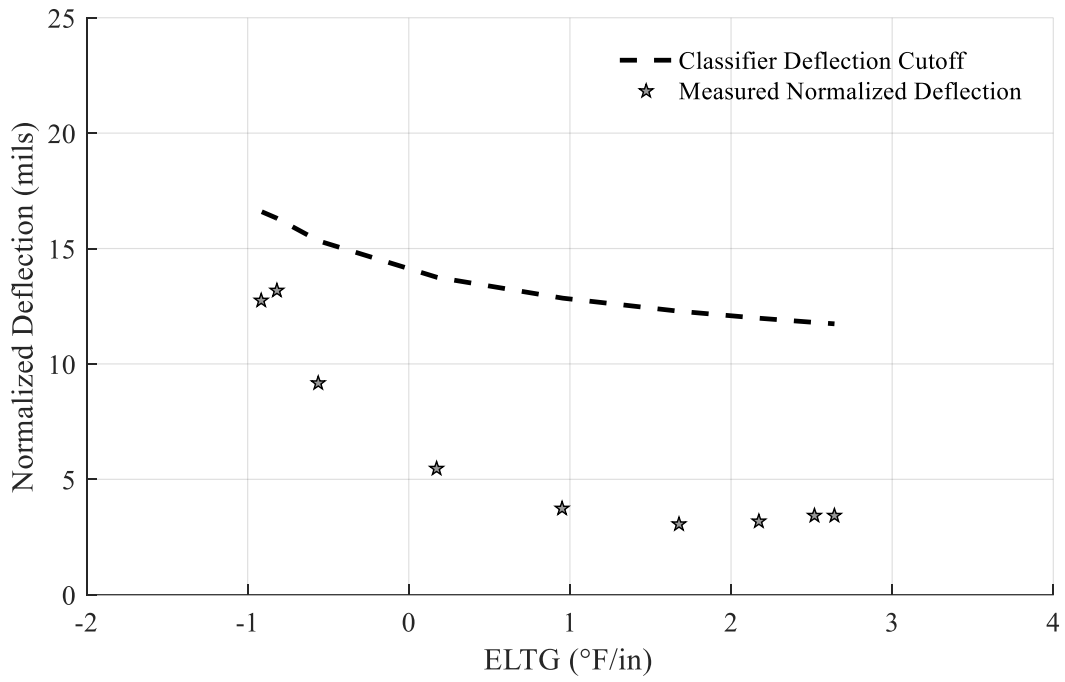


Figure 5.31. LASSO classifier validation (I-79, Joint 4)

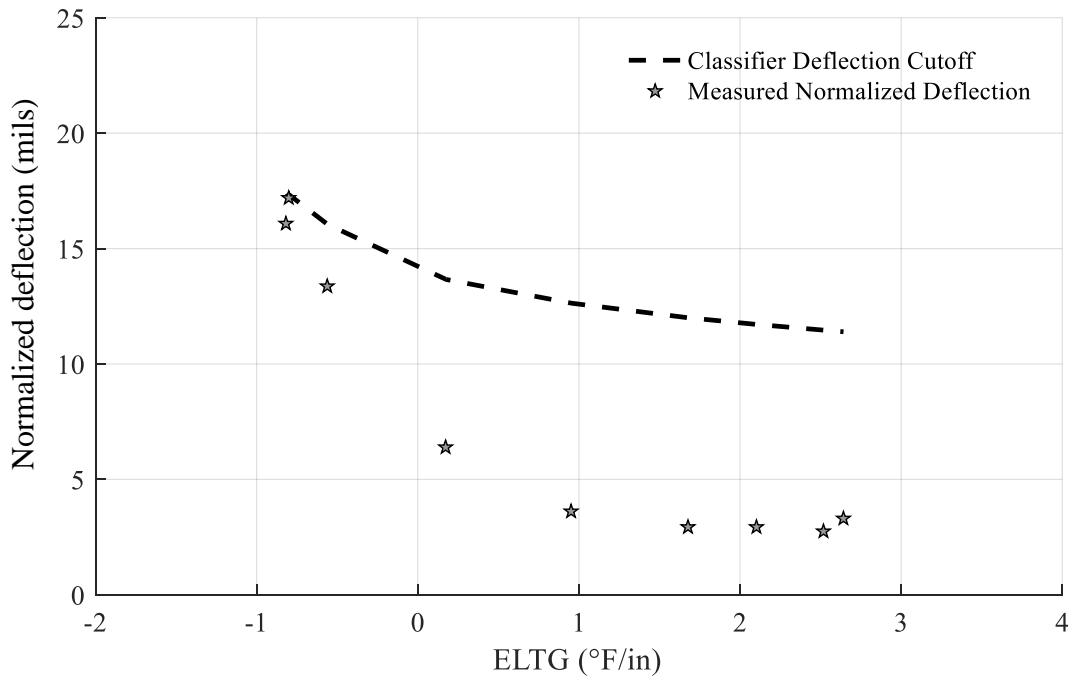


Figure 5.32. LASSO classifier validation (I-79, Joint 5)

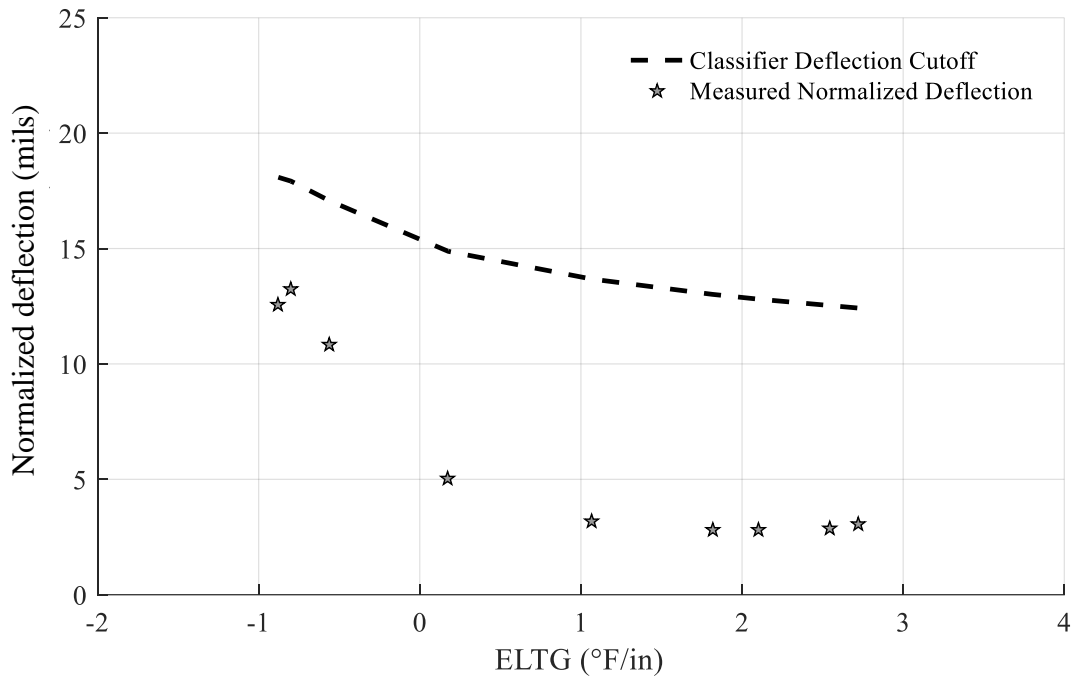


Figure 5.33. LASSO classifier validation (I-79, Joint 6)

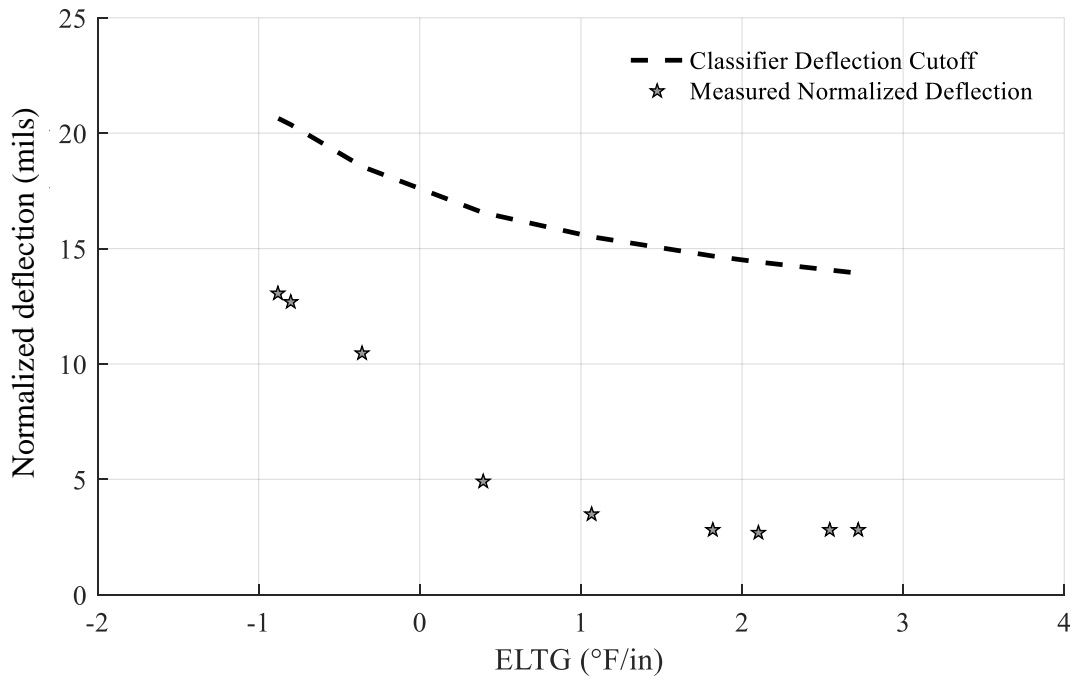


Figure 5.34. LASSO classifier validation (I-79, Joint 7)

For SR-22, the LASSO classifier shows that there is unlikely to be a void present at any of the joints, as the measured normalized deflections are well below the deflection cutoff value. This agrees with the observations from MnROAD and the LTPP database, where deflections more than doubled when a void was present. An example of this can be seen in Figure 5.1. The shape of the LASSO classifier cutoff follows approximately the same general shape as the field test data.

For I-79, the LASSO classifier predicts that there is no void for all tests. However, the tests with a negative ELTG are closer to this deflection cutoff than the tests with a positive ELTG. As previously mentioned, a vast majority of the sections with voids in the training database have a 15-ft joint spacing. Therefore, joint spacing was unable to be considered as an input into the classifier. A pavement with a 20-ft skewed joint spacing will have larger upward deflections due to curvature when a negative ELTG is present than a pavement with a 15-ft joint spacing. This additional curling deflection will lead to a higher normalized deflection parameter and void parameter as the corner of the pavement must deflect further when loaded. This likely contributes to the classifier having less specificity at negative gradients when applied to pavements with a 20-ft joint spacing. The LASSO classifier should be used with caution on pavements with a 20-ft joint spacing when negative ELTGs are present at the time of testing.

Both of the pavement sections evaluated do not likely contain any voids. Therefore, to observe the behavior of the classifier on pavements where a void is present, two other pavement sections were considered. The first of these sections is the driving lane of Cell 8 at MnROAD, which was determined to have voids develop between 2007 and 2009 at all of the tested joints. This cell consists of a 7.5-in thick slab on an asphalt treated base, with a 15-foot joint spacing, and 1 in diameter dowels. Figures 5.35 to 5.38 show the “deflection cutoff” and test results from Cell

8. The deflection cutoff was determined using the classifier trained without Cell 8 in the training set.

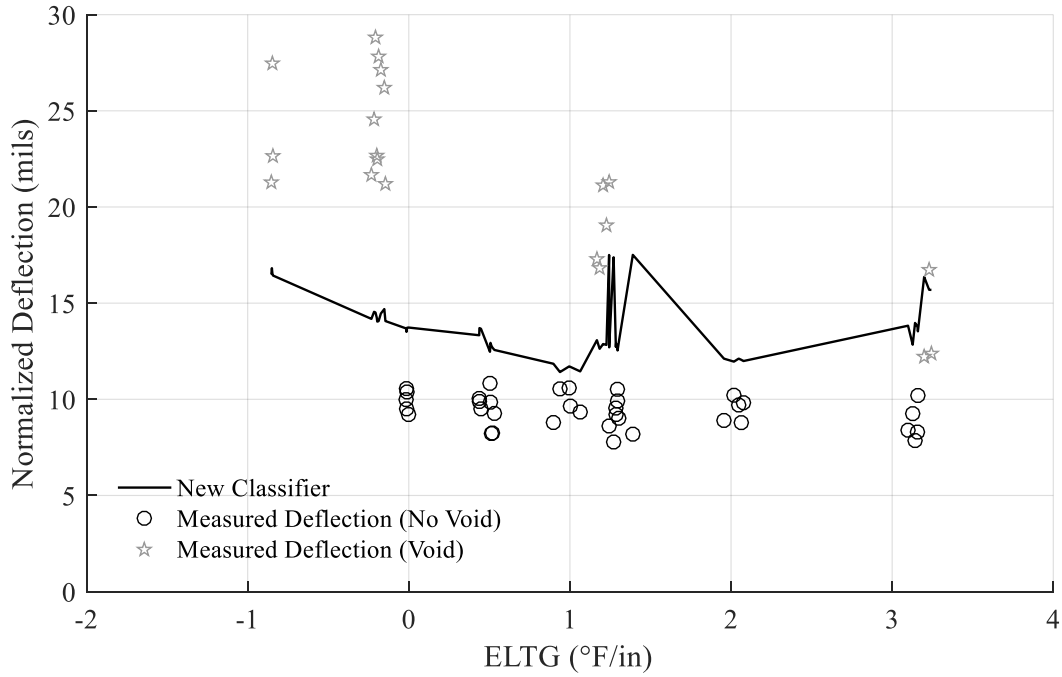


Figure 5.35. LASSO classifier validation (MnROAD Cell 8, Joint 4)

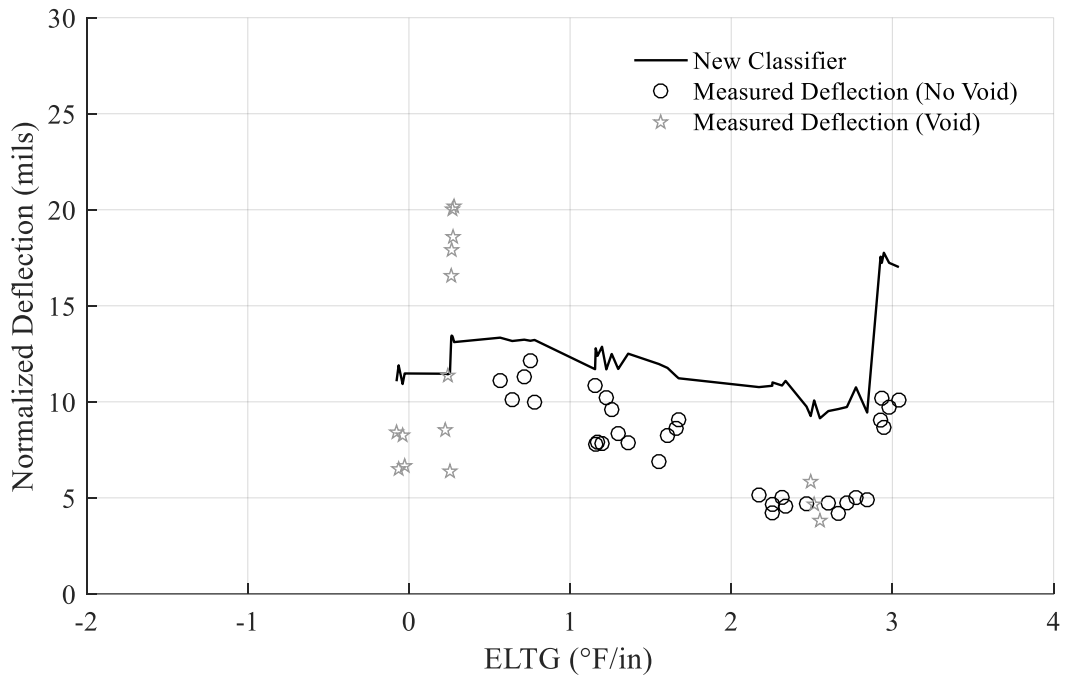


Figure 5.36. LASSO classifier validation (MnRoad Cell 8, Joint 3)

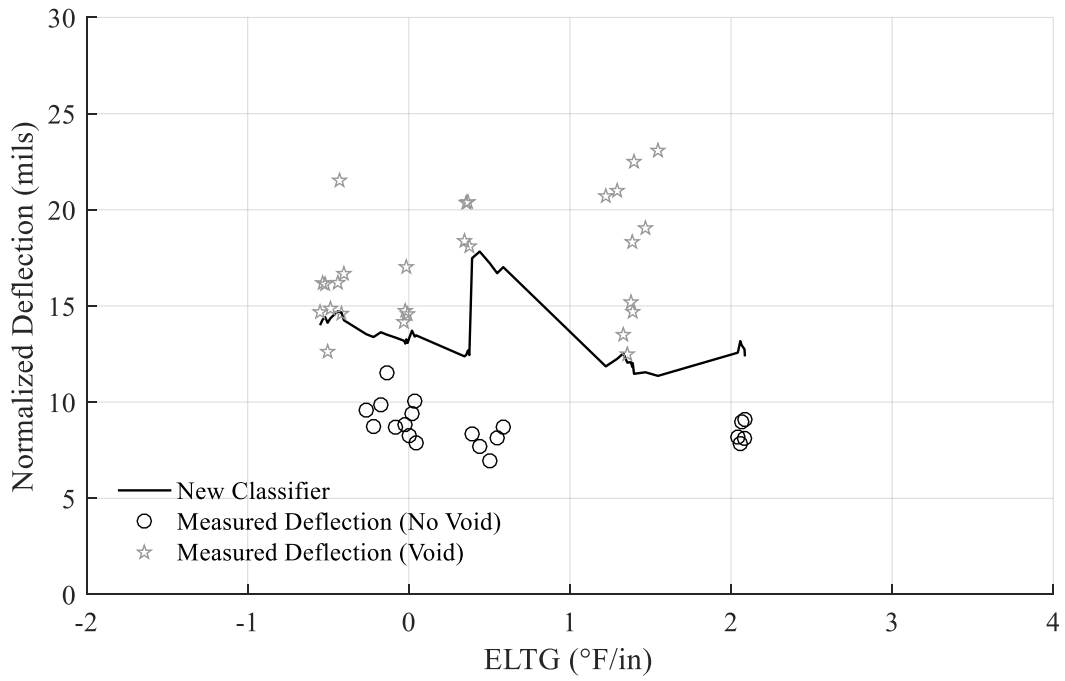


Figure 5.37. LASSO classifier validation (MnROAD Cell 8, Joint 10)

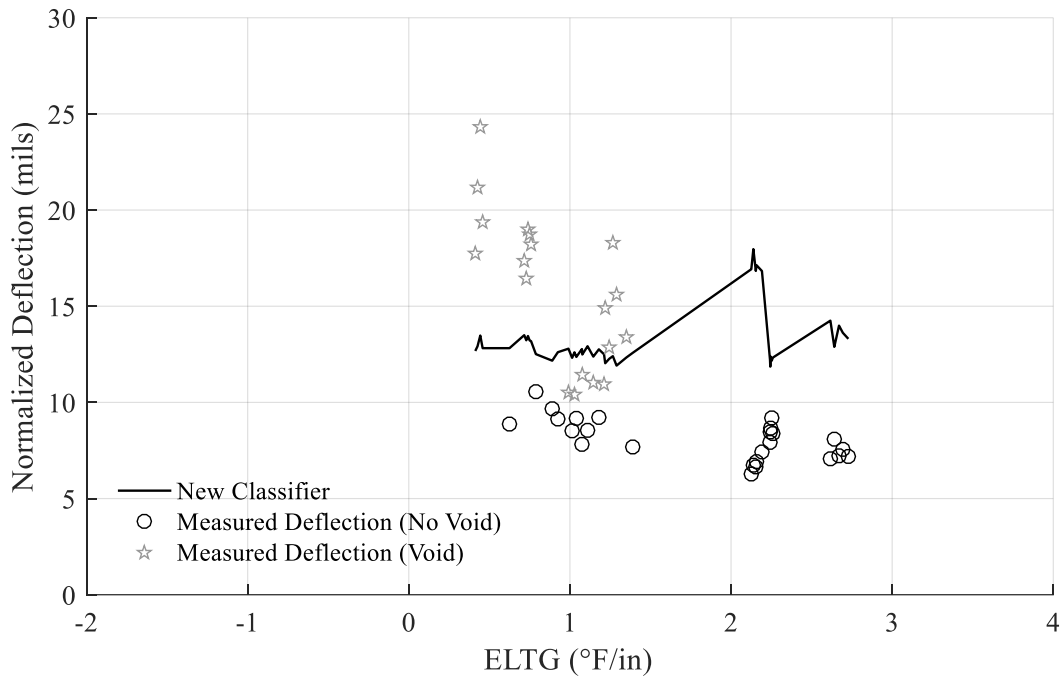


Figure 5.38. LASSO classifier validation (MnROAD Cell 8, Joint 9)

Of the 187 tests performed when no void is likely present, there were 5 false positives, for a specificity of 97%. Of the 92 tests when a void is likely present, there are 24 false negatives, for a sensitivity of 74%. False positives and false negatives occur at all temperature gradients.

The classifier was also tested on LTPP Section 05-0215, on I-30 in Arkansas, a wet, non-freeze environment. This section was not included in the training dataset. The section consists of an 11.5 in thick slab on a granular base, with a 15-ft joint spacing, and 1.25 in diameter dowels. It was constructed in 1995. This section was chosen because 0.09 in of average faulting occurred in the first 10 years indicating that voids may have developed. The test results and the LASSO classifier deflection cutoff for LTPP Section 05-0215 can be seen in Figure 5.39.

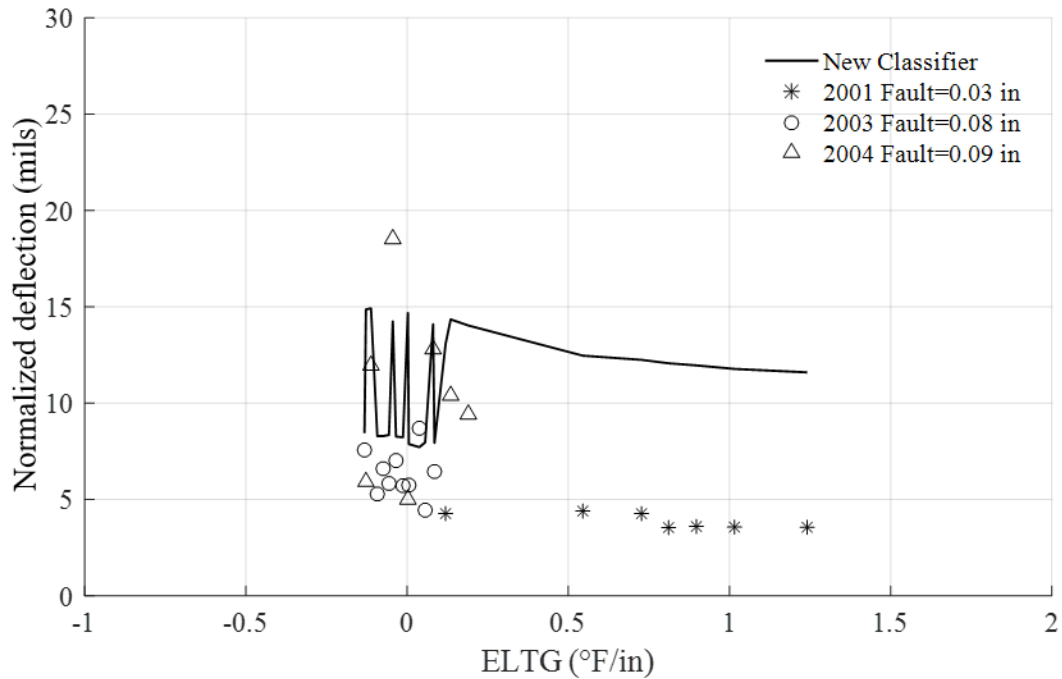


Figure 5.39. Lasso classifier performance (LTPP Section 05-0215, all joints)

Based on the test results, it is evident that voids are developing at 5 of the 7 joints tested when testing was performed in 2004. The classifier classifies 3 of the 5 joints as having a void that likely developed in 2004. The deflection measured at two joints are near the deflection cutoff. These tests are likely false negatives. The deflection at the remaining two joints are similar to the deflection measurements from 2001 and 2003. It is likely that a void did not develop at these locations, and the classifier accurately indicates that no void occurs. The classifier does detect a void at a single location in 2003. This location has the largest normalized deflection in both 2003 and 2004. It is likely that a void was beginning to develop at this location in 2003, and became larger in 2004.

5.2.3 Sensitivity analysis

While the classifier appears to be performing accurately on the validation sections, it is important to review the sensitivity of the parameter to each of the input variables. This was performed by calculating the deflection cutoff, varying a single input at a time for Joint 1 on I-79. The sensitivity of the model to k-value, ℓ , LTE, and void parameter can be seen in Figure 5.40 to 5.43.

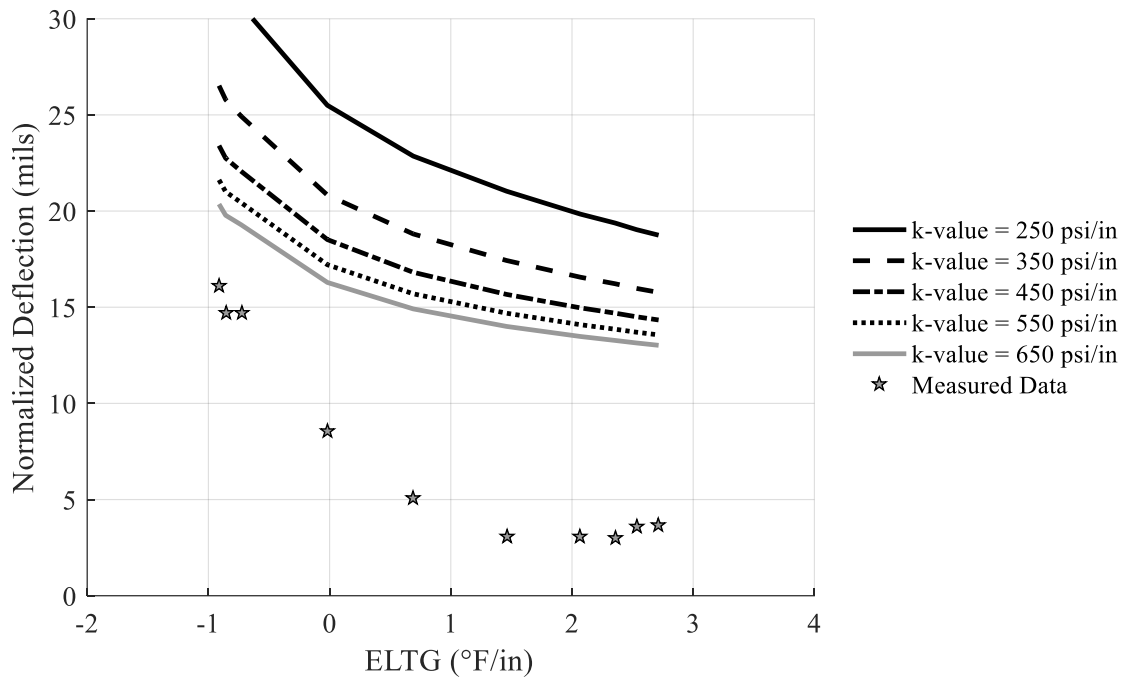


Figure 5.40. Sensitivity of classifier to k-value

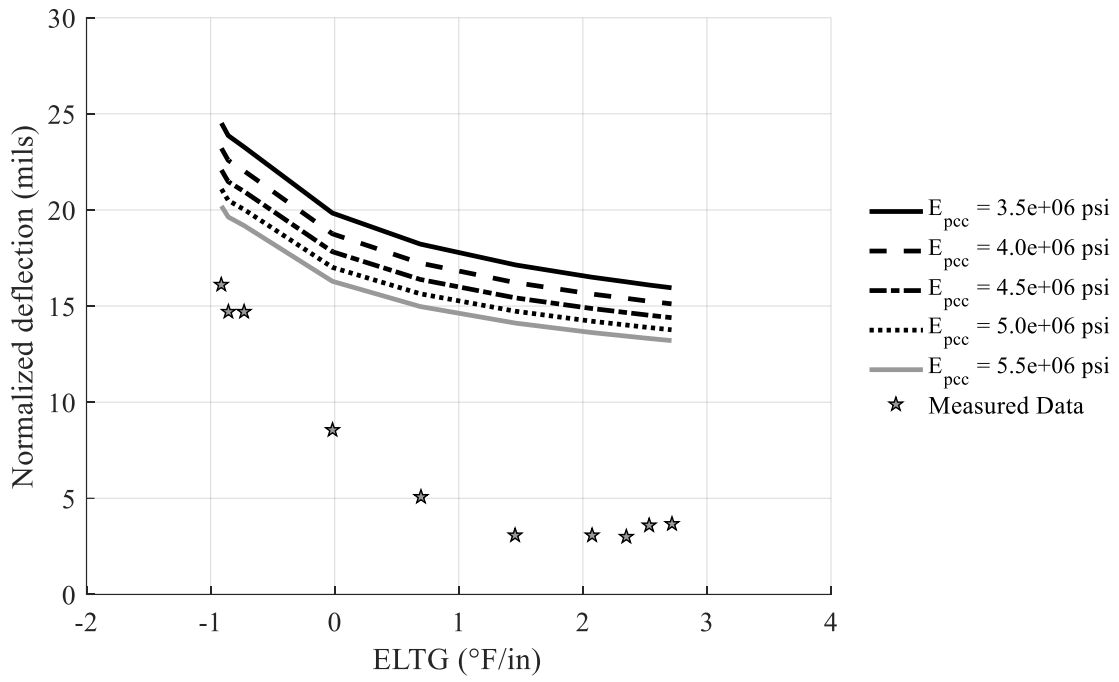


Figure 5.41. Sensitivity of classifier to elastic modulus of the PCC layer

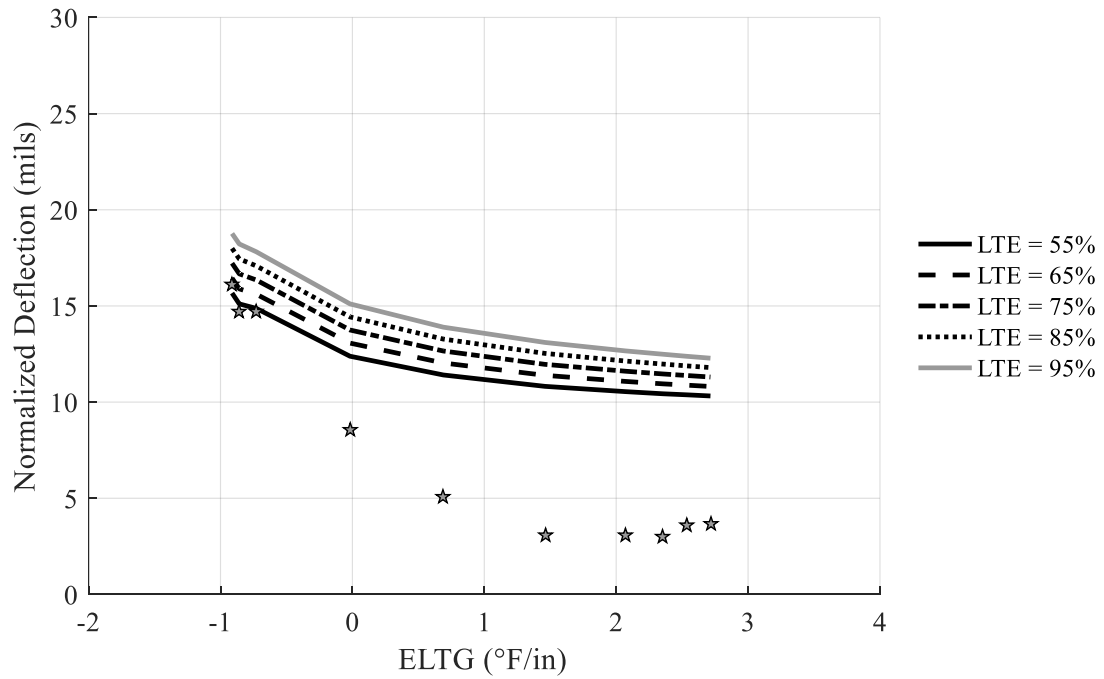


Figure 5.42. Sensitivity of classifier to LTE

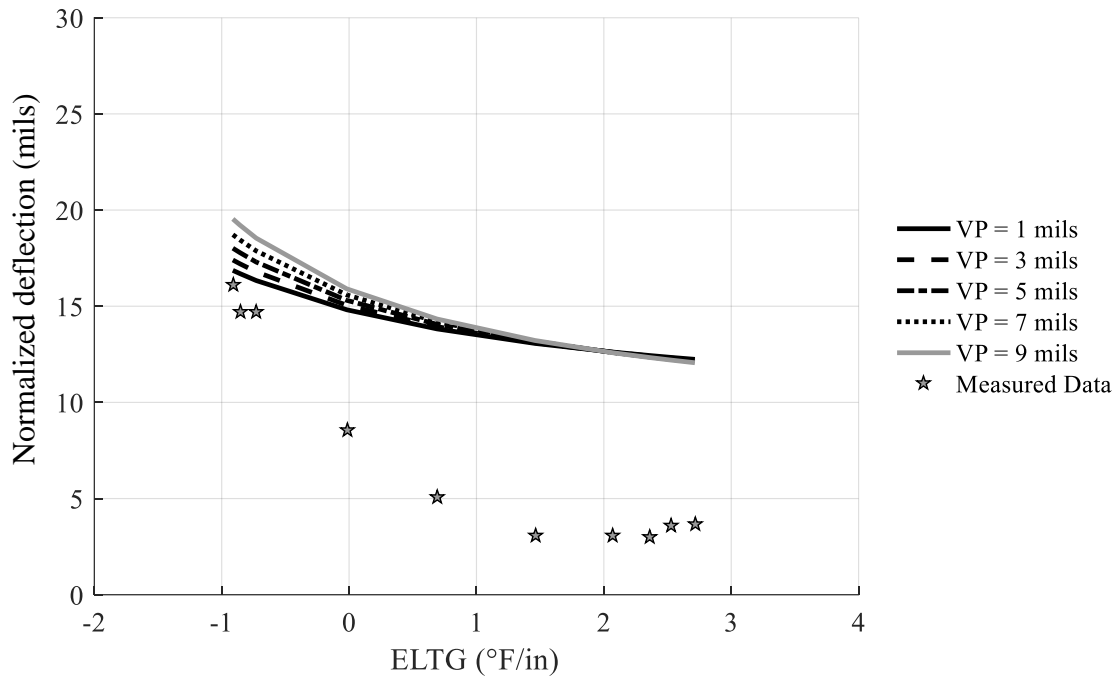


Figure 5.43. Sensitivity of classifier to void parameter

Increasing both the k-value, and the elastic modulus of the concrete layer results in a decrease in the normalized deflection required to detect a void. This is as expected, as increasing these parameters should result in a lower theoretical deflection. If the same normalized deflection occurs on a stiffer pavement structure as a less stiff pavement structure, then a void is more likely under the stiffer pavement structure. The deflection required to detect a void increases as LTE increases. This may be due to voids being more likely to develop at joints with a low LTE than joints with a high LTE. In effect, the LTE parameter may provide information on the “prior” probability of a void occurring at a joint. At a negative ELTG, a higher void parameter increases the normalized deflection required to detect a void, whereas at a positive ELTG a higher void parameter decreases the normalized deflection required to detect a void. It is expected that a void developing would increase the void parameter, regardless of the ELTG. However, this would be accompanied by an increase in deflection. Therefore, a high void parameter may not necessarily be expected to

decrease the normalized deflection required to detect a void. At a positive ELTG, a large void parameter is likely indicative of a void, whereas at a negative ELTG a large void parameter is likely indicative of curvature. Therefore, the interaction behavior shown in Figure 5.43 is reasonable. In general, all of the trends shown in the sensitivity analysis are as expected.

5.3 CONCLUSION

The LTPP and MnROAD database were used to develop and estimate the performance of existing void detection methods, and a new statistical classifier was developed using LASSO logistic regression for the detection of voids. Of the existing methods, deflection based void identification methods perform better than the variable load corner deflection based methods. The estimated performance of the LASSO classifier exceeds the performance of any of the existing analysis methods. Based on field trials, the LASSO classifier appears to perform well on pavements with a 15-ft joint spacing. The LASSO classifier may not perform well on pavements with joint spacing longer than 15 ft, especially when a negative temperature gradient is present. A sensitivity analysis shows that the behavior of the tool in response to each of the inputs is as expected.

6.0 TEMPERATURE PROFILE PREDICTION

6.1 INTRODUCTION

The tools developed as part of this research project for backcalculating pavement layer properties, evaluating joint efficiency, and detecting voids (Chapters 3 -5) require an estimate of the ELTG in the pavement at the time of testing. The length of the slab, which is influenced by the WAT, can also affect FWD testing results. Therefore, only FWD tests with a pavement WAT less than 75 °F were considered in the models developed for measuring joint performance and detection voids (Chapters 4 and 5). As a result, it is critical to be able to measure or estimate the pavement temperature profile during testing.

A procedure was developed as part of the LTPP testing protocol to measure the temperature profile of the slab using holes drilled in the pavement (Schmalzer 2011) . This practice is suitable for the LTPP program where FWD testing is performed on relatively short sections (500 ft) and the lane is closed to traffic throughout testing. Practical considerations, such as the time, equipment, and traffic control required to drill the holes, make temperature holes difficult to implement for routine FWD testing. Therefore, it is useful to develop a tool that can be used to predict the temperature gradient in the pavement based on the weather conditions prior to and during FWD testing.

Temperature gradients in concrete pavements are the result of the movement of heat into and through the pavement structure. This movement of heat is controlled by:

- Shortwave radiation absorbed on the pavement surface
- Longwave irradiation emitted by the pavement surface
- Convection at the pavement surface
- Conduction within the concrete slab and to the supporting layers
- Latent heat of evaporation at the pavement of moisture within the slab
- Heat of cement hydration

A schematic of heat flow through a pavement structure is shown in Figure 6.1.

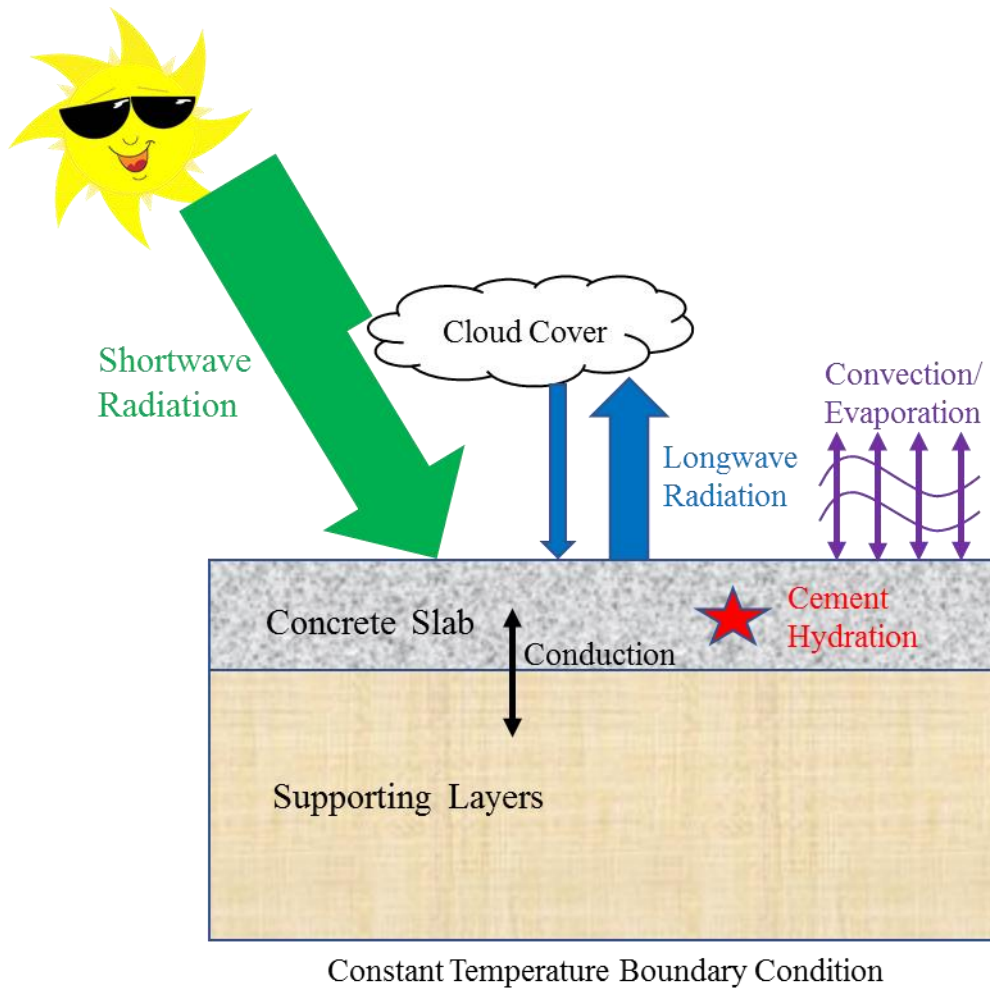


Figure 6.1. Heat transfer in concrete pavements

6.2 LITERATURE REVIEW

Several models have been developed to predict the temperature profile within a pavement. These models typically fall within two categories: statistics-based models and heat transfer-based models. Statistics-based models are most commonly used for asphalt pavements, where the magnitude of the temperature is more important than the temperature gradient (Lukanen et al. 2000). Heat transfer-based models are generally based on one-dimensional heat flow through a pavement using the differential equation shown in Equation 6.1.

$$K * T_{xx} + Q_H = \rho * C_p * T_t \quad (6.1)$$

Where:

K = thermal conductivity

T_{xx} = second depth derivative of temperature

Q_H = the heat generated during hydration

ρ = density

C_p = specific heat

T_t = the first time derivative of temperature

Some research has been performed using a 2-D axisymmetric heat transfer model (Wang et al. 2009). However, the boundary conditions of concrete pavements are not axisymmetric.

6.2.1 Existing Heat Transfer Models

6.2.1.1 CMS/EICM Model One of the first heat transfer-based temperature prediction models for pavements was developed as part of the Climatic-Materials-Structural (CMS) Analysis Program at the University of Illinois (Dempsey et al. 1986). This model is still in use today as part

of the Enhanced Integrated Climatic Model (EICM), which is integrated into the Pavement ME Design Guide (ARA Inc. 2004). The CMS solves Equation 6.1 by using a 1-dimensional finite difference model (FDM). The heat flux at the surface is calculated using Equation 6.2.

$$Q = Q_s + Q_a - Q_e + Q_c \quad (6.2)$$

Where:

Q_s = absorbed shortwave radiation

Q_a = absorbed longwave radiation

Q_e = emitted longwave radiation

Q_c = heat flux due to convection

The individual components of the heat flux are estimated as follows:

- The absorbed shortwave solar radiation is estimated using Equation 6.3.

$$Q_s = (1 - a) * R(A + B * (1 - cf)) \quad (6.3)$$

Where:

a = albedo of the pavement

R = extraterrestrial radiation

cf = cloud fraction (expressed as a decimal)

A, B = regression coefficients

For the EICM implementation of the CMS model, A is assumed to be 0.202 and B is assumed to be 0.531. The extraterrestrial radiation, R , is assumed to vary parabolically from sunrise to sunset.

- The emitted and absorbed radiation are based on Equations 6.4 through 6.7 (Geiger et al. 1950).

$$Q_e = Q_x \left(1 - N \left(\frac{cf}{100} \right) \right) \quad (6.4)$$

$$Q_x = 1.72 * 10^{-9} (T_{surf} + 460.7)^4 \quad (6.5)$$

$$Q_a = Q_z \left(1 - N \left(\frac{cf}{100} \right) \right) \quad (6.6)$$

$$Q_z = 1.72 * 10^{-9} (T_{air} + 460.7)^4 (0.77 - .28 * 10^{-.074 * P}) \quad (6.7)$$

Where:

Q_e = emitted longwave radiation in $\left(\frac{\text{BTU}}{\text{hr} * \text{ft}^2} \right)$

N = emissivity of the concrete

T_{surf} = pavement surface temperature ($^{\circ}\text{F}$)

T_{air} = ambient temperature ($^{\circ}\text{F}$)

P = vapor pressure (mm Hg)

- The heat transfer due to convection is estimated using Equation 6.8.

$$Q_c = H * (T_{air} - T_{surf}) \quad (6.8)$$

Where H is the convection coefficient, which is determined by Equation 6.9 (Vehrencamp 1953).

$$H = 122.93 \left(.00144 * \left((T_{avg} - 32) * \frac{5}{9} \right)^3 * \frac{ws^{.7}}{2.24} + 0.00097 * \left((T_{air} - T_{surf}) * \frac{5}{9} \right)^{0.3} \right) \quad (6.9)$$

Where:

ws = wind speed (mph)

T_{avg} = the mean of the surface and air temperatures (°F)

The default (Level 3) thermal material properties for the Pavement ME implementation of the CMS model are shown in Table 6.1. It is important to note that the CMS model does not consider the effect of latent heat of evaporation or heat of hydration.

Table 6.1. CMS/EICM model material properties

Parameter	Estimate
Thermal Conductivity	$3.47 * 10^{-4} \frac{BTU}{s * ft * ^\circ F}$
Emissivity	0.92
Albedo	0.1-0.3
Specific Heat Capacity	0.20-0.28 $\frac{BTU}{lb * ^\circ F}$

Several studies have evaluated the accuracy of the CMS model for its inclusion in the Pavement ME Design Guide. A study at MnROAD found that the distribution of temperature gradients matches the measured distribution of temperature gradients better if a thermal conductivity of $2.67 \times 10^{-4} \frac{BTU}{lb \cdot ^\circ F}$ is used (Johanneck 2010).

6.2.1.2 HIPERPAV I The first version of the HIgh PERformance concrete PAVing software (HIPERPAV I) included a model that estimates the temperature of concrete immediately after paving (McCullough and Rasmussen 1999). This model is similar to the CMS model; however, the HIPERPAV model incorporates the heat of cement hydration in the temperature prediction.

The HIPERPAV model estimates the heat flux at the surface using Equation 6.10.

$$Q = Q_s + Q_r + Q_c + Q_d \quad (6.10)$$

Where:

Q_r = net heat flux due to longwave radiation

Q_d = heat flux due to conduction to a curing compound or blanket

The individual components of the heat flux are estimated as follows:

- The absorbed shortwave radiation is modeled using Equation 6.11.

$$Q_s = a * R_{pk} * I \quad (6.11)$$

Where:

I = intensity factor

R_{pk} = peak solar radiation

The intensity factor is a sinusoidal function. The peak radiation is defined in Table 6.2.

Table 6.2. HIPERPAV I model solar radiation

Sky Condition	Peak Radiation (BTU/ft ² /hr)
Clear	317
Partly Cloudy	221
Overcast	95

- The net longwave radiation is estimated using Equation 6.12.

$$Q_r = 0.176 * N(4.8 + 0.0042(T_{air} - 41))(T_{air} + T_{surf}) \quad (6.12)$$

Where T_{surf} and T_{air} are in °F.

- The heat transfer due to convection is modeled using Equation 6.8. However, unlike the CMS model, the convection coefficient, H, is defined using Equation 6.13 (McCullough and Rasmussen 1999).

$$H = 0.318 * \left(-0.0022 * \left(\frac{ws}{2.23} \right)^2 + 0.06522 * \left(\frac{ws}{2.23} \right) + 1.9521 \right) \quad (6.13)$$

Where wind speed, ws, is in miles per hour.

The thermal material properties of the concrete assumed within HIPERPAV I are shown in Table 6.3.

Table 6.3. HIPERPAV I model material properties

Parameter	Estimate
Thermal Conductivity	$9.8 * 10^{-5} \frac{BTU}{s * ft * ^\circ F}$
Emissivity	0.88
Albedo	0.45
Specific Heat Capacity	$0.18-0.22 \frac{BTU}{lb * ^\circ F}$

The HIPERPAV model considers heat due to conduction to a curing compound and the heat of cement hydration. These factors are integral for the HIPERPAV model, as it is intended to analyze concrete pavements soon after construction. However, heat due to conduction to a curing compound and heat of hydration are negligible for the mature pavements, which are typically evaluated using FWD testing.

6.2.1.3 HIPERPAV II The second version of HIPERPAV contains a modified temperature prediction model (Ruiz et al. 2004).

The equation for absorbed solar radiation is consistent with the previous version. However, HIPERPAV II uses the 95-percentile values of peak solar radiation from a solar radiation database, rather than assuming the values in Table 6.2. The methods for estimating net long wave irradiation and convection were also modified. The updated methods are as follows:

- The net longwave radiation is estimated using the Stefan-Boltzman equation presented in Equation 6.14.

$$Q_r = N * \sigma * (T_{surf}^4 - T_{\infty}^4) \quad (6.14)$$

Where:

σ = Stefan-Boltzman constant $\left(4.761 * 10^{-13} \frac{BTU}{s * ft^2 * ^\circ F^4}\right)$
 T_{∞} = sky temperature, which is defined in Equation 6.15.

$$T_{\infty} = (A_r / \sigma)^4 - 459.7 \quad (6.15)$$

Where A_r is the atmospheric longwave radiation, presented in Equation 6.16.

$$A_r = N_{app} * \sigma * T_{amb}^4 \quad (6.16)$$

where:

N_{app} = apparent emissivity of all atmospheric layers.

This value is defined for three layers of the atmosphere. The apparent emissivity is a function of the density-length product of water vapor and the ratio of carbon dioxide to water vapor densities in each layer. The water vapor density at a given height is estimated as a function of the water vapor density at the ground. A full description of this method is provided in Ruiz et al. 2004. The cloud cover is not directly considered.

- The heat transfer due to convection is defined using Equation 6.8. However, unlike the HIPERPAV I model, the convection coefficient, H, is defined using Equation 6.17. This equation is also used in ASTM C680 (Heilman 1929).

$$H = 1.217 * C * (T_{avg})^{-0.181} * (T_{surf} - T_{amb})^{.266} * \sqrt{1 + WS} \quad (6.17)$$

Where:

C = a constant depending on the shape and heat flow condition (1.79 for horizontal plates warmer than air and 0.89 for horizontal plates cooler than air)

The recommended thermal material properties can be seen in Table 6.4.

Table 6.4. HIPERPAV II model material properties

Parameter	Estimate
Thermal Conductivity	$4.2 * 10^{-4}$ to $6.6 * 10^{-4} \frac{\text{BTU}}{\text{s} * \text{ft} * ^\circ\text{F}}$ *
Emissivity	0.88
Albedo	0.45
Specific Heat Capacity	0.19-0.29 $\frac{\text{BTU}}{\text{lb} * \text{v}}$

**The HIPERPAV II model recommends the thermal conductivity of the concrete slab to be between $4.2 * 10^{-4} \frac{\text{BTU}}{\text{s} * \text{ft} * ^\circ\text{F}}$ and $6.6 * 10^{-4} \frac{\text{BTU}}{\text{s} * \text{ft} * ^\circ\text{F}}$, which is the range of values recommended by ACI Committee 207. The actual value of thermal conductivity used for the analysis depends on the aggregate type. This typical range of values is much higher than the values used in the HIPERPAV I model. It is*

noted in the technical appendices of Ruiz et al. 2004 that these values are much higher than the experimental work conducted at McGill University, which found the thermal conductivity of hardened concrete to be around $1.85 \cdot 10^{-4} \frac{BTU}{s \cdot ft \cdot ^\circ F}$ (De Schutter and Taerwe 1995) . The recommended values did return reasonable results in validation studies (Ruiz et. al 2004).

6.2.1.4 NIST Model A model was developed at the National Institute of Standards and Technology (NIST) to predict the temperature and time of wetness of concrete pavements and bridges decks (Bentz 2000). The heat flux at the surface is calculated using Equation 6.10. The individual components of the heat flux at the surface are estimated as follows:

- The solar radiation is input directly from the National Solar Radiation Database (NSRDB), which includes solar radiation values spanning from 1961-2014.
- The net longwave radiation is determined using Equation 6.14. However, the sky temperature, T_∞ , is calculated using Equation 6.18 (Walton 1983).

$$T_\infty = (N_{app})^{1/4} * T_{amb} \quad (6.18)$$

Where N_{app} is defined by Equation 6.19.

$$N_{app} = 2.487 + 2.414 * \ln\left(\frac{T_{dew}}{459.67}\right) * F_{cloud} \quad (6.19)$$

Where F_{cloud} is a cloud factor, which is presented in Equation 6.20.

$$F_{cloud} = 1 + .024 * cf - .0035 * cf^2 + .00028 * cf^3 \quad (6.20)$$

- Heat transfer due to convection is estimated using Equations 6.8. However, the convection coefficient, H, is defined using Equations 6.21 and 6.22.

$$H = 1.68 + ws/2.24 \quad (\text{for } ws < 14.3 \text{ mph}) \quad (6.21)$$

$$H = 2.17 * (ws/2.24)^{.78} \quad (\text{for } ws > 14.3 \text{ mph}) \quad (6.22)$$

The default thermal material properties for the NIST model are presented in Table 6.5.

Table 6.5. NIST model material properties

Parameter	Estimate
Thermal Conductivity	$2.41 * 10^{-4} \frac{BTU}{s * ft * ^\circ F}$
Emissivity	0.88
Albedo	0.35
Specific Heat Capacity	$0.239 \frac{BTU}{lb * ^\circ F}$

6.2.2 Research Utilizing Heat Transfer Models

6.2.2.1 Establishing Permanent Curling and Warping Gradients in Pennsylvania A model was developed to predict the temperatures in newly placed pavements in Pennsylvania for use in estimating the set time, and built in temperature gradients of concrete slabs (Nassiri 2011). This analysis used the models established in HIPERPAV I, along with direct measurements of the temperature, wind speed, relative humidity, and solar radiation adjacent to the pavement, to predict the temperature profile of instrumented slabs. The model tended to predict the temperature very

well after the first 6 hours of placement. A sensitivity analysis conducted as part of this study, found the model to be sensitive to the thermal conductivity of the slab, but less sensitive to the thermal conductivity of the base, and insensitive to the thermal conductivity of the subgrade.

6.2.2.2 Qin and Hiller A model was developed to investigate the sensitivity of the temperature and temperature gradient in a concrete slab to various climatic inputs (Qin and Hiller 2011a). The absorbed shortwave radiation is calculated using Equation 6.11. The peak solar radiation, R , is assumed to be a randomly distributed variable with a mean equal to halfway between the maximum and minimum monthly solar radiation and a standard deviation of 1. The maximum and minimum peak radiation are collected from weather stations. The net longwave irradiation is estimated using the procedures in the NIST model (Equations 6.18 through 6.20).

It was determined that changing the solar absorptivity from 0.65 to 0.85 can cause a large enough change in the maximum ELTG to increase the temperature related stress in the slab by 10%. It was also found that the weather history (i.e. whether the previous day was cloudy or sunny) has an effect on the temperature at the bottom of the slab, which impacts the temperature gradient (Qin and Hiller 2011b). Finally, thermal irradiation models that consider the dew point temperature, such as the NIST or HIPERPAV II models, were found to better predict pavement temperature than models that did not consider the dew point temperature (Qin and Hiller 2011a).

6.3 DEVELOPMENT OF A TEMPERATURE PROFILE PREDICTION MODEL FOR FWD TESTING

While several models have been developed to predict pavement temperature, none are currently viable for evaluating the temperature of a slab during FWD testing. First, the data sources used by each of the models discussed in the previous sections do not update frequently enough to allow analysis soon after testing. In addition, validation studies of the CMS/EICM model have focused on whether the distribution of predicted temperatures and temperature gradients matches the distribution of actual temperatures and temperature gradients throughout the life of the pavement. This is reasonable for pavement design since a temperature analysis is intended to evaluate the effect of climate on long-term pavement performance. The HIPERPAV models are intended to be used for newly constructed pavements when heat of cement hydration is a large component of heat transferred in and out of the pavement. Validation of the HIPERPAV models has focused on this time period (Schindler 2004; Ruiz et al. 2001; Ruiz et al. 2004).

A temperature profile prediction model for use with FWD testing must account for the effect of weather on the pavement at the time of testing. Therefore, it is necessary to compare the measured and predicted temperature profile at specific points in time to accurately gauge the performance of a temperature profile prediction model for this purpose. For example, consider a model that accurately predicts the shape and amplitude of the daily variation in ELTG and WAT for a pavement, but with a phase lag. This model would work well for pavement design since it would predict the correct distribution of ELTG and WAT. However, this model may have considerable errors when predicting the temperature profile for FWD testing. Therefore, it is desirable to build a temperature profile prediction model that can utilize weather data sources soon after testing. The data sources must also be tuned and validated for accurate prediction.

6.3.1 Data Sources

The existing temperature profile prediction models are intended to capture the climate at a given location and commonly use a sample of historical data. The CMS model implemented in the Pavement ME Design Guide uses hourly climatic data (.hcd) files. The files for the weather stations included in Pavement ME are available from AASHTO. This data was originally based on the Unedited Local Climatic Dataset (ULCD) and the Quality Controlled Local Climatic Dataset (QCLCD) from NOAA (Diamond et al. 2013). The datasets primarily consist of information collected from ASOS and its predecessor, the Automated Weather Observation System (AWOS). Both of these systems have weather stations primarily situated at airports (Mannarano 1998). The most recent version of the files are based on the North American Regional Reanalysis Dataset (NARR) from NOAA (Mesinger et al. 2006). The .hcd files based on NARR data only contain data up to 2015. In addition, .hcd files based on the MERRA2 dataset are available from the LTPP Infopave website (Gelaro et al. 2017). This data is available until the end of 2016. The temperature profile prediction models that directly input solar radiation typically use the NSRD, which contains data until the end of 2010, or measure the data directly (Sengupta et al. 2014). A comparison between the QCLCD and MERRA (version 1) dataset, a predecessor to the MERRA2 dataset, found that the temperatures from the MERRA dataset were, on average, slightly higher than temperatures from the QCLCD (usually less than 2 °F). However, this did not lead to a large difference in distress predictions using the Pavement ME design procedure (Schwartz et al. 2015).

The pavement temperature profile at the time of FWD testing is affected by the weather at the test location immediately prior to and during testing, rather than the long-term climate. The .hcd infrastructure is set up to provide a sample of the historic climatic data, not short-term weather data. Therefore, weather data must be downloaded directly from the source datasets. The NARR

dataset is based on a northern conical projection and has a finer spatial grid than the MERRA2 dataset at lower latitudes (Mesinger et al. 2006). However, the grid spacings are similar in Pennsylvania. The NARR dataset also has a coarser temporal coverage (3 hours) than the MERRA2 and ASOS datasets (1 hour), which is not an issue when looking at climatic effects, but may cause errors when looking at weather (i.e. a storm or cloud system passes through a location within a 3-hour period of time) between data points. Therefore, the NARR dataset may not be suitable for predicting pavement temperature profiles during FWD testing. The suitability of the two remaining data sources, the ASOS and MERRA2 datasets, for inclusion in the pavement temperature profile prediction tool are evaluated.

6.3.1.1 ASOS The ASOS system is run by the National Weather Service (NWS) in collaboration with the FAA and DoD. The system consists of over 1000 weather stations throughout the country, which are primarily situated at airports. The data is typically available at an hourly resolution, with more frequent measurements provided during weather events, such as precipitation. Each station consists of one or more of the following sensors (Mannarano 1998):

- Ceilometer (cloud height indicator)
 - The number of ceilometer hits is used to calculate the sky coverage percentage. This value is then used to determine a sky condition presented in Table 6.6.

Table 6.6. ASOS sky condition estimates

Sky Cover (From Ceilometer)	Sky Condition
0% to 5%	Clear
5% to 25%	Mostly Clear
25% to 50%	Partly Cloudy
50% to 87%	Mostly Cloudy
87% to 100%	Overcast

The sky condition is also used in estimating the shortwave solar radiation.

- Visibility sensor
- Precipitation identifier
- Freezing rain sensor
- Lightning sensor
- Pressure sensor
- Ambient temperature sensor (Dry Bulb)
 - The dry bulb sensor is used to calculate the relative humidity (RH).
- Dew point temperature sensor (Wet Bulb)
 - The wet bulb sensor is used to calculate the relative humidity (RH).
- Anemometer (wind speed and direction)
 - The wind speed is typically measured at a height of 33 ft above the touchdown zone at the airport.
- Heated tipping bucket (precipitation accumulation)

The values used for the temperature profile prediction tool developed as part of this study include the ambient temperature, relative humidity, wind speed, and sky condition. This data is automatically downloaded from the Synoptic Labs Application Program Interface (API) run by the Mesowest group from the University of Utah Department of Atmospheric Sciences, in collaboration with the Western Division of NOAA (Horel et al. 2002). The ASOS data is available almost immediately. A map of the ASOS stations located in and near the Commonwealth of Pennsylvania is shown in Figure 6.2.

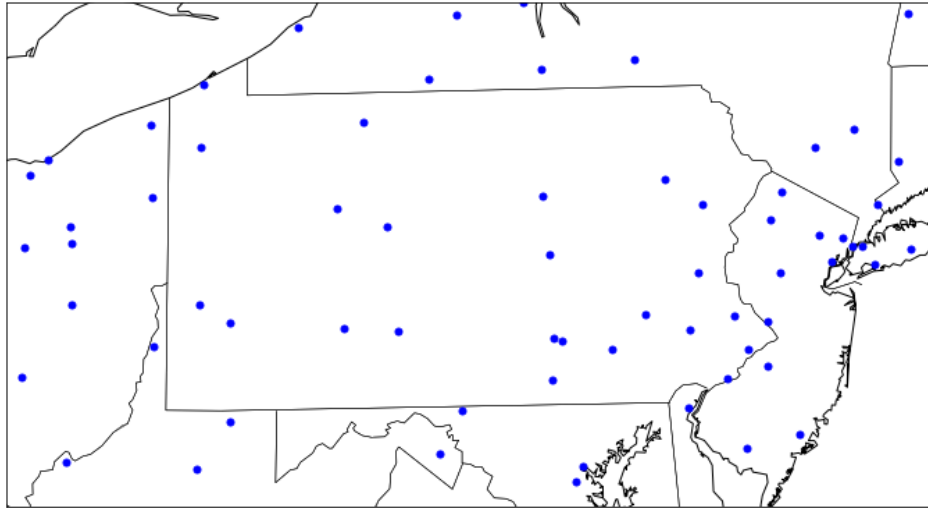


Figure 6.2. ASOS stations in and near Pennsylvania

6.3.1.2 MERRA2 The MERRA2 dataset is compiled by NASA as part of the Global Assimilation and Modeling Office (GAMO). The MERRA2 system consists of the GEOS physical atmospheric model and the GSI analysis methodology (Rienecker et al. 2011). In this system, “background states,” predictions of atmospheric conditions, are estimated in 6-hour increments using the GEOS model. These results are then compared to observations from land, sea, air and satellite-based data sources. From the comparison, a corrector variable set is applied to achieve agreement between the predicted and measured data. This correction is applied gradually using incremental analysis units (IAUs) to avoid unreasonable discontinuities in the observations and to avoid nonconvergence (Rienecker et al. 2011; Gelaro et al. 2017). The combination of a computational model tied to physical observations allows the dataset to include observations on a regular grid (0.5° Latitude x 0.625 °Longitude). The MERRA2 variables used in the temperature profile prediction tool developed as part of this study are presented in Table 6.7.

Table 6.7. MERRA2 variables used in temperature profile prediction tool

Collection	Variable	Description
Time Averaged (1 Hour) Radiation Diagnostics (RAD)	CLDTOT	Total cloud area fraction (high, medium and low)
	SWGDN	Surface incoming shortwave radiation
Time Averaged (1 Hour) Single Level Diagnostics (SLV)	T2M	Ambient Temperature 6.6 ft above the ground
	T2MDEW	Dew point Temperature 6.6 ft above the ground
	U10M	Eastward wind speed 33 ft above the ground
	V10M	Northward wind speed 33 ft above the ground

The U10M and V10M variables (wind speed 33 ft above the ground) are used instead of the U2M and V2M variables (wind speed 6.6 ft above the ground) for two reasons. First, a wind speed height of 33 ft agrees with the height of the ASOS wind speed measurements. Also, the zero-displacement height is averaged over the cell and can be close to or greater than 6.6 ft due to obstacles such as hills, trees, and buildings. However, wind will often move more freely over a pavement. Therefore, the wind speed at 33 ft is used and adjusted to account for the difference in height.

MERRA2 data is available for automated download from the NASA Goddard Earth Sciences Data and Information Services Center (DISC) (GMAO 2015). The reanalysis process is computationally extensive, which delays the availability of the data. A map of the MERRA2 grid point locations in and near the Commonwealth of Pennsylvania is shown in Figure 6.3.

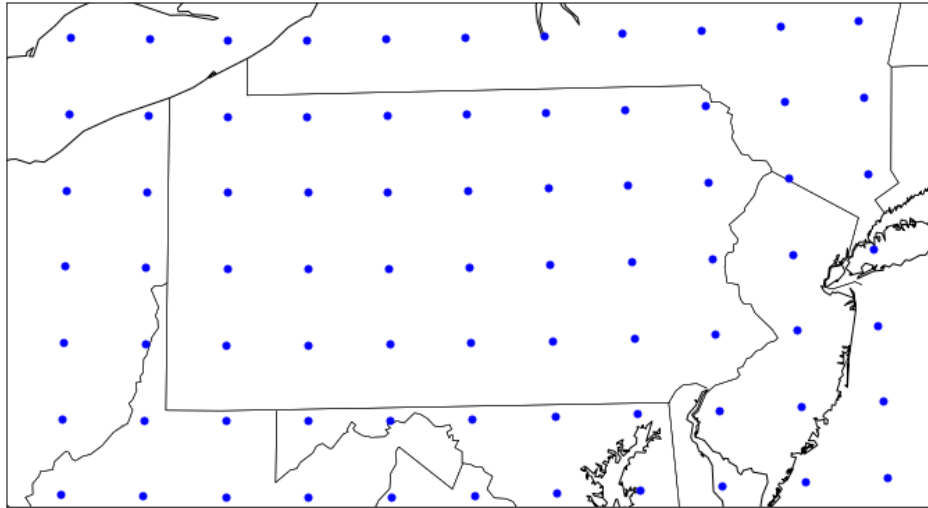


Figure 6.3. MERRA2 grid points in and near Pennsylvania

6.3.2 Processing Weather Datasets

The weather data from each source must be processed to calculate the five inputs needed for the temperature profile prediction model: shortwave radiation at the ground, ambient temperature, wind speed, relative humidity, and cloud cover.

6.3.2.1 ASOS The first step in generating the input data from the ASOS dataset is to choose the stations for interpolation. To account for two-dimensional variations in weather, the weather data from each station is interpolated by a set of three stations using barycentric interpolation. This requires three stations to be chosen to form a triangle, which contains the testing location. An

example of barycentric interpolation is shown for a test location on I-79 near Bridgeville, PA in Figure 6.4.

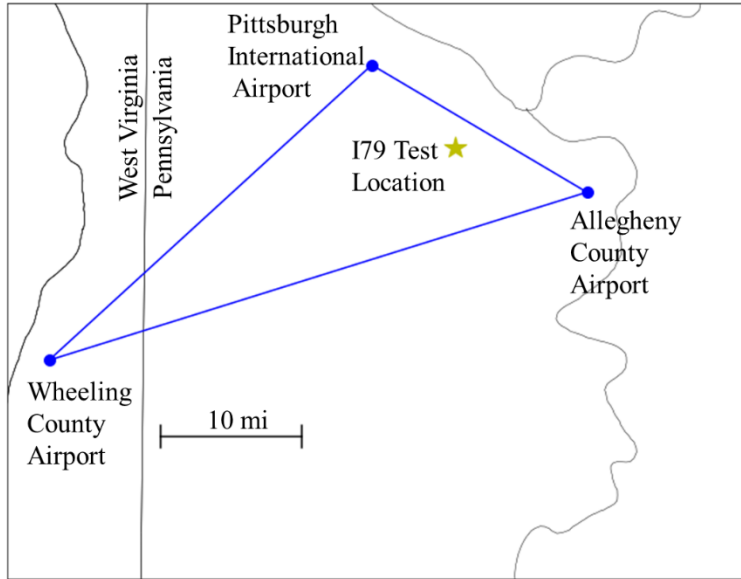


Figure 6.4. ASOS stations used for barycentric interpolation (I-79)

The optimum set of three stations is determined by developing a factorial of all possible combinations of three weather stations, which are in proximity to the testing location. Each set of stations is then checked to determine if the testing location is within the formed triangle. The sum of the distance between each of the stations and the test location is then calculated for each set of stations. The set of stations with the smallest total distance is chosen to perform interpolation. Before interpolation can be performed, the solar radiation needs to be estimated from the cloud fraction.

The cloud fraction is estimated from the sky condition using the values in Table 6.8. These values are the middle of the range shown in Table 6.6.

Table 6.8. Estimate of cloud fractions for ASOS sky conditions

Sky Condition	Cloud Fraction
Clear (CLR)	2.5%
Mostly Clear (FEW)	17.25%
Partly Cloudy (SCT)	37.5%
Mostly Cloudy (BKN)	68.5%
87% to 100% (OVC)	93.5%

The total clear sky, extraterrestrial radiation in a given day is calculated using a method developed by the American Society of Civil Engineers (ASCE) Environmental and Water Resources Institute (EWRI) and is shown in Equation 6.23 (Allen et al. 2005).

$$R_{24} = \frac{24}{\pi} * G_{sc} d_r (w_s * \sin\delta + \cos\phi \cos\delta \sin\omega_s) \quad (6.23)$$

Where:

R_{24} = the cumulative solar radiation in a period of 24 hours

G_{sc} = the solar constant

ω_s = the sunset angle (radians)

Φ = the latitude (radians)

δ = the solar declination (radians)

d_r = a term to account for the elliptical nature of the earth's orbit, which is based on the Julian day.

The solar declination can be determined using the equations in the NOAA Solar Calculator (Meeus 1991, NOAA 2017). The sunset angle is given in Equation 6.24.

$$\omega_s = \arccos(-\tan\phi \tan\delta) \quad (6.24)$$

The solar intensity is assumed to vary sinusoidally from sunrise to sunset, as with HIPERPAV and NIST models. The time from sunrise to sunset is assumed to be a full period of a sine wave with an amplitude equal to half the peak solar radiation and an offset of half the peak solar radiation. Therefore, the cumulative radiation in 24 hours can be expressed in terms of the peak radiation using Equation 6.25.

$$\int_{SR}^{SS} \left(R/2 * \sin \left(\frac{(x - SR) * 2\pi}{(SS - SR)} - \pi/2 \right) + R/2 \right) dx = R_{24} \quad (6.25)$$

Where:

SR = sunrise time

SS = sunset time

These values are calculated using the NOAA sunrise and sunset calculator within a 1 minute margin of error for latitudes less than 72° (Meeus 1991; NOAA 2017) and a 10 minute margin of error for higher latitudes. Equation 6.26, which is a simplification of Equation 6.25, can be used to calculate the peak solar radiation as the integral of a full period sine wave is 0.

$$R = \frac{2 * R_{24}}{(SR - SS)} \quad (6.26)$$

The clear sky radiation at a given time of day can then be calculated using Equation 6.11. The effect of clouds on solar radiation is accounted for using Equation 6.3, along with the regression coefficients used in Pavement ME (ARA Inc. 2004).

The wind speed at the ASOS stations is measured at a height of 33 ft above the ground. The wind at this height will be greater than wind on the ground due to the roughness of the ground.

Wind speed can be adjusted for elevation based on the log wind and power wind profiles. The log wind profile is considered more accurate within 60 ft the ground. The wind power law conversion can be approximated using Equation 6.27 (Oke 2002).

$$ws(z_2) = ws \frac{(z_1) * \ln((z_2 - d)/z_0)}{\ln((z_1 - d)/z_0)} \quad (6.27)$$

Where:

z_1 = the height of the anemometer

z_2 = the target height

d = zero-displacement height

z_0 = the characteristic roughness of the ground

Unfortunately, this formula is undefined when calculating the wind speed directly at the ground. Therefore, the wind speed driving convection is estimated using the wind speed 3.3 ft above the ground. If a characteristic roughness of 4 in is assumed, which corresponds to an open terrain with occasional obstacles, the previous equation can be simplified. Equation 6.28 shows that the wind speed used to calculate convection is half of the measured wind speed.

$$ws(3.3ft) = 0.5 * ws(33ft) \quad (6.28)$$

Ambient temperature is also influenced by elevation. This can lead to errors when the weather stations are at a different elevation than the testing location. Therefore, the ambient temperatures of the weather stations are adjusted to the elevation of the testing location using a lapse rate of 23.2 °F/mi for weather stations at a higher elevation than the pavement and 18.8 °F/mi for weather

stations at a lower elevation than the pavement. The difference in lapse rate is due to adiabatic cooling (Schwartz et al. 2015).

6.3.2.2 MERRA2 The structured nature of the MERRA2 grid allows the weather conditions at a location to be estimated using bilinear interpolation. An example of a MERRA2 interpolation box for the I-79 test location is shown in Figure 6.5.

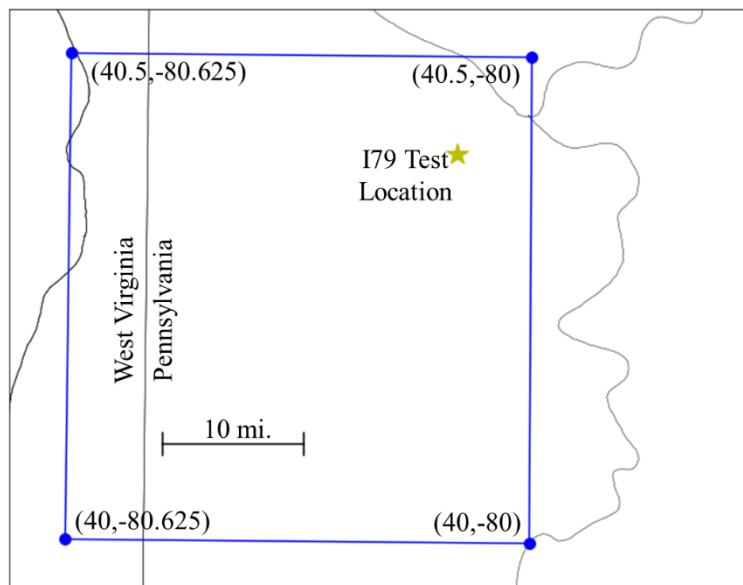


Figure 6.5. MERRA2 grid points used for bilinear interpolation (I-79)

The shortwave solar radiation at the ground is given and does not need to be estimated. The relative humidity is calculated using Equation 6.29 (Alduchov and Eskridge 1996).

$$RH = \frac{100 * \exp(9.8 * (T_{dew} - 32)) / (-48 + 5/9 * T_{dew})}{(\exp(9.8 * (T_{amb} - 32)) / (-48 + 5/9 * T_{amb}))} \quad (6.29)$$

The wind speed measurements are adjusted to a height of 3.3 ft and the ambient temperature is adjusted to the elevation of the test location utilizing the same procedures as the ASOS Dataset.

6.3.3 Finite Difference Method

Mathematical modeling of one-dimensional heat transfer in a pavement requires the boundary conditions and heat movement through the pavement to be described mathematically for each time step. The boundary condition at the top of the slab is defined as a heat flux boundary condition. The boundary condition at the bottom of the model, which is located deep in the subgrade, is defined as a constant temperature boundary condition. The movement of heat through the pavement structure is calculated by approximating Equation 6.1 using FDM, similar to the existing models (LeVeque 2007).

6.3.3.1 Heat Flux at the Pavement Surface The heat flux at the surface of the pavement is calculated as the summation of heat absorbed from shortwave radiation, heat transfer from net longwave irradiation, and heat transfer from convection. The heat of cement hydration and latent heat of evaporation are not considered. The heat of cement hydration is negligible in mature pavements where FWD testing will be performed. In addition, it is difficult to estimate the amount of water lost due to evaporation and previous studies have shown adequate results without considering the effect of the latent heat of evaporation (Nassiri 2011). The net longwave irradiation was estimated using the equations in the HIPERPAV I, HIPERPAV II, and NIST models and compared in a sensory analysis. The convection coefficient was estimated using Equation 6.17

(HIPERPAV II model) since it considers the differences in the shape of heat flow between convective heating and convective cooling.

6.3.3.2 Initial Conditions and Constant Temperature Depth The ground temperature is constant at a certain depth below the pavement layer. This depth is typically 33 to 66 ft below the ground. A sensitivity analysis was performed to determine if the depth of the constant temperature layer affects the results of the temperature profile prediction. In this model, the depth of the constant temperature layer is 33 ft below the top of the subgrade since the results of the analysis indicate the depth of the constant temperature layer, between 16 and 66 ft, does not affect the results of the prediction. The temperature at this deep node is approximated as the mean annual ambient temperature (MAT) at the test location. The initial temperature condition in the concrete slab is assumed to be the mean monthly ambient temperature (MMT). The initial temperature in the base, subbase, and subgrade are linearly interpolated between the MAT and MMT.

6.3.3.3 Computational Structure The one-dimensional heat transfer equation shown in Equation 6.1 is approximated using an FDM model, like the existing heat transfer models. The model space is discretized into four layers: the slab, base, subbase, and subgrade. The thickness, density, specific heat capacity, and thermal conductivity of each layer are inputs. The domain spaced is discretized into elements, with a maximum element thickness of 1 in in the slab, base, and subbase and a maximum element thickness of 10 in in the subgrade. The model is solved using

the explicit stencil (forward time, centered space). The maximum time step for this model to achieve stability is defined by Equation 6.30 (LeVeque 2007).

$$\Delta t \leq \frac{\Delta X^2}{\frac{4 * k}{\rho C_p}} \quad (6.30)$$

Where:

ΔX = the minimum element thickness

Δt is the time step

A conservative estimate of the maximum time step is around 180 seconds for 1-in thick elements. For maximum computational efficiency, this time step was used in the analysis. The Crank-Nicolson (implicit stencil) could increase this time step but was not used due to the difficulty of applying a flux boundary condition and achieving reasonable computation times. The boundary conditions are updated each time step to account for changes in the surface temperature and the weather conditions used to estimate the boundary conditions are changed every hour based on the time discretization of the data sources. The model results are output every 5 time steps (15 minutes).

6.3.3.4 Convergence Previous research has shown that the temperature profile in a pavement depends on recent weather at the pavement location (Qin and Hiller 2011b). Therefore, it is important to determine the length of analysis necessary to capture the effects of recent weather. Three pavement structures were evaluated at the location of the SR-22 SMART Pavement in

Murrysville, PA (Wells et al. 2005). The pavement structures include a 7 in slab (low-volume concrete pavement), 12 in slab (highway concrete pavement), and 20 in slab (airfield pavement). The pavement temperature profile was estimated using the MERRA2 dataset for three randomly selected days in April 2014. Analysis of the strain gauges at the SR-22 SMART Pavement, using the procedure demonstrated in Figure 4.1, performed as part of this research showed that joint lock-up commonly occur in May, June, July and August. In addition, PennDOT does not commonly test in these months to avoid having joint lock-up present during testing. An analysis of the thermocouples at the SR-22 SMART Pavement, as part of this research, indicates that the largest temperature gradients of the remaining months occurs in April. Therefore, April was chosen for the convergence analysis. For each of these days, the estimates were made using the prior 1, 3, 7, 14, 28, and 56 days in the analysis. The results of this convergence study are shown in Figure 6.6 to 6.14.

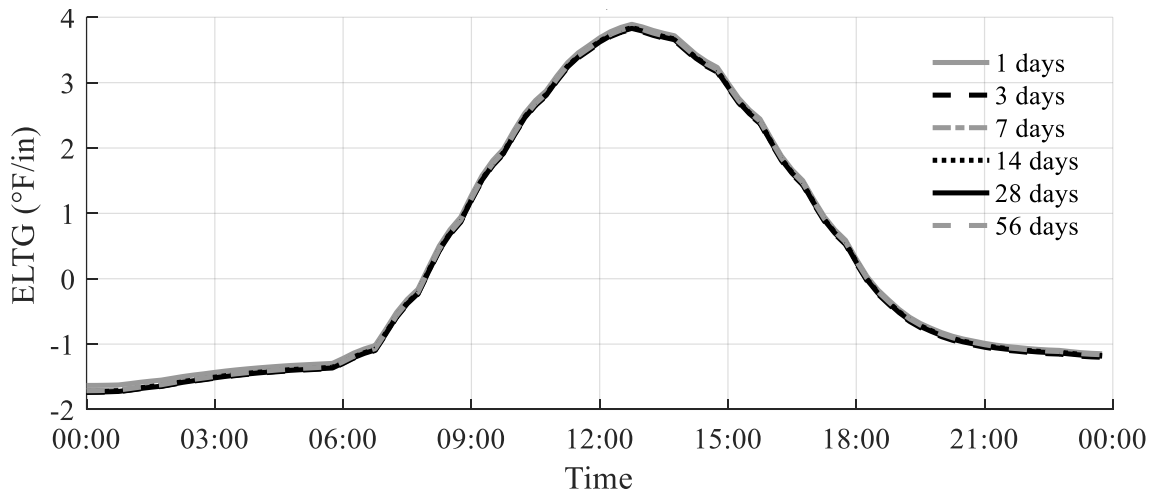


Figure 6.6. Analysis length required for convergence (4/6/2014, 7-in slab)

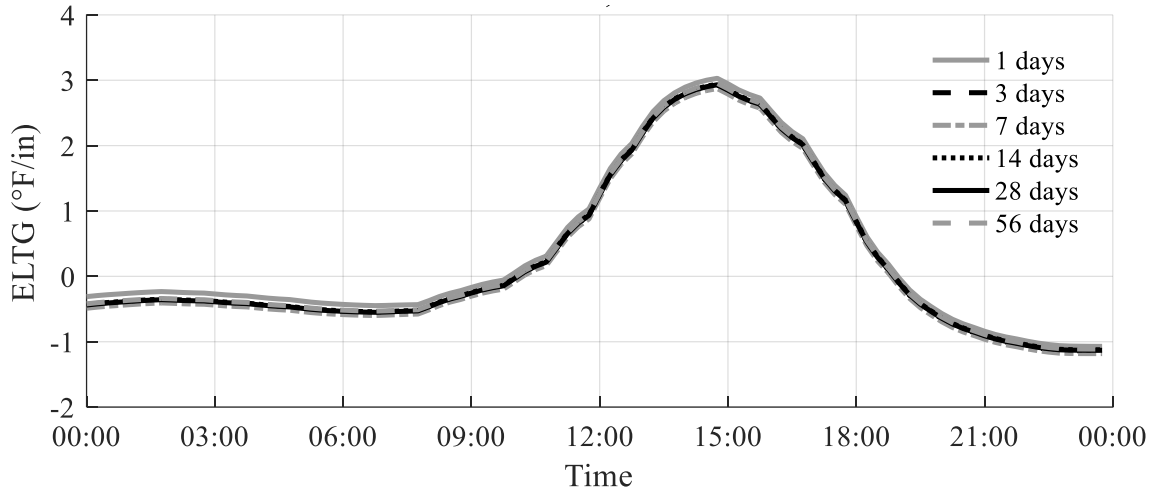


Figure 6.7. Analysis length required for convergence (4/8/2014, 7-in slab)

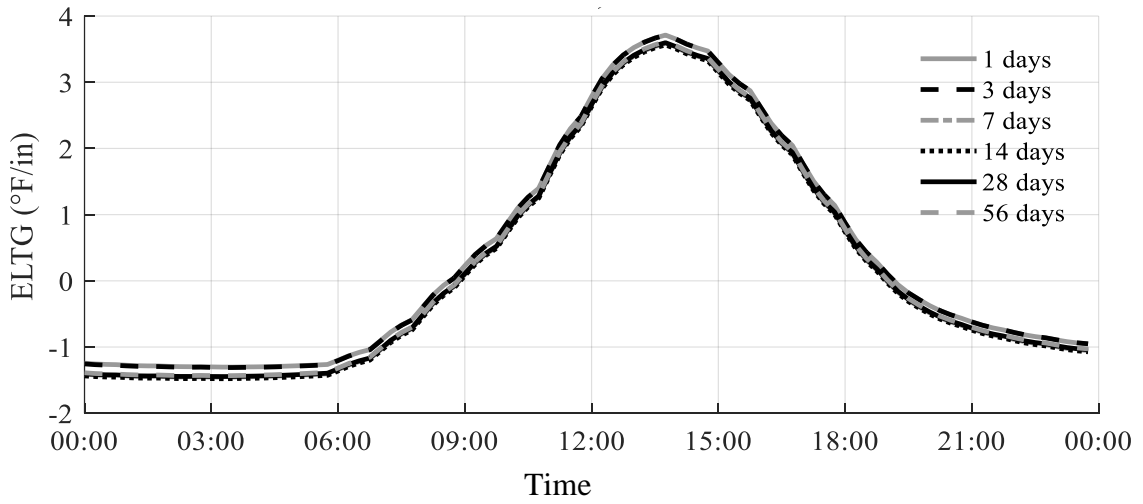


Figure 6.8. Analysis length required for convergence (4/18/2014, 7-in slab)

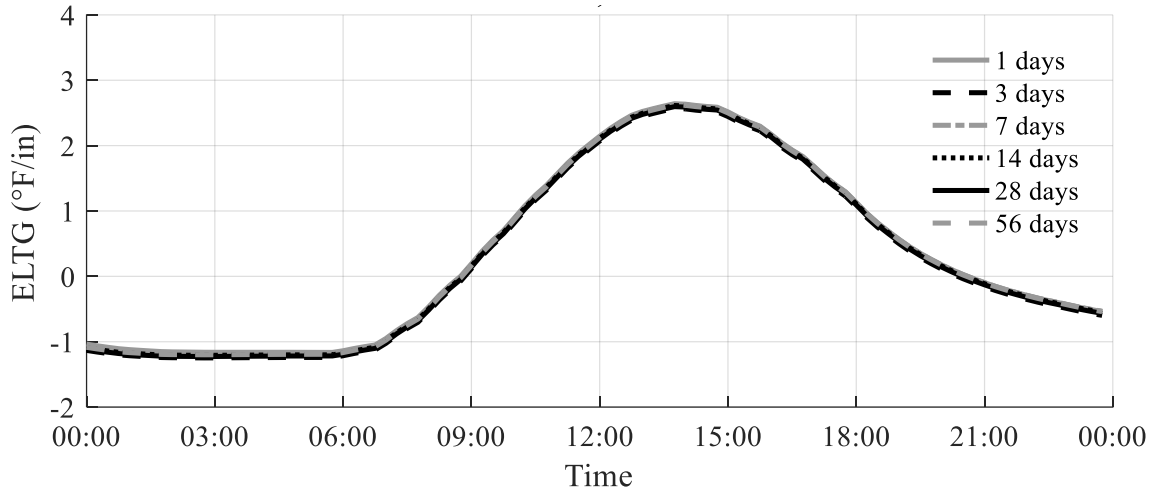


Figure 6.9. Analysis length required for convergence (4/6/2014, 12-in slab)

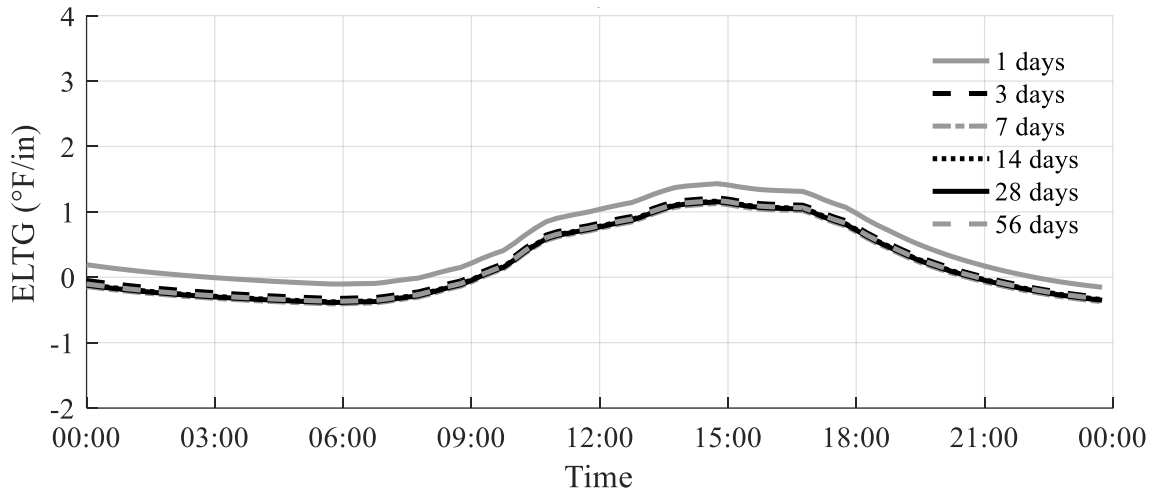


Figure 6.10. Analysis length required for convergence (4/14/2014, 12-in slab)

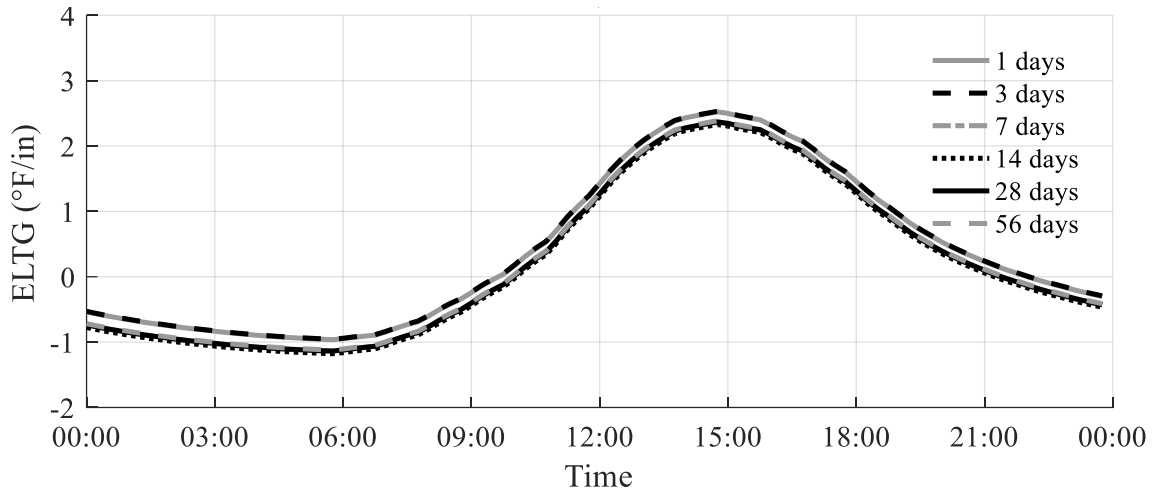


Figure 6.11. Analysis length required for convergence (4/18/2014, 12-in slab)

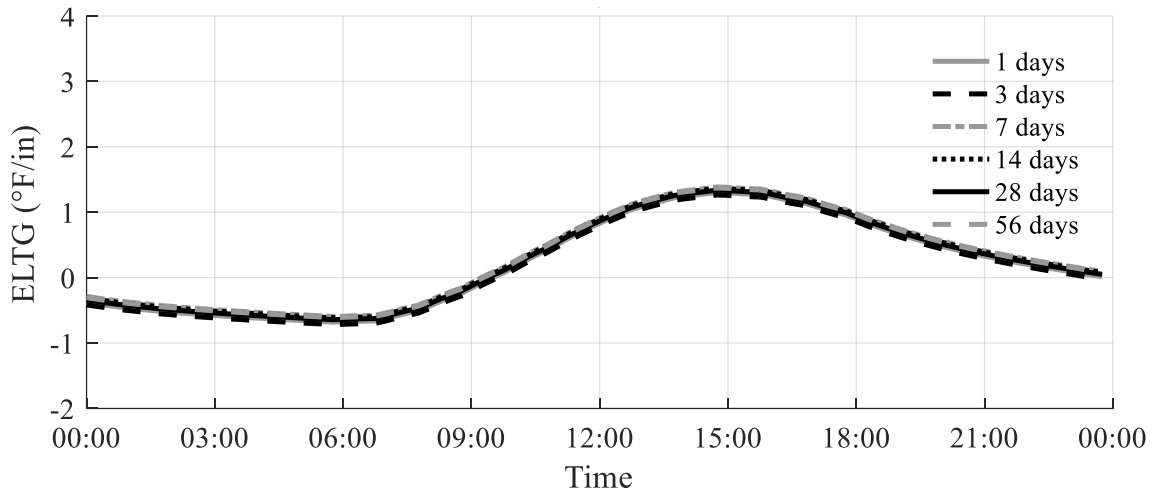


Figure 6.12. Analysis length required for convergence (4/6/2014, 20-in slab)

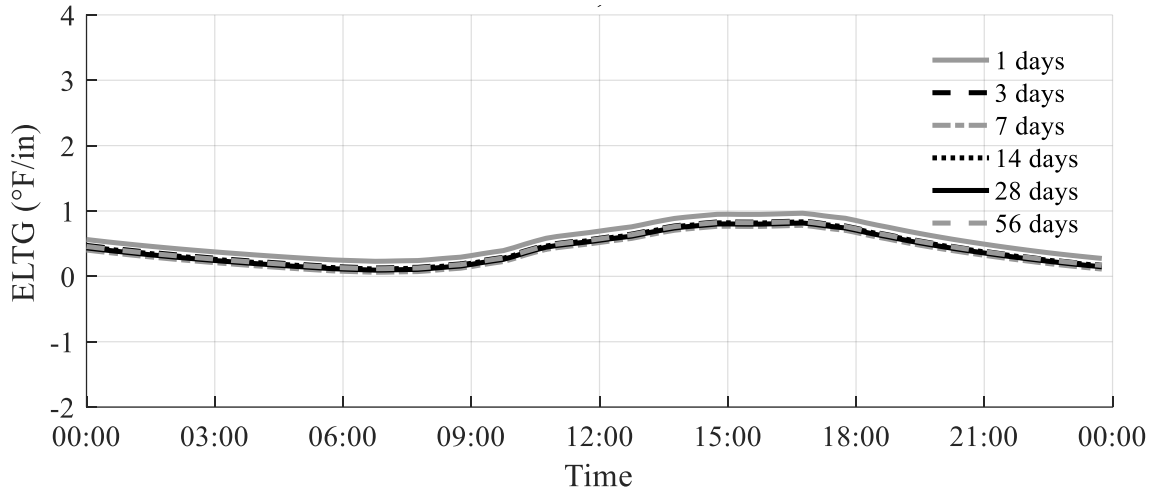


Figure 6.13. Analysis length required for convergence (4/14/2014, 20-in slab)

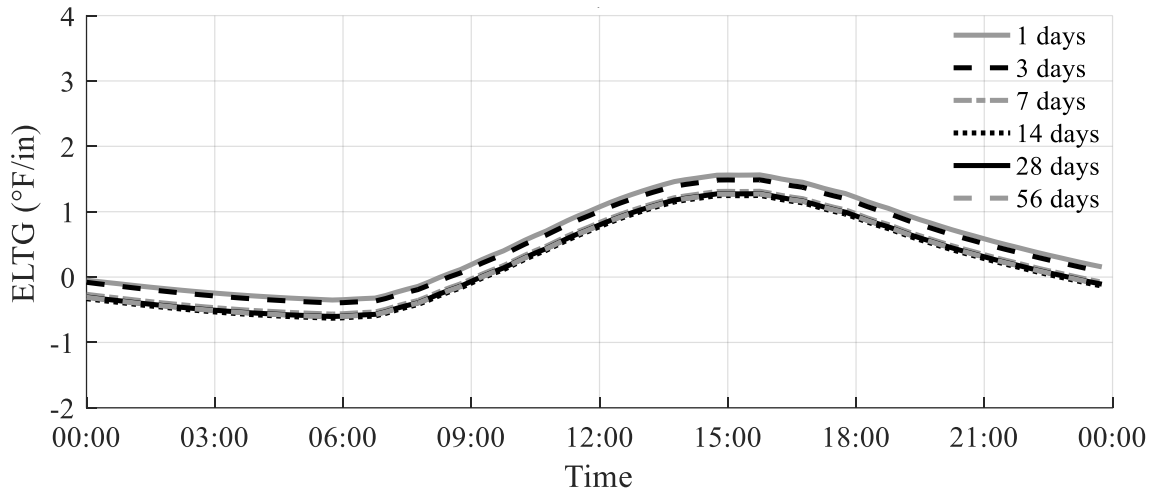


Figure 6.14. Analysis length required for convergence (4/24/2014, 20-in slab)

Each of these analyses converged to a stable solution after 7 days. Therefore, at least 7 days of weather data, including the test date, must be analyzed for accurate pavement temperature profile predictions.

6.3.4 Sensitivity Analysis

A sensitivity analysis was conducted to determine the effect of the thermal material properties and procedure used to calculate net longwave irradiation on the predicted ELTG and WAT. The structure and location of the SR-22 Smart Pavement near Murrysville, PA was used in this analysis. The pavement consists of a 12.5 in thick concrete slab on an asphalt-treated base, and is located at approximately 40.1 °N, 79.8°W. The analysis was performed using all the 2014 weather data in the MERRA2 dataset for this location. The baseline values for the sensitivity analysis are shown in Table 6.9.

Table 6.9. Baseline values for the sensitivity analysis

Property	Baseline Value
Slab Thermal Conductivity	$2.41 * 10^{-4} \frac{BTU}{s * ft * ^\circ F}$
Base Thermal Conductivity	$1.28 * 10^{-4} \frac{BTU}{s * ft * ^\circ F}$
Emissivity	0.88
Solar Absorptivity	0.60
Specific Heat Capacity	$0.239 \frac{BTU}{lb * ^\circ F}$
Long Wave Irradiation Method	NIST

The thermal properties were cycled through a range of typical values, while all other properties remained constant. The sensitivity of the predicted ELTG and WAT to the procedure used to estimate net longwave irradiation was evaluated by comparing the NIST, HIPERPAV I, and HIPERPAV II models. For each sensitivity parameter, the ELTG and WAT were plotted and evaluated for each day from March 1, 2014 through May 31, 2014. The graphs for April 10, 2014, which was a typical sunny day, are shown for each parameter in Figure 6.15 to 6.20 and discussed in the following subsections.

6.3.4.1 Thermal Conductivity of the Concrete Existing literature has reported a wide range of thermal conductivity of concrete measurements, ranging from $1.8 * 10^{-4}$ to $6.4 * 10^{-4} \frac{BTU}{s * ft * ^\circ F}$ (Dempsey et. al. 1986; Ruiz et. al. 2001; Schindler et al. 2004; De Schutter and Taerwe 1995;

Johanneck 2010). Figure 6.15 shows the sensitivity of ELTG and WAT predictions to thermal conductivity of the concrete.

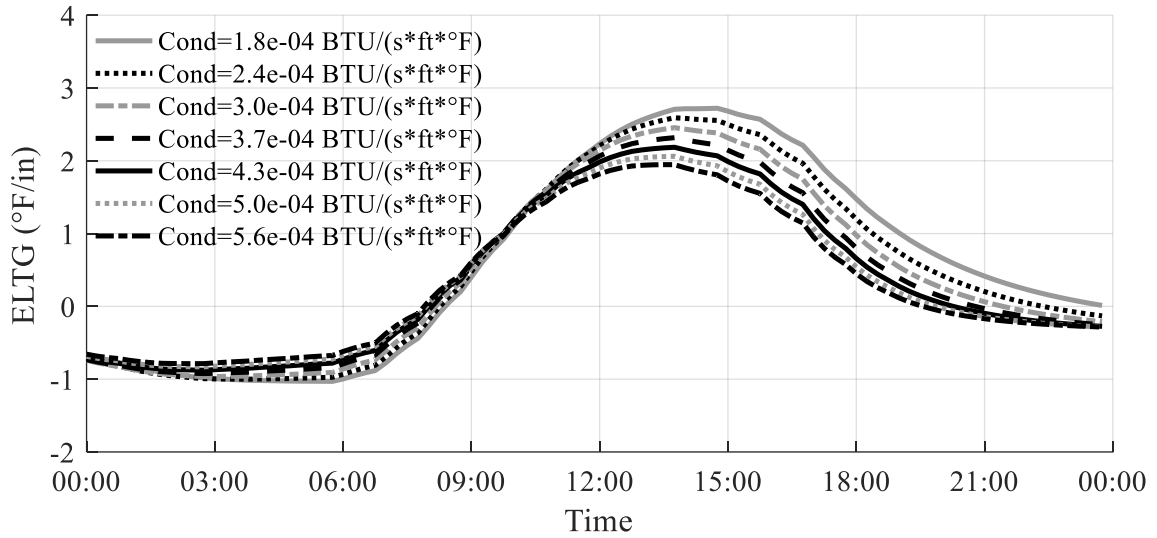


Figure 6.15a. Sensitivity of ELTG to concrete thermal conductivity (4/10/2014)

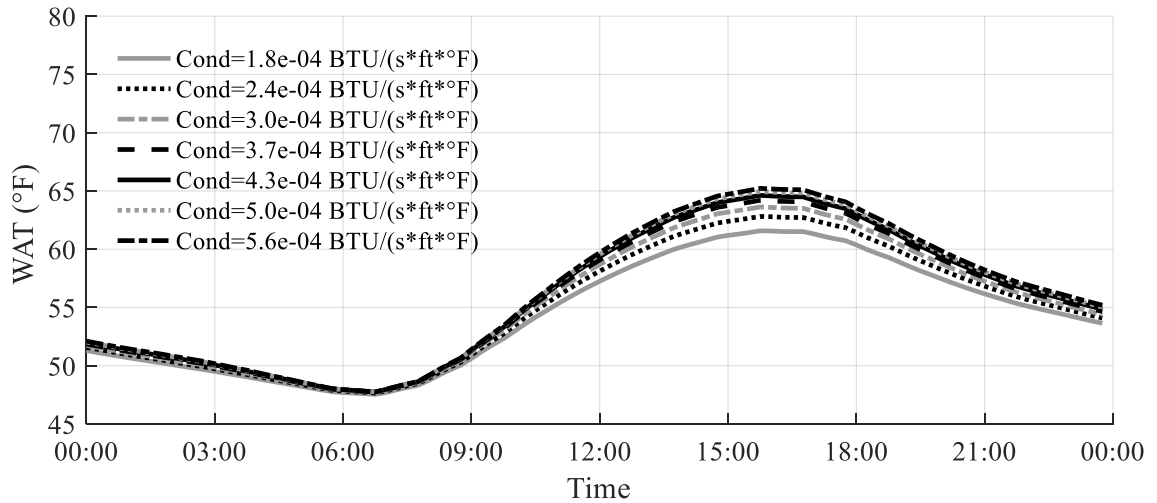


Figure 6.15b. Sensitivity of WAT prediction to concrete thermal conductivity (4/10/2014)

The magnitude and time of the predicted ELTG are both sensitive to thermal conductivity. As thermal conductivity decreases, it takes longer for the heat generated at the pavement surface to conduct to the bottom of the slab. This results in larger magnitudes of positive and negative temperature gradients. In addition, the peak ELTG of the least conductive concrete is approximately 1 hour later than the peak ELTG of the most conductive concrete. The ELTG does not begin decreasing following the peak ELTG due to a decrease in temperature at the top of the slab, but rather an increase in temperature at the bottom of the slab. The temperature at the bottom of a slab with concrete having a low thermal conductivity will take longer to increase, therefore delaying the peak temperature gradient.

The magnitude of the daily peak WAT is also affected by thermal conductivity, but the minimum WAT, and time of the daily maximum WAT are not affected. Over all the peak WAT varies by less than 3 °F with slab thermal conductivity. This difference is unlikely to have a large effect on the interpretation of the FWD testing results.

6.3.4.2 Thermal Conductivity of the Base Layer The thermal conductivity of the base can vary with the type of material and moisture content used to construct the base. For instance, a dry granular layer will have a low conductivity, whereas a wet stabilized layer will have conductivity values similar to that of concrete. The effect of the conductivity of the base is shown in Figure 6.16.

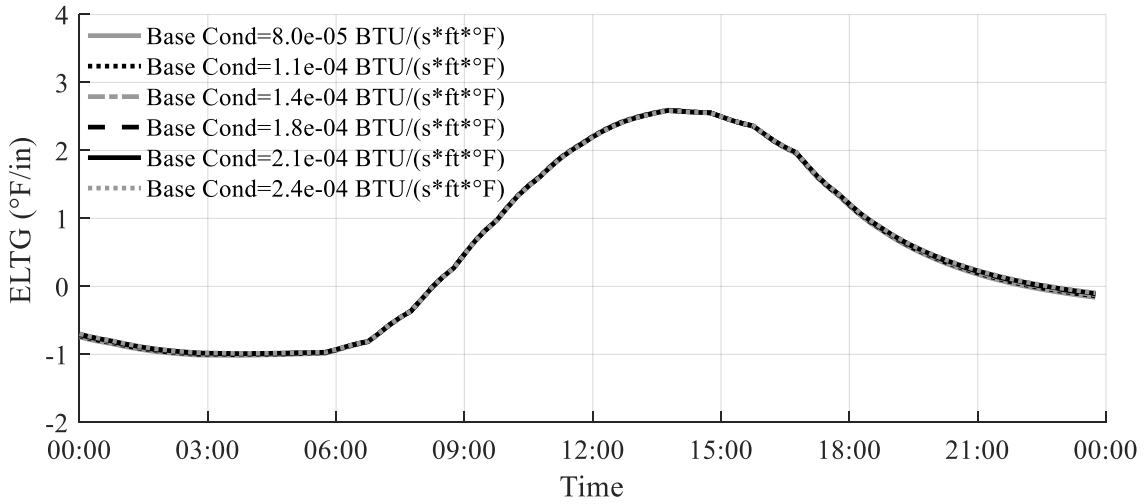


Figure 6.16a. Sensitivity of ELTG prediction to base conductivity (4/10/2014)

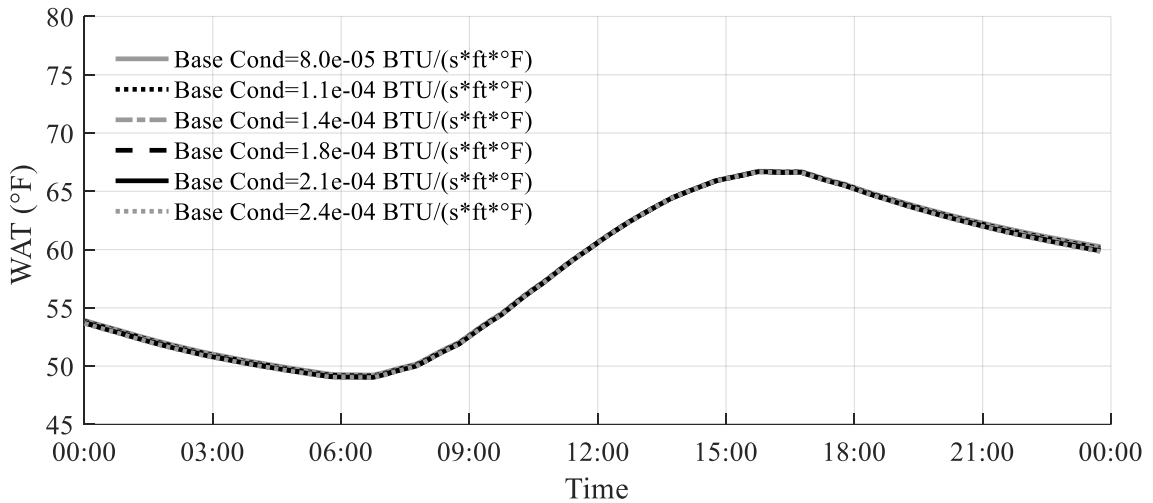


Figure 6.16b. Sensitivity of WAT prediction to base conductivity (4/10/2014)

The thermal conductivity of the base does not appear to have a large effect on the predicted ELTG or WAT. This is likely due to the relatively small diurnal temperature cycles experienced at the concrete layer. A previous study showed that in the first three days after casting, the conductivity of the base does have an effect on the temperature at the bottom of the slab (Nassiri 2011). This is

likely a result of the heat generated near the bottom of the slab due to cement hydration dissipating into the base layer. For mature slabs, heat mostly enters or leaves the system at the pavement surface, which makes the conductivity of the base less influential.

6.3.4.3 Emissivity The effect of emissivity of the concrete layer is shown in Figure 6.17. Most existing models use an emissivity between 0.88 and 0.95.

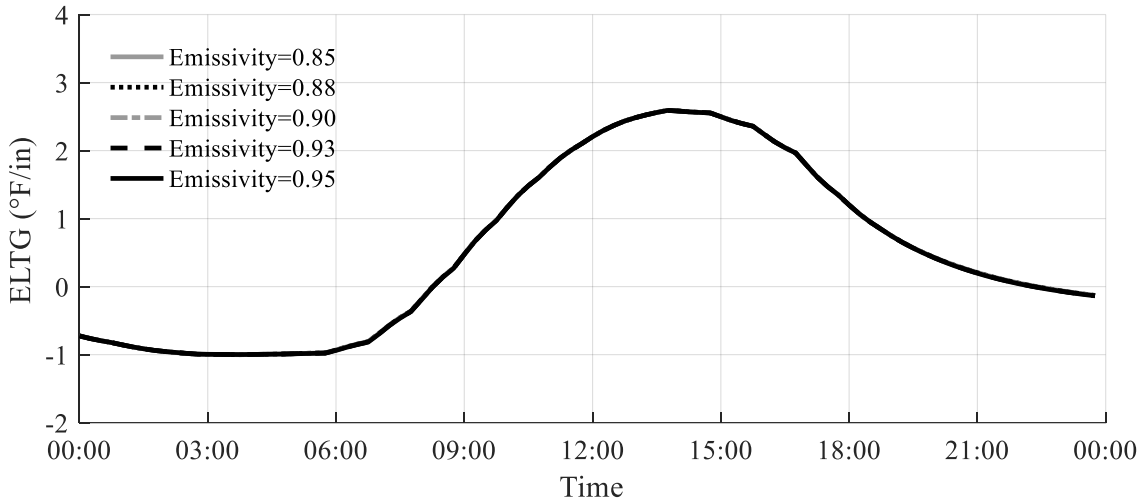


Figure 6.17a. Sensitivity of ELTG prediction to emissivity (4/10/2014)

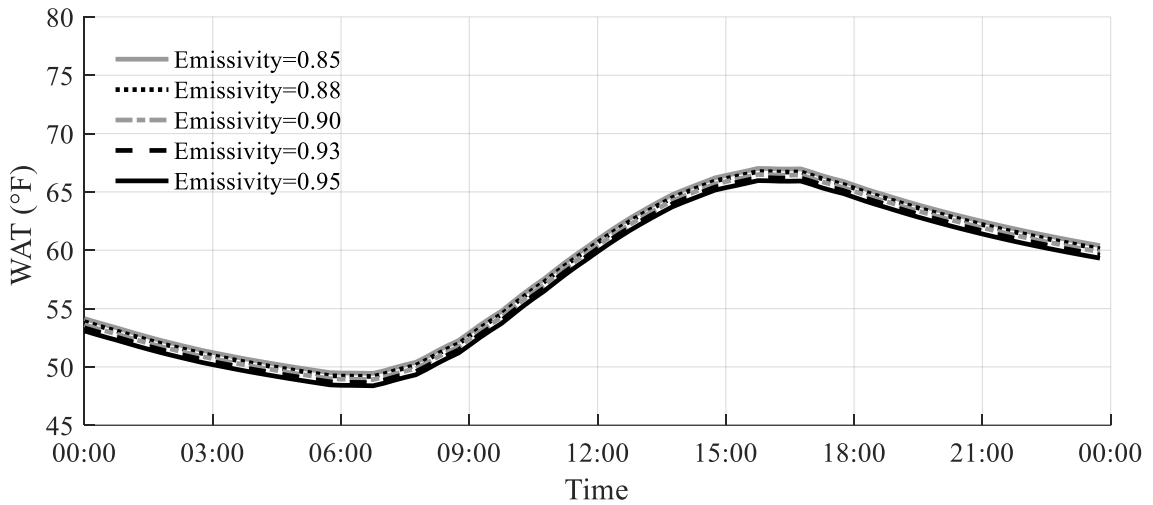


Figure 6.17b. Sensitivity of WAT prediction to emissivity (4/10/2014)

The emissivity of the concrete has very little effect on the estimated ELTG and only a minor effect on the estimated WAT. This could be due to the relatively narrow range of emissivity values reported in the literature.

6.3.4.4 Albedo

A wide range of albedo values, between 0.1 and 0.5, have been reported in existing literature. The effect of albedo can be seen in Figure 6.18.

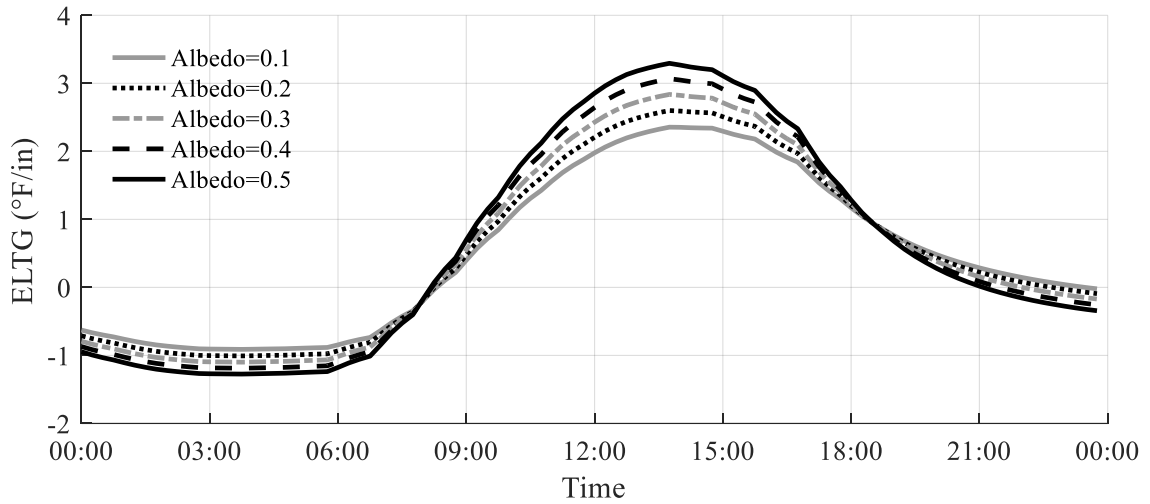


Figure 6.18a. Sensitivity of ELTG prediction to albedo (4/10/2014)

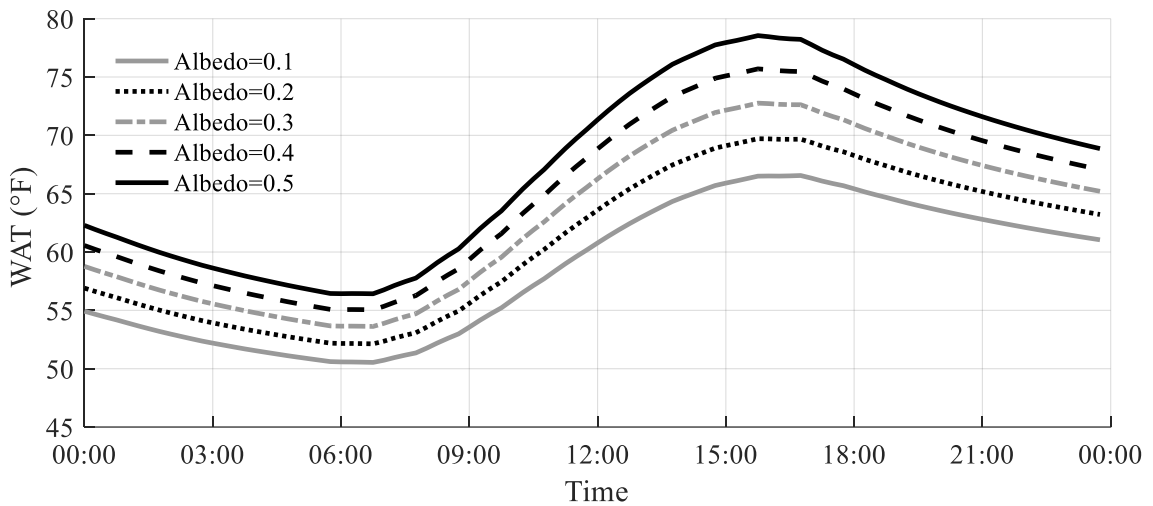


Figure 6.18b. Sensitivity of WAT prediction to albedo (4/10/2014)

As expected, albedo is a very important parameter for both ELTG and WAT. A lower albedo, which corresponds to high solar absorptivity, leads to higher magnitudes of positive and negative gradients. However, unlike slab conductivity, albedo does not influence the time when peak gradients occur. Additionally, a lower albedo results in higher temperatures throughout the day. This contrasts with slab conductivity, which does not affect the WAT overnight. A lower albedo increases the heat budget of the pavement, whereas a higher thermal conductivity only results in the redistribution of heat through the pavement layers.

6.3.4.5 Specific Heat Capacity The effect of specific heat capacity is shown in Figure 6.19. Existing literature has reported the specific heat capacity of concrete to be between 0.19 and 0.29

$$\frac{BTU}{lb \cdot ^\circ F}$$

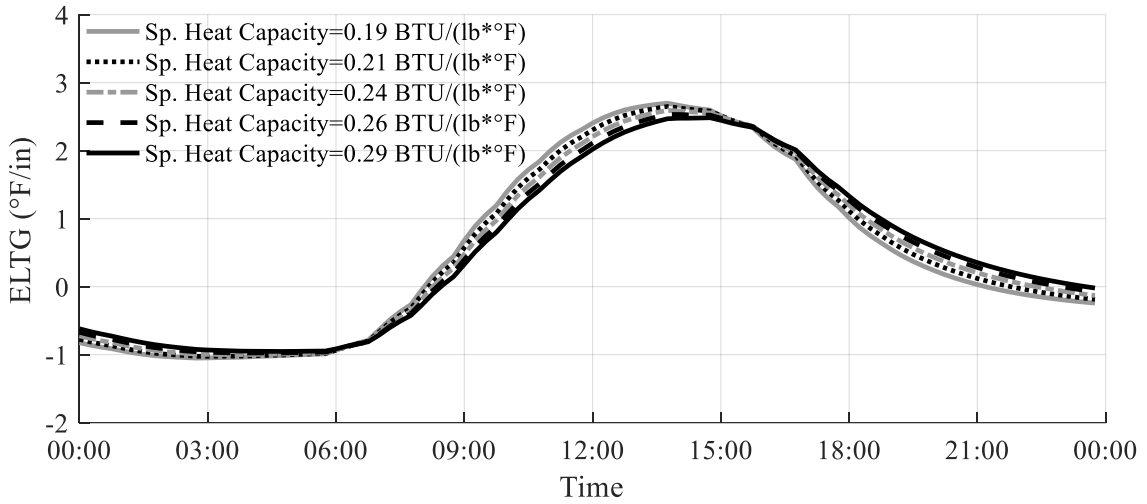


Figure 6.19a. Sensitivity of ELTG prediction to specific heat capacity (4/10/2014)

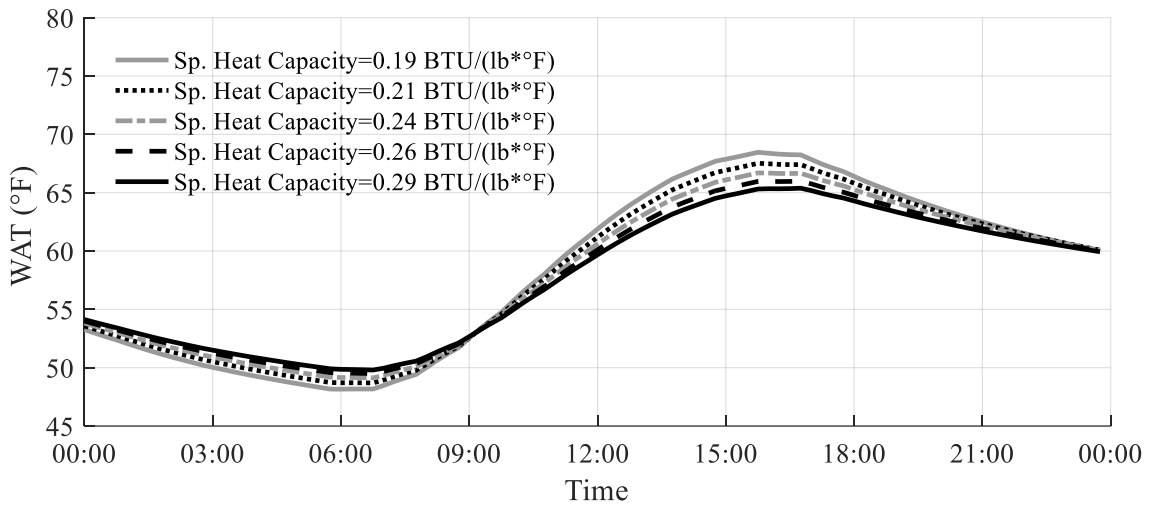


Figure 6.19b. Sensitivity of WAT prediction to specific heat capacity (4/10/2014)

An increased specific heat capacity will slightly decrease the magnitude of positive and negative ELTG. It also results in a delay of the peak temperature gradient. This delay is expected. The diffusion of heat through the slab is driven by temperature differentials, not heat differentials. With a higher heat capacity, it takes more shortwave radiation, and therefore more time, for the

temperature at the top of the slab to increase in the morning. In addition, it will require more heat conducting from the top to the bottom of the slab in the afternoon to cause the ELTG to begin decreasing. As a result, the specific heat capacity only has a small effect on the magnitude of the peak ELTG but does influence the time of the peak ELTG. In addition, the magnitude but not the shape of the daily swing in WAT is affected by specific heat capacity. The heat flux at the top and bottom of the slab is independent of specific heat capacity. Therefore, a slab made of concrete with a high heat capacity will experience a similar heat flux to a slab made with concrete having a low heat capacity, which will result in a smaller change in temperature.

6.3.4.6 Net Longwave Irradiation Model The effect of the method used to predict net longwave irradiation can be seen in Figure 6.20.

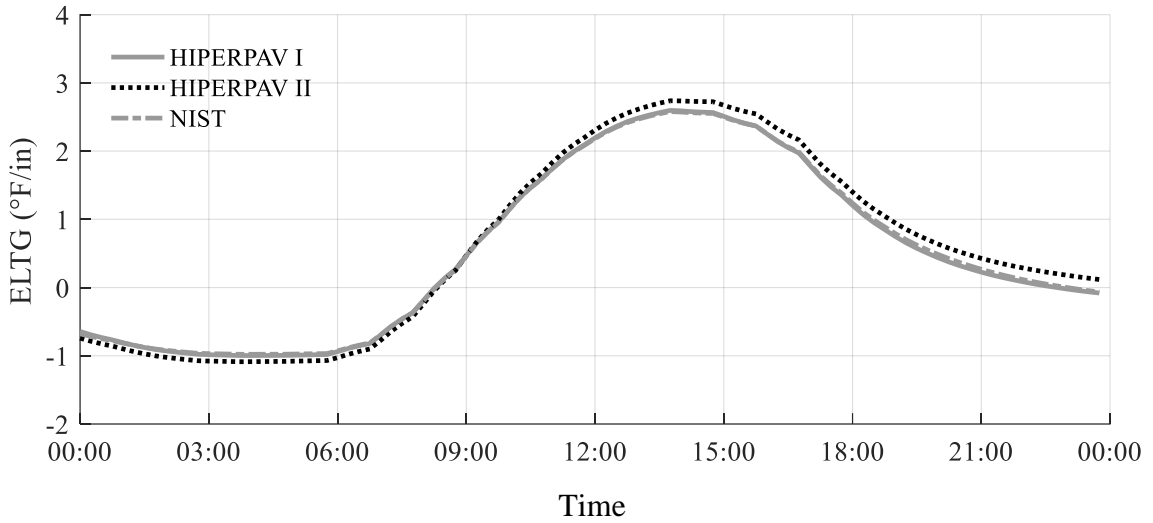


Figure 6.20a. Sensitivity of ELTG prediction to net longwave irradiation model (4/10/2014)

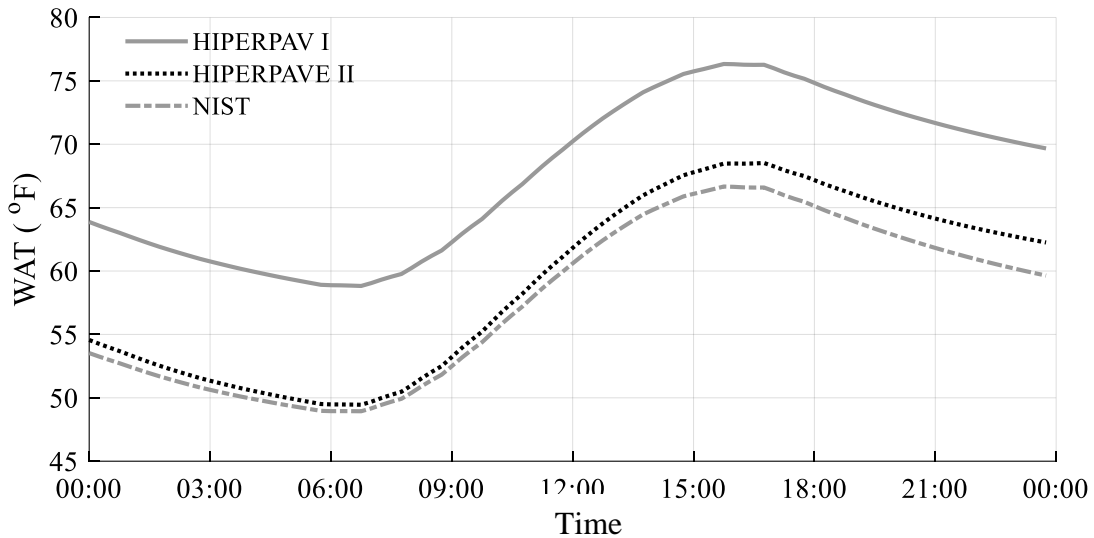


Figure 6.20b. Sensitivity of WAT prediction to net longwave irradiation model (4/10/2014)

The method of estimating net longwave irradiation does not appear to have a significant effect on the predicted ELTG. The HIPERPAV II model predicts a slightly different peak ELTG than the other two models. The difference in predictions may be due to the HIPERPAV II model estimating the sky emissivity based solely on the relative humidity, whereas the NIST and HIPERPAV I

model estimate sky emissivity based on the cloud cover and relative humidity. There appears to be a significant difference in the predicted WAT when comparing the HIPERPAV I model to the other two models. The HIPERPAV II and NIST models both estimate net longwave irradiation based on the difference between the pavement surface temperature to the fourth power and the sky temperature to the fourth power (Equation 6.14). In contrast, the HIPERPAV I model estimates net longwave irradiation based on a first order relationship with ambient temperature (Equation 6.12).

6.3.5 Comparison Between Data Sources

It is important to verify the agreement between the ASOS and MERRA2 data sources to evaluate the feasibility of using both data sources to predict the temperature profile. An analysis has previously been performed evaluating the relationship between predictions between the MERRA (version 1) dataset (Rienecker et al. 2011), the predecessor to MERRA2, and the QCLCD, which is primarily based on ASOS measurements. The comparison focused on ambient temperature and showed that the MERRA temperatures were, on average, slightly warmer than the QCLCD temperatures (Schwartz et al. 2015). The MERRA2 dataset includes observational data sources that were not included in the original MERRA analysis (Gelaro et al. 2017). This may affect the temperatures in the dataset.

Studies have shown the most important factor when predicting the temperature gradient in a concrete slab is shortwave radiation (Qin and Hiller 2011b). However, the previous comparison between the MERRA and QCLCD datasets did not evaluate incoming shortwave radiation, as it is not a direct measurement in the ASOS dataset. An analysis was performed as part of this study to

compare the two datasets at 100 randomly chosen locations in Pennsylvania between 2011 and 2015. The locations of the randomly selected points are shown in Figure 6.21.

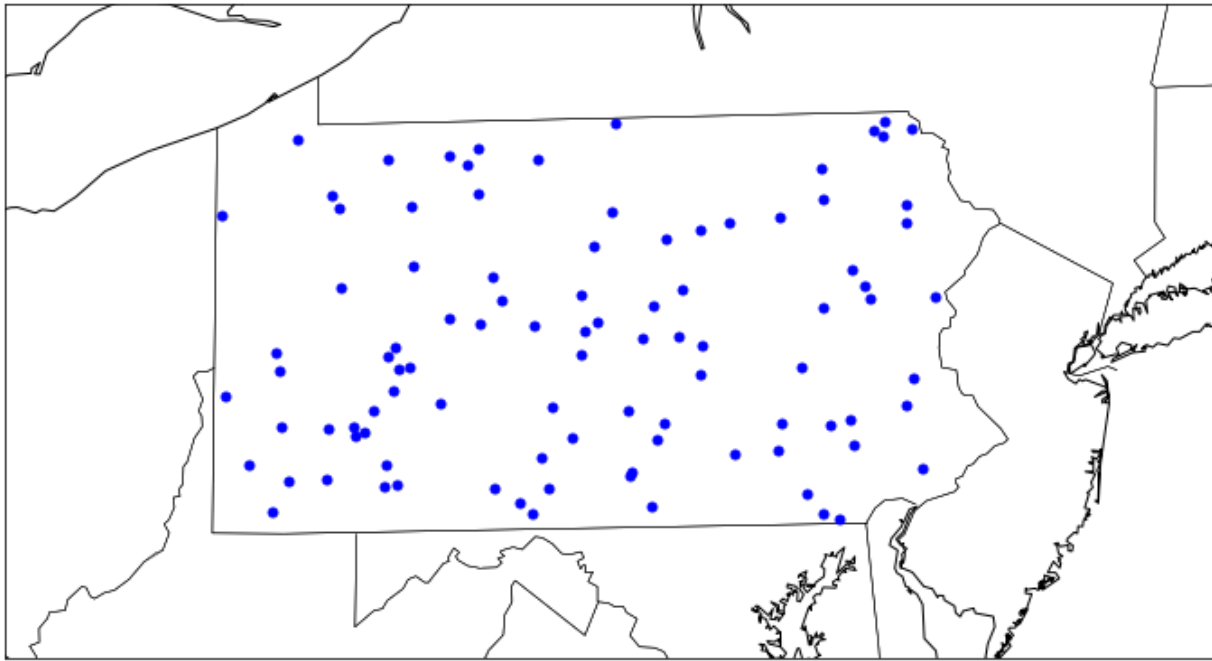


Figure 6.21. Randomly selected locations for comparing MERRA2 and ASOS datasets

The weather conditions at each location were estimated using barycentric interpolation of the ASOS dataset and bilinear interpolation of the MERRA2 dataset. The agreement between the datasets for the five parameters of interest (shortwave radiation, ambient temperature, wind speed, relative humidity and cloud fraction) was compared using a linear regression between the ASOS interpolated values and the MERRA2 interpolated values. The shortwave radiation was only considered during daylight hours, whereas the other factors were compared at all time points. This prevents the trivial result that both data sources indicate shortwave radiation does not occur at night, causing an artificially optimistic measure of agreement between the data sources.

The relationship and coefficient of determination of the linear regression comparison is presented in Table 6.10.

Table 6.10. Evaluation of the agreement between the MERRA2 and ASOS datasets

Measurement	Slope	Intercept	R²
Shortwave Radiation	1.00	0.004 BTU/s/ft ²	0.75
Temperature	0.93	4.5 °F	0.85
Wind Speed	0.70	0.7 mph	0.29
Cloud Fraction	0.15	0.47	0.03
Relative Humidity	0.08	75%	0.01

**Regression Format: MERRA = Slope * ASOS + Intercept*

The estimated shortwave radiation from the ASOS measurements is slightly lower than the MERRA2 measured shortwave radiation. This may be due to the cloud fraction in the ASOS dataset being higher than the cloud fraction in the MERRA2 dataset. In the future, it may be possible to reduce the bias between MERRA2 and ASOS shortwave radiation by modifying the relationship between shortwave radiation and cloud cover (Equation 6.3).

The temperature from the MERRA2 dataset is slightly less than the temperature estimated from the ASOS dataset. This observation disagrees with previous research that has found the MERRA temperature to be slightly higher than the ASOS temperature (Schwartz et al. 2015). This discrepancy may be due to differences between the MERRA and MERRA2 datasets. The previous study did not consider interpolation, but rather compared locations where the QCLCD station was within the MERRA cell (Schwartz et al. 2015). The current analysis uses bilinear and barycentric interpolation to estimate the weather conditions at randomly generated locations within Pennsylvania. This may explain the additional disagreement found between the datasets.

There is also poor agreement between the cloud cover and relative humidity. These parameters are used to estimate sky emissivity when calculating the net long wave irradiation. The HIPERPAV II model calculates sky emissivity based on the moisture distribution through the atmospheric column. This distribution is estimated based on the relative humidity at the surface. In contrast, the NIST model estimates sky emissivity as a function of the dew point and cloud cover. The dew point is influenced by both relative humidity and ambient temperature. Therefore, it is expected that the NIST model, which uses the dew point rather than relative humidity, would be less sensitive to the disagreement between the relative humidity of the two datasets.

Cloud cover is used for estimating the net longwave irradiation in the NIST model and shortwave radiation for the ASOS dataset. As previously mentioned, the shortwave radiation in the MERRA2 dataset is, on average, slightly higher than the shortwave radiation in the ASOS dataset, which may be attributed to differences in cloud fraction. This disagreement is likely caused by several factors:

- The datasets use different means for measuring the cloud fraction.
 - MERRA2 uses satellite measurements.
 - ASOS uses ground-based ceilometers, which cannot detect clouds above 12,000 ft (Mannarano 1998).
- ASOS cloud cover is grouped into sky conditions rather than presented as a continuous variable.
- Cloud cover is stochastic and difficult to estimate using barycentric or bilinear interpolation. Cloud cover can vary between ASOS stations, MERRA2 grid points, and the testing location.

It should be noted that the MERRA2 dataset does not consider all clouds to have the same reflectivity. Some data points have a large cloud fraction, but the shortwave radiation at the ground is close to the clear sky shortwave radiation at the ground. This may account for the much stronger agreement between the shortwave radiation in the datasets than the cloud cover. It is important to

note that the temperature profile prediction model is very sensitive to cloud fraction when the ASOS dataset is used. This error could be reduced by manually recording the sky condition during FWD testing or installing a pyranometer on the roof of the FWD truck to record the shortwave radiation during testing.

There is also significant bias between the measured wind speeds. The wind speed from the ASOS dataset is, on average, larger than the wind speed from the MERRA2 dataset. This is despite the wind speed from each dataset being measured 33 ft above the ground and adjusted using the log wind law to 3.3 ft above the ground. The difference in wind speed may be because the average wind speed of the entire GEOS analysis cell is reported in the MERRA2 dataset. In contrast, the wind speed measured at the ASOS station is at airports, usually near the center of the airfield. Airfields are defined as large, flat areas with no obstructions, which would result in higher wind speeds.

Overall, there are significant differences between the two datasets. However, the agreement is best for shortwave radiation and ambient temperature, which are the most important factors when estimating the pavement temperature profile. Therefore, both datasets were deemed suitable to predict the pavement temperature profile. It is possible that the differences between the datasets can be accounted for by adjusting the thermal properties of the concrete using tuning sections.

6.3.6 Validation and Tuning

The ability of the temperature profile prediction to accurately estimate the temperature profile was evaluated using five tuning sections and six validation sections. As previously discussed, a wide range of values have been reported for the thermal properties of concrete pavements. Therefore, it is critical to determine which of these values provide the best prediction of the pavement

temperature profile. The three parameters used for tuning the model, albedo, thermal conductivity of the concrete layer, and specific heat capacity of the concrete layer, were selected based on the results of the sensitivity analysis, which revealed the emperature profile prediction is sensitive to these parameters. Five instrumented sections were used to estimate these properties. Information about the instrumented pavements used for validation is presented in Table 6.11.

Table 6.11. Tuning section pavement information

Section	State	Thickness (in)	Base Type	Coarse Aggregate Type
LTPP Section 37-0201 (LTPP370201) (412) (412)	North Carolina	9	Granular	Crushed Stone
MnROAD Cell 52 (MNR52) (Burnham 2001)	Minnesota	7.5	Granular	Natural Gravel
MnROAD Cell 53 (MNR53) (Rohne 2009)	Minnesota	12	Granular	Natural Gravel
Atlanta Hartsfield-Jackson International Airport (ATL) (Brill et al. 2007)	Georgia	19	Lean Concrete	Unknown
SR-22 Smart Pavement (SR-22) 418	Pennsylvania	12.5	Asphalt Treated	Limestone

The HIPERPAV models estimate the thermal material parameters based on the characteristics of the concrete, such as aggregate type and water cement ratio. However, the concrete mix properties may not be known for mature pavements where FWD testing is performed. In addition, as stated in the literature review, these models disagree with values determined using lab studies and field analysis (Johanneck et al. 2010; De Schutter and Taerwe 1995). Therefore, these estimates cannot be used directly, and would need to be tuned. Only five sections are available to tune the temperature profile prediction model. Attempting to tune this model while accounting for

additional variables, such as the aggregate type, can lead to over-fitting. Therefore, measured data from the instrumented sections is used to estimate a single value for these three parameters. The tuning sections include mixes with both natural gravel and crushed limestone coarse aggregate. In addition, the albedo of a concrete pavement is known to increase with time. However, the relationship between albedo and time has been shown to be logarithmic in nature. Most of this increase occurs in the first few years after construction. After the first few years, the change in albedo with time is much smaller than the variation in albedo between different sections. FWD testing is not typically performed in the first few years after construction. Therefore, a single static value is tuned for albedo rather than a time dependent value.

Each of these pavements is instrumented, with data recorded at least once an hour. The measured and predicted temperature profiles of each section are compared for each temperature profile measurement for one year. The year chosen for analysis was based on the completeness of the measured data. The first four pavements were constructed with embedded thermocouples. These thermocouples estimate the temperature at a minimum of five depths throughout the slab. The LTPP section is part of the Seasonal Monitoring Program (SMP). Pavements in this program were retrofitted after construction with three thermistors throughout the depth of the pavement. Each of these thermistors were embedded in the same steel tube. One thermistor is 1 in from the top of the concrete layer, one thermistor is at mid-depth of the concrete layer and one thermistor is 1 in from the bottom of the concrete layer.

The NIST model provides the best prediction of temperature profiles and was therefore used for all analyses. In this analysis, the ELTG and WAT were calculated using the measured pavement temperatures and the predicted pavement temperatures for both data sources. The material properties for the optimum fit can be seen in Table 6.12.

Table 6.12. Tuned thermal material properties for each dataset

Parameter	MERRA2	ASOS
Thermal Conductivity	$2.41 * 10^{-4} \frac{BTU}{s * ft * ^\circ F}$	$2.09 * 10^{-4} \frac{BTU}{s * ft * ^\circ F}$
Albedo	0.32	0.12
Specific Heat Capacity	$3.11 * 10^{-1} \frac{BTU}{lb * ^\circ F}$	$2.15 * 10^{-1} \frac{BTU}{lb * ^\circ F}$

It is expected that the optimum albedo for the MERRA2 dataset is higher than the optimum albedo for the ASOS dataset, as the shortwave radiation in the MERRA2 dataset is, on average, slightly higher than the ASOS dataset. It is unknown why the tuned model for ASOS utilizes a lower thermal conductivity and specific heat capacity. The lower values may be because, on average, the wind speeds are higher in the ASOS Dataset, leading to more convection.

For comparison purposes, temperature profile predictions were also calculated using EICM, which uses the CMS model. The EICM infrastructure is not suited for continuously adding data to the analysis database, which is required for analyzing data soon after testing. In addition, solar noon for the EICM database is always assumed to be 12:00 pm. In reality, solar noon depends on the longitude. This is irrelevant for pavement design as it will not affect the distribution of temperatures or temperature gradients, however it can cause a phase lag when attempting to predict the temperature profile at a particular time. Therefore, the EICM model was not independently tuned as a candidate model. The material properties estimated using the ASOS dataset were utilized for comparison.

For each analysis, a linear regression line was fit between the measured and predicted values. The intercepts of the regressions were forced to zero, so the slope of the regression line accurately describes differences in the peak positive and negative ELTG. The coefficient of

determination provides information on any differences in the shape of the plot, either due to a phase lag or disagreement between the interpolated and true weather conditions. It should be noted that fitting the intercept caused the coefficient of determination to be slightly lower for all comparisons, less than a 0.05 difference, than would be observed if both an intercept and slope had been fit. In addition, the measured ELTG and WAT, along with the predicted ELTG and WAT from the MERRA2, ASOS, and NARR datasets, were plotted for the month of April to visually observe differences between the measured and predicted values. These plots are included in Appendix A. The fit between the measured and predicted ELTG and WAT is presented in Tables 6.13 and Table 6.14, respectively. In addition, daily plots of measured and predicted ELTG of the sections were made for each day in the month of April and shown in Appendix A.

Table 6.13. Comparison between measured and predicted ELTG for the tuning sections

		MERRA2		ASOS		EICM	
Section	Year	R ²	Slope	R ²	Slope	R ²	Slope
LTPP 370201	2003	0.80	1.33	0.76	1.09	0.46	1.29
MNR 52	2011	0.85	0.92	0.74	0.85	0.57	1.08
MNR 53	2011	0.80	1.05	0.73	1.05	0.48	1.03
ATL	2009	0.81	1.00	0.78	1.02	0.25	0.71
SR-22	2014	0.86	1.03	0.79	0.86	0.77	1.10

Table 6.14. Comparison between measured and predicted WAT for the tuning sections

		MERRA2		ASOS		EICM	
Section	Year	R ²	Slope	R ²	Slope	R ²	Slope
LTPP 370201	2003	0.96	1.02	0.92	0.96	0.80	1.04
MNR 52	2011	0.97	0.98	0.95	1.00	0.85	0.98
MNR 53	2011	0.95	1.00	0.94	1.03	0.84	1.01
ATL	2009	0.98	0.97	0.82	0.96	0.85	0.96
SR-22	2014	0.96	1.01	0.95	0.95	0.97	1.02

The MERRA2 dataset provides a better fit than the ASOS dataset for each section. An F-test was used to compare the variance of the residuals for the temperature predictions using MERRA2 and the temperature predictions using ASOS. The results of this testing can be seen in Table 6.15.

Table 6.15. Hypothesis testing results comparing the variability of temperature prediction model residuals using the MERRA2 dataset and ASOS dataset

Section	p-value	95% confidence interval on $\sigma^2_{MERRA2}/\sigma^2_{ASOS}$
LTPP 370201	$6.7 \cdot 10^{-14}$	0.77 to 0.86
MNR 52	0	0.55 to 0.58
MNR 53	$3.0 \cdot 10^{-253}$	0.68 to 0.71
ATL	$1.0 \cdot 10^{-9}$	0.78 to 0.88
SR-22	$2.4 \cdot 10^{-25}$	0.76 to 0.83

The reduction in variance by utilizing the MERRA2 dataset, rather than the ASOS dataset is statistically significant at the 95% confidence level for all 5 sections. This is likely because the MERRA2 dataset provides direct measurements of shortwave radiation, whereas the ASOS dataset estimates the shortwave radiation from the sky condition. It should be noted that all the instrumented pavements are near ASOS stations and the ATL section is directly at an ASOS station. The difference in performance may be larger for sections further from the nearest airport. Overall, the temperature prediction model for both the ASOS and MERRA2 datasets provides relatively accurate predictions of ELTG.

The ASOS and MERRA2 datasets both predict ELTG with a higher magnitude than the measured ELTG at LTPP 37-0201, but accurately predict the WAT. This is likely due to the thermistors being installed in a steel tube. The steel tube acts as a “thermal bridge,” which artificially reduces the measured temperature gradient in the slab.

As expected, the fit between the measured and predicted WAT is stronger than the fit between the measured and predicted ELTG. This is because the WAT experiences diurnal and seasonal changes, whereas the ELTG only experiences diurnal changes. The seasonal changes are primarily driven by the ambient air temperature and occur slowly, making them easier to predict. It is interesting that the agreement between the measured and predicted WAT for both datasets is greater than the agreement of the ambient temperatures.

Although these sections are used for tuning the thermal properties of the concrete, only three degrees of freedom are used for tuning and the predicted temperature profile is not sensitive to the parameters of interest. The results of the sensitivity analysis indicate these parameters can control the magnitude of the peak positive and negative ELTG and the time of peak ELTG within a few hours. However, the shape of both the ELTG and WAT curve is primarily driven by the

weather data, which is not adjusted. Therefore, the predictive power of the model on these tuned sections is not expected to widely vary from sections not used for tuning.

To evaluate the ability of the model to predict ELTG and WAT for sections outside of the dataset used for tuning, the model was evaluated using temperature hole measurements taken during FWD testing. Temperature holes are created by drilling various 0.5 in diameter holes in the pavement, at least 1.6 ft apart. Mineral oil is placed in the bottom of the hole to provide conductivity between the location of the temperature measurement and the pavement (Schmalzer 2011). The temperature holes do not suffer the same “thermal bridge” conditions as the SMP thermistors since the measurements are taken in separate holes. A total of six sections were evaluated on ten test dates. The first section is the I-79 section in Pennsylvania, which was tested as part of the field trials described in Chapter 2. The coarse aggregate in this section is a natural gravel. The remaining four sections are part of the LTPP SPS section in Delaware County, Ohio. These sections were chosen due to the proximity to Pennsylvania and the use of four temperature holes on the test date. The coarse aggregate in these sections is natural gravel. There are no LTPP test dates in Pennsylvania that use at least four temperature holes.

The ASOS weather stations and MERRA2 grid points used to interpolate the I-79 test section are shown in Figures 6.4 and 6.5. The ASOS weather stations and MERRA2 grid points used to interpolate the Ohio SPS sections can be seen in Figure 6.22.

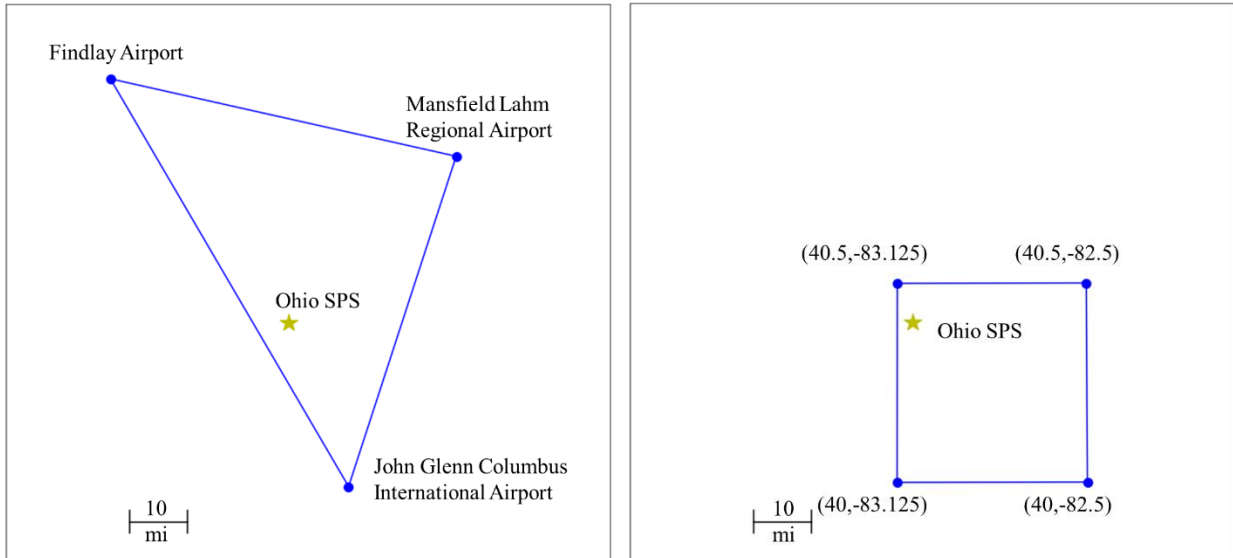


Figure 6.22. Location of ASOS station and MERRA2 grid points used for interpolation (Ohio SPS sections)

The I-79 test section is near an urban area. The ASOS locations used for interpolation are, on average, closer to the test section than the MERRA2 grid points. In contrast, the Ohio SPS sections are in a rural area. The sections are closer to the MERRA2 grid points than the ASOS stations. The structures of the pavement sections used for validation are summarized in Table 6.16.

Table 6.16. Validation section information

Section	Thickness (in)	Base Type
I-79 (Bridgeville, PA)	12	Granular
LTPP 39-0203	11	Lean Concrete
LTPP 39-0205	8	Lean Concrete
LTPP 39-0207	11	Asphalt Treated Base
LTPP 39-0260	11.6	Cement Treated Base
LTPP 39-0262	11.5	Granular

The measured and predicted ELTG and WAT for all test dates at the I-79 test section and a selection of test dates at the Ohio SPS test sections can be seen in Figure 6.23 to 6.32.

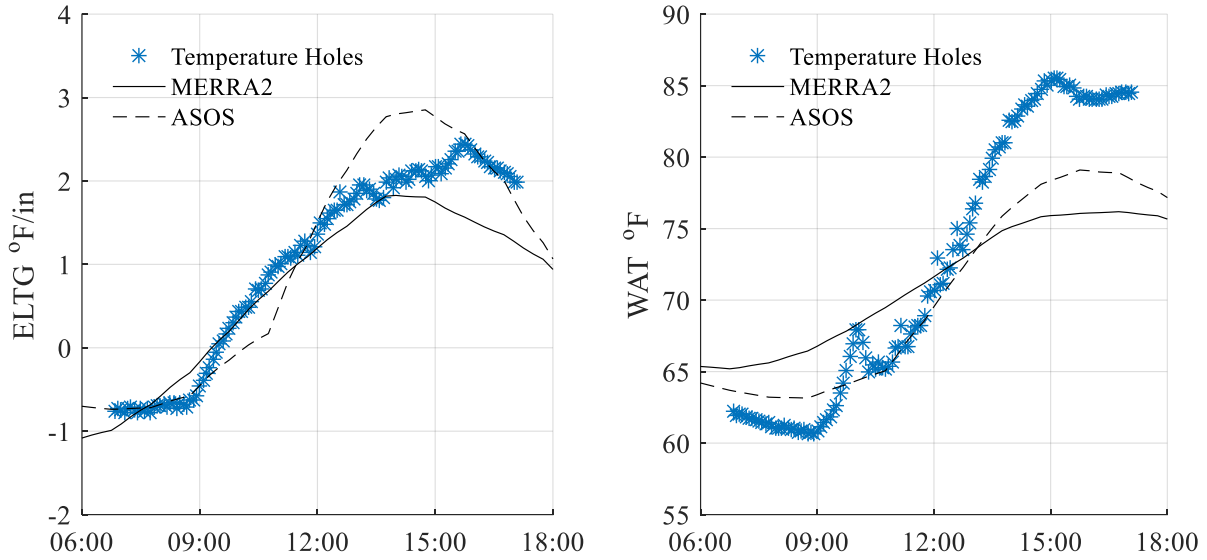


Figure 6.23. Comparison between measured and predicted temperature profile (I-79, 5/8/2016)

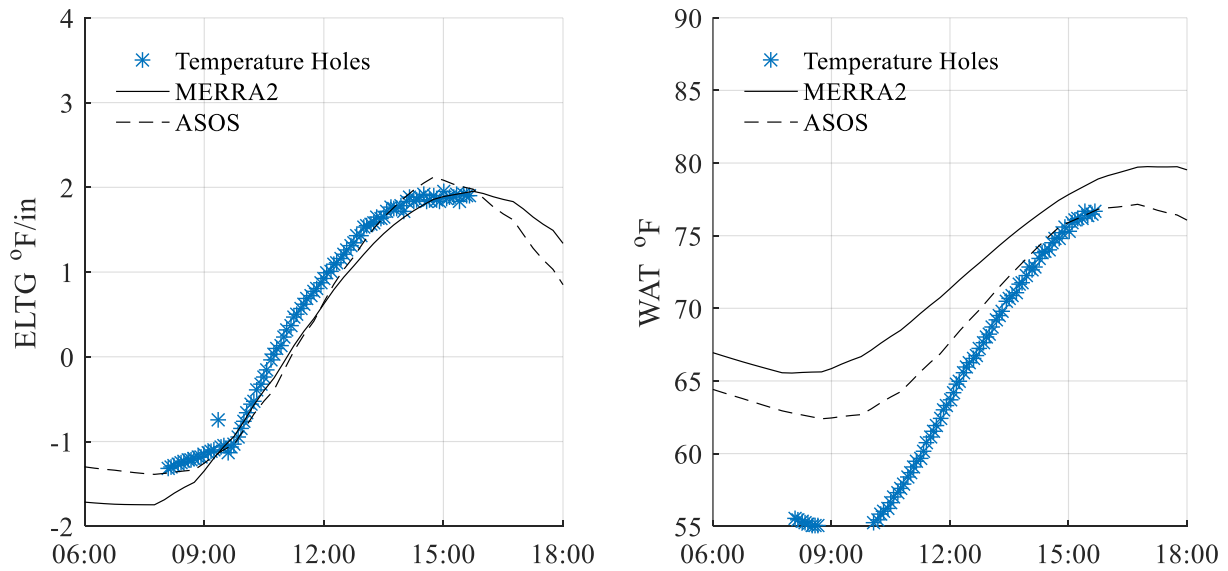


Figure 6.24. Comparison between measured and predicted temperature profile (I-79, 10/1/2017)

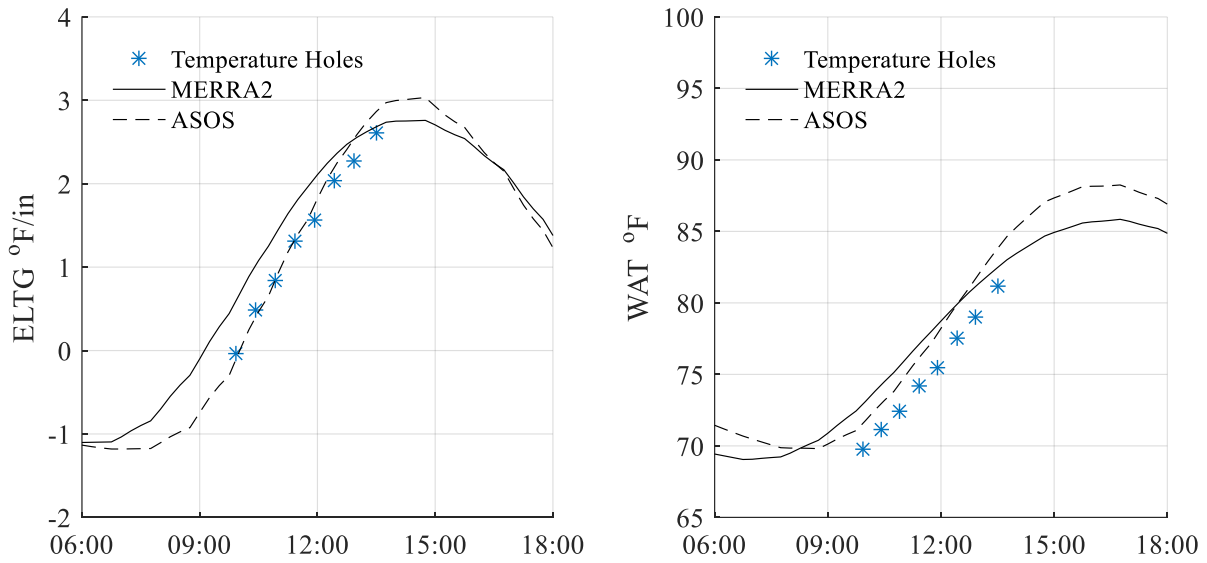


Figure 6.25. Comparison between measured and predicted temperature profile (39-0203, 9/22/2004)

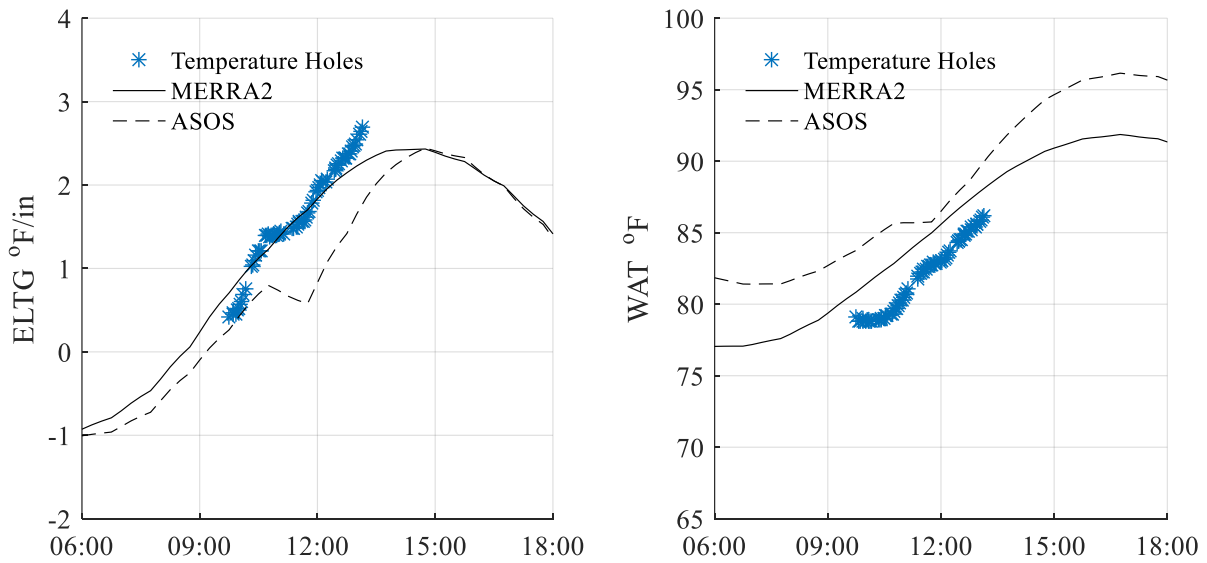


Figure 6.26. Comparison between measured and predicted temperature profile (39-0203, 6/17/2014)

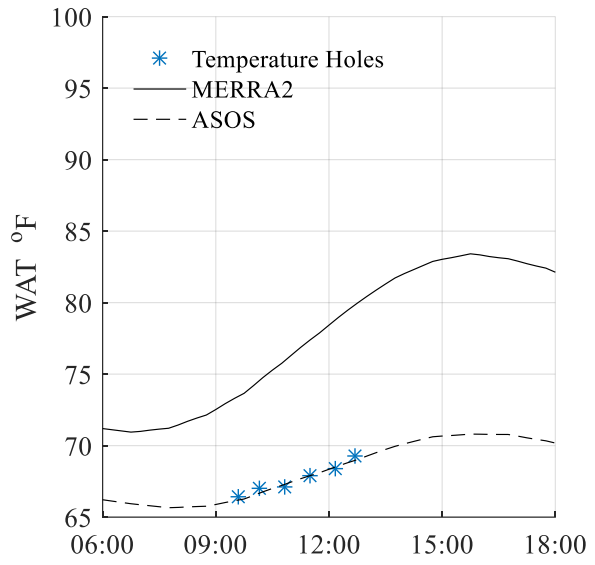
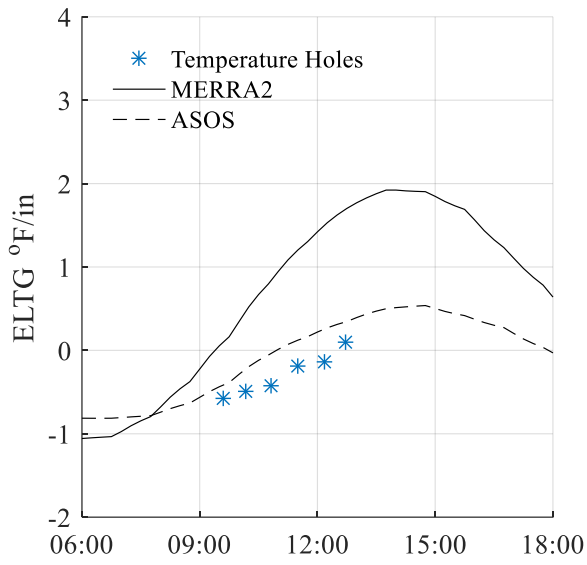


Figure 6.27. Comparison between measured and predicted temperature profile (39-0205, 9/9/2004)

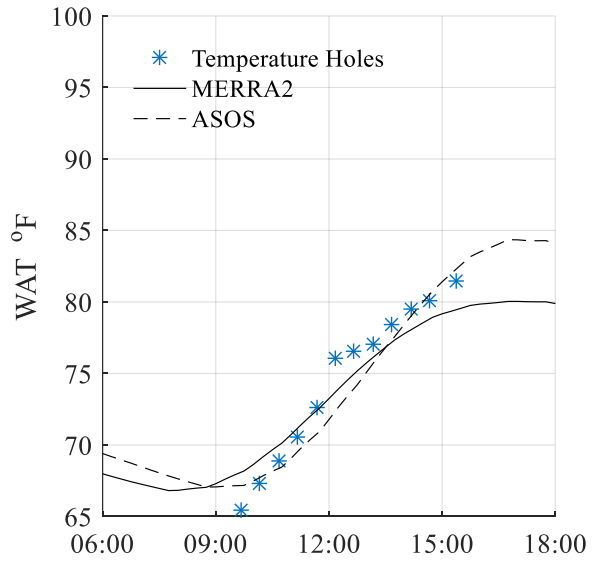
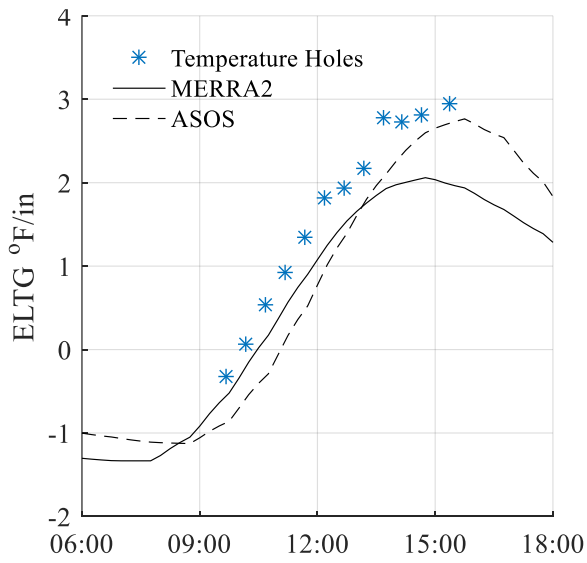


Figure 6.28. Comparison between measured and predicted temperature profile (39-0207, 9/21/2004)

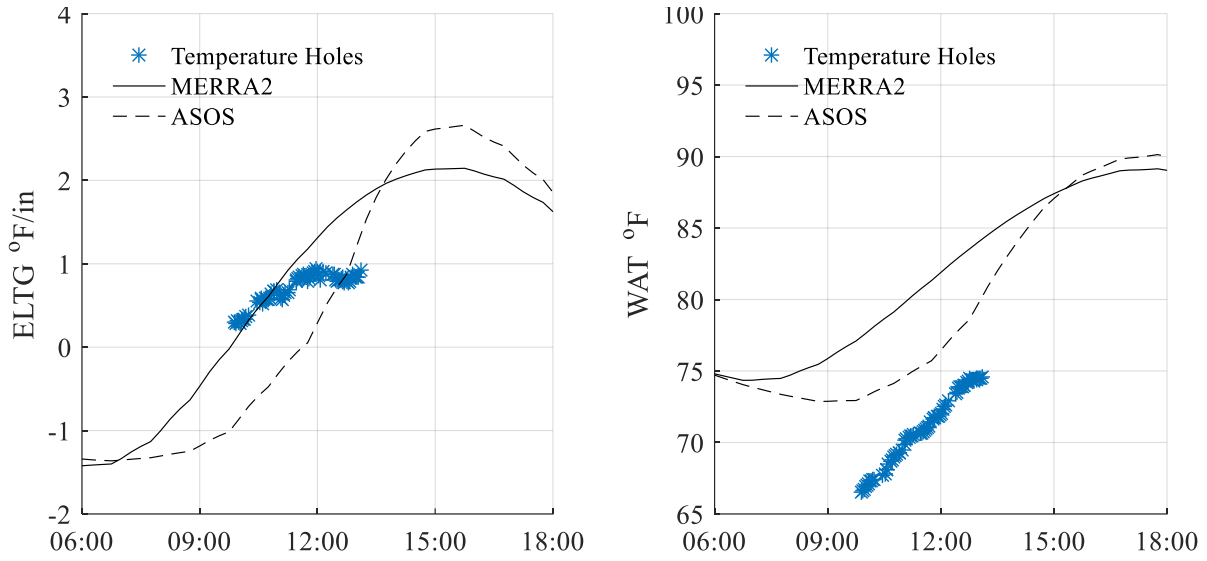


Figure 6.29. Comparison between measured and predicted temperature profile (39-0207, 6/5/2014)

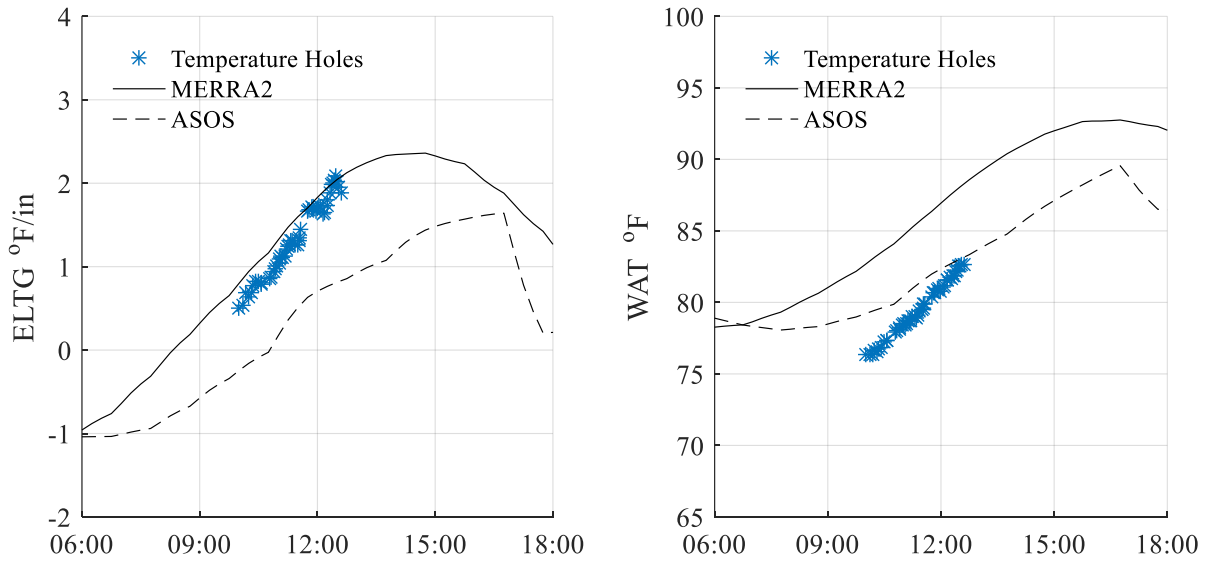


Figure 6.30. Comparison between measured and predicted temperature profile (39-0260, 6/3/2014)

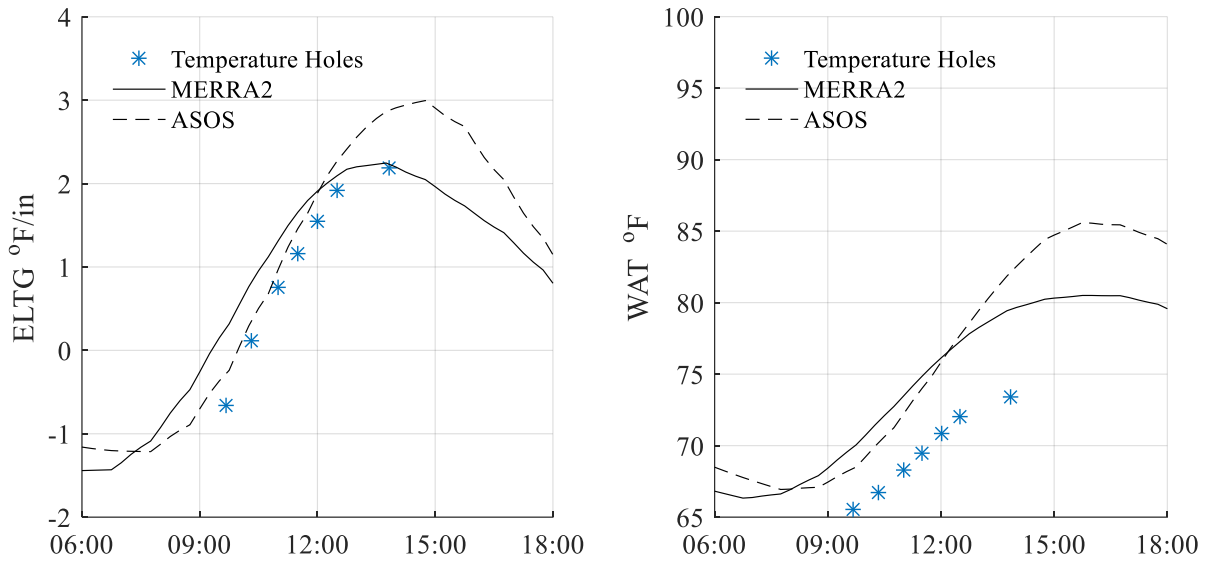


Figure 6.31. Comparison between measured and predicted temperature profile (39-0262, 9/21/2004)

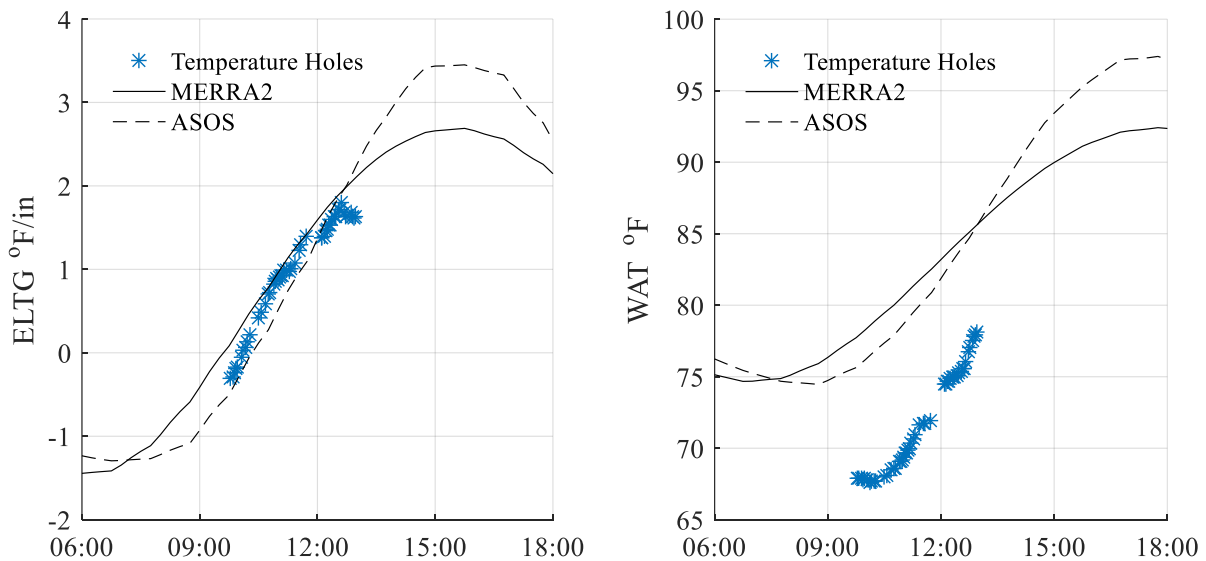


Figure 6.32. Comparison between measured and predicted temperature profile (39-0262, 6/6/2014)

The predicted WAT could vary from the measured WAT by as much as 8 °F. This could lead to testing being allowed when the joints are locked up, or valid testing not being considered for analysis. Due to this possibility of a large error, to avoid joint lockup, current recommendations

should be followed. For example, PennDOT 408 specifies testing should be restricted to times when the peak ambient temperature is less than 75 °F, regardless of the WAT prediction (PennDOT 2011).

Both datasets accurately predict the ELTG in the validation sections with a few exceptions. For example, analysis using the MERRA2 dataset over predicts both the ELTG and WAT during testing of LTPP 39-0205 on 9/9/2004. The FWD operator reported the sky condition as cloudy during testing. However, the MERRA2 dataset estimates that the weather was mostly sunny with a cloud cover of less than 10% during testing. The disagreement between the estimated cloud cover of the MERRA2 and ASOS datasets, shown in Table 6.8, demonstrates the difficulty in estimating cloud cover. Cloud cover is stochastic in nature, making it difficult to estimate using linear interpolation. One possible solution is to record shortwave radiation estimates on site, which could be accomplished by mounting a pyranometer on the roof of the FWD test vehicle. This instrument can provide direct estimates of shortwave radiation during testing. A second option is to have the FWD operator record the estimated cloud cover throughout testing. However, there are several drawbacks to this strategy. First, cloud cover is a subjective measurement that FWD operators are not trained to take. Also, cloud packing can lead to errors in estimating the cloud cover. The ASOS ceilometers measure straight up and the MERRA2 satellite measurements are directly looking down, allowing unbiased observation of cloud cover. The observation angle of distant clouds causes human observers to see more clouds than are present. An example of the cloud packing effect is shown in Figure 6.33.

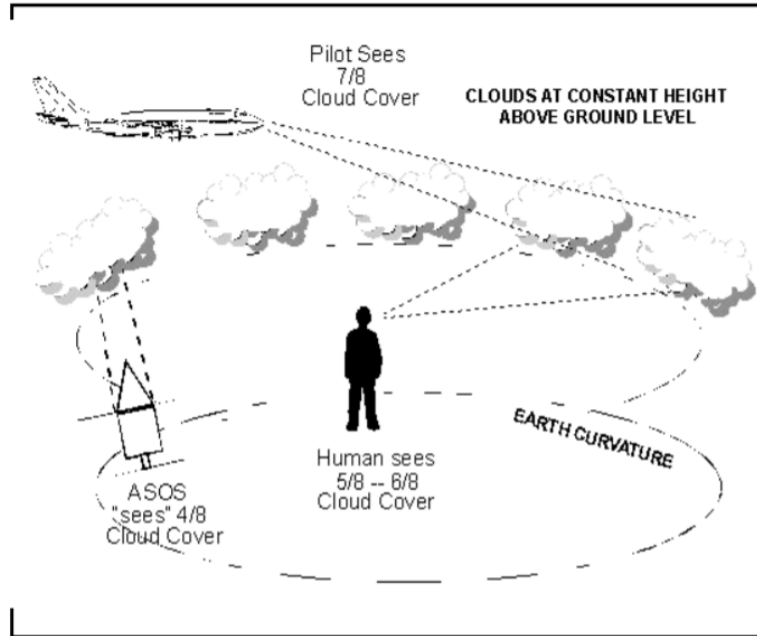


Figure 6.33. Cloud packing effect (Mannarano 1998)

Despite these issues, the observed cloud fraction can be used as a tool to effectively prevent large differences between the interpolated and on site shortwave radiation. The shortwave radiation can be adjusted for the observed cloud fraction using Equation 6.31.

$$Q_{adj} = R(A + B(1 - cf_{onsite})) \quad (6.31)$$

Where:

Q_{adj} = adjusted shortwave radiation to be used in temperature prediction

R = Extraterrestrial shortwave radiation

cf_{onsite} = cloud fraction estimated by the FWD operator

A, B = regression coefficients used in Equation 6.3

For example, during testing of LTPP Section 39-0205 on 9/9/2004, the FWD operator indicated the sky condition was overcast throughout testing period day. The shortwave radiation and cloud cover was estimated using Equation 6.31. The estimated ELTG and WAT using the corrected cloud cover can be seen in Figure 6.34.

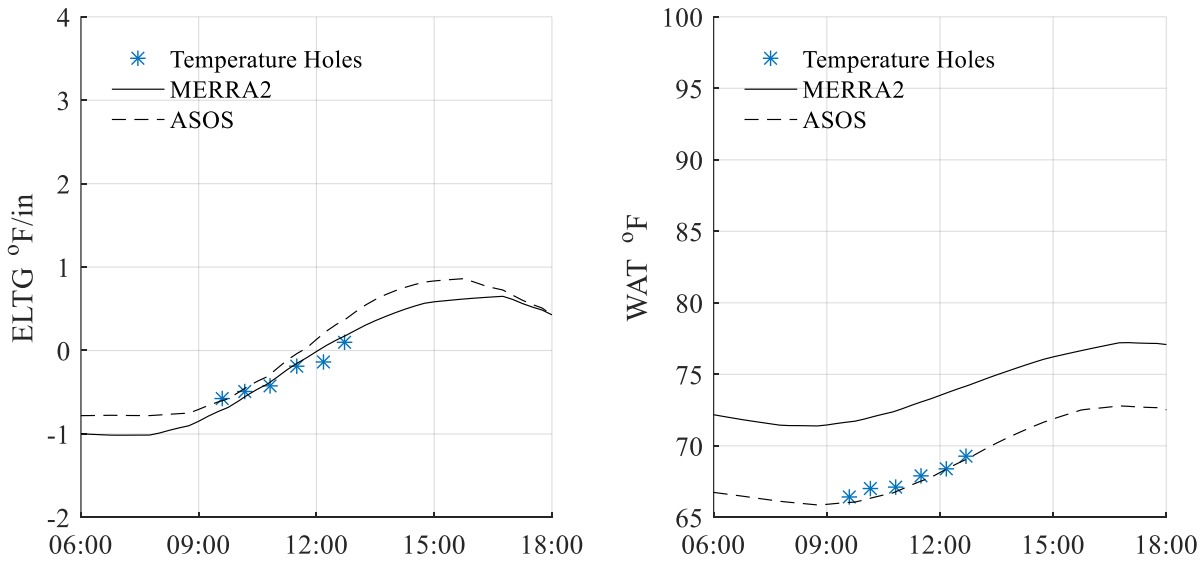


Figure 6.34. Example of improved performance of temperature prediction using estimated sky condition (LTPP Section 39-0205, 9/9/2004)

A comparison of Figure 6.27 and Figure 6.34 clearly shows that utilizing the cloud fraction estimated by the FWD operator improved the estimated temperature profile.

6.4 ALLOWABLE TESTING TIMES

In 3.0 , it was shown that slab curvature can cause inaccurate estimates of pavement layer stiffness when the ELTG exceeds 0.5 °F/in. However, an accurate estimate of the ELTG during testing can

only be determined after testing has occurred. To effectively schedule FWD testing while avoiding this threshold, it is necessary to estimate when the temperature gradient will be less than this threshold for both cloudy and sunny days. The temperature prediction model developed, utilizing the MERRA2 dataset, can estimate the threshold by simulating cloudy and sunny conditions on the day of interest.

Eleven locations near the geographic center of each PennDOT Engineering District were used in this analysis. Five structures were evaluated with concrete pavement thicknesses of 6, 8, 10, 12, and 14 in. Analyses were conducted for each day in the five year period of January 1, 2011 through December 31, 2015 for each structure. Each analysis uses 14 days of weather data ending on the day of interest. The first 13 days of the analysis use the measured weather data from the MERRA2 dataset. The fourteenth day was adjusted to be completely cloudy (CF=1.0), for the cloudy day analyses, or completely sunny (CF=0.0), for the sunny day analyses. The shortwave radiation corresponding to the assumed cloud cover is calculated using Equation 6.32.

$$Q_{adj} = R \left(A + 294294B(1 - CF_{analysis}) \right) \quad (6.32)$$

Where:

$CF_{analysis}$ = cloud fraction corresponding to the analysis (1.0 for cloudy day analyses and 0.0 for sunny day analyses)

The measured ambient temperature, wind speed, and relative humidity were used on the fourteenth day. The estimated ELTG on the fourteenth day (the day of interest) was recorded at 15-minute intervals. This process was repeated for each day in the five-year analysis period at each location, for each structure, and for cloudy and sunny days resulting in a total of over 200,000 analyses.

The 95% prediction interval could then be calculated at each location for each structure for every 15-minute interval in a year. The recorded data was divided based on the date of the day of interest and the time of day. For each 15-minute interval on each day of the year, all the data within one week of the day was pooled into a sample with 70 observations (14 days over 5 years). The single-sided 95% Bonferroni prediction interval was calculated for each of these samples, using Equation 6.33.

$$ELTG_{pred} < \overline{ELTG} + t_{95,69}\sigma_{ELTG} \left(1 + \sqrt{\frac{1}{70}} \right) \quad (6.33)$$

Where:

$ELTG_{pred}$ = predicted ELTG

\overline{ELTG} = mean ELTG in the sample

$t_{95,69}$ = t-variate at a 95% confidence level with 69 degrees of freedom

σ_{ELTG} = standard deviation of the ELTG in the sample.

The time of day the 95% prediction interval crosses the 0.5 °F/in threshold in the morning and afternoon was then calculated using linear interpolation. However, the date of daylight saving time changes each year, which causes errors if daylight saving time is considered when estimating the threshold times. Therefore, the threshold times were all calculated in Eastern Standard Time (Universal Time Coordinated (UTC) -5 hours). These threshold times were then plotted against the day of the year. Noise in these plots were reduced using LOWESS smoothing with a bandwidth of 10% of the data points (Royston 1992). The resulting plots are shown in Figures 6.35 to 6.56.

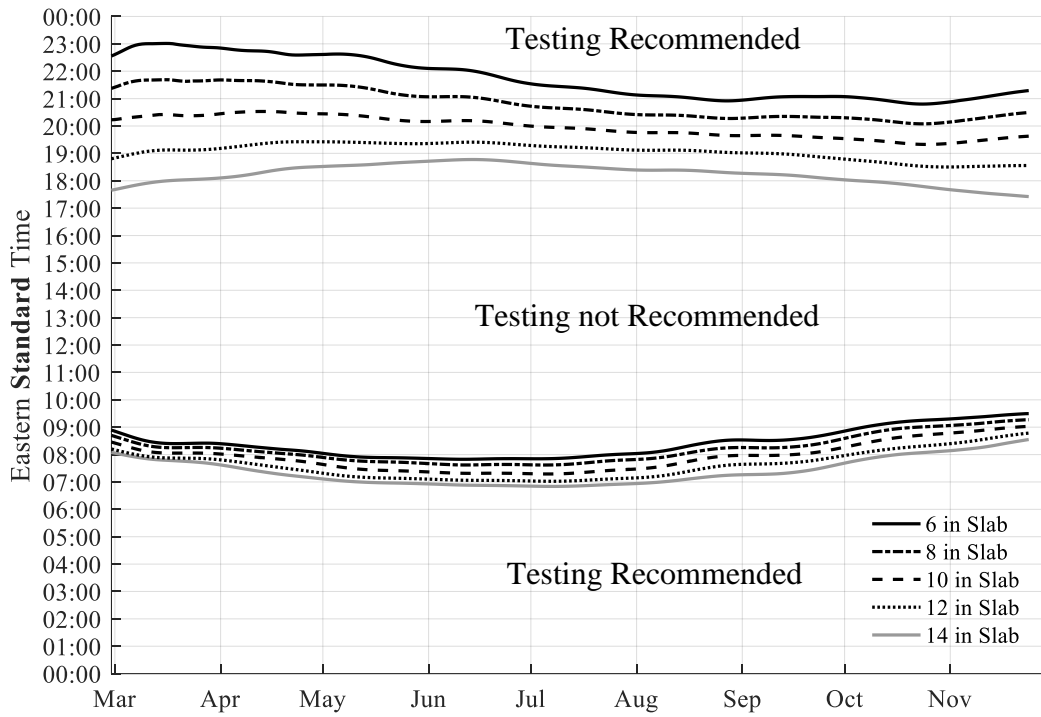


Figure 6.35. Allowable testing times for PennDOT Engineering District 1 (sunny days)

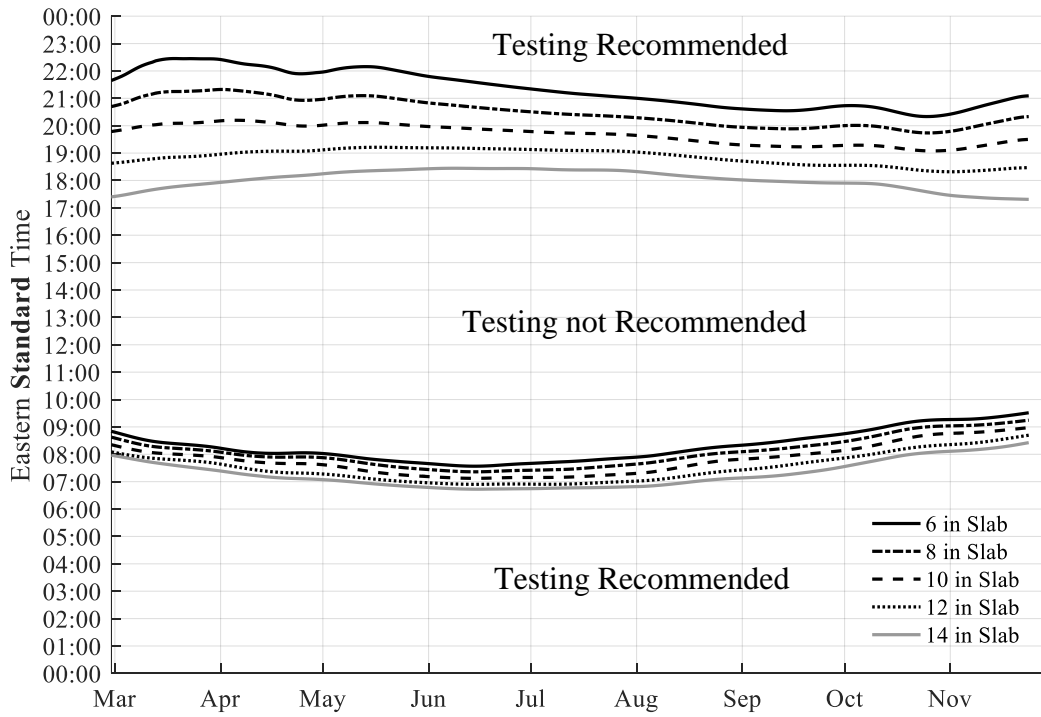


Figure 6.36. Allowable testing times for PennDOT Engineering District 2 (sunny days)

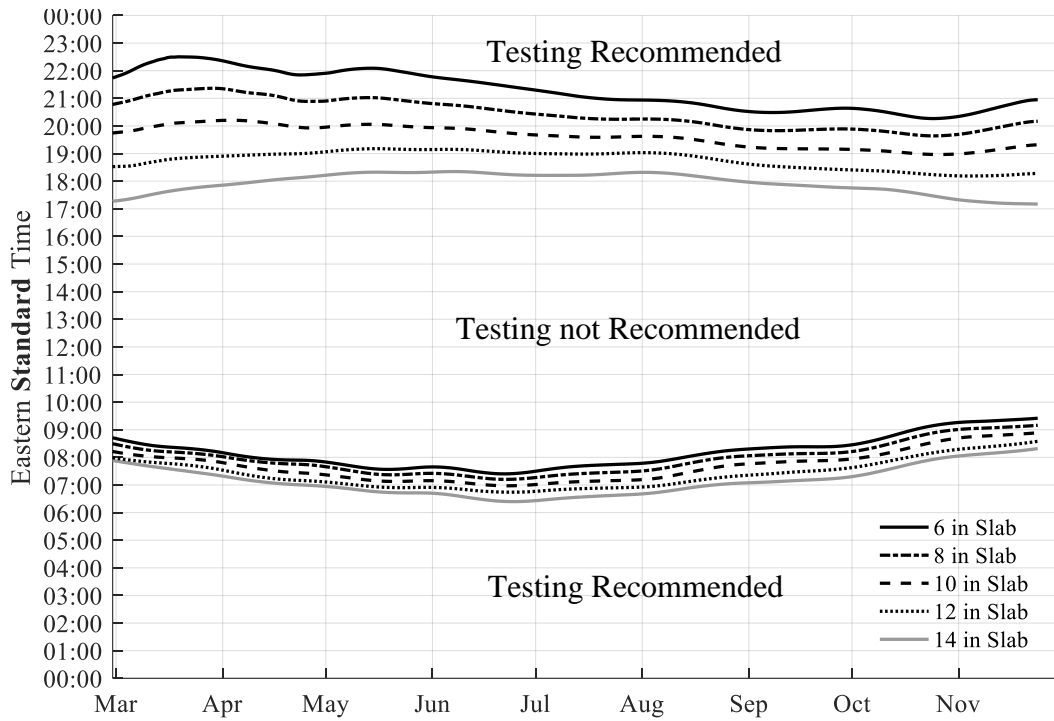


Figure 6.37. Allowable testing times for PennDOT Engineering District 3 (sunny days)

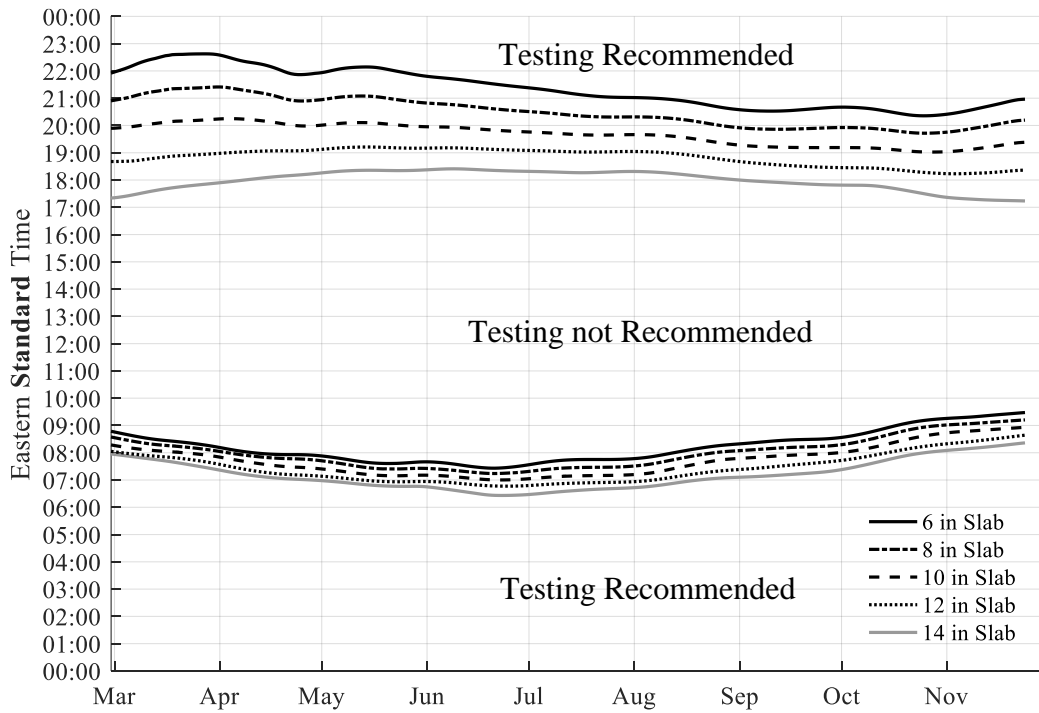


Figure 6.38. Allowable testing times for PennDOT Engineering District 4 (sunny days)

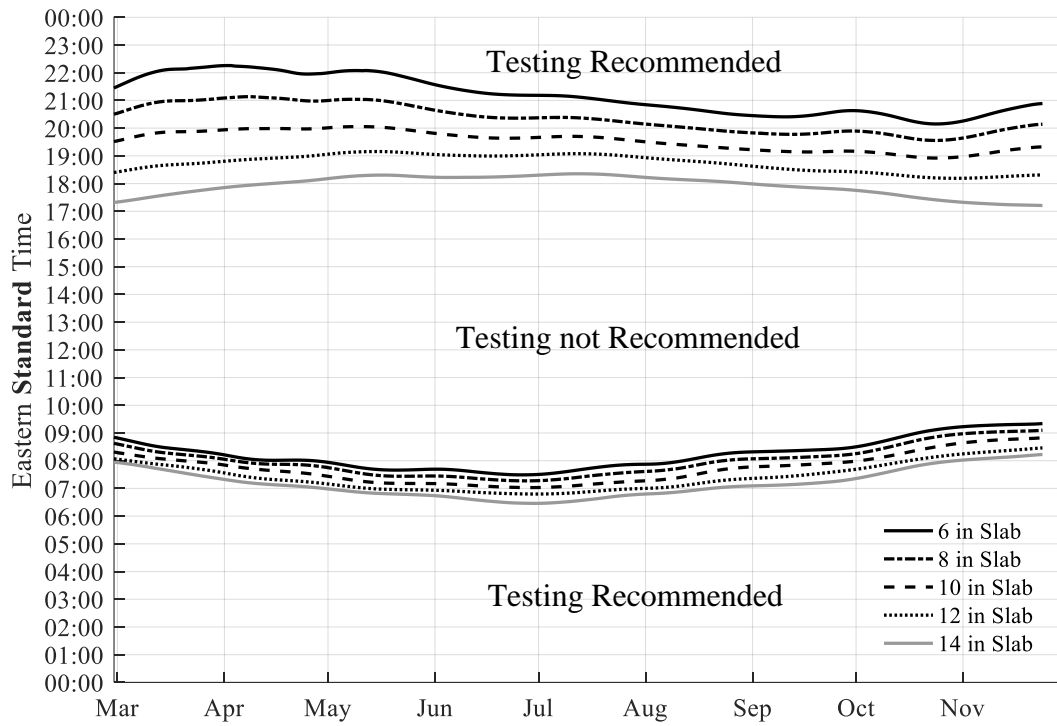


Figure 6.39. Allowable testing times for PennDOT Engineering District 5 (sunny days)

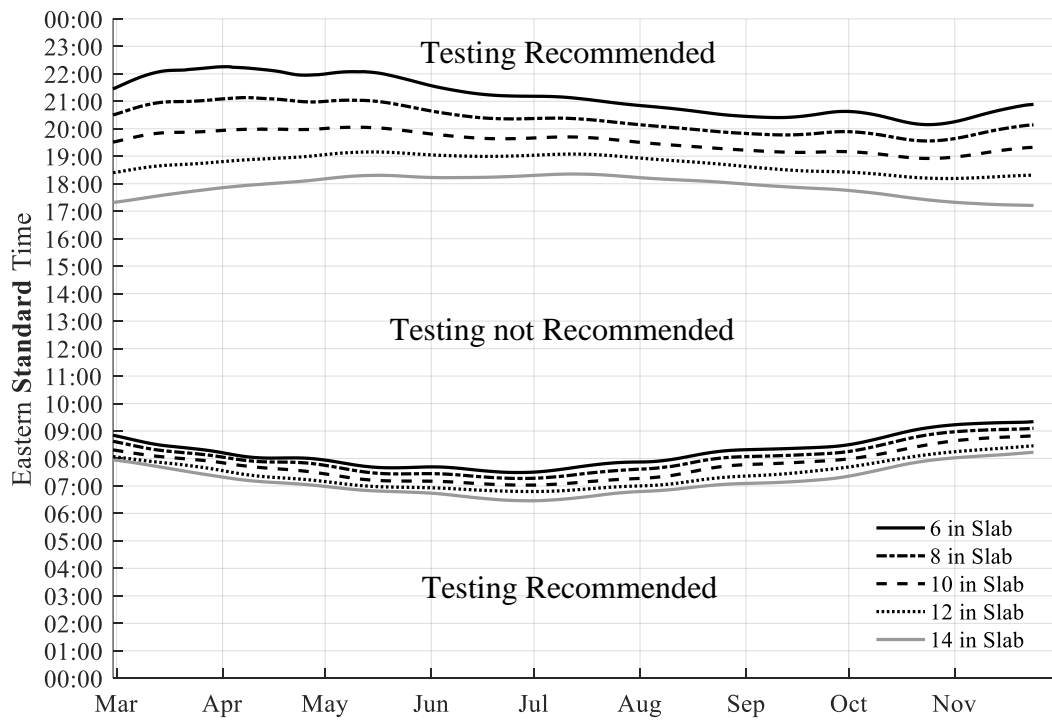


Figure 6.40. Allowable testing times for PennDOT Engineering District 6 (sunny days)

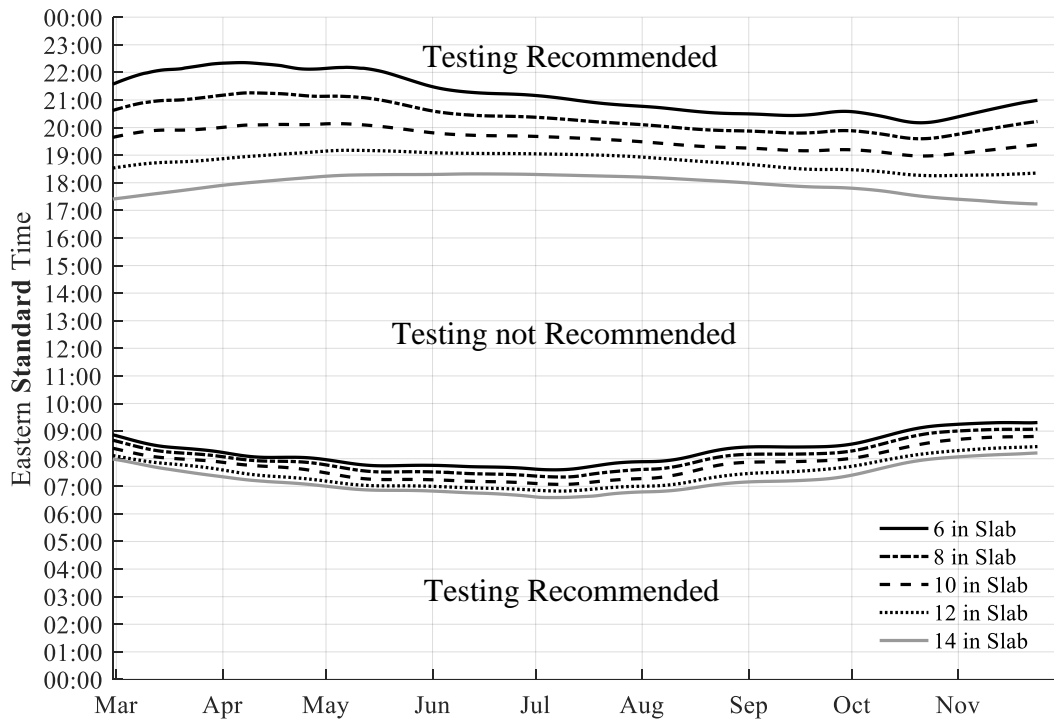


Figure 6.41. Allowable testing times for PennDOT Engineering District 8 (sunny days)

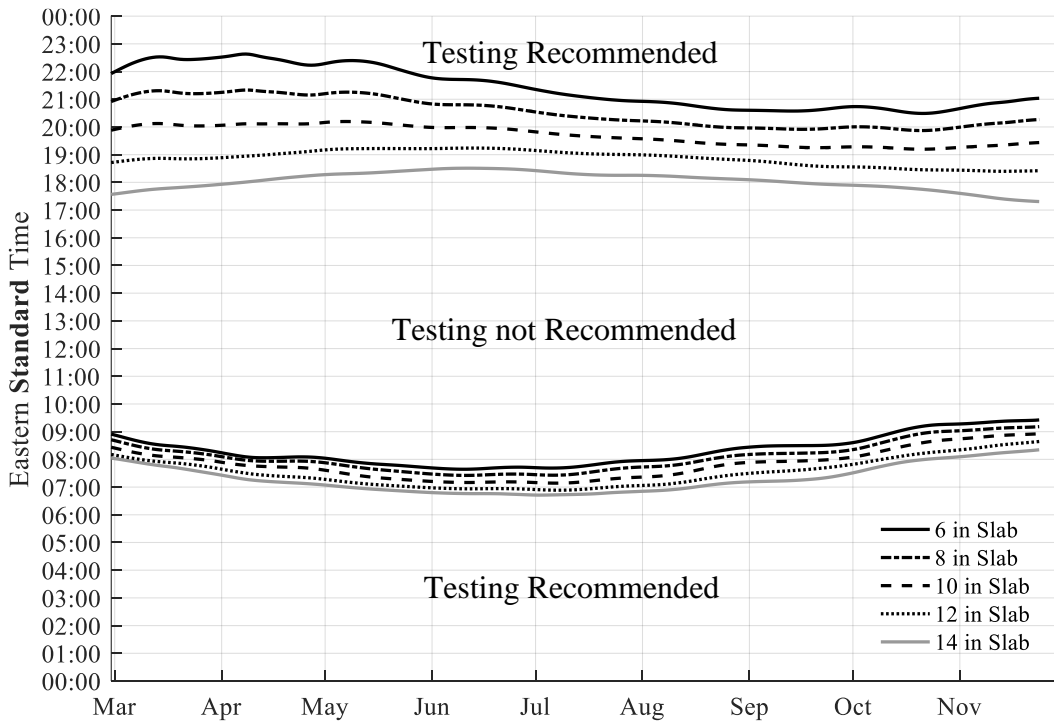


Figure 6.42. Allowable testing times for PennDOT Engineering District 9 (sunny days)

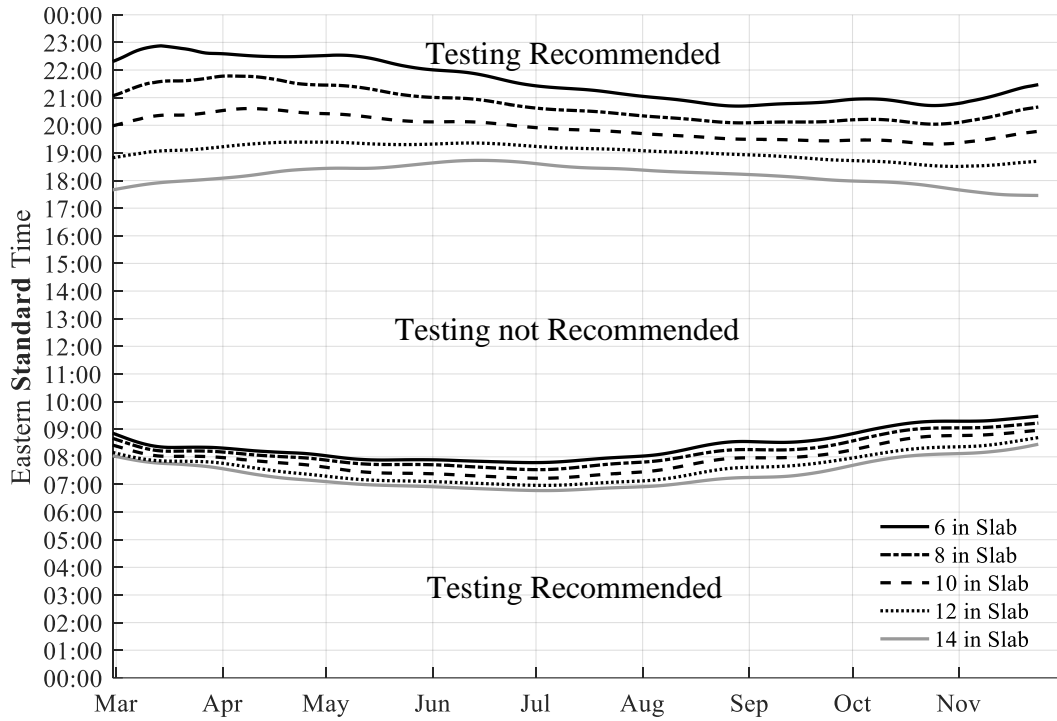


Figure 6.43. Allowable testing times for PennDOT Engineering District 10 (sunny days)

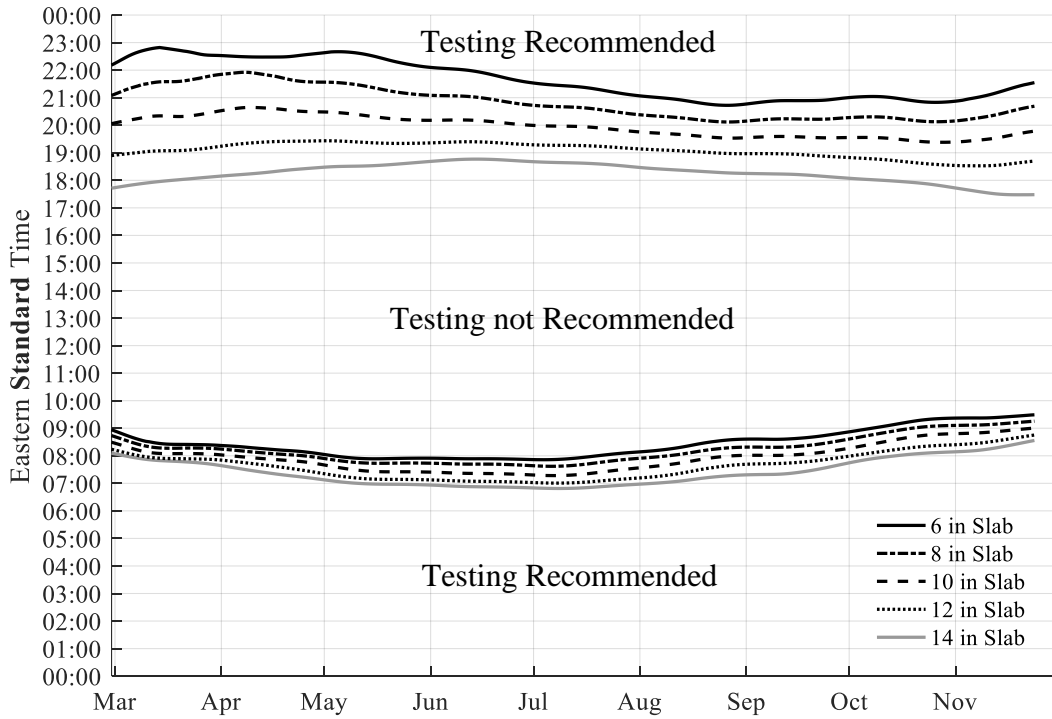


Figure 6.44. Allowable testing times for PennDOT Engineering District 11 (sunny days)

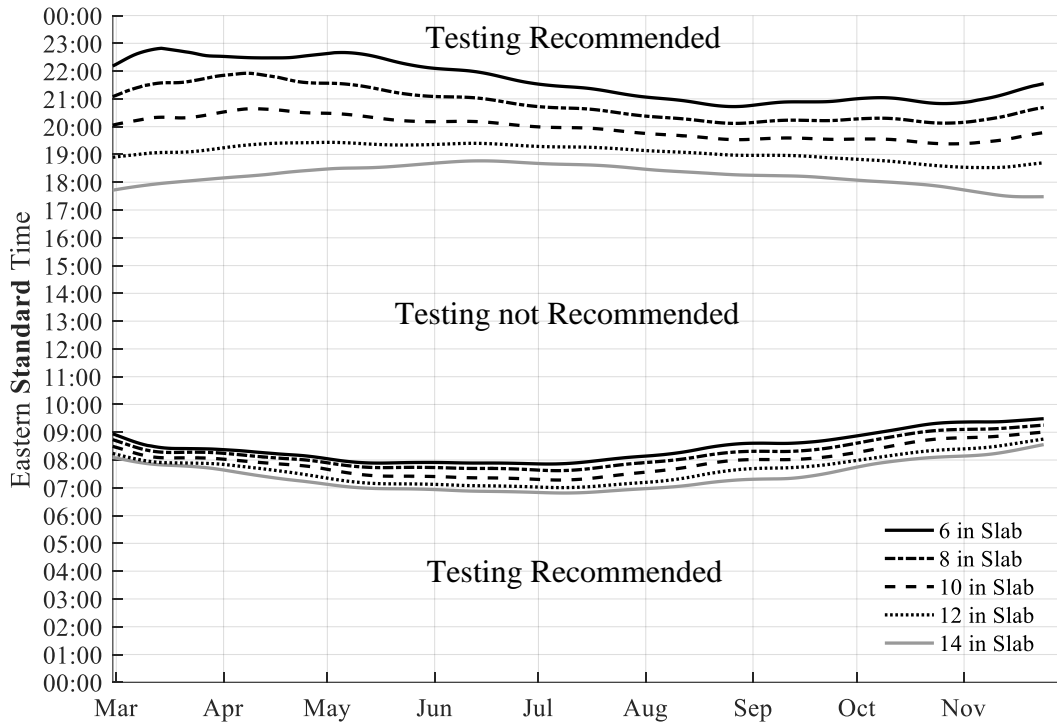


Figure 6.45. Allowable testing times for PennDOT Engineering District 12 (sunny days)

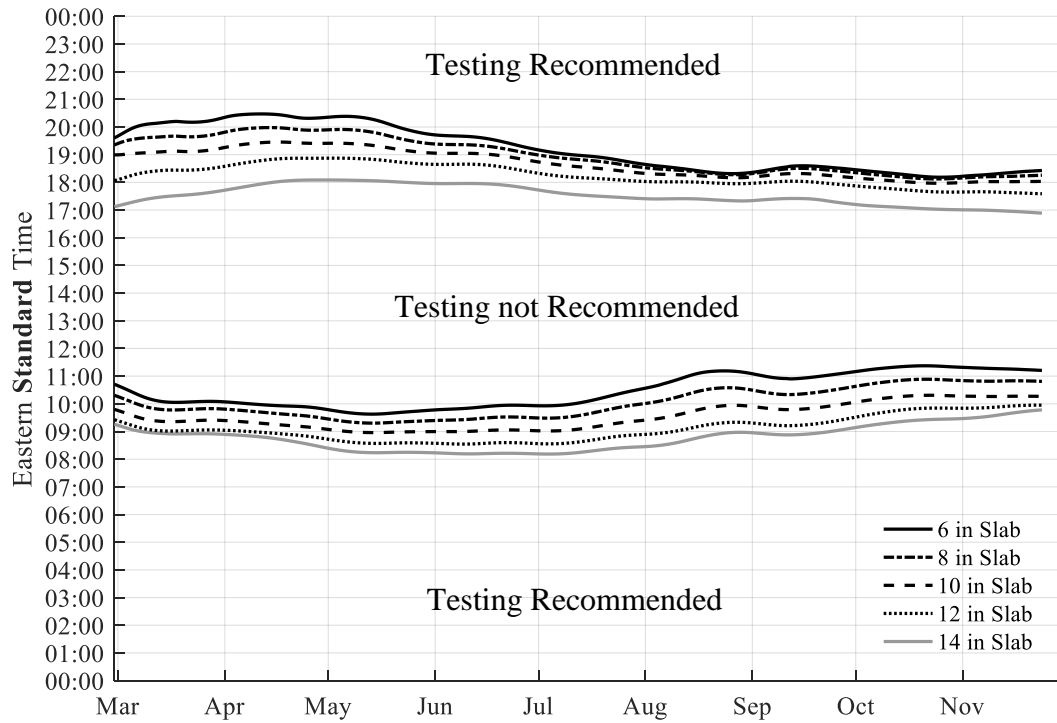


Figure 6.46. Allowable testing times for PennDOT Engineering District 1 (cloudy days)

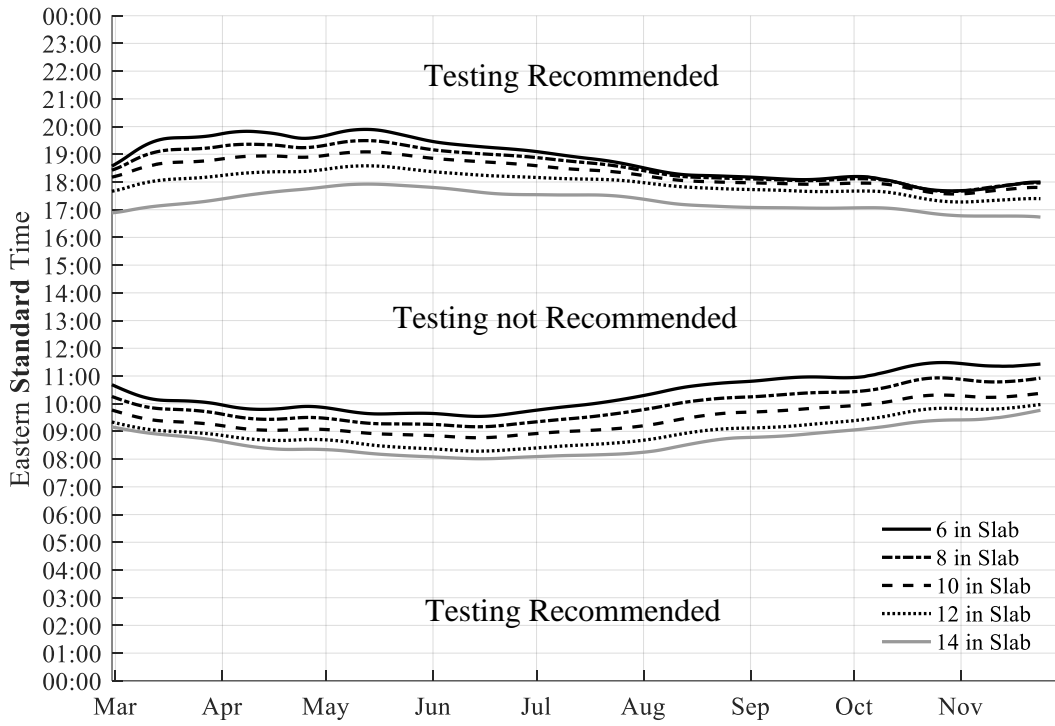


Figure 6.47. Allowable testing times for PennDOT Engineering District 2 (cloudy days)

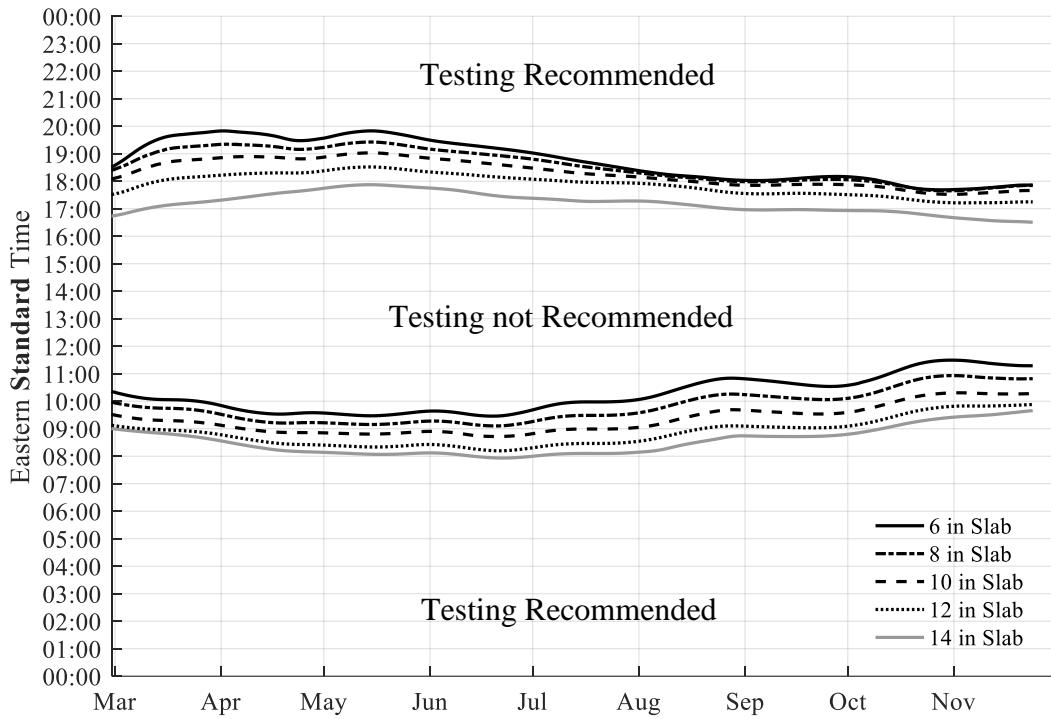


Figure 6.48. Allowable testing times for PennDOT Engineering District 3 (cloudy days)

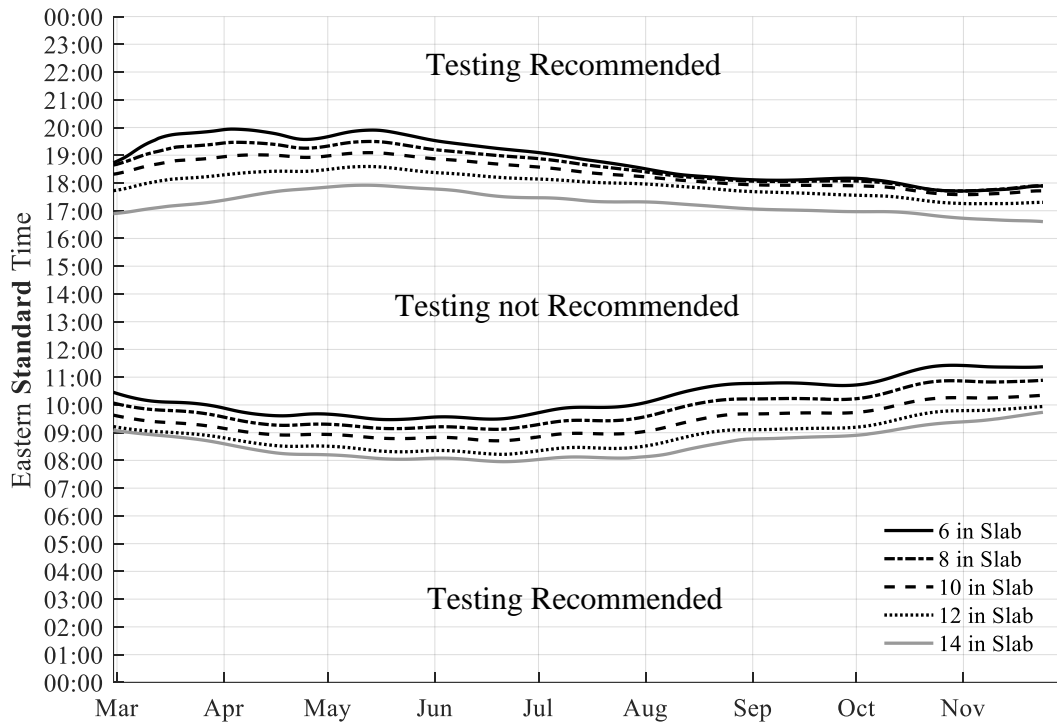


Figure 6.49. Allowable testing times for PennDOT Engineering District 4 (cloudy days)

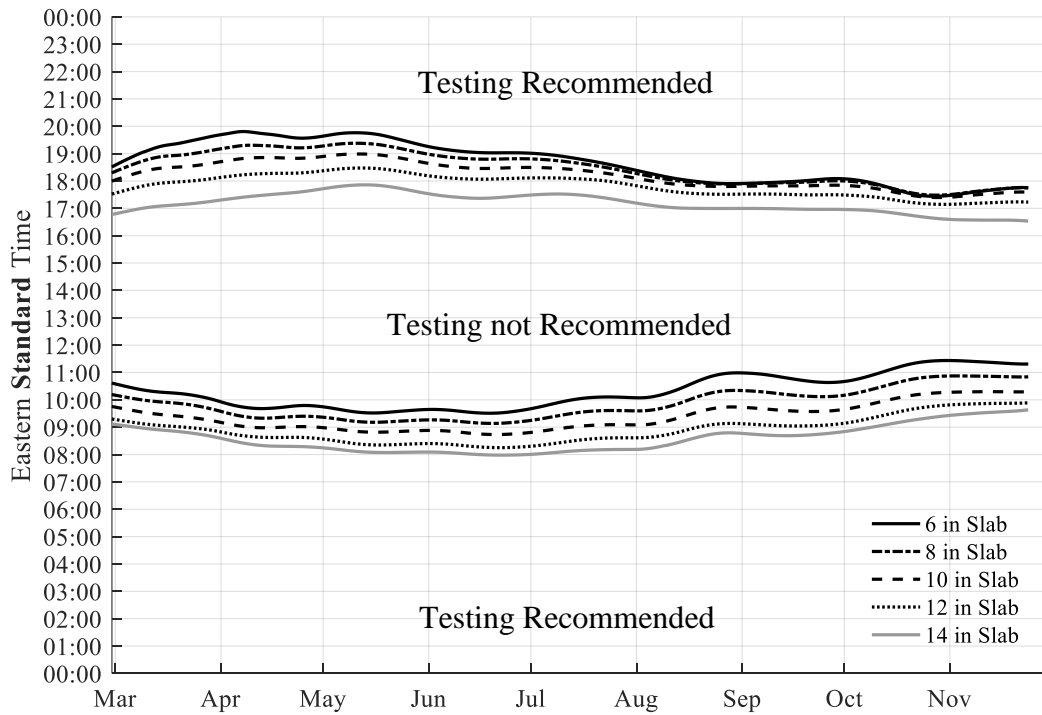


Figure 6.50. Allowable testing times for PennDOT Engineering District 5 (cloudy days)

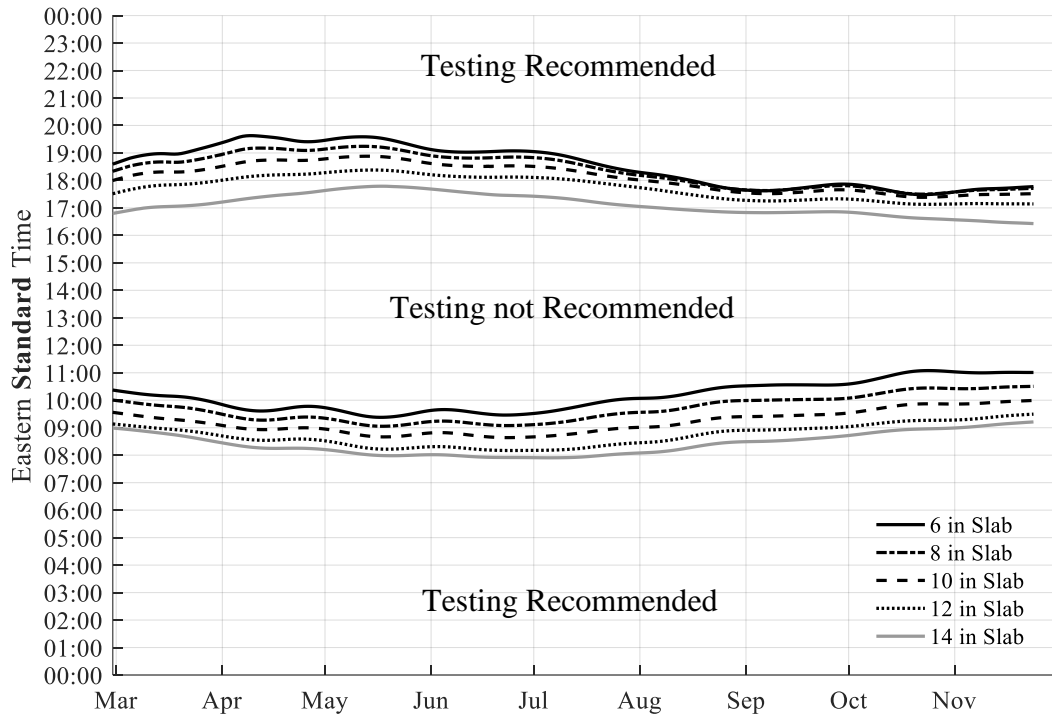


Figure 6.51. Allowable testing times for PennDOT Engineering District 6 (cloudy days)

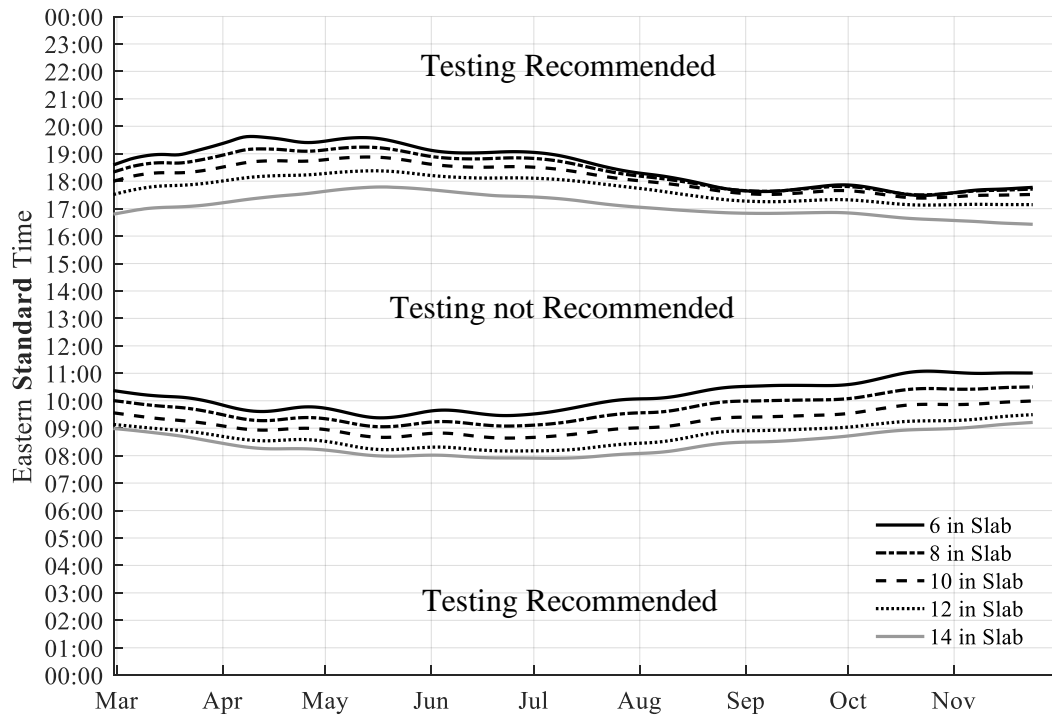


Figure 6.52. Allowable testing times for PennDOT Engineering District 8 (cloudy days)

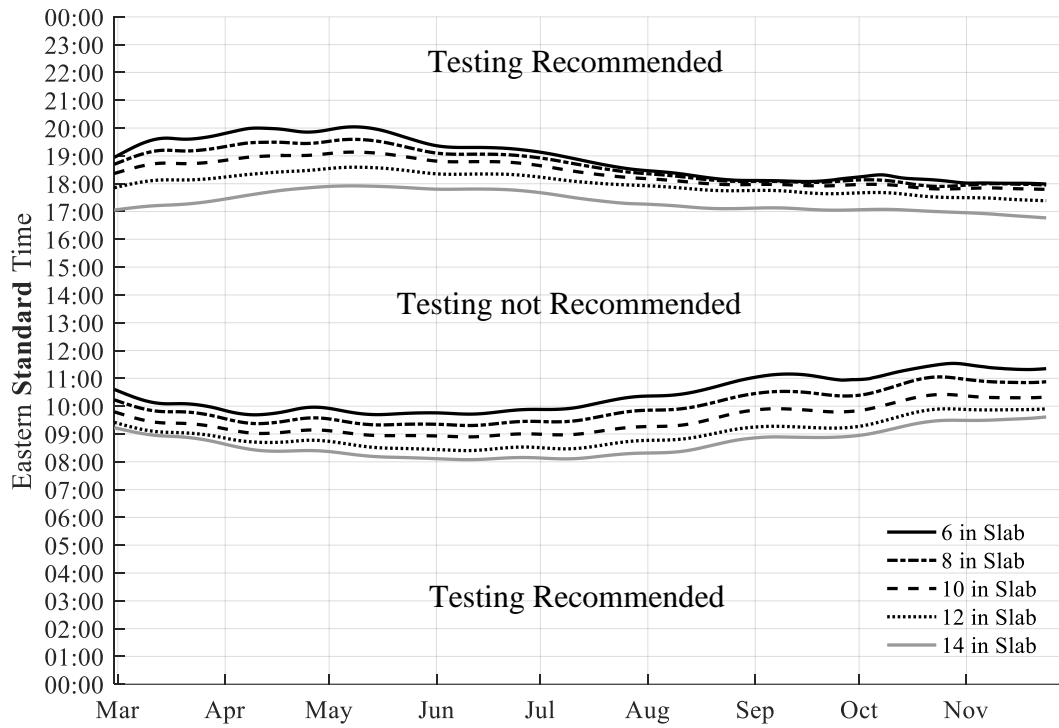


Figure 6.53. Allowable testing times for PennDOT Engineering District 9 (cloudy days)

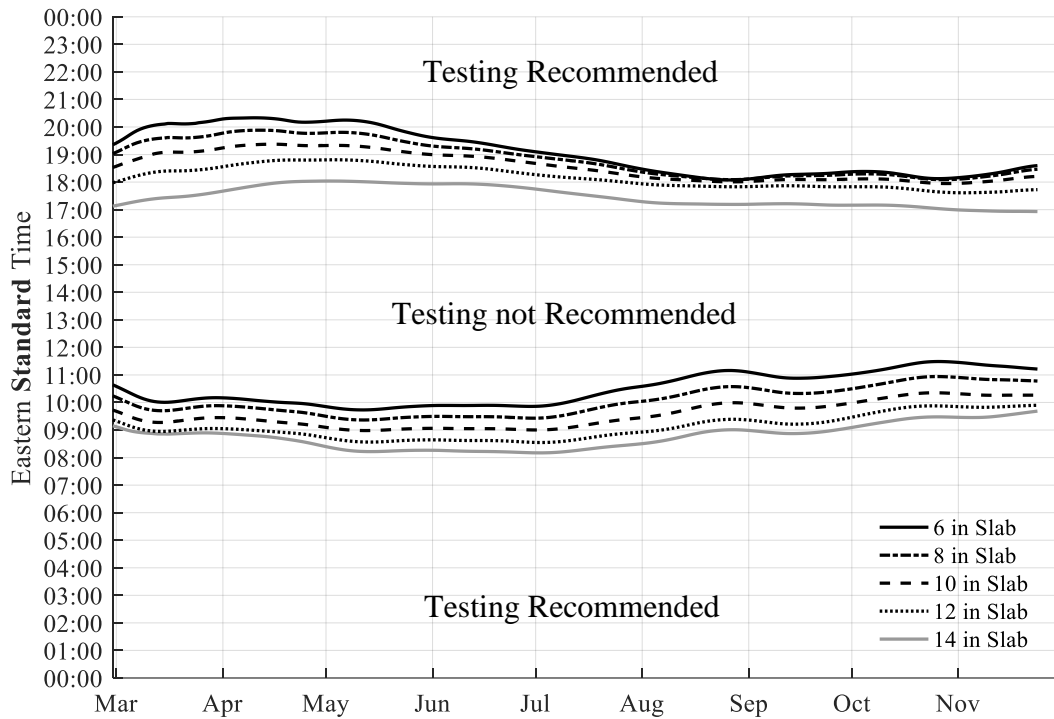


Figure 6.54. Allowable testing times for PennDOT Engineering District 10 (cloudy days)

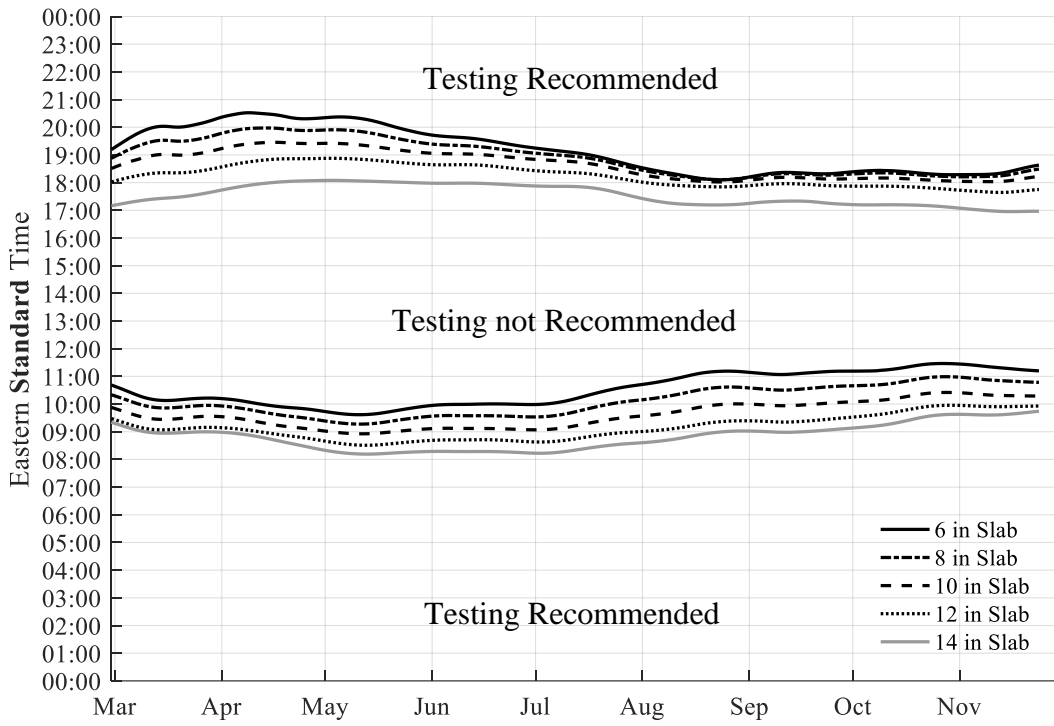


Figure 6.55. Allowable testing times for PennDOT Engineering District 11 (cloudy days)

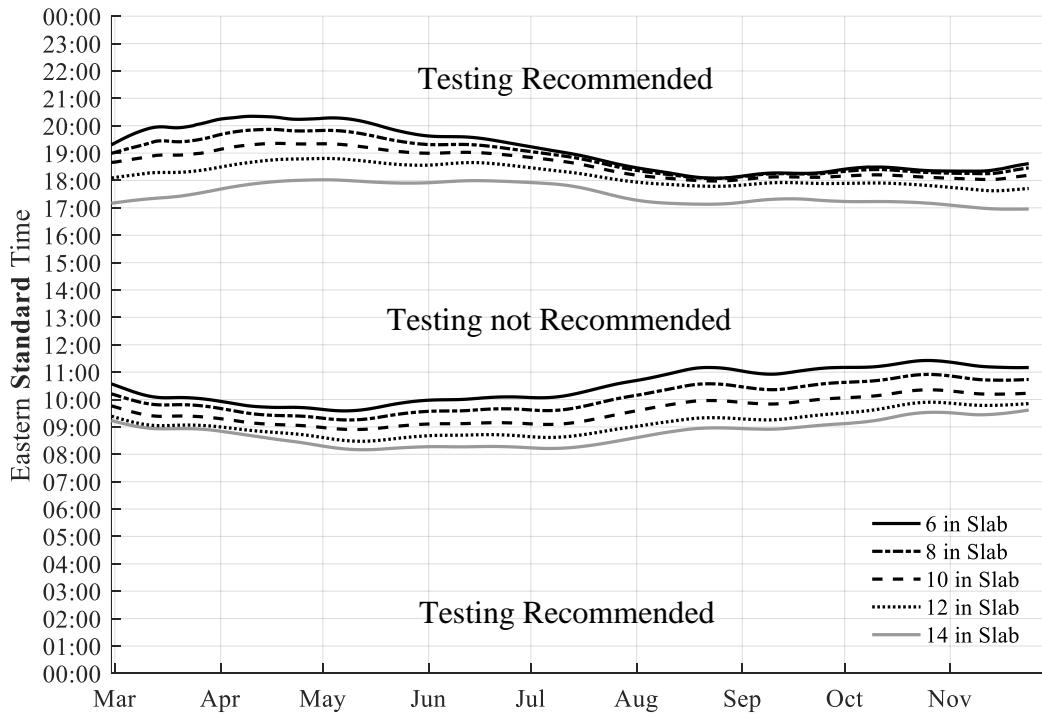


Figure 6.56. Allowable testing times for PennDOT Engineering District 12 (cloudy days)

The analysis indicates thicker structures allow for slightly later testing at midslab in the morning but require testing at midslab to occur later in the evening. Geographical location causes a small difference in these plots. Thresholds for allowable testing times in District 6 (near Philadelphia) are approximately 20 minutes earlier than the allowable testing times in District 11 (near Pittsburgh). This corresponds with the sunrise in Pittsburgh occurring approximately 20 minutes later than the sunrise in Philadelphia.

6.5 CONCLUSION

A temperature prediction model has been developed to accurately estimate the temperature profile of a concrete pavement during FWD testing. This model can utilize the MERRA2 or ASOS datasets and requires slightly different material properties based on the specific dataset to produce correct results. It should be noted that the sections used for this analysis were primarily on the eastern half of the United States. Recalibration may be necessary for use in the Western United States or internationally. The MERRA2 dataset tends to generate more accurate predictions of the pavement temperature profile than the ASOS dataset. There are some instances where interpolation from the datasets does not accurately represent the cloud cover conditions at the pavement location during testing. This is likely due to the stochastic nature of cloud cover and could be addressed by installing a pyranometer on the roof of the FWD test vehicle, such that the shortwave radiation during testing is measured directly. Finally, the MERRA2 dataset was used to estimate times in which the ELTG is less than 0.5 °F/in, which is required to accurately backcalculate pavement layers using FWD testing results.

7.0 CONCLUDING REMARKS AND FUTURE WORK

In this research effort the effect of slab curvature during FWD testing was evaluated for the backcalculated k-value, LTE, DD, and the detection of voids. This research effort found that the backcalculated k-value using previous methods will decrease as ELTG increases for ELTGs greater than 0.5 °F/in. The magnitude of this effect depends on the “true” stiffness of the foundation. The backcalculated k-value is relatively insensitive to slab curvature for pavements on a weak foundation. However, the backcalculated k-value is very sensitive to k-value for a stiff foundation. When a large positive ELTG is present, the k-value has only a negligible effect on the deflection basin. Therefore, it is not possible to accurately backcalculate the k-value when a positive ELTG is present using FWD tests at midslab. A model was developed that allows backcalculation to be performed using FWD testing in the wheelpath on the leave side of the joint when a positive ELTG is present.

This research determined that for doweled JPCP pavements LTE is at a minimum when the slab is approximately flat and increases as the ELTG increases or decreases. For slabs with little looseness around the dowel, the maximum DD occurs when the slab is approximately flat and decreases when large positive or negative ELTGs are present. For slabs with significant dowel looseness, the maximum DD occurs when a negative ELTG is present. A computational analysis shows that discreetly modeling a gap around the dowel to simulate dowel looseness is able to capture this phenomenon. However, this model does not replicate field data directly. Future

research is required to determine the best method of modeling the interaction between dowels and the surrounding concrete. One possible approach would be to use non-linear or piecewise linear spring between the dowel and the concrete.

The relationship between LTE and DD and k-value was evaluated using a logistic regression model to predict the probability that a fault greater than 0.12 in will develop. With raw LTE and DD values, DD is a statistically significant predictor of faulting at the 95% confidence level. However, LTE is not a statistically significant predictor. If the parameters are adjusted for ELTG, both parameters are statistically significant predictors at the 95% confidence level. One limitation to evaluating the relationship between LTE and DD and faulting is that very few joints in the LTPP database faulted. In the future, as more states continue to develop pavement management systems (PMS), a more robust dataset for evaluating the relationship between these parameters and faulting may be available.

A void detection model was developed, which predicts the probability of a void while accounting for curling and warping. A major challenge in developing this model is developing the physical void locations. The method developed for this analysis was only able to estimate void locations with enough accuracy for training the model at test sections where many FWD tests were performed. The model performs better on a test set developed using the currently available models at all ranges of temperature gradients on this test set. The necessity for frequent repetitive testing to establish the void locations with enough certainty to be used in training limited the database to 14 test sections, and prevented factors such as the joint spacing, or an estimate of moisture warping to be included in the model. In the future, it may be possible to develop another method of non-destructive testing for identifying whether voids occur, which is independent of FWD testing. This

method could be used to develop a more robust database for developing a statistical model to detect voids.

A temperature prediction model was developed to estimate the pavement temperature profile during FWD testing, utilizing both the ASOS and MERRA2 data sources. The MERRA2 dataset, which contains a direct estimate of incoming shortwave radiation reaching the ground, resulted in a better prediction of the temperature gradient at each of the five tuning and validation sections. The predicted ELTG using the temperature prediction model performs well on most days. However, due to the stochastic nature of cloud cover, there are some days where the cloud cover at the testing location does not match the cloud cover at the ASOS weather stations or the MERRA2 grid points. This can lead to inaccurate ELTG predictions. One method of lowering this error would be to install a Pyranometer on the roof of the FWD test van to record the shortwave radiation during testing. Another option would be to have the FWD operator manually estimate the cloud cover during testing. Using the FWD operator estimated cloud cover in the analysis increased the accuracy of the model on an example test date. However, there is not sufficient data available for a robust validation of these possible improvements. In the future, it may be necessary to adjust the tuned thermal material properties, if shortwave radiation measured by the pyranometer is biased from the shortwave radiation from the MERRA2 dataset or measured from the ASOS dataset.

All of the statistical models and tools developed in this research have been packaged into the University of Pittsburgh FWD Analysis of Concrete Slabs (Pitt-FACS) web tool. This tool will provide engineers a user-friendly method to utilize the research to more accurately make pavement rehabilitation and design decisions. The User's Manual of the web tool can be seen in Appendix B.

APPENDIX A

DAILY PLOTS OF TEMPERATURE PREDICTIONS AT VALIDATION SECTIONS

MNROAD CELL 52

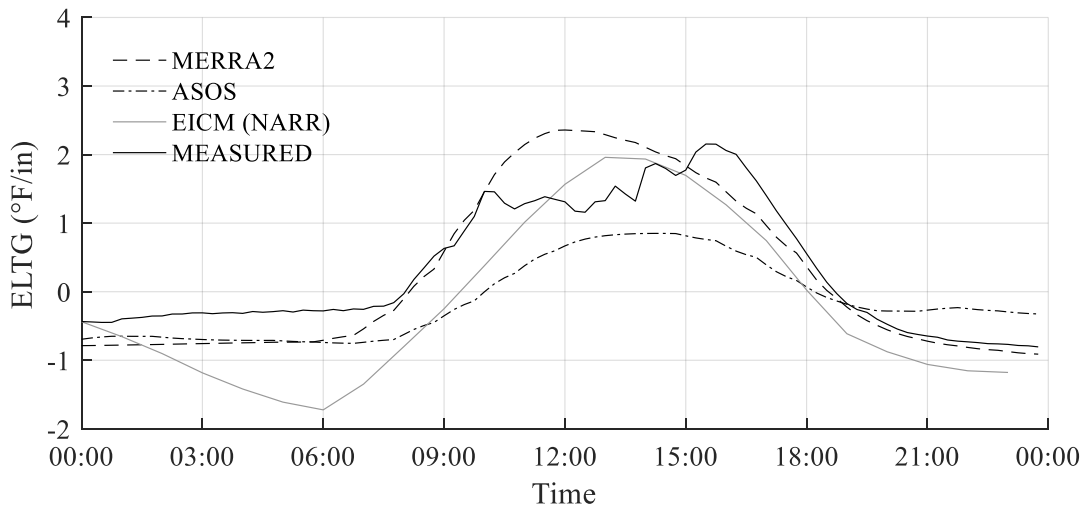


Figure A.1. MnROAD Cell 52 (4/1/2011)

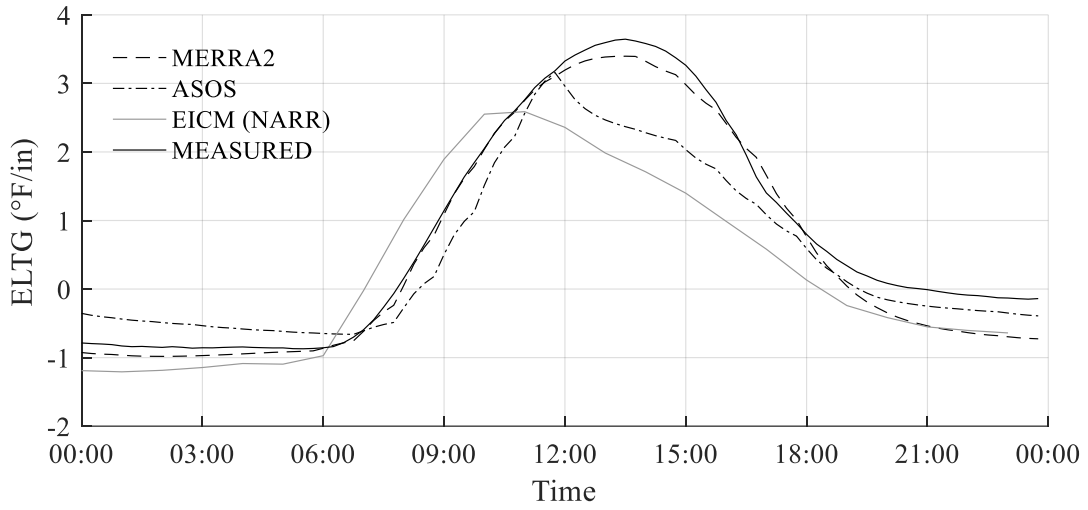


Figure A.2. MnROAD Cell 52 (4/1/2011)

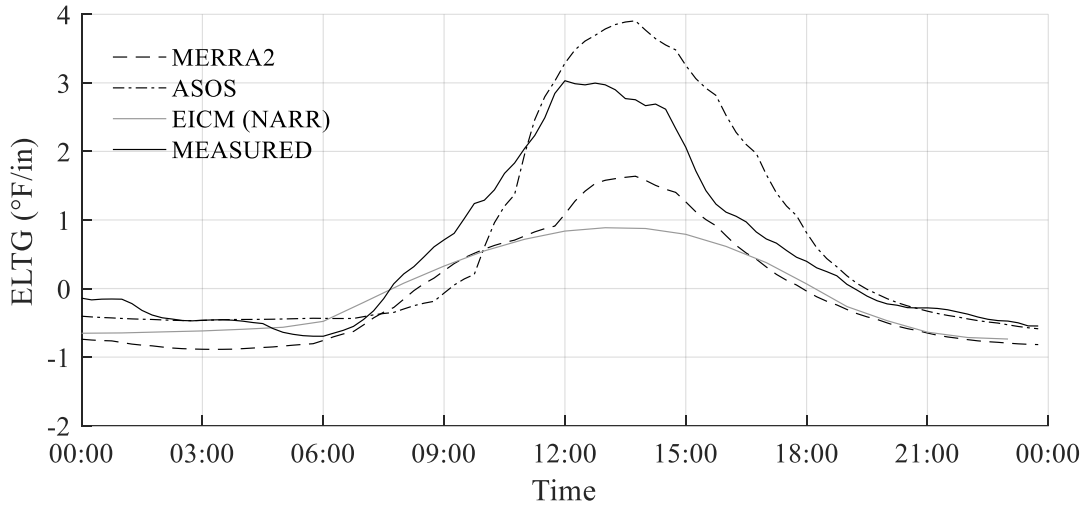


Figure A.3. MnROAD Cell 52 (4/3/2011)

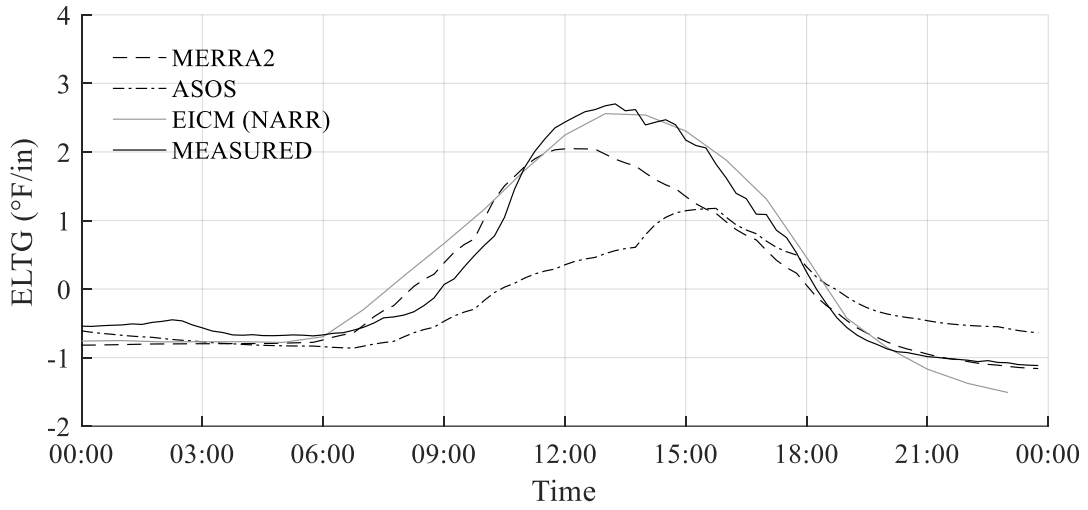


Figure A.4. MnROAD Cell 52 (4/4/2011)

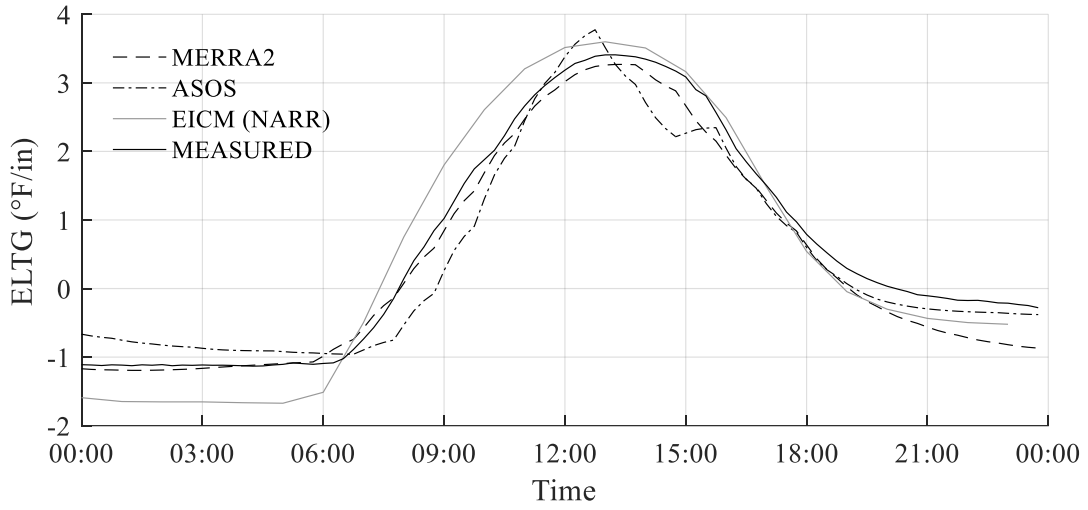


Figure-A.5. MnROAD Cell 52 (4/5/2011)

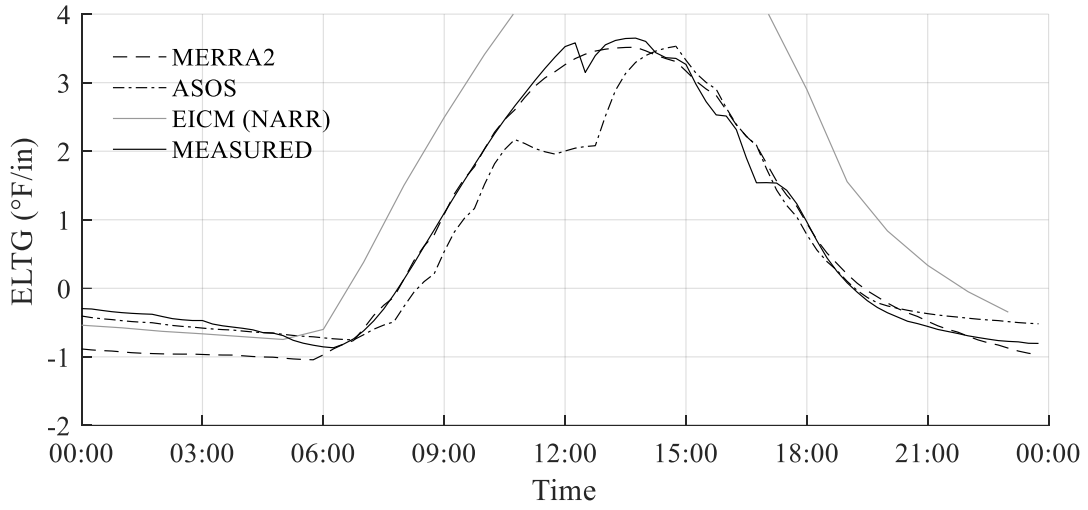


Figure A.6. MnROAD Cell 52 (4/6/2011)

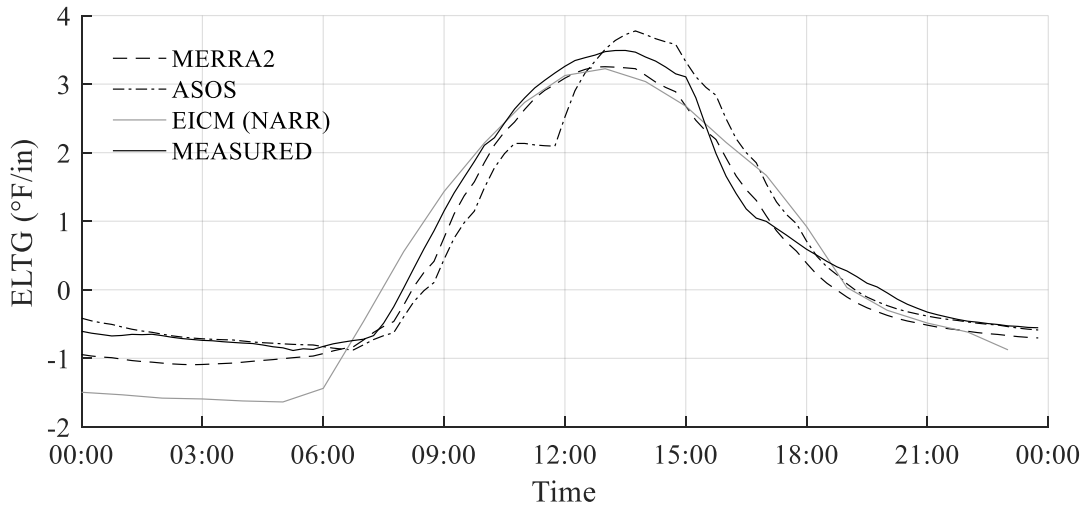


Figure A.7. MnROAD Cell 52 (4/8/2011)

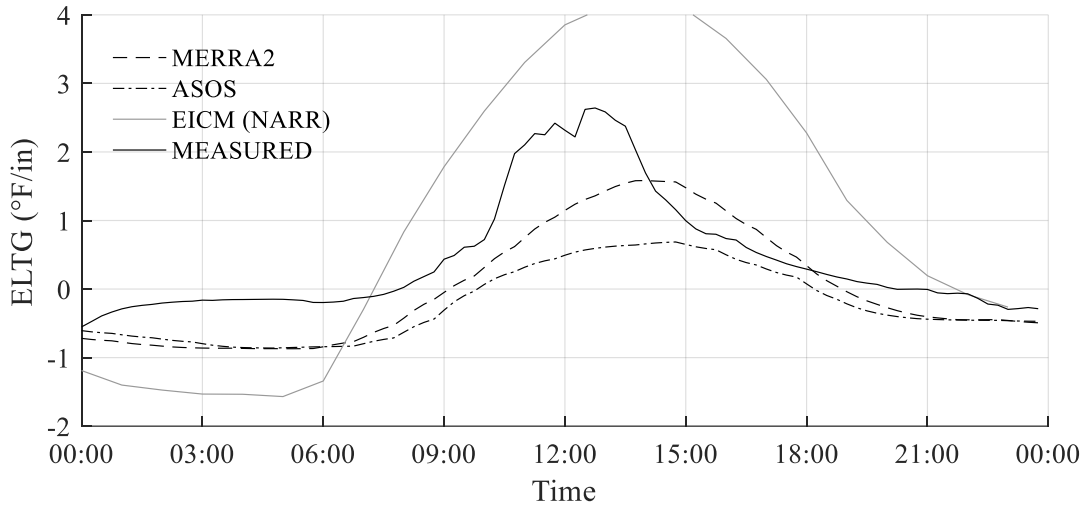


Figure A.8. MnROAD Cell 52 (4/9/2011)

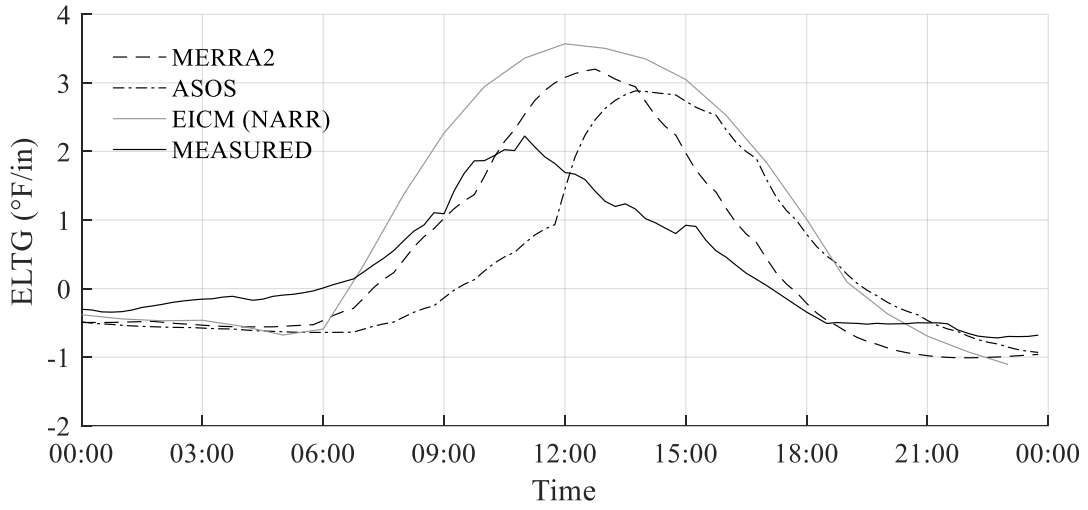


Figure A.9. MnROAD Cell 52 (4/10/2011)

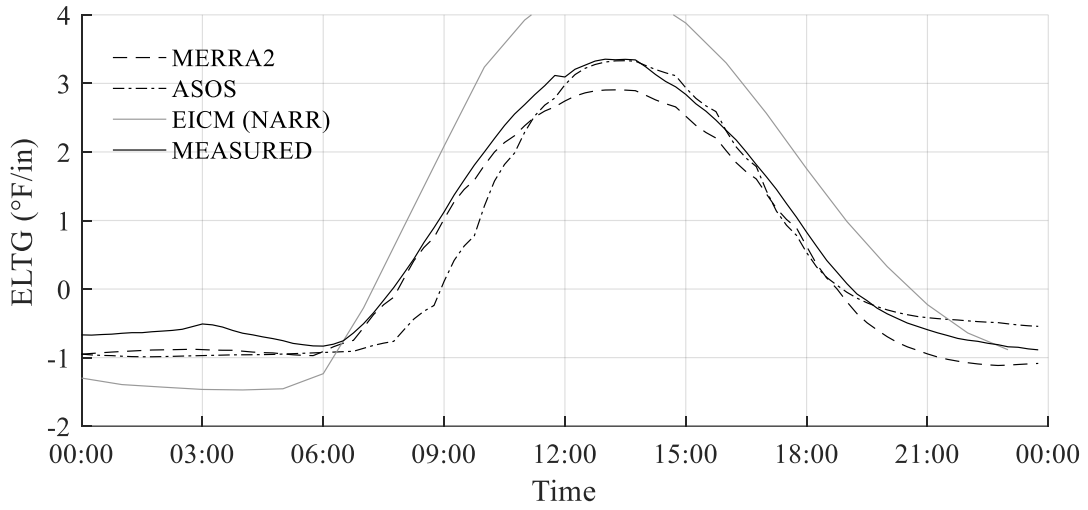


Figure A.10. MnROAD Cell 52 (4/11/2011)

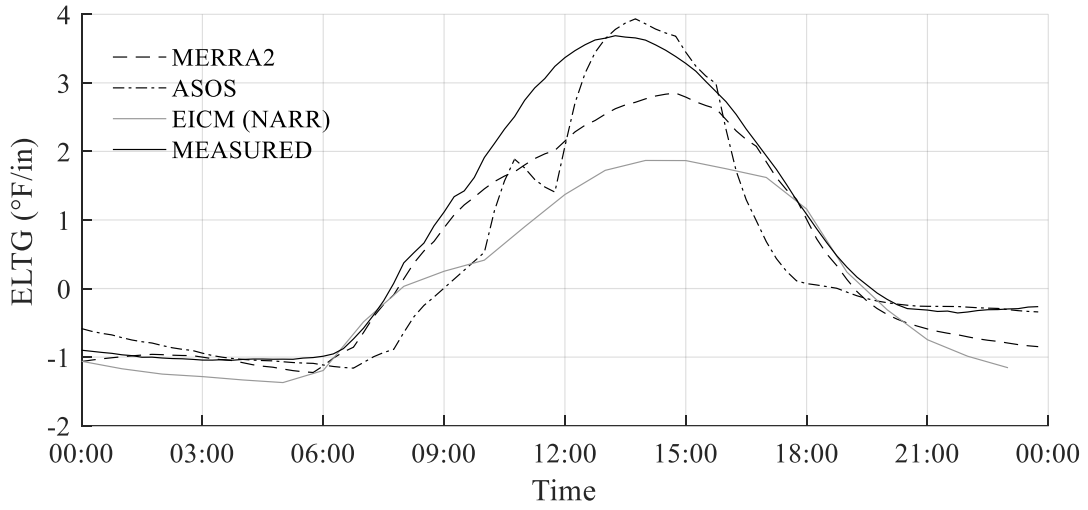


Figure A.11. MnROAD Cell 52 (4/12/2011)

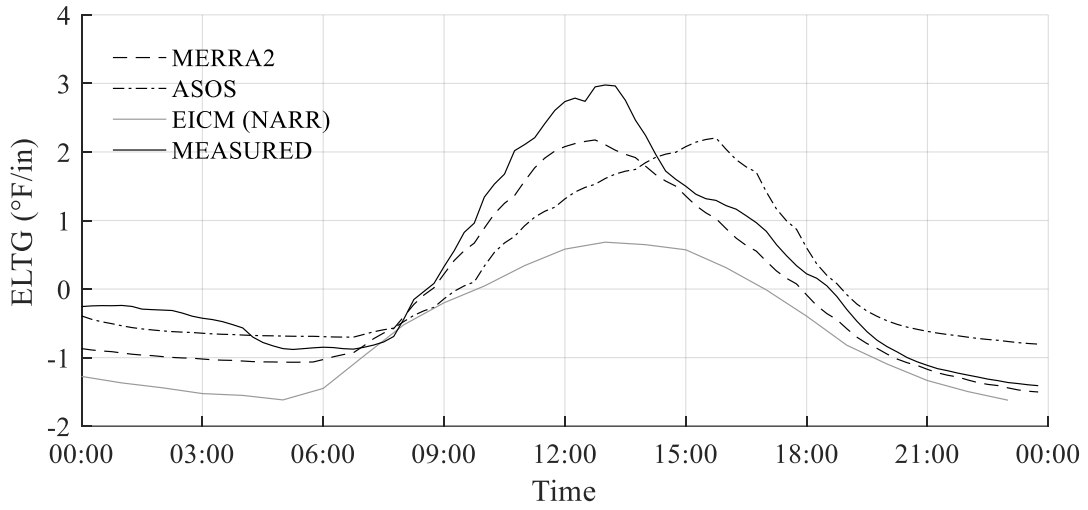


Figure A.12. MnROAD Cell 52 (4/13/2011)

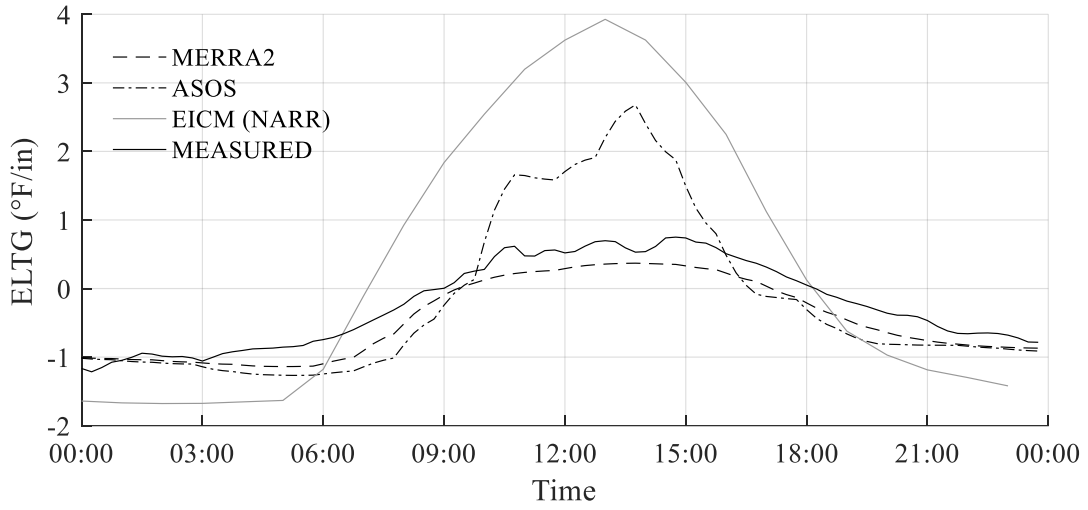


Figure A.13. MnROAD Cell 52 (4/15/2011)

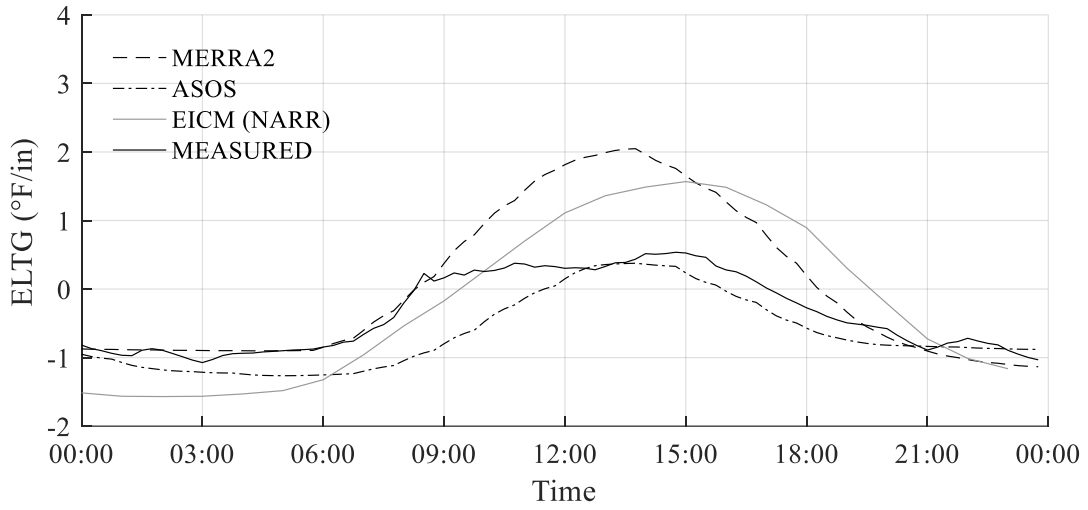


Figure A.14. MnROAD Cell 52 (4/16/2011)

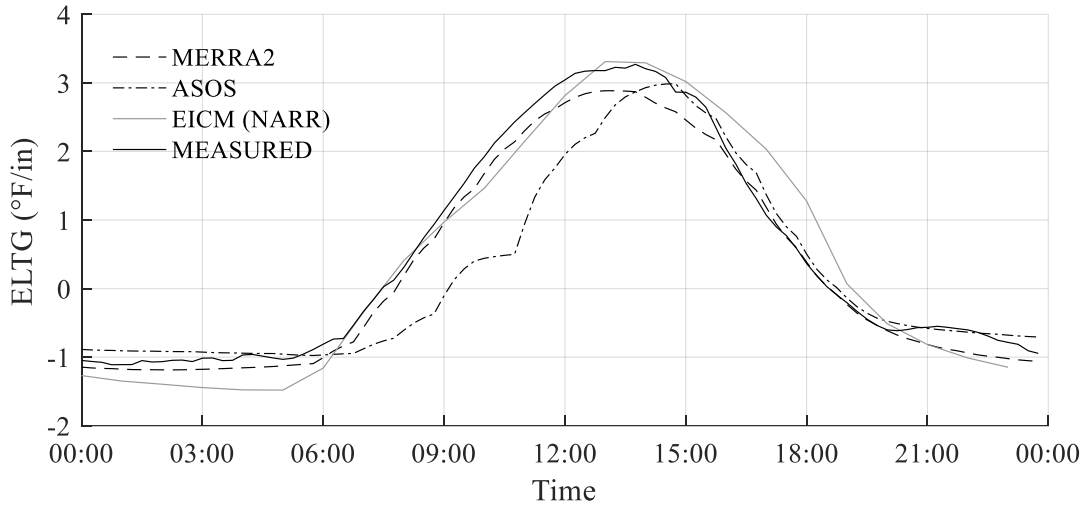


Figure A.15. MnROAD Cell 52 (4/17/2011)

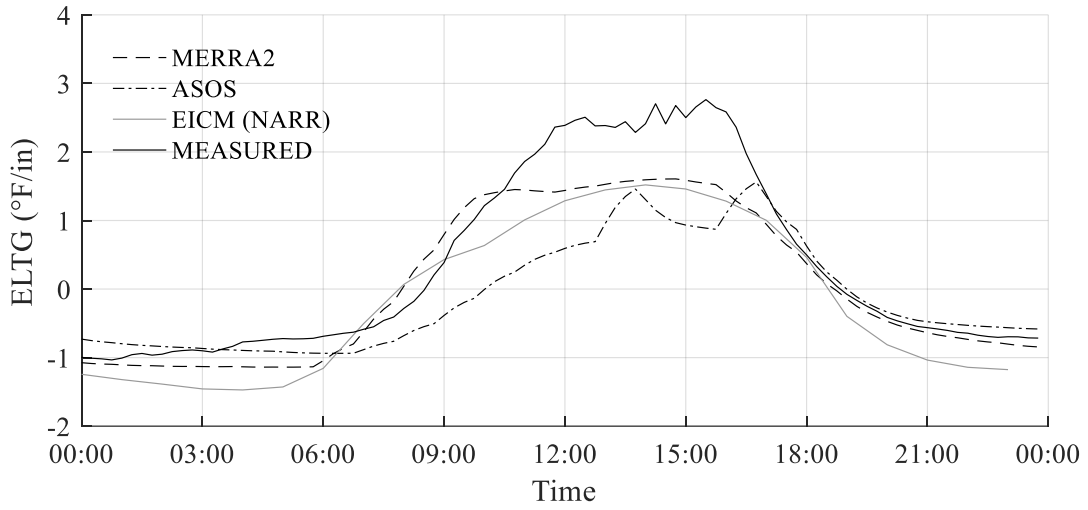


Figure A.16. MnROAD Cell 52 (4/18/2011)

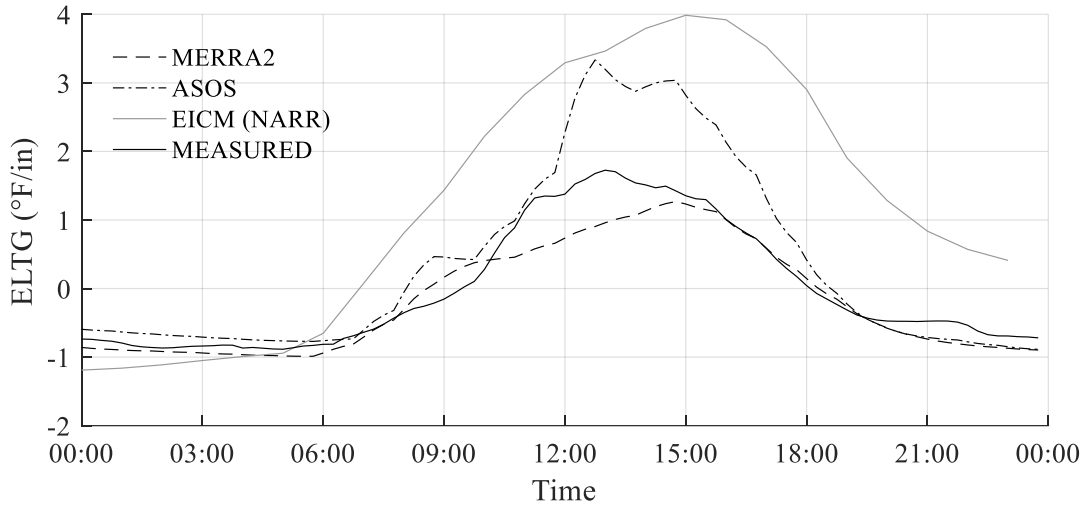


Figure A.17. MnROAD Cell 52 (4/19/2011)

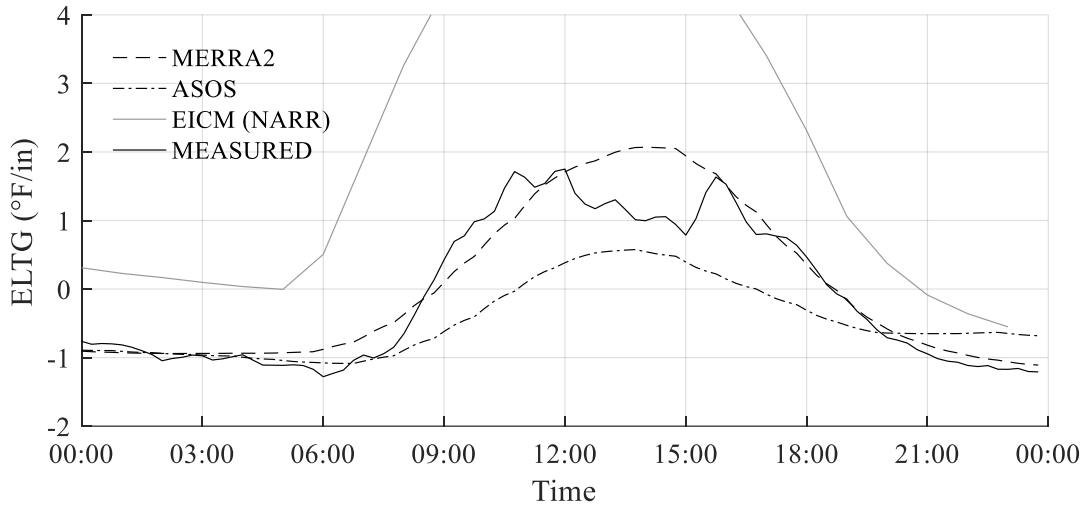


Figure A.18. MnROAD Cell 52 (4/20/2011)

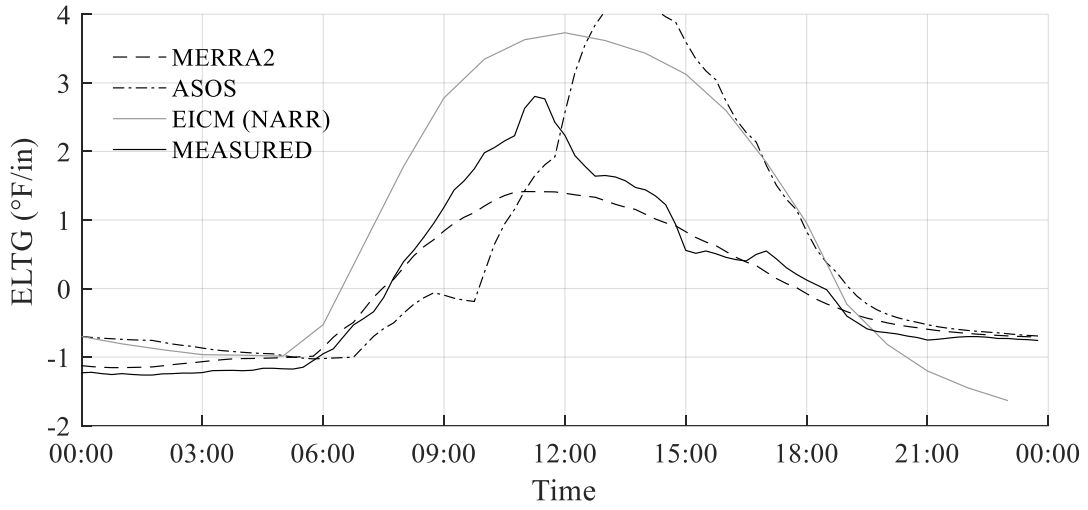


Figure A.19. MnROAD Cell 52 (4/21/2011)

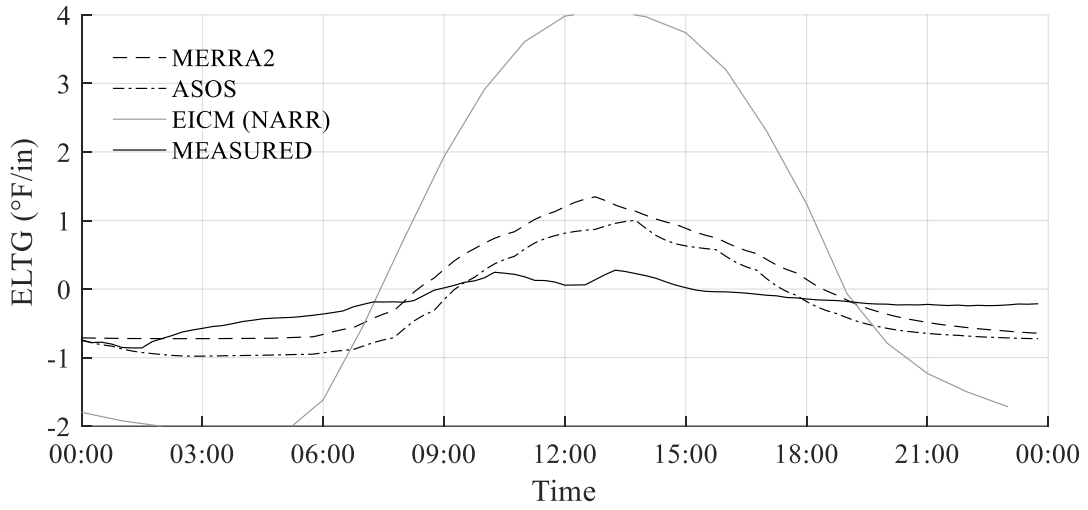


Figure A.20. MnROAD Cell 52 (4/22/2011)

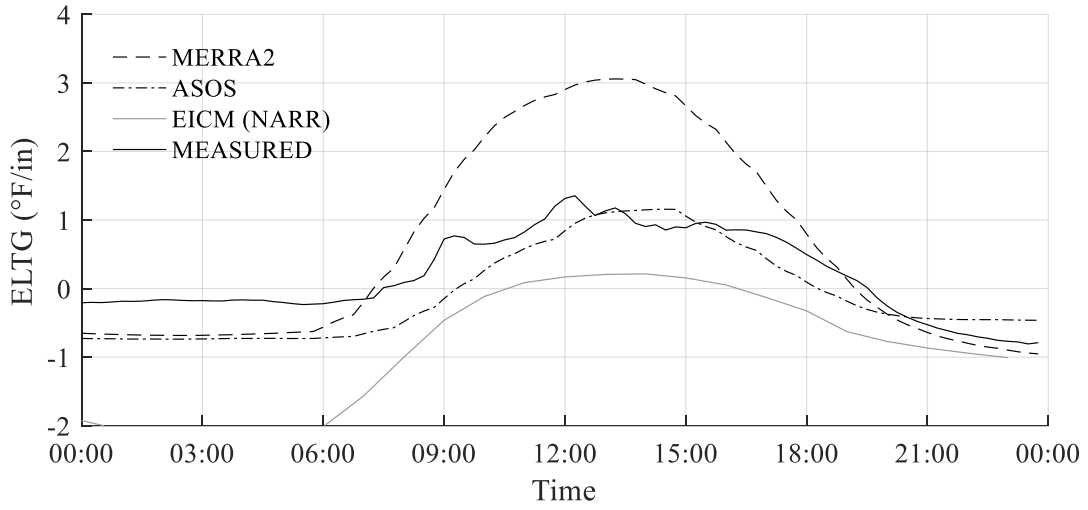


Figure A.21. MnROAD Cell 52 (4/23/2011)

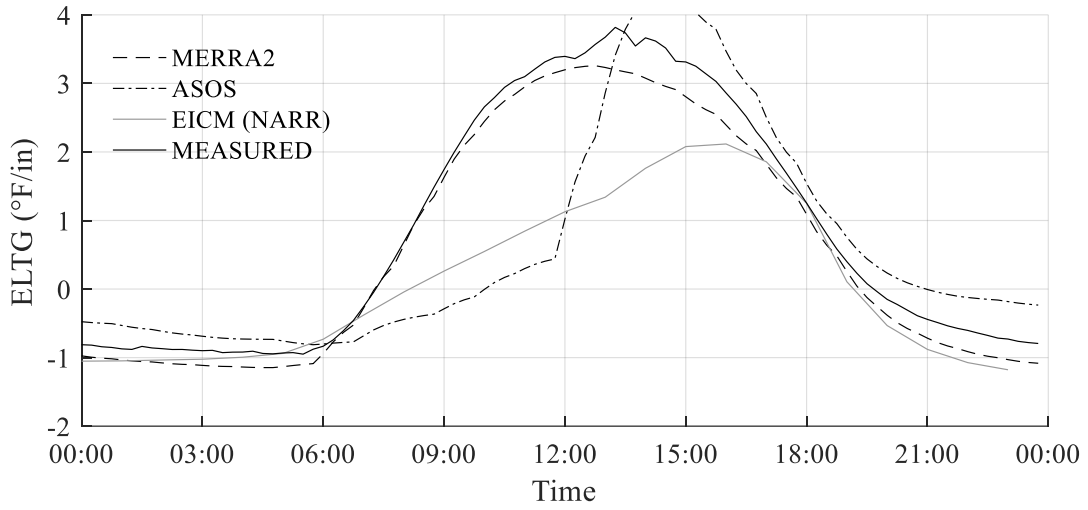


Figure A.22. MnROAD Cell 52 (4/24/2011)

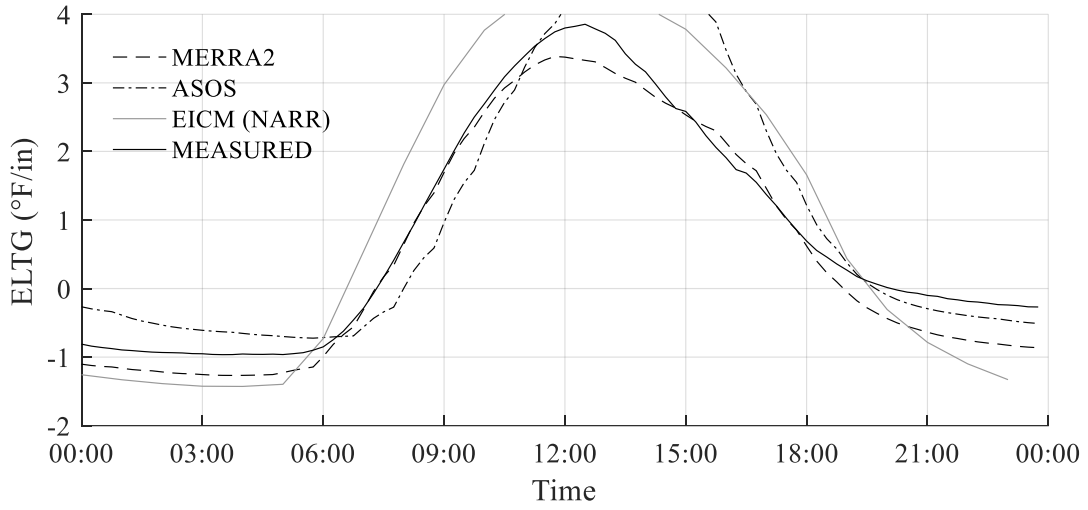


Figure A.23. MnROAD Cell 52 (4/25/2011)

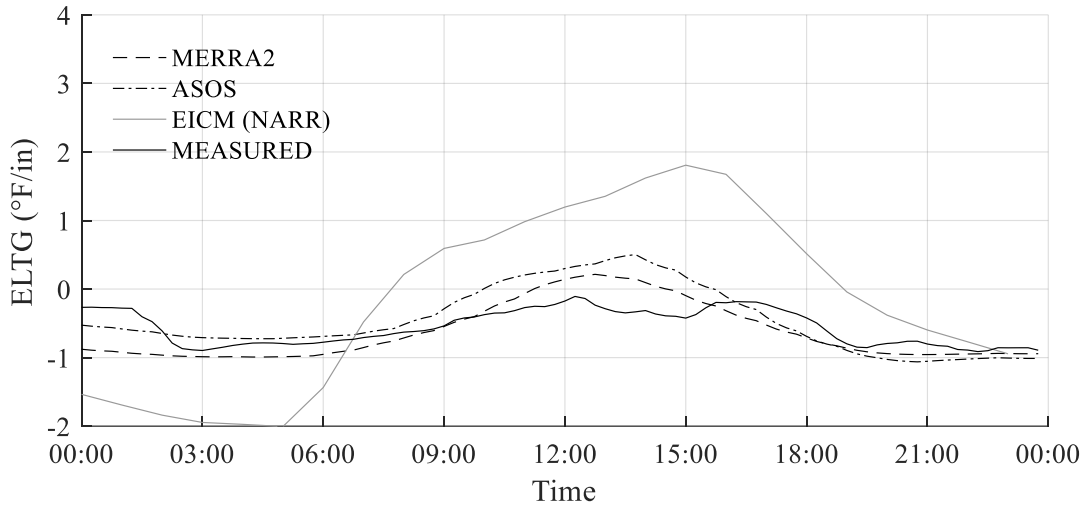


Figure A.24. MnROAD Cell 52 (4/26/2011)

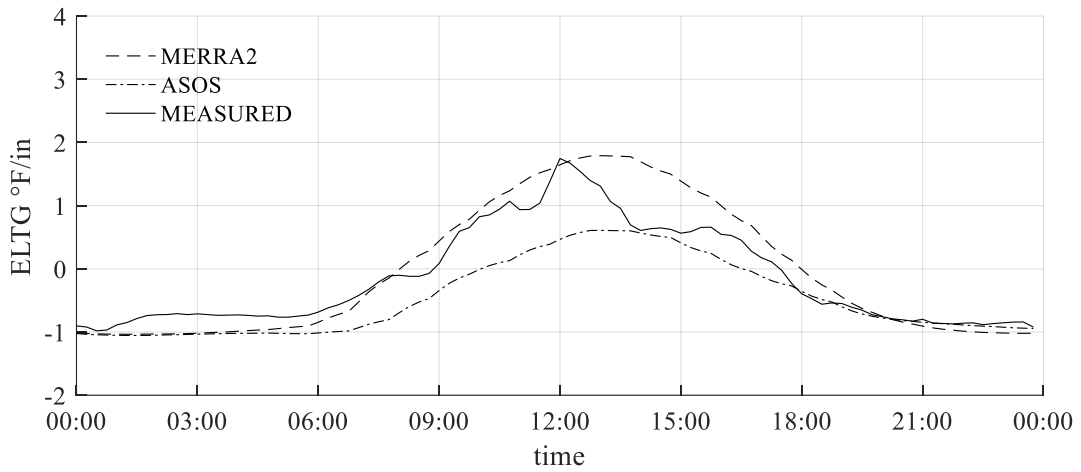


Figure A.25. MnROAD Cell 52 (4/27/2011)

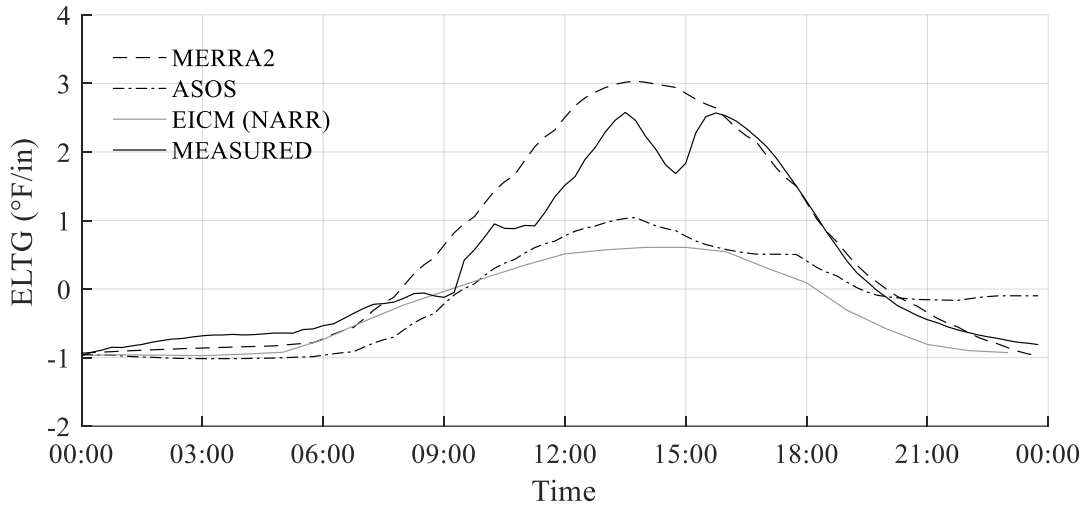


Figure A.26. MnROAD Cell 52 (4/28/2011)

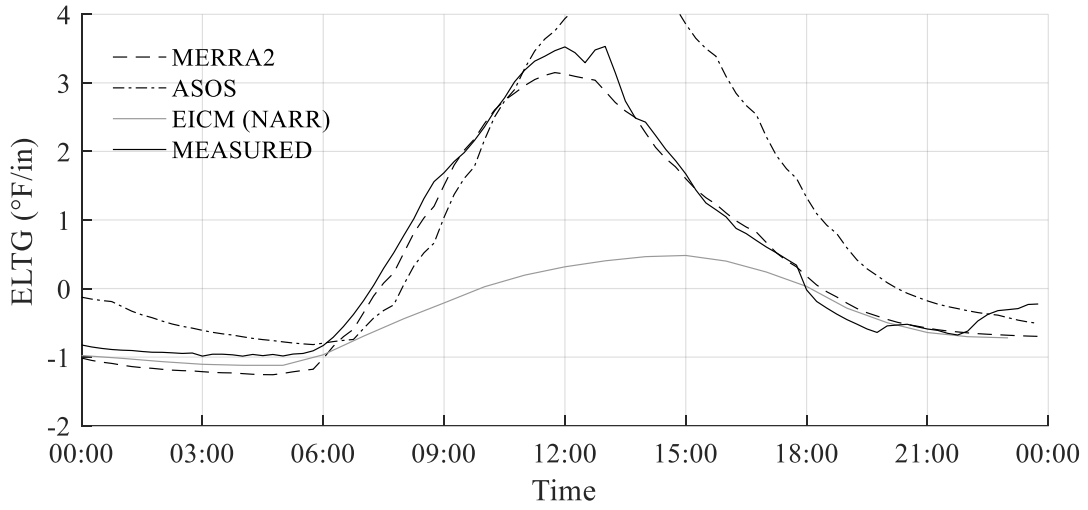


Figure A.27. MnROAD Cell 52 (4/29/2011)

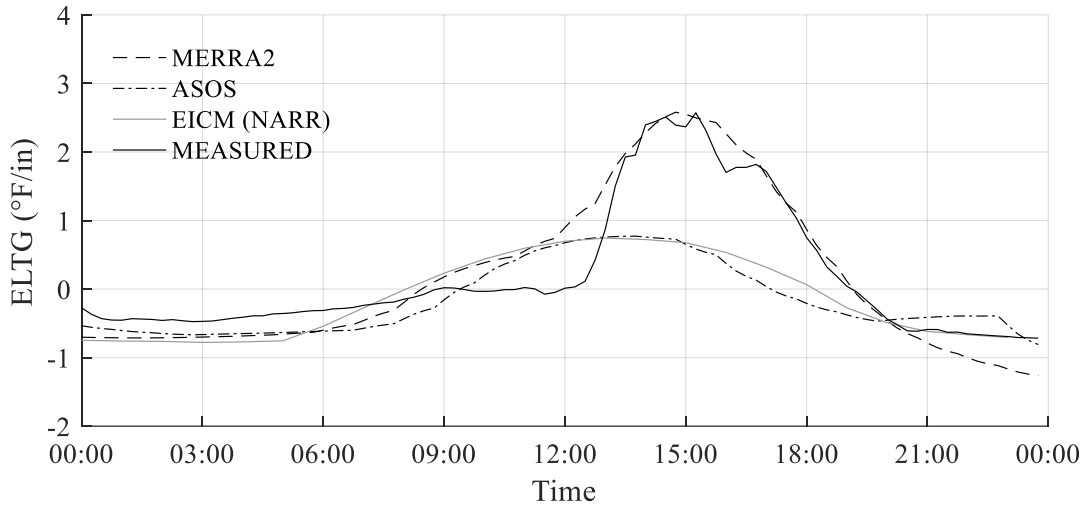


Figure A.28. MnROAD Cell 52 (4/30/2011)

MNROAD CELL 53

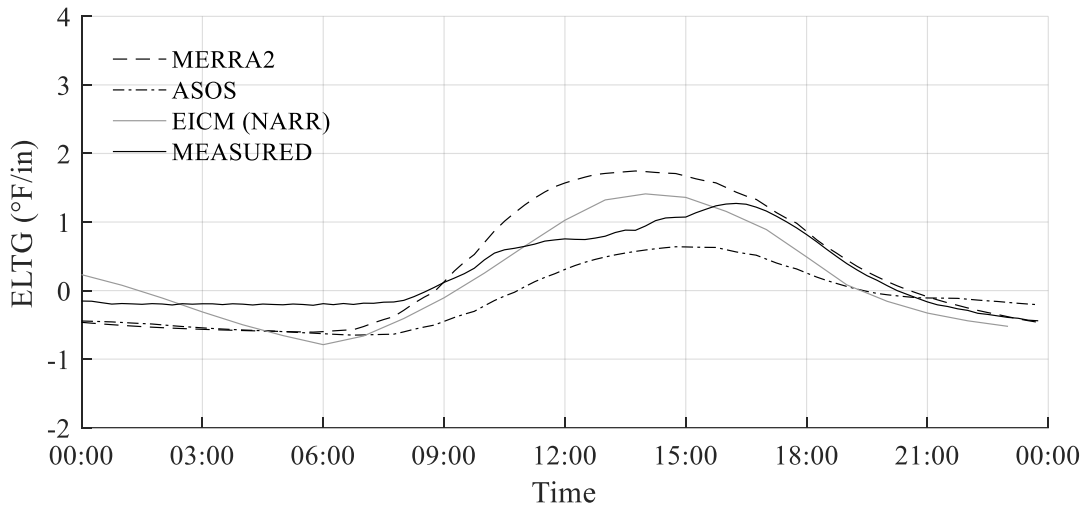


Figure A.29. MnROAD Cell 53 (4/1/2011)

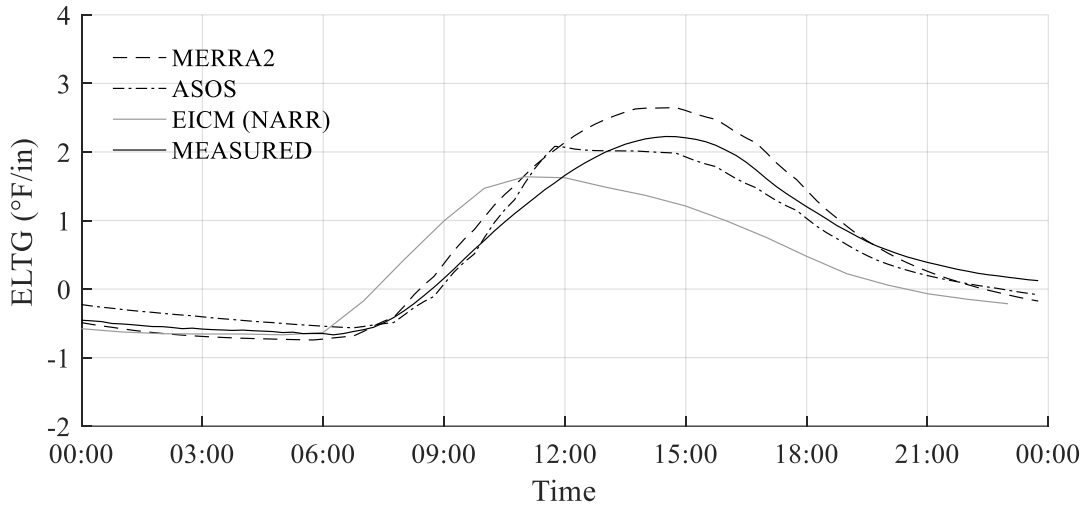


Figure A.30. MnROAD Cell 53 (4/2/2011)

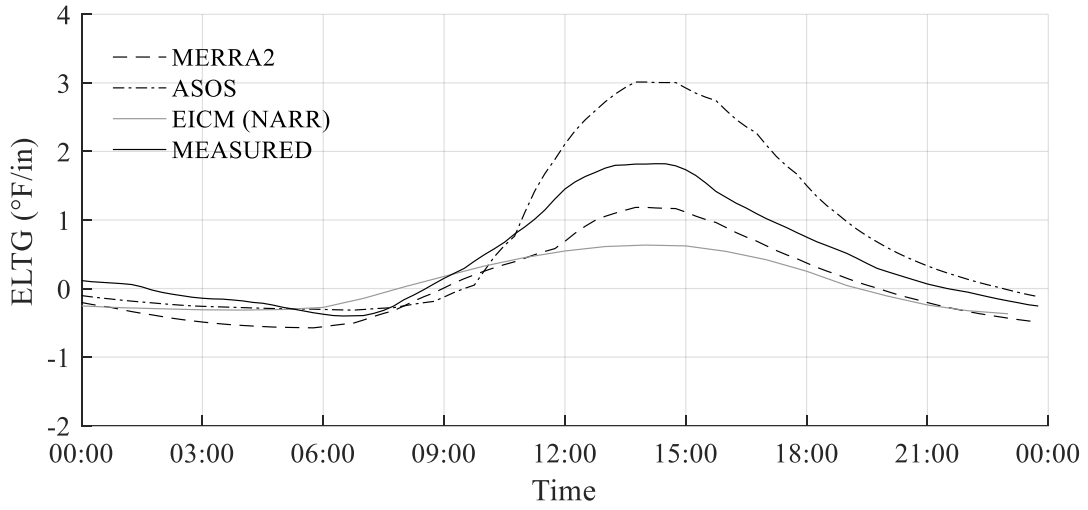


Figure A.31. MnROAD Cell 53 (4/3/2011)

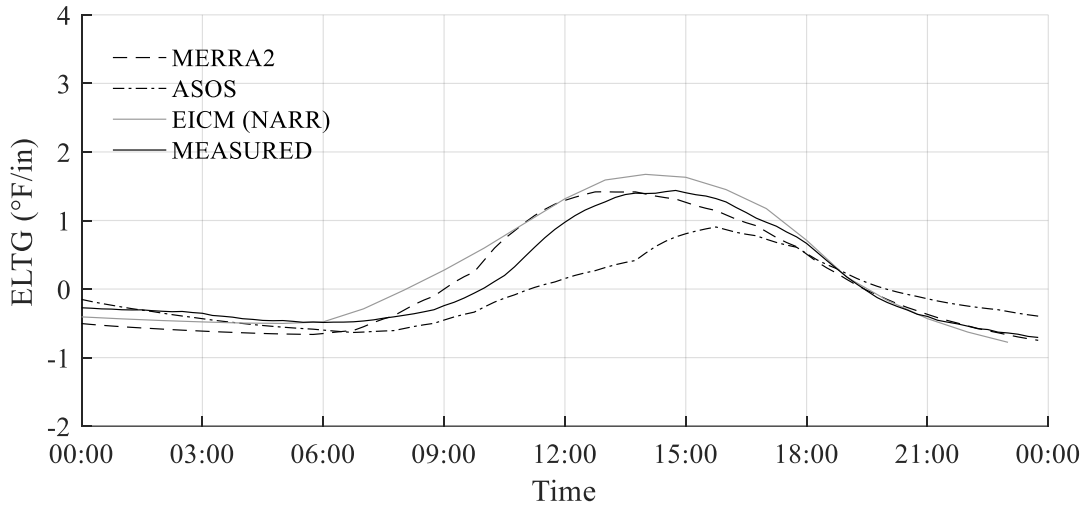


Figure A.32. MnROAD Cell 53 (4/4/2011)

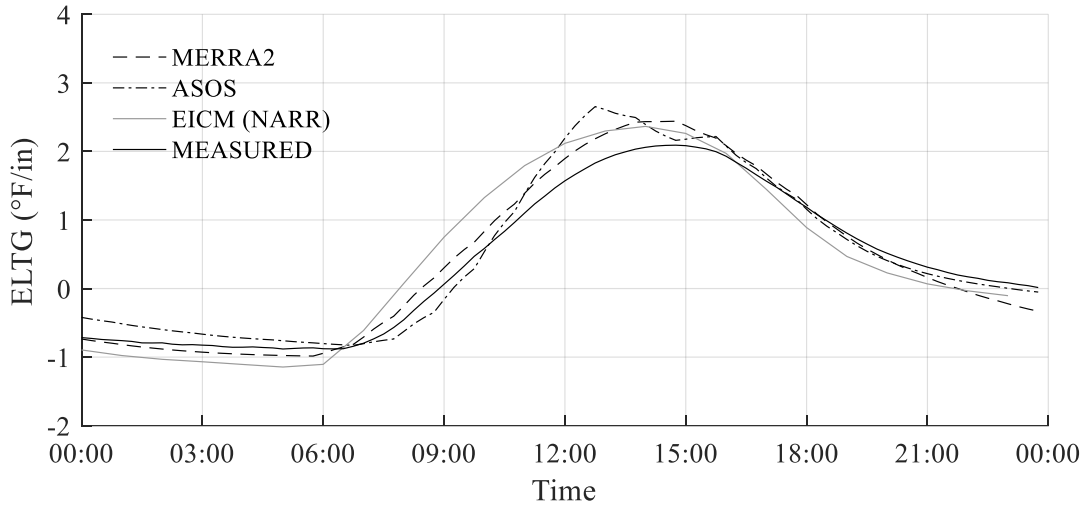


Figure A.33. MnROAD Cell 53 (4/5/2011)

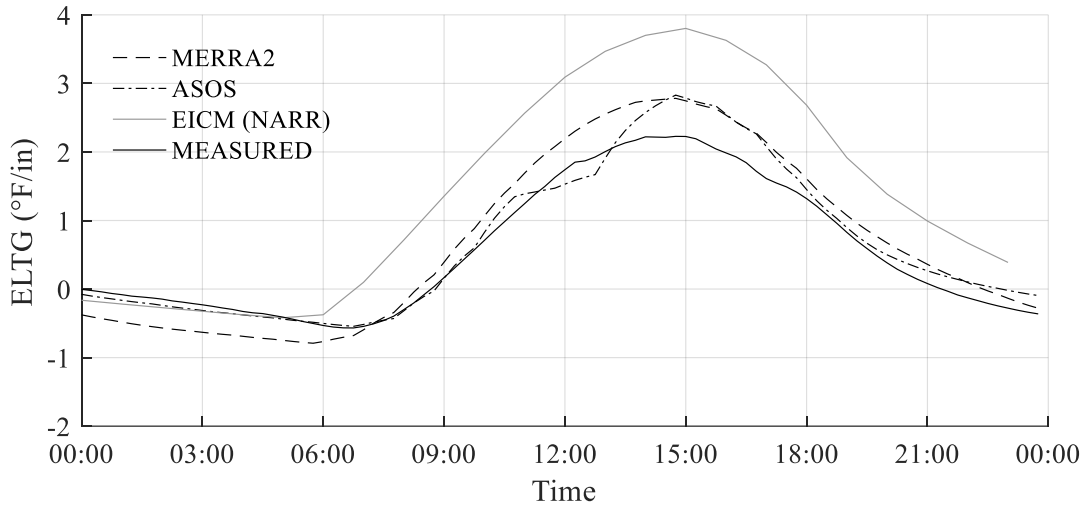


Figure A.34. MnROAD Cell 53 (4/6/2011)

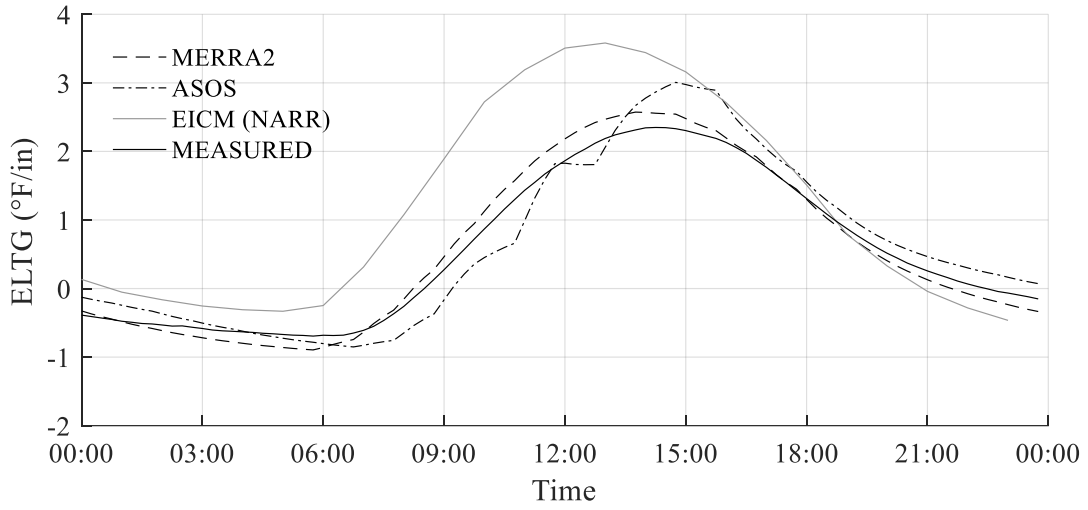


Figure A.35. MnROAD Cell 53 (4/7/2011)

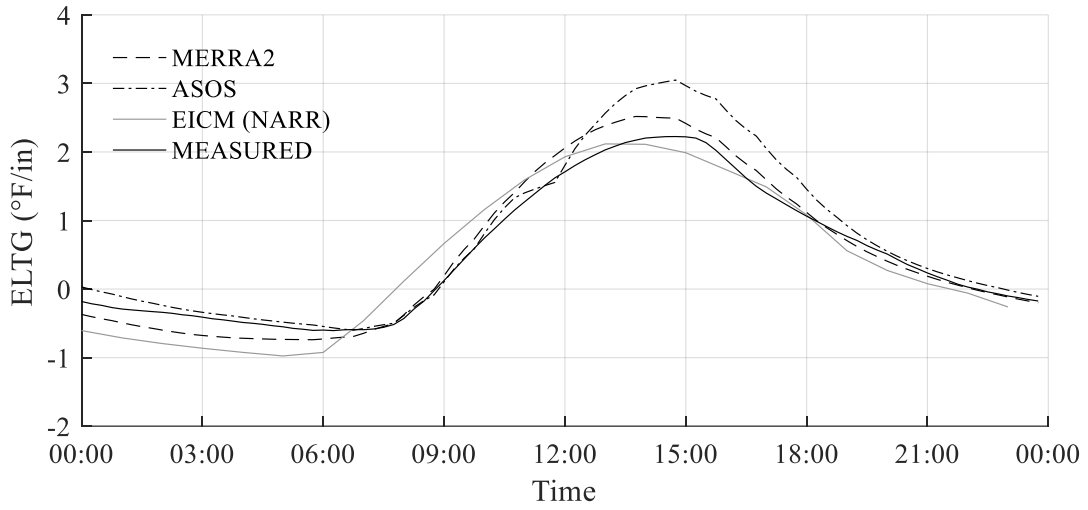


Figure A.36. MnROAD Cell 53 (4/8/2011)

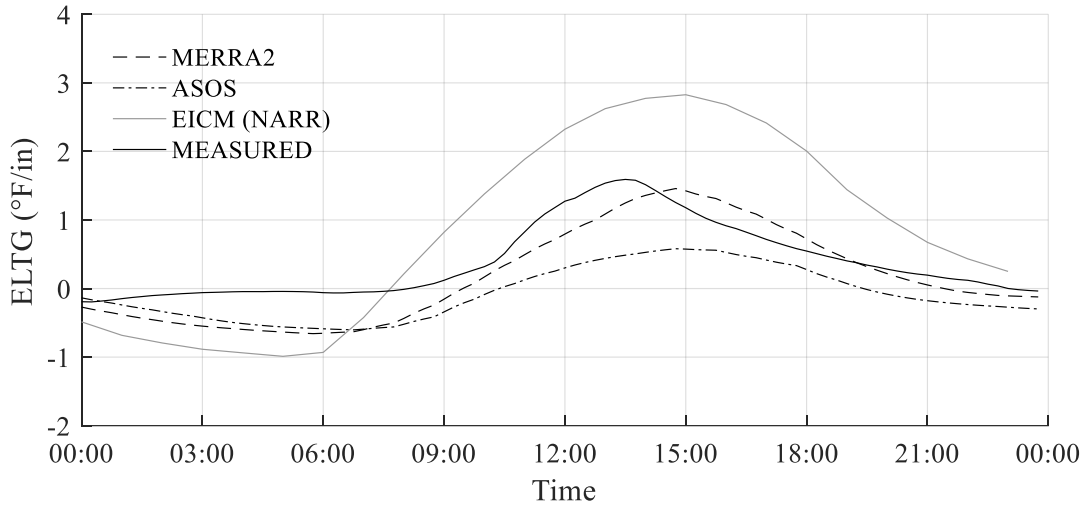


Figure A.37. MnROAD Cell 53 (4/9/2011)

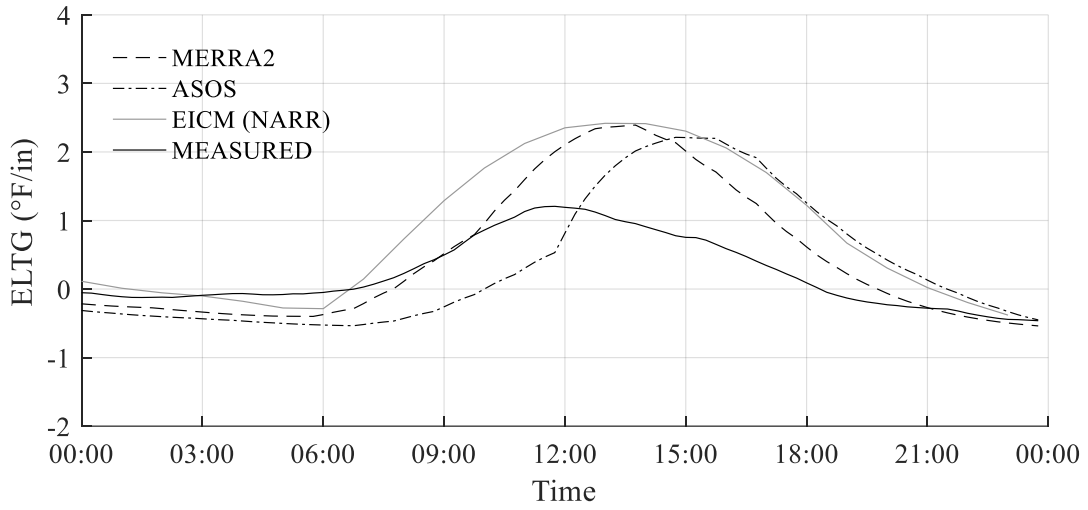


Figure A.38. MnROAD Cell 53 (4/10/2011)

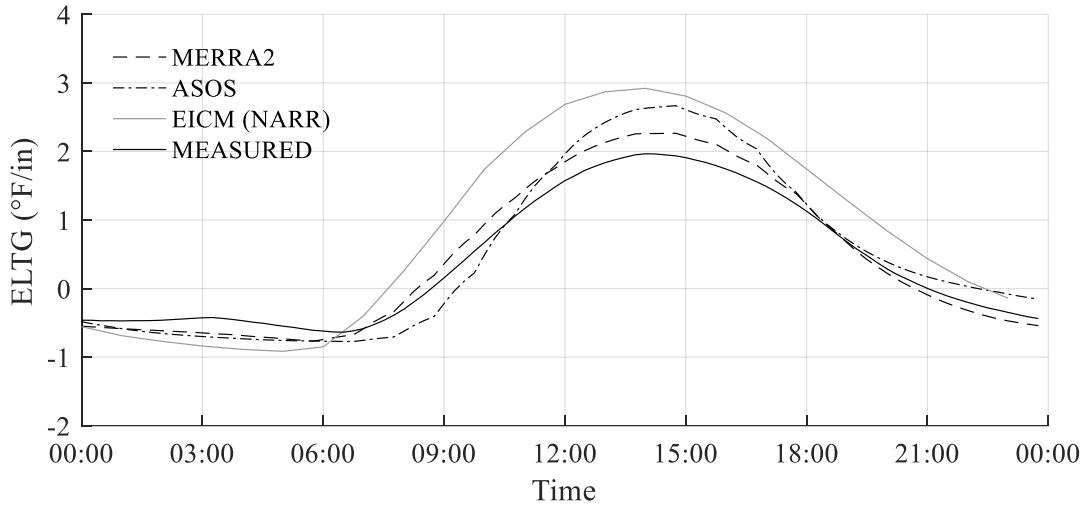


Figure A.39. MnROAD Cell 53 (4/11/2011)

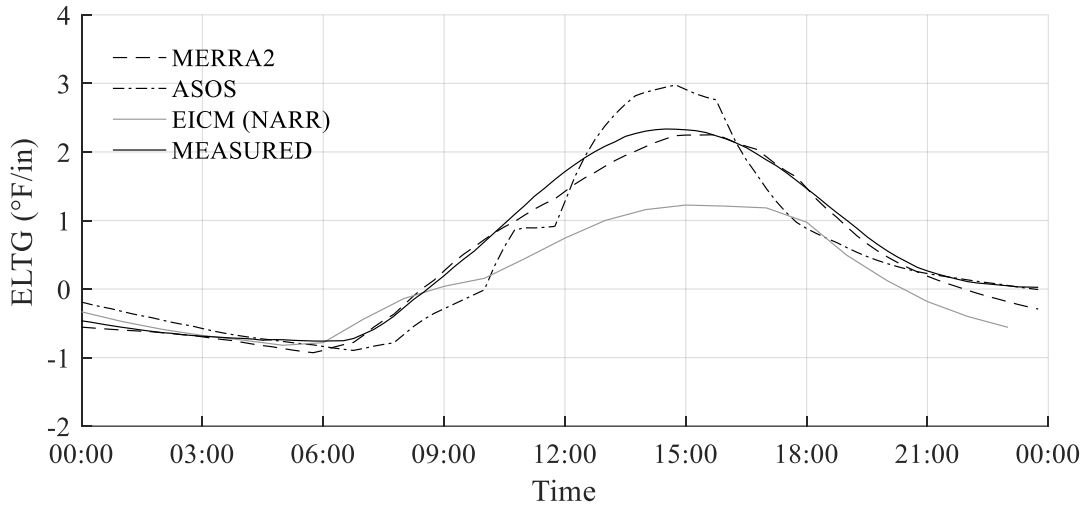


Figure A.40. MnROAD Cell 53 (4/12/2011)

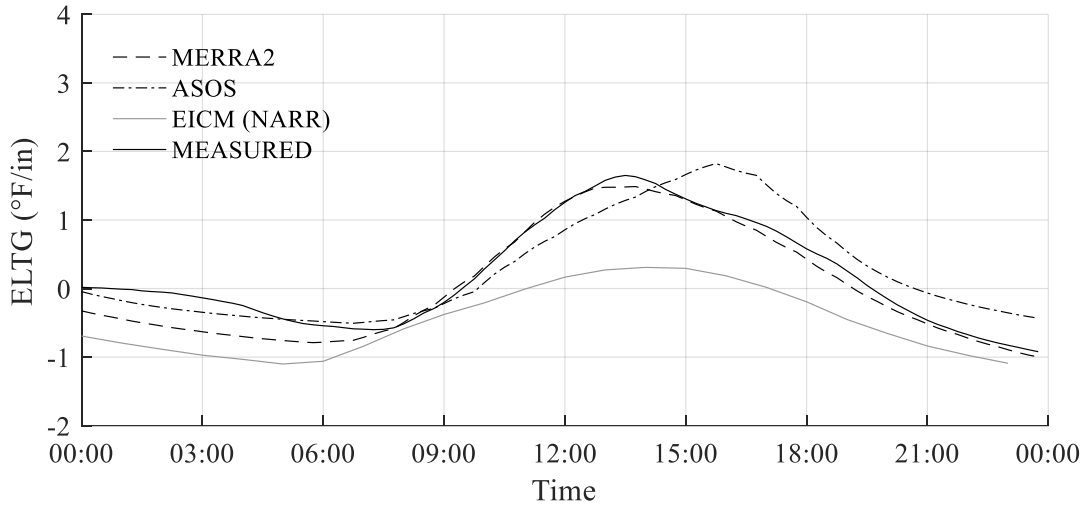


Figure A.41. MnROAD Cell 53 (4/13/2011)

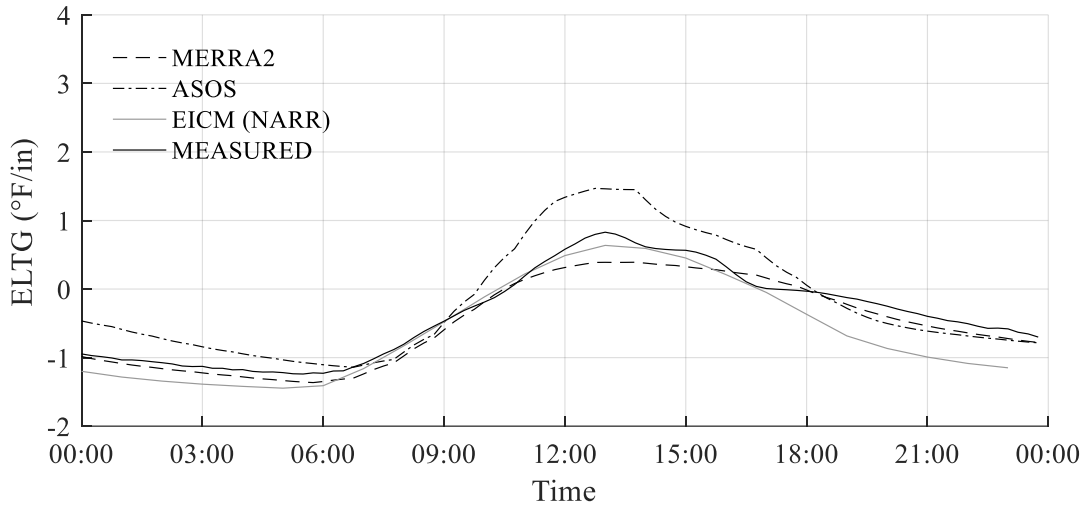


Figure A.42. MnROAD Cell 53 (4/14/2011)

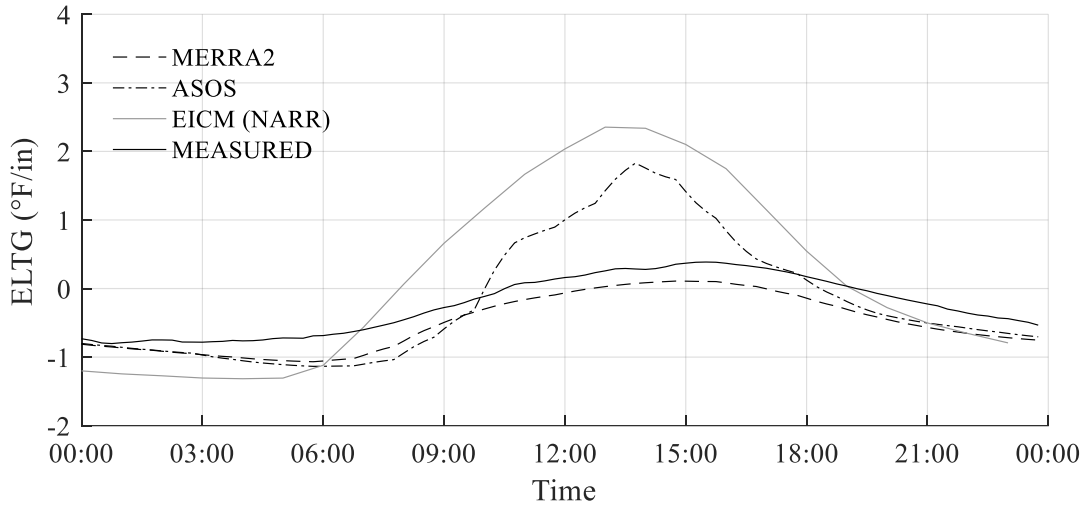


Figure-A.43. MnROAD Cell 53 (4/15/2011)

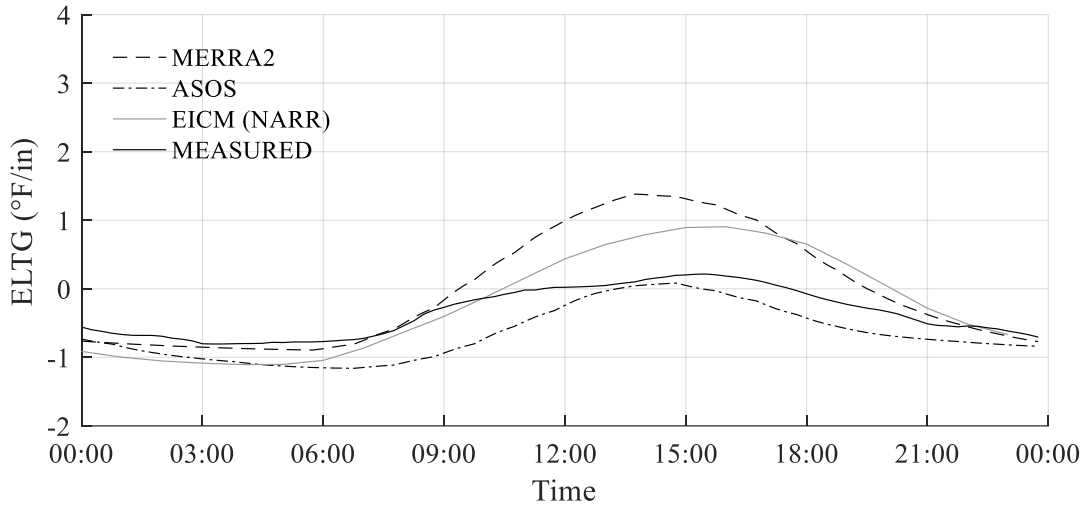


Figure A.44. MnROAD Cell 53 (4/16/2011)

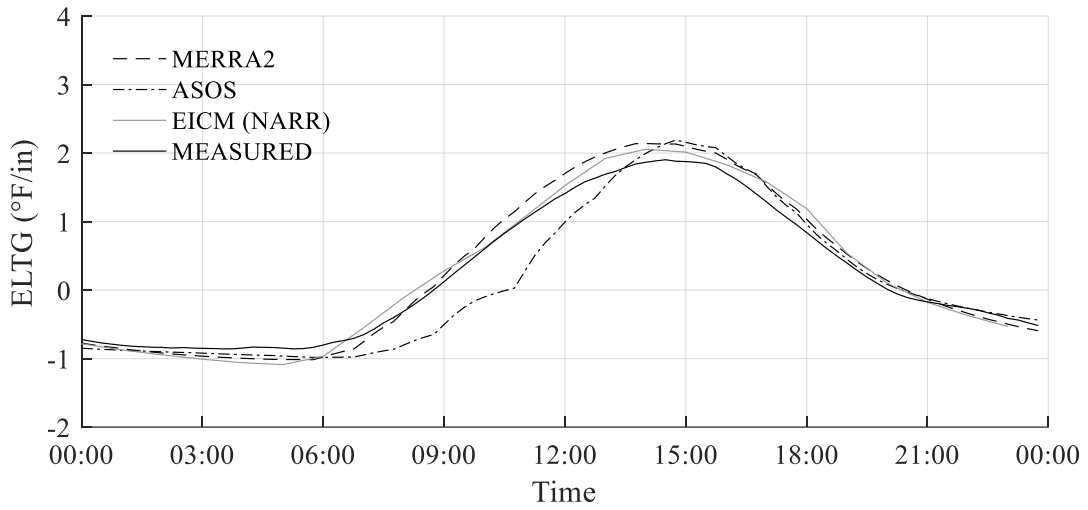


Figure A.45. MnROAD Cell 53 (4/17/2011)

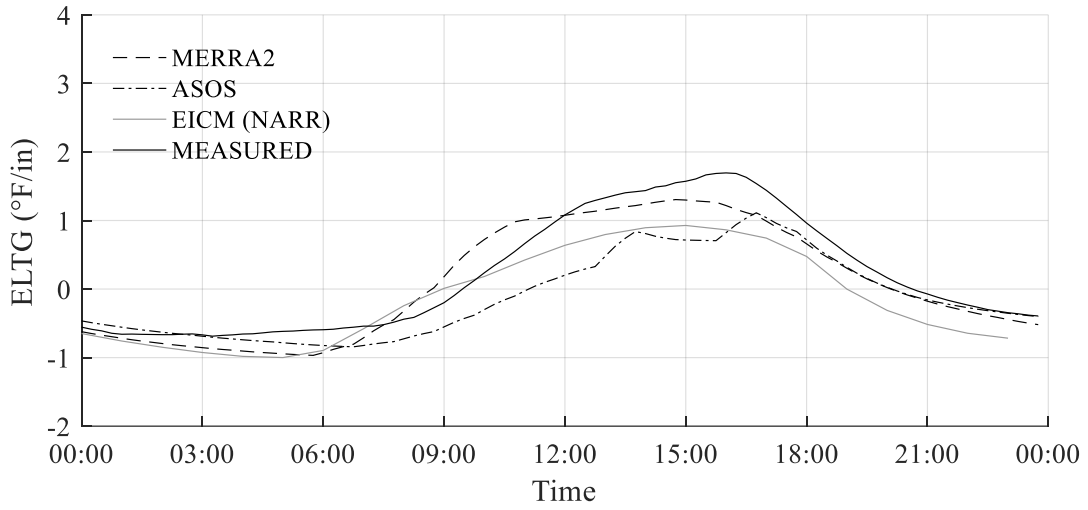


Figure A.46. MnROAD Cell 53 (4/18/2011)

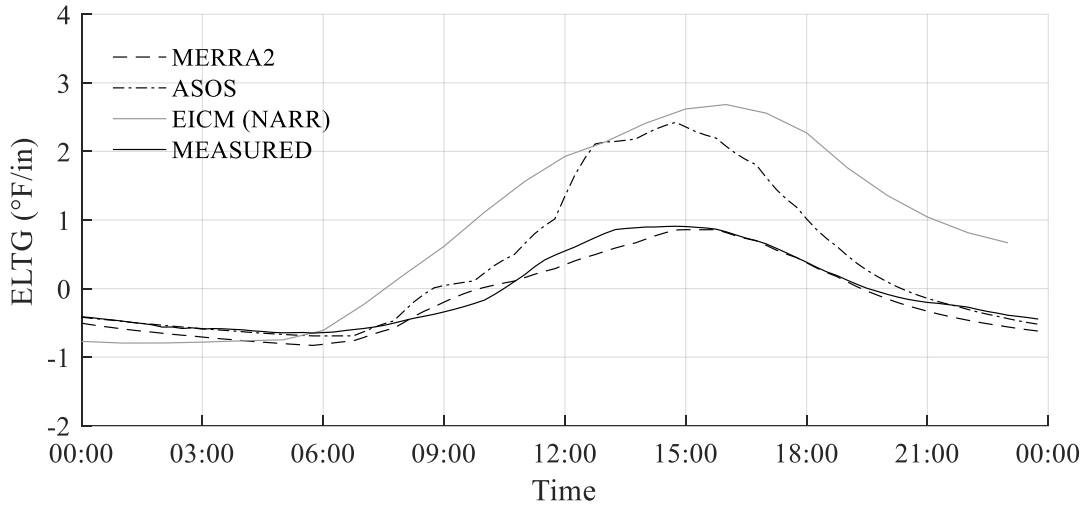


Figure A.47. MnROAD Cell 53 (4/19/2011)

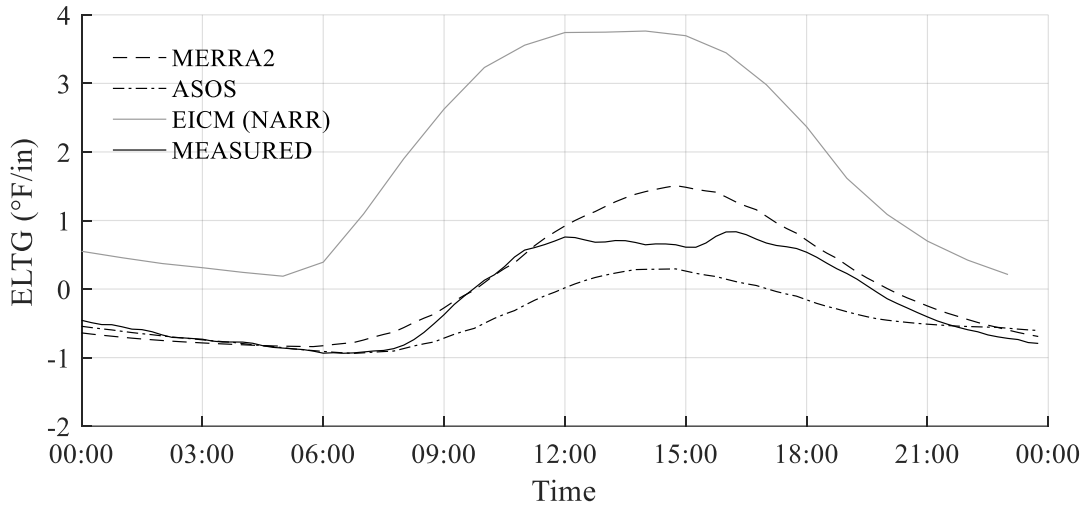


Figure A.48. MnROAD Cell 53 (4/20/2011)

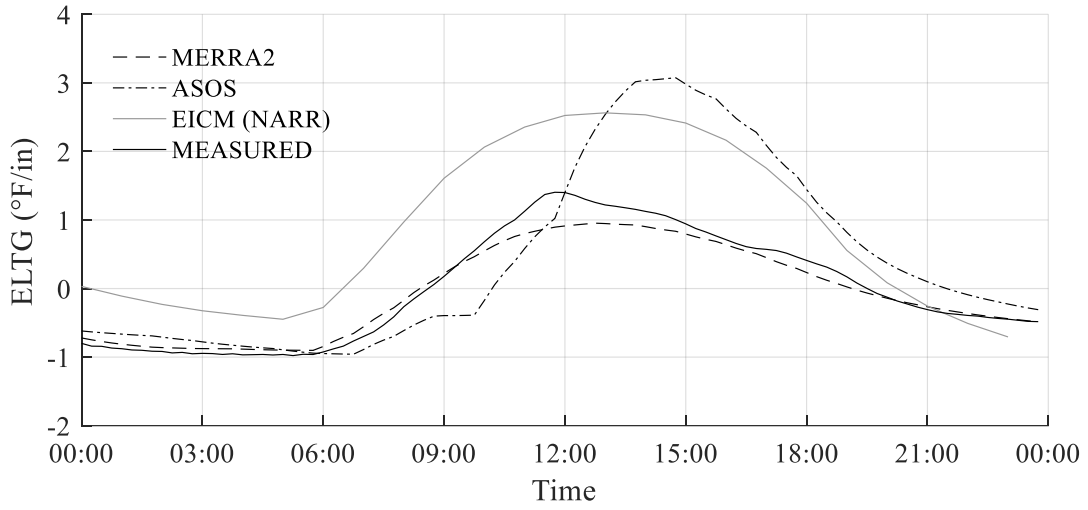


Figure A.49. MnROAD Cell 53 (4/21/2011)

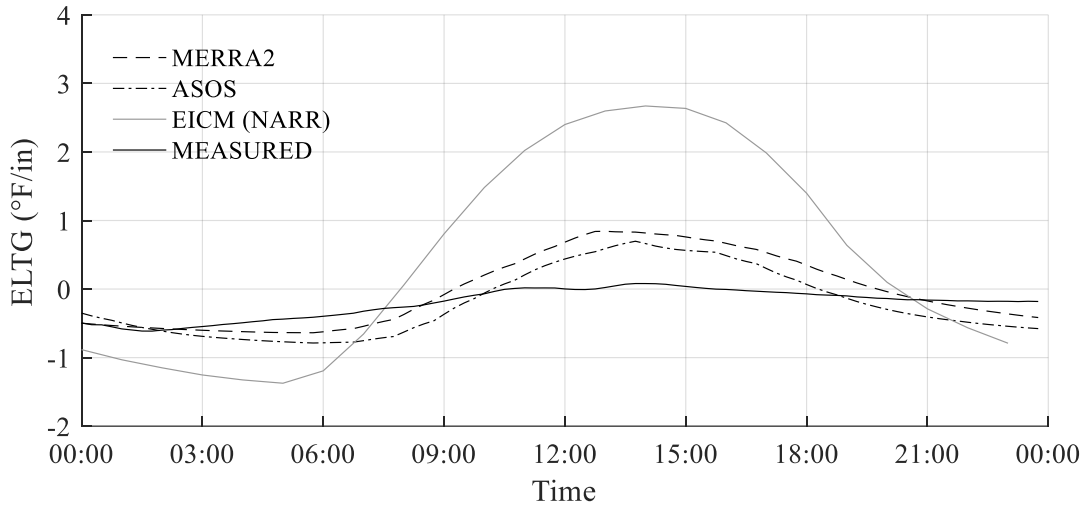


Figure A.50. MnROAD Cell 53 (4/22/2011)

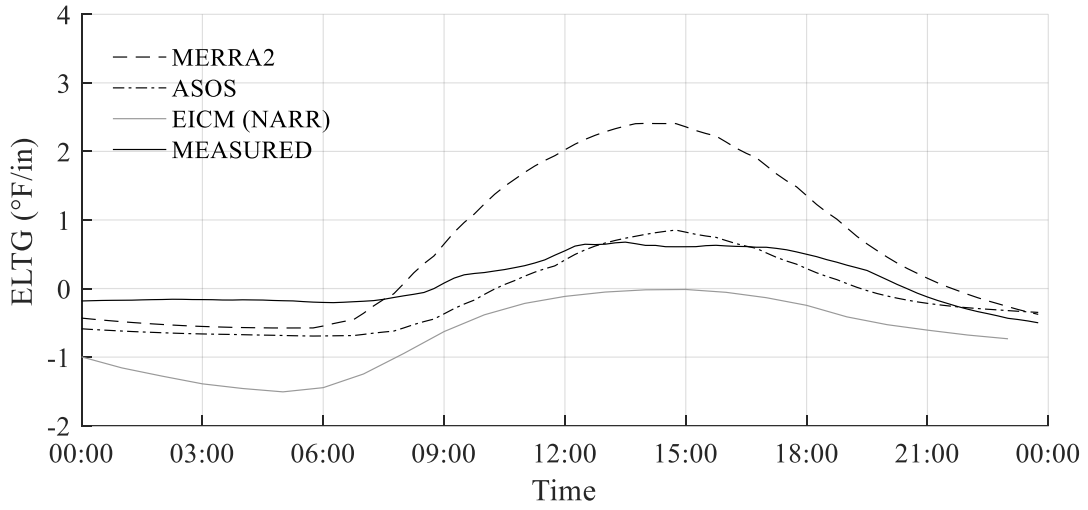


Figure A.51. MnROAD Cell 53 (4/23/2011)

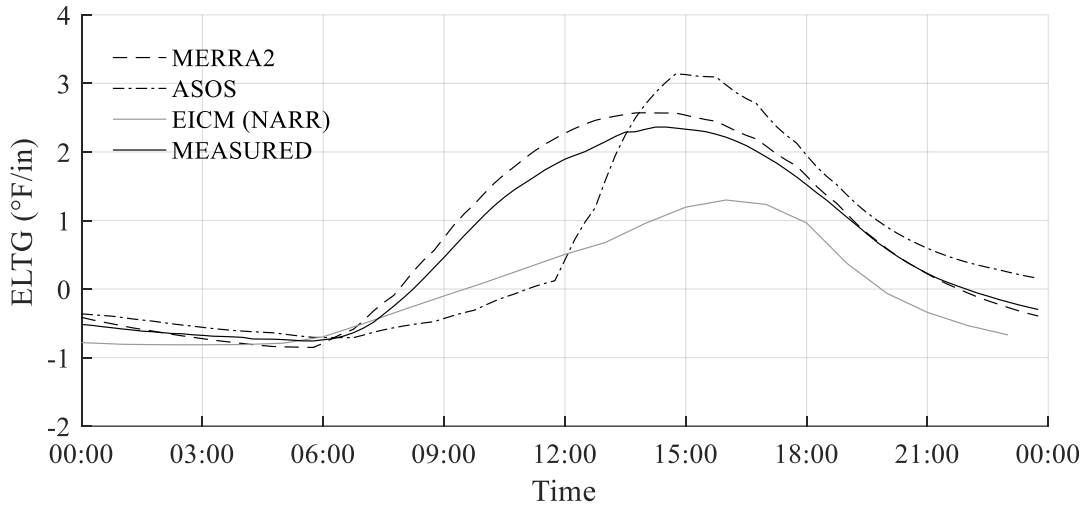


Figure A.52. MnROAD Cell 53 (4/24/2011)

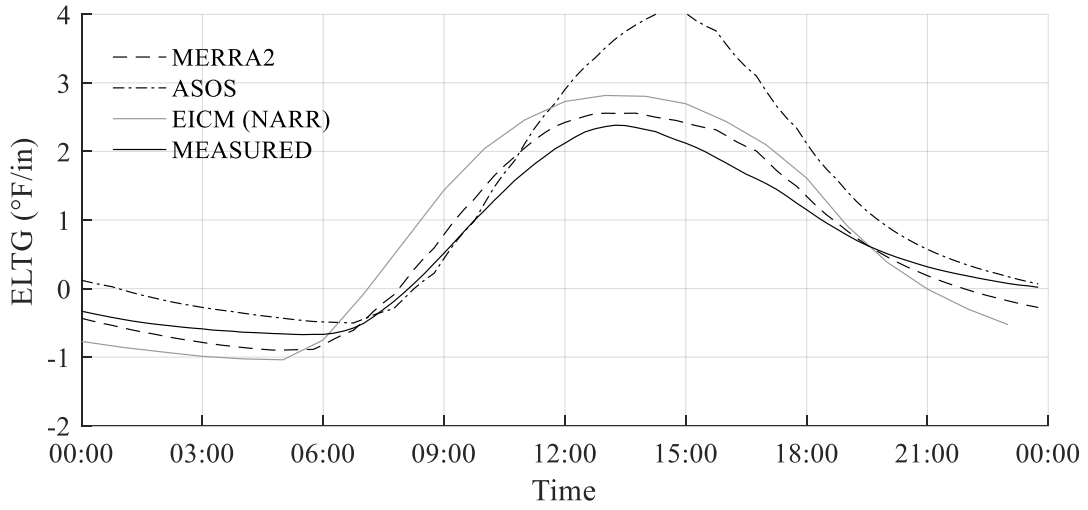


Figure A.53. MnROAD Cell 53 (4/25/2011)

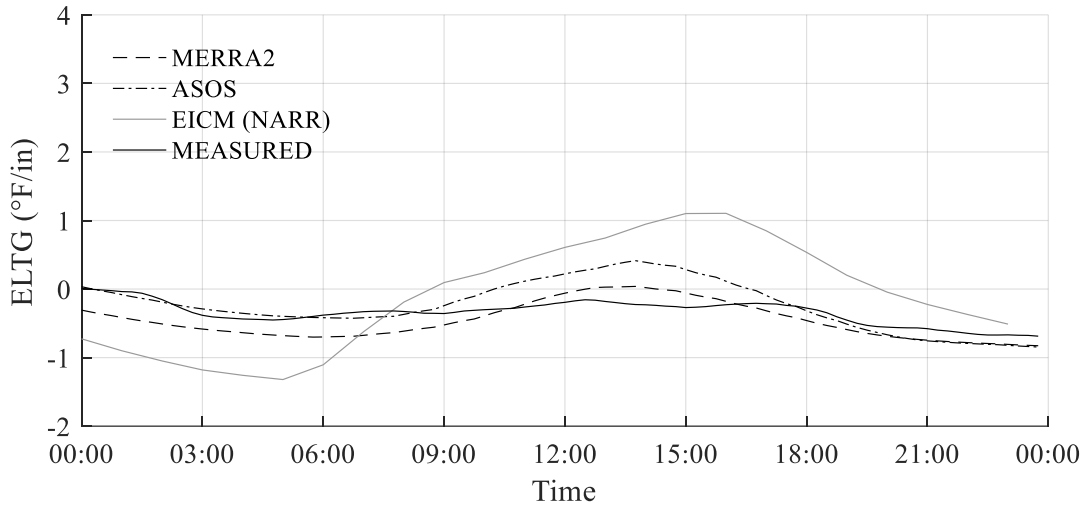


Figure A.54. MnROAD Cell 53 (4/26/2011)

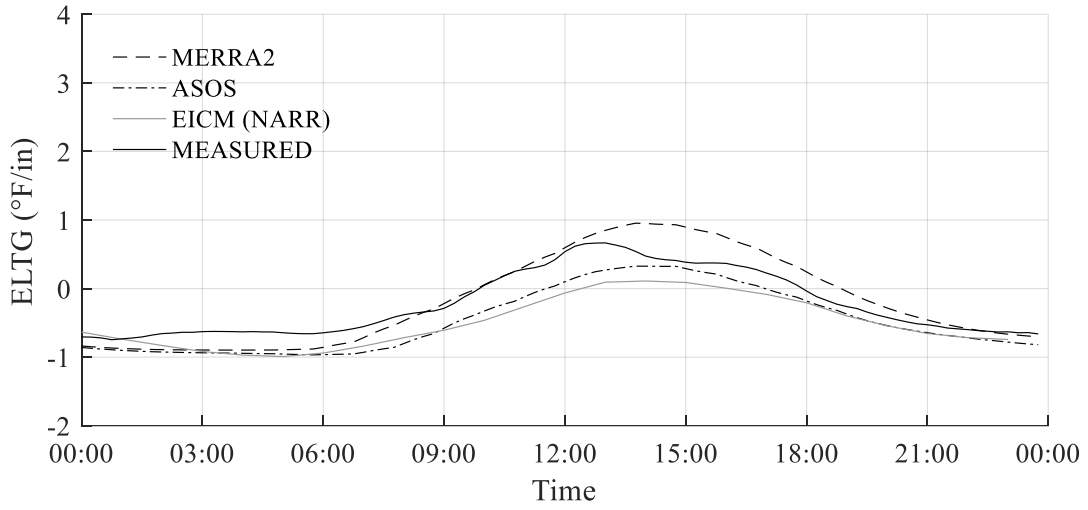


Figure A.55. MnROAD Cell 53 (4/27/2011)

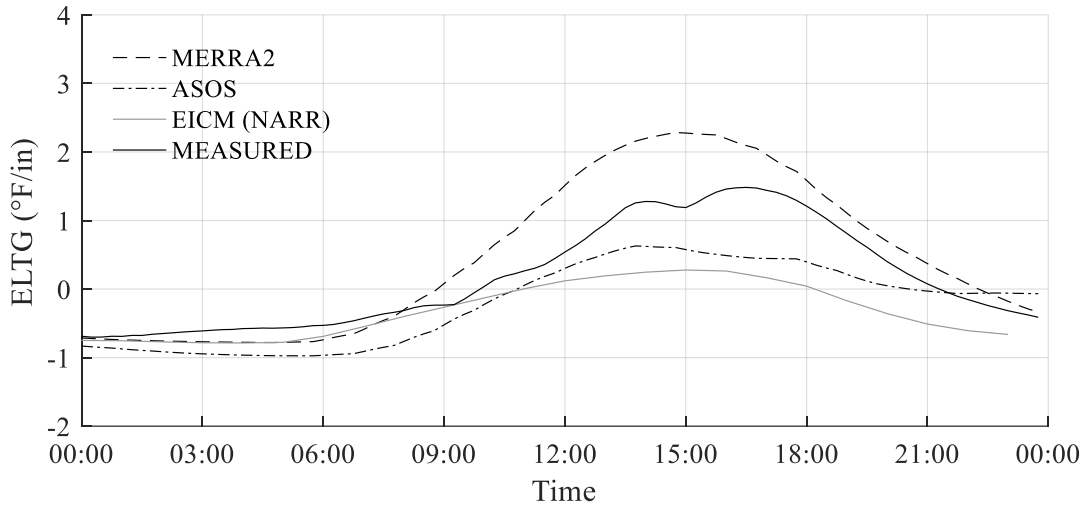


Figure A.56. MnROAD Cell 53 (4/28/2011)

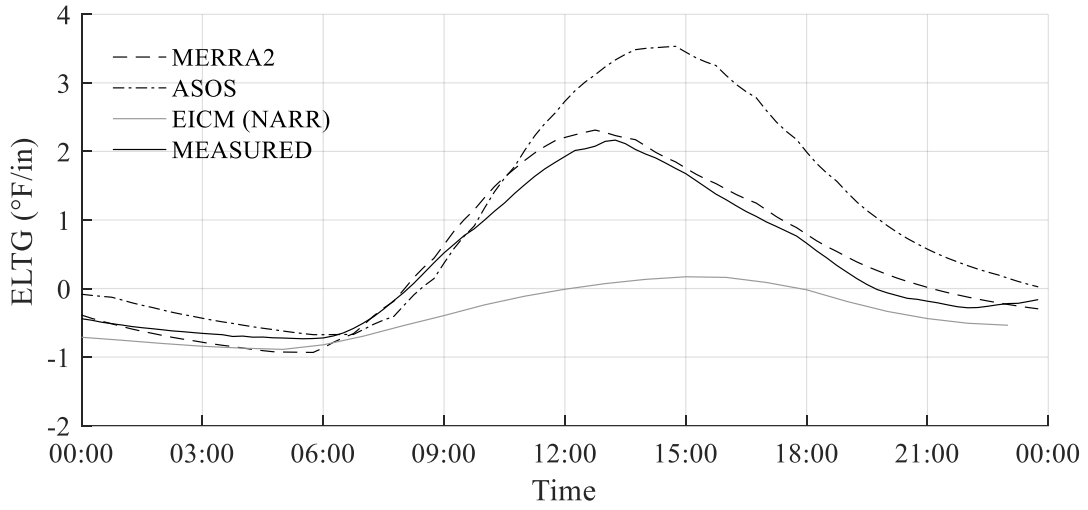


Figure A.57. MnROAD Cell 53 (4/29/2011)

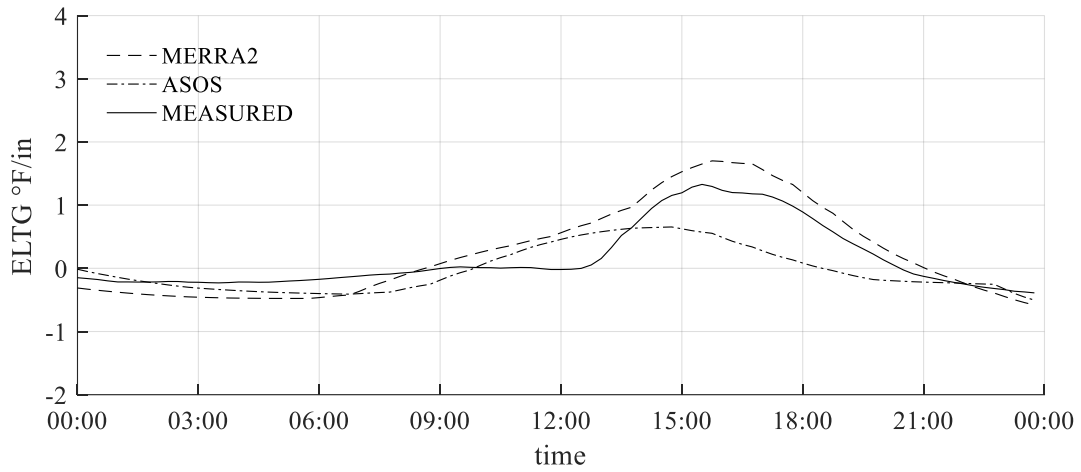


Figure A.58. MnROAD Cell 53 (4/30/2011)

ATLANTA HARTSFIELD-JACKSON INTERNATIONAL AIRPORT

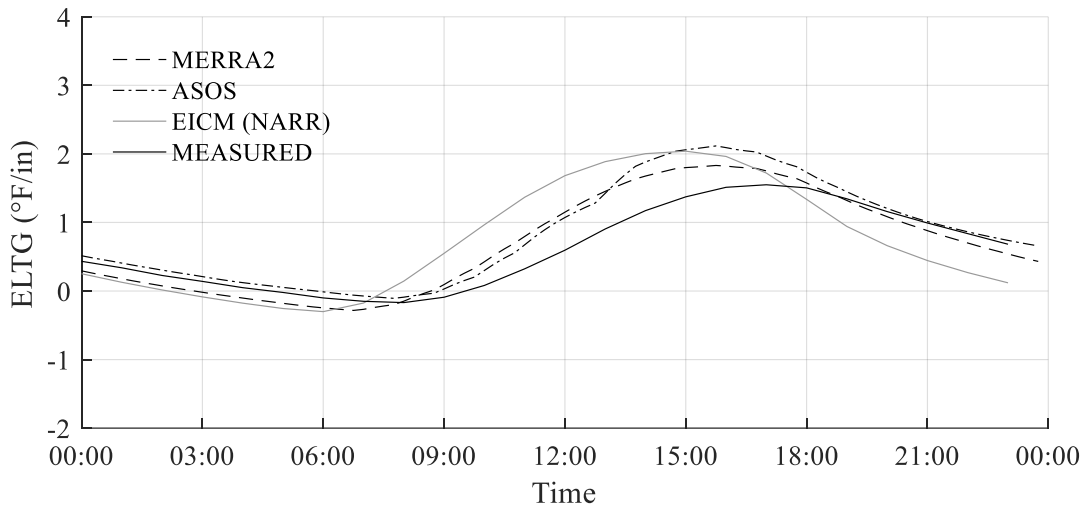


Figure A.59. Atlanta Hartsfield-Jackson Airport (4/1/2010)

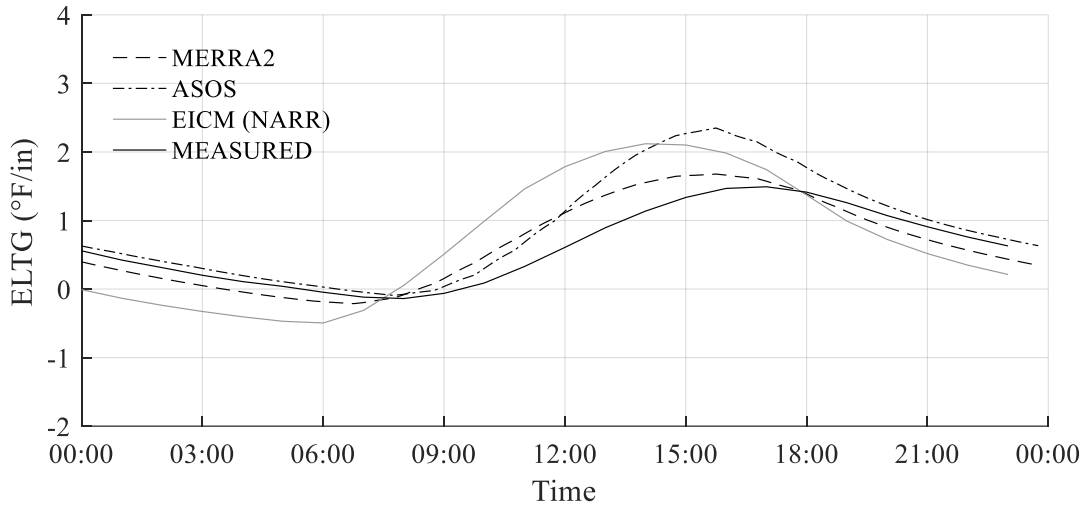


Figure A.60. Atlanta Hartsfield-Jackson Airport (4/2/2010)

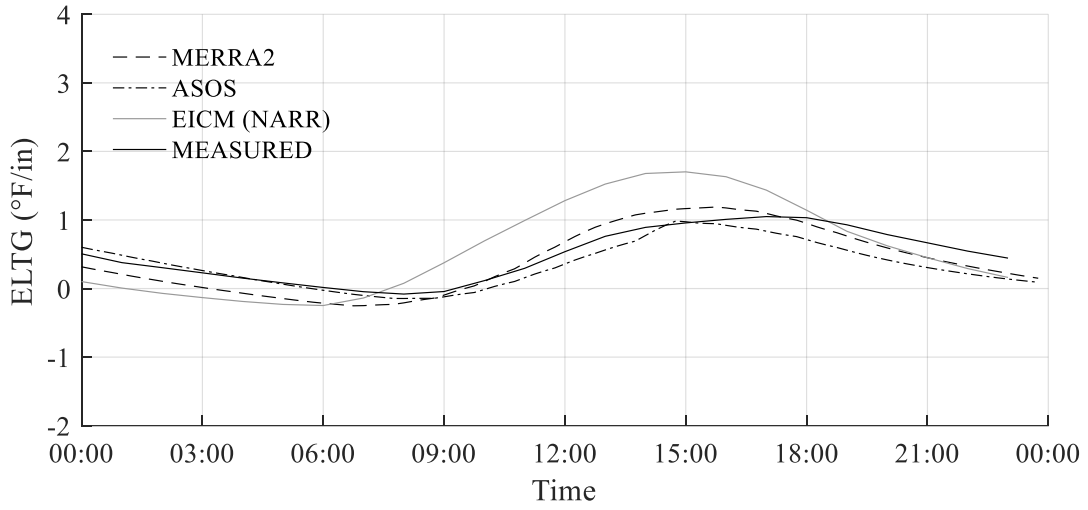


Figure A.61. Atlanta Hartsfield-Jackson Airport (4/3/2010)

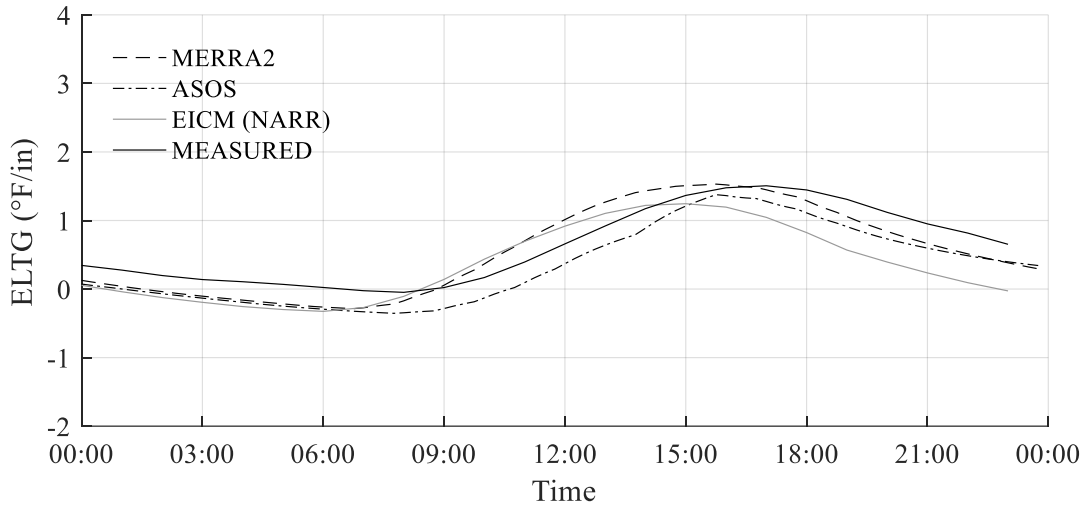


Figure A.62. Atlanta Hartsfield-Jackson Airport (4/4/2010)

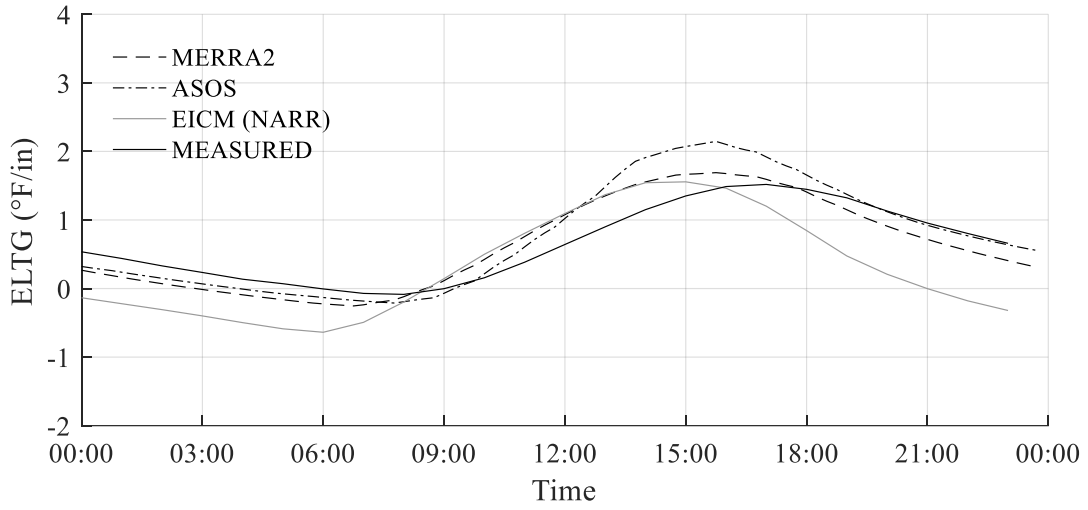


Figure A.63. Atlanta Hartsfield-Jackson Airport (4/5/2010)

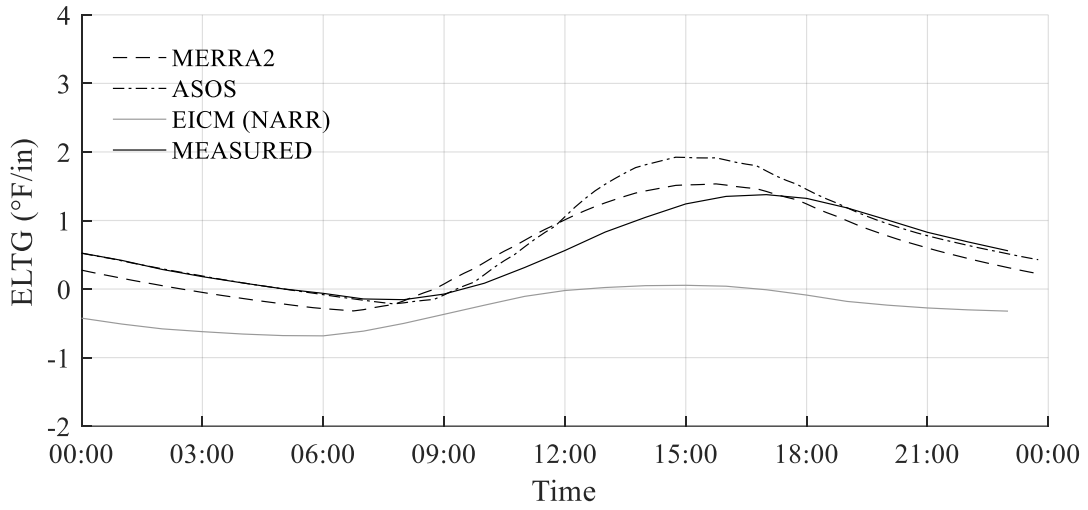


Figure A.64. Atlanta Hartsfield-Jackson Airport (4/6/2010)

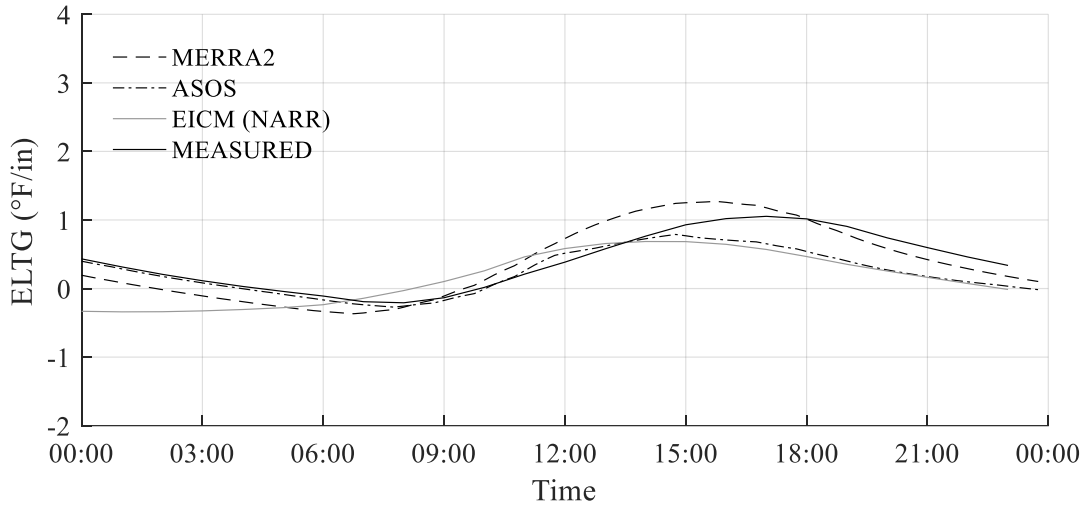


Figure A.65. Atlanta Hartsfield-Jackson Airport (4/7/2010)

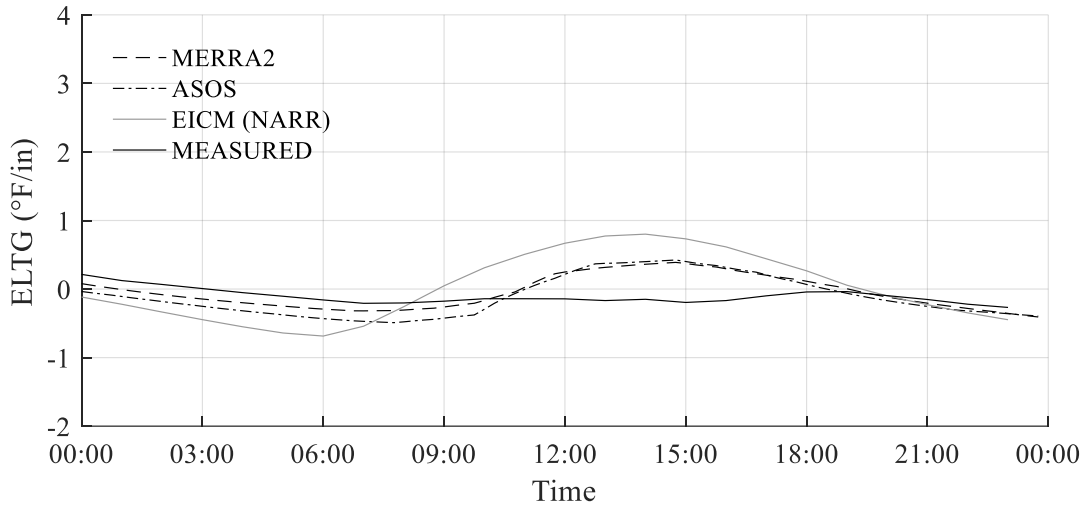


Figure A.66. Atlanta Hartsfield-Jackson Airport (4/8/2010)

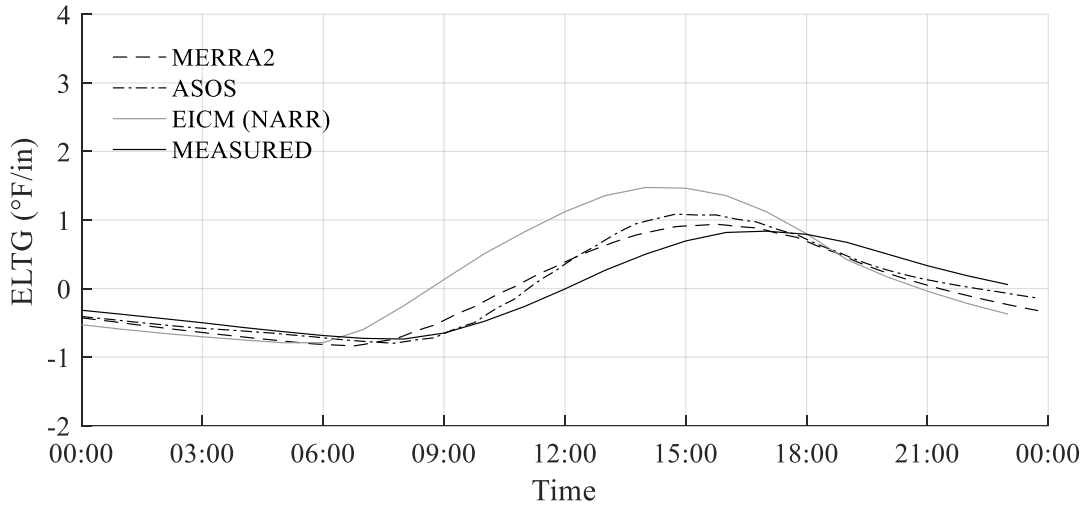


Figure A.67. Atlanta Hartsfield-Jackson Airport (4/9/2010)

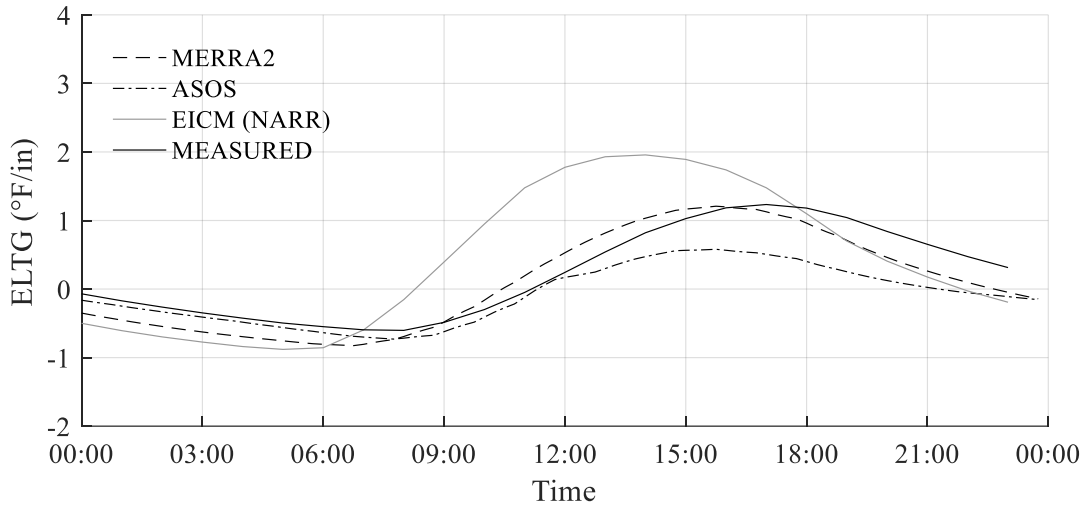


Figure A.68. Atlanta Hartsfield-Jackson Airport (4/10/2010)

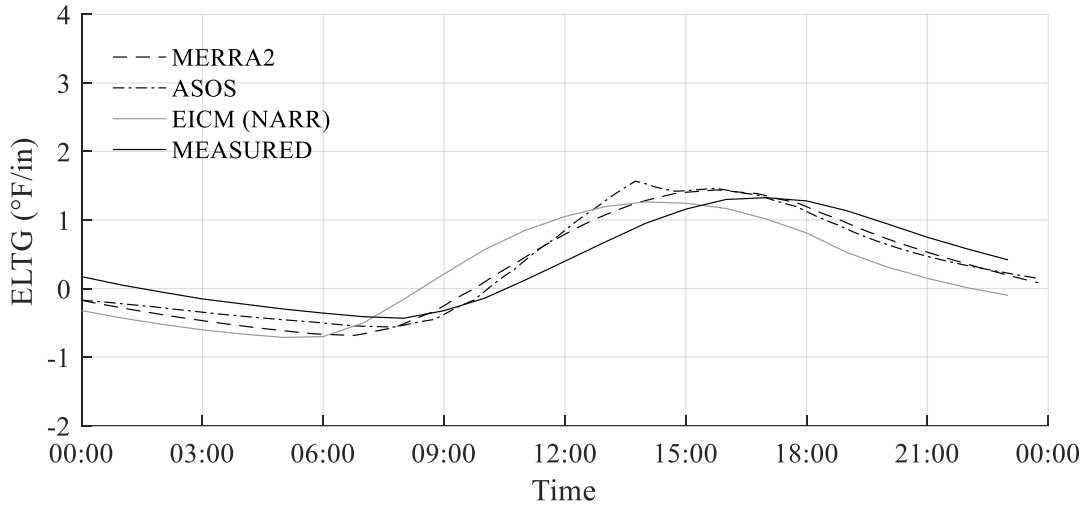


Figure A.69. Atlanta Hartsfield-Jackson-Airport (4/11/2010)

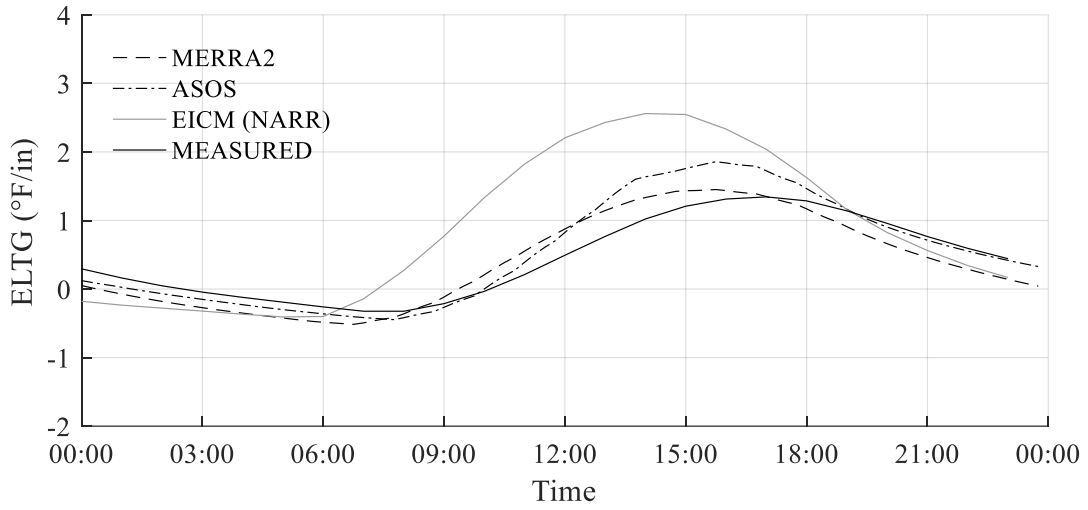


Figure A.70. Atlanta Hartsfield-Jackson Airport (4/12/2010)

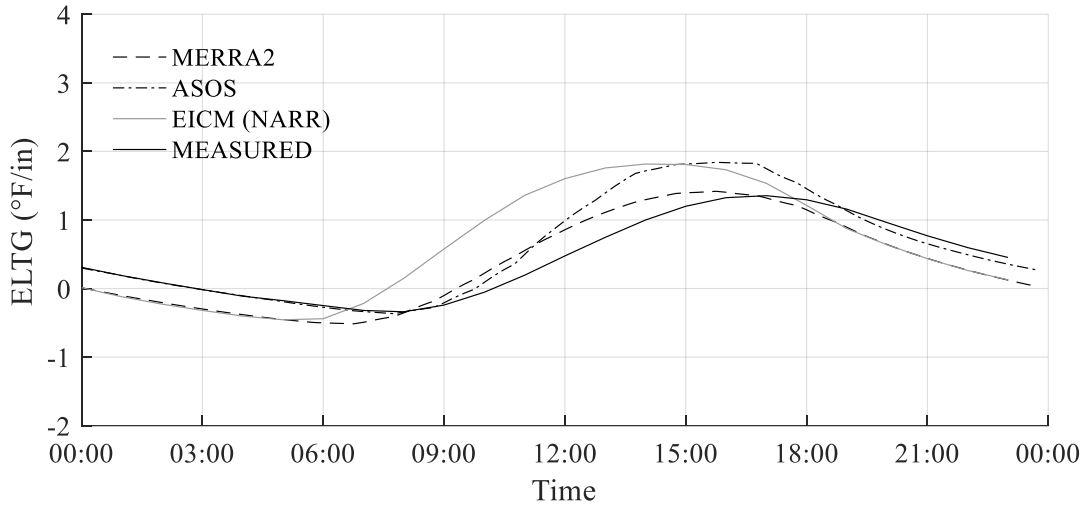


Figure A.71. Atlanta Hartsfield-Jackson Airport (4/13/2010)

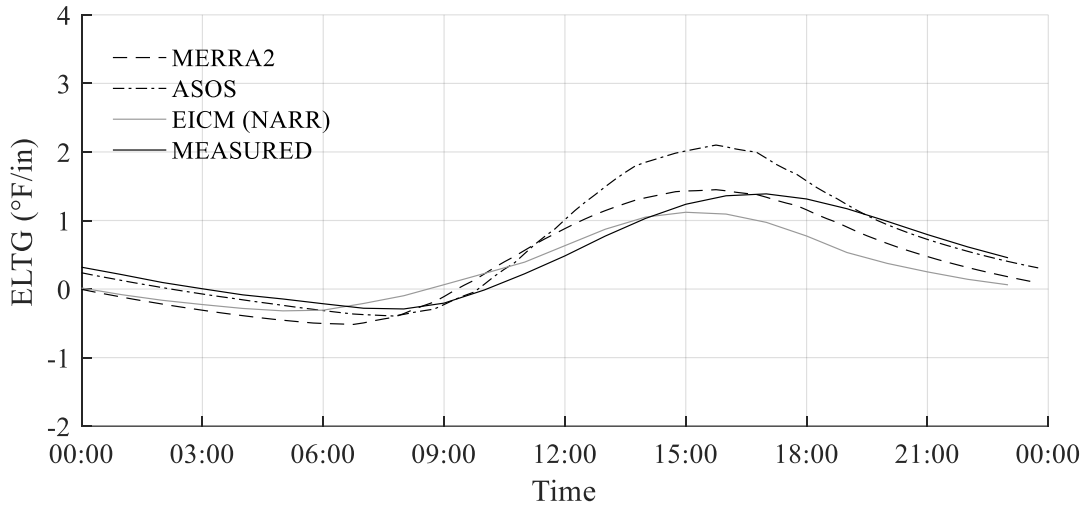


Figure A.72. Atlanta Hartsfield-Jackson Airport (4/14/2010)

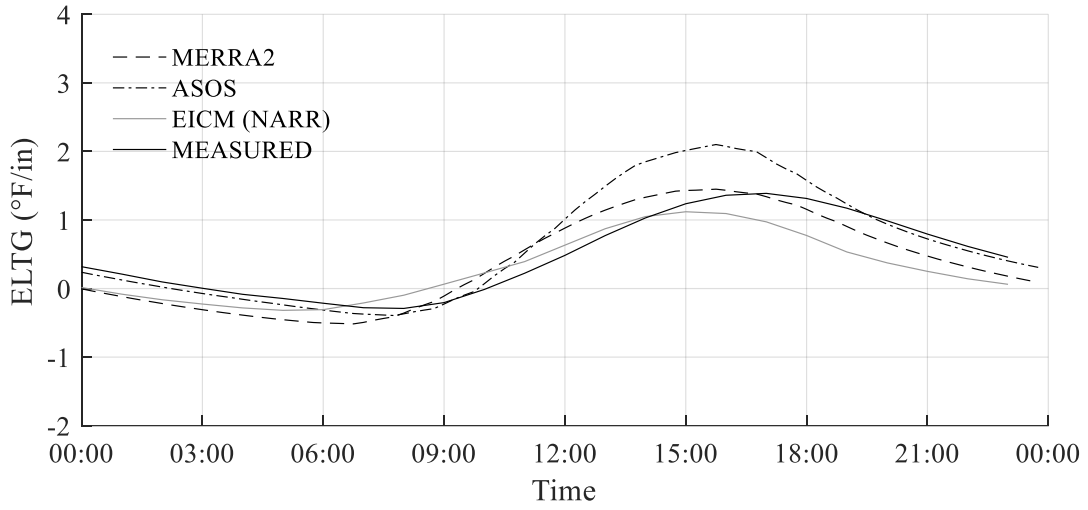


Figure A.73. Atlanta Hartsfield-Jackson Airport (4/15/2010)

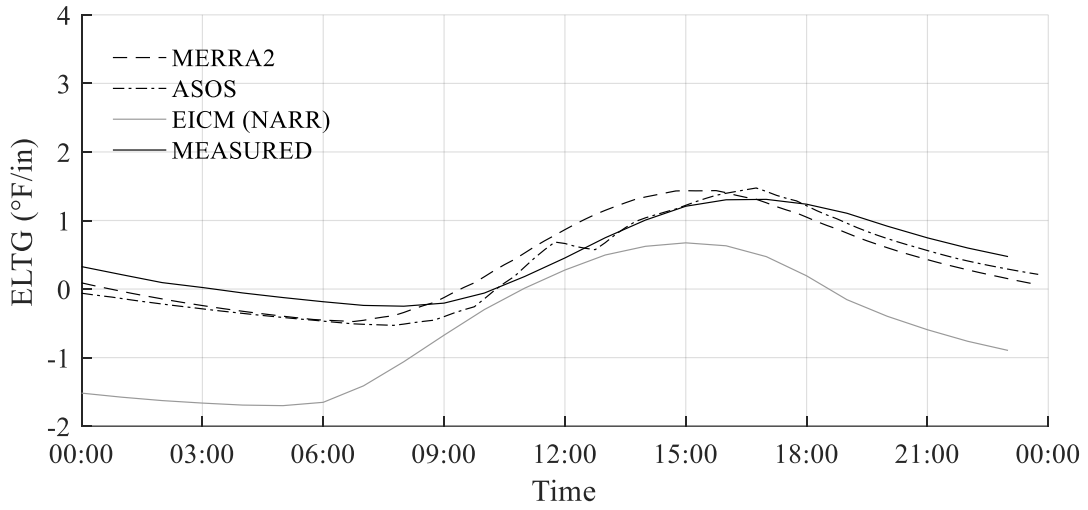


Figure A.74. Atlanta Hartsfield-Jackson Airport (4/16/2010)

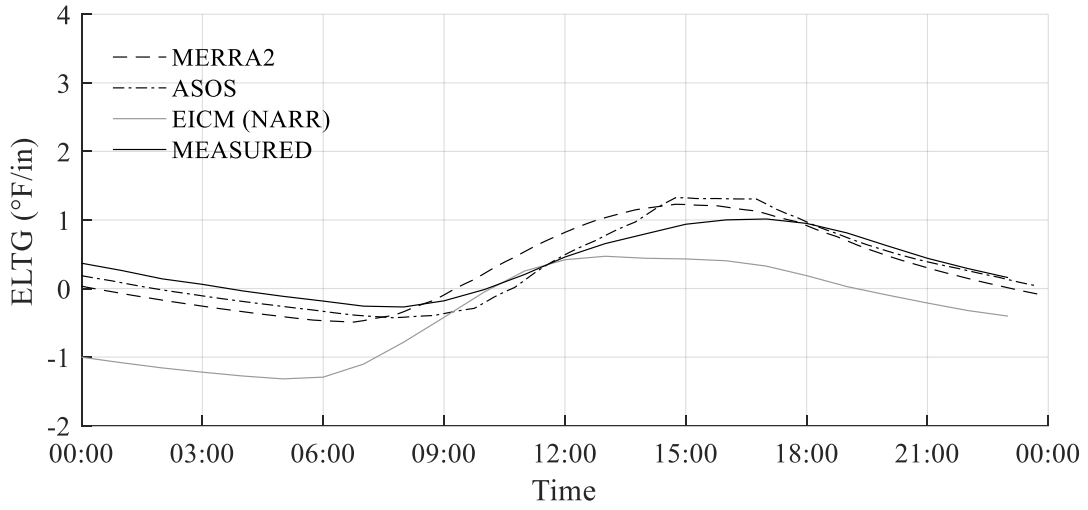


Figure A.75. Atlanta Hartsfield-Jackson Airport (4/17/2010)

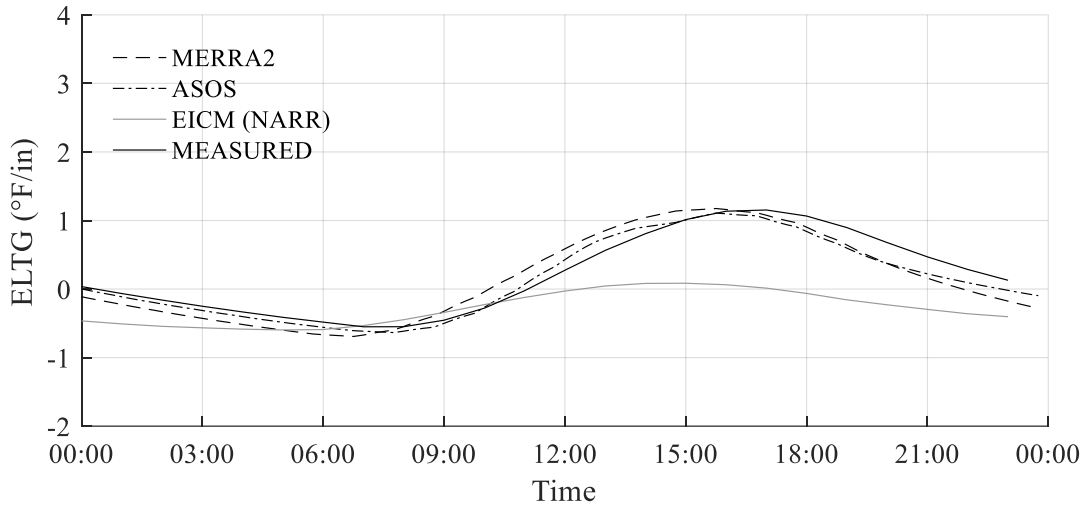


Figure A.76. Atlanta Hartsfield-Jackson Airport (4/18/2010)

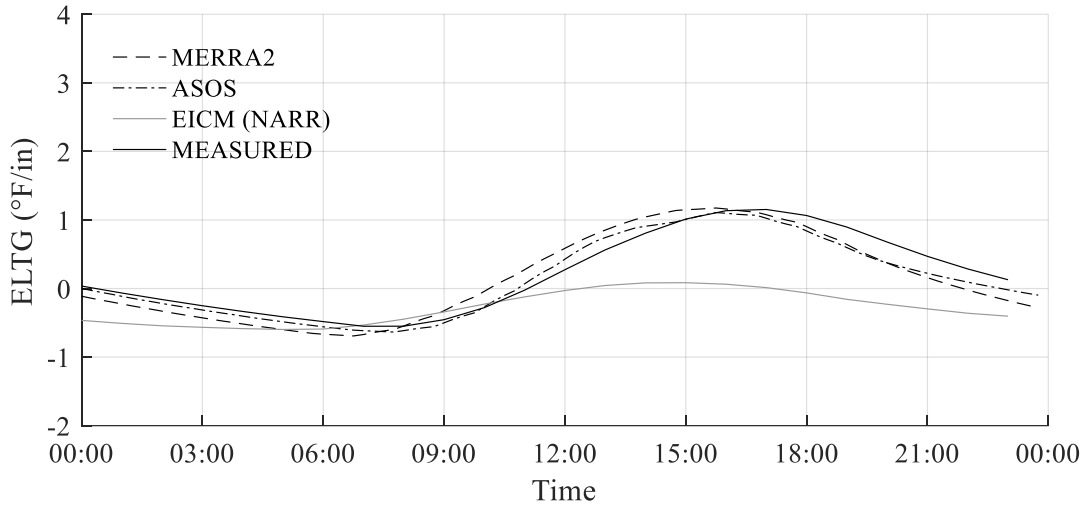


Figure A.77. Atlanta Hartsfield-Jackson Airport (4/19/2010)

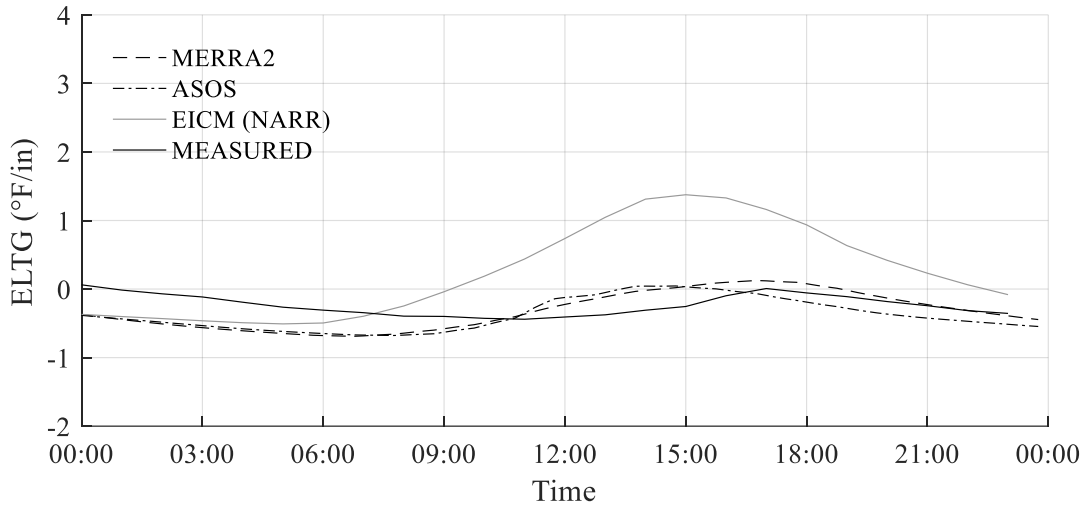


Figure A.78. Atlanta Hartsfield-Jackson Airport (4/20/2010)

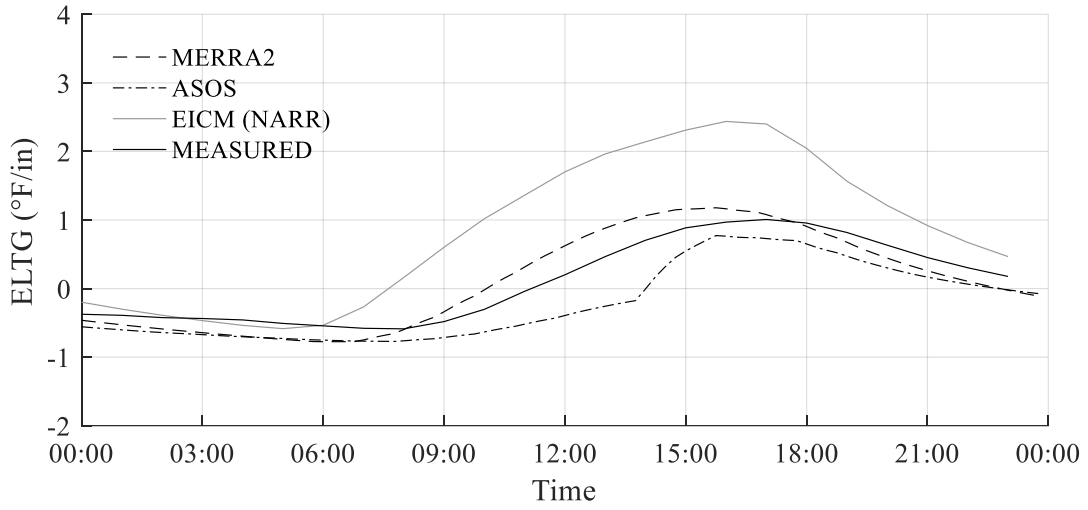


Figure-A.79. Atlanta Hartsfield-Jackson Airport (4/21/2010)

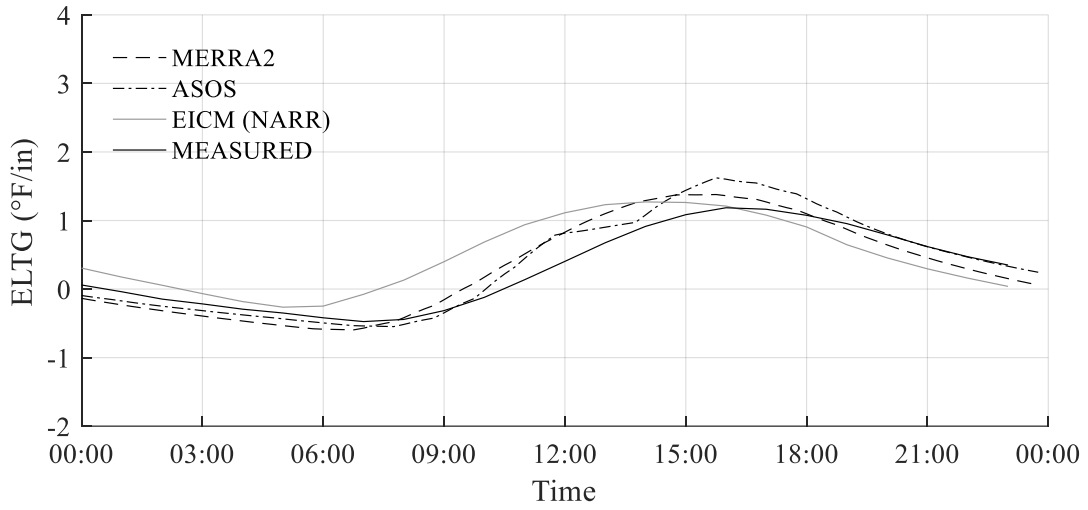


Figure A.80. Atlanta Hartsfield-Jackson Airport (4/22/2010)

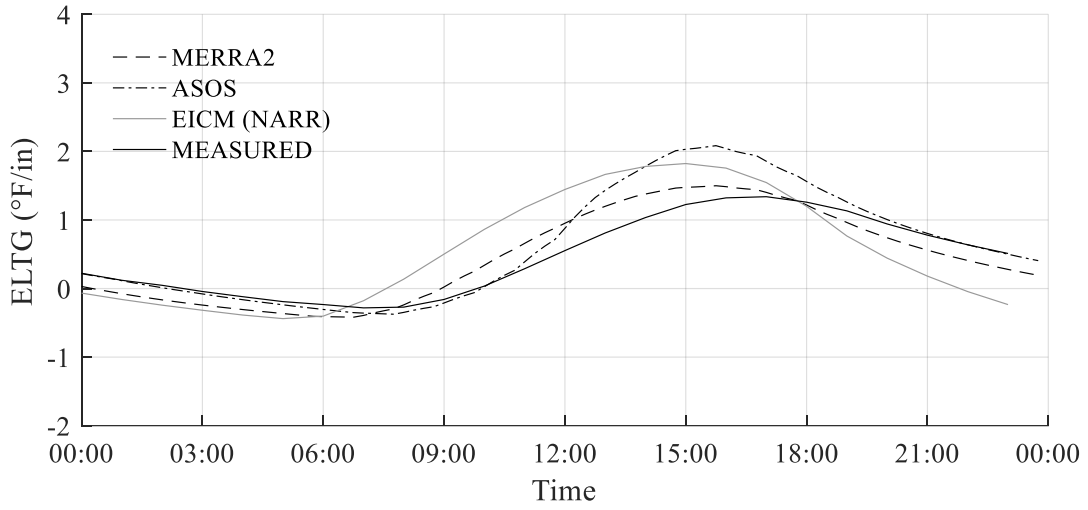


Figure A.81. Atlanta Hartsfield-Jackson Airport (4/23/2010)

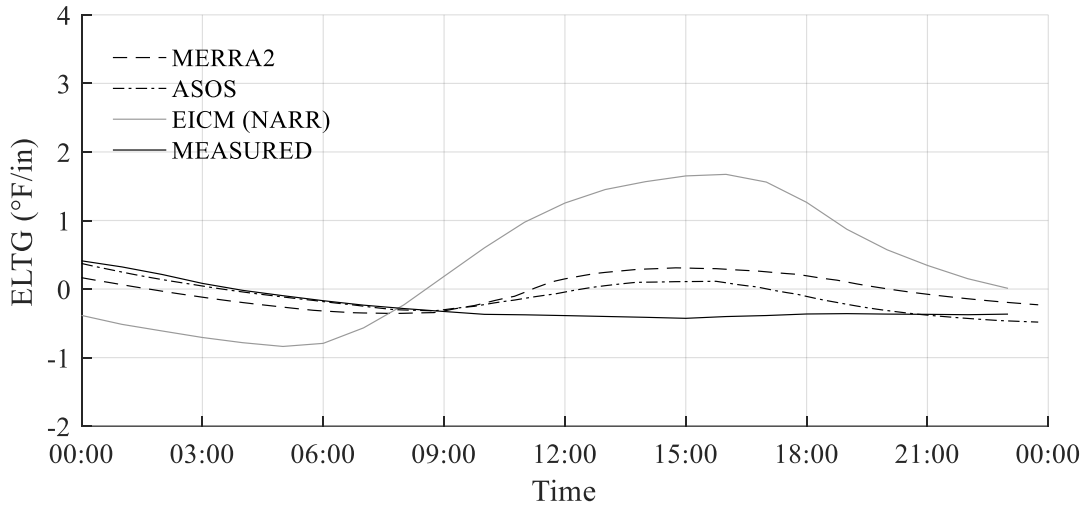


Figure A.82. Atlanta Hartsfield-Jackson Airport (4/24/2010)

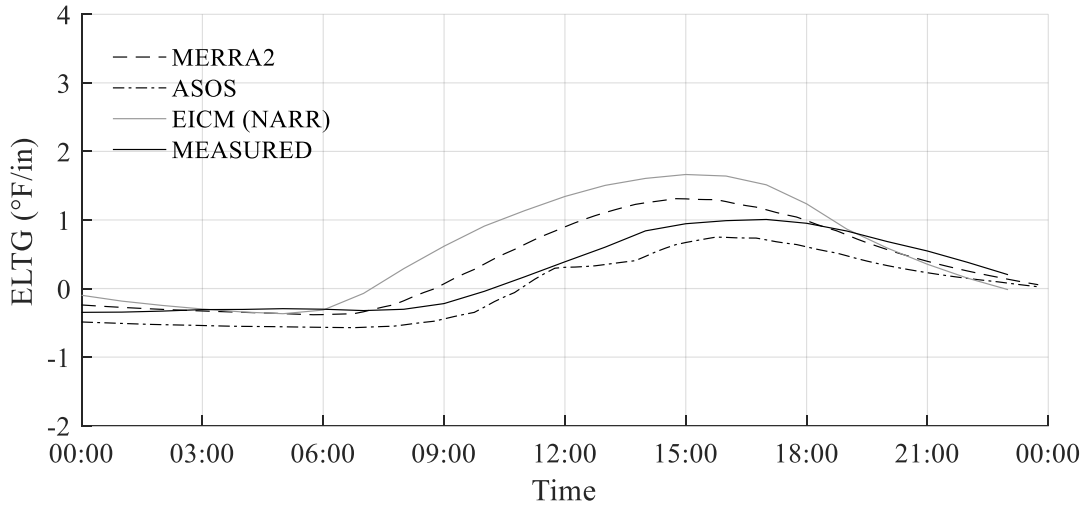


Figure A.83. Atlanta Hartsfield-Jackson Airport (4/25/2010)

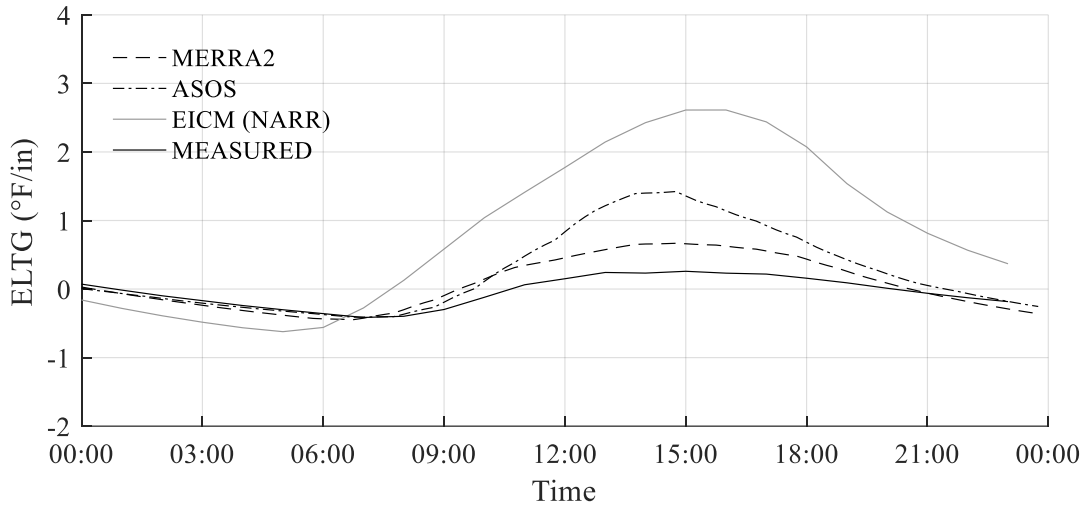


Figure A.84. Atlanta Hartsfield-Jackson Airport (4/26/2010)

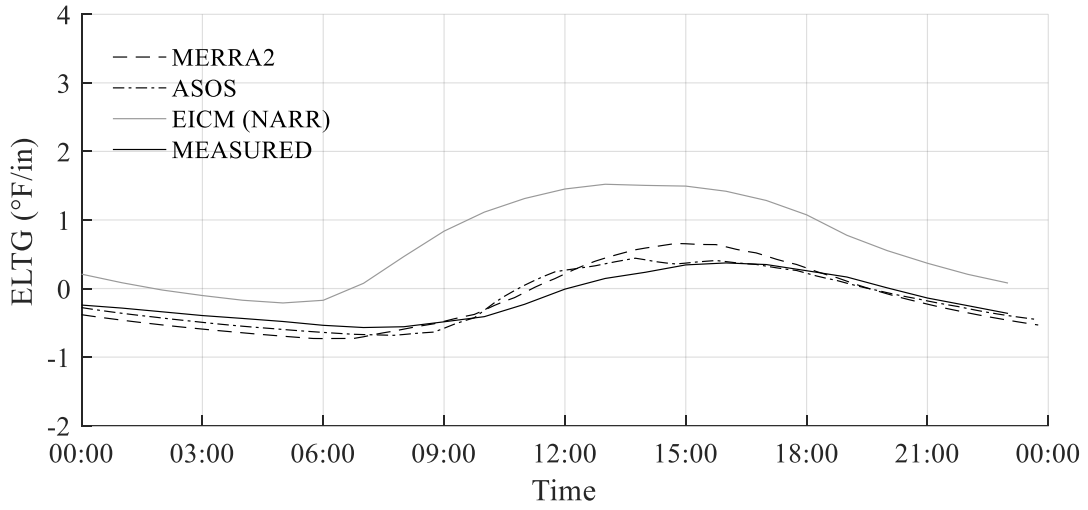


Figure A.85. Atlanta Hartsfield-Jackson Airport (4/27/2010)

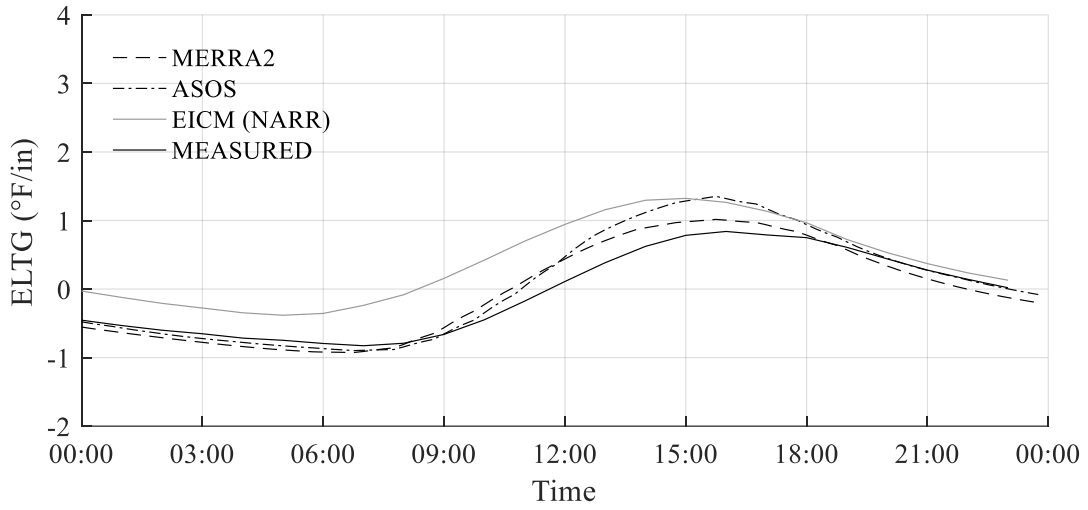


Figure A.86. Atlanta Hartsfield-Jackson Airport (4/28/2010)

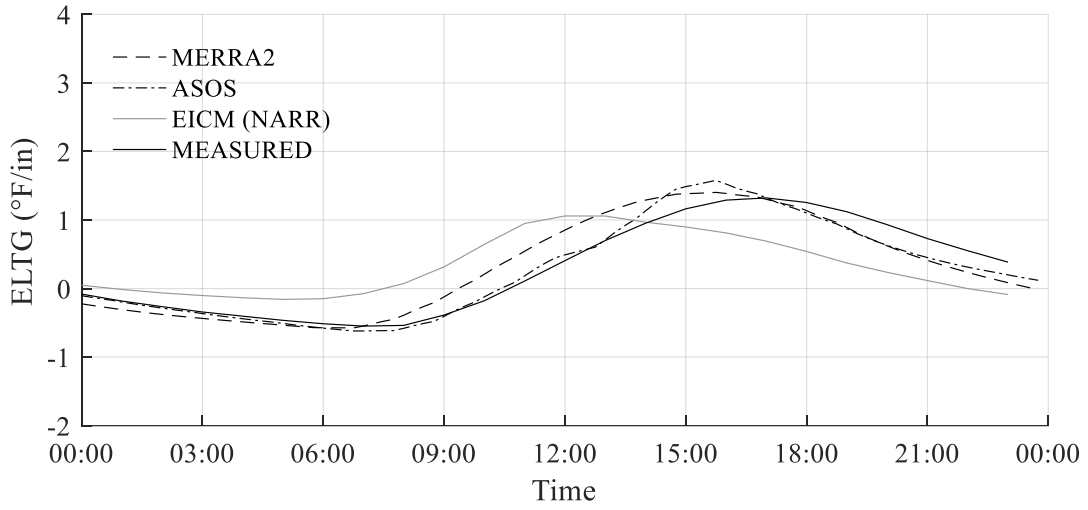


Figure A.87. Atlanta Hartsfield-Jackson Airport (4/29/2010)

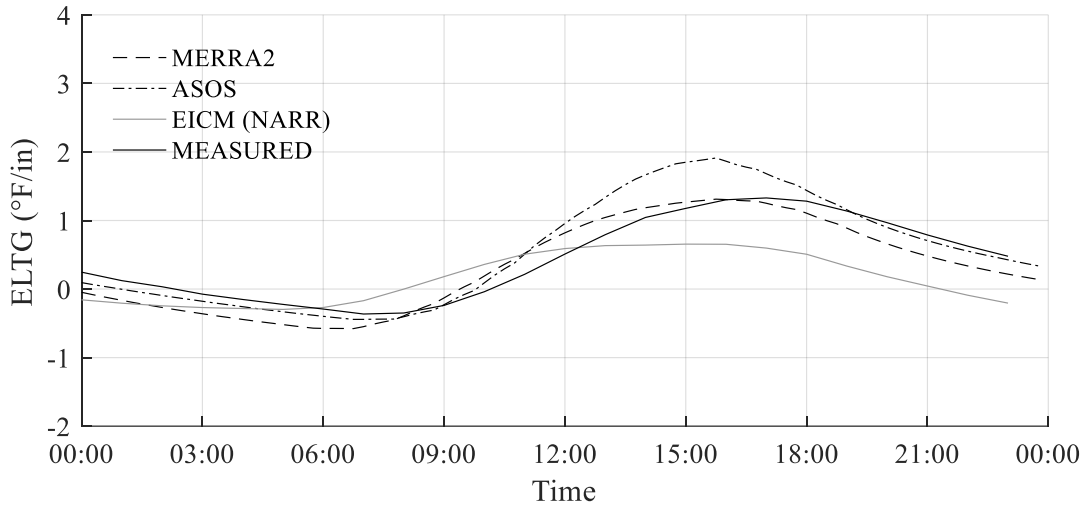


Figure A.88. Atlanta Hartsfield-Jackson Airport (4/30/2010)

SR-22 SMART PAVEMENT

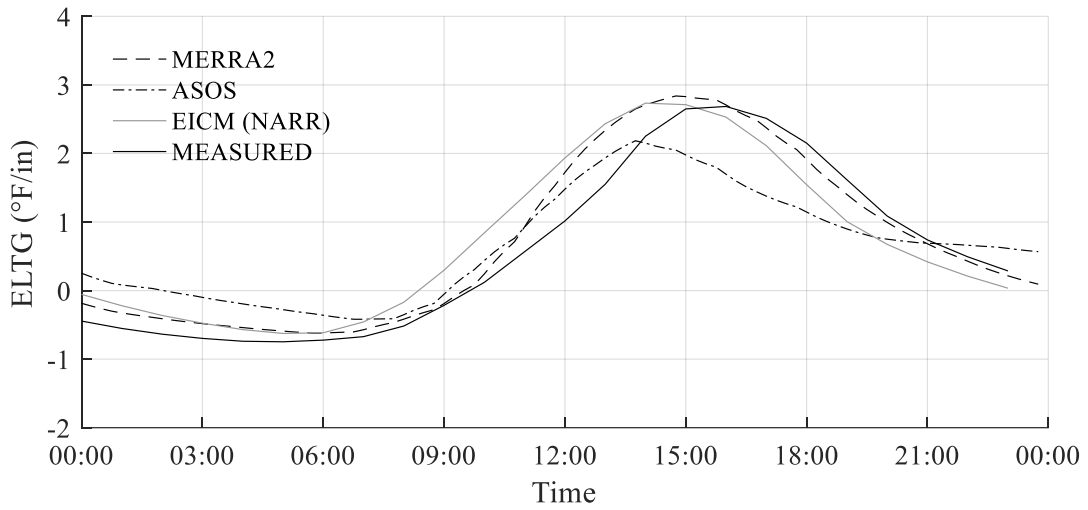


Figure A.89. SR-22 Smart Pavement (4/1/2014)

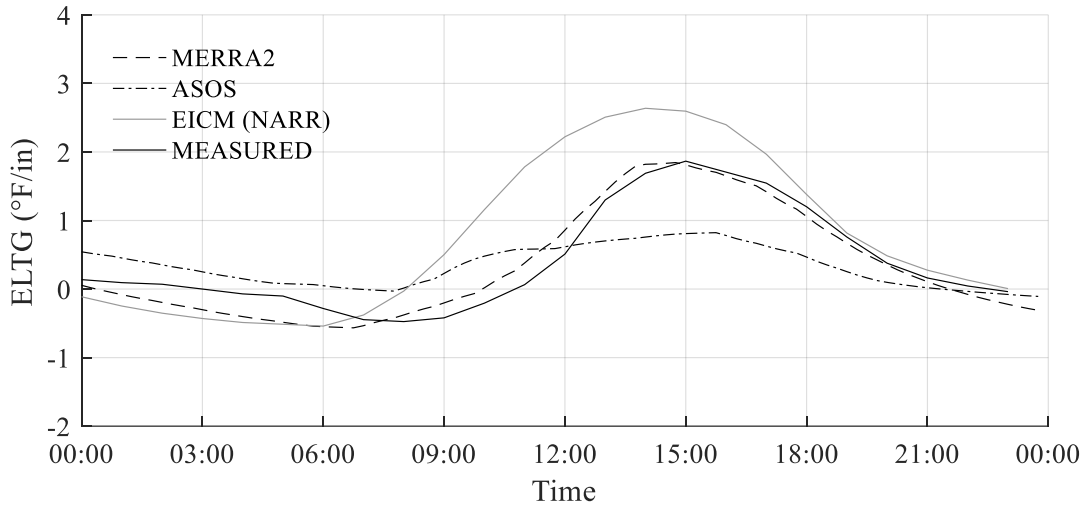


Figure A.90. SR-22 Smart Pavement (4/2/2014)

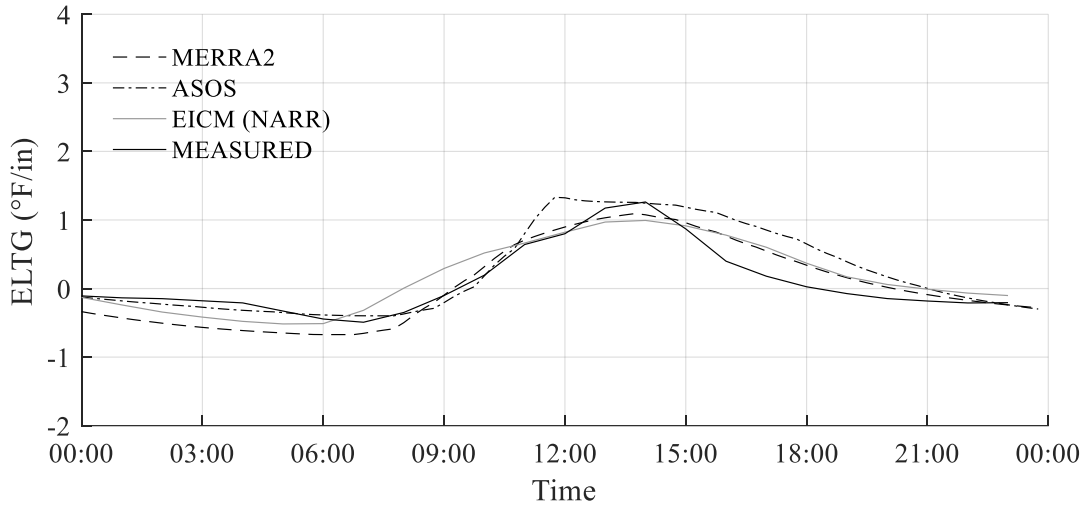


Figure A.91. SR-22 Smart Pavement (4/3/2014)

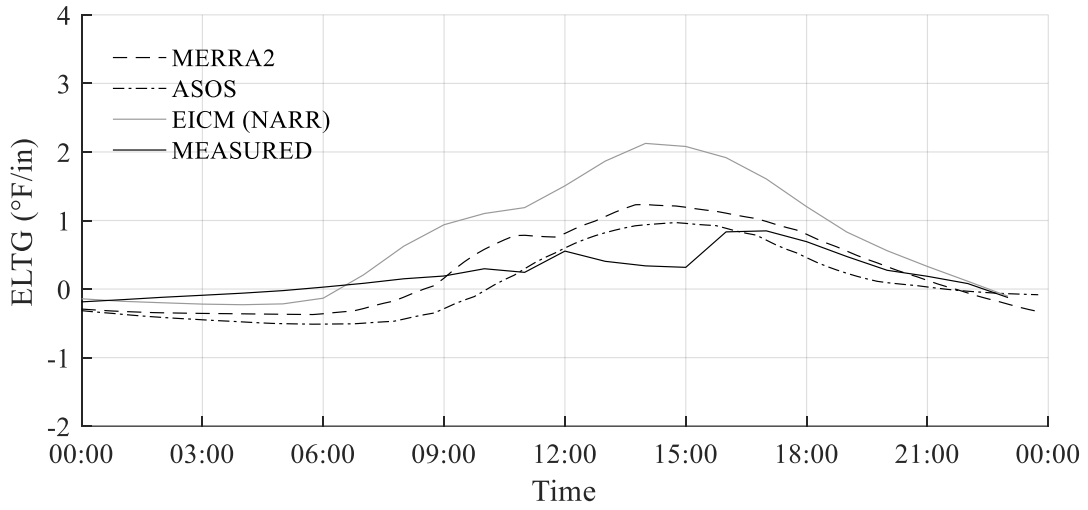


Figure A.92. SR-22 Smart Pavement (4/4/2014)

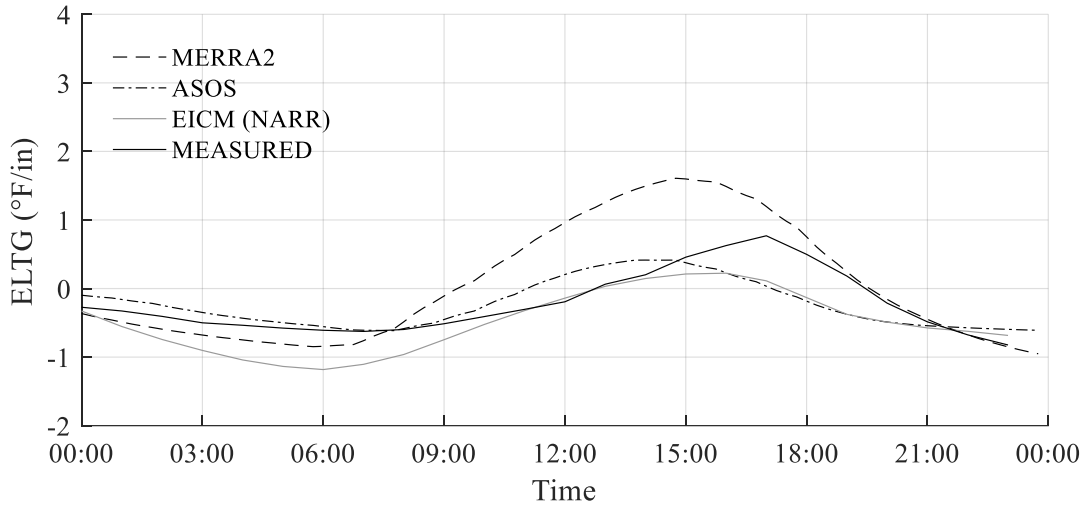


Figure A.93. SR-22 Smart Pavement (4/5/2014)

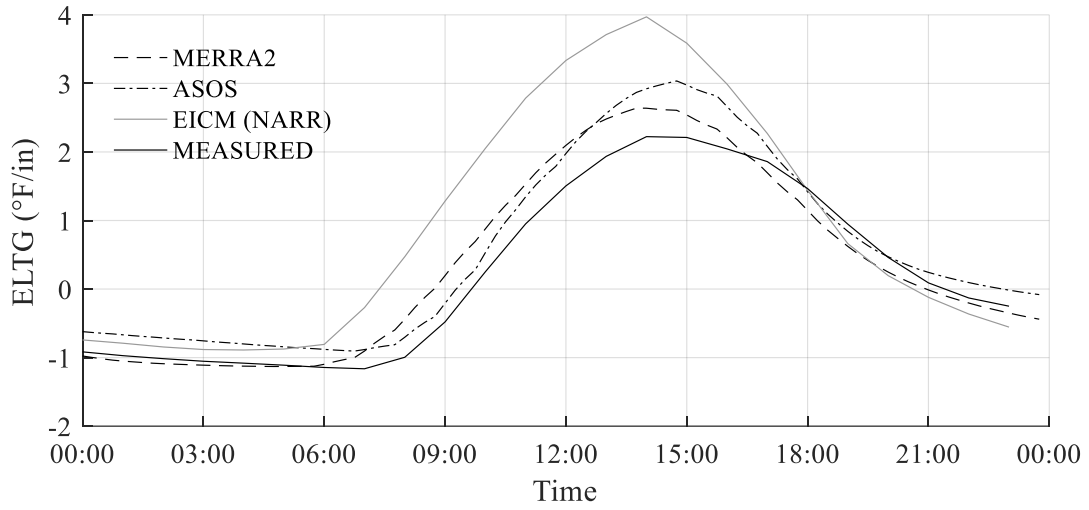


Figure A.94. SR-22 Smart Pavement (4/6/2014)

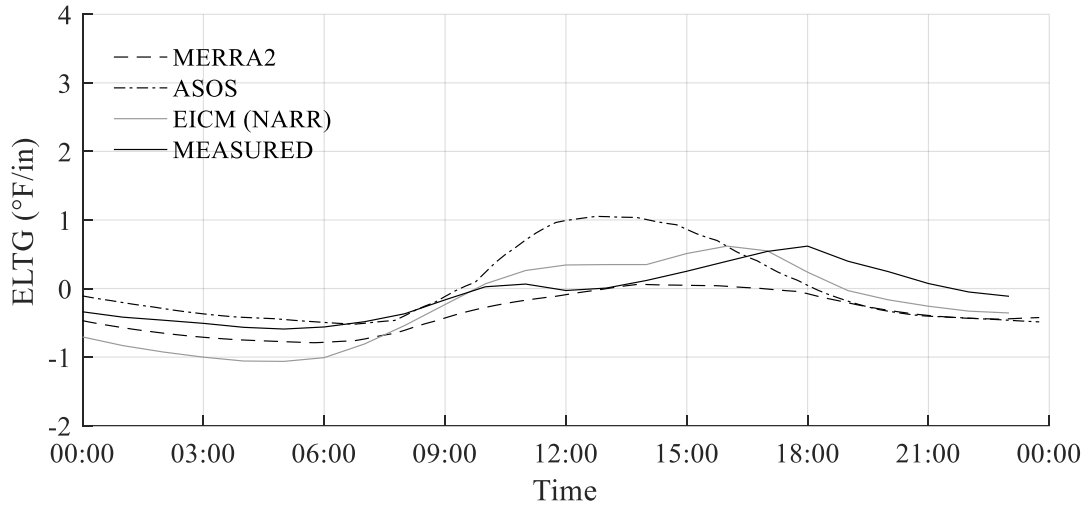


Figure A.95. SR-22 Smart Pavement (4/7/2014)

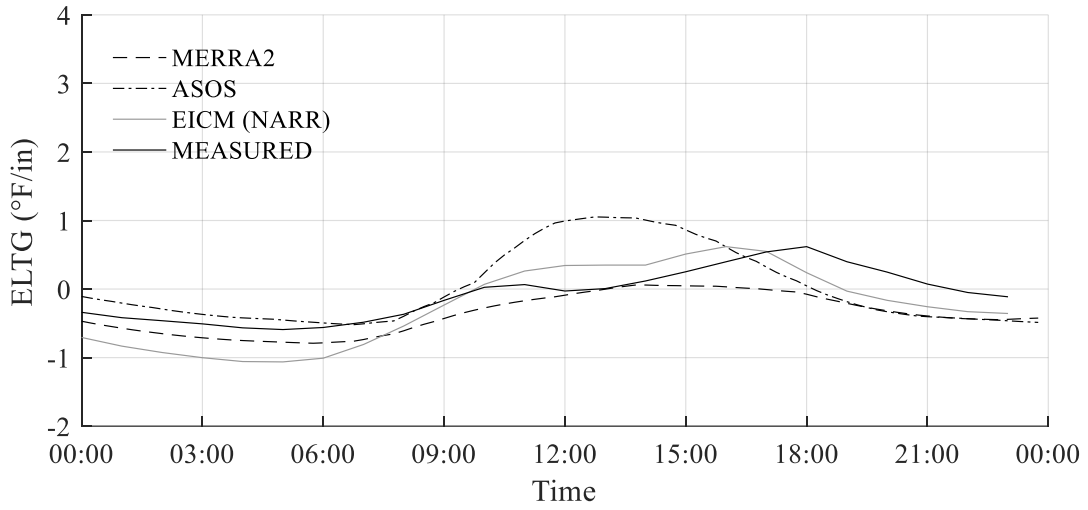


Figure A.96. SR-22 Smart Pavement (4/8/2014)

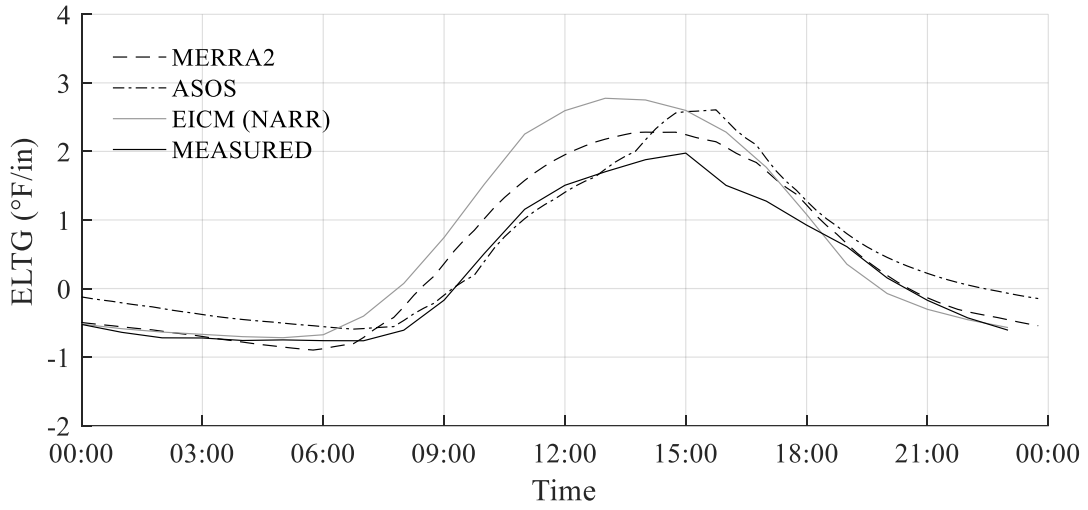


Figure A.97. SR-22 Smart Pavement (4/9/2014)

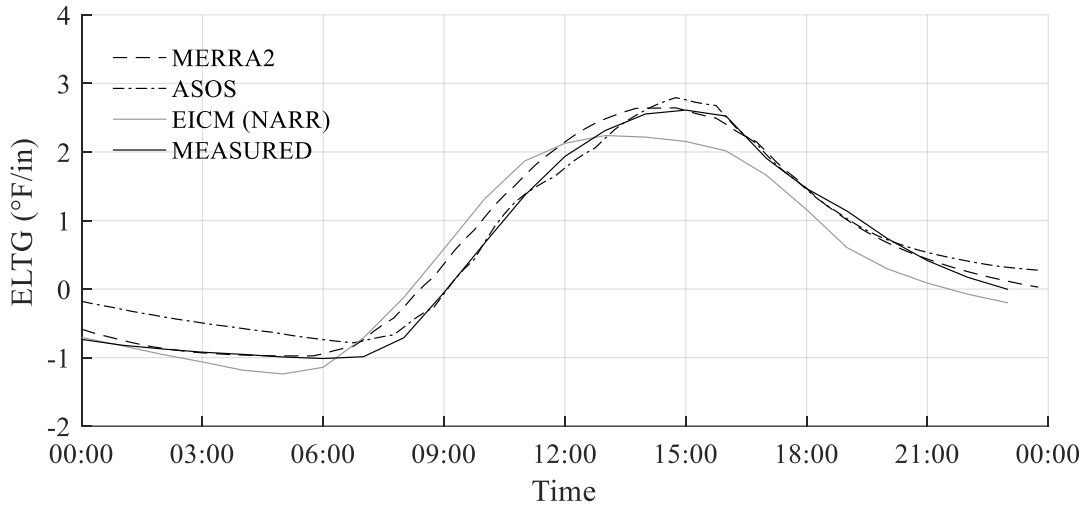


Figure A.98. SR-22 Smart Pavement (4/10/2014)

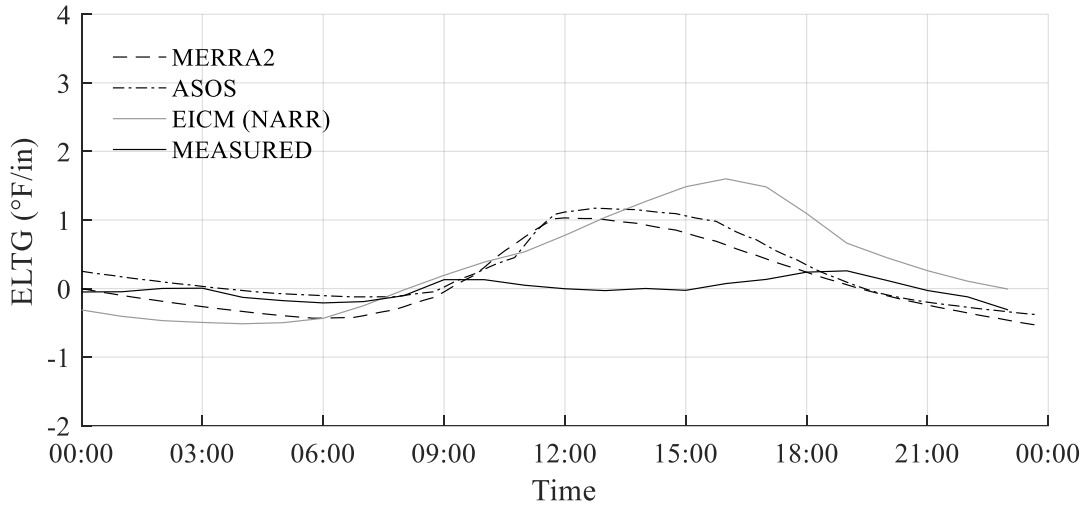


Figure A.99. SR-22 Smart Pavement (4/11/2014)

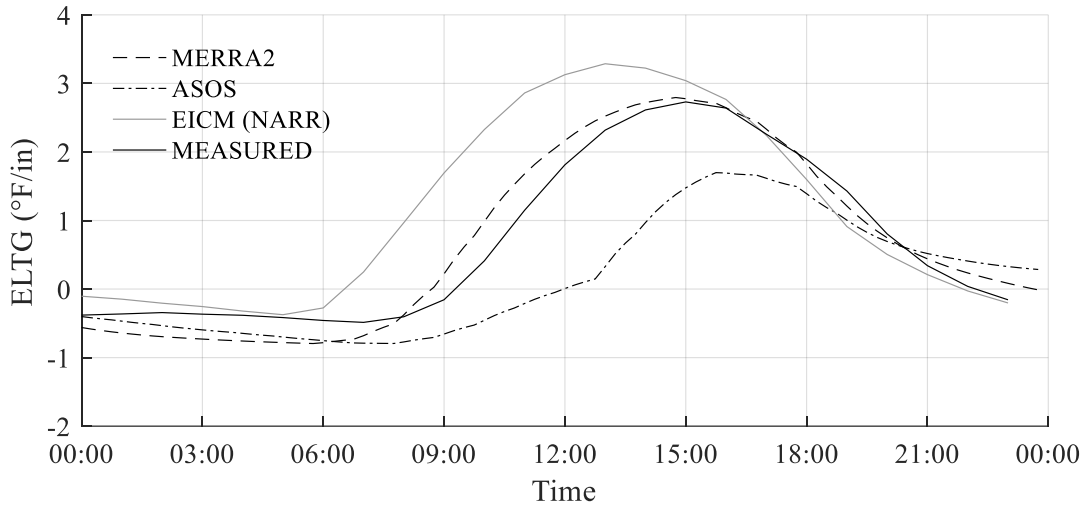


Figure A.100. SR-22 Smart Pavement (4/12/2014)

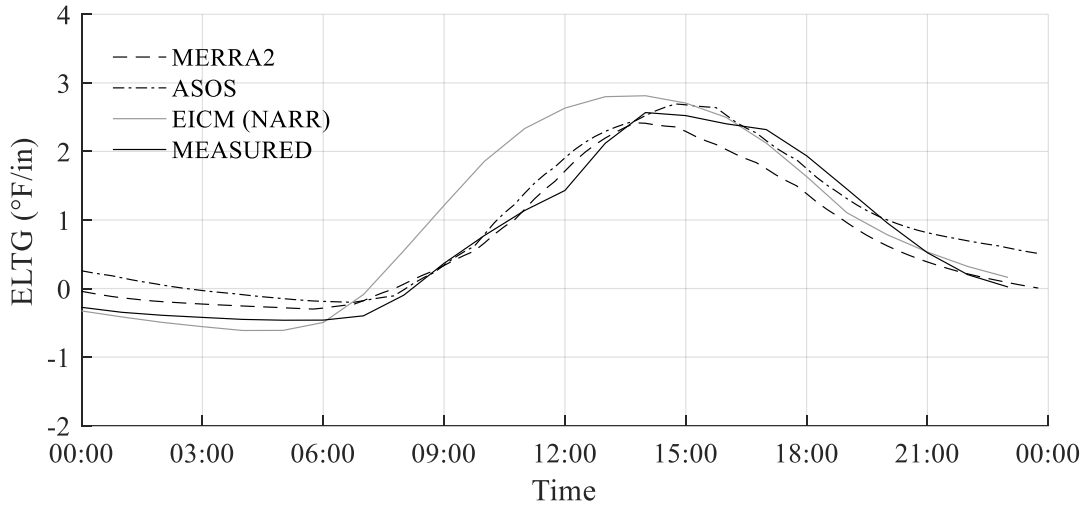


Figure A.101. SR-22 Smart Pavement (4/13/2014)

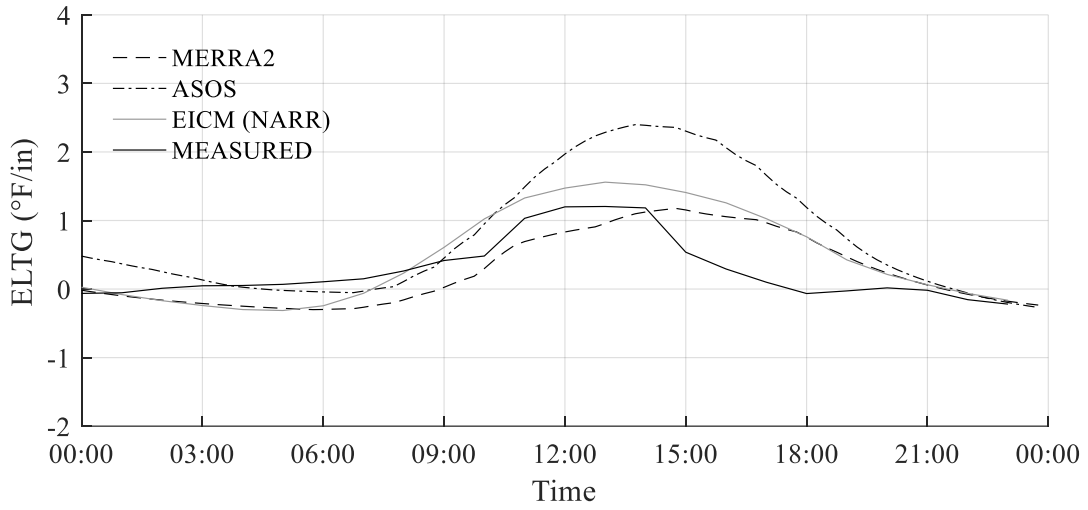


Figure A.102. SR-22 Smart Pavement (4/14/2014)

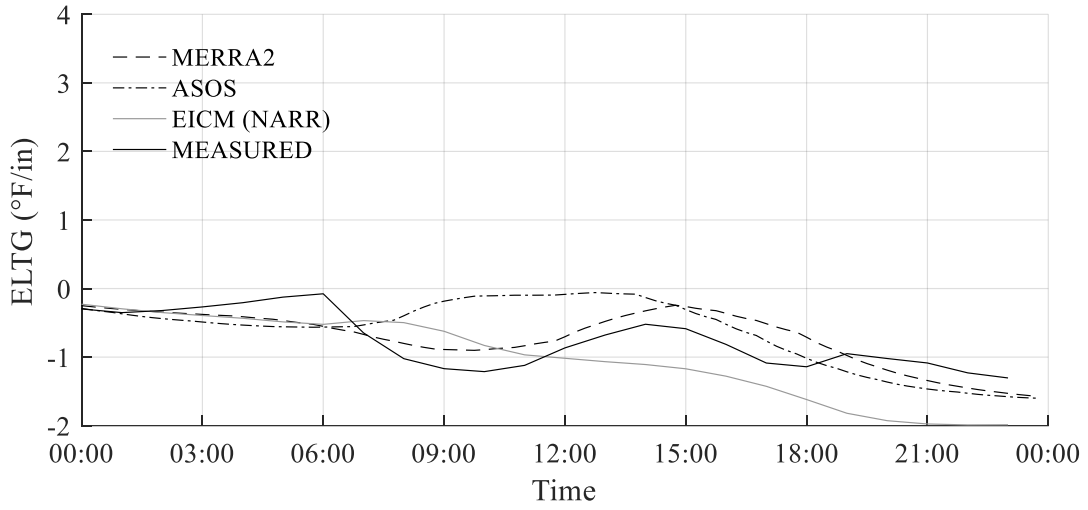


Figure A.103. SR-22 Smart Pavement (4/15/2014)

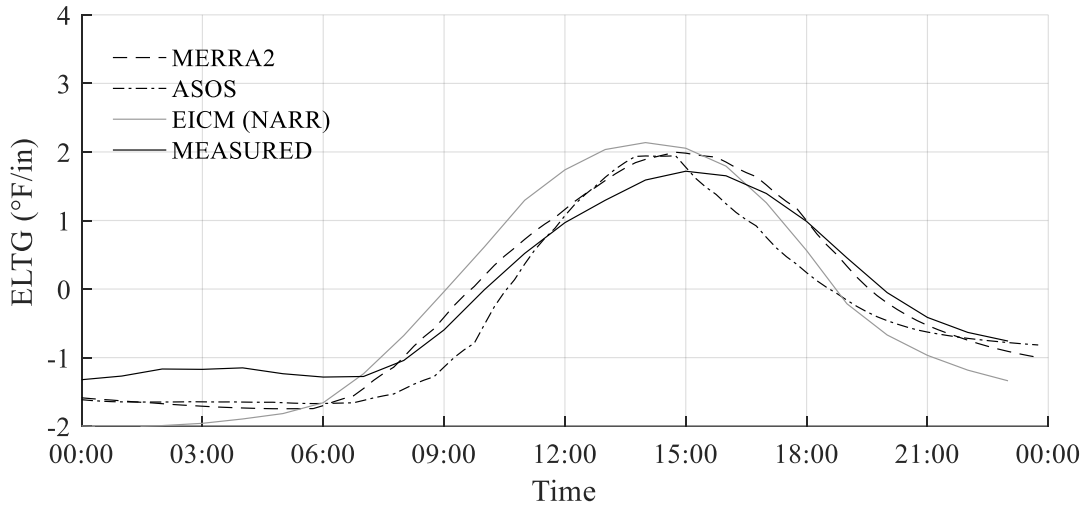


Figure A.104. SR-22 Smart Pavement (4/17/2014)

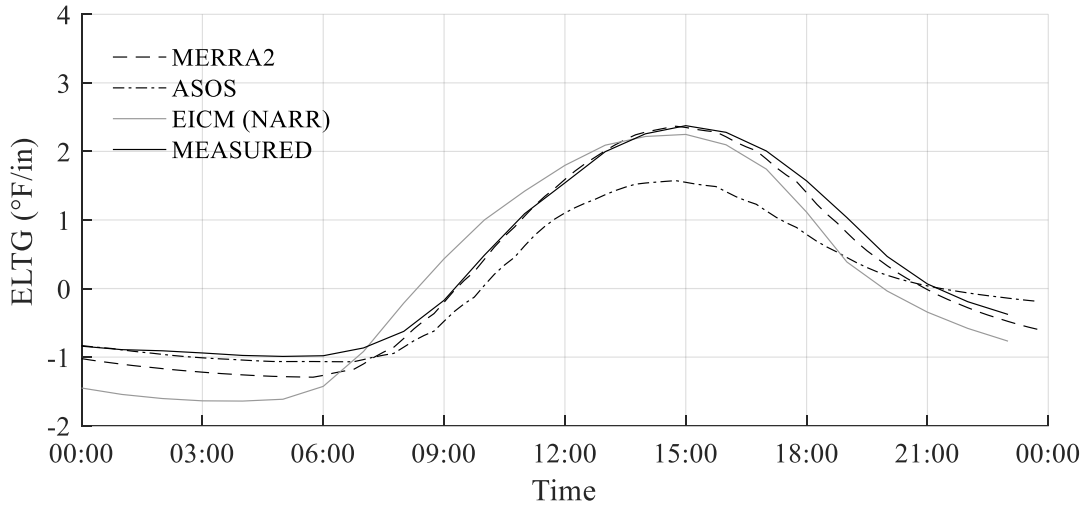


Figure A.105. SR-22 Smart Pavement (4/18/2014)

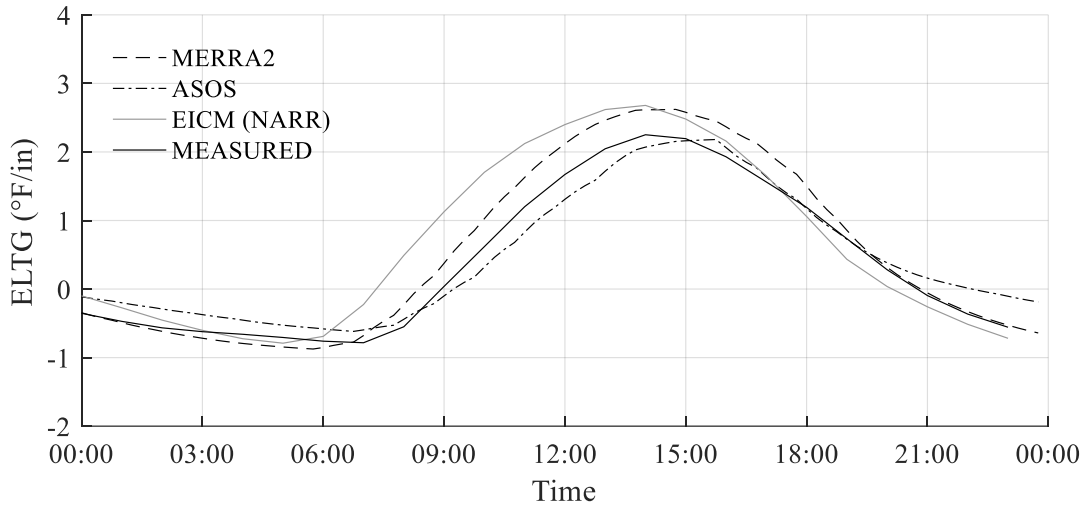


Figure A.106. SR-22 Smart Pavement (4/19/2014)

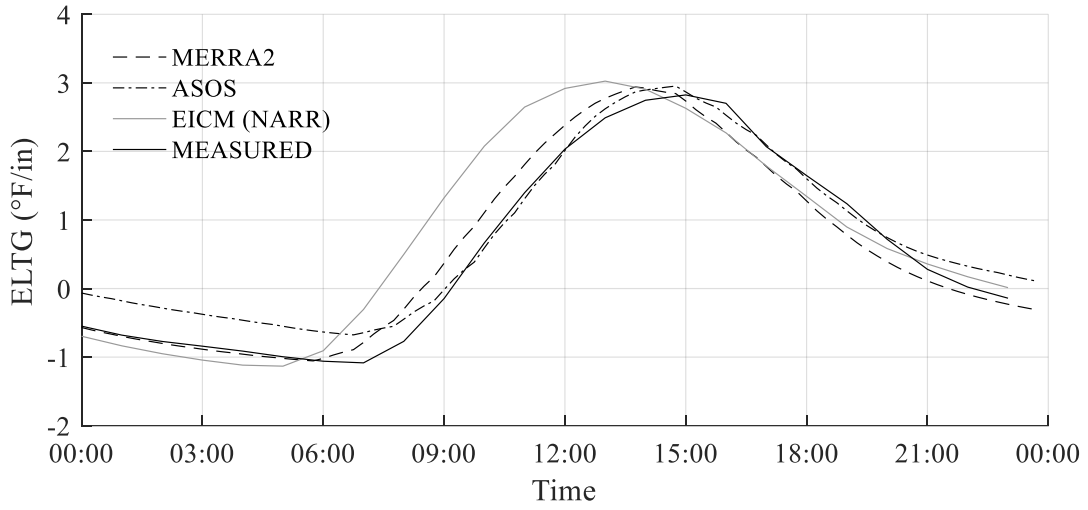


Figure A.107. SR-22 Smart Pavement (4/21/2014)

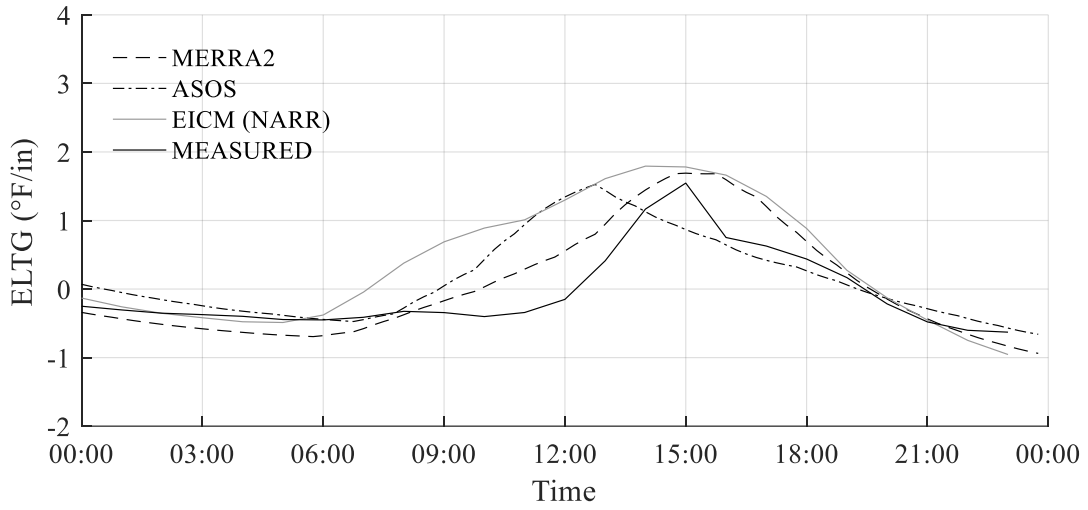


Figure A.108. SR-22 Smart Pavement (4/22/2014)

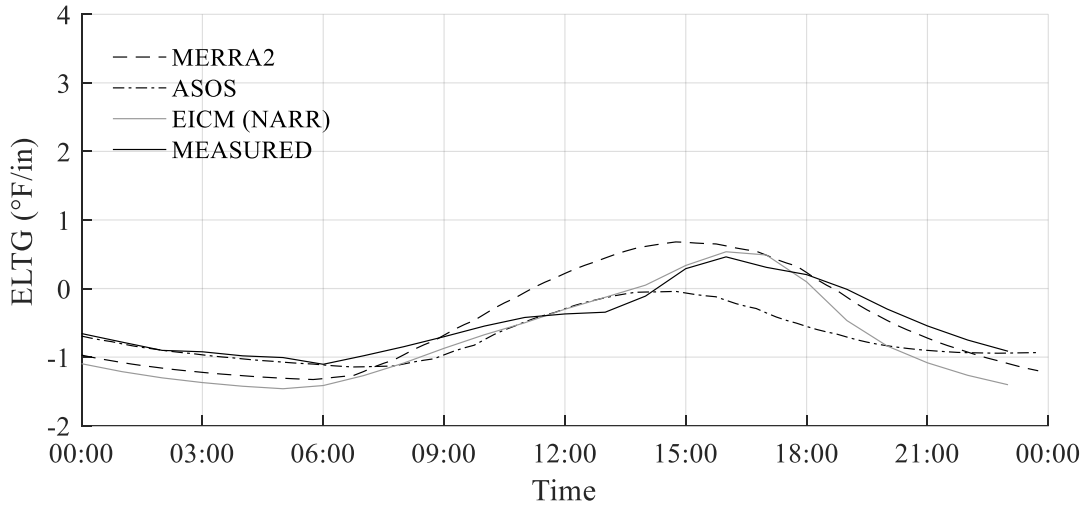


Figure A.109. SR-22 Smart Pavement (4/23/2014)

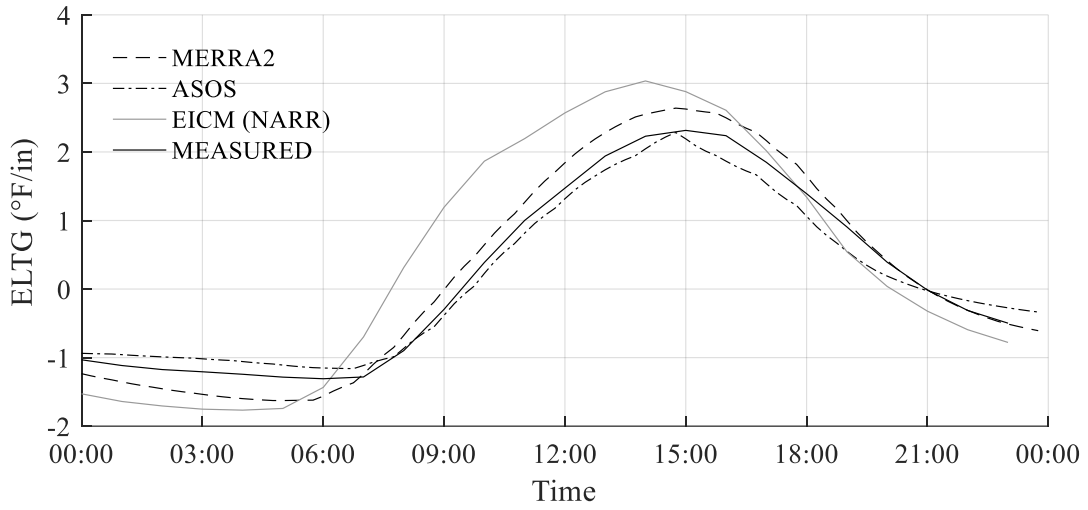


Figure A.110. SR-22 Smart Pavement (4/24/2014)

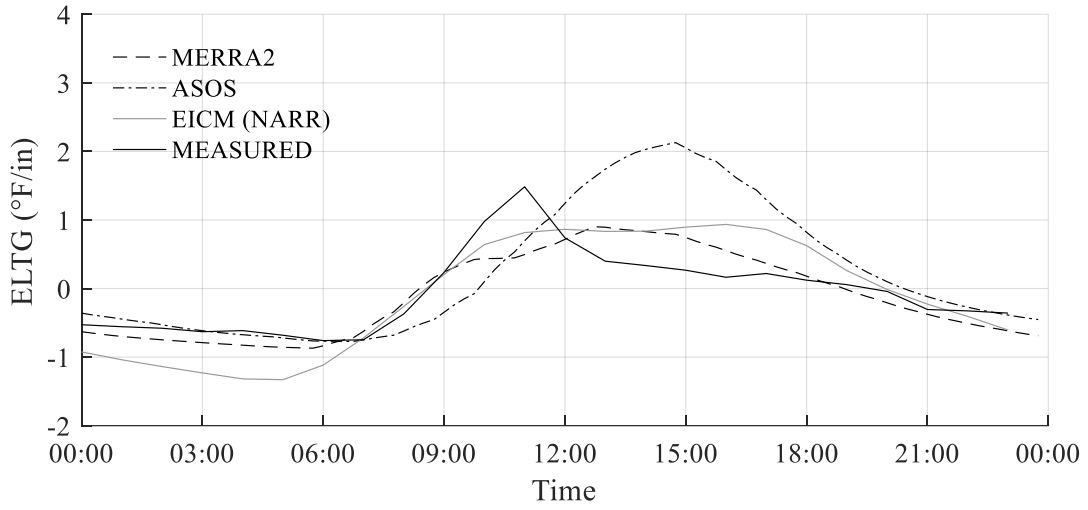


Figure A.111. SR-22 Smart Pavement (4/25/2014)

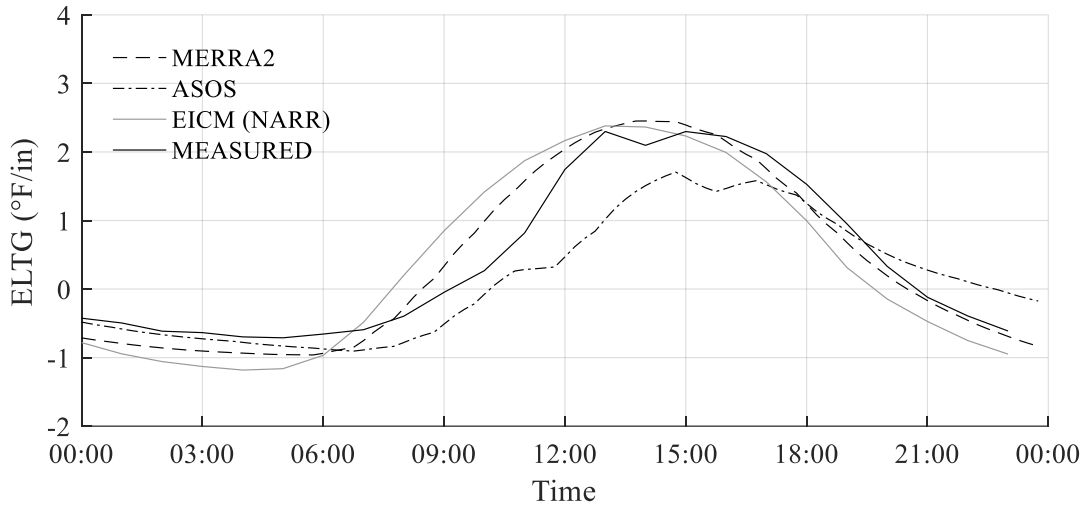


Figure A.112. SR-22 Smart Pavement (4/26/2014)

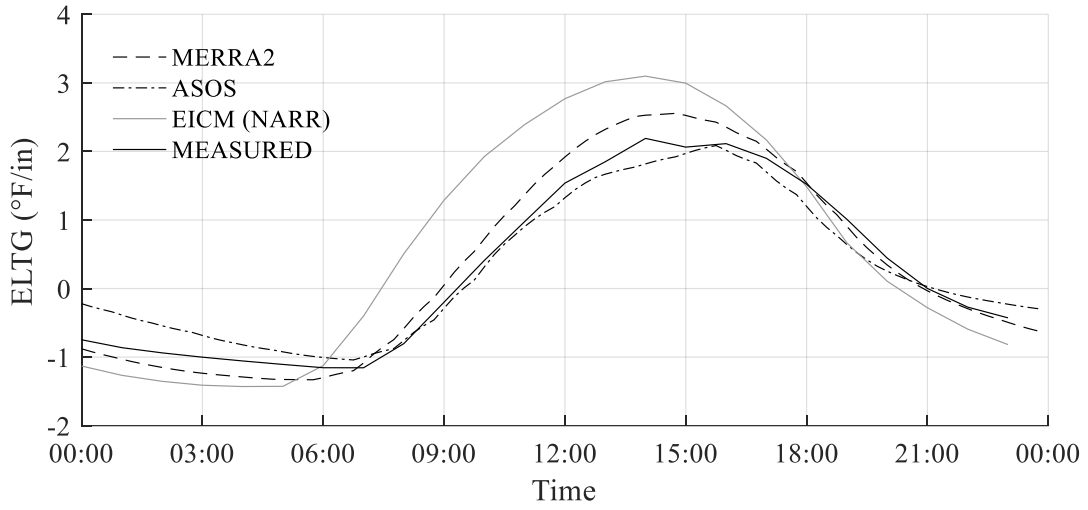


Figure A.113. SR-22 Smart Pavement (4/27/2014)

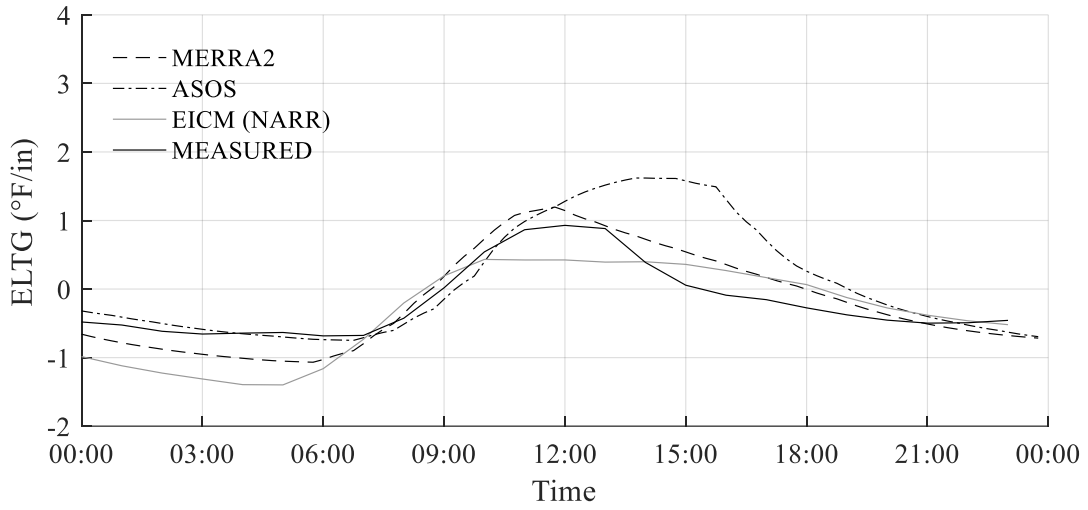


Figure A.114. SR-22 Smart Pavement (4/28/2014)

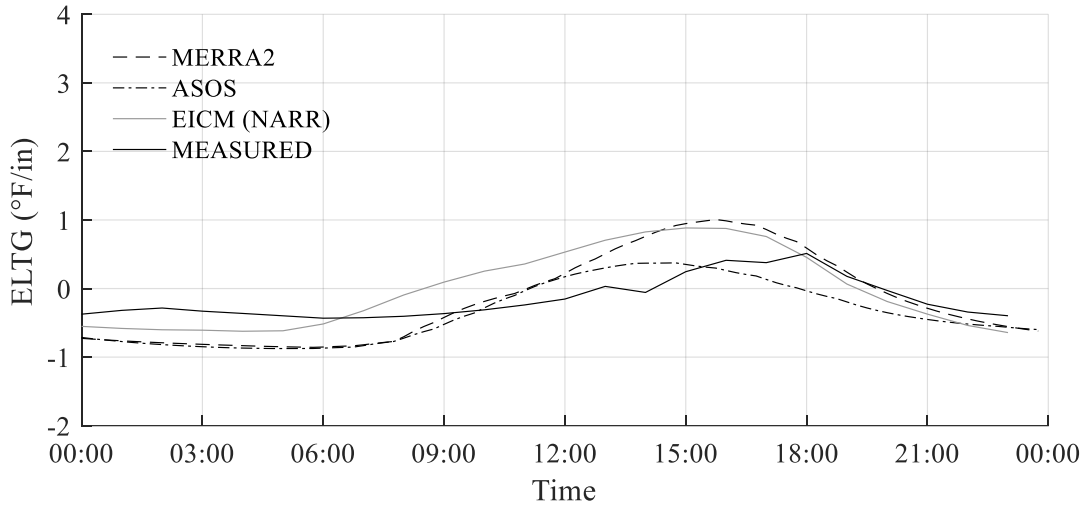


Figure A.115. SR-22 Smart Pavement (4/29/2014)

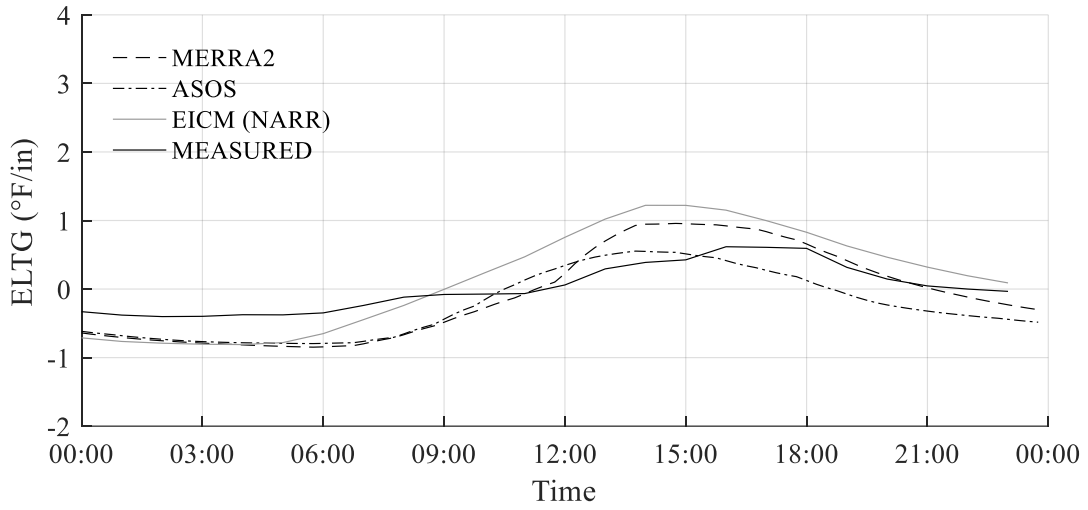


Figure A.116. SR-22 Smart Pavement (4/30/2014)

LTPP SECTION 37-0201

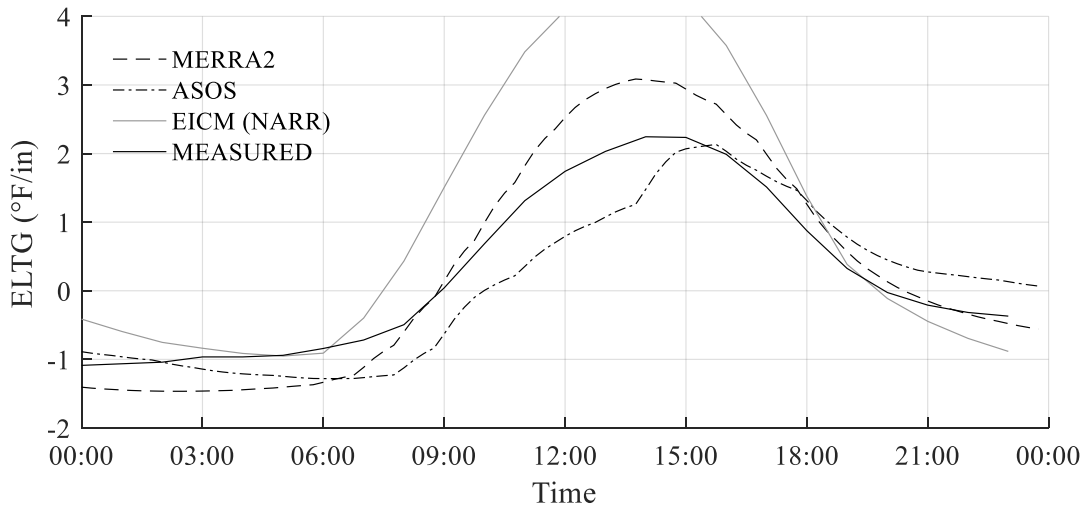


Figure-A.117. LTPP Section 37-0201 (4/1/2003)

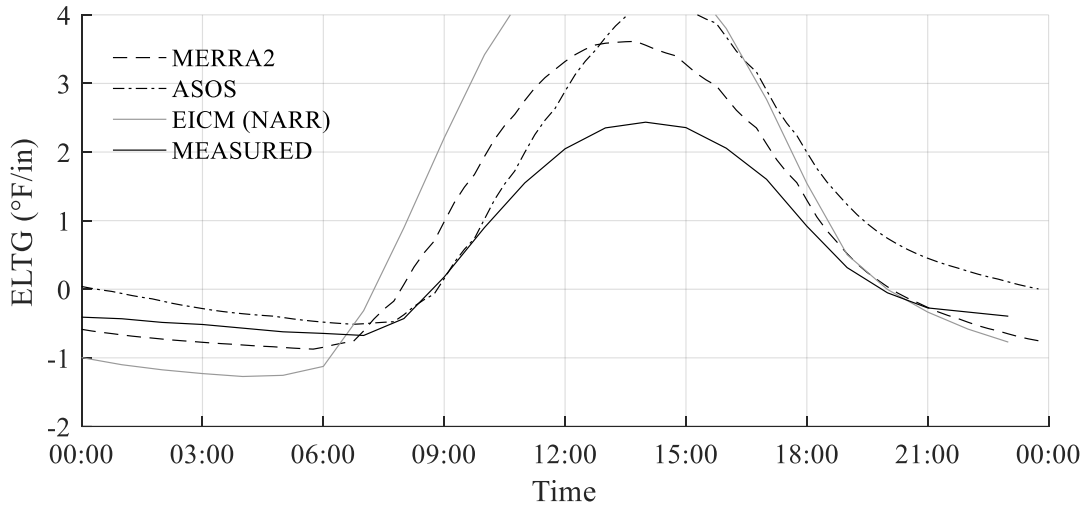


Figure A.118. LTPP Section 37-0201 (4/2/2003)

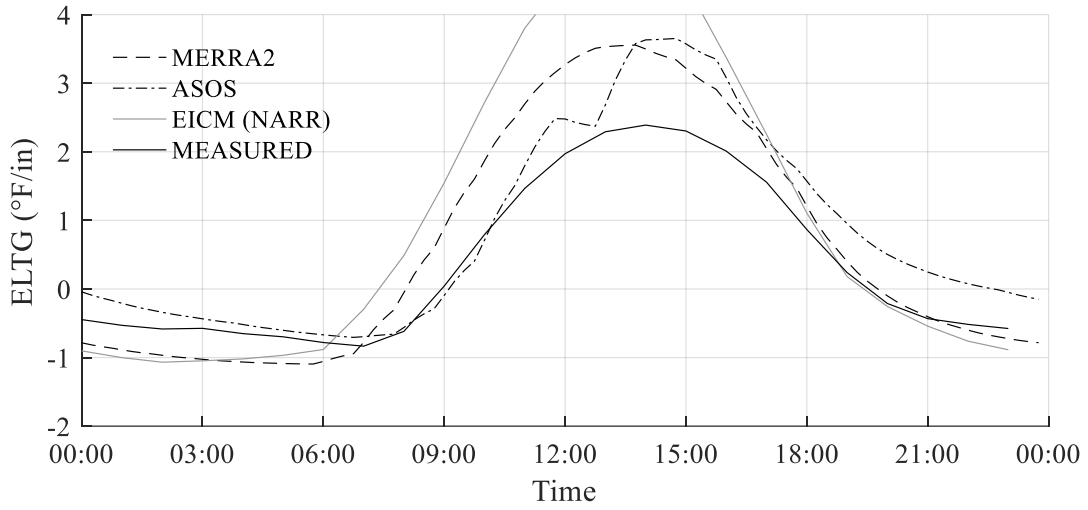


Figure A.119. LTPP Section 37-0201 (4/3/2003)

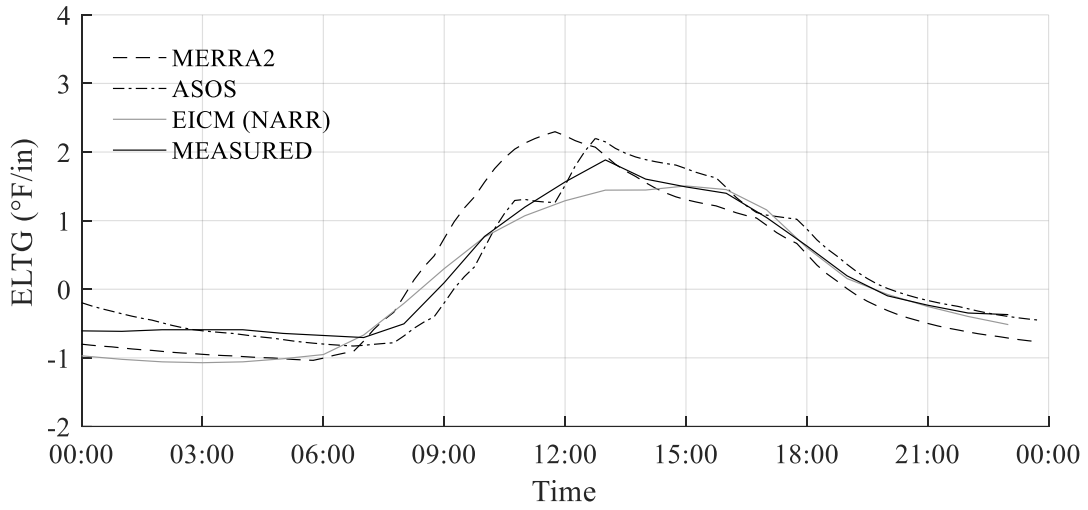


Figure A.120. LTPP Section 37-0201 (4/4/2003)

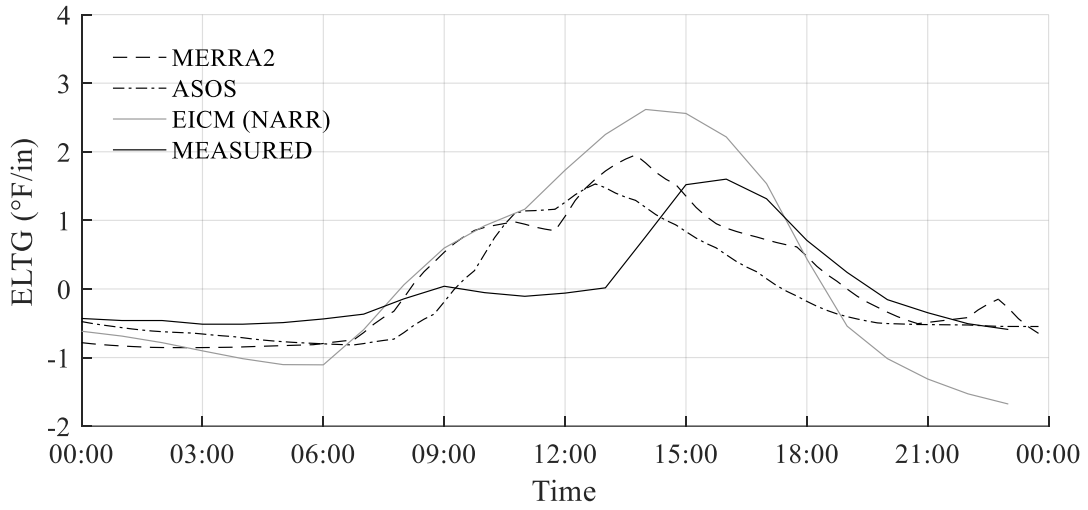


Figure A.121. LTPP Section 37-0201 (4/5/2003)

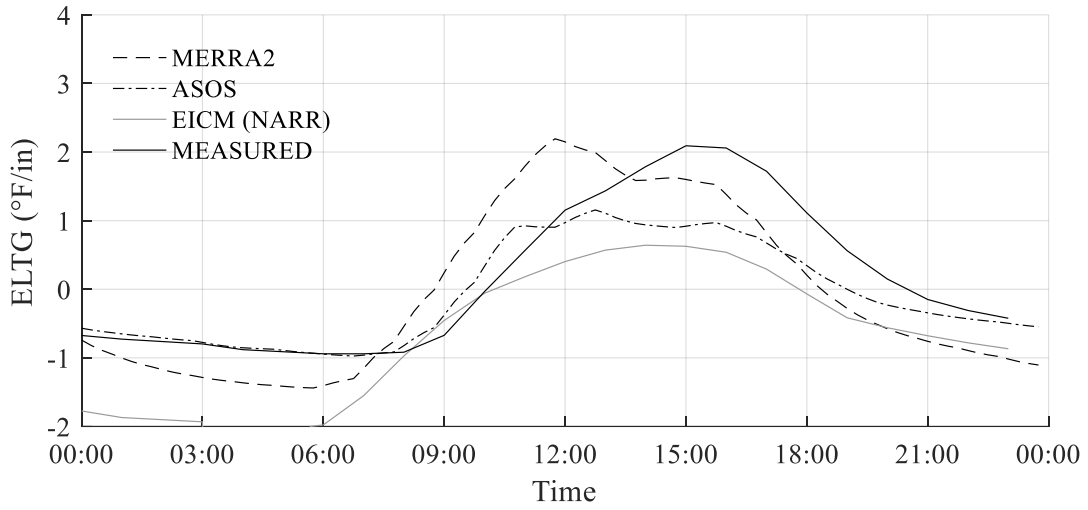


Figure A.122. LTPP Section 37-0201 (4/6/2003)

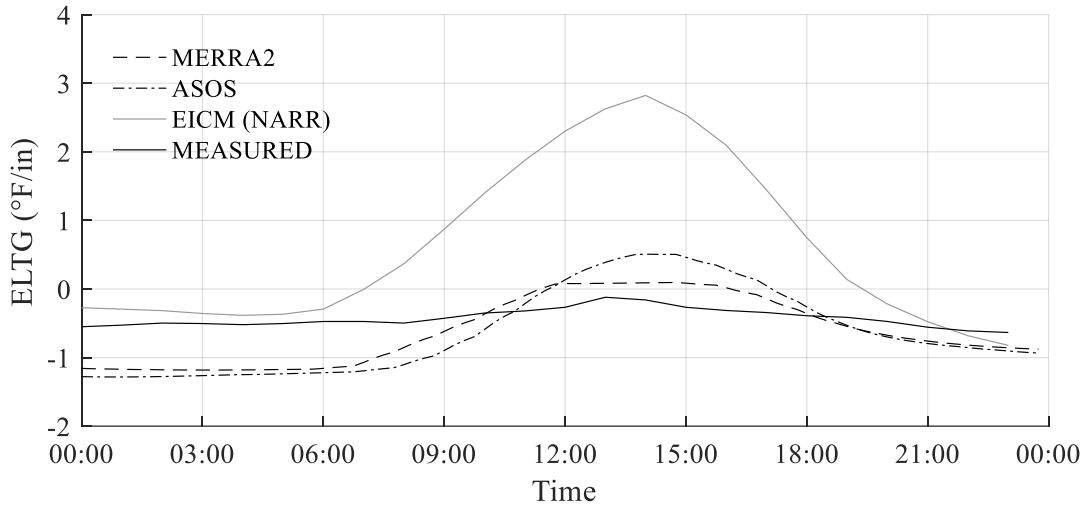


Figure A.123. LTPP Section 37-0201 (4/8/2003)

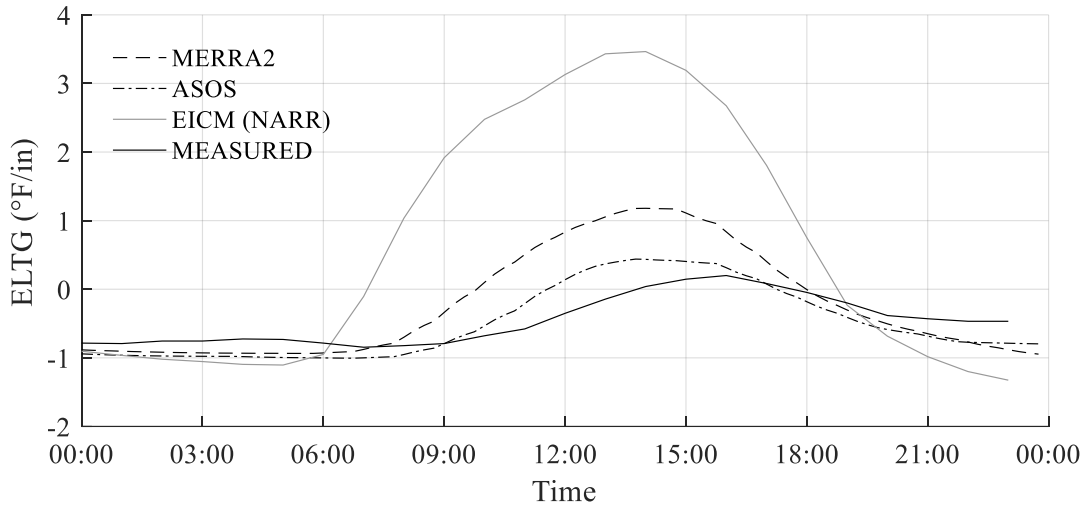


Figure A.124. LTPP Section 37-0201 (4/9/2003)

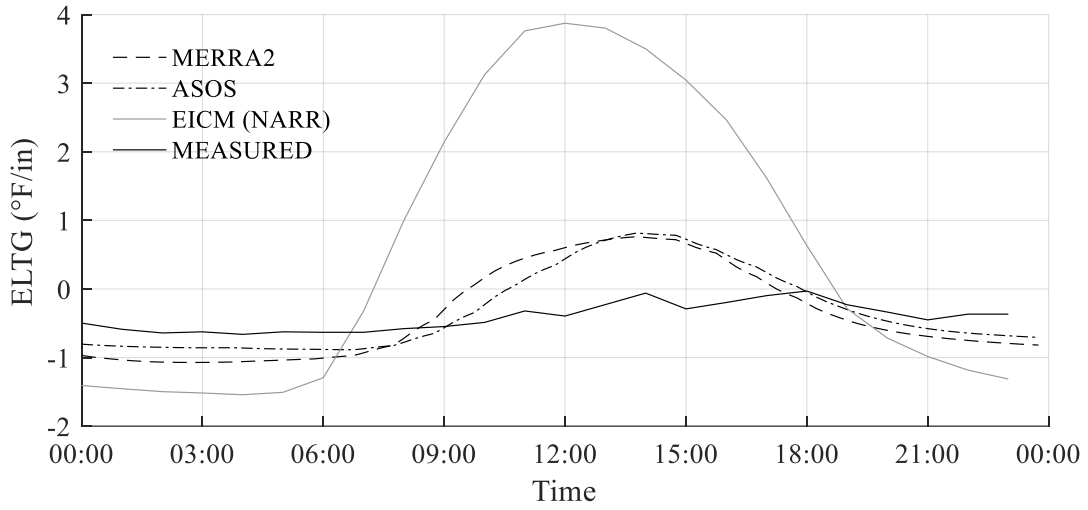


Figure A.125. LTPP Section 37-0201 (4/10/2003)

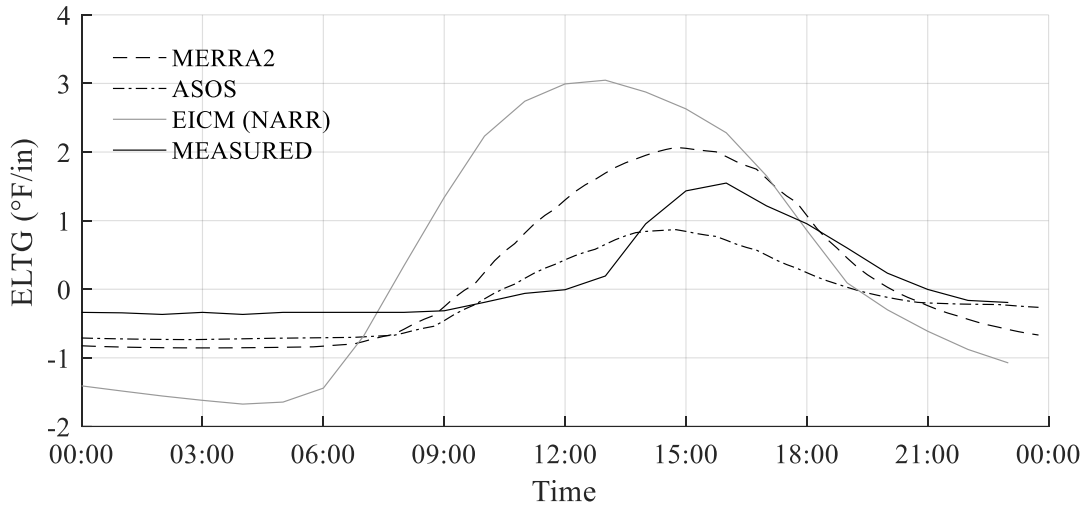


Figure A.126. LTPP Section 37-0201 (4/11/2003)

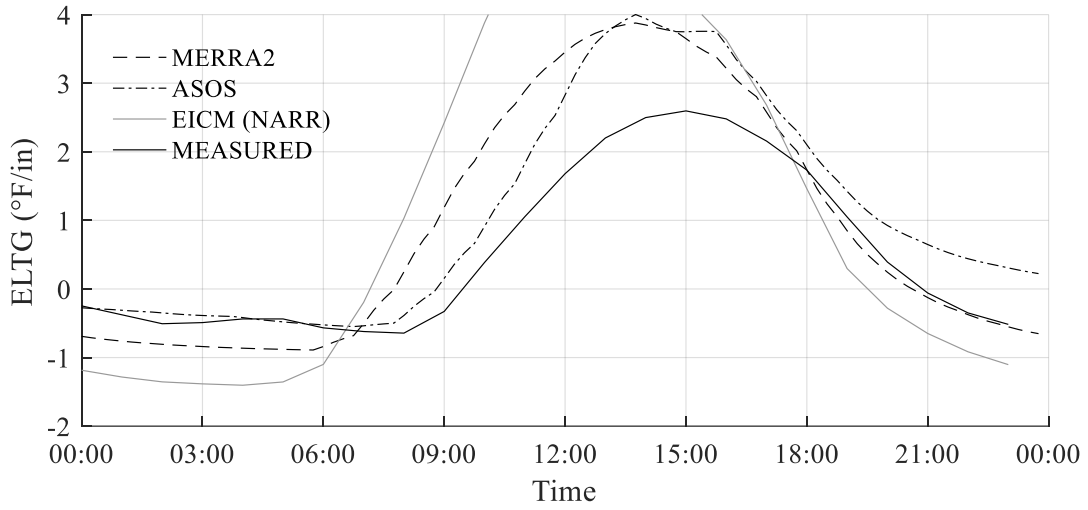


Figure A.127. LTPP Section 37-0201 (4/12/2003)

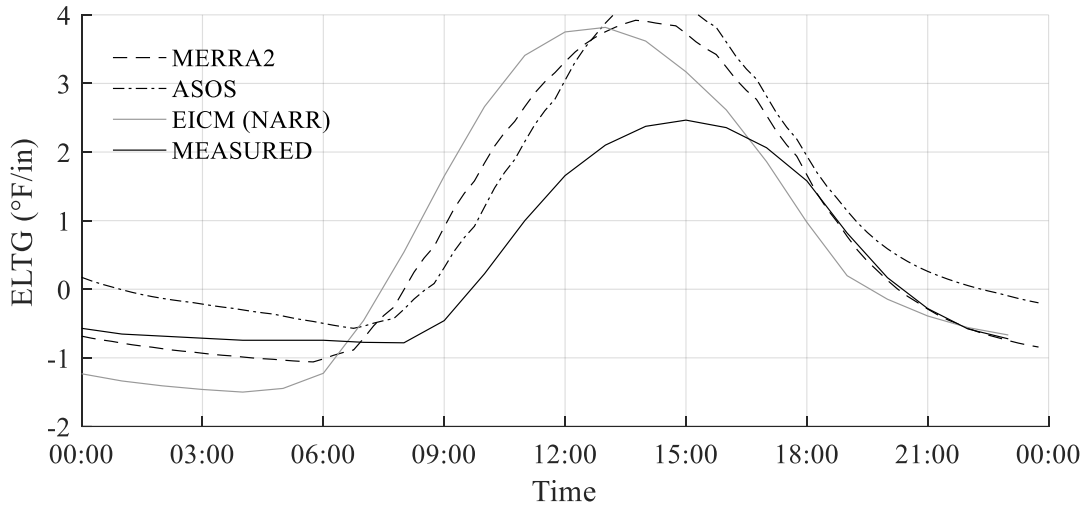


Figure A.128. LTPP Section 37-0201 (4/13/2003)

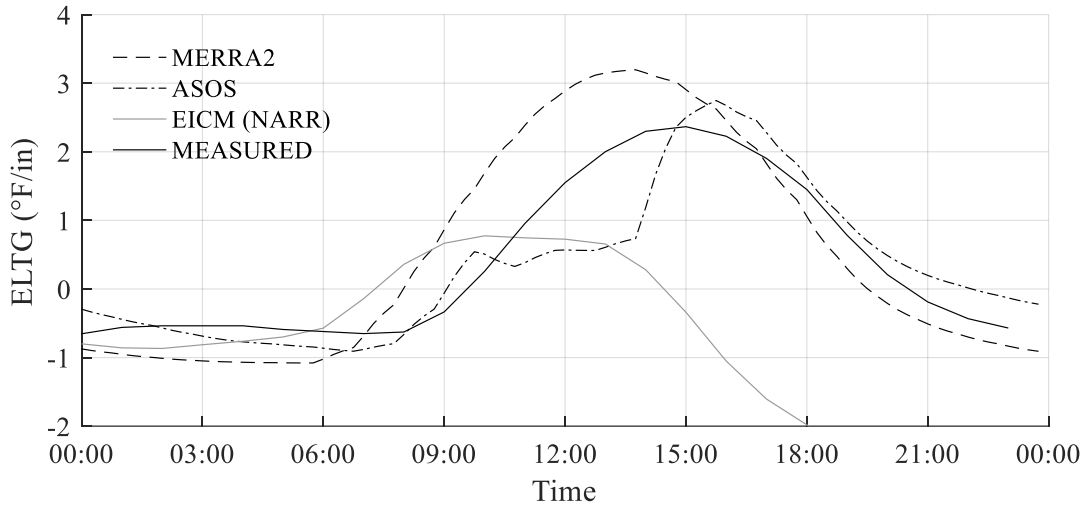


Figure A.129. LTPP Section 37-0201 (4/15/2003)

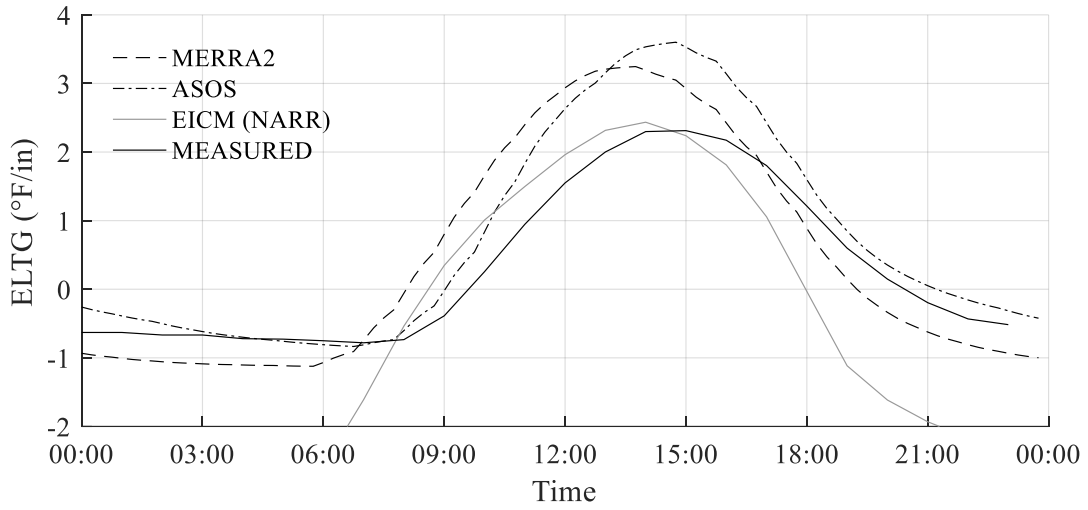


Figure A.130. LTPP Section 37-0201 (4/16/2003)

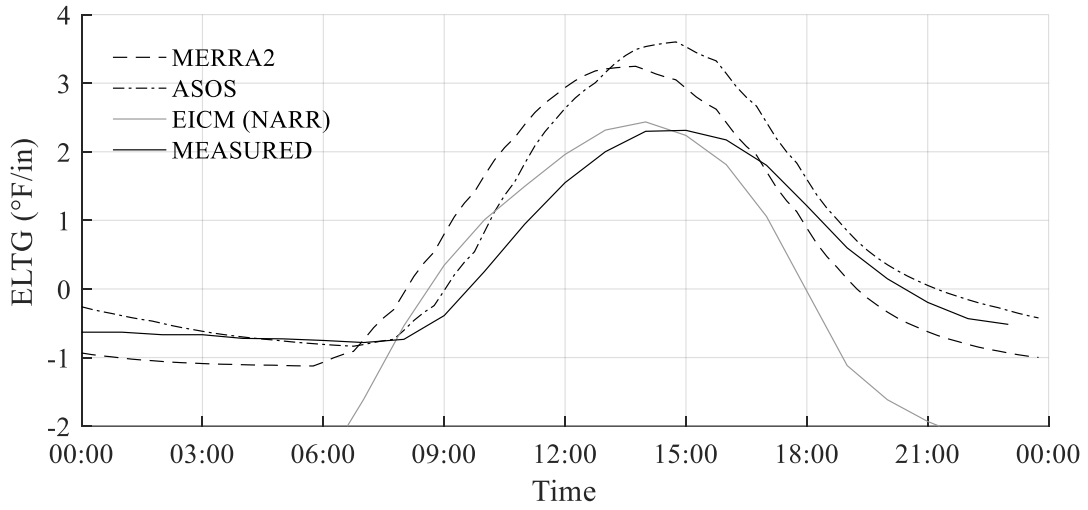


Figure A.131. LTPP Section 37-0201 (4/17/2003)

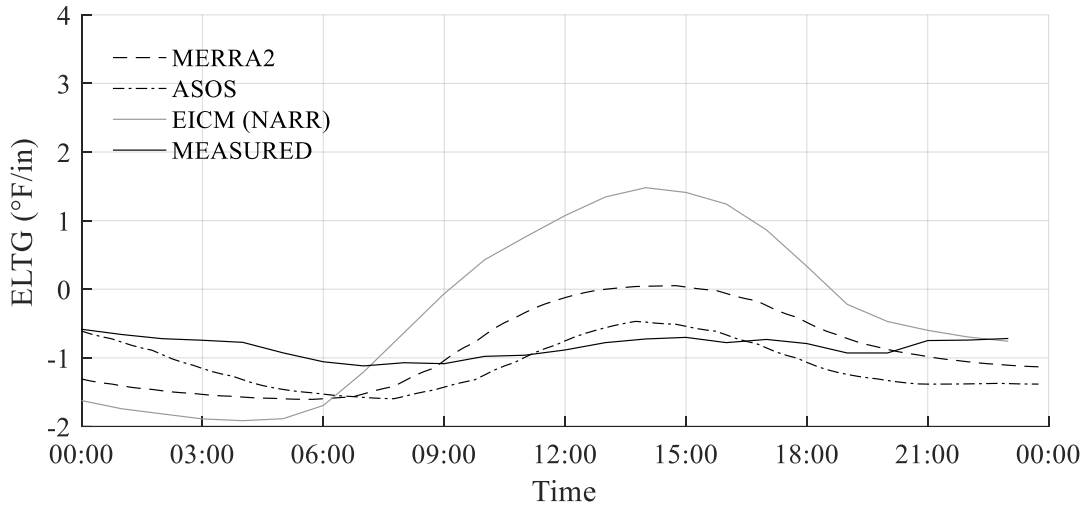


Figure A.132. LTPP Section 37-0201 (4/18/2003)

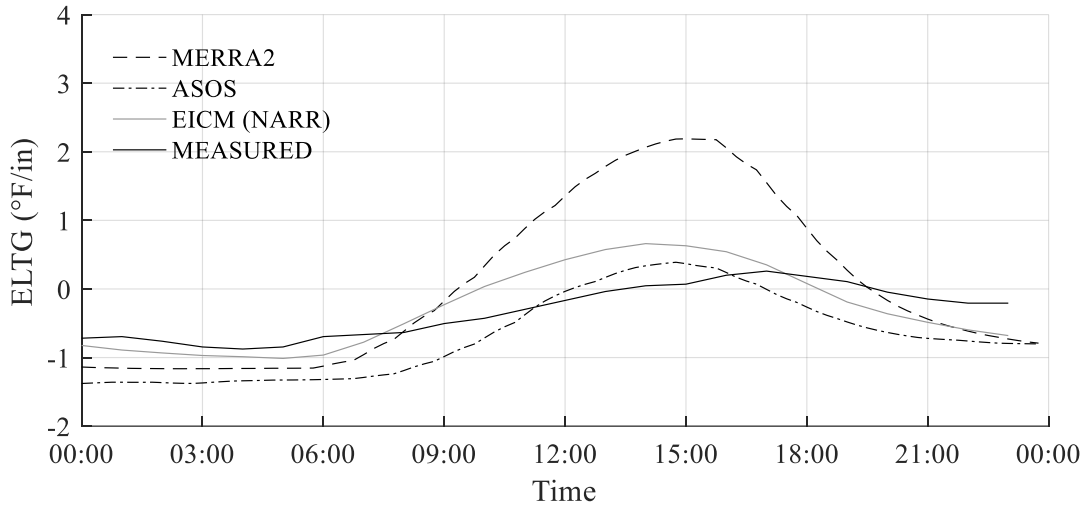


Figure A.133. LTPP Section 37-0201 (4/19/2003)

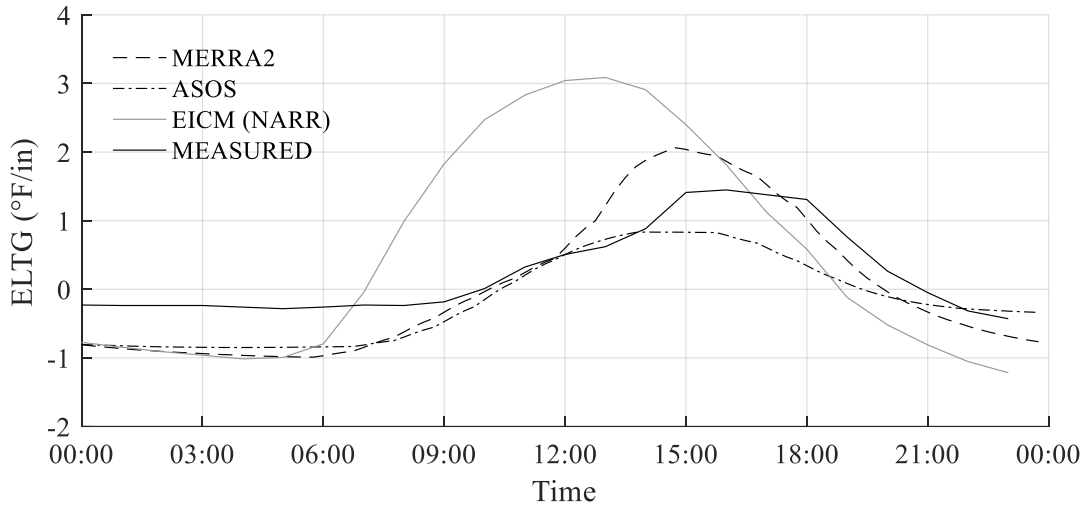


Figure A.134. LTPP Section 37-0201 (4/20/2003)

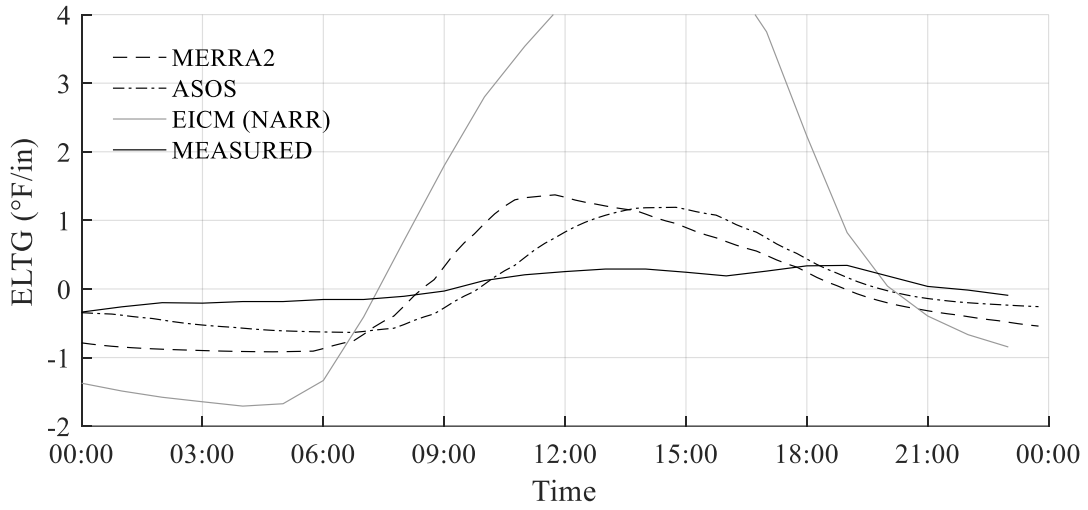


Figure A.135. LTPP Section 37-0201 (4/21/2003)

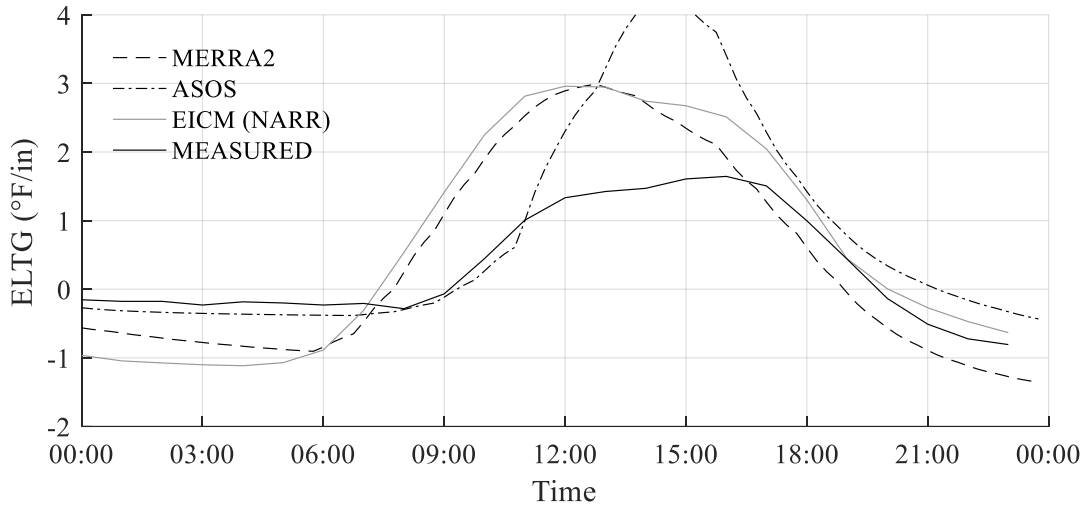


Figure A.136. LTPP Section 37-0201 (4/22/2003)

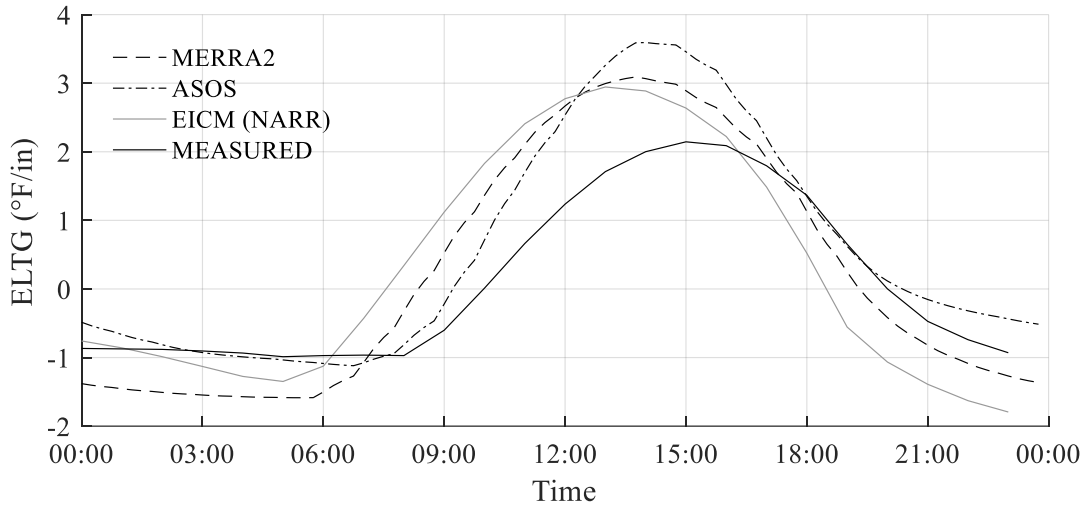


Figure A.137. LTPP Section 37-0201 (4/23/2003)

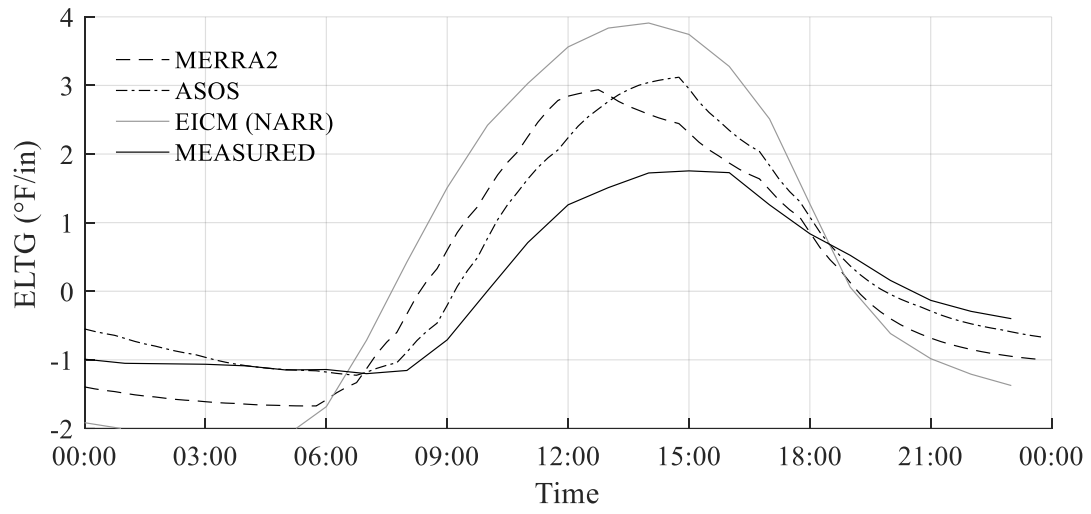


Figure A.138. LTPP Section 37-0201 (4/24/2003)

APPENDIX B

PITT-FACS WEB TOOL USER'S GUIDE

This instruction manual is intended to be used along with the Pitt-FACS web tool. A list of definitions for all abbreviations is provided at the end of the instruction manual. This tool is only intended for JPCP.

FIELD DATA COLLECTION NOTES

In order for the Pitt-FACS tool to work correctly, the following steps must be taken during field data collection:

- Testing must be performed in three locations
 - Midslab (label “Center” in FWD data file)
 - Wheelpath on the leave side of the joint (label “Lower Right” in FWD data file)
 - Corner of the slab on the leave side of the joint (label “Corner” in FWD data file)
- All three FWD test passes should be stored in the same FWD data file
- The DMI should be zeroed between passes to ensure consistency between stations

STEP 1: ACCESS THE WEBSITE

The tool can be found at: https://www.engineering.pitt.edu/Sub-Sites/Faculty-Subsites/J_Vandenbossche/FWD-Analysis-Tool/FWD-Analysis-Tool-Page/

STEP 2: ENTER THE REQUIRED INFORMATION ABOUT THE PAVEMENT TESTED.

- **Project Title:** The project title will be included in the output file.

- **User:** The user will be included in the output file.
- **Pavement Thickness:** The mean thickness of the concrete layer, in inches.
- **Base Type:** The base type should be selected between Granular, Asphalt Stabilized, Lean, Concrete, Cement Stabilized, and None. The None option should be chosen when the slab is placed directly on a natural subgrade. The Lean Concrete option should be chosen for any plant mixed cement based material. The cement treated option should be used for cement or lime treated subgrades or cement aggregate mixtures.
- **Base Thickness:** The thickness of the base, in inches.
- **Shoulder:** The shoulder should be selected to be either tie concrete, or other for a granular, asphalt surfaced or untied concrete surfaced shoulder.
- **Dowel Size:** The size of the dowel should be chosen to be equal to 1.5 in, less than 1.5 in, or none from the drop-down menu. These sizes assume solid steel dowel bars. If an alternative dowel bar, such as FRP or hollow steel is chosen, and equivalent steel dowel bar should be selected.
- **Joint Spacing:** Enter the joint spacing in feet. Currently the web tool does not support random joint spacing.
- **Slab width:** The width of the tested slabs in feet.

STEP 3: SELECT WHETHER TEMPERATURE HOLES WERE USED TO MEASURE THE PAVEMENT TEMPERATURE PROFILE.

STEP 4: IF THE PAVEMENT TEMPERATURE PROFILE WAS NOT MEASURED, ENTER GEOGRAPHICAL INFORMATION FOR THE PAVEMENT, SO THAT THE PAVEMENT TEMPERATURE PROFILE CAN BE MEASURED.

- Enter the latitude of the pavement section in °N (value will be positive in PA). This information can be obtained from the link marked “Geographical Information”
- Enter the longitude of the pavement section in °E (value will be negative in PA). This information can be obtained from the link marked “Geographical Information.”
- Enter the elevation of the pavement section in ft. This information can be obtained from the link marked “Geographical Information”.
- An example of the geographical information tool (from Veloroutes.org) can be seen in Figure B.1.

[Home](#)

[Create a route](#) (profiles)

[Calculate hill grade](#)

Find elevation of these places:

- [Seattle](#)
- [Atlanta](#)
- [Mt. Kilimanjaro](#)
- [Mexico City](#)
- [San Francisco](#)
- [New York, NY](#)
- [Los Angeles](#)
- [London](#)
- [Chicago](#)
- [Lhasa](#)
- [The White House](#)
- [Eiffel Tower, Paris, Fr](#)
- [Yankee Stadium](#)

Address:

units:

Elevation for 3700 Ohara St Pittsburgh PA is 980 feet

- The latitude for this location is: 40.4442959
- The longitude for this location is: -79.9577917
- Click [here](#) to create a route at this location.



Figure B.1 . Geographical information tool

Mark whether the pavement is in Pennsylvania. The Pitt-FACS tool was developed with funding by PennDOT. Therefore, the tool automatically downloads and stores weather data for Pennsylvania so that analysis can be performed in real time. Analysis outside of Pennsylvania is supported, but it will require additional analysis time to download the required weather data.

- Select the weather data source. The Pitt-FACS tool supports two weather sources MERRA2 and ASOS.
 - The MERRA2 data source, is a data source developed by NASA, which combines data from land, sea, air and satellite sources with a retrospective analysis. This allows data to be provided on a 0.625 °Longitude x 0.5° Latitude grid for the entire planet. This allows excellent distribution of data points, especially in rural areas.

MERRA2 provides direct estimates of the solar radiation reaching the ground, allowing it to provide better estimates of the pavement temperature. This data requires intensive reanalysis, which is performed once a month and can therefore lead to a delay in data becoming available. The Pitt-FACS tool will download MERRA2 data for a given month on the last day of the next month. For example, data for the month of February will be downloaded March 31.

- The ASOS data source is a system of over 900 land-based weather stations operated by a collaboration between the National Oceanic and Atmospheric Administration (NOAA), the Federal Aviation Administration (FAA) and the Department of Defense (DoD). These stations are primarily based at airports and provide data every hour. These locations tend to cluster in urban locations, and some pavements may be some distance from the nearest weather station. These stations provide a sky condition, which can be used to estimate the incoming shortwave radiation, but do not provide a direct estimate of shortwave radiation. Therefore, temperature gradients predicted using ASOS data tend to be less accurate than temperature gradients predicted with MERRA2 data. This data does not require reanalysis and is available nearly immediately. ASOS weather data for a given week will be downloaded on the Saturday of the following week. This data is the basis of the QCLCD data was, until recently, used to generate the .hcd files used in the Pavement ME Guide temperature analysis.
- If the pavement is outside of Pennsylvania, provide climate normals.
 - The Pitt-FACS tool requires the mean monthly temperature (MMT), and mean annual temperature (MAT) for pavements outside of Pennsylvania.
 - This information can be found using a tool from NOAA, which can be seen in Figure B.2.

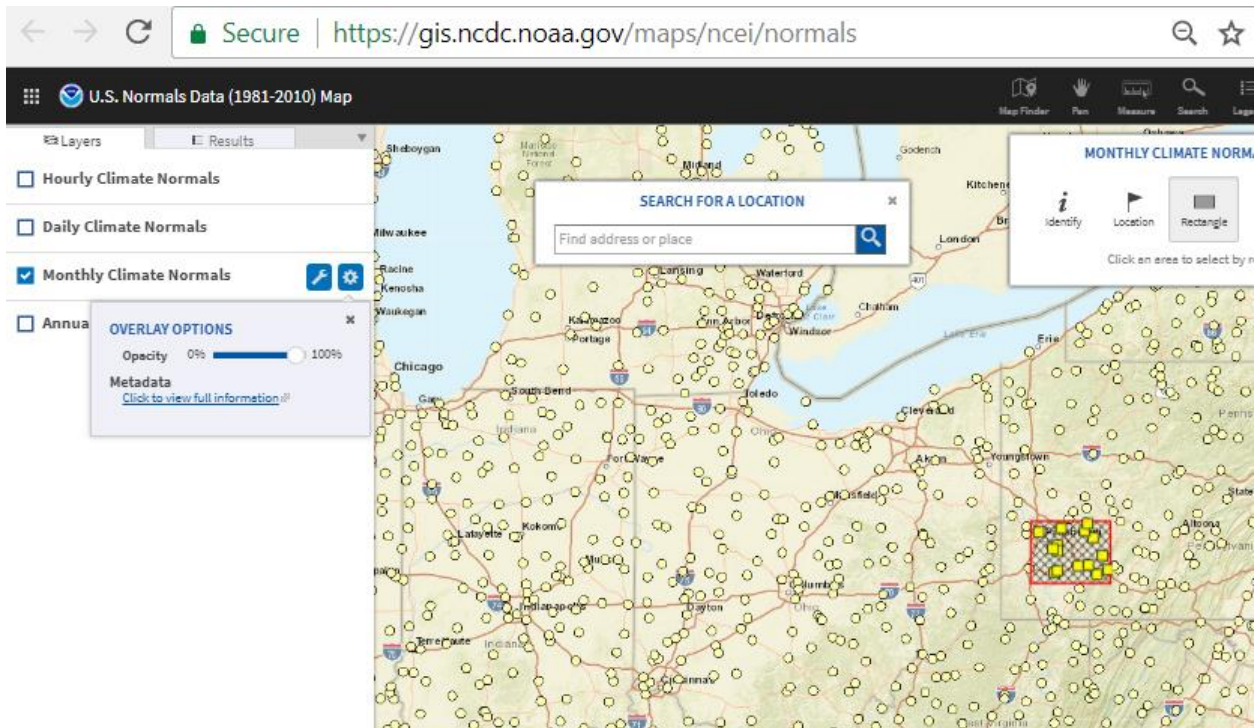


Figure B.2. NOAA climatic normals tool

- The data selection tools are made available by selecting the “wrench” icon, next to “Monthly Climatic Norms”
- Select a station near the pavement and click “Get Station Details”
- Scroll to “View Station Data”, select 2010 as the year and click view data.
- The mean monthly temperatures will be provided in the generated .pdf file.
- The mean annual temperature is listed in the summary row of that table.
- An example of the output can be seen in Figure B.3.

Temperature (°F)												
Mean							Cooling Degree Days					
							Base (above)					
Month	Daily Max	Daily Min	Mean	Long Term Max Std Dev	Long Term Min Std Dev	Long Term Avg Std Dev	55	57	60	65	70	72
01	37.1	20.8	29.0				-7777	-7777	0	0	0	0
02	40.1	21.9	31.0				1	-7777	-7777	0	0	0
03	49.8	29.6	39.7				7	5	2	-7777	-7777	0
04	61.9	38.6	50.3				51	35	18	5	1	-7777
05	71.2	50.8	61.0				215	170	113	48	16	9
06	79.4	60.6	70.0				451	392	306	176	78	51
07	83.2	65.7	74.5				603	541	448	294	152	106
08	81.9	63.4	72.7				547	485	392	240	111	72
09	75.4	55.3	65.4				318	262	184	83	26	14
10	63.7	44.2	54.0				85	60	33	9	2	1
11	52.8	34.4	43.6				11	6	2	-7777	0	0
12	40.7	25.2	33.0				2	1	1	-7777	0	0
Summary	61.4	42.5	52.0	0.0	0.0	0.0	2291	1957	1499	855	386	253

-7777: a non-zero value that would round to zero

Empty or blank cells indicate data is missing or insufficient occurrences to compute value

Figure B.3. Climatic normals output file

STEP 5: FORMAT THE INPUT DATA FILES.

- Automated file formatting and unit conversion should be performed using the provided excel spreadsheet. This spreadsheet can be downloaded using the “Download Excel File Formatting Spreadsheet” button.
- The macro enabled spreadsheet should then be opened using Microsoft Excel. The interface of the tool can be seen in Figure B.4. Be sure to enable editing, and to enable macros, as both are required for the file formatting tool.



This tool can be used to format data from FWD testing MS-Access (.mdb, .accdb) files into the format required for PITT-FACS. Please select the units used in FWD data collection, and identify any supplementary data which was collected. Then click the button to select the FWD data file.

Deflection Units	mils
Station Units	ft
Force Units	lbs
Sensor Offset Units	in
Supplementary Information	<input type="radio"/> Temperature Holes <input checked="" type="radio"/> Pyranometer Readings <input type="radio"/> Cloud Cover Estimates <input type="radio"/> None
Solar Radiation Units	BTU/hr/ft ²
Number of Times Supplemental Data is Collected	15
<input type="button" value="Select FWD Data File"/>	

Figure B.4. File formatting tool interface

- The units used in the FWD file for deflection, station, force, and sensor offset should be selected from the drop-down menus. The file formatting tool will convert these parameters to the US customary units, which are used in Pitt-FACS.
- If supplemental data (temperature hole measurements, pyranometer measurements or sky condition estimates) is available, select the appropriate option.
 - If the temperature hole measurements option is selected, a prompt will appear requesting the number of temperature holes used. Fields will then appear on the

user interface for the units used to measure the depth of the temperature holes, the depth of each hole, and the number of time points measured during testing. This can be seen in Figure B.5.



This tool can be used to format data from FWD testing MS-Access (.mdb, .accdb) files into the format required for PITT-FACS. Please select the units used in FWD data collection, and identify any supplementary data which was collected. Then click the button to select the FWD data file.

Deflection Units	mils
Station Units	ft
Force Units	lbs
Sensor Offset Units	in
Supplementary Information	<input checked="" type="radio"/> Temperature Holes <input type="radio"/> Pyranometer Readings <input type="radio"/> Cloud Cover Estimates <input type="radio"/> None
Temperature Units	°F
Hole Depth Units	in
Depth 1	1
Depth 2	2
Depth 3	4
Depth 4	8
Depth 5	12
Supplemental Data is Collected	15

Select FWD Data File

Figure B.5. Fields for temperature hole information

- If the pyranometer readings option is select, fields will appear asking for the units of the pyranometer readings, and the number of time points. This can be seen in Figure B.6.

University of Pittsburgh

FWD Analysis of Concrete Slabs

This tool can be used to format data from FWD testing MS-Access (.mdb, .accdb) files into the format required for PITT-FACS. Please select the units used in FWD data collection, and identify any supplementary data which was collected. Then click the button to select the FWD data file.

Deflection Units mils
Station Units ft
Force Units lbs
Sensor Offset Units in

Supplementary Information

- Temperature Holes
- Pyranometer Readings
- Cloud Cover Estimates
- None

Solar Radiation Units BTU/hr/ft²
Supplemental Data is Collected 15

Select FWD Data File

Figure B.6. Fields for pyranometer reading information

- If the sky condition estimates option is selected, a field will appear for the number of time points estimated, as can be seen in Figure B.7.



This tool can be used to format data from FWD testing MS-Access (.mdb, .accdb) files into the format required for PITT-FACS. Please select the units used in FWD data collection, and identify any supplementary data which was collected. Then click the button to select the FWD data file.

Deflection Units	mils
Station Units	ft
Force Units	lbs
Sensor Offset Units	in
Supplementary Information	<input type="radio"/> Temperature Holes <input type="radio"/> Pyranometer Readings <input checked="" type="radio"/> Cloud Cover Estimates <input type="radio"/> None
Supplemental Data is Collected	15
<input type="button" value="Select FWD Data File"/>	

Figure B.7 . Field for sky condition estimate information

- Click the button to generate files.
- A prompt will appear to select the location of the Access test files, as shown in Figure B.8. Use the explorer to select the FWD file location, and click “Open”.

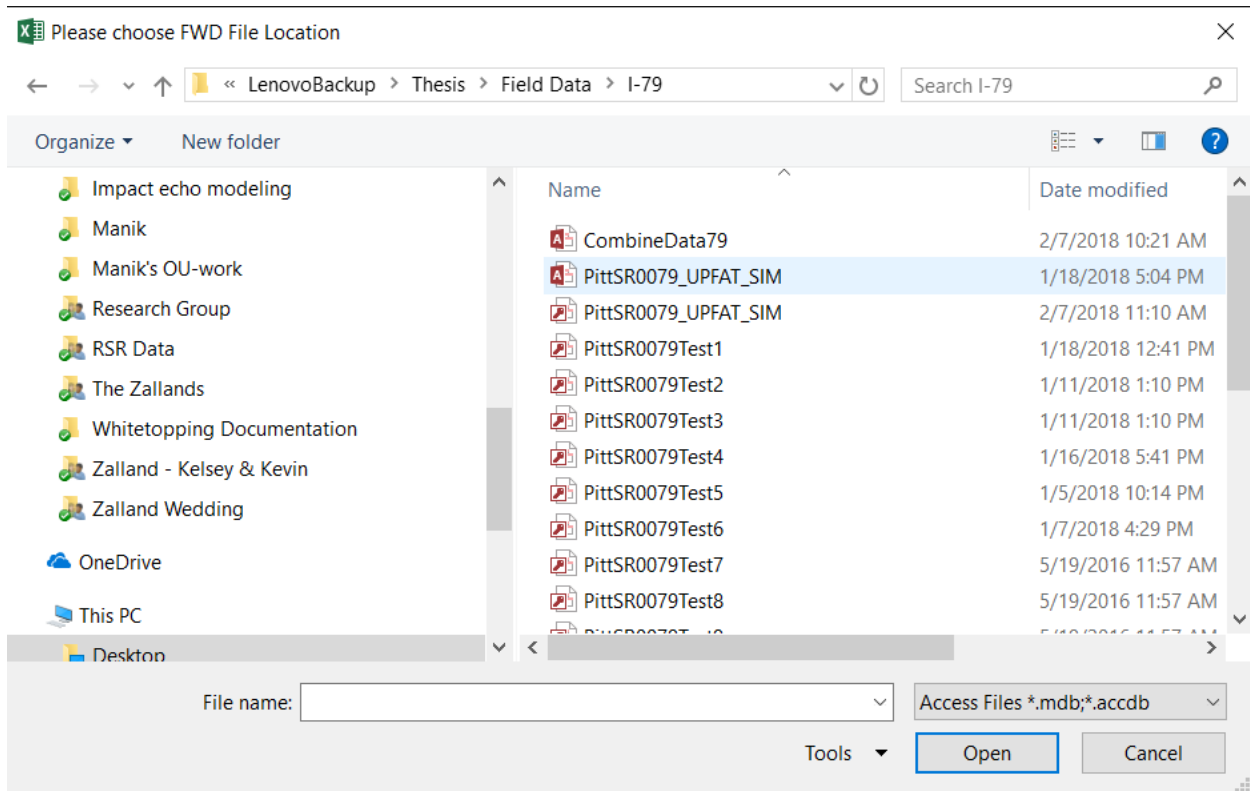


Figure B.8. Selection of FWD file location

- If no supplemental data is to be used, no further action is required, and the excel tool should be closed without saving. The .csv file will be saved with the same name, at the same location as your Access Database test file, with the extension .csv.
- If supplemental data is to be used, a worksheet will activate with a table for the time and measurements for each of the supplemental data time points. The format of the worksheet for temperature hole measurements can be seen in Figure B.9. The format of the worksheet for pyranometer measurements can be seen in Figure B.10. The format of the worksheet for sky condition estimates can be seen in Figure B.11. *Note: this worksheet contains hidden information which is required by Pitt-FACS. Do not attempt to format the supplemental data without using the provided button.*



Save
Supplemental
Data File

Date and Time	Temp. @ Depth 1	Temp. @ Depth 2	Temp. @ Depth 3	Temp. @ Depth 4	Temp. @ Depth 5
5/27/2017 13:45	9	3	2	1	0

Example

Figure B.9. Form for temperature hole measurements



Save
Supplemental
Data File

Date and Time	Solar Radiation
5/27/2017 13:45	132.1

Example

Figure B.10. Form to record pyranometer measurements



Save Supplemental Data File

Date and Time	Sky Condition
5/27/2017 13:45	Clear

Example

Sky Condition	Octas Filled
Clear	<1/2
Few	1/2 to 2
Partly Cloudy	2 to 4
Mostly Cloudy	4 to 7
Overcast	>7

Figure B.11. Form to record sky conditions

- The form should be filled out with the date and time of the measurement time point, and in the units selected on the User Interface sheet.
- Once the table is filled out, the supplemental data file, in the format required by Pitt-FACS, can be generated by clicking the “Save Supplemental Data File” button. A file will be saved with the same name and location as the FWD test file, with the ending “SUPPLEMENTAL.csv”.

STEP 6: UPLOAD THE FWD DATA FILE, AND SUPPLEMENTAL DATA FILE

STEP 7: ENTER THE USER'S EMAIL ADDRESS

The analysis results will be sent out through email. The email address is not saved for any purpose and is deleted once the data is generated and sent.

An example screenshot of the tool is shown in Figure B.12 and B.13.



GENERAL INFORMATION

Project Title:

User Name:

Pavement Thickness (in):

Base Type: [BASE TYPE DESCRIPTIONS](#)

Base Thickness (in):

Dowel Diameter:

Shoulder:

Joint Spacing (ft):

Slab Width(ft):

Figure B.12. Screenshot of Pitt-FACS interface

TIME ZONE

Time zone represented by the timestamp in the FWD Data File: Eastern Time (DST is consid ▼)

TEMPERATURE

Was the pavement temperature profile measured? Yes No

Latitude (degrees): [GEOGRAPHIC INFORMATION](#)

Longitude (degrees):

Elevation (ft):

Is the Pavement in Pennsylvania? Yes No

Weather Data Source: [EXPLANATION OF DATA SOURCES](#)

UPLOAD FILES

Automated FWD and supplemental data file formatting can be performed using this excel file. [DOWNLOAD EXCEL FILE](#)

FWD Data File: No file chosen

Supplemental Data File: No file chosen

EMAIL

Your Email Address:

[ANALYZE](#)

Figure B.13. Screenshot of Pitt-FACS interface (continued)

AN EXAMPLE OF THE OUTPUT FILE IS INCLUDED ON THE FOLLOWING PAGES:



Pavement Information

Project Title: UPFAT TOOL EXAMPLE
 Analyzed by: John Doe
 Analysis Date: 01/12/2018
 Pavement Thickness: 12.0 in
 Base Type: Granular
 Base Thickness: 4.0 in
 Dowel Size: 1.5 in
 Joint Spacing: 15.0 ft
 Slab Width: 12.0 ft
 Tied PCC Shoulder: True

Testing Information

Test Date: 05/08/2016
 Stations: 0 ft to 861 ft

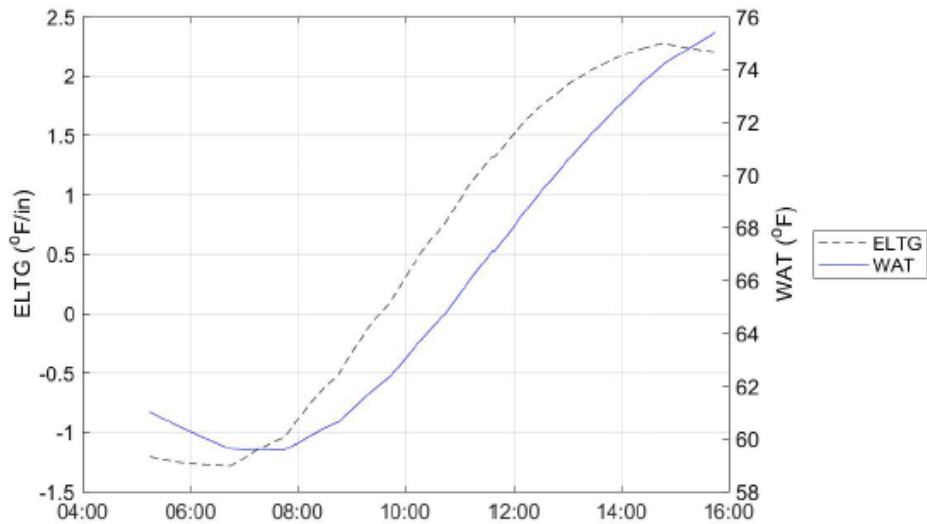
Sensor Offsets (in)

Sensor 1	Sensor 2	Sensor 3	Sensor 4	Sensor 5	Sensor 6	Sensor 7	Sensor 8	Sensor 9
0	-12	8	12	18	24	36	60	

Pavement Temperature Profile Was: Estimated
 Weather Data Source: MERRA2

This page contains the information about the Pavement and FWD testing for records purposes. Some fields are inputs into the tool, some fields, such as the testing date and sensor offsets are generated from the input files.

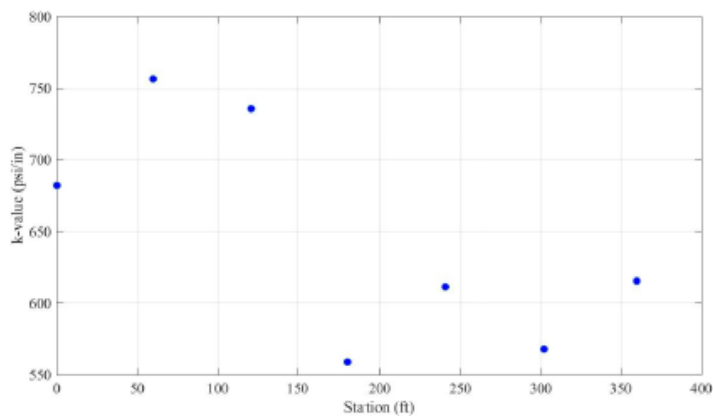
Pavement Temperature Information



ELTG Range: -1.3 °F/in to 2.3 °F/in, WAT Range: 60 °F to 75 °F

This section contains a plot of the estimated or measured equivalent linear temperature gradient (ELTG), and weighted average slab temperature (WAT) during testing. These values are used in the other analysis modules and are provided for reference.

Backcalculation Results



Average k-value (midslab): 647 psi/in
 Average Epcc (midslab): 6.4e+06 psi

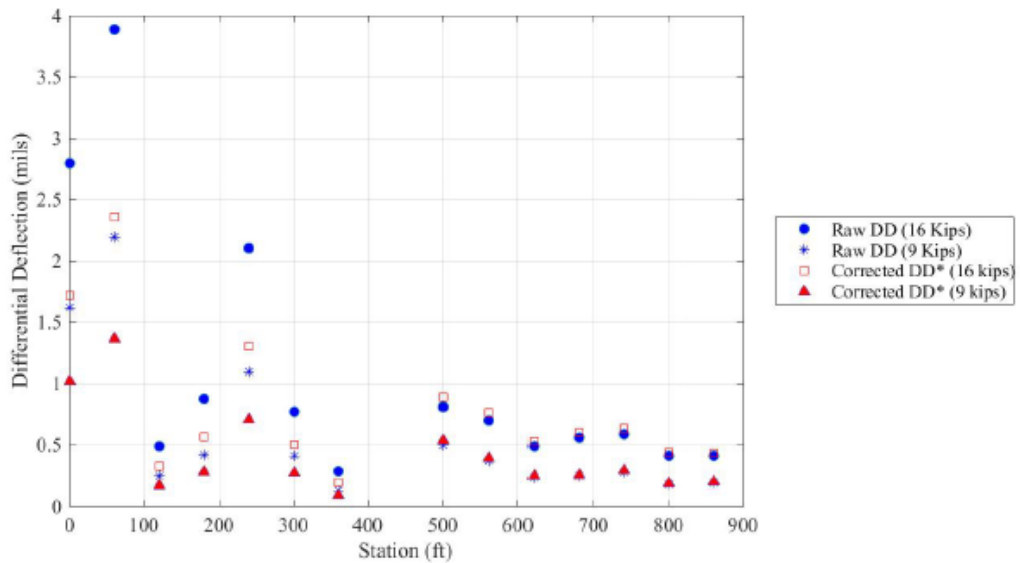
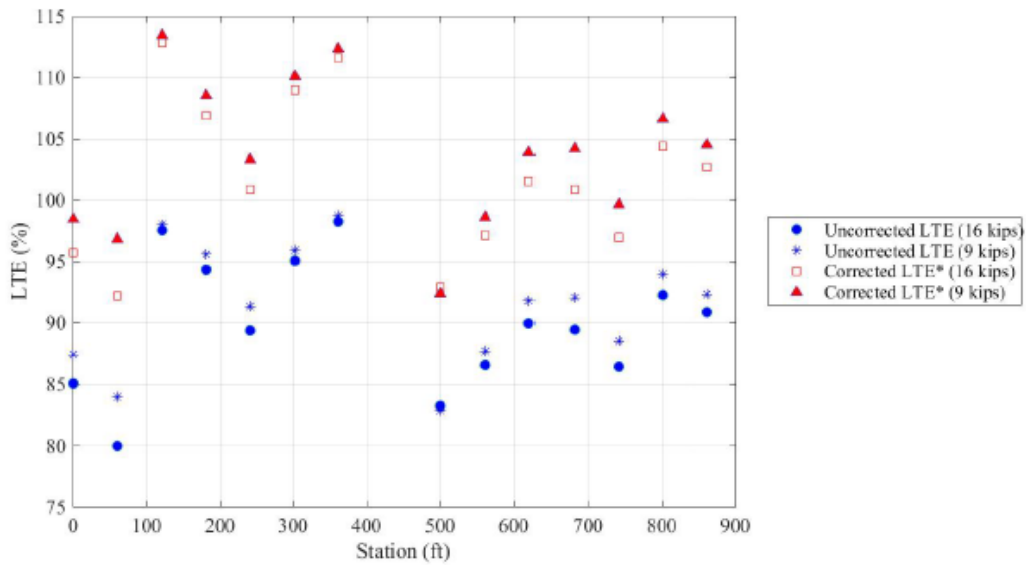
Backcalculation Results (cont.)

Station	ELTG (°F/in)	WAT (°F)	k (psi/in)	E (psi)
0	-1.2	60	682	6.1e+06
60	-1.2	60	756	5.7e+06
121	-1.2	60	735	7.3e+06
181	-1.2	60	559	7.0e+06
241	-1.2	60	611	7.2e+06
302	-1.1	60	568	4.9e+06
360	-1.1	60	615	6.4e+06

*Backcalculation is only performed at midslab tests where $ELTG < 0.5$ °F/in. See the User's Guide and Theory Manual for more Information.

*This section contains the backcalculated **dynamic** k-value at each station where valid midslab or wheelpath tests were performed. It also contains the backcalculated **dynamic** elastic modulus of the slab when valid midslab tests were performed. Tests at midslab are considered valid if the ELTG at the time of testing is less than 0.5 °F/in. Information on the ELTG restrictions for testing at midslab is available in the theory manual.*

Joint Performance Results



*LTE is corrected for ELTG and bending, DD is corrected for ELTG.

This section provides plots of the LTE and DD measurements at all the joints which are tested. FHWA guidelines suggest load transfer restoration be performed if bending corrected LTE is less than 60% or DD is greater than 10 mils.

If the pavement is doweled, corrections to LTE are for bending of the slab, and the ELTG at the time of testing. Corrections to DD are for the ELTG at the time of testing. Tests which are

performed with a WAT greater than 75 °F are not plotted. The corrections for ELTG at the time of testing are based on log-normal distributions in the LTPP database. See the theory manual for more information.

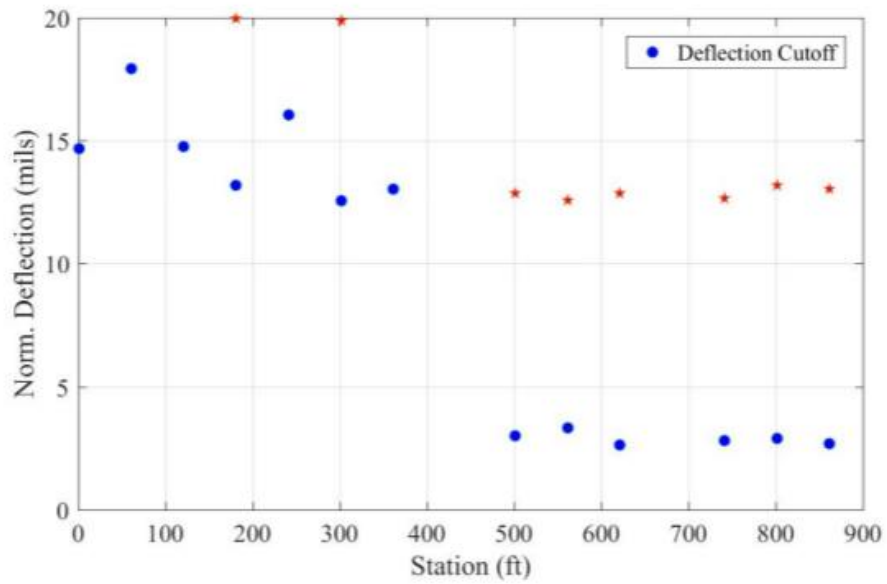
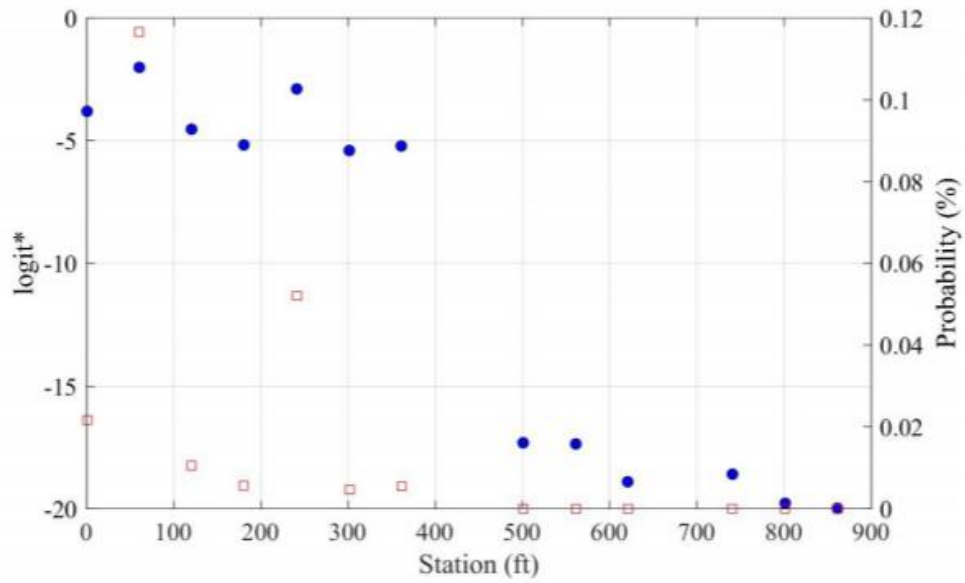
If the pavement is undoweled, the LTE is adjusted for bending only, and the DD is not adjusted.

Joint Performance Results (cont.)

Station	ELTG (°F/in)	WAT (°F)	N. Load (kips)	Raw LTE (%)	Raw DD (mils)	Adj. LTE (%)	Adj. DD (mils)
1	-1.3	60	16	85	2.8	96	1.7
61	-1.3	60	16	80	3.9	92	2.4
121	-1.2	60	16	98	0.5	113	0.3
181	-1.2	60	16	94	0.9	107	0.6
241	-1.2	60	16	89	2.1	101	1.3
302	-1.2	60	16	95	0.8	109	0.5
361	-1.2	60	16	98	0.3	112	0.2
501	2.2	74	16	83	0.8	93	0.9
562	2.2	74	16	87	0.7	97	0.8
621	2.2	74	16	90	0.5	101	0.5
681	2.3	74	16	89	0.6	101	0.6
741	2.3	74	16	86	0.6	97	0.6
801	2.3	74	16	92	0.4	104	0.4
861	2.3	74	16	91	0.4	103	0.4
1	-1.3	60	9	87	1.6	98	1.0
61	-1.3	60	9	84	2.2	97	1.4
121	-1.2	60	9	98	0.2	113	0.2
181	-1.2	60	9	96	0.4	108	0.3
241	-1.2	60	9	91	1.1	103	0.7
302	-1.2	60	9	96	0.4	110	0.3
361	-1.2	60	9	99	0.1	112	0.1
501	2.2	74	9	83	0.5	92	0.5
562	2.2	74	9	88	0.4	99	0.4
621	2.2	74	9	92	0.2	104	0.2
681	2.3	74	9	92	0.2	104	0.3
741	2.3	74	9	88	0.3	100	0.3
801	2.3	74	9	94	0.2	107	0.2
861	2.3	74	9	92	0.2	105	0.2

This section contains the measured LTE and DD at each joint. Tests with a WAT > 75°F (which are not plotted) are shown in this table in red and marked with an asterisk.

Void Detection Results



Void Detection Results (cont.)

Station	ELTG (°F/in)	WAT (°F)	VP (mils)	Normalized Defl (mils)	Prob. (%)	Cutoff (mils)*
1.2	-1.1	63	6.1	14.7	2	20.2
61.09	-1.1	63	9.8	17.9	12	21.3
121	-1.1	63	3.9	14.8	1	20.9
180.89	-1.0	63	3.5	13.2	1	20.0
241.6	-1.0	63	6.6	16.1	5	20.3
301.89	-1.0	63	4.1	12.6	0	19.9
361.39	-1.0	63	3.3	13.0	1	20.2
501.2	2.2	77	0.3	3.0	0	12.9
561.5	2.2	77	0.2	3.3	0	12.6
621	2.2	77	0.2	2.6	0	12.9
741.2	2.2	77	0.2	2.8	0	12.7
801.5	2.2	77	0.1	2.9	0	13.2
861.4	2.2	77	0.1	2.7	0	13.0

*The void detection model is based on logistic regression model. This model estimates the logit, the natural log of the odds ratio, as a linear regression. The odds ratio is defined as the $\text{Pr}(\text{void})/(1-\text{Pr}(\text{void}))$. A 50% probability of a void would have an odds ratio of 1, and a logit of 0. The logit is plotted along with probability to show changes in the prediction model in the linear form before transformation. A logit value greater than 0 indicates that the probability of a void is greater than 50%. Engineering judgement should also be used. If one or more joints have a higher logit than the others they may indicate a void even if the logit is not greater than 0. See the User's Guide and Theory Manual for more information

**The void detection analysis considers several factors. Some tests which have a small void parameter and high LTE will not detect a void at any deflection level.

This section provides information about the void detection algorithm. The probability of a void is calculated as:

$$\ln\left(\frac{\text{Pr}(\text{Void})}{\text{Pr}(\text{No Void})}\right) = \beta_0 + \beta X$$

Where β_0 and β are a scalar and vector of regression coefficients respectively and X is the vector of inputs, which includes pavement information and FWD testing information. The term $\ln\left(\frac{\text{Pr}(\text{Void})}{\text{Pr}(\text{No Void})}\right)$ is considered the natural log of the odds, or logit, and is plotted on the left y axis of the first plot. A logit equal to zero corresponds to a 50% probability of a void. This algorithm shows better accuracy than using normalized deflection, or the void parameter alone for detecting

voids. However, engineering judgement should still be used in detecting voids. For example, if the tool predicts that the deflection at one or more joints is near the deflection cutoff, while a vast majority of the joints are not near the cutoff, this may indicate a void is present at these locations.

ABBREVIATIONS

ASOS-Automated Surface Observation System

DMI-Distance Measuring Instrument

ELTG-Equivalent Linear Temperature Gradient

FRP-Fiber Reinforced Plastic

FWD-Falling Weight Deflectometer

LTE-Load Transfer Efficiency

MERRA2-Modern Era Retrospective Analysis for Research and Applications Version 2

NASA-National Aeronautics and Space Administration

NOAA-National Oceanic and Atmospheric Administration

Pitt-FACS-University of Pittsburgh Falling Weight Deflectometer Analysis of Concrete
Slabs

VP-Void Parameter (the deflection intercept of the load vs. deflection plot for corner FWD
testing)

WAT-Weighted Average Temperature

BIBLIOGRAPHY

- AASHTO (1993). AASHTO Guide for Design of Pavement Structures, 1993. AASHTO Guide for Design of Pavement Structures, AASHTO, Washington, DC. (Chapter III-3)
- Alduchov, O. A., and Eskridge, R. E. (1996). "Improved Magnus Form Approximation of Saturation Vapor Pressure." *Journal of Applied Meteorology*, American Meteorological Society, 35(4), 601–609.
- Alland, K. and Vandenbossche, J.M. (2017). "Daily Cycles of Temperature-Independent Curvature in Jointed Plain Concrete Pavements" *Journal of Transportation Engineering, Part A: Systems*, American Society of Civil Engineers, 143(8) DOI: 04017034.
- Allen, R. G., Walter, I. A., Elliott, R., Howell, T., Itenfisu, D., and Jensen, M. (2005). *The ASCE Standardized Reference Evapotranspiration Equation*. American Society of Civil Engineers, Reston, VA.
<https://www.kimberly.uidaho.edu/water/asceewri/ASCE_Standardized_Ref_ET_Eqn_Phoenix2000.pdf>
- Applied Pavement Technology (2001). PCC Pavement Evaluation and Rehabilitation Reference Manual. Federal Highway Administration, McLean, VA. (Module 2-3) 2-3.1-2-3.30.
- ARA Inc. (2004). *Guide for Mechanistic-Empirical Design of New and Rehabilitated Pavement Structures*. NCHRP 1-37A. National Cooperative Highway Research Program, Washington, DC. (Part 3) 3.4.37.
- Asbahan, R, and Vandenbossche, J.M. (2011). "Effects of Temperature and Moisture Gradients on Slab Deformation for Jointed Plain Concrete Pavements." *Journal of Transportation Engineering*, American Society of Civil Engineers, 163(8), 563-570.
- Bayrak, M. B., and Ceylan, H. (2007). "Effect of slab curling and warping on pavement layer backcalculation." (Presentation) *Falling Weight Deflectometer (FWD) User's Group Conference*. Ames, IA.
<[https://docs.google.com/file/d/0BwRtUOIxzIF4\\$FU3UFdQR29hV2M/edit](https://docs.google.com/file/d/0BwRtUOIxzIF4$FU3UFdQR29hV2M/edit)>
- Bayrak, M. B., and Ceylan, H. (2009). "Neural Network-Based Approach for Analysis of Rigid Pavement Systems Using Deflection Data." *Transportation Research Record*, Transportation Research Board, 2068(1), 61-70.

- Bentz, D. P. (2000). *A Computer Model to Predict The Surface Temperature and Time-of Wetness of Concrete Pavements and Bridge Decks*. National Institute of Standards and Technology, Gaithersburg, MD. 1-19. <<https://www.nist.gov/publications/computer-model-predict-surface-temperature-and-time-wetness-concrete-pavements-and>>
- Bhattacharya, B. B., Raghunathan, D., Selezneva, O., Wilke, P., Darter, M. I., and Von Quintus, H. L. (2017). *PennDOT Pavement ME Design Preliminary User Input Guide (Draft Report)*. Pennsylvania Department of Transportation, Harrisburg, PA. 1-136.
- Brill, D., Flynn, R., and Pecht, F. (2007). *FAA Rigid Pavement Instrumentation at Atlanta Hartsfield-Jackson International Airport*. FAA Airport Technology R&D Branch, Atlantic City, New Jersey. <<http://www.airporttech.tc.faa.gov/Airport-R-D/Conference-and-Workshop/Airport-RD-Conference-Detail/dt/Detail/ItemID/396/FAA-Rigid-Pavement-Instrumentation-at-Atlanta-Hartsfield-Jackson-International-Airport>>
- Buch, N., and Zollinger, D. G. (1996). “Development of Dowel Looseness Prediction Model for Jointed Concrete Pavements.” *Transportation Research Record*, Transportation Research Board, 1525 (1), 21–27.
- Burnham, T. R. (2001). *Construction Report for Mn/ROAD PCC Test Cells 32, 52 and 53*. Minnesota Department of Transportation, Office of Research Services, St. Paul, MN. 1-121<<https://www.lrrb.org/pdf/200204.pdf>>
- Byrum, C., Kohn, S., Gemayel, C., Tayabji, S., Barton, P., Ye, D., Rollings, R., Ioannides, A., and Perera, R. (2011). *Joint Load Transfer in Concrete Airfield Pavements: Final Report*. Federal Aviation Administration, Innovative Pavement Research Foundation, Rosemont, IL. (Chapter 5) 131-164.
- Chapin, L. T., and White, T. D. (1993). “Validating Loss of Support for Concrete Pavements.” *Fifth International Conference on Concrete Pavement Design and Rehabilitation [Proceedings]*, West Lafayette, IN. 163-193.
- Crovetti, J. A. (1994). *Design and Evaluation of Jointed Concrete Pavement Systems Incorporating Open-Graded Permeable Bases* (Doctoral Dissertation). University of Illinois. Urbana-Champaign, IL. (Chapter 6) 127-177
- Crovetti, J. A., and Darter, M. I. (1985). “Void Detection for Jointed Concrete Pavements.” *Transportation Research Record*, Transportation Research Board, 1041(1), 59-68.
- Darter, M. I., Barenberg, E. J., and Yrjanson, W. A. (1985). *NCHRP Report 281: Joint Repair Methods for Portland Cement Concrete Pavements*. National Cooperative Highway Research Program. Washington, DC. (Chapter 4-3) 39-47.
- Darter, M. I., Becker, J. M., and Snyder, M. B. (1984). *Concrete Pavement Evaluation System (COPES)*. University of Illinois, Urbana-Champaign, IL. (Chapter 3) 12-24.

- Davids, W. G. (1998). *Modeling of Rigid Pavements: Joint Shear Transfer Mechanisms and Finite Element Solution Strategies* (Doctoral Dissertation). University of Washington, Seattle, WA. (Chapters 3-8) 27-180.
- Davids, W. G. (2000). "Effect of Dowel Looseness on Response of Jointed Concrete Pavements." *Journal of Transportation Engineering*, American Society of Civil Engineers, 126(1), 50–57.
- Davids, W. G. (2003). "EverFE Theory Manual, Version 2. 24." Computer Software. <<https://civil.umaine.edu/everfe-2/>>
- DeSantis, J., Sachs, S., Vandenbossche J. (*In Print*). "Faulting Mechanisms in Concrete Pavements and Overlays. *International Journal of Pavement Engineering*. Chinese Society of Civil Engineers.
- Dempsey, B. J., Hierlache, W. A., and Patel, A. J. (1986). "Climatic-Materials-Structural Pavement Analysis Program." *Transportation Research Record*, Transportation Research Board, (1095), 111–123.
- Diamond, H. J., Karl, T. R., Palecki, M. A., Baker, C. B., Bell, J. E., Leeper, R. D., Easterling, D. R., Lawrimore, J. H., Meyers, T. P., and Helfert, M. R. (2013). "US Climate Reference Network After One Decade of Operations: Status and Assessment." *Bulletin of the American Meteorological Society*, American Meteorological Society, 94(4), 485–498.
- Dupont, W. D. (2009). *Statistical Modeling for Biomedical Researchers: A Simple Introduction to the Analysis of Complex Data*. Cambridge University Press. Chapter 11, 248-260.
- Elkins, G., Schmalzer, P., Thompson, T., and Simpson, A. (2003). *FHWA-RD-03-088: Long-Term Pavement Performance Information Management System Pavement Performance Database User Reference Guide*. Federal Highway Administration, McLean, VA. 1-171.
- FHWA. (2017). "Long Term Pavement Performance Database." <<https://infopave.fhwa.dot.gov/>> (Jan. 1, 2017).
- Friberg, B. F. (1940). "Design of Dowels in Transverse Joints of Concrete Pavements." *Transactions, American Society of Civil Engineers*, American Society of Civil Engineers 105(2081), 1076-1095.
- Geiger, R., Aron, R. H., and Todhunter, P. (1950). *The Climate Near the Ground*. Rowman & Littlefield. (Part I) 2-46.
- Gelaro, R., McCarty, W., Suárez, M. J., Todling, R., Molod, A., Takacs, L., Randles, C. A., Darmenov, A., Bosilovich, M. G., Reichle, R., Wargan, K., Coy, L., Cullather, R., Draper, C., Akella, S., Buchard, V., Conaty, A., da Silva, A. M., Gu, W., Kim, G. K., Koster, R., Lucchesi, R., Merkova, D., Nielsen, J. E., Partyka, G., Pawson, S., Putman, W., Rienecker, M., Schubert, S. D., Sienkiewicz, M., and Zhao, B. (2017). "The Modern-Era Retrospective Analysis for Research and Applications, Version 2 (MERRA-2)." *Journal of Climate*, American Meteorological Society, 30(14), 5419–5454.

- Giam, X., and Olden, J. D. (2015). "A New R2-based Metric to Shed Greater Insight on Variable Importance in Artificial Neural Networks." *Ecological Modeling*, Elsevier Inc, 313, 307-313.
- GMAO. (2015). "MERRA-2 tavg1_2d_slv_Nx: 2d,1-Hourly, Time-Averaged, Single Level, Assimilation, Single-Level Diagnostics V5.12.4." Goddard Earth Sciences Data and Information Services Center (GES DISC), Greenbelt, MD.
- Guo, H. (1992). *Mathematical Modeling for Dowel Load Transfer Systems* (Doctoral Dissertation). Michigan State University, East Lansing, MI. (Chapters 4-5) 62-117.
- Guo, H., Sherwood, J. A., and Snyder, M. B. (1995). "Component Dowel-Bar Model for Load Transfer Systems in PCC Pavements." *Journal of Transportation Engineering*, American Society of Civil Engineers 121(3), 289–298.
- Hall, K.T. (1992). *Backcalculation Solutions for Concrete Pavements*. Technical Memo Prepared for SHRP Contract P-020, "Long Term Pavement Performance Analysis." Transportation Research Board, Washington, DC.
- Hastie, T., Tibshirani, R., and Friedman, J. (2009). *The Elements of Statistical Learning*. Springer, New York, NY. (Chapter 11) 389-415.
- Heilman, R. H. (1929). "Surface Heat Transmission." *Transactions of the Society of Mechanical Engineers*, Society of Mechanical Engineers, 51(1), 287–302.
- Horel, J., Splitt, M., Dunn, L., Pechmann, J., White, B., Ciliberti, C., Lazarus, S., Slemmer, J., Zaff, D., and Burks, J. (2002). "Mesowest: Cooperative Mesonets in the Western United States." *Bulletin of the American Meteorological Society*, American Meteorological Society, 83(2), 211–225.
- Ioannides, A., Barenberg, E., and Lary, J. (1989). "Interpretation of Falling Weight Deflectometer Results Using Principles of Dimensional Analysis." *4th International Conference on Concrete Pavement Design and Rehabilitation [Proceedings]*, West Lafayette, IN. 231-247.
- Janssen, D.J. (1987). "Moisture in Portland Cement Concrete." *Transportation Research Record*, Transportation Research Board, 1121(1), 40-44.
- Janssen, D. J., and Snyder, M. B. (2000). "Temperature-Moment Concept for Evaluating Pavement Temperature Data." *Journal of Infrastructure Systems*, American Society of Civil Engineers, 6(2), 81–83.
- Jeong, J., Lee, J., Suh, Y.-C., and Zollinger, D. (2006). "Effect of Slab Curling on Movement and Load Transfer Capacity of Saw-Cut Joints." *Transportation Research Record*, Transportation Research Board, 1947(1), 69-78.

- Johanneck, L., Tompkins, D., and Khazanovich, L. (2010). Design and Construction Guidelines for Thermally Insulated Concrete Pavements: Task 3. Minnesota Department of Transportation, St. Paul, MN. 25-54. <<http://www.dot.state.mn.us/mnroad/projects/Thermally%20Insulated%20Concrete%20Pavements/pdfs/T3%20-%20EICM%20Validation.pdf>>
- Khazanovich, L., and Gotlif, A. (2003). Evaluation of Joint and Crack Load Transfer Final Report. Federal Highway Administration, McLean, VA. 1-110. <<https://www.fhwa.dot.gov/publications/research/infrastructure/pavements/ltpa/reports/02088/02088.pdf>>
- Khazanovich, L., Hoegh, K., and Snyder, M. (2008). NCHRP Report 637: Guidelines for Dowel Alignment in Concrete Pavements. National Cooperative Highway Research Program, Washington, DC. (Appendix D) D2-D47.
- Khazanovich, L., and Roesler, J. (1997). "DIPLOBACK: Neural-Network-Based Backcalculation Program for Composite Pavements." *Transportation Research Record*, Transportation Research Board, 1570(1), 143–150.
- Khazanovich, L., Tayabji, S. D., and Darter, M. I. (2001). *Backcalculation of Layer Parameters for LTPP Test Sections, Volume I: Slab on Elastic Solid and Slab on Dense-Liquid Foundation Analysis of Rigid Pavements*. Federal Highway Administration, McLean, VA. 3-89.
- Korenev, B. G. (1954). "Problems of Analysis of Beams and Plates on Elastic Foundation". *Gosudarstvennoe Izdatel'stvo Literatury po Stroitel'stvu i Arkhitekture*, Moscow, USSR.
- Larralde, J. S. (1984). *Structural Analysis of Rigid Pavement with Pumping* (Doctoral Dissertation). Purdue University, West Lafayette, IN. (Chapter 5) 74-116.
- LeVeque, R. J. (2007). *Finite Difference Methods for Ordinary and Partial Differential Equations*. Society for Industrial and Applied Mathematics, Philadelphia, PA. (Chapter 5) 113-145.
- Lukanen, E. O., Stubstad, R., and Briggs, R. (2000). *Temperature Predictions and Adjustment Factors for Asphalt Pavement*. FHWA-RD-98-085. Federal Highway Administration, Washington, DC. (Chapter 4) 21-27.
- Lytton, R. L., Tsai, F.-L., Lee, S. I., Luo, R., Hu, S., and Zhou, F. (2010). *Models for Predicting Reflection Cracking of Hot-Mix Asphalt Overlays*. NCHRP Report 669. National Cooperative Highway Research Program, Washington, DC. (Chapter 3) 48-56.
- MacKay, D. J. C. (1992). "A Practical Bayesian Framework for Backpropagation Networks." *Neural Computation*, Massachusetts Institute of Technology Press Journals, 4(3), 448–472.
- Mackiewicz, P. (2015). "Finite-Element Analysis of Stress Concentration around Dowel Bars in Jointed Plain Concrete Pavement." *Journal of Transportation Engineering*, American Society of Civil Engineers, 141(1993), 1-8.

- Maitra, S. R., Reddy, K. S., and Ramachandra, L. S. (2009). “Experimental Evaluation of Interface Friction and Study of Influence on Concrete Pavement Response.” *Journal of Transportation Engineering*, American Society of Civil Engineers, 135(8), 563–572.
- Mannarano, D. (1998). *Automated Surface Observing System (ASOS) User’s Guide*. National Oceanic and Atmospheric Administration, Washington, DC. 1-74. <<https://www.weather.gov/media/asos/aum-toc.pdf>>
- McCullough, B. F., and Rasmussen, R. O. (1999). *Fast Track Paving: Concrete Temperature Control and Traffic Opening Criteria for Bonded Concrete Overlays Volume I -Final Report. HIPPERPAV User’s Manual*, Federal Highway Administration, McLean, VA. (Chapter 4) 53-101.
- Meeus, J. H. (1991). *Astronomical Algorithms*. Willmann-Bell, Incorporated, Richmond, VA. (Chapter 15) 101-105.
- Mesinger, F., DiMego, G., Kalnay, E., Mitchell, K., Shafran, P. C., Ebisuzaki, W., Jović, D., Woollen, J., Rogers, E., Berbery, E. H., Ek, M. B., Fan, Y., Grumbine, R., Higgins, W., Li, H., Lin, Y., Manikin, G., Parrish, D., and Shi, W. (2006). “North American Regional Reanalysis.” *Bulletin of the American Meteorological Society*, American Meteorological Society, 87(3), 343–360.
- MoDOT. (2013). “Void Detection and Undersealing Verification Testing of Concrete Pavement with a Falling Weight Deflectometer.” *Missouri Department of Transportation Engineering Policy Guide*, <http://epg.modot.org/index.php?title=106.3.2.64_TM64%2C_Void_Detection_and_Undersealing_Verification_Testing_of_Concrete_Pavement_with_a_Falling_Weight_Deflectometer> (Jan. 7, 2016).
- Nassiri, S. and Vandenbossche, J.M. (2012). “Establishing Built-In Temperature Gradient for Jointed Plain Concrete Pavements in Pennsylvania.” *International Journal of Pavement Research and Technology*, Chinese Society of Pavement Engineering, 5(4), 245-256.
- Nassiri, S. (2011). *Establishing Permanent Curl/Warp Temperature Gradient in Jointed Plain Concrete Pavements* (Doctoral Dissertation). University of Pittsburgh, Pittsburgh, PA. (Chapters 4-5) 174-199.
- Nishizawa, T., Fukuda, T., and Matsuno, S. (1989). “A Refined Model of Doweled Joints for Concrete Pavement Using FEM Analysis.” *International Conference on Concrete Pavement Design and Rehabilitation* [Proceedings], West Lafayette, IN. 735-745.
- “NOAA Solar Calculator.” (n.d.). Earth Science Research Laboratory, <<https://www.esrl.noaa.gov/gmd/grad/solcalc/>> (Jan. 1, 2017).
- Oke, T. R. (2002). *Boundary Layer Climates*. Routledge London, England and New York, NY. (Appendix A.2) 358-364.
- PennDOT. (2011). Publication 408/2011 *Specifications. Pennsylvania Department of Transportation*, Harrisburg, PA. (Section 5:Concrete Pavements)

- Prabhu, M., Varma, A., and Buch, N. (2009). “Analytical Investigation of the Effects of Dowel Misalignment on Concrete Pavement Joint Opening Behavior.” *International Journal of Pavement Engineering*, Elsevier, Inc. 10(1), 49–62.
- Qin, Y., and Hiller, J. E. (2011a). “Modeling Temperature Distribution in Rigid Pavement Slabs: Impact of Air Temperature.” *Construction and Building Materials*, Elsevier Ltd, 25(9), 3753–3761.
- Qin, Y., and Hiller, J. E. (2011b). “Modeling the Temperature and Stress Distributions in Rigid Pavements: Impact of Solar Radiation Absorption and Heat History Development.” *KSCE Journal of Civil Engineering*, Korean Society of Civil Engineers, 15(8), 1361–1371.
- Rao, S., and Roesler, J. R. (2005). “Nondestructive Testing of Concrete Pavements for Characterization of Effective Built-in Curling.” *Journal of Testing and Evaluation*, ASTM International, 33(5), 356–363.
- Rohne, J. (2009). *Sixty-Year Design Concrete Pavement-Performance Model Development: MnROAD Cell 53 Construction Report*. Minnesota Department of Transportation, St. Paul, MN. 1-29.
- Rienecker, M. M., Suarez, M. J., Gelaro, R., Todling, R., Bacmeister, J., Liu, E., Bosilovich, M. G., Schubert, S. D., Takacs, L., Kim, G. K., Bloom, S., Chen, J., Collins, D., Conaty, A., Da Silva, A., Gu, W., Joiner, J., Koster, R. D., Lucchesi, R., Molod, A., Owens, T., Pawson, S., Pegion, P., Redder, C. R., Reichle, R., Robertson, F. R., Ruddick, A. G., Sienkiewicz, M., and Woollen, J. (2011). “MERRA: NASA’s Modern-Era Retrospective Analysis for Research and Applications.” *Journal of Climate*, American Meteorological Society, 24(14), 3624–3648.
- Royston, P. (1992). “Lowess Smoothing.” *Stata Technical Bulletin*, StataCorp LP, 1(3).
- Ruiz, J. M., Kim, P. J., Schindler, A. K., and Rasmussen, R. O. (2001). “Validation of HIPERPAV for Prediction of Early-Age Jointed Concrete Pavement.” *Transportation Research Record*, Transportation Research Board, 1778(1), 17–25.
- Ruiz, J. M., Rasmussen, R. O., Chang, G. K., and Dick, J. C. (2004). *Computer-Based Guidelines for Concrete Pavements Volume III—Technical Appendices*. Federal Highway Administration, McLean, VA. (Appendix E), 299-322.
- Sachs, S. (2016). *Development of a Joint Faulting Model for Unbonded Concrete Overlays of Existing Concrete Pavements Through a Laboratory and Numerical Analysis* (Doctoral Dissertation). University of Pittsburgh, Pittsburgh, PA. (Chapter 5.5) 116-121.
- Sachs, S., Vandenbossche, J.M., and Snyder, M.B. (2015). “Calibration of National Rigid Pavement Performance Models for the Pavement Mechanistic–Empirical Design Guide.” *Transportation Research Record*, Transportation Research Board, 2524(1), 59–67.
- Schindler, A. K. (2004). “Effect of Temperature on Hydration of Cementitious Materials.” *ACI Materials Journal*, American Concrete Institute, 101(1), 72-81.

- Schmalzer, P. N. (2011). *Long-Term Pavement Performance Program Manual for Falling Weight Deflectometer Measurements*. Federal Highway Administration, McLean, VA. 1-79.
- De Schutter, G., and Taerwe, L. (1995). "Specific Heat and Thermal Diffusivity of Hardening Concrete." *Magazine of Concrete Research*, ICE Publishing, 47(172), 203–208.
- Schwartz, C. W., Forman, B. A., and Leininger, C. W. (2015). "Alternative Source of Climate Data for Mechanistic- Empirical Pavement Performance Prediction." *Transportation Research Record*, Transportation Research Board, 2524 (1), 83-91.
- Sengupta, M., Habte, A., Gotseff, P., Weekley, A., Lopez, A., Anderberg, M., Molling, C., and Heidinger, A. (2014). "Physics-Based GOES Product for Use in NREL's National Solar Radiation Database." *European Photovoltaic Solar Energy Conference and Exhibition [Proceedings]*, Amsterdam, The Netherlands. NREL/CP-5D00-62776. <<https://www.nrel.gov/docs/fy14osti/62776.pdf>>
- Snyder, M. B. (1989). *Dowel Load Transfer Systems for Full-Depth Repairs of Jointed Portland Cement Concrete Pavements* (Doctoral Dissertation). University of Illinois, Urbana-Champaign, IL. (Chapter 4) 124-190.
- Teller, L. W., and Cashell, H. D. (1959). "Performance of Doweled Joints Under Repetitive Loading." *Highway Research Board Bulletin*, Highway Research Board, (217), 8-49.
- Titus-Glover, L., Bhattacharya, B. B., Raghunathan, D., Mallela, J., and Lytton, R. L. (2016). "Adaptation of NCHRP Project 1-41 Reflection Cracking Models for Semi-Rigid Pavement Design in AASHTOWare Pavement ME Design." *Transportation Research Record*, Transportation Research Board, 2590(1), 122-131.
- Titus-Glover, L., Owusu-Antwi, E. B., and Darter, M. I. (1999). *Design and Construction of PCC Pavements, Volume III: Improved PCC Performance Models*. Federal Highway Administration, McLean, VA. (Chapter 4), 15-49.
- Vandenbossche, J.M. (2001). "The Measured Response of Ultra-Thin and Thin Whitetopping to Environmental Loads." *7th International Conference on Concrete Pavements [Proceedings]*, Orlando, FL. 807-823.
- Vandenbossche, J.M. (2007). "Effects of Slab Temperature Profiles on Use of Falling Weight Deflectometer Data to Monitor Joint Performance and Detect Voids." *Transportation Research Record*, Transportation Research Board, 2005(1), 75–85.
- Vandenbossche, J.M. (2017). "Full-scale Testing of the Performance of 1.5 in Dia. Epoxy Coated Dowel Bars in the Accelerated Loading Frame, (Unpublished)" University of Pittsburgh, Pittsburgh, PA.
- Vandenbossche, J.M. (2003). *Interpreting Falling weight Deflectometer Results for Curled and Warped Portland Cement Concrete Pavements* (Doctoral Dissertation). University of Minnesota, Minneapolis, MN. (Chapter 3-5) 55-114.

- Vandenbossche, J.M., and Snyder, M. B. (2004). “Interpreting the Effects of Curled / Warped Pavements on the Analysis of FWD Data.” *The 5th International CROW Workshop on Fundamental Modeling of the Design and Performance of Concrete Pavements* [Proceedings], CROW Technology Center of the Netherlands, Istanbul, Turkey. (CD-ROM)
- Vanwijk, B. A. J., Larralde, J., Lovell, C. W., and Chen, W. F. (1989). “Pumping Prediction Model for Highway Concrete Pavements.” *Journal of Transportation Engineering*, American Society of Civil Engineers, 115(2), 161-175.
- Vehrencamp, J. E. (1953). “Experimental Investigation of Heat Transfer at an Air Earth Interface.” *Eos, Transactions American Geophysical Union*, Wiley Online Library, 34(1), 22–30.
- Walton, G. N. (1983). *Thermal Analysis Research Program Reference Manual*. United States Department of Commerce. (Chapter I) 71-79.
- Wang, D., Roesler, J. R., and Guo, D.-Z. (2009). “Analytical Approach to Predicting Temperature Fields in Multilayered Pavement Systems.” *Journal of Engineering Mechanics*, American Society of Civil Engineers, 135(4), 334–344.
- Wells, S. A., Phillips, B. M., and Vandenbossche, J. M. (2005). *SR-22 Smart Pavement Phase I: Early-Age Material Properties and Pavement Response Characteristics for Jointed Plain Concrete Pavements, Phase I Final Report*. Pennsylvania Department of Transportation and the Federal Highway Administration. Harrisburg, PA. 1-165.
- Wells, S. A., Phillips, B. M., and Vandenbossche, J. M. (2006). “Characterizing Strain Induced by Environmental Loads in Jointed Plain Concrete Pavements Immediately After Paving and Throughout First 10 Months.” *Transportation Research Record*, Transportation Research Board, 1947(1), 36–48.
- Wu, C. L., Mack, J. W., Okamoto, P. A., and Packard, R. G. (1993). “Prediction of Faulting of Joints in Concrete Pavements.” *Fifth International Conference on Concrete Pavement Design and Rehabilitation* [Proceedings]. 53-70.
- Ye, D. (2017). “Comparing Best-Fit Backcalculation Approach Incorporating Curling to Conventional Backcalculation Methods for JPCP Sections of LTPP Seasonal Monitoring Program Study.” *Transportation Research Board Annual Meeting* [Compendium of Papers], Washington, DC. <<http://amonline.trb.org/63532-trb-1.3393340/t025-1.3403719/6311.3404024/17-04489-1.3404034/17-04489-1.3501288?qr=1>>
- Yu, H. T., Smith, K. D., Darter, M. I., Jiang, J., and Khazanovich, L. (1998). *Performance of Concrete Pavements. Volume III: Improving Concrete Pavement Performance*. Federal Highway Administration, McLean, VA. 7-34.
- Zeger, S. L., Liang, K.-Y., and Albert, P. S. (1988). “Models for Longitudinal Data: a Generalized Estimating Equation Approach.” *Biometrics*, JSTOR, 1049–1060.